VENOMS, ANIMAL AND MICROBIAL TOXINS, VOLUME II

EDITED BY: Jean-Marc Sabatier, Herve Kovacic, Delavar Shahbazzadeh, Jing-Lin Wang, Zhijian Cao, Patrick Michael McNutt, Heike Wulff and Yuri N. Utkin

PUBLISHED IN: Frontiers in Pharmacology

frontiers Research Topics

ISSN 1664-8714
ISBN 978-2-83250-114-6
DOI 10.3389/978-2-83250-114-6

About Frontiers

Frontiers is more than just an open-access publisher of scholarly articles: it is a pioneering approach to the world of academia, radically improving the way scholarly research is managed. The grand vision of Frontiers is a world where all people have an equal opportunity to seek, share and generate knowledge. Frontiers provides immediate and permanent online open access to all its publications, but this alone is not enough to realize our grand goals.

Frontiers Journal Series

The Frontiers Journal Series is a multi-tier and interdisciplinary set of open-access, online journals, promising a paradigm shift from the current review, selection and dissemination processes in academic publishing. All Frontiers journals are driven by researchers for researchers; therefore, they constitute a service to the scholarly community. At the same time, the Frontiers Journal Series operates on a revolutionary invention, the tiered publishing system, initially addressing specific communities of scholars, and gradually climbing up to broader public understanding, thus serving the interests of the lay society, too.

Dedication to Quality

Each Frontiers article is a landmark of the highest quality, thanks to genuinely collaborative interactions between authors and review editors, who include some of the world's best academicians. Research must be certified by peers before entering a stream of knowledge that may eventually reach the public - and shape society; therefore, Frontiers only applies the most rigorous and unbiased reviews.
Frontiers revolutionizes research publishing by freely delivering the most outstanding research, evaluated with no bias from both the academic and social point of view. By applying the most advanced information technologies, Frontiers is catapulting scholarly publishing into a new generation.

What are Frontiers Research Topics?

Frontiers Research Topics are very popular trademarks of the Frontiers Journals Series: they are collections of at least ten articles, all centered on a particular subject. With their unique mix of varied contributions from Original Research to Review Articles, Frontiers Research Topics unify the most influential researchers, the latest key findings and historical advances in a hot research area! Find out more on how to host your own Frontiers Research Topic or contribute to one as an author by contacting the Frontiers Editorial Office: frontiersin.org/about/contact

VENOMS, ANIMAL AND MICROBIAL TOXINS, VOLUME II

Topic Editors:
Jean-Marc Sabatier, Aix-Marseille Université, France
Herve Kovacic, Aix Marseille Université, France
Delavar Shahbazzadeh, Pasteur Institute of Iran (PII), Iran
Jing-Lin Wang, Beijing Institute of Microbiology and Epidemiology, China
Zhijian Cao, Wuhan University, China
Patrick Michael McNutt, Wake Forest School of Medicine, United States
Heike Wulff, University of California, Davis, United States
Yuri N. Utkin, Institute of Bioorganic Chemistry (RAS), Russia

Citation: Sabatier, J.-M., Kovacic, H., Shahbazzadeh, D., Wang, J.-L., Cao, Z., McNutt, P. M., Wulff, H., Utkin, Y. N., eds. (2022). Venoms, Animal and Microbial Toxins, Volume II. Lausanne: Frontiers Media SA. doi: 10.3389/978-2-83250-114-6

Table of Contents

frontiers | Frontiers in Pharmacology

TYPE Editorial
PUBLISHED 19 August 2022
DOI 10.3389/fphar.2022.973628

OPEN ACCESS

EDITED AND REVIEWED BY
Diana Conte Camerino,
University of Bari Aldo Moro, Italy

*CORRESPONDENCE
Jean-Marc Sabatier,
sabatier.jm1@libertysurf.fr

SPECIALTY SECTION
This article was submitted to Pharmacology of Ion Channels and Channelopathies, a section of the journal Frontiers in Pharmacology

RECEIVED 20 June 2022
ACCEPTED 06 July 2022
PUBLISHED 19 August 2022

CITATION
Cao Z, Shahbazzadeh D, Kovacic H, McNutt PM, Wang J-L, Wulff H, Utkin Y and Sabatier J-M (2022), Editorial: Venoms, animal and microbial toxins, volume II.
Front. Pharmacol. 13:973628.
doi: 10.3389/fphar.2022.973628

Editorial: Venoms, animal and microbial toxins, volume II

Zhijian Cao[1], Delavar Shahbazzadeh[2], Hervé Kovacic[3], Patrick Michael McNutt[4], Jing-Lin Wang[5], Heike Wulff[6], Yuri Utkin[7] and Jean-Marc Sabatier[3]*

[1]College of Life Sciences, Wuhan University, Wuhan, China, [2]Pasteur Institute of Iran (PII), Tehran, Iran, [3]UMR7051 Institut de NeuroPhysiopathologie, Aix-Marseille Université, Marseille, France, [4]Wake Forest Institute for Regenerative Medicine, Wake Forest School of Medicine, Winston-Salem, NC, United States, [5]Beijing Institute of Microbiology and Epidemiology, Beijing, China, [6]Department of Pharmacology, University of California, Davis, Davis, CA, United States, [7]Laboratory of Molecular Toxinology, Shemyakin-Ovchinnikov Institute of Bioorganic Chemistry RAS, Moscow, Russia

KEYWORDS

venom, animal toxin, plant toxin, bacterial toxin, viral toxin, structure

Editorial on the Research Topic
Venoms, animal and microbial toxins, volume II

Our Research Topic titled *Venoms, animal and microbial toxins, volume II* is centered on the characteristics of animal, plant, microbial toxins, and their molecular/cellular targets. It also addresses whole animal venoms, which contain a complex mixture of diverse toxins. Venomous animals and microbes are the natural sources of many toxins. These toxins vary in size, nature, and mode of action. They mainly act on ion channels, enzymes, receptors, and neurotransmitter release to produce an acute pathophysiological effect. Animal venom and microbial molecules behave as candidate therapeutics or biological weapons because of their unique potencies, rapid mode of action and wide range of bioactivities.

This Research Topic compiles twenty research and review articles to describe venoms and toxins (or derivatives), through an "in-depth" analysis of their structure, pharmacology, synergistic effects, and structure-function relationship.

Several articles are focused on the structural and/or functional characterization of animal and microbial toxins, as well as other animal venom compounds. A first article by Ullah et al. describes the three-dimensional (3-D) structure of the exfoliative toxin D (ETD) from the pathogenic bacterium *Staphylococcus aureus* responsible for skin disorders. The authors predicted the 3-D structure of ETD using optimized molecular modeling techniques, and compared it to those of four other known exfoliative toxins (A, B, C and E). The authors then used the predicted ETD structure for *in silico* docking simulations of natural and synthetic inhibitors, which is important to inform the design of new potent inhibitors to treat staphylococcal scalded skin syndrome. The article by Peng et al. reports on the isolation and characterization of δ-theraphotoxin-Gr4b, a novel toxin (37-residue peptide crosslinked by 3 disulfide bridges) from the venom of the spider *Grammostola*

rosea. Interestingly, this toxin inhibits the fast inactivation of the $Na_v1.9$ channel through a unique mechanism: binding to domains III and IV voltage sensors. Since $Na_v1.9$ plays a key role in pain perception, these finding may inform a therapeutic development of novel analgesics. In another article, Dongol et al. screened venoms from Australian theraphosid spider species against the human pain target $hNa_V1.7$ and isolated Ssp1a, a 33-residue peptide with an "inhibitor cystine knot" motif. Functional characterization of recombinant Ssp1a on neuronal hNav subtypes suggested Ssp1a interacts with the voltage-sensing domain II of $hNa_V1.7$ to trap the channel in a resting state. George et al. investigated the effects of synthetic peptide toxins predicted from Arizona bark scorpion venom on the voltage-gated sodium channel $Na_v1.8$, another channel involved in pain signaling. The authors found the peptide NaTx36 inhibited sodium current recorded from a recombinant grasshopper mouse $Na_V1.8$ channel ($OtNa_V1.8$) via interactions with the domain I voltage sensor and domain II pore module. Ho et al. described the structural and functional properties of an α-conotoxin OmIA isolated from *Conus omaria* venom. OmIA behaves as a potent antagonist of α7 nicotinic acetylcholine receptors (nAChRs). The authors analyzed a co-crystal structure of OmIA with the acetylcholine binding protein of gasteropod *Lymnae stagnalis*, and highlighted key amino acid residues responsible for the high potency of OmIA against these receptors. Huynh et al. characterized α-elapitoxin-Oh3a, a 72-residue post-synaptic neurotoxin derived from venom of the Asian *Ophiophagus hannah* king cobra. This toxin, which causes neuromuscular paralysis, inhibited the contractile responses of tissues to exogenous carbachol and acetylcholine in chick *Biventer cervicis* nerve-muscle samples. King cobra antivenom prevented α-elapitoxin-Oh3a-induced neurotoxicity *in vitro*, suggesting an active role for α-elapitoxin-Oh3a during king cobra intoxication. Yu et al. focused on *Nemopilema nomurai* jellyfish envenomation, a threat to humans in Asian waterways. Metalloproteinases are reportedly the main toxic components of the venom, causing inflammation and damage. The authors isolated and characterized high proteinase activity fractions in tentacle autolysis using complementary purification techniques. Unexpectedly, these fractions did not show any proteinase activity except when mixed together, highlighting some synergistic effects among components of the fractions. Elrayess et al. characterized Smp24 and Smp43, two "novel" cationic antimicrobial peptides (AMPs) from the venom of the scorpion *Scorpio maurus palmatus*. The authors examined peptide-induced cytotoxicity on various cell lines, including leukaemia and non-cancer cells. The peptides were found to alter the viability of all cells tested (although HaCaT human skin keratinocytes were less sensitive). This decreased cell viability was accompanied by a selective up-regulation of the caspase-1 gene (except for HaCaT cells), whereas all tested cells showed an increase in downstream interleukin-1β expression. These data suggested scorpion venom AMPs activate pyroptosis, a highly inflammatory signaling cascade leading to a lytic programmed cell death.

Other articles of the Research Topic are focused on the structural characteristics, mode of action, targets and fields of application of toxins, venom components or whole venoms. For example, Wu et al. characterized FM-CATH, a "novel" cathelicidin from the *Fejervarya multistriata* paddy frog skin. FM-CATH has potent antimicrobial properties against both bacteria and fungi. It binds to lipopolysaccharides and lipoteichoid acid, and induces agglutination of bacteria. It also alters enzymatic activities (plasmin, thrombin, tissue plasminogen activator, β-tryptase) thus inhibiting the coagulation process both *in vitro* and *in vivo*. FM-CATH increased survival of septic mice, suggesting it might be of value in the treatment of sepsis. Wang et al. studied PcActx, a toxic peptide from the zoantharian *Palythoa caribaeorum* with potential inhibitory activity on the transient receptor potential cation channel subfamily V member 1 (TRPV1). TRPV1 conducts Ca^{2+}, is widely expressed in sensory neurons but is also expressed in epileptic brain areas and is thought to be a potential target to prevent epileptic seizures. At non-toxic doses, PcActx peptides (reduced and folded oxidized forms) reversed pentylenetetrazol-induced seizure-related behavior in zebrafish larvae by limiting the production of reactive oxygen species (ROS) and modulating the expression of genes involved in Ca2+ and GABA-glutamate signaling. The authors conclude PcActx is a potential novel treatment for epilepsy. Another study by Wu et al. focused on Cath-MH, an AMP from the skin of the frog *Microhyla heymonsivogt*. The authors investigated the antimicrobial potential of Cath-MH on *Propionibacterium acnes*. Cath-MH had bacteriocidal effects through membrane disruption. *In vivo*, Cat-MH showed agglutination activity, and reduced edema and infiltration of inflammatory cells in an acne mouse model. Cath-MH also suppressed bacterial growth and production of pro-inflammatory cytokines *in vivo*, suggesting it might be useful to manage acne vulgaris and related skin disorders. Gutierres et al. examined the protective effects of the phospholipase A2 inhibitor Varespladib on the deleterious actions of the venom from the southern American bushmaster *Lachesis muta rhombeata* pit viper snake. The enzymatic, coagulant and hemorrhagic activities of venom were studied in the presence of varespladib (with or without addition of a commercial antivenom). Varespladib potently antagonized PLA2 activity preventing venom-induced coagulation, whereas it had little or no effects on esterasic, caseinolytic, and hemorrhagic activities. Eisele et al. studied the binary C2 toxin of the highly pathogenic *Clostridium botulinum* bacteria. The binary C2 toxin consists of two proteins: C2I (enzyme) and C2II (binding/transport) subunits. To exert toxic effects on mammal cells, C2II needs to be proteolytically cleaved to the pore-forming subunit C2IIa. The authors

demonstrate that C2IIa reduces the chemotactic translocation of human neutrophils (polymorphonuclear leukocytes), thus have potential to down-modulate the excessive and deleterious recruitment of neutrophils into organs after trauma. Barros et al. reviews bioactive peptides and alkaloids identified in skin secretions of Urodele amphibians, which include antimicrobials, antioxidants, immune system modulators, vasoactive and coagulation-acting compounds and which could serve as "new" scaffolds for drug design.

Another set of articles of the Research Topic are focused on the potential treatment of envenomation using antibodies or other compounds. Johnston et al. introduced the "Australian Snakebite Project" (ASP-24), and detailed the epidemiology and clinical presentation of Australian sea snake envenoming. The efficacies of antivenoms in preventing myotoxicity and neurotoxicity are presented. The morbidity and mortality related to sea snake envenoming are discussed and it is concluded that early antivenom treatment after host envenomation is a key therapeutic intervention to prevent severe myotoxicity and death. Hmaidi et al. described the molecular basis of the interaction between the cardiotoxic α-neurotoxin AahII (scorpion *Androctonus australis hector*) and the (cardiac) voltage-gated $Na_v1.5$ channel. The authors showed that AahII slows the fast inactivation of $Na_v1.5$ channels expressed in HEK293 cells. A highly neutralizing anti-AahII nanobody (previously produced Nb10) was shown to fully reverse the effects of AahII on the kinetics of channel inactivation. Computer-aided docking experiments suggest that at AahII molecule, Nb10 might bind to the same binding sites as $Na_v1.5$. Sachetto et al. studied the neutralization of toxins in venom from the lethal Brazilian pit viper *Bothrops jararaca*. The bioflavonoids rutin and its water-soluble derivative rutin succinate were used to assess their protective potential against the snake venom in *in vitro* and *in vivo* assays (*in vivo*, mice were injected with venom, or venom preincubated with rutin or rutin succinate). The data indicated that both flavonoids prevent venom-induced lethality through multiple mechanisms (e.g., coagulation, metalloproteinases). Interestingly, rutin, and rutin succinate showed different modes of action on homeostasis, which would deserve a more detailed analysis of the structure-activity relationships. A similar approach was followed by Heber et al. using ambroxol to neutralize exotoxins TcdA and TcdB from the enterobacterium *Clostridioides difficile*. TcdA and TcdB are the main virulence factors produced by the bacterium and the cause of *C. difficile* associated diseases (CDAD). To exert their toxic effects, the two exotoxins are internalized into the cells via receptor-mediated endocytosis. Translocation of exotoxins from endosomal vesicles into the cytosol requires the acidification of endosomes; ambroxol prevents such acidification. The authors therefore examined the potential protective effects of ambroxol on TcdA- and TcdB-induced cytotoxicity. Ambroxol was found to inhibit key (exotoxin-induced) events (i.e., endosome acidification, morphological changes, glucosylation of Rac1), whereas it also unexpectedly decreases the intracellular enzyme activity of exotoxins. Ambroxol thus behaves as a candidate therapeutic against CDAD. Silva et al. discussed translational concerns regarding the use of rodent lethality models to evaluate antivenoms for human envenoming. To illustrate this problem, it was shown that human nicotinic acetylcholine receptors (nAChRs) have an exceptionally low affinity for the short-chain α-neurotoxins compared to long-chain α-neurotoxins, while both types of α-neurotoxins bind to mouse nAChRs with high affinity. The authors pointed out that the effects of purified toxins or animal venoms on natural prey species are likely to be different from the effects on non-prey species, including humans.

A final article by Hirschenberger et al. describes CRISPA, a transient and non-viral technique to deliver Cas9 endonuclease into specific cells. The strategy developed by the authors is based on the translocation machinery of the *Bacillus anthracis* anthrax toxin, PA (protective antigen). The PA transporter, which normally mediates the entry of anthrax lethal factor and edema factor into the cells, might be optimized for a cell-type specific delivery of Cas9. Therefore, CRISPA potentially represents a step forward, in the translation of the CRISP/Cas9 genome editing technology into clinics.

Taken together, Volume II of this Research Topic contributes to a better understanding of venoms, venom compounds and toxins (or derivatives) opening the way to new exciting research and discoveries. We do believe that these articles exploring a particularly complex world, will inspire researchers and clinicians worldwide.

Author contributions

All authors listed have made a substantial, direct, and intellectual contribution to the work and approved it for publication.

Conflict of interest

The authors declare that the research was conducted in the absence of any commercial or financial relationships that could be construed as a potential conflict of interest.

Publisher's note

frontiers in Pharmacology

ORIGINAL RESEARCH
published: 16 August 2021
doi: 10.3389/fphar.2021.731056

FM-CATH, A Novel Cathelicidin From *Fejervarya Multistriata*, Shows Therapeutic Potential for Treatment of CLP-Induced Sepsis

Jiena Wu[1,2†], Haiyun Zhang[1†], Xiaoxin Chen[2], Jinwei Chai[2], Yunrui Hu[2], Weichen Xiong[2], Wancheng Lu[2], Maolin Tian[2], Xin Chen[1] and Xueqing Xu[2*]*

[1]Department of Pulmonary and Critical Care Medicine, Zhujiang Hospital, Southern Medical University, Guangzhou, China, [2]Guangdong Provincial Key Laboratory of New Drug Screening, School of Pharmaceutical Sciences, Southern Medical University, Guangzhou, China

OPEN ACCESS

Edited by:
Zhijian Cao,
Wuhan University, China

Reviewed by:
Wen-Hui Lee,
Kunming Institute of Zoology (CAS), China
Keith Miller,
Sheffield Hallam University, United Kingdom

***Correspondence:**
Xin Chen
chen_xin1020@163.com
Xueqing Xu
xu2003@smu.edu.cn

†These authors have contributed equally to this work and share first authorship

Specialty section:
This article was submitted to Translational Pharmacology, a section of the journal Frontiers in Pharmacology

Received: 26 June 2021
Accepted: 04 August 2021
Published: 16 August 2021

Citation:
Wu J, Zhang H, Chen X, Chai J, Hu Y, Xiong W, Lu W, Tian M, Chen X and Xu X (2021) FM-CATH, A Novel Cathelicidin From Fejervarya Multistriata, Shows Therapeutic Potential for Treatment of CLP-Induced Sepsis. Front. Pharmacol. 12:731056. doi: 10.3389/fphar.2021.731056

Sepsis is an exacerbated inflammatory reaction induced by severe infection. As important defensive molecules in innate immunity, several AMPs are reported to prevent septic shock. In this study, we characterized a novel cathelicidin, FM-CATH, from the frog skin of *F. multistriata*. FM-CATH was found to adopt an amphipathic α-helix structural in membrane-mimetic environments and possess favorable antimicrobial effects against bacteria and fungus. In addition, it triggered the agglutination of bacteria. It could also strongly bind to LPS and LTA. Additionally, FM-CATH affected the enzymatic activities of thrombin, plasmin, β-tryptase, and tPA, leading to coagulation inhibition *in vitro* and *in vivo*. Finally, we observed that FM-CATH improved survival rate and inhibited pathological alteration, bacterial count, serum biochemistry, and pro-inflammatory cytokine expression in the cecal ligation and puncture-induced sepsis mice. Taken together, these findings suggest that FM-CATH might be served as a promising agent for the treatment of sepsis.

Keywords: antimicrobial peptide, cathelicidin, sepsis, lipopolysaccharide and lipoteichoic acid-neutralizing, coagulation, cecal ligation and puncture, *F. multistriata*

INTRODUCTION

Sepsis is a syndrome associated with pathological, physiological, and biochemical abnormalities, which is induced by infection and is a life-threatening condition (Huang et al., 2019). Due to the anti-infection effects, the utility of antibiotic therapy in patients with sepsis is widely accepted (Gonçalves de Sousa et al., 2008). However, many antibiotics can stimulate the release of endotoxin and thus increase the occurrence of symptoms (Uppu et al., 2015). Antimicrobial peptide (AMP) is attracting widespread interest as an alternative to traditional antibiotic by augmenting the host response and inhibiting bacterial virulence (Hancock and Sahl, 2006). Lipoteichoic acid (LTA) and lipopolysaccharide (LPS) are important components of the cell wall of many Gram-positive bacteria and the outer membrane of Gram-negative bacteria, respectively (Erridge et al., 2002; Ray et al., 2013), which constitute important virulence factors in bacterial infection and are able to stimulate innate immune responses (Ginsburg, 2002; Heumann and Roger, 2002). LTA and LPS recognize and bind to specific toll-like receptors (TLRs), causing the production and release of many pro-inflammatory mediators from mammal cells (Guha and Mackman, 2001; Rockel and Hartung, 2012). Concurrently, coagulation activated *via* pattern recognition receptors (PRRs) (Ishii et al., 2008; van der Poll and Opal, 2008; van der Poll and Levi, 2012) may promote the development of

sepsis (Remick, 2007; Kimbrell et al., 2008; van der Poll and Opal, 2008; Castellheim et al., 2009). Molecules with LPS- and/or LTA-neutralizing activities directly bind to the pro-inflammatory membrane constituents and prevent them from binding to the PRRs (Skovbakke and Franzyk, 2017). Due to their important roles in innate host defense, AMPs have recently received increasing attention in sepsis because they can inhibit proinflammatory responses by directly destroying bacteria or neutralizing LPS or LTA (Vaara and Porro, 1996; Park et al., 2000; Giacometti et al., 2002; Heinbockel et al., 2013; Bosso et al., 2017).

Cathelicidins are one of the largest AMP families which commonly contain a N-terminal signal peptide region, a highly conserved cathelin-like domain and a C-terminal mature peptide (Zanetti et al., 2000). In addition to broad spectrum antimicrobial activity against bacteria, fungi, viruses, and parasites, cathelicidin AMPs also possess diverse biological activities including LPS neutralization, antioxidant, direct chemotaxis, and wound healing effects (Wei et al., 2013; Mu et al., 2017; Cao et al., 2018; Wu et al., 2018). There are abundant studies related to neutralization of LPS or LTA-elicited excessive inflammation during bacterial infection. However, peptides with both LPS and LTA neutralizing activity have been sporadically investigated. In the present study, we characterized a novel cathelicidin from the frog skin of *F. multistriata*. FM-CATH exhibits typical α-helical structure in the membrane mimetic environment and possesses favorable antimicrobial activity, bacterial agglutination activity with high stability and low cytotoxicity to normal mammalian cells. Besides, FM-CATH is able to bind both LPS and LTA, affecting its secondary structure and antimicrobial activity. In addition, our results showed that FM-CATH inhibits coagulation *in vitro* and *in vivo* by affecting the activity of serine protease. Moreover, FM-CATH significantly improves the survival rates and inhibits pathological abnormalities and inflammatory cytokine expression of the CLP-induced septic mice.

MATERIALS AND METHODS

Animals and Ethics Statement

All BALB/c mice (six-week-old) were purchased from the Laboratory Animal Center of Southern Medical University and were housed in the SPF facility at Southern Medical University. The animal experiments were carried out in the light of the approval and guidelines of Animal Care and Use Committee of Southern Medical University. All procedures in this study strictly complied with the Animal Welfare Act and principles stated in the Guide for the Care and Use of Laboratory Animals, National Research Council, 1996.

Sample Collection, Molecular Cloning, and cDNA Synthesizing

Both sexes of adult *F. multistriata* (n = 3; weighing about 40 g) with no specific permissions in need for sampling were captured from Guangzhou city, Guangdong Province, China (23.12°N, 113.28°E) and were euthanized by CO_2 before their skins were subsequently sheared and preserved in liquid nitrogen. Total RNA of the *F. multistriata* frog skin was extracted with Trizol (Life Technologies, CA, United States) according to the manufacturer's protocols and prepared as temples for PCR amplifications as previously reported by us (Chai et al., 2021). The sense primer (5′-GGATGAAGGTCTGGCAGTGTGTGC-3′) was used for the 5′ sequence PCR amplifications of cDNA as described in our previous study (Chai et al., 2021). Prediction of physical and chemical parameters of FM-CATH was done by the ExPASy-ProtParam tool (http://web.expasy.org/protparam/).

Peptide Synthesis

The peptide ordered from GL Biochem Ltd. (Shanghai, China) was purified to 95% with an Inertsil ODS-SP (C18) reverse-phase HPLC column (SHIMAZU, osumi, Japan) before being lyophilized and further confirmed by MALDI-TOF Mass Spectrometry.

Circular Dichroism Measurement

Circular dichroism (CD) was conducted to identify the secondary structure and the stability of FM-CATH in solutions using Jasco-810 spectropolarimeter (Jasco, Tokyo, Japan) as described in our previous study (Zeng et al., 2018). For secondary structure investigation, peptide at the final concentration of 50 μM were dissolved in 0, 30, 60, 90, and 120 mM SDS solutions. For stability evaluation, FM-CATH (50 μM) dissolved in 60 mM SDS was incubated in 25, 37, 50, 70, and 90°C or 0, 100, 200, and 400 mM NaCl for 1 h before CD spectra measurement. To characterize the binding of peptide to bacteria polysaccharides, 0.2 mg/ml of LPS (L2880, *Escherichia coli* O55:B5, Sigma-Aldrich, St. Louis, Missouri, MO) and LTA (L2512, Staphylococcus aureus, Sigma-Aldrich, St. Louis, MO) were dissolved in H_2O or 30 mM SDS solution, respectively. FM-CATH was added to the sugar suspension at the final concentration of 50 μM for 1 h at room temperature. Binding of the peptide to LPS and LTA aggregates was studied by monitoring the change in the secondary structure of peptide (Nankar and Pande, 2013). CD data were expressed as the mean residue ellipticity (θ) of three consecutive scans per sample in deg $cm^2 \cdot dmol^{-1}$.

Antimicrobial Assay

The antimicrobial activity of FM-CATH was measured using two-fold dilution method as reported previously by us (Ye et al., 2020). Microorganisms bought from Guangdong Institute of Microbiology were cultured in Muller-Hinton (MH) broth at 37°C to exponential phase and subsequently diluted with fresh MH broth to reach 10^6 CFU/ml of density. An equal volume of microbial inoculums in 96-well plates was incubated with different concentrations of FM-CATH at 37°C for 14 h. The absorbance at 600 nm was measured by a microplate spectrophotometer (Infinite M1000 Pro, Tecan Company, Switzerland) to calculate the minimal inhibitory concentration (MIC) values. To measure the inhibitory effect of LPS and LTA on the antimicrobial activity of FM-CATH, LPS or LTA at final concentration of 0.2 mg/ ml was pre-incubation with FM-CATH for 1 h at room temperature before MIC values were measured. Ampicillin and polymyxin B were used as positive controls.

Stability Analysis

The salt, thermal and serum stabilities of FM-CATH were investigated with antimicrobial assays as described previously by us (Zeng et al., 2018). Briefly, the activities of FM-CATH against *E. coli* ATCC 25922 were measured after peptide incubated with 0, 50, 100, 150, 200, and 400 mM NaCl at room temperature or at 25, 37, 50, 70 and 90°C for 1 h. For serum stability, FM-CATH solubilized in saline was incubated with human serum in a volume ratio of 1:4 for 0–6 h at 37°C before their MICs were determined at 0, 1, 2, 4, and 6 h. All experiments were repeated at least three times.

Bacterial Agglutination Assay

The agglutination assay was performed with *S. aureus* ATCC 25923 and *E. coli* ATCC 25922. Bacteria at exponential phase were harvested, washed twice and diluted to 10^9 CFU/ml of density with fresh MH broth. The microorganisms were treated with BSA in TBS, FM-CATH (25 μM), FM-CATH (25 μM) plus equal volume of 0.2 mg/ ml LPS or 0.2 mg/ ml LTA for 30 min at room temperature. The incubation solution was dropped on a glass slide and dyed with a Gram staining kit (Solarbio Technology Co., Ltd., Beijing), and the result was observed under an oil microscope (Nikon Corporation, Japan).

Cytotoxicity and Hemolytic Assay

The cytotoxicity of FM-CATH on different mammal cells was detected by MTT. Three tumor cell lines (A549, HepG2, and MDA-MB-231) and two normal mammalian cell lines (MH-S and MDCK) were seeded in 96-well plates at a density of 5,000 cells per well. Cells were grown in DMEM or RPMI 1640 medium, or medium containing continuous concentrations of FM-CATH (2.5, 5, 10, 20, 40 μM) at 37°C for 24 h before MTT was added in the dark and the culture was continued for 4 h. The supernatant was removed and DMSO was added before the absorbance at 490 nm was measured. Hemolytic assay was carried out with fresh blood from mouse heart as reported in our previous article with minor modification (Chai et al., 2021). In short, 2% of mouse erythrocyte suspension in TBS solution (v/v) was treated with 2.5, 5, 10, 20, and 40 μM FM-CATH in a 96-V-well plate at room temperature for 2 h. 1% Triton X-100 and PBS were applied as the positive and negative control, respectively. The absorbance of the supernatant at 540 nm was measured with a microplate spectrophotometer. The hemolysis rate was calculated using the following formula: percentage hemolysis = $(OD_{sample}—OD_{PBS})/(OD_{Triton}—OD_{PBS}) \times 100\%$.

Isothermal Titration Calorimetry Assay

ITC assay was carried out to investigate the thermodynamics of interactions between peptides and LPS or LTA using MicroCal PEAQ-ITC (Malvern; United Kingdom). 50 mM of PBS (pH 7.2) was used to prepare stock solutions of peptide, LPS, and LTA. With a constant stirring of 250 rpm/s at 25°C, 1.5 μL aliquots of FM-CATH or polymyxin B at concentration of 1 mM were titrated into the sample cell filled with 280 μL of 50 μM LPS. In LTA binding experiment, 100 μM LTA in the syringe was titrated into 280 μL of 50 μM FM-CATH in the cell with the condition described above. Instrument was operated in high feedback mode. After the heats derived from dilution were subtracted, the equilibrium disassociation constant (K_D) and the enthalpy change (ΔH) were analyzed by fitting to a single-site binding model using the MicroCal Origin software. The Gibb's free energy change (ΔG) and entropy change (ΔS) were obtained from the basic thermodynamic equations, respectively.

Surface Plasmon Resonance Imaging Measurement

PlexArrayTM HT A100 system (Plexera LLC, Bothell, Washington, United States) and bare gold SPRi chip (Nanocapture gold chip, with a gold layer or 47.5 nm thickness) was used to explore the real-time binding reaction of FM-CATH with LPS, LTA, and proteases as described in our previous method (Chai et al., 2021). In detail, FM-CATH (2 mM) and BSA dissolved in PBS were spotted in multiplex onto the gold chip surface and then stored at 4°C for 14 h in a humid box according to the instruction of the manufacturer. The SPRi chip was washed with PBS and blocked with 1 M ethanolamine/H_2O solution (pH 8.5) for 30 min, and then mounted in the instrument. Different concentrations of proteinase factors were flowed over the chip at the speed of 2 μL/ s 0.5% (v/v) H_3PO_4 in H_2O was added to regenerate the chip surface. Data were analyzed with the PLEXEA data analysis module and ORIGINLab software (OriginLab).

Chromogenic Substrate Assay

The chromogenic substrate assay was performed to identify effects of FM-CATH on blood clotting factors. In brief, FM-CATH at final concentrations of 12.5, 25, and 50 μM was mixed with thrombin, plasmin, β-tryptase, tPA for 10 min at room temperature before chromogenic substrates (S2238 for thrombin and β-tryptase; S2302 for plasmin; S2288 for tPA) were added into the mixtures. Substrate hydrolysis at 37°C was measure by reading the absorbance 405 nm at 1-min time intervals with microplate spectrophotometer.

Anticoagulant Assay *in Vitro*

The anticoagulant activity of FM-CATH was examined by the plasma recalcification time (PRT) and activated partial thromboplastin time (APTT) assays of normal human platelet-free plasma. For PRT measurement, 50 μL of the platelet-poor plasma was mixed with 50 μL of FM-CATH in a 96-well microplate and incubated at 37°C for 10 min before addition of 50 μL of 25 mM $CaCl_2$. Absorbance was measured at 405 nm at intervals of 1 min using microplate spectrophotometer. For APTT assay, 90 μL of the platelet-poor plasma was incubated with 10 μL of FM-CATH (final concentration 12.5, 25, and 50 μM) at 37°C for 10 min before 100 μL of pre-warmed APTT assay reagent (Shanghai yuanyeBio-Technology Co., Ltd, China) was added. The 200 μL of mixture was continued to incubate at 37°C for another 5 min before 100 μL of pre-warmed 25 mM $CaCl_2$ was added and the clotting time was recorded.

Bleeding Time Assay

The bleeding time of the transected-tail mice was measured as reported in our previous paper (Ma et al., 2011). Briefly, mice

FIGURE 1 | The nucleotide and the deduced amino acid sequences of FM-CATH. The signal peptide is framed in pink and followed by a cathelin-like domain with RR residues at the end in red bole. The sequence of mature FM-CATH is boxed, and the stop codon is displayed by *.

were injected intravenously *via* the tail vein with saline or FM-CATH dissolved in saline (10 mg/ kg). After 1 h, the distal 2 mm segment of the tail was transected and vertically immersed into saline at 37°C. Bleeding time was calculated from bleeding to termination and the end point was the arrest of bleeding lasting for more than 30 s.

Cecal Ligation and Puncture Sepsis

CLP was carried out as described by us with minor modifications (Chai et al., 2021). In brief, six-week-old BALB/c mice of either gender were randomly grouped to sham, CLP, and FM-CATH-treated groups (n = 6). Each group was weighed and anesthetized with ketamine and xylazine. The cecum was isolated under a sterile environment and ligated at 1.0 cm from its tip before a single puncture was performed in the middle of the ligated cecum with a 20-gauge needle. Subsequently, small amount of feces was extruded and the cecum was returned to the abdomen before the abdomen was sewn up. Sham controls underwent the same surgical procedure but CLP was not performed. Immediately after surgery, percutaneous injection of 1 ml of pre-warmed saline was done into the recovering mice. 2 h after the sham or CLP procedure, mice were intraperitoneally administrated with FM-CATH (10 mg/ kg) or saline, and then the survival rate was recorded every 12 h for up to 3 days. Another set of mice were prepared as described above and the serum, bronchoalveolar lavage fluid (BALF), peritoneal lavage fluid and lung tissues were collected 24 h after the CLP operation for histopathological analysis, pathological scoring, wet/dry weight ratio, bacterial colony forming unit (CFU) counts, cytokine and signaling pathway assays.

Statistical Analyses

All data were presented as mean ± SEM. Data were analyzed using one-way ANOVA. $^{*}p < 0.05$, $^{**}p < 0.01$, and $^{***}p < 0.001$ were considered statistically significant as compared to control.

RESULTS

Identification of FM-CATH

The cDNA encoding one novel antimicrobial peptide named FM-CATH was obtained by PCR-based cDNA cloning method from the cDNA library of *F. multistriata*. The complete nucleotide sequence and translated amino acid sequence of FM-CATH precursor were shown in **Figure 1**. The cDNA sequence encoding FM-CATH was composed of 557 bp and the deduced amino acid precursor contained 148 amino acids. The sequence of mature FM-CATH was LKTKALNKLKQKLQAVGNLIGSVIKG which displayed high sequence similarities with other representative cathelicidins. FM-CATH had a theoretical PI of 10.70 with + 6 net charge and GRAVY index was -0.004. Its relative mass was measured to 2762.37.

CD Determination

The secondary structure of FM-CATH as well as its stability in different solution environments were investigated through CD. As presented in **Figure 2A**, a small negative peak at 198 nm was observed in the CD spectra of H_2O-dissolved peptide, suggesting that FM-CATH might contain random coil construction. Meanwhile, while dissolved in membrane-like SDS solution, the CD spectra presented a big positive peak at 192 nm and two small negative peaks at 208 and 222 nm, suggesting the presence of α-helix in the secondary structure of FM-CATH. In addition, some slight changes in the secondary structure components of FM-CATH were also observed in different

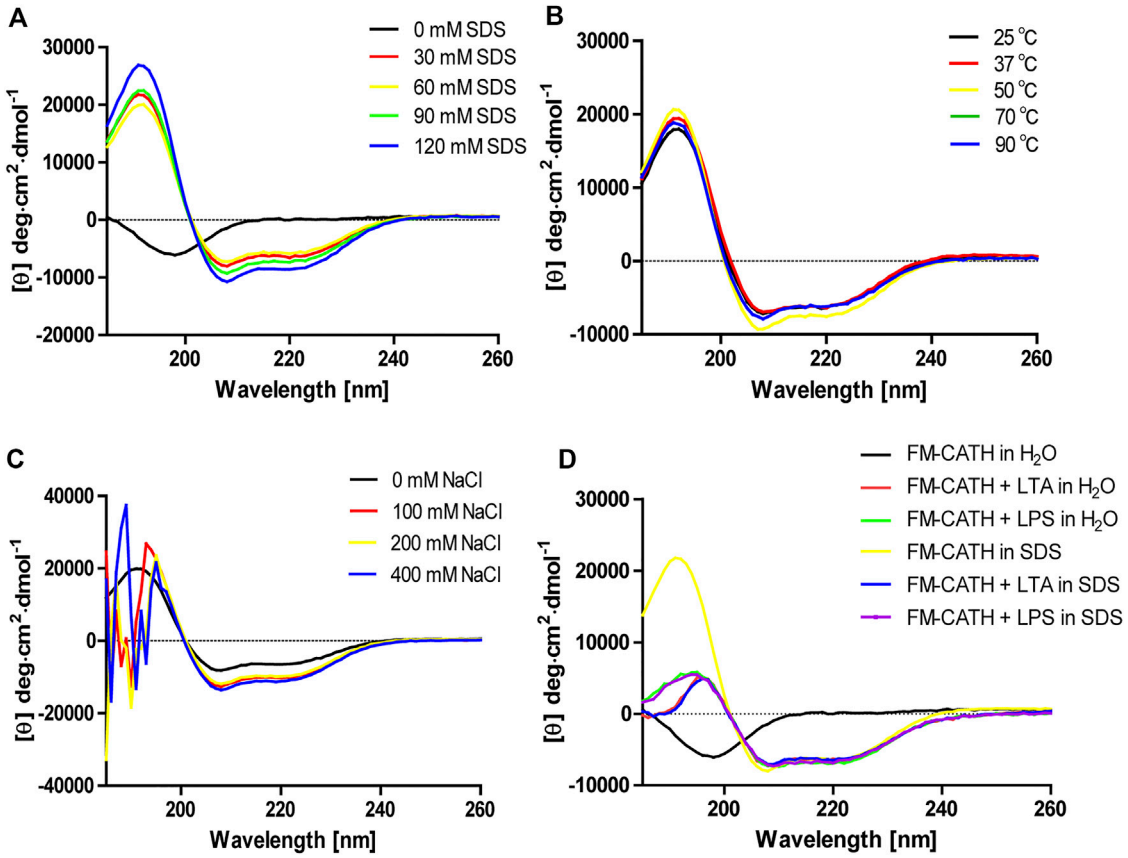

FIGURE 2 | CD analysis of FM-CATH in **(A)** membrane-like SDS solutions, **(B)** 60 mM SDS solution under different temperatures, **(C)** various NaCl concentrations or **(D)** the aqueous solution or 30 mM SDS solution containing LPS or LTA for 1 h before CD spectra measurement.

TABLE 1 | The secondary structure components of FM-CATH in different solution.

Solution	Helix (%)	Parallel (%)	Beta-turn (%)	Random-coil (%)
H_2O	2.30	42.30	26.00	30.90
SDS (mM)				
30	98.60	1.30	5.10	0.20
60	98.40	1.30	5.50	0.20
90	98.80	1.30	5.20	0.20
120	99.70	0.00	3.80	0.00
NaCl (mM)				
100	92.50	0.70	10.40	0.70
200	99.10	0.10	5.00	0.20
400	99.00	0.20	5.10	0.20
Temperature (°C)				
25	99.20	0.20	3.90	0.30
37	99.30	0.10	3.80	0.20
50	99.40	0.10	3.60	0.20
70	99.30	0.10	3.90	0.20
90	99.50	0.10	3.60	0.20
Bacterial polysaccharides				
FM-CATH + LPS in H_2O	96.60	0.50	6.70	0.80
FM-CATH + LTA in H_2O	96.00	0.50	7.70	0.80
FM-CATH + LPS in 30 mM SDS	96.80	0.40	6.90	0.70
FM-CATH + LTA in 30 mM SDS	94.90	0.60	8.30	0.90

TABLE 2 | Antimicrobial activity of FM-CATH.

Microorganisms	MIC (μM)		
	FM-CATH	Ampicillin	Polymyxin B
Pseudomonas aeruginosa ATCC 27853	50	>100	50
Staphylococcus aureus ATCC 25923	>100	25	>100
Propionibacterium acnes ATCC 6919	6.25	>100	6.25
Bacillus subtilis CMCC 63501	12.5	>100	25
Candida albicans ATCC 10231	6.25	>100	25
Escherichia coli ATCC 25922	6.25	12.5	12.5
Escherichia coli ATCC 25922[a]	>100	12.5	12.5
Escherichia coli ATCC 25922[b]	>100	12.5	12.5

[a]*Samples were pre-incubated with LPS (0.2 mg/ ml).*
[b]*Samples were pre-incubated with LTA (0.2 mg/ ml).*

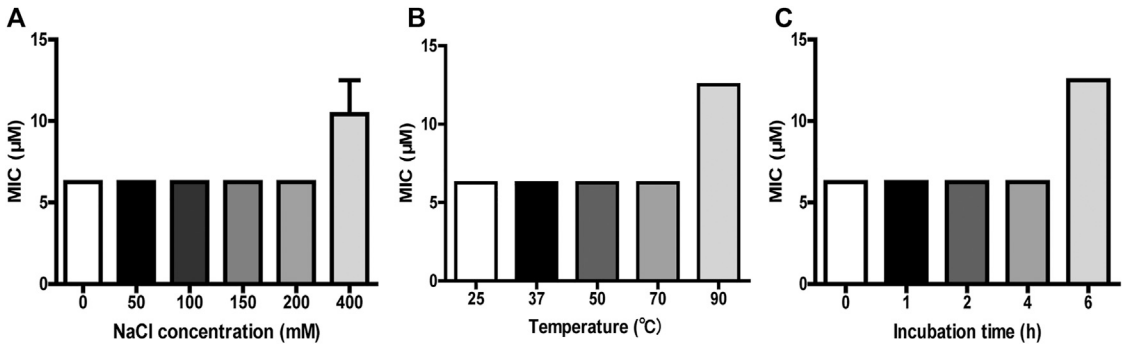

FIGURE 3 | Stability detection of FM-CATH. FM-CATH was incubated **(A)** with different concentrations of NaCl solution at room temperature for 1 h, **(B)** at the indicated temperatures for 1 h, or **(C)** with human serum [1:4 (v/v)] at 37°C for the indicated duration before its MICs against *E. coli* ATCC 25922 were determined. Data are expressed as mean ± SEM (n = 3).

concentration of SDS solution (**Table 1**). Furthermore, the CD spectra of FM-CATH treated with different temperatures also displayed highly identical peaks (**Figure 2B**). However, though it showed some changes in various NaCl concentrations (100, 200 and 400 mM), the α-helix structure of FM-CATH was preserved (**Figure 2C**). Peptides binding to LPS/LTA are known to adopt significant α-helical structures (Nankar and Pande, 2013). To determinate the LPS- and LTA-binding ability of FM-CATH, peptide was individually incubated with the LPS or LTA dissolved in H_2O or 30 mM SDS solution before the CD spectra were determined, respectively. As presented in **Figure 2D**, in the presence of LPS or LTA, FM-CATH showed obviously different CD spectra which are features of α-helical structure including two negative bands at 222 and 208 nm and a positive band at 192 nm, suggesting FM-CATH binds to LPS and LTA.

Antimicrobial Activity of FM-CATH

The MICs of FM-CATH against Gram-positive bacteria, Gram-negative bacteria and fungi were presented in **Table 2**. Under our condition, FM-CATH could suppress the growth of *E. coli* ATCC 25922, *P. acnes* ATCC 6919, *B. subtilis* CMCC 63501, *C. albicans* ATCC 10231, and *P. aeruginosa* ATCC 27853 within a range of 6.25–50 μM, which were more potent or equal to those of polymyxin B. However, its antimicrobial activity against *S. aureus* ATCC 25923 was more than 100 μM. Moreover, the antimicrobial activity of FM-CATH against *E. coli* ATCC 25922 was abrogated after its incubation with LPS and LTA. However, our result showed that the antibacterial activity of polymyxin B at 100 μM was not inhibited in the presence of LPS (0.2 mg/ ml), which is line with the report by Krishnakumari et al. (Krishnakumari et al., 2020).

Stability of FM-CATH

The antimicrobial ability of many AMPs is usually affected by temperature condition, salt concentration, and serum components like proteases (Travis et al., 2000). To further confirm the results from CD experiment, the antimicrobial activity of FM-CATH under different NaCl concentrations and temperature conditions was investigated. As shown in **Figure 3**, FM-CATH maintained the antibacterial activity against *E. coli* ATCC 25922 at the tested temperatures, NaCl solutions and serum. Although the antibacterial activity decreased after incubation with 400 mM NaCl, solubilization in saline at 90°C for 1 h or human serum (1:4 (v/v)) at 37°C for 6 h, FM-CATH still possessed antibacterial activity. The results indicated that FM-CATH has good stability.

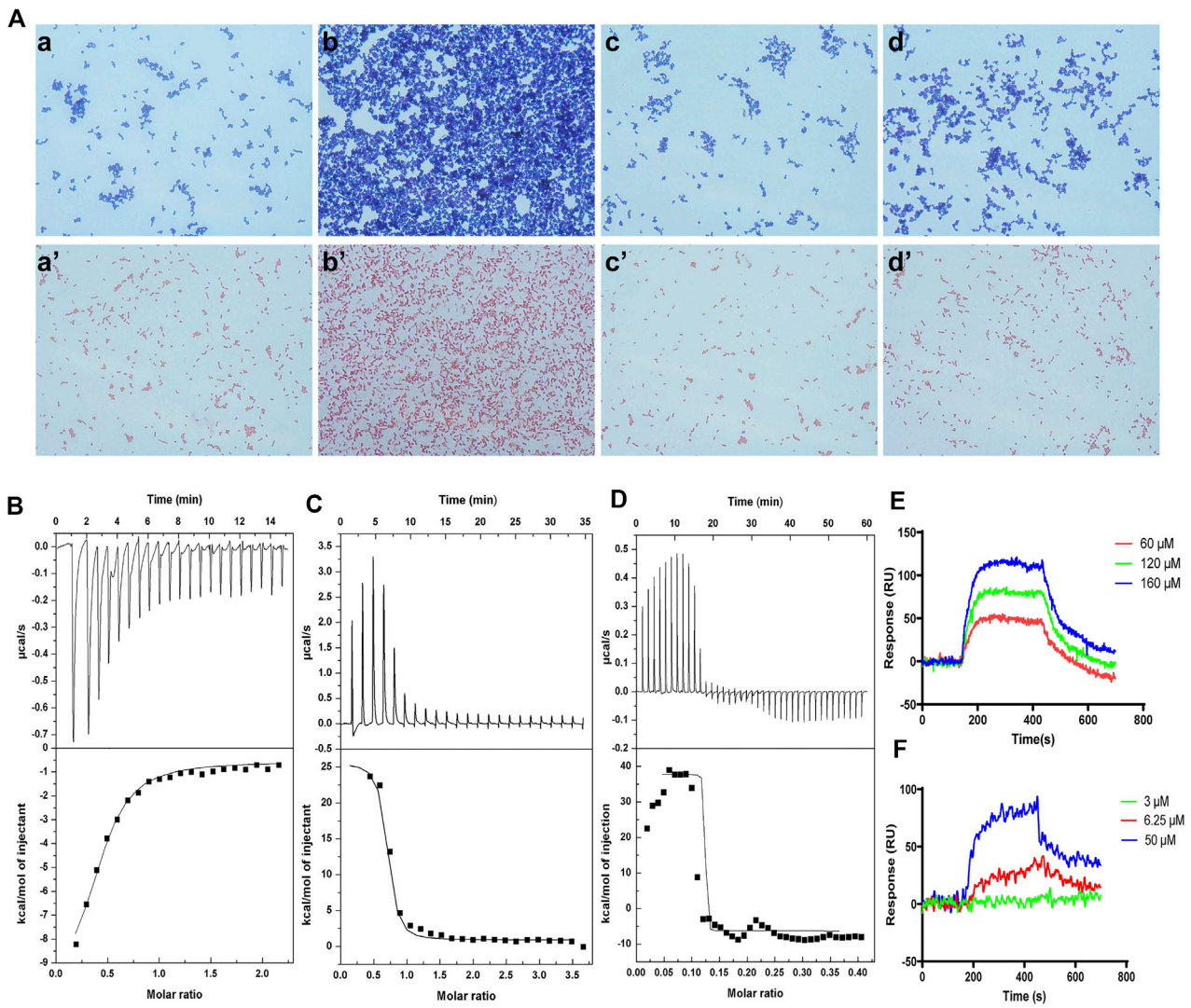

FIGURE 4 | Binding reactions of FM-CATH with LPS and LTA **(A)** Bacterial agglutination of *S. aureus* ATCC 25923 (the upper row) and *E. coli* ATCC 25922 (the lower row), respectively. Bacteria treated with BSA in TBS (a, a'), FM-CATH (25 μM) (b, b'), FM-CATH (25 μM) plus equal volume of 0.2 mg/ ml LPS (c, c') and 0.2 mg/ ml LTA (d, d') for 30 min before being stained with Gram staining kit. **(B), (C), (D)** ITC analysis of FM-CATH binding to LPS, polymyxin B binding to LPS, and FM-CATH binding to LTA, respectively. **(E), (F)** SPRi analysis of LPS and LTA binding to FM-CATH immobilized on a gold chip, respectively.

Interaction Between FM-CATH and LPS or LTA

The bacterial agglutination of FM-CATH against *S. aureus* ATCC 25923 and *E. coli* ATCC 25922 was tested. As illustrated in **Figure 4A**, agglutination occurred in the presence of FM-CATH (25 μM) after 30 min of incubation. However, it was totally abolished by LPS and LTA. ITC experiment was next performed to investigate the binding of FM-CATH to LPS and LTA, respectively (**Figures 4B,D**). Binding saturation occurred at 12 min while the molar ration of peptide to LPS reach to 20 while the molar ration of LTA to peptide reach to 2at 40 min, respectively. Furtherly, LPS and LTA bound to FM-CATH with K_D values of about 4.90 μM and 0.714 nM, respectively (**Table 3**). However, as shown in **Figure 4C** and **Table 3**, the K_D value for polymyxin B binding to LPS was about 0.414 μM, indicating that the binding ability of polymyxin B to LPS was stronger than that of FM-CATH to LPS. SPRi is an optical method monitoring and quantifying biomolecular interactions (Homola, 2008). In agreement, there was strong SPRi signal when LPS and LTA were flowed through the gold chip containing FM-CATH and BSA (**Figures 4E,F**). Resonance units increased in a concentration-dependent manner and the K_D values of FM-CATH binding to LPS and LTA were 2.57 μM and 6.21 nM, which was relatively consistent with the ITC results. FM-CATH could thus directly bind to both LPS and LTA.

Cell Toxicity and Hemolytic Activity of FM-CATH

The application of AMPs is usually limited due to their cytotoxicity to erythrocytes and mammalian cells (Gajski

TABLE 3 | Thermodynamic parameters from ITC. The parameters (ΔH, ΔS, ΔG, K_D) are obtained from the ITC experiments for the interaction of FM-CATH with LPS and LTA plus polymyxin B with LPS, respectively.

Thermodynatic parameters	FM-CATH		Polymyxin B
	LPS	LTA	LPS
ΔH (KJ·mol^{-1})	−12.0 ± 0.657	170 ± 5.62	24.7 ± 0.651
TΔS (KJ·mol^{-1})	18.3	222	− 61.2
ΔG (KJ·mol^{-1})	− 30.3	− 52.3	− 36.5
K_D (M)	(4.90 ± 0.495) × 10^{-6}	(7.14 ± 2.27) × 10^{-10}	(0.414 ± 0.08) × 10^{-6}

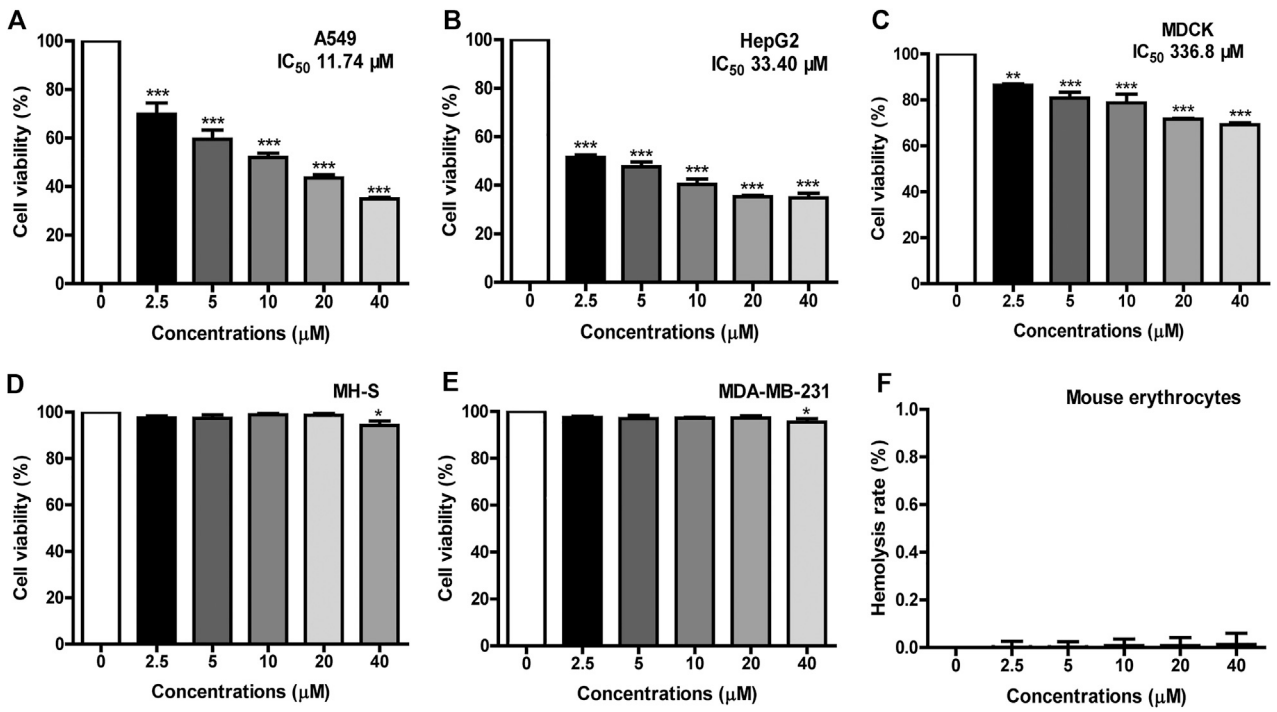

FIGURE 5 | Cytotoxicity and hemolysis of FM-CATH. Cell viability of **(A)** A549, **(B)** HepG2, **(C)** MDCK, **(D)** MH-S, and **(E)** MDA-MB-231 were tested by MTT after incubation with the indicated concentration of FM-CATH for 24 h. The blank medium without any treatment was used as a control. **(F)** Hemolysis rate of mouse erythrocytes with different concentration of FM-CATH. Data are mean ± SEM (n = 3). $^{**}p < 0.01$ and $^{***}p < 0.001$ were thought statistically significant as compared to the corresponding control groups.

et al., 2016). The cytotoxicity of FM-CATH against different cells were measured by MTT. As illustrated in **Figures 5A–E**, FM-CATH concentration-dependently inhibited the proliferation of A549, HepG2 and MDCK cells and the IC_{50} values were 11.74, 33.40 and 336.8 μM, respectively. However, it showed very low cytotoxicity against MH-S and MDA-MB-231. Accordingly, we speculated that FM-CATH exerts strong killing activity against some of cancer cells and a low toxicity to normal mammalian cells *in vitro*. Additionally, the hemolytic activity of FM-CATH was measured using mouse heart blood. The hemolysis rates of mouse heart blood at different concentration of FM-CATH were presented in **Figure 5F** and at the highest concentration, 40 μM, FM-CATH had almost no hemolytic activity.

Effects of FM-CATH on Coagulation

To explore whether FM-CATH affected the activities of proteases, its binding reactions were measured by SPRi. As illustrated in **Figure 6A**, FM-CATH could bind to thrombin, plasmin, β-tryptase, and tPA in a dose-dependent manner but not BSA. In addition, chromogenic substrate assay revealed that FM-CATH increased the activity of tPA while suppressed the one of thrombin, plasmin, β-tryptase (**Figure 6B**). Given that FM-CATH reacted with serine proteases related to the coagulation cascade, the activity of FM-CATH on plasma was further investigated by PRT and APTT measurements. FM-CATH had ability to prolonged PRT and APTT in a dose-dependent manner, suggesting that coagulation could be inhibited by FM-CATH (**Figures 6C,D**). To clarify whether FM-CATH had anticoagulant

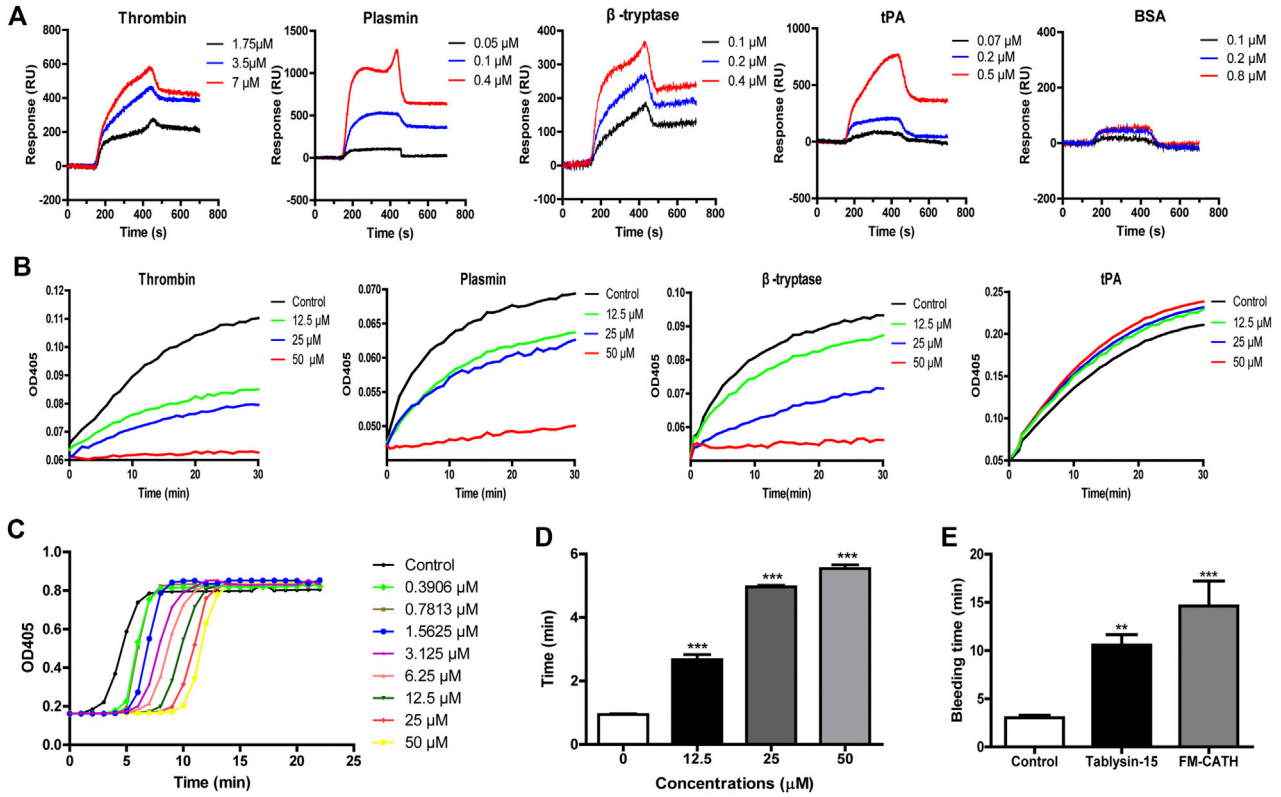

FIGURE 6 | The effects of FM-CATH on coagulation **(A)** SPRi analysis of thrombin, plasmin, β-tryptase, tPA, and BSA binding to FM-CATH immobilized on a gold chip. **(B)** Effects of FM-CATH on chromogenic substrate hydrolysis by serine proteases. The anticoagulation effect of FM-CATH measured by PRT **(C)** and APTT **(D)** assays. **(E)** Effect of FM-CATH on mice tail bleeding time. Data are reported as mean ± SEM (n = 6). $^{**}p < 0.01$ and $^{***}p < 0.001$ was considered statistically significant compared with the control group.

effect *in vivo*, tail bleeding was observed in mice. As shown in **Figure 6E**, the duration of tail bleeding in the saline-treated group was 3.03 ± 0.52 min. However, the tail bleeding time in the group treated by 10 mg/ kg FM-CATH at a dose of was markedly prolonged to 14.29 ± 4.12 min. The positive control, Tablysin-15, which was described in our previous study (Ma et al., 2011), also significantly extended the tail bleeding time to 10.57 ± 2.67 min at a dose of 2.5 mg/ kg.

Effects of FM-CATH on CLP-Induced Septic Mice

To assess the effect of FM-CATH on polymicrobial sepsis, CLP-induced sepsis mice model was established. Interestingly, FM-CATH obviously improved the prognosis of the septic mice. The survival rate at the assay end point had increased to 43% in the group intraperitoneally injected with FM-CATH while 0% in the control CLP group (**Figure 7A**). Histological staining of the lung tissue with hematoxylin and eosin in the CLP group showed a severe organ damage including the increase of alveolar wall thickness and inflammatory cell infiltration accompanied by destruction of the alveolar structures and reductions in the alveolar spaces (**Figure 7B,** panel b). It was found that administration of FM-CATH protected against CLP-induced organ damage in the lung (**Figure 7B,** panel c) and lung damage scores were obviously lower than those in the CLP model group (**Figure 7C**). In line with the above data, the lung wet/dry ratio and BALF total protein level were clearly increased after CLP induction and FM-CATH effectively decreased their levels (**Figures 7D,E**). Furthermore, MPO activity of lung was evidently abated after treatment with FM-CATH (**Figure 7F**). Consistently, the FM-CATH treatment also definitely cut down the contents of the inflammatory cytokines IL-1β, IL-6 and TNF-α in the lung tissue (**Figures 7G–I**) and serum (**Figures 7J–L**). It was also confirmed that the FM-CATH treatment significantly decreased the contents of some blood biochemical factors like aspartate aminotransferase (AST), urea nitrogen (BUN) as well as alanine aminotransferase (ALT) (**Figures 7M–O**). Additionally, the FM-CATH treatment reduced the bacterial colony forming unit (CFU) counts in peritoneal fluid (**Figure 7P**). To further explore the protective mechanism of FM-CATH in CLP-induced sepsis, the expression of MAPK signaling in lung was investigated by western blotting. The activation of ERK, JNK, and p38 were markedly enhanced after CLP administration, which was significantly alleviated by post-treatment with FM-CATH (**Figures 7Q,R**). Altogether,

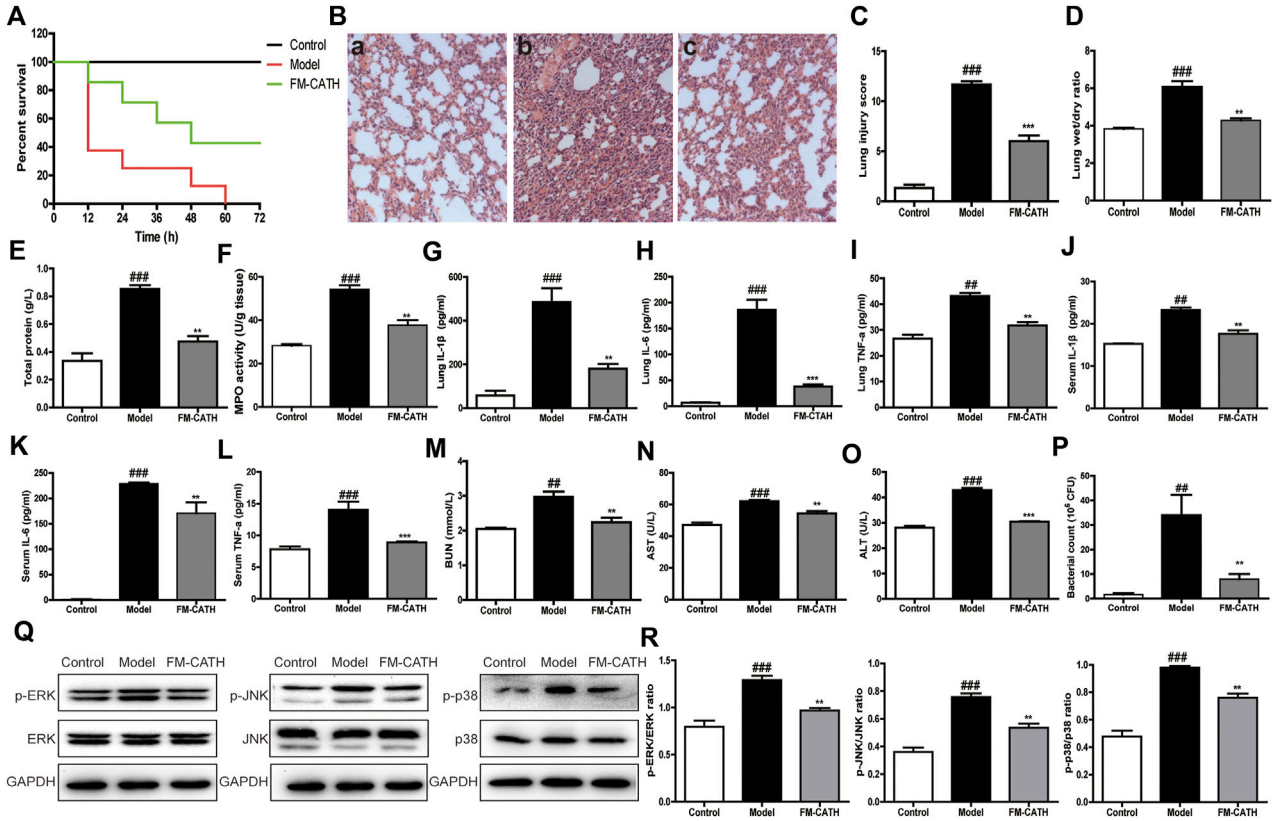

FIGURE 7 | Effects of FM-CATH on CLP-induced mice **(A)** Effects of FM-CATH on the survival rates of CLP-induced mice. **(B)** Representative histological staining images of lung tissues with haematoxylin and eosin. Sham-operated mice were served as negative controls (a), mice were treated with PBS (b), or FM-CATH treatment after CLP induction (c) (magnification × 100) **(C)** Lung injury scores of CLP induction. **(D)** W/D ratio of lung tissues **(E)** The total protein levels of BALF. **(F)** MPO activity of lung **(G–I)** Effects of FM-CATH on pro-inflammatory cytokine expression in lung tissues. **(J–L)** Effects of FM-CATH on pro-inflammatory cytokine expression in serum. **(M–O)** Effects of FM-CATH on BUN, AST, and ALT in serum. **(P)** CFU quantification in the peritoneal lavage fluid **(Q)** Western blotting images of ERK, JNK and p38 expression. **(R)** Ratio of phosphorylated ERK, JNK, and p38 to their total proteins. Data presented are mean ± SEM (n = 5). $^{\#\#}p < 0.01$, and $^{\#\#\#}p < 0.001$ significantly different compared to the control group; $^{**}p < 0.01$, $^{***}p < 0.001$ significantly different compared to the model group.

these data demonstrated that the FM-CATH treatment can significantly increase survival rate, and decrease disease severity in CLP-induced septic mice.

DISCUSSION

Sepsis is an exacerbated inflammatory reaction induced by severe infection. Thus, it may be more beneficial to inhibit the initial signaling pathways in the infection-related host response. Bacterial products including LPS and LTA, recognized by TLR4 and TLR2, are involved in Gram-negative and -positive bacterial infections, respectively (Mukherjee et al., 2016). Recognition and induction of TLR signaling lead to release of cytokines including IL-1β, IL-6, and TNF-α, which are crucial for the anti-infective immune response (Akira et al., 2006). In addition to direct antibacterial action, several AMPs have been modulators of host responses and prevent inflammation and sepsis (Giacometti et al., 2002; Vonk et al., 2008; Lee et al., 2010). In this study, a cathelicidin is identified from the skin of *F. multistriata* and demonstrated to be a promising new candidate therapeutic for sepsis.

AMPs are relatively small size, cationicity, and amphipathicity in membrane mimetic environment which empower them to damage bacterial membranes selectively (Bosso et al., 2017). FM-CATH possesses a net charge of + 6, indicating its potential to interact with negatively charged bacterial membrane components by electrostatic attraction. Furthermore, like most cathelicidins (Ling et al., 2014; Zeng et al., 2018), FM-CATH adopts an amphipathic α-helix structure in membrane-mimetic environments (**Figure 2A**). In agreement, FM-CATH possesses a favorable effect against some of bacteria and fungus (**Table 2**). Additionally, FM-CATH can avoid bacteria moving around and protect the host from pathogenic attack by trapping them together. Though FM-CATH has no exhibit lethal activity against *S. aureus*, its agglutination activity may contribute to prevent the spread of infection (**Figures 4A,B**).

LPS and LTA play important roles in sepsis and septic shock through hyperactivation of the innate immune system and induction of abnormal coagulation by binding TLRs and PRRs

(Guha and Mackman, 2001; Rockel and Hartung, 2012). Our compelling evidences demonstrate that FM-CATH possesses not only direct antibacterial activity, but also direct LPS- and LTA-neutralizing activity (**Figure 4**). Thus, it is rational to speculate that FM-CATH can effectively control sepsis. Consistently, FM-CATH increases the survival rate, reduces serum biochemistry and the degree of lung injury of CLP mice (**Figure 7**). Meanwhile, the ability of peritoneal cavity to clear bacteria is enhanced in septic mice. During sepsis, LPS/LTA can activate the MAPK signaling pathway, and further accelerate the production of proinflammatory cytokines, such as IL-1β, IL-6, and TNF-α, which form the cytokine cascade, and eventually leads to cell apoptosis and multiple organ dysfunction (Zhang et al., 2015; Wang et al., 2020). In agreement, the excessive release of inflammatory factors and activation of ERK, JNK, and p38 are inhibited by treatment with FM-CATH.

Coagulation is triggered once plasma tissue factor is induced to express on the surface of monocytes and endothelial cells stimulated by proinflammatory cytokines or bacterial products (Mackman et al., 2007). Therefore, sepsis is almost invariably associated with coagulation abnormalities (van der Poll and Levi, 2012). Surprisingly, our results show that FM-CATH can affect the activity of thrombin, plasmin, β-tryptase and tPA, inhibit plasma coagulation *in vitro*, and prolong the bleeding time *in vivo* (**Figure 6**). Thrombin is increased during sepsis and plays a role in dysregulated coagulation, and antithrombin is beneficial for patients with severe infection and sepsis in experimental and initial clinical trials (Woodman et al., 2000; Levi and van der Poll, 2017). Furthermore, in sepsis, coagulation abnormalities promote the recruitment of profibrinolytic enzymes including plasmin (Gould et al., 2015). Finally, β-tryptase promotes early pulmonary fibrosis in sepsis-induced lung injury and anti-tryptase treatment with nafamostat mesilate significantly improves the experimental colitis (Isozaki et al., 2006; Villar et al., 2015). Given to the observed anticoagulation effect and protease inhibition/promotion activities of FM-CATH, we cannot exclude that these functions also contributed to its anti-sepsis role *in vivo*.

Alone with the strong and broad-spectrum antibacterial ability, the new AMPs must show low cytotoxicity against human normal cells before their therapeutic use can be considered (Kosikowska and Lesner, 2016). However, as the main target of most AMPs is the cell membrane, part of them also is toxic to host cells, and lead to cytotoxic and haemolytic activity, which are usually major limiting factors for their application (Lee et al., 2014; Kumar et al., 2017). Our results show that FM-CATH exhibits relatively low cytotoxic activities toward the tested normal mammalian cells and low hemolytic activity at the present concentration (**Figure 5**). In addition to cytotoxicity, stability is also a major reason impeding AMPs from becoming therapeutic agents (Zhu et al., 2015; Wang et al., 2018). As shown in **Figure 3**, FM-CATH showed better stability in NaCl solution, serum or at different temperature. These characteristics suggest its promising therapeutic potential as anti-microbial drugs.

In conclusion, a novel cathelicidin, FM-CATH, from the skin of frog *F. multistriata* is identified and characterized at present study. FM-CATH contains single α-helix structure in membrane-mimetic environments and favorable antimicrobial, bacterial agglutination, LPS- and LTA-binding activities. In addition, FM-CATH can affect the activities of thrombin, plasmin, β-tryptase and tPA, inhibit plasma coagulation *in vitro*, and prolong the bleeding time *in vivo*. Moreover, FM-CATH significantly protects mice against CLP-induced sepsis. Thus, FM-CATH has the potential for the treatment of sepsis.

DATA AVAILABILITY STATEMENT

The original contributions presented in the study are included in the article/Supplementary Material, further inquiries can be directed to the corresponding authors.

ETHICS STATEMENT

The studies involving human participants were reviewed and approved by The Ethics Committee of Zhujiang Hospital. The patients/participants provided their written informed consent to participate in this study. The animal study was reviewed and approved by Animal Care and Use Committee of Southern Medical University.

AUTHOR CONTRIBUTIONS

JW, HZ, XC, JC, YH, WX, WL, and MT performed experiments and analyzed data; XX and XC designed experiments, supervised the study, evaluated the data and revised the manuscript for publication. All authors contributed to the manuscript and have given approval to the final version of the manuscript.

FUNDING

This research was funded by the National Natural Science Foundation of China, grant number 31772476, 31861143050, 31911530077, and 82070038.

REFERENCES

Akira, S., Uematsu, S., and Takeuchi, O. (2006). Pathogen Recognition and Innate Immunity. *Cell* 124, 783–801. doi:10.1016/j.cell.2006.02.015

Bosso, A., Pirone, L., Gaglione, R., Pane, K., Del Gatto, A., Zaccaro, L., et al. (2017). A New Cryptic Host Defense Peptide Identified in Human 11-hydroxysteroid Dehydrogenase-1 β-like: from In Silico Identification to Experimental Evidence. *Biochim. Biophys. Acta Gen. Subjects* 1861, 2342–2353. doi:10.1016/j.bbagen.2017.04.009

Cao, X., Wang, Y., Wu, C., Li, X., Fu, Z., Yang, M., et al. (2018). Cathelicidin-OA1, a Novel Antioxidant Peptide Identified from an Amphibian, Accelerates Skin Wound Healing. *Sci. Rep.* 8, 943. doi:10.1038/s41598-018-19486-9

Castellheim, A., Brekke, O.-L., Espevik, T., Harboe, M., and Mollnes, T. E. (2009). Innate Immune Responses to Danger Signals in Systemic Inflammatory Response Syndrome and Sepsis. *Scand. J. Immunol.* 69, 479–491. doi:10.1111/j.1365-3083.2009.02255.x

Chai, J., Chen, X., Ye, T., Zeng, B., Zeng, Q., Wu, J., et al. (2021). Characterization and Functional Analysis of cathelicidin-MH, a Novel Frog-Derived Peptide with Anti-septicemic Properties. *Elife* 10. doi:10.7554/eLife.64411

Erridge, C., Bennett-Guerrero, E., and Poxton, I. R. (2002). Structure and Function of Lipopolysaccharides. *Microbes Infect.* 4, 837–851. doi:10.1016/S1286-4579(02)01604-0

Gajski, G., Domijan, A.-M., Žegura, B., Štern, A., Gerić, M., Novak Jovanović, I., et al. (2016). Melittin Induced Cytogenetic Damage, Oxidative Stress and Changes in Gene Expression in Human Peripheral Blood Lymphocytes. *Toxicon* 110, 56–67. doi:10.1016/j.toxicon.2015.12.005

Giacometti, A., Cirioni, O., Ghiselli, R., Mocchegiani, F., Del Prete, M. S., Viticchi, C., et al. (2002). Potential Therapeutic Role of Cationic Peptides in Three Experimental Models of Septic Shock. *Antimicrob. Agents Chemother.* 46, 2132–2136. doi:10.1128/AAC.46.7.2132-2136.2002

Ginsburg, I. (2002). Role of Lipoteichoic Acid in Infection and Inflammation. *Lancet Infect. Dis.* 2, 171–179. doi:10.1016/S1473-3099(02)00226-8

Gonçalves de Sousa, A., José Fernandes Junior, C., de Paula Dias Santos, G., Regina Laselva, C., Polessi, J., Fernando Lisboa, L., et al. (2008). The impact of each action in the Surviving Sepsis Campaign measures on hospital mortality of patients with severe sepsis/septic shock Impacto de cada ação dos pacotes da Surviving Sepsis Campaign na mortalidade hospitalar de pacientes portadores de sepse. *Einstein* 6, 323–330.

Gould, T. J., Vu, T. T., Stafford, A. R., Dwivedi, D. J., Kim, P. Y., Fox-Robichaud, A. E., et al. (2015). Cell-Free DNA Modulates Clot Structure and Impairs Fibrinolysis in Sepsis. *Arterioscler. Thromb. Vasc. Biol.* 35, 2544–2553. doi:10.1161/ATVBAHA.115.306035

Guha, M., and Mackman, N. (2001). LPS Induction of Gene Expression in Human Monocytes. *Cell Signal.* 13, 85–94. doi:10.1016/S0898-6568(00)00149-2

Hancock, R. E. W., and Sahl, H.-G. (2006). Antimicrobial and Host-Defense Peptides as New Anti-infective Therapeutic Strategies. *Nat. Biotechnol.* 24, 1551–1557. doi:10.1038/nbt1267

Heinbockel, L., Sánchez-Gómez, S., Martinez de Tejada, G., Dömming, S., Brandenburg, J., Kaconis, Y., et al. (2013). Preclinical Investigations Reveal the Broad-Spectrum Neutralizing Activity of Peptide pep19-2.5 on Bacterial Pathogenicity Factors. *Antimicrob. Agents Chemother.* 57, 1480–1487. doi:10.1128/AAC.02066-12

Heumann, D., and Roger, T. (2002). Initial Responses to Endotoxins and Gram-Negative Bacteria. *Clinica Chim. Acta* 323, 59–72. doi:10.1016/S0009-8981(02)00180-8

Homola, J. (2008). Surface Plasmon Resonance Sensors for Detection of Chemical and Biological Species. *Chem. Rev.* 108, 462–493. doi:10.1021/cr068107d

Huang, M., Cai, S., and Su, J. (2019). The Pathogenesis of Sepsis and Potential Therapeutic Targets. *Int. J. Mol. Sci.* 20, 5376. doi:10.3390/ijms20215376

Ishii, K. J., Koyama, S., Nakagawa, A., Coban, C., and Akira, S. (2008). Host Innate Immune Receptors and Beyond: Making Sense of Microbial Infections. *Cell Host Microbe* 3, 352–363. doi:10.1016/j.chom.2008.05.003

Isozaki, Y., Yoshida, N., Kuroda, M., Handa, O., Takagi, T., Kokura, S., et al. (2006). Anti-tryptase Treatment Using Nafamostat Mesilate Has a Therapeutic Effect on Experimental Colitis. *Scand. J. Gastroenterol.* 41, 944–953. doi:10.1080/00365520500529470

Kimbrell, M. R., Warshakoon, H., Cromer, J. R., Malladi, S., Hood, J. D., Balakrishna, R., et al. (2008). Comparison of the Immunostimulatory and Proinflammatory Activities of Candidate Gram-Positive Endotoxins, Lipoteichoic Acid, Peptidoglycan, and Lipopeptides, in Murine and Human Cells. *Immunol. Lett.* 118, 132–141. doi:10.1016/j.imlet.2008.03.009

Kosikowska, P., and Lesner, A. (2016). Antimicrobial Peptides (AMPs) as Drug Candidates: a Patent Review (2003-2015). *Expert Opin. Ther. Patents* 26, 689–702. doi:10.1080/13543776.2016.1176149

Krishnakumari, V., Binny, T. M., Adicherla, H., and Nagaraj, R. (2020). Escherichia coli Lipopolysaccharide Modulates Biological Activities of Human-β-Defensin Analogues but Not Non-Ribosomally Synthesized Peptides. *ACS Omega* 5, 6366–6375. doi:10.1021/acsomega.9b03770

Kumar, A., Mahajan, M., Awasthi, B., Tandon, A., Harioudh, M. K., Shree, S., et al. (2017). Piscidin-1-analogs with Double L- and D-Lysine Residues Exhibited Different Conformations in Lipopolysaccharide but Comparable Anti-endotoxin Activities. *Sci. Rep.* 7, 39925. doi:10.1038/srep39925

Lee, J.-K., Park, S.-C., Hahm, K.-S., and Park, Y. (2014). A helix-PXXP-helix Peptide with Antibacterial Activity without Cytotoxicity against MDRPA-Infected Mice. *Biomaterials* 35, 1025–1039. doi:10.1016/j.biomaterials.2013.10.035

Lee, S.-H., Jun, H.-K., Lee, H.-R., Chung, C.-P., and Choi, B.-K. (2010). Antibacterial and Lipopolysaccharide (LPS)-neutralising Activity of Human Cationic Antimicrobial Peptides against Periodontopathogens. *Int. J. Antimicrob. Agents* 35, 138–145. doi:10.1016/j.ijantimicag.2009.09.024

Levi, M., and van der Poll, T. (2017). Coagulation and Sepsis. *Thromb. Res.* 149, 38–44. doi:10.1016/j.thromres.2016.11.007

Ling, G., Gao, J., Zhang, S., Xie, Z., Wei, L., Yu, H., et al. (2014). Cathelicidins from the Bullfrog Rana catesbeiana Provides Novel Template for Peptide Antibiotic Design. *PLoS One* 9, e93216. doi:10.1371/journal.pone.0093216

Ma, D., Xu, X., An, S., Liu, H., Yang, X., Andersen, J. F., et al. (2011). A Novel Family of RGD-Containing Disintegrins (Tablysin-15) from the Salivary Gland of the Horsefly Tabanus Yao Targets αIIbβ3 or αVβ3 and Inhibits Platelet Aggregation and Angiogenesis. *Thromb. Haemost.* 105, 1032–1045. doi:10.1160/TH11-01-0029

Mackman, N., Tilley, R. E., and Key, N. S. (2007). Role of the Extrinsic Pathway of Blood Coagulation in Hemostasis and Thrombosis. *Arterioscler. Thromb. Vasc. Biol.* 27, 1687–1693. doi:10.1161/ATVBAHA.107.141911

Mu, L., Zhou, L., Yang, J., Zhuang, L., Tang, J., Liu, T., et al. (2017). The First Identified Cathelicidin from Tree Frogs Possesses Anti-inflammatory and Partial LPS Neutralization Activities. *Amino Acids* 49, 1571–1585. doi:10.1007/s00726-017-2449-7

Mukherjee, S., Karmakar, S., and Babu, S. P. S. (2016). TLR2 and TLR4 Mediated Host Immune Responses in Major Infectious Diseases: A Review. *Braz. J. Infect. Dis.* 20, 193–204. doi:10.1016/j.bjid.2015.10.011

Nankar, S. A., and Pande, A. H. (2013). Physicochemical Properties of Bacterial Pro-inflammatory Lipids Influence Their Interaction with Apolipoprotein-Derived Peptides. *Biochim. Biophys. Acta Mol. Cel Biol. Lipids* 1831, 853–862. doi:10.1016/j.bbalip.2013.01.006

Park, C. B., Yi, K.-S., Matsuzaki, K., Kim, M. S., and Kim, S. C. (2000). Structure-activity Analysis of Buforin II, a Histone H2A-Derived Antimicrobial Peptide: The Proline Hinge Is Responsible for the Cell-Penetrating Ability of Buforin II. *Proc. Natl. Acad. Sci.* 97, 8245–8250. doi:10.1073/pnas.150518097

Ray, A., Cot, M., Puzo, G., Gilleron, M., and Nigou, J. (2013). Bacterial Cell wall Macroamphiphiles: Pathogen-/microbe-Associated Molecular Patterns Detected by Mammalian Innate Immune System. *Biochimie* 95, 33–42. doi:10.1016/j.biochi.2012.06.007

Remick, D. G. (2007). Pathophysiology of Sepsis. *Am. J. Pathol.* 170, 1435–1444. doi:10.2353/ajpath.2007.060872

Rockel, C., and Hartung, T. (2012). Systematic Review of Membrane Components of Gram-Positive Bacteria Responsible as Pyrogens for Inducing Human Monocyte/Macrophage Cytokine Release. *Front. Pharmacol.* 3. doi:10.3389/fphar.2012.00056

Skovbakke, S. L., and Franzyk, H. (2017). Anti-inflammatory Properties of Antimicrobial Peptides and Peptidomimetics: LPS and LTA Neutralization. *Methods Mol. Biol.*, 369–386. doi:10.1007/978-1-4939-6737-7_27

Travis, S. M., Anderson, N. N., Forsyth, W. R., Espiritu, C., Conway, B. D., Greenberg, E. P., et al. (2000). Bactericidal Activity of Mammalian Cathelicidin-Derived Peptides. *Infect. Immun.* 68, 2748–2755. doi:10.1128/IAI.68.5.2748-2755.2000

Uppu, D. S. S. M., Ghosh, C., and Haldar, J. (2015). Surviving Sepsis in the Era of Antibiotic Resistance: Are There Any Alternative Approaches to Antibiotic Therapy?. *Microb. Pathog.* 80, 7–13. doi:10.1016/j.micpath.2015.02.001

Vaara, M., and Porro, M. (1996). Group of Peptides that Act Synergistically with Hydrophobic Antibiotics against Gram-Negative Enteric Bacteria. *Antimicrob. Agents Chemother.* 40, 1801–1805. doi:10.1128/AAC.40.8.1801

van der Poll, T., and Levi, M. (2012). Crosstalk between Inflammation and Coagulation: The Lessons of Sepsis. *Curr. Vasc. Pharmacol.* 10, 632–638. doi:10.2174/157016112801784549

van der Poll, T., and Opal, S. M. (2008). Host-pathogen Interactions in Sepsis. *Lancet Infect. Dis.* 8, 32–43. doi:10.1016/S1473-3099(07)70265-7

Villar, J., Cabrera-Benítez, N. E., Valladares, F., García-Hernández, S., Ramos-Nuez, Á., Martín-Barrasa, J. L., et al. (2015). Tryptase Is Involved in the Development of Early Ventilator-Induced Pulmonary Fibrosis in Sepsis-Induced Lung Injury. *Crit. Care* 19, 138. doi:10.1186/s13054-015-0878-9

Vonk, M. J., Hiemstra, P. S., and Grote, J. J. (2008). An Antimicrobial Peptide Modulates Epithelial Responses to Bacterial Products. *Laryngoscope* 118, 816–820. doi:10.1097/MLG.0b013e31816422d7

Wang, J., Chou, S., Yang, Z., Yang, Y., Wang, Z., Song, J., et al. (2018). Combating Drug-Resistant Fungi with Novel Imperfectly Amphipathic Palindromic Peptides. *J. Med. Chem.* 61, 3889–3907. doi:10.1021/acs.jmedchem.7b01729

Wang, X., Xing, Y., Tang, Z., Tang, Y., Shen, J., and Zhang, F. (2020). Thioredoxin-2 Impacts the Inflammatory Response *via* Suppression of NF-κB and MAPK Signaling in Sepsis Shock. *Biochem. Biophys. Res. Commun.* 524, 876–882. doi:10.1016/j.bbrc.2020.01.169

Wei, L., Yang, J., He, X., Mo, G., Hong, J., Yan, X., et al. (2013). Structure and Function of a Potent Lipopolysaccharide-Binding Antimicrobial and Anti-inflammatory Peptide. *J. Med. Chem.* 56, 3546–3556. doi:10.1021/jm4004158

Woodman, R. C., Teoh, D., Payne, D., and Kubes, P. (2000). Thrombin and Leukocyte Recruitment in Endotoxemia. *Am. J. Physiol. Heart Circulatory Physiol.* 279, H1338–H1345. doi:10.1152/ajpheart.2000.279.3.H1338

Wu, J., Yang, J., Wang, X., Wei, L., Mi, K., Shen, Y., et al. (2018). A Frog Cathelicidin Peptide Effectively Promotes Cutaneous Wound Healing in Mice. *Biochem. J.* 475, 2785–2799. doi:10.1042/BCJ20180286

Ye, T., Wu, J., Xu, Z., Chai, J., Zeng, Q., Zeng, B., et al. (2020). Esc-1GN Shows Therapeutic Potentials for Acne Vulgaris and Inflammatory Pain. *J. Pep Sci.* 26, e3269. doi:10.1002/psc.3269

Zanetti, M., Gennaro, R., Scocchi, M., and Skerlavaj, B. (2000). Structure and Biology of Cathelicidins. *Adv. Exp. Med. Biol.* 479, 203–218. doi:10.1007/0-306-46831-X_17

Zeng, B., Chai, J., Deng, Z., Ye, T., Chen, W., Li, D., et al. (2018). Functional Characterization of a Novel Lipopolysaccharide-Binding Antimicrobial and Anti-Inflammatory Peptide *In Vitro* and *In Vivo*. *J. Med. Chem.* 61, 10709–10723. doi:10.1021/acs.jmedchem.8b01358

Zhang, J., Wang, Z., Wang, Y., Zhou, G., and Li, H. (2015). The Effect of Dexmedetomidine on Inflammatory Response of Septic Rats. *BMC Anesthesiol* 15, 68. doi:10.1186/s12871-015-0042-8

Zhu, X., Zhang, L., Wang, J., Ma, Z., Xu, W., Li, J., et al. (2015). Characterization of Antimicrobial Activity and Mechanisms of Low Amphipathic Peptides with Different α-helical Propensity. *Acta Biomater.* 18, 155–167. doi:10.1016/j.actbio.2015.02.023

Conflict of Interest: The authors declare that the research was conducted in the absence of any commercial or financial relationships that could be construed as a potential conflict of interest.

Publisher's Note: All claims expressed in this article are solely those of the authors and do not necessarily represent those of their affiliated organizations, or those of the publisher, the editors and the reviewers. Any product that may be evaluated in this article, or claim that may be made by its manufacturer, is not guaranteed or endorsed by the publisher.

frontiers in Pharmacology

ORIGINAL RESEARCH
published: 18 October 2021
doi: 10.3389/fphar.2021.770283

CRISPA: A Non-viral, Transient Cas9 Delivery System Based on Reengineered Anthrax Toxin

Maximilian Hirschenberger[1,2], Nicole Stadler[1], Maximilian Fellermann[1], Konstantin M. J. Sparrer[2], Frank Kirchhoff[2], Holger Barth[1†] and Panagiotis Papatheodorou[1*†]*

[1]Institute of Pharmacology and Toxicology, Ulm University Medical Center, Ulm, Germany, [2]Institute of Molecular Virology, Ulm University Medical Center, Ulm, Germany

OPEN ACCESS

Edited by:
Jean-Marc SABATIER,
Aix-Marseille Université, France

Reviewed by:
Ekaterina Nestorovich,
Catholic University of America,
United States
Johanna Rivera,
Albert Einstein College of Medicine,
United States

***Correspondence:**
Holger Barth
holger.barth@uni-ulm.de
Panagiotis Papatheodorou
panagiotis.papatheodorou@uni-ulm.de

[†]These authors have contributed equally to this work and share last authorship

Specialty section:
This article was submitted to Pharmacology of Ion Channels and Channelopathies, a section of the journal Frontiers in Pharmacology

Received: 03 September 2021
Accepted: 01 October 2021
Published: 18 October 2021

Citation:
Hirschenberger M, Stadler N, Fellermann M, Sparrer KMJ, Kirchhoff F, Barth H and Papatheodorou P (2021) CRISPA: A Non-viral, Transient Cas9 Delivery System Based on Reengineered Anthrax Toxin. Front. Pharmacol. 12:770283. doi: 10.3389/fphar.2021.770283

Translating the CRISPR/Cas9 genome editing technology into clinics is still hampered by rather unspecific, unsafe and/or inconvenient approaches for the delivery of its main components - the Cas9 endonuclease and a guide RNA - into cells. Here, we describe the development of a novel transient and non-viral Cas9 delivery strategy based on the translocation machinery of the *Bacillus anthracis* anthrax toxin, PA (protective antigen). We show that Cas9 variants fused to the N-terminus of the lethal factor or to a hexahistidine tag are shuttled through channels formed by PA into the cytosol of human cells. As proof-of-principle, we applied our new approach, denoted as CRISPA, to knock out lipolysis-stimulated lipoprotein receptor (LSR) in the human colon cancer cell line HCT116 and green-fluorescent protein (GFP) in human embryonic kidney 293T cells stably expressing GFP. Notably, we confirmed that the transporter PA can be adapted to recognize specific host cell-surface receptor proteins and may be optimized for cell type-selective delivery of Cas9. Altogether, CRISPA provides a novel, transient and non-viral way to deliver Cas9 into specific cells. Thus, this system is an additional step towards safe translation of the CRISPR/Cas9 technology into clinics.

Keywords: CRISPR/Cas9, genome editing, cell targeting, bacterial toxin, pore-forming toxin, translocation channel, protein translocation

INTRODUCTION

CRISPR/Cas9 emerged over the last years as a key technology for targeted genome editing. The cooperative assembly of the Cas9 endonuclease and a target gene-specific guide RNA (gRNA) allows the introduction of a site-specific double-strand-break (DSB). Repair of the DSB via error-prone non-homologous end joining (NHEJ) eventually leads to frequent base pair insertions or deletions (indels), which disrupt gene expression (Mali et al., 2013). Conventionally, Cas9 and the gRNA sequence are transiently or stably introduced into cells via plasmid- or viral-based delivery methods. To this end a plethora of different delivery methods, including electroporation, cell penetrating peptides or as Cas9-gRNA ribonucleoproteins (RNPs), were described (Nelson and Gersbach, 2016; Liu et al., 2017; Lino et al., 2018; Wang et al., 2019). Most *in vivo* Cas9-based genome editing trials aimed to eradicate integrated E6 and E7 HPV (human papilloma virus) oncogenes in accessible cervical cancer. Cas9-guided therapy has been applied to the eye, e.g. for the repair of inherited retinal disorders (Hirakawa et al., 2020). However, the lack of cell-type/tissue selectivity remains a drawback and a major hurdle in translating CRISPR/Cas9 genome editing into clinical applications. Increasing

cell specificity of CRISPR/Cas9 genome editing would allow to expand its therapeutic applications to a larger number of diseases, beyond easily accessible tissues.

A delivery system based on bacterial toxins can be engineered to become highly cell type-specific (Beilhartz et al., 2017). In principle, the receptor-binding domain of the toxin can be substituted with a protein ligand for a cell surface receptor that is expressed exclusively in a specific cell type. Anthrax lethal toxin, the main virulence factor of the anthrax-causing pathogen *Bacillus anthracis*, is a binary combination of a protein transporter system (PA) and the executor factor (lethal factor, LF). LF is a protease which specifically cleaves mitogen-activated protein kinases (MAPKs), ultimately leading to cell cycle arrest and an accompanying inhibition of cell proliferation (Moayeri and Leppla, 2009). PA acts as the binding and translocation component for the biologically active toxin complex. Upon binding to its target cell receptors ANTXR1 (TEM8) and ANTXR2 (CMG2) (van der Goot and Young, 2009), a 20 kD fragment of the 83 kD PA (PA83) is released by proteolytic cleavage. Processed PA (now PA63) forms heptamers or octamers at the cell surface and recruits up to three LF molecules to the PA63 oligomer/receptor complex. Following receptor-mediated endocytosis and acidification of endosomes by vesicular proton pumps (vATPases), PA63 oligomers form channels in endosomal membranes, facilitating the translocation of LF into the host cell cytosol (Young and Collier, 2007; Moayeri et al., 2015).

More than 2 decades ago, it was shown that foreign proteins can be delivered into mammalian cells via PA, when fused to the PA recognition domain of LF (N-terminus, LF_N) (Arora and Leppla, 1993, Arora and Leppla, 1994; Milne et al., 1995). PA-dependent delivery to the cytosol is also facilitated when a short polybasic sequence of lysine, arginine or histidine residues is fused to cargo proteins (Blanke et al., 1996; Sharma and Collier, 2014). Importantly, a conventional, N-terminal hexahistidine tag (His6-tag), which is commonly used as a purification tag for recombinant proteins, is also sufficient for promoting cell entry of foreign proteins into cells via the PA channel (Beitzinger et al., 2012). To date more than 30 different non-native cargos have been delivered into the cytosol of cells by using PA as non-toxic delivery platform to probe intracellular biological functions (Rabideau and Pentelute, 2016; Piot et al., 2021).

In the present study, the PA-mediated delivery platform was established as a non-viral, transient Cas9 system for RNA-guided CRISPR/Cas9 genome engineering. As proof-of-concept, we generated a knockout of the gene encoding the protein LSR (lipolysis-stimulated lipoprotein receptor) in the human colon carcinoma cell line HCT116, since we previously succeeded in knocking out the lsr gene with the conventional CRISPR/Cas9 mutagenesis approach in this cell line (Hemmasi et al., 2015). LSR serves as host entry receptor for the AB-type binary actin-ADP-ribosylating *Clostridium difficile* toxin CDT (*Clostridium difficile* transferase) (Papatheodorou et al., 2011). LSR-deficient HCT116 cell clones are CDT-resistant and can easily be selected after toxin treatment. In addition, the system was translated to a different setting by targeting stably integrated GFP in the commonly used human embryonic kidney cell line 293T. Finally, we demonstrate cell specificity with a mutated PA variant fused to a growth factor, which enabled the specific transport of a toxic cargo protein into cells expressing the corresponding growth factor receptor.

This novel modular PA-based Cas9 delivery method, denoted as CRISPA (a portmanteau of CRISPR and PA), represents an innovative tool in molecular biology with future clinical potential especially for *ex vivo* gene therapy purposes. Moreover, CRISPA can be further developed for targeted, cell type-selective delivery of Cas9 by changing the receptor-specificity of PA.

MATERIALS AND METHODS

Cell Culture and Transfection

HEK293T cells (ATCC: #CRL-3216) were cultured in Dulbecco's Modified Eagle's Medium (DMEM) supplemented with 10% (v/v) fetal calf serum (FCS), 1% (v/v) penicillin/streptomycin, and 2 mM L-glutamine. Wild-type HCT116 (ATCC: #CCL-247) and LSR-deficient HCT116/ΔLSR_{CRISPR} cells (Hemmasi et al., 2015) were cultivated in DMEM supplemented with 10% (v/v) FCS, 1% (v/v) penicillin/streptomycin, and 2 mM L-glutamine. HeLa cells were grown in Minimum Essential Medium (MEM) supplemented with 10% (v/v) FCS, 1% (v/v) penicillin/streptomycin, 2 mM L-glutamine, and 1 mM sodium pyruvate. A431 cells were grown in Roswell Park Memorial Institute (RPMI) 1640 Medium supplemented with 10% (v/v) FCS, 1% (v/v) penicillin/streptomycin, and 2 mM L-glutamine.

For HCT116 cells, Lipofectamine 2000 Transfection Reagent (Thermo Fisher Scientific, Waltham, United States) and for 293T-GFP cells, TransIT-LT1 Transfection Reagent (Mirus Bio LLC, Madison, United States) were used for transfection, according to the manufacturer's protocols.

Cell Viability Assay

Cell viability measurements with cultured cells were performed with the CellTiter 96 AQ_{ueous} One Solution Cell Proliferation Assay (MTS) from Promega (Madison, United States), according to the manufacturer's protocol. Briefly, cells were seeded in 96-well plates and the next day the medium (100 µL) was exchanged with medium (100 µL) containing the respective toxin components at indicated concentrations. Mock- and DMSO (10% (v/v))-treated cells served as positive and negative control for cell viability, respectively. Following an incubation period of 24 h at 37°C, MTS (3-(4,5-dimethylthiazol-2-yl)-5-(3-carboxymethoxyphenyl)-2-(4-sulfophenyl)-2H-tetrazolium) was added to the medium of each well and the absorption was measured at 490 nm using a microtiter plate reader.

Limited Dilution Cloning

Monoclonal cell populations were obtained by limited dilution cloning. Briefly, suspensions of trypsinized cells were adjusted with growth medium to a cell density of 5 cells per ml and transferred to 96-well plates in 100 µL portions (corresponding to 0.5 cells per well). An inverted microscope Axiovert ProgRess C10 plus was used to detect wells that contained only one defined cell clone after 7 days of growth. Single cell colonies were then

removed by trypsinization and transferred to culture dishes for expansion.

Generation of HEK293T Cells Stably Expressing GFP

GFP expressing HEK293T cells were generated with third generation lentiviral particles (Dull et al., 1998) as described previously (Koepke et al., 2020). In short, third generation lentiviruses were produced using pCSC-SP-PW-GFP and helper plasmids and then used to transduce HEK293T cells. Three days post transduction, the cells were sorted using the BD FACSAria II. Cells with moderate GFP MFIs were pooled and cultivated at 37°C with 5% (v/v) CO_2 under humidified conditions. The pCSC-SP-PW-GFP plasmid (aka pBOB-eGFP) was kindly provided by Inder Verma (Addgene, #12337 (Marr et al., 2004)).

Recombinant Toxins or Toxin Components

Recombinantly expressed and purified toxins or toxin components, such as His-TccC3hvr, C2I, C2II, CDTa, CDTb, PA (PA83) and the receptor-binding domain (RBD) of CDTb, are described elsewhere (Barth et al., 2000; Tonello et al., 2004; Lang et al., 2010; Schwan et al., 2011; Papatheodorou et al., 2013). The RBD of CDTb was used as a glutathione S-transferase (GST) fusion protein. The binding components of CDT, C2 and anthrax toxin, namely CDTb, C2II and PA83, respectively, were used as protease-activated proteins, whereas protease-activated PA83 is denoted as PA63 (Singh et al., 1989; Barth et al., 2000; Blöcker et al., 2001; Sterthoff et al., 2010). Unnicked diphtheria toxin (DT) from *Corynebacterium diphtheriae* was purchased from Sigma-Aldrich (order number: D0564). His-TccC3hvr, both CDT components (CDTa and CDTb) and the RBD of CDTb were provided by the laboratory of Klaus Aktories (University of Freiburg, Germany). The PA variants mPA83 and mPA83-EGF as well as LF_N-DTA were provided by R. John Collier (Harvard Medical School, Boston, United States).

Subconfluent monolayers of cultured cells were intoxicated by direct addition of toxins or toxin components into the growth medium. If required, toxin dilutions were performed with growth medium or phosphate-buffered saline. If not otherwise stated, the final concentrations of the toxins during the intoxication were as follows: CDTa/CDTb (5 nM/1 nM), C2I/C2II (1 nM, 1.67 nM), PA63/His-TccC3hvr (10 nM/50 nM), DT (10 nM), and the combinations PA83, PA63, mPA83 or mPA83-EGF (20 nM) plus LF_N-DTA (10 nM), respectively. The intoxication of cells was analyzed by microscopic evaluation of the cell morphology, by measuring cell viability or by immunodetection of target substrate modification.

Generation, Expression and Purification of His- and LF_N-Cas9

For the recombinant production of His-Cas9, *Escherichia coli* XJb (DE3) Autolysis strain (T3051, Zymo Research Europe, Freiburg, Germany) was transformed with Addgene plasmid #53261 (pET28a/Cas9-Cys (Ramakrishna et al., 2014)). Briefly, transformants were grown in liquid LB medium at 37°C until an $OD_{600\ nm}$ of 0.6–0.8 was reached. Then, 0.5 mM IPTG and 3 mM arabinose were added to the medium for His-Cas9 and lambda lysozyme expression, respectively, followed by incubation for 4 h at 37°C under shaking. After harvesting of the cells by centrifugation, cells were resuspended in buffer, containing 50 mM NaH_2PO_4 (pH 8), 300 mM NaCl, 5 mM imidazole, 0.03% (v/v) Triton X-100, and stored at −20°C. A cell lysate for subsequent protein purification was generated by thawing the cell pellet, followed by addition of 1 mM PMSF and 1 mM DTT to the cell suspension. Next, cell debris was removed by centrifugation (30,000 g, 30 min, 4°C) and the supernatant filtered through a 0.45 and 0.2 µm sterile filter. Finally, the filtrate was subjected to PureCube 1-step batch Midi Plus Columns (Cube Biotech, Monheim, Germany) for purification of His-Cas9 by nickel affinity chromatography. Washing and elution buffers were 50 mM NaH_2PO_4 (pH 8), 300 mM NaCl, 20 mM imidazole, 0.03% (v/v) Triton X-100 and 50 mM NaH_2PO_4 (pH 8), 300 mM NaCl, 250 mM imidazole, respectively. Eventually, a buffer exchange of the eluate to phosphate-buffered saline (PBS) was performed with Vivaspin 20 columns (Sigma-Aldrich Chemie GmbH, Munich, Germany).

LF_N-Cas9 was expressed and purified essentially as described for His-Cas9 above. However, the initial cloning of the LF_N-Cas9 fusion construct was necessary. The Addgene plasmid #62933 (pET-Cas9-NLS-6xHis (Zuris et al., 2015)) served as backbone for insertion of an LF_N-encoding fragment upstream of the Cas9 sequence by seamless assembly (NEBuilder HiFi DNA Assembly Cloning Kit; #E5520; New England BioLabs GmbH, Frankfurt am Main, Germany). The LF_N-encoding fragment was generated by PCR and with Addgene plasmid #11075 (pET-15b LFN-DTA (Milne et al., 1995)) as template. The NEBuilder Assembly Tool (New England BioLabs GmbH, Frankfurt am Main, Germany) was used to design primers for the seamless cloning procedure.

Purified His- and LF_N-Cas9 proteins were tested for dsDNA cleavage activity by performing an *in vitro* Cas9 cleavage assay with the CRISPRcraft S. p. Cas9 Control Kit (Lucigen, Middleton, United States), which includes a substrate DNA, a substrate DNA-specific gRNA and a set of DNA primers. For the *in vitro* cleavage assay, ~300 ng of a 1083 bp DNA fragment (generated by PCR and by using the supplied substrate DNA as template) was incubated for 10 min together with the gRNA and 20 nM or 40 nM His-Cas9- and LF_N-Cas9, respectively, and cleavage products were analyzed by agarose gel electrophoresis. The gRNA-directed cleavage of the 1083 bp fragment results into two fragments with the size of 800 and 283 bp, respectively. Commercial Cas9 protein (EnGen® Spy Cas9 NLS from New England Biolabs (NEB); M0646T) was used as positive control for *in vitro* DNA cleavage.

For the detection of His- and LF_N-Cas9 via immunoblotting and enhanced chemiluminescence (ECL) imaging, a mouse anti-His (AD1.1.10) antibody (Santa Cruz Biotechnology, Dallas, United States) as primary antibody in combination with mouse IgGκ light chain binding protein coupled to horseradish peroxidase (m-IgGκ BP-HRP) was used.

Immunodetection of Proteins in Whole-Cell Lysates

Whole-cell lysates were generated directly in well plates or culture dishes by washing cell monolayers first with PBS and then by resuspending them in Laemmli buffer. Prior to SDS-PAGE followed by immunoblotting, lysate samples were heated at 95°C for 5 min. For the detection of LSR, Hsp90 and GAPDH, commercial primary antibodies (rabbit anti-LSR (X-25); mouse anti-Hsp90 α/β (F-8); mouse anti-GAPDH (G-9)) and secondary antibodies (m-IgGκ BP-HRP and goat anti-rabbit IgG-HRP) were used. All antibodies were purchased from Santa Cruz Biotechnology, Dallas, United States.

Light Microscopy

An inverted Axiovert 40 CFL microscope (Carl Zeiss Microscopy, Jena, Germany) equipped with a ProgRess C10 plus camera (Jenoptik, Jena, Germany) was used in this study for light microscopic analyses, such as monitoring cell intoxication, identification of growing cell clones in wells and cell confluence estimation, respectively.

Verification of Cas9-Induced Indel Mutations in LSR Knockout Clones

First, genomic DNA was isolated from 1×10^6 cells using the MyTaq Extract-PCR Kit (Bioline GmbH, Luckenwalde, Germany) or innuPREP DNA Mini Kit (Analytik Jena, Jena, Germany) following the manufacturer's recommendations. Next, a 403 bp DNA fragment within the lsr gene that contains the LSR-specific gRNA binding site was amplified by PCR with oligonucleotides 5′-GTCCAACCCCTACCACGTGGTG-3′ and 5′- GCTTTCAGATGGGGACTCCAGG-3′ and by using genomic DNA as template (Hemmasi et al., 2015). Eventually, the PCR product was purified with the my-Budget Double Pure Kit (BioBudget Technologies GmbH, Krefeld, Germany) and subjected to DNA sequencing (Eurofins Genomics Europe Sequencing GmbH, Konstanz, Germany). Indels in the sequenced DNA fragments were identified by performing sequence alignments with the lsr reference sequence.

Sequential ADP-Ribosylation

The sequential ADP-ribosylation assay served to estimate *in vitro* the ADP-ribosylation status of cellular actin after intoxication of cells by the actin ADP-ribosylating toxin CDT (Kaiser et al., 2011). First, intoxicated cells (and mock-treated cells as negative controls) were washed twice with PBS and frozen at −20°C. Then, cell lysis was induced by thawing, after which the lysed cells were collected with a cell scraper and resuspended in buffer containing 20 mM Tris-HCl (pH 7.5), 5 mM $MgCl_2$, 1 mM EDTA, 1 mM DTT, and cOmplete protease Inhibitor Cocktail (Roche, Rotkreuz, Switzerland). Cell lysate (20 µL) was incubated for 30 min at 4°C together with purified CDTa (100 ng) and 250 pmol biotinylated NAD^+ (Trevigen, Gaithersburg, United States), prior to addition of Laemmli buffer and heating for 10 min at 95°C to stop the ADP-ribosylation reaction. Eventually, *in vitro* sequentially ADP-ribosylated (and thus biotinylated) actin was visualized by Western Blotting and ECL and by the use of peroxidase-conjugated streptavidin (Merck, Darmstadt, Germany).

Flow Cytometry

For the analysis of cell surface binding, purified proteins were fluorescently labelled with DyLight 488 NHS Ester (Thermo Fisher Scientific, Waltheim, United States) following manufacturer's instructions and as described earlier (Papatheodorou et al., 2013). Zebra Spin Desalting Columns (Thermo Fisher Scientific, Waltham, United States) were used to remove excess fluorescent dye after the labelling reaction. Labelling efficiency and protein concentration were determined by performing spectrophotometric analyses on a NanoDrop OneC spectrophotometer (Thermo Fisher Scientific, Waltham, United States). Next, cultured cell monolayers were detached by incubation for 15–30 min at 37°C with PBS containing 25 mM EDTA (and without trypsin) to preserve proteins at the cell surface. The detached cells were resuspended in growth medium and the cell density of the cell suspension adjusted to 1×10^6 cells per ml. Then, DyLight-labelled protein at indicated amounts was incubated with 2×10^5 cells (200 µL cell suspension) for 30 min on ice to prevent cellular uptake of cell surface-bound proteins. Finally, cells were washed up to 5 times by centrifugation (500 g, 5 min, 4°C) and resuspension in PBS to remove any non-bound DyLight-labelled protein, prior to flow cytometric analysis of the cell suspensions using the BD FACSCelesta flow cytometer run by the FACSDiva software (BD Biosciences, San Jose, United States). The results of the flow cytometric measurements (typically 1×10^4 cells per sample) were further analyzed using Flowing software version 2.5.1 (University of Turku, Finland).

The sorting of HEK293T cells expressing moderate GFP levels was done using the BD FACSAria III. To measure GFP fluorescence of cells applied to the CRISPA method the Beckman-Coulter CytoFLEX was used.

Guide RNA Expression Plasmids

Guide RNA (gRNA) expression plasmids including the protospacer sequences 5′- GGACAGCGTGCGCACCGTCA-3 for LSR and 5′-GTGAACCGCATCGAGCTGAA-3′ for GFP were used in this study that are described elsewhere (Hemmasi et al., 2015; Koepke et al., 2020).

T7EI Mismatch Detection Assay

293T-GFP cells were cultivated in a 24-well to half-confluency, then transfected with a plasmid encoding a GFP-specific gRNA, followed by medium renewal after 6 h. The next day, the cells were incubated for 24 h with 10 nM PA63 together with 100 nM His- and LF_N-Cas9, respectively, or a commercially available His-Cas9 protein (EnGen® Spy Cas9 NLS from New England Biolabs (NEB); M0646T). Cells were then harvested for T7 endonuclease I (T7EI) mismatch detection using the GeneArt® Genomic Cleavage Detection Kit (Thermo Scientific). In short, total genomic DNA was extracted from harvested cells and the locus, which is targeted by the GFP-

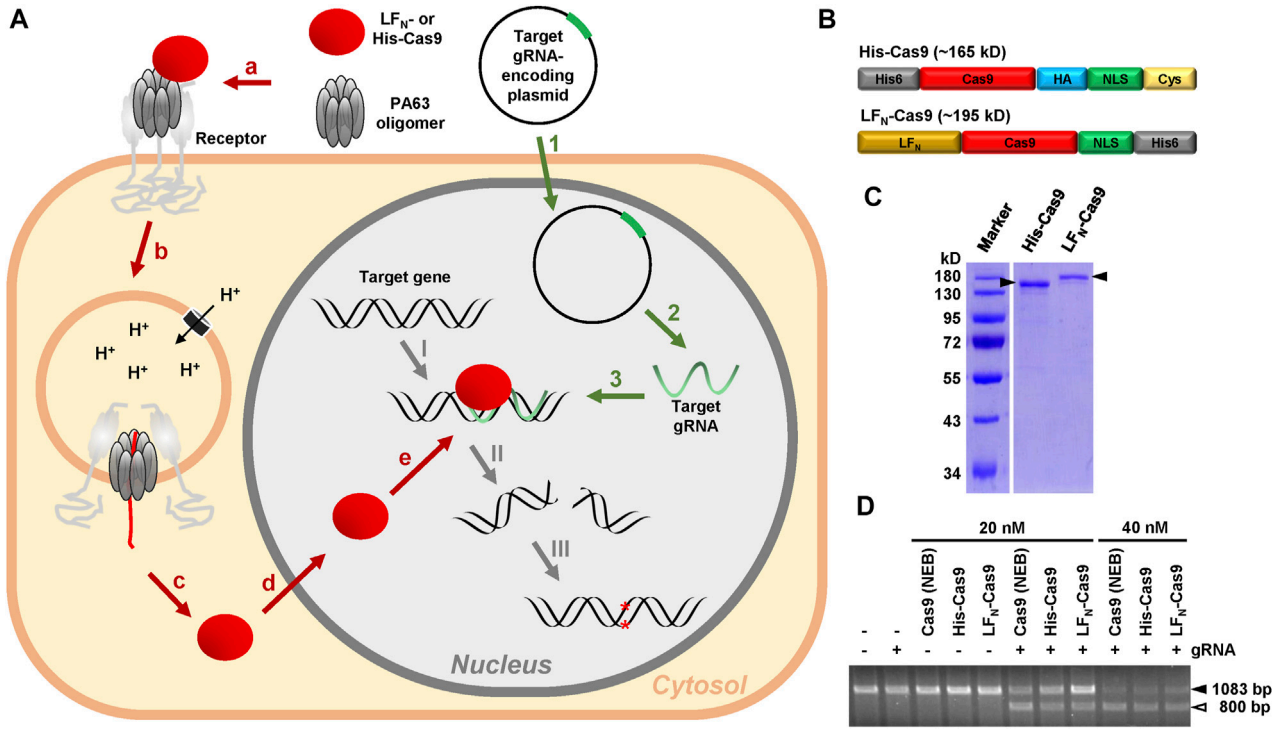

FIGURE 1 | Rationale of the modular CRISPA concept and characterization of His- and LF_N-Cas9. **(A)** 1: A plasmid for the expression of the target gRNA is introduced into cells via transfection; 2: Target gRNA is expressed by the cells; 3: Target gRNA forms a RNA-DNA-heteroduplex at its target position within the genomic DNA; a: PA63 binds as oligomer to its receptor on the cell surface and forms a complex with LF_N- or His-Cas9; b: Receptor-mediated endocytosis promotes entry of the PA63 oligomer–LF_N-/His-Cas9–receptor complex into cells via endosomes; c: Acidification of the endosomes leads to channel formation of the PA63 oligomer into the endosomal membrane and translocation of unfolded LF_N-/His-Cas9 into the cytosol; d: The nuclear localization signal (NLS) promotes entry of refolded LF_N-/His-Cas9 into the nucleus; e: LF_N-/His-Cas9 is recruited to the RNA-DNA-heteroduplex formed by the gRNA at its target position: I: A LF_N-/His-Cas9–gRNA complex is formed at the target gene. II: LF_N-/His-Cas9 leads to a double-strands cleavage of the target gene; III: Non-homologous end joining (NHEJ) generates indels into the target gene, which in turn lead to premature stop codons within the open reading frame (ORF) of the targeted gene, resulting in the knockout of the respective gene **(B)** Schematic representation of the modular composition of His-Cas9 (~165 kD) and LF_N-Cas9 (~195 kD). Please note that the size of the boxes is not related to the size of the modules. His6, hexahistidine tag; HA, human influenza hemagglutinin epitope tag; NLS, nuclear localization sequence; Cys, cysteine residue **(C)** Coomassie-stained polyacrylamide gel for size and purity control of purified His- (0.55 µg) and LF_N-Cas9 (0.425 µg) indicated by filled arrowheads **(D)** Cas9 cleavage assay. Cleavage of approx. 300 ng target DNA (1083 bp; filled arrowhead) after incubation with 20 nM or 40 nM His- or LF_N-Cas9, respectively, or commercial Cas9 (Cas9 (NEB)) alone or in combination with the respective guide RNA (gRNA) was monitored by agarose gel electrophoresis. The open arrowhead indicates the 800 bp cleavage product of the target DNA. bp, base pairs.

specific gRNA was amplified by PCR using the primers 5′-ACA GCTCGTCCATGC-’3 (GFP-rev) and 5′-TGCTTCAGCCGC TACC-’3 (GFP-fwd). Subsequently, the PCR product was heat-denatured and reannealed to generate mismatch strands. These mismatches were then detected and cleaved by the Detection Enzyme (T7EI) and the resulting products were separated by agarose gel electrophoresis and visualized by gel imaging (Gel Doc XR + Gel Documentation System; Biorad). DNA band intensity was analyzed with ImageJ (Schneider et al., 2012) and the cleavage efficiency calculated essentially as described in the GeneArt® Genomic Cleavage Detection Kit manual.

Statistics

Bar diagrams were generated with mean values calculated from triplicates or from three samples performed in parallel and with error bars representing standard deviation (SD). Significance differences were calculated with Microsoft Excel (Student´s) *t*-test. Resulting *p* values were indicated by asterisks as follows: $^{*}p < 0.05$, $^{**}p < 0.01$, $^{***}p < 0.001$.

RESULTS

Establishing CRISPA in HCT116 Cells

Here, we describe a novel modular PA-based Cas9 delivery concept, denoted as CRISPA, that can be subdivided into three main processes. The first is the transfection of a plasmid encoding the target guide RNA into cells. The second step is the delivery of Cas9 into cells via PA. As a consequence of both processes, a third process is initiated, the Cas9-dependent cleavage of the target gene, eventually resulting in the knockout of the respective gene (**Figure 1A**).

The CRISPA method requires purified recombinant Cas9 protein, either fused to an N-terminal His6-tag (denoted as His-Cas9) or to the N-terminus of the *Bacillus anthracis*

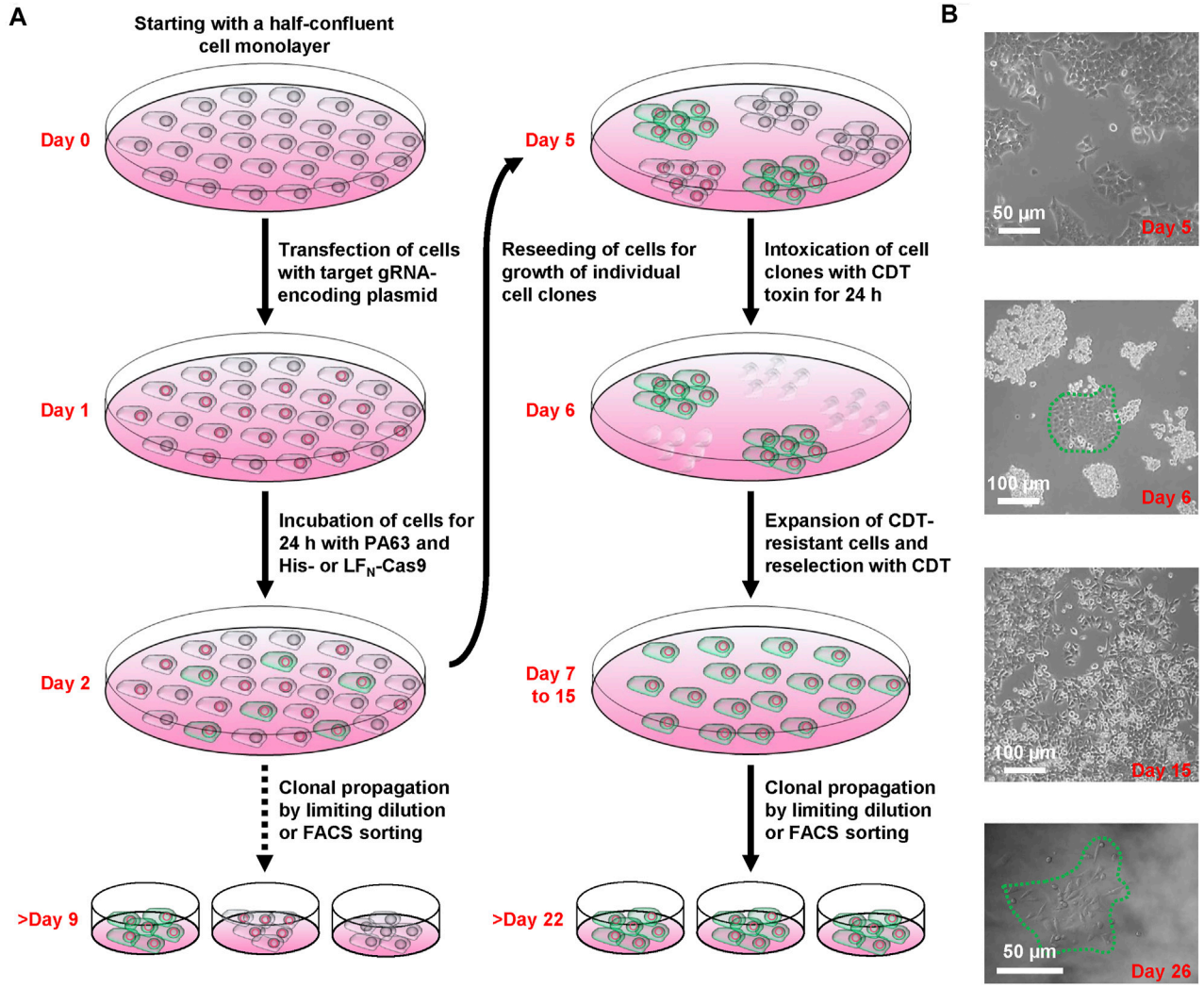

FIGURE 2 | Working scheme of the CRISPA mutagenesis protocol. **(A)** Illustration of the successive steps of the CRISPA approach with images of key steps shown in **(B)**.

lethal factor (denoted as LF_N-Cas9). Suitable Cas9 constructs must also possess a nuclear localization signal (NLS), in order to reach the nucleus of target cells. As His-Cas9, we used a recently described Cas9 construct consisting of an N-terminal His6-tag and Cas9 followed by an HA tag, an NLS and a single cysteine residue (Ramakrishna et al., 2014). As LF_N-Cas9, a Cas9 construct consisting of Cas9 followed by an NLS and a His6-tag was used, where we fused the N-terminus of the lethal factor (LF_N) at its N-terminus by Gibson cloning (Zuris et al., 2015) (**Figure 1B**). Both Cas9 fusion proteins were expressed in *Escherichia coli* and purified as His-tagged proteins by nickel affinity chromatography. The purity of both Cas9 preparations (~87% for His- and 82% for LF_N-Cas9) was determined by SDS-PAGE and Coomassie staining (**Figure 1C**). Both Cas9 preparations were almost as active as commercial Cas9 protein in an *in vitro* Cas9 cleavage assay (**Figure 1D**).

We have chosen the HCT116 cell line as a model cell line for our CRISPA approach, because we previously succeeded in knocking out a gene of interest via the conventional CRISPR/Cas9 approach in these cells (Hemmasi et al., 2015). To examine whether HCT116 cells are a suitable target for the CRISPA approach, we first determined whether PA (in particular PA63 was applied in this study) is able to promote translocation of foreign cargo proteins into HCT116 cells. Here, we used His-tagged TccC3hvr (actin ADP-ribosyltransferase domain of the *Photorhabdus luminescens* PTC3 toxin) as toxic cargo protein for PA, since it was reported that this combination is toxic to various mammalian cell lines, such as HeLa and Vero (Lang et al., 2010; Ernst et al., 2017). Beitzinger et al. utilized 3 µg/ml (~50 nM) proteolytically-activated PA (PA63) for transport of a His- or LF_N-fused cargo protein into human umbilical vein endothelial cells (HUVECs) (Beitzinger et al., 2012). We tested whether 10 nM PA63 would already be sufficient for translocating His-

TccC3hvr at three different concentrations (20, 50, 100 nM) into HCT116 cells.

Mock-treated HCT116 cells or HCT116 cells treated for up to 24 h with 100 nM His-TccC3hvr or 10 nM PA63 alone did not show any morphological signs of intoxication (**Supplementary Figure S1A**). However, HCT116 cells incubated with the combination of 10 nM PA63 plus 20, 50 or 100 nM His-TccC3hvr, displayed strong cell rounding, a typical hallmark of TccC3hvr intoxication due to its molecular action on the actin cytoskeleton, already after 6 h of incubation (**Supplementary Figure S1B and S1C**). Thus, 10 nM PA63 is sufficient for translocating His- or LF_N-fused cargo proteins into HCT116 cells.

These results indicated that HCT116 cells express host receptor(s) for PA and permit transport of its cargo protein.

Generation of HCT116 LSR Knockout Cells via CRISPA

We next set about knocking out LSR in HCT116 cells by applying the CRISPA method (**Figure 2A**). At first, HCT116 cells were cultivated in a 24-well plate to half-confluency (day 0), then transiently transfected with a plasmid encoding the LSR-specific gRNA and the medium renewed 6 h after transfection. At day 1, cells were treated for 24 h with 10 nM PA63 together with 100 nM His-Cas9 or LF_N-Cas9, respectively, to induce the Cas9-based knockout of LSR. It is of note that already at this stage (day 2), single cell clones for further analysis and identification of cell clones carrying the desired gene knockout may be isolated.

LSR is the host entry receptor for CDT. This enabled us to further select for LSR-deficient HCT116 cells simply by intoxicating the cells after CRISPA with CDT. To this end, cells were trypsinized at day 2 and one-tenth of the cells was re-seeded into a 6-well to obtain segregated colonies of clonal derivatives at the plastic bottom. Grown cell colonies were then incubated twice for 24 h with CDT at day 5 and day 6. At day 7, CDT-resistant cell clones could easily be discriminated microscopically from non-resistant cell clones that exhibited massive CDT-induced cell rounding. Only a few CDT-resistant cell clones were observed in each 6-well (typically up to 10), independent of whether His- or LF_N-Cas9 was used together with PA63. Notably, CDT-resistant cell clones were only detected when all components of the CRISPA approach (LSR-specific guide RNA-expressing plasmid, PA63 and His-/LF_N-Cas9) were used in combination, indicating that CDT-resistant cell clones did not arise from random mutations due to genetic instability. CDT-resistant cells were expanded and reselected again with CDT (days 7–15, **Figure 2B**). Eventually, single cell clones were obtained in 96-wells by limiting dilution and cell colonies were clearly visible after approximately 1 week of incubation (>day 22) (**Figure 2B**).

Verification of the LSR Knockout in HCT116 Cell Clones

To test whether the CRISPA approach was successful, we analyzed a single LF_N-Cas9- (HCT116/$\Delta LSR_{CRISPA/LFN\text{-}Cas9}$) and a single His-Cas9-derived cell clone (HCT116/$\Delta LSR_{CRISPA/His\text{-}Cas9}$), respectively, via LSR immunoblotting. To this end, whole-cell lysates were generated from both CRISPA-derived LSR knockout cell clones and, for direct comparison, from wildtype HCT116 cells (HCT116/WT). Whole-cell lysates from LSR-deficient HCT116 cells generated using conventional CRISPR/Cas9 approach (denoted here as HCT116/ΔLSR_{CRISPR}) (Hemmasi et al., 2015) were used as negative controls for LSR immunodetection. LSR immunoblotting confirmed the lack of LSR expression in HCT116/ΔLSR_{CRISPR}, but also in HCT116/$\Delta LSR_{CRISPA/LFN\text{-}Cas9}$ and HCT116/$\Delta LSR_{CRISPA/His\text{-}Cas9}$ cells (**Figure 3A**).

Next, we analyzed whether indel mutations in our target gene LSR are present in both CRISPA-derived LSR knockout clones. For that purpose, genomic DNA was isolated from each cell clone and from HCT116/WT and HCT116/ΔLSR_{CRISPR} cells and a region including the guide RNA target site of the LSR gene was amplified by PCR and sequenced. In comparison to HCT116 wildtype cells, both the LF_N-Cas9- and the His-Cas9-derived cell clone exhibited a frameshift mutation (single-guanine insertion) directly within the Cas9 cleavage site of the LSR guide RNA target site. A single-thymine insertion was found in HCT116/ΔLSR_{CRISPR} cells at this position (**Figure 3B**). Both mutations lead to premature stop codons within the open reading frame (ORF) of LSR, resulting in a loss of expression of LSR.

We then examined whether CRISPA-derived LSR knockout cell clones became resistant towards CDT intoxication, either (I) via microscopic analysis of cell morphology or (II) by probing the ADP-ribosylation status of actin. Here, the *Clostridium botulinum* C2 toxin served as a control, as it enters the target cells independent of LSR (Papatheodorou et al., 2011). Consequently, HCT116/$\Delta LSR_{CRISPA/His\text{-}Cas9}$ and HCT116/$\Delta LSR_{CRISPA/LFN\text{-}Cas9}$ cells were intoxicated for 24 h with CDT or C2 toxin, followed by microscopic analysis of the cell morphology. Wildtype and HCT116/ΔLSR_{CRISPR} cells served as controls in the intoxication assay. As expected, cell rounding induced by the cell cytoskeleton-disrupting activity of CDT was observed in wildtype HCT116 cells, while LSR-deficient HCT116/ΔLSR_{CRISPR}, HCT116/$\Delta LSR_{CRISPA/His\text{-}Cas9}$ and HCT116/$\Delta LSR_{CRISPA/LFN\text{-}Cas9}$ cells were resistant to CDT (**Figure 4A**). All cells were readily intoxicated by C2 toxin (**Figure 4A**), indicating that general endocytic processes are still functional in these cells.

To substantiate our finding that HCT116/$\Delta LSR_{CRISPA/His\text{-}Cas9}$ and HCT116/$\Delta LSR_{CRISPA/LFN\text{-}Cas9}$ cells are resistant to CDT intoxication, we probed the ADP-ribosylation state of actin in lysates of CDT-treated and non-treated HCT116/$\Delta LSR_{CRISPA/His\text{-}Cas9}$ and HCT116/$\Delta LSR_{CRISPA/LFN\text{-}Cas9}$ cells using an *in vitro* actin-ADP-ribosylation assay. Importantly, the amount of actin amendable to sequential ADP-ribosylation upon CDT intoxication was only decreased in HCT116 wildtype but not in LSR-deficient HCT116/ΔLSR_{CRISPR}, HCT116/$\Delta LSR_{CRISPA/His\text{-}Cas9}$ and HCT116/$\Delta LSR_{CRISPA/LFN\text{-}Cas9}$ cells (**Figure 4B**).

To verify lack of the LSR receptor, we demonstrated that CDT is no longer able to bind to HCT116/ΔLSR_{CRISPR}, HCT116/$\Delta LSR_{CRISPA/His\text{-}Cas9}$ and HCT116/$\Delta LSR_{CRISPA/LFN\text{-}Cas9}$ cells. CDT is an AB-type binary toxin, where its B (binding/

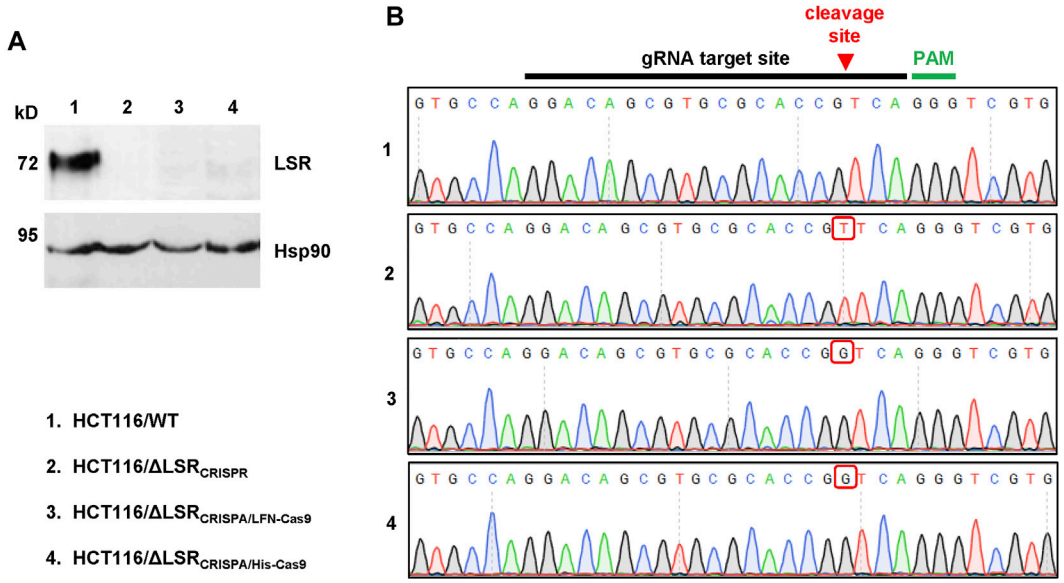

FIGURE 3 | Confirmation of the CRISPA-mediated LSR knockout mutation in HCT116 cells. **(A)** Immunoblot for the detection of LSR and Hsp90 (loading control) in whole-cell lysates of wildtype and LSR-deficient HCT116 cells (a detailed description of the cells is provided in the legend of numbers within the figure) **(B)** Chromatograms obtained by Sanger sequencing are shown, comprising the gRNA target site, the Cas9 cleavage site (red arrow) and the PAM sequence with the LSR gene of wildtype and LSR-deficient HCT116 cells (a detailed description of the cells is provided in the legend of numbers within the figure). Red box points towards a nucleotide insertion (mutation) that has been generated as a result of Cas9 cleavage and non-homologous end joining.

translocation) component (CDTb) mediates binding to LSR via a C-terminal receptor-binding domain (RBD) (Papatheodorou et al., 2013). Thus, the RBD of CDTb was labelled with the fluorescent dye DyLight 488 and its binding to suspension cells from wildtype and LSR-deficient HCT116/ΔLSR$_{CRISPR}$, HCT116/ΔLSR$_{CRISPA/His-Cas9}$ and HCT116/ΔLSR$_{CRISPA/LFN-Cas9}$ cells at 4°C (no endocytic uptake) was analyzed by flow cytometry. Only wildtype HCT116 cells exhibited an increase in cell surface-bound fluorescence after incubation with the fluorescent RBD, confirming that HCT116/ΔLSR$_{CRISPR}$, HCT116/ΔLSR$_{CRISPA/His-Cas9}$ and HCT116/ΔLSR$_{CRISPA/LFN-Cas9}$ cells are lacking LSR expression at the cell surface (**Figure 4C**).

In summary, our results showed that the CRISPA method allowed knockout of a specific gene in a human cell line.

Application of CRISPA to HEK293T Cells

We next sought to determine if the CRISPA approach is applicable in other cell lines and for different target genes. For that purpose, we used a HEK293T cell line stably expressing green-fluorescent protein (GFP). In a previous study it was already shown that HEK293T cells are susceptible to the lethal toxin of *B. anthracis* (Chavarría-Smith and Vance, 2013). Here, the target gene for the CRISPA approach was the non-native, chromosomally integrated coding sequence of GFP. Thus, GFP-expressing 293T cells (293T-GFP cells) transiently expressing a GFP-targeting gRNA were incubated with PA63 in combination with His- or LF$_N$-Cas9, respectively. Cells were then incubated for 6 days, due to long half-life (~26 h) of GFP in mammalian cells (Corish and Tyler-Smith, 1999) and GFP expression subsequently analyzed via flow cytometry. A clear decrease of the median fluorescence intensity (~15–25%) of the 293T GFP cell population was observed, only if PA63 was added together with 80 nM His-Cas9 and LF$_N$-Cas9, respectively (**Figure 5A**). Single treatment with either PA63 or any Cas9 variant did not affect GFP expression. This confirms cell entry of both Cas9 variants and consequently knockout of GFP via the PA transporter.

In order to estimate the genome editing efficiency in CRISPA-targeted 293T-GFP cells, a commercial kit-based T7 endonuclease 1 (T7EI) mismatch detection assay was performed. 293T-GFP cells transiently expressing a GFP-targeting gRNA were treated with PA63 and His- and LF$_N$-Cas9. 293T-GFP cells co-transfected with a Cas9-expressing plasmid or treated with PA63 together with commercial Cas9 protein were used as controls. We observed genome editing efficiencies of 3.6/3.8% for His-Cas9, 2.4/2.6% for LF$_N$-Cas9, 3.8/5.7% for commercial Cas9 (NEB), 20.4/20.5% for transfected Cas9 plasmid, and 7.8/8.8% for the internal control of the commercial kit (**Figure 5B**).

These results confirm that CRISPA approach can be applied to different cell lines and native or non-native target genes.

Application of CRISPA to Selectively Target EGF Receptors Expressing Cells

The modular CRISPA approach has advantages over other non-viral and transient Cas9 delivery methods, because it offers the possibility for a cell-specific genome engineering. Previous studies have shown that PA can be engineered to bind to other host entry receptors. For instance, a mutated PA83 variant unable to bind to its native receptors due to mutations

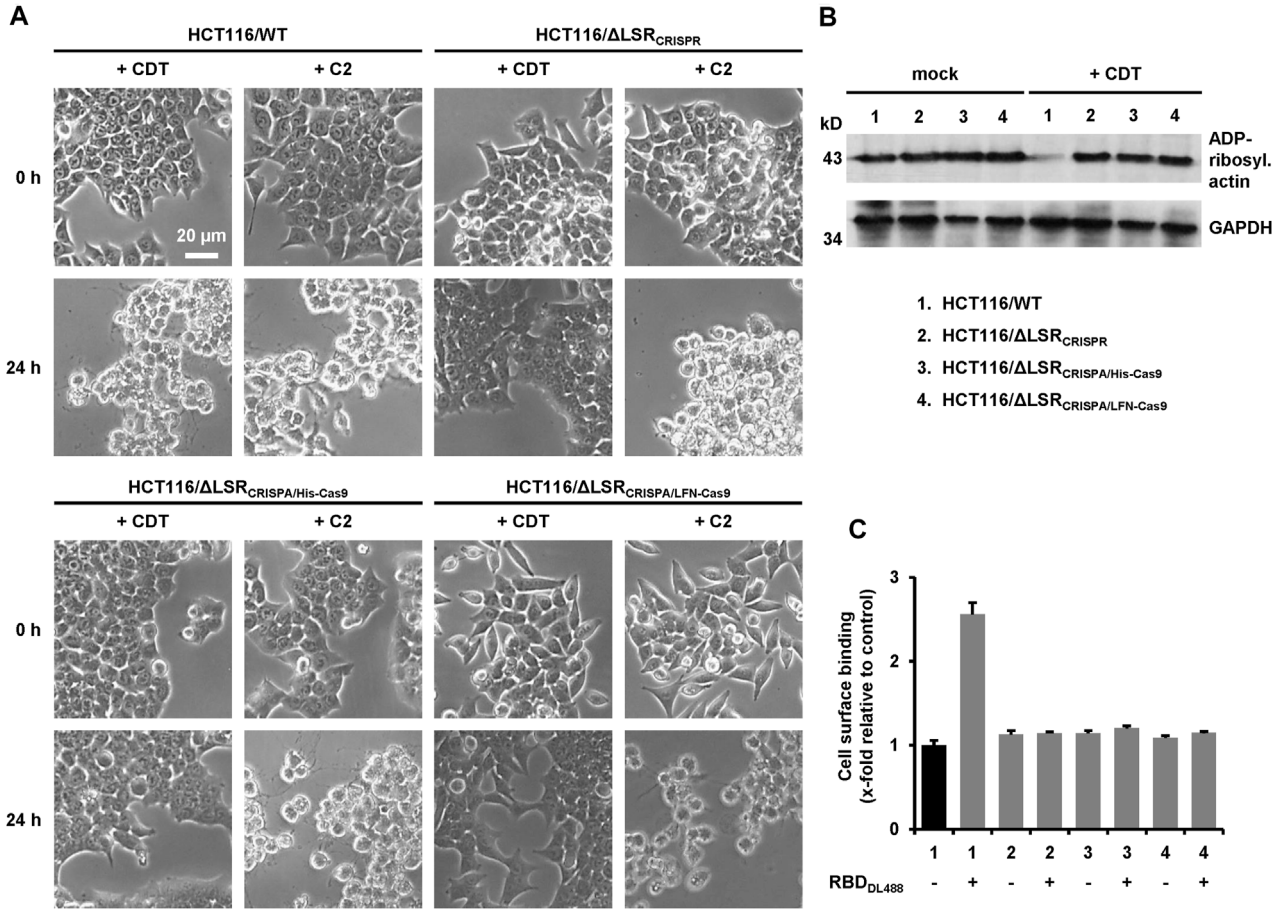

FIGURE 4 | Characterization of LSR-deficient HCT116 cells with CDT. **(A)** Wildtype HCT116 cells (HCT116/WT) as wells as LSR-deficient HCT116/ΔLSR$_{CRISPR}$, HCT116/ΔLSR$_{CRISPA/His-Cas9}$ and HCT116/ΔLSR$_{CRISPA/LFN-Cas9}$ cells were intoxicated with CDT (5 nM CDTa/1 nM CDTb) or C2 toxin (1 nM C2I/1.67 nM C2II) and images were obtained microscopically after 0 and 24 h to monitor morphological changes (cell rounding) of the cells. A scale bar representative for all images is shown in the upper left image **(B)** Wildtype and LSR-deficient HCT116 cells as described in the legend of numbers were intoxicated for 24 h with CDT (5 nM CDTa/1 nM CDTb) or were left untreated (mock), followed by a sequential ADP-ribosylation assay. Immunodetection of GAPDH served as loading control **(C)** Binding of DyLight 488-labeled CDTb-RBD (RBD$_{DL488}$) on wildtype and LSR-deficient HCT116 cells as described in the legend of numbers in **(B)** was analyzed via FACS and fluorescence intensity (cell surface-binding) is shown in the bar diagram (n = 3, ±SD) as x-fold relative to control (black bar; mock-treated wildtype HCT116 cells), which was set to 1.

in the receptor-binding domain (termed mPA83), was fused to EGF (epidermal growth factor) and thus redirected to EGF receptors (EGFR), which are highly expressed in many cancer cells (Mechaly et al., 2012; Zahaf et al., 2017).

To confirm that mPA83-EGF selectively targets EGFR-positive cells, we used A431 and HeLa cells, which are characterized by high (A431 cells) and low (HeLa cells) levels of EGFR expression, respectively (Zhang et al., 2015). Both cell lines were intoxicated with 20 nM mPA83-EGF as the EGFR-specific transporter and 10 nM LF_N-DTA as the toxic cargo component. In LF_N-DTA, the N-terminus of the anthrax toxin lethal factor (LF_N) is fused to the enzyme portion of the diphtheria toxin (DTA), which ADP-ribosylates the eukaryotic elongation factor 2 (eEF2) and thereby inhibits protein synthesis (Milne et al., 1995). Measuring the cell viability after 24 h of intoxication revealed that A431 (**Supplementary Figure S2**; black bars), but not HeLa cells (**Supplementary Figure S2**; white bars), were intoxicated with mPA83-EGF plus LF_N-DTA. Importantly, a decrease in cell viability in both cell lines was obvious with 20% (v/v) DMSO or when cells were intoxicated with positive controls (10 nM native diphtheria toxin (DT) and the combinations of 20 nM PA83 or 20 nM PA63 plus 10 nM LF_N-DTA, respectively), but not with negative controls (the combination of 20 nM mPA83 alone plus 10 nM LF_N-DTA or the single toxin components) (**Supplementary Figure S2**).

These results demonstrate that cell specificity of the CRISPA approach can be achieved by the use of a mutated PA variant fused to a cell surface-specific ligand.

DISCUSSION

CRISPR/Cas9 genome engineering requires the formation of a gRNA:Cas9 complex directly at the target gene in the cell nucleus. Nowadays, a plethora of methods are available for the viral or non-viral delivery of both components into target cells, each with

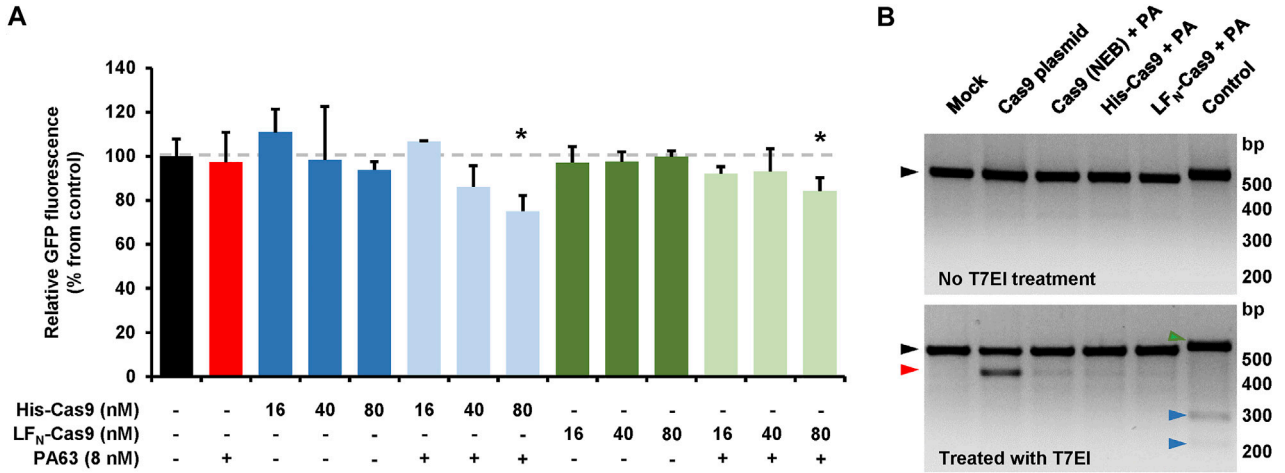

FIGURE 5 | CRISPA-mediated knockout of GFP in 293T GFP cells. **(A)** 293T GFP cells transfected with a gRNA-expressing plasmid targeting GFP were incubated the following day either with indicated concentrations of His- or LF_N-Cas9 alone (dark colored blue and green bars) or together with 8 nM PA63 (light colored blue and green bars). Red bar indicates cells treated with 8 nM PA63 only. Black bar represents mock-treated cells (control). Bar diagram shows the median GFP fluorescence of cells after 6 days of incubation relative to control, which was set to 100%. Results shown are mean values calculated from three samples performed in parallel and with error bars indicating $n = 3 \pm$ SD (*$p < 0.05$) **(B)** T7 endonuclease I mismatch detection assay. 293T-GFP cells transfected with a plasmid encoding a GFP-specific gRNA were incubated for 24 h with 10 nM PA63 (PA) together with 100 nM His- and LF_N-Cas9, respectively, or a commercial Cas9 protein carrying an N-terminal His-tag (denoted as Cas9 (NEB)). Cells co-transfected with a Cas9-expressing plasmid (Cas9 plasmid) served as positive control and cells without Cas9 as negative control (mock). A T7 endonuclease I (T7EI) mismatch detection assay was performed with all cell populations and subsequently analyzed by agarose gel electrophoresis. Black triangles indicate PCR-derived DNA templates from all Cas9-treated cell populations with (lower panel) or without (upper panel) T7EI treatment. The red triangle indicates the T7EI-derived cleavage product in the Cas9-treated cell populations. Green and blue triangles indicate DNA template (516 bp) and cleavage products (225 and 291 bp) of the internal kit control (control), respectively. bp, base pairs **(A, B)** Experiments were performed at least twice with identical results.

its own specific advantages and disadvantages (Liu et al., 2017). Here, we describe a novel, modular CRISPA approach for the transient, non-viral delivery of Cas9 protein into mammalian cells via the transport machinery (PA) of the anthrax toxin.

As proof-of-concept for this CRISPA approach, we knocked out the gene encoding LSR in HCT116 colon cancer cells. Besides its physiological roles in lipoprotein uptake and stability of tricellular junctions, LSR acts also as entry receptor for the *C. difficile* binary toxin CDT (Papatheodorou et al., 2011, Papatheodorou et al., 2018). The latter helped us in selecting homozygous/biallelic CRISPA-derived, LSR-deficient HCT116 cells that are resistant to CDT. CRISPA introduced a nucleotide insertion (frameshift mutation) exactly at the Cas9 cleavage site, targeted by the LSR-specific gRNA. Transfer of the CRISPA approach to 293T cells stably expressing GFP, indicates that the CRISPA approach may be applicable to a wide range of target cells and genes. In order to reach cell specificity, the receptor-binding domain of PA has to be replaced with the respective protein ligand of a given cell surface-marker.

We used two different recombinant Cas9 variants for PA-mediated entry into target cells. One of them already carried a His6-tag at its N-terminus and the other Cas9 variant (with a His6-tag at its C-terminus) was fused to the N-terminus of the anthrax lethal factor (LF_N). Notably, the His6-tag is very convenient for purification of recombinant Cas9 proteins and, if preferred, various His6-tagged Cas9 variants are commercially available. Both N-terminal sequences (His6-tag and LF_N) enable the interaction with and translocation of cargo proteins through the PA pore formed in endosomal membranes upon acidification of the endosomal lumen (Rabideau and Pentelute, 2016). In our hands, both N-termini showed similar efficiencies in knocking out GFP in 293T-GFP cells, as estimated by a T7 endonuclease I mismatch detection assay.

The use of mPA83-EGF instead of PA in our CRISPA approach would thus enable a selective genome engineering in EGFR-expressing cells. Accordingly, fusions of mPA83 with other receptor ligands will allow CRISPA to adapt to specific cell types. Other non-viral and transient CRISPR/Cas9 delivery systems, such as cell penetrating peptides, lack this possibility. Verdurmen and others succeeded in retargeting mPA83 to epithelial adhesion molecule (EpCAM)-expressing cells by fusion with an EpCAM-targeting designed ankyrin repeat protein (DARPin) (Verdurmen et al., 2015). Such cell-specific CRISPA approaches would pave the way for *in vivo* clinical applications.

It has been shown by several groups that *Streptococcus pyogenes* Cas9 does not dissociate from the cleaved DNA due to an extremely slow rate of turnover (Sternberg et al., 2014; Richardson et al., 2016; Jones et al., 2017; Gong et al., 2018; Raper et al., 2018). We therefore speculate that this prominent feature of *S. pyogenes* Cas9 might explain the rather low gene-editing efficiency that we calculated via the T7EI assay for our CRISPA approach in dividing cells. Yourik and others reported the first multiple-turnover Cas9 from *Staphylococcus aureus* and speculated that a faster rate of turnover by *S. aureus* Cas9 should result in more attempts to re-introduce the double-stranded DNA break at the site of interest and thus might result in

a higher degree of editing (Yourik et al., 2019). We are planning to test this Cas9 ortholog in a follow-up study, whether it is more efficient in gene-editing after delivery into cells via PA.

Inefficient unfolding prior and/or refolding after transport of Cas9 into the cytosol, as well as quick degradation of Cas9 in the cell might also contribute to the rather low gene-editing efficiency of our CRISPA approach. However, the CRISPA approach should also function with hyper-accurate Cas9 variants or even with Cas9 alternatives, such as Cpf1, Cas12a and Cas12b, and smaller Cas9 orthologues (e.g. CjCas9) (Broeders et al., 2020). Future studies are needed to clarify, whether smaller or stabilized Cas9 variants might increase the efficiency of the CRISPA approach. In addition, these Cas9 variations might help to reduce off-target effects.

Transient and non-viral delivery of gRNA molecules into cells remains a challenge. One option is the *in vitro* assembly of ribonuclearprotein (RNP) complexes between the Cas9 protein and the guide RNA (DeWitt et al., 2017). However, such Cas9-gRNA-RNPs are delivered transiently into cells for instance via electroporation, which is rather unspecific and not applicable in a clinical setting. However, it was reported that Cas9 protein and single guide RNA can be coupled to cell-penetrating peptides (CPPs) to yield RNP nanoparticles, which led to efficient gene disruption in treated cells (Ramakrishna et al., 2014). In comparison, the CRISPA approach most likely lacks the possibility to transport such RNP nanoparticles into cells, because the translocation across the channel formed by PA in endosomes requires unfolding of cargo proteins.

However, a disarmed anthrax toxin was used by Dyer and others for the cytosolic delivery of antisense oligonucleotides (ASOs) and siRNA (Dyer et al., 2015). Transport of ASOs or siRNA via PA was achieved via LF_N fusions of either *Saccharomyces cerevisiae* GAL4 or human protein kinase R (PKR), both of which are capable of binding dsDNA or dsRNA, respectively. But it remained unclear, how the ASOs and siRNA were transported through the channel, given the fact that the pore diameter of the channel is too small to allow the transport of GAL4:dsDNA or PKR:dsRNA complexes in an unfolded state.

Nevertheless, piggyback-transport of sgRNA through the PA channel via a sgRNA-binding protein fused to LF_N would allow simultaneous delivery of Cas9 and sgRNA into target cells. However, in its current state, the CRISPA approach needs to be combined with other viral or non-viral methods that are capable of delivering the single guide RNA into cells. Notably, a transient toxin-based siRNA delivery strategy was developed just recently on the basis of an attenuated diphtheria toxin (Arnold et al., 2020).

The approach presented in this study represents an additional step towards safe translation of the powerful CRISPR/Cas9 genome engineering technology into clinics, especially with respect to *ex vivo* applications. Using CRISPA cell-type specificity in transient systems may reduce off-target effects. Moreover, the CRISPA approach provides another example of the power of bacterial protein toxins as cellular transport systems and potential therapeutic agents.

DATA AVAILABILITY STATEMENT

The raw data supporting the conclusions of this article will be made available by the authors, without undue reservation.

AUTHOR CONTRIBUTIONS

All authors listed have made a substantial, direct, and intellectual contribution to the work and approved it for publication.

FUNDING

KMJS is supported by the German Research Foundation (DFG; SP1600/4-1) and the BMBF (IMMUNOMOD). FK, HB and KMJS are further funded by the CRC 1279. MH and MF are members of the International Graduate School for Molecular Medicine, Ulm. The work in the Barth group was supported by the German Research Foundation project number 316249678-CRC 1279 (project C02).

ACKNOWLEDGMENTS

The authors would like to thank Ina Felix for help in protein purification, Anna Anastasia for technical assistance, Amani Alharbi for help in the initial phase of this project, and Klaus Aktories (University of Freiburg, Germany) for critical reading of the manuscript and, together with R. John Collier (Harvard Medical School, Boston, United States), for sharing material. We also thank the staff of the Core Facility Flow Cytometry of the University of Ulm for help in cell sorting.

SUPPLEMENTARY MATERIAL

The Supplementary Material for this article can be found online at: https://www.frontiersin.org/articles/10.3389/fphar.2021.770283/full#supplementary-material

REFERENCES

Arnold, A. E., Smith, L. J., Beilhartz, G. L., Bahlmann, L. C., Jameson, E., Melnyk, R. A., et al. (2020). Attenuated Diphtheria Toxin Mediates siRNA Delivery. *Sci. Adv.* 6. doi:10.1126/sciadv.aaz4848

Arora, N., and Leppla, S. H. (1994). Fusions of Anthrax Toxin Lethal Factor with Shiga Toxin and Diphtheria Toxin Enzymatic Domains Are Toxic to Mammalian Cells. *Infect. Immun.* 62, 4955–4961. doi:10.1128/IAI.62.11.4955-4961.1994

Arora, N., and Leppla, S. H. (1993). Residues 1-254 of Anthrax Toxin Lethal Factor Are Sufficient to Cause Cellular Uptake of Fused Polypeptides. *J. Biol. Chem.* 268, 3334–3341. doi:10.1016/s0021-9258(18)53698-x

Barth, H., Blocker, D., Behlke, J., Bergsma-Schutter, W., Brisson, A., Benz, R., et al. (2000). Cellular Uptake of Clostridium Botulinum C2 Toxin Requires Oligomerization and Acidification. *J. Biol. Chem.* 275, 18704–18711. doi:10.1074/jbc.M000596200

Beilhartz, G. L., Sugiman-Marangos, S. N., and Melnyk, R. A. (2017). Repurposing Bacterial Toxins for Intracellular Delivery of Therapeutic Proteins. *Biochem. Pharmacol.* 142, 13–20. doi:10.1016/j.bcp.2017.04.009

Beitzinger, C., Stefani, C., Kronhardt, A., Rolando, M., Flatau, G., Lemichez, E., et al. (2012). Role of N-Terminal His6-Tags in Binding and Efficient Translocation of Polypeptides into Cells Using Anthrax Protective Antigen (PA). *PLoS One* 7, e46964. doi:10.1371/journal.pone.0046964

Blanke, S. R., Milne, J. C., Benson, E. L., and Collier, R. J. (1996). Fused Polycationic Peptide Mediates Delivery of Diphtheria Toxin A Chain to the Cytosol in the Presence of Anthrax Protective Antigen. *Proc. Natl. Acad. Sci. U. S. A.* 93, 8437–8442. doi:10.1073/pnas.93.16.8437

Blöcker, D., Behlke, J., Aktories, K., and Barth, H. (2001). Cellular Uptake of the *Clostridium perfringens* Binary iota-toxin. *Infect. Immun.* 69, 2980–2987. doi:10.1128/IAI.69.5.2980-2987.2001

Broeders, M., Herrero-Hernandez, P., Ernst, M. P. T., van der Ploeg, A. T., and Pijnappel, W. W. M. P. (2020). Sharpening the Molecular Scissors: Advances in Gene-Editing Technology. *iScience* 23, 100789. doi:10.1016/j.isci.2019.100789

Chavarría-Smith, J., and Vance, R. E. (2013). Direct Proteolytic Cleavage of NLRP1B Is Necessary and Sufficient for Inflammasome Activation by Anthrax Lethal Factor. *Plos Pathog.* 9, e1003452. doi:10.1371/journal.ppat.1003452

Corish, P., and Tyler-Smith, C. (1999). Attenuation of green Fluorescent Protein Half-Life in Mammalian Cells. *Protein Eng.* 12, 1035–1040. doi:10.1093/protein/12.12.1035

DeWitt, M. A., Corn, J. E., and Carroll, D. (2017). Genome Editing via Delivery of Cas9 Ribonucleoprotein. *Methods* 121-122, 9–15. doi:10.1016/j.ymeth.2017.04.003

Dull, T., Zufferey, R., Kelly, M., Mandel, R. J., Nguyen, M., Trono, D., et al. (1998). A Third-Generation Lentivirus Vector with a Conditional Packaging System. *J. Virol.* 72, 8463–8471. doi:10.1128/jvi.72.11.8463-8471.1998

Dyer, P. D. R., Shepherd, T. R., Gollings, A. S., Shorter, S. A., Gorringe-Pattrick, M. A. M., Tang, C. K., et al. (2015). Disarmed Anthrax Toxin Delivers Antisense Oligonucleotides and siRNA with High Efficiency and Low Toxicity. *J. Control Release* 220, 316–328. doi:10.1016/j.jconrel.2015.10.054

Ernst, K., Schmid, J., Beck, M., Hägele, M., Hohwieler, M., Hauff, P., et al. (2017). Hsp70 Facilitates Trans-membrane Transport of Bacterial ADP-Ribosylating Toxins into the Cytosol of Mammalian Cells. *Sci. Rep.* 7, 2724. doi:10.1038/s41598-017-02882-y

Gong, S., Yu, H. H., Johnson, K. A., and Taylor, D. W. (2018). DNA Unwinding Is the Primary Determinant of CRISPR-Cas9 Activity. *Cell Rep* 22, 359–371. doi:10.1016/j.celrep.2017.12.041

Hemmasi, S., Czulkies, B. A., Schorch, B., Veit, A., Aktories, K., and Papatheodorou, P. (2015). Interaction of the *Clostridium difficile* Binary Toxin CDT and its Host Cell Receptor, Lipolysis-Stimulated Lipoprotein Receptor (LSR). *J. Biol. Chem.* 290, 14031–14044. doi:10.1074/jbc.M115.650523

Hirakawa, M. P., Krishnakumar, R., Timlin, J. A., Carney, J. P., and Butler, K. S. (2020). Gene Editing and CRISPR in the Clinic: Current and Future Perspectives. *Biosci. Rep.* 40. doi:10.1042/BSR20200127

Jones, D. L., Leroy, P., Unoson, C., Fange, D., Ćurić, V., Lawson, M. J., et al. (2017). Kinetics of dCas9 Target Search in *Escherichia coli*. *Science* 357, 1420–1424. doi:10.1126/science.aah7084

Kaiser, E., Kroll, C., Ernst, K., Schwan, C., Popoff, M., Fischer, G., et al. (2011). Membrane Translocation of Binary Actin-ADP-Ribosylating Toxins from *Clostridium difficile* and *Clostridium perfringens* Is Facilitated by Cyclophilin A and Hsp90. *Infect. Immun.* 79, 3913–3921. doi:10.1128/IAI.05372-11

Koepke, L., Winter, B., Grenzner, A., Regensburger, K., Engelhart, S., van der Merwe, J. A., et al. (2020). An Improved Method for High-Throughput Quantification of Autophagy in Mammalian Cells. *Sci. Rep.* 10, 12241. doi:10.1038/s41598-020-68607-w

Lang, A. E., Schmidt, G., Schlosser, A., Hey, T. D., Larrinua, I. M., Sheets, J. J., et al. (2010). Photorhabdus Luminescens Toxins ADP-Ribosylate Actin and RhoA to Force Actin Clustering. *Science* 327, 1139–1142. doi:10.1126/science.1184557

Lino, C. A., Harper, J. C., Carney, J. P., and Timlin, J. A. (2018). Delivering CRISPR: a Review of the Challenges and Approaches. *Drug Deliv.* 25, 1234–1257. doi:10.1080/10717544.2018.1474964

Liu, C., Zhang, L., Liu, H., and Cheng, K. (2017). Delivery Strategies of the CRISPR-Cas9 Gene-Editing System for Therapeutic Applications. *J. Control Release* 266, 17–26. doi:10.1016/j.jconrel.2017.09.012

Mali, P., Yang, L., Esvelt, K. M., Aach, J., Guell, M., DiCarlo, J. E., et al. (2013). RNA-guided Human Genome Engineering via Cas9. *Science* 339, 823–826. doi:10.1126/science.1232033

Marr, R. A., Guan, H., Rockenstein, E., Kindy, M., Gage, F. H., Verma, I., et al. (2004). Neprilysin Regulates Amyloid Beta Peptide Levels. *J. Mol. Neurosci.* 22, 5–11. doi:10.1385/JMN:22:1-2:5

Mechaly, A., McCluskey, A. J., and Collier, R. J. (2012). Changing the Receptor Specificity of Anthrax Toxin. *MBio* 3. doi:10.1128/mBio.00088-12

Milne, J. C., Blanke, S. R., Hanna, P. C., and Collier, R. J. (1995). Protective Antigen-Binding Domain of Anthrax Lethal Factor Mediates Translocation of a Heterologous Protein Fused to its Amino- or Carboxy-Terminus. *Mol. Microbiol.* 15, 661–666. doi:10.1111/j.1365-2958.1995.tb02375.x

Moayeri, M., and Leppla, S. H. (2009). Cellular and Systemic Effects of Anthrax Lethal Toxin and Edema Toxin. *Mol. Aspects Med.* 30, 439–455. doi:10.1016/j.mam.2009.07.003

Moayeri, M., Leppla, S. H., Vrentas, C., Pomerantsev, A. P., and Liu, S. (2015). Anthrax Pathogenesis. *Annu. Rev. Microbiol.* 69, 185–208. doi:10.1146/annurev-micro-091014-104523

Nelson, C. E., and Gersbach, C. A. (2016). Engineering Delivery Vehicles for Genome Editing. *Annu. Rev. Chem. Biomol. Eng.* 7, 637–662. doi:10.1146/annurev-chembioeng-080615-034711

Papatheodorou, P., Barth, H., Minton, N., and Aktories, K. (2018). Cellular Uptake and Mode-Of-Action of *Clostridium difficile* Toxins. *Adv. Exp. Med. Biol.* 1050, 77–96. doi:10.1007/978-3-319-72799-8_6

Papatheodorou, P., Carette, J. E., Bell, G. W., Schwan, C., Guttenberg, G., Brummelkamp, T. R., et al. (2011). Lipolysis-stimulated Lipoprotein Receptor (LSR) Is the Host Receptor for the Binary Toxin *Clostridium difficile* Transferase (CDT). *Proc. Natl. Acad. Sci. U. S. A.* 108, 16422–16427. doi:10.1073/pnas.1109772108

Papatheodorou, P., Hornuss, D., Nölke, T., Hemmasi, S., Castonguay, J., Picchianti, M., et al. (2013). *Clostridium difficile* Binary Toxin CDT Induces Clustering of the Lipolysis-Stimulated Lipoprotein Receptor into Lipid Rafts. *MBio* 4, e00244–13. doi:10.1128/mBio.00244-13

Piot, N., van der Goot, F. G., and Sergeeva, O. A. (2021). Harnessing the Membrane Translocation Properties of AB Toxins for Therapeutic Applications. *Toxins (Basel)* 13, 36. doi:10.3390/toxins13010036

Rabideau, A. E., and Pentelute, B. L. (2016). Delivery of Non-native Cargo into Mammalian Cells Using Anthrax Lethal Toxin. *ACS Chem. Biol.* 11, 1490–1501. doi:10.1021/acschembio.6b00169

Ramakrishna, S., Kwaku Dad, A. B., Beloor, J., Gopalappa, R., Lee, S. K., and Kim, H. (2014). Gene Disruption by Cell-Penetrating Peptide-Mediated Delivery of Cas9 Protein and Guide RNA. *Genome Res.* 24, 1020–1027. doi:10.1101/gr.171264.113

Raper, A. T., Stephenson, A. A., and Suo, Z. (2018). Functional Insights Revealed by the Kinetic Mechanism of CRISPR/Cas9. *J. Am. Chem. Soc.* 140, 2971–2984. doi:10.1021/jacs.7b13047

Richardson, C. D., Ray, G. J., DeWitt, M. A., Curie, G. L., and Corn, J. E. (2016). Enhancing Homology-Directed Genome Editing by Catalytically Active and Inactive CRISPR-Cas9 Using Asymmetric Donor DNA. *Nat. Biotechnol.* 34, 339–344. doi:10.1038/nbt.3481

Schneider, C. A., Rasband, W. S., and Eliceiri, K. W. (2012). NIH Image to ImageJ: 25 Years of Image Analysis. *Nat. Methods* 9, 671–675. doi:10.1038/nmeth.2089

Schwan, C., Nölke, T., Kruppke, A. S., Schubert, D. M., Lang, A. E., and Aktories, K. (2011). Cholesterol- and Sphingolipid-Rich Microdomains Are Essential for Microtubule-Based Membrane Protrusions Induced by *Clostridium difficile* Transferase (CDT). *J. Biol. Chem.* 286, 29356–29365. doi:10.1074/jbc.M111.261925

Sharma, O., and Collier, R. J. (2014). Polylysine-mediated Translocation of the Diphtheria Toxin Catalytic Domain through the Anthrax Protective Antigen Pore. *Biochemistry* 53, 6934–6940. doi:10.1021/bi500985v

Singh, Y., Chaudhary, V. K., and Leppla, S. H. (1989). A Deleted Variant of Bacillus Anthracis Protective Antigen Is Non-toxic and Blocks Anthrax Toxin Action *In Vivo*. *J. Biol. Chem.* 264, 19103–19107. doi:10.1016/s0021-9258(19)47273-6

Sternberg, S. H., Redding, S., Jinek, M., Greene, E. C., and Doudna, J. A. (2014). DNA Interrogation by the CRISPR RNA-Guided Endonuclease Cas9. *Nature* 507, 62–67. doi:10.1038/nature13011

Sterthoff, C., Lang, A. E., Schwan, C., Tauch, A., and Aktories, K. (2010). Functional Characterization of an Extended Binding Component of the Actin-ADP-Ribosylating C2 Toxin Detected in Clostridium Botulinum Strain (C) 2300. *Infect. Immun.* 78, 1468–1474. doi:10.1128/IAI.01351-09

Tonello, F., Naletto, L., Romanello, V., Dal Molin, F., and Montecucco, C. (2004). Tyrosine-728 and Glutamic Acid-735 Are Essential for the Metalloproteolytic Activity of the Lethal Factor of Bacillus Anthracis. *Biochem. Biophys. Res. Commun.* 313, 496–502. doi:10.1016/j.bbrc.2003.11.134

van der Goot, G., and Young, J. A. (2009). Receptors of Anthrax Toxin and Cell Entry. *Mol. Aspects Med.* 30, 406–412. doi:10.1016/j.mam.2009.08.007

Verdurmen, W. P., Luginbühl, M., Honegger, A., and Plückthun, A. (2015). Efficient Cell-specific Uptake of Binding Proteins into the Cytoplasm through Engineered Modular Transport Systems. *J. Control Release* 200, 13–22. doi:10.1016/j.jconrel.2014.12.019

Wang, L., Zheng, W., Liu, S., Li, B., and Jiang, X. (2019). Delivery of CRISPR/Cas9 by Novel Strategies for Gene Therapy. *Chembiochem* 20, 634–643. doi:10.1002/cbic.201800629

Young, J. A., and Collier, R. J. (2007). Anthrax Toxin: Receptor Binding, Internalization, Pore Formation, and Translocation. *Annu. Rev. Biochem.* 76, 243–265. doi:10.1146/annurev.biochem.75.103004.142728

Yourik, P., Fuchs, R. T., Mabuchi, M., Curcuru, J. L., and Robb, G. B. (2019). *Staphylococcus aureus* Cas9 Is a Multiple-Turnover Enzyme. *Rna* 25, 35–44. doi:10.1261/rna.067355.118

Zahaf, N. I., Lang, A. E., Kaiser, L., Fichter, C. D., Lassmann, S., McCluskey, A., et al. (2017). Targeted Delivery of an ADP-Ribosylating Bacterial Toxin into Cancer Cells. *Sci. Rep.* 7, 41252. doi:10.1038/srep41252

Zhang, F., Wang, S., Yin, L., Yang, Y., Guan, Y., Wang, W., et al. (2015). Quantification of Epidermal Growth Factor Receptor Expression Level and Binding Kinetics on Cell Surfaces by Surface Plasmon Resonance Imaging. *Anal. Chem.* 87, 9960–9965. doi:10.1021/acs.analchem.5b02572

Zuris, J. A., Thompson, D. B., Shu, Y., Guilinger, J. P., Bessen, J. L., Hu, J. H., et al. (2015). Cationic Lipid-Mediated Delivery of Proteins Enables Efficient Protein-Based Genome Editing *In Vitro* and *In Vivo*. *Nat. Biotechnol.* 33, 73–80. doi:10.1038/nbt.3081

Conflict of Interest: The authors declare that the research was conducted in the absence of any commercial or financial relationships that could be construed as a potential conflict of interest.

Publisher's Note: All claims expressed in this article are solely those of the authors and do not necessarily represent those of their affiliated organizations, or those of the publisher, the editors and the reviewers. Any product that may be evaluated in this article, or claim that may be made by its manufacturer, is not guaranteed or endorsed by the publisher.

frontiers in Pharmacology

ORIGINAL RESEARCH
published: 25 November 2021
doi: 10.3389/fphar.2021.791847

Synergistic Effect of Proteinase Activity by Purification and Identification of Toxic Protease From *Nemopilema nomurai*

Chunlin Yu[1,2], *Rongfeng Li*[1,3], *Xiujing Yin*[1,2], *Huahua Yu*[1,3]* *and Pengcheng Li*[1,3]*

[1]CAS and Shandong Province Key Laboratory of Experimental Marine Biology, Center for Ocean Mega-Science, Institute of Oceanology, Chinese Academy of Sciences, Qingdao, Qingdao, China, [2]College of Earth and Planetary Sciences, University of Chinese Academy of Sciences, Beijing, China, [3]Laboratory for Marine Drugs and Bioproducts, Pilot National Laboratory for Marine Science and Technology, Qingdao, China

Scyphozoan *Nemopilema nomurai* envenomation is an unresolved threat to human health in Asian waters. *Nemopilema nomurai* venom metalloproteinases show important toxicities in skin damage and inflammation, but there is still no purified protein for further studies. In this study, high proteinase activity fractions in tentacle autolysis were isolated by ammonium sulfate precipitation, DEAE Sepharose Fast Flow, and Superdex 75 chromatography successively. Purification was guided by azocasein hydrolysis activity and SDS-PAGE. The final products were analyzed by LC-MS/MS. Four elution peaks purified by Superdex 75 chromatography had multiple protein bands but did not show proteinase activity. These fractions would recover proteinase activity after mixing again. Regulation mechanisms were speculated as binding metalloproteinase regulator or disaggregating metalloproteinase inhibitor by LC-MS/MS analysis. For the first time, a synergistic effect in *N. nomurai* proteinase activity was found in the purification process.

Keywords: jellyfish *Nemopilema nomurai*, purification, protease, metalloprotease, synergistic effect

OPEN ACCESS

Edited by:
Zhijian Cao,
Wuhan University, China

Reviewed by:
Aifeng Li,
Ocean University of China, China
Anwar Ullah,
COMSATS Institute of Information Technology, Pakistan

***Correspondence:**
Huahua Yu
yuhuahua@qdio.ac.cn
Pengcheng Li
pcli@qdio.ac.cn

Specialty section:
This article was submitted to Pharmacology of Ion Channels and Channelopathies, a section of the journal Frontiers in Pharmacology

Received: *09 October 2021*
Accepted: *02 November 2021*
Published: *25 November 2021*

Citation:
Yu C, Li R, Yin X, Yu H and Li P (2021) Synergistic Effect of Proteinase Activity by Purification and Identification of Toxic Protease From Nemopilema nomurai. *Front. Pharmacol. 12:791847. doi: 10.3389/fphar.2021.791847*

INTRODUCTION

Jellyfish sting is an important health problem for persons engaged in marine activities, and the symptoms of victims range from itch, pain, inflammation, and edema to cutaneous necrosis and even death (Cegolon et al., 2013). Venom from jellyfish *Nemopilema nomurai* is responsible for the symptoms of jellyfish envenomation. *N. nomurai* is widely distributed in the Yellow Sea and East China Sea every summer season (Sun et al., 2015a; Sun et al., 2015b). It has been regarded as a synonymy of *Stomolophus meleagris* in some research literatures (Liumin et al., 2011). In recent decades, blooms of *N. nomurai* have been of frequent occurrence and became more of a threat to humans in Chinese, Japanese, and Korean waters (Kawahara et al., 2006; Liumin et al., 2011; Xu et al., 2013; Yoon et al., 2014; Sun et al., 2015a; Sun et al., 2015b). This makes *N. nomurai* venom research more necessary and important.

Jellyfish *N. nomurai* venom is a complex mixture of peptides and proteins (Li et al., 2014) and has a variety of bioactivities such as hemolytic and antioxidant activities (Yu et al., 2005; Li et al., 2012; Li et al., 2013; Yue et al., 2021). According to the proteome and transcriptome analyses, metalloproteinases are main components in *N. nomurai* venom (Li et al., 2014). The crude venom extracted from nematocysts was identified to have significant metalloproteinase activity (Yue et al., 2017b) and played an important role in pro-inflammatory activity, edematogenic effects,

lethality, and cytotoxicity (Lee et al., 2011; Yue et al., 2017b; Li et al., 2018; Yue et al., 2021). Through chromatography, some *N. nomurai* toxins were partially purified, such as hemolytic toxin SmTX (Li et al., 2013) and lethal toxin NnLF (Li et al., 2020). Protease in *N. nomurai* venom, isolated and identified by zymogram, was identified to contain many other protein components (Yue et al., 2017a). A purified protease with only one SDS-PAGE band was isolated from *N. nomurai* venom by HiPrep 26/60 Sephacryl S-200 column, which did not match any high similarity protease in LC-MS/MS analysis (Yue et al., 2021).

Several protein toxins were successfully purified from jellyfish venom by chromatography, such as cytotoxin CcTX-1 and antioxidant protein SmP90 (Rottini et al., 1995; Yang et al., 2003; Helmholz et al., 2008; Lassen et al., 2011; Lassen et al., 2012; Li et al., 2012; Horiike et al., 2015). But more toxins from jellyfish were partially purified (Bloom et al., 1998; Chung et al., 2001; Sanchez-Rodriguez et al., 2006; Li et al., 2011; Li et al., 2013; Li et al., 2018; Li et al., 2020). For example, Rastogi et al. (2017) identified a 95 kDa metalloproteinase in a partially purified product of *Rhizostoma pulmo* (barrel jellyfish) venom. But there are still no single metalloproteinase purified from the jellyfish venom, which limits the analysis of its molecular structure and action mechanism. In addition to the small amount of toxin and instability, synergistic effects of toxins may increase the difficulty of single metalloproteinase purification.

Synergistic effects in snake venom have been demonstrated to occur between different toxins with different patterns owing to the amounts of toxin purification, characterization, and pathological researches (Doley and Kini, 2009; Xiong and Huang, 2018). The synergetic pain activation mechanism of scorpion toxin BmP01 was deeply revealed based on its molecular structure researches (Yang et al., 2017). Metalloproteinases in snake venom showed different interactions to other subunits and components (Doley and Kini, 2009; Xiong and Huang, 2018). However, there is no report on the synergistic effects of jellyfish toxins, and the regulation mechanism of jellyfish venom metalloproteinase has not been revealed.

In the present study, the toxic protease components in *N. nomurai* tentacle tissue autolysis were purified by activity-guided chromatography. Protein components of the final purified products, which showed a synergistic effect of proteinase activity, were identified by LC-MS/MS analysis to explore the possible active components and regulation mechanism. This study may provide references for further research on the NnVMP and therapy of jellyfish stings.

MATERIALS AND METHODS

Venomous Sample Collection

The venomous sample used in protease purification was collected from the supernatant of *N. nomurai* tentacle autolysis. *N. nomurai* was collected from the coastal waters of Huangshan Village, in the Yellow Sea, on August 29, 2018. Tentacle tissues were cut off from *N. nomurai* and immediately transported back to the laboratory in an ice bath. Every package of the samples was a mixture of multiple *N. nomurai* individuals. The tentacle tissues were mixed with 50% (v/v) precooled filtered natural seawater and autolyzed at 4°C for 3 days. Then, autolysis solutions were centrifuged at 3000 *g* for 15 min. The supernatant was collected as venomous samples for protease purification. Protein concentrations were determined using FolinCiocalteu's phenol reagent (Dingguo Changsheng Biotechnology Co. Ltd., Beijing, China) according to the manufacturer's instructions.

Ammonium Sulfate Fractional Precipitation

Ammonium sulfate fractional precipitation was performed in a 0°C chromatography freezer with sustained magnetic stirring. An appropriate amount of solid ammonium sulfate was added in small amounts repeatedly to 1 L of the venomous samples and stirred overnight in a 0°C freezer. Then, the sample solutions were centrifuged at 10000 *g*, at 4°C for 5 min. All of the supernatants were collected for the preparation of protein precipitation in the subsequent ammonium sulfate saturation. The protein precipitation was redissolved in 100 ml PBS (20 mM, pH 7.4) and dialyzed in the same PBS solution at 4°C for 48 h by Spectra/Por CE dialysis tubing, 500–1000 MWCO. Then, the sample solutions were centrifuged at 4°C, 10000 *g* for 5 min and the supernatant collected for further experiment. The ammonium sulfate saturations set in this experiment were 20, 30, 40, 50, 60, 70, and 80%.

Chromatography Purification

About 30 mg protein precipitation collected from 80% ammonium sulfate saturation was used in DEAE Sepharose Fast Flow chromatography. First, the sample solutions were concentrated by Millipore concentrators, 3,000 Da MWCO, at 4°C, 6000 g, and filtered with a 22 μm membrane. The protein samples were purified with a Hiprep DEAE FF 16/10 chromatography column (GE Healthcare, Princeton, NJ) that was coupled to a fast protein liquid AKTA pure chromatography system. The proteins were eluted by a discontinuous NaCl gradient (0.1–2 M), 3 ml/min. The equilibration buffer was 20 mM PBS. Elution buffer A was 20 mM PBS with 2 M NaCl, pH 7.4. Each elution peak was pooled and concentrated to test SDS-PAGE and metalloprotease activity. The concentrated fraction of 0.2 M NaCl elution peak was then filtered and submitted to a HiLoad 16/60 Superdex 75 column (GE Healthcare) with elution buffer B (0.15 M NaCl, 20 mM PBS, pH 7.4), 1 ml/min. Each elution peak was pooled, concentrated, and tested in SDS-PAGE for metalloprotease activity. The whole chromatography system worked in a 4°C freezer.

SDS-PAGE

SDS-PAGE was performed according to Laemmli's method (Laemmli, 1970). Briefly, 20 μg of the protein sample mixed with nonreducing 5× Protein Loading Buffer (Nanjing Jiancheng Bioengineering Institute, Nanjing, China) was incubated for 5 min at 100°C and then loaded into a 12% SurePAGE precast gel (GenScript, New Jersey, United States).

Protein samples were separated in Tris-MOPS-SDS running buffer (GenScript, New Jersey, United States) in a Bio-Rad Mini-PROTEAN Tetra System (Bio-Rad, California, United States) at 120 V for approximately 90 min. Gels were stained with 0.5% Coomassie brilliant blue R-250 and then photographed and analyzed by a Bio-Rad Gel Doc EZ Imager (Bio-Rad, California, United States). The low molecular standard (Yuanye, Shanghai, China) includes rabbit phosphorylase b, 97.4 kDa; bovine serum albumin, 66.2 kDa; rabbit actin, 43.0 kDa; bovine carbonic anhydrase, 31.0 kDa; trypsin inhibitor, 20.1 kDa; and hen egg-white lysozyme, 14.4 kDa.

Proteinase Activity

Proteinase activity was detected using azocasein according to a previously reported method (Wang et al., 2004) with minor modifications. Briefly, 12.5 μg of protein sample was added to 100 μL of 5 mg/ml azocasein (in 50 mM Tris-HCl, 100 mM NaCl, 5 mM $CaCl_2$, pH 8.8) in a 1.5 ml centrifuge tube and then incubated at 37°C for 90 min. The reaction was stopped by adding 200 μL of 5% trichloroacetic acid at room temperature for 30 min. After centrifugation at 10,000 *g* for 20 min, 150 μL of the supernatant was transferred to a 96-well plate and mixed with 150 μL of 0.5 M NaOH. The absorbance was measured by an Infinite M100 plate reader (Tecan Group Ltd., Männedorf, Switzerland) at 450 nm. The PBS group was set as the negative control. Proteinase activity was shown as U/mg.

LC-MS/MS Identification and Analysis

The protein components identification of fractions C and D was conducted by LC-MS/MS detection and spectra analysis. Briefly, SDT buffer was added to the protein powder sample. The lysate was sonicated and then boiled for 15 min. After being centrifuged at 14000 *g* for 40 min, the supernatant was quantified with the BCA Protein Assay Kit (Bio-Rad, United States). Then, 20 μg of proteins from each sample were mixed with 5× loading buffer and boiled for 5 min. The proteins were separated on 12.5% SDS-PAGE. Protein bands were visualized by Coomassie blue R-250 staining. 50 μg of sample was added to UA buffer, and DTT and iodoacetamide were then added to reduce and block the cysteine residues. Then trypsin was added. The mixtures were all incubated at 37°C for 16–18 h. Each fraction was injected for nano LC-MS/MS analysis. The peptide mixture was loaded onto a reverse-phase trap column (Thermo Scientific Acclaim PepMap100, 100 μm × 2 cm, NanoViper C18) connected to the C18 reversed phase analytical column (Thermo Scientific Easy Column, 10 cm long, 75 μm inner diameter, 3 μm resin) in buffer A (0.1% formic acid) and separated with a linear gradient of buffer B (84% acetonitrile and 0.1% formic acid) at a flow rate of 300 nL/min controlled by IntelliFlow technology. LC-MS/MS analysis was performed on a Q Exactive mass spectrometer (Thermo Scientific) that was coupled to Easy-nLC (Proxeon Biosystems, now Thermo Fisher Scientific) for 30 min. The mass spectrometer was operated in the positive ion mode. MS data were acquired using a data-dependent top10 method dynamically choosing the most abundant precursor ions from the survey scan (300–1,800 m/z) for HCD fragmentation.

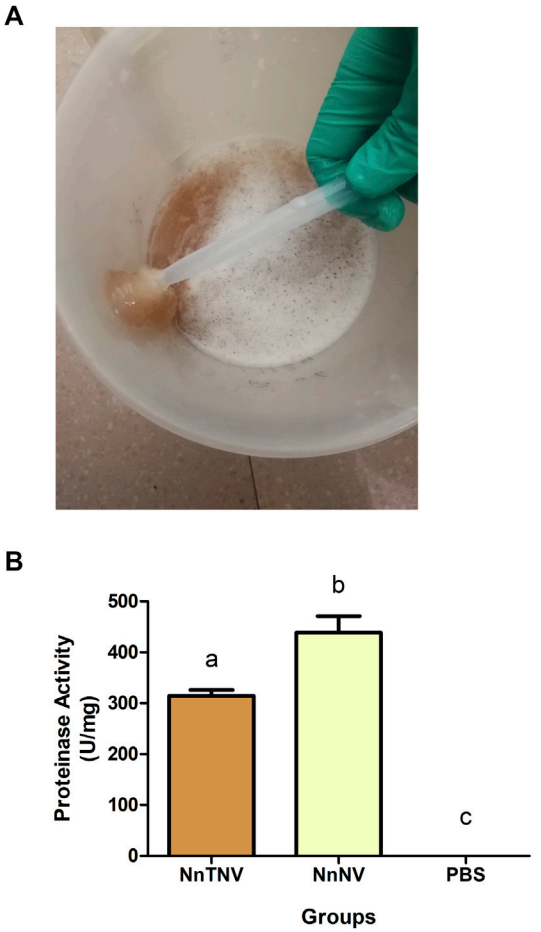

FIGURE 1 | Venomous sample preparation and proteinase activity assay. **(A)** Fresh *Nemopilema nomurai* tentacle tissues mixed with 50% (v/v) filtered natural seawater and completely autolyzed in 3–5 days. Supernatant was used in further experiments. **(B)** Proteinase activity of venomous samples. NnTNV: *Nemopilema nomurai* tentacle autolysis; NnNV: *Nemopilema nomurai* nematocyst venom. Both venomous samples showed significant proteinase activity, $p < 0.05$. NnNV was 438.6 U/mg. NnTNV was 314.4 U/mg.

Automatic gain control target was set to 3e6 and maximum inject time to 10 ms. Dynamic exclusion duration was 40.0 s. Survey scans were acquired at a resolution of 70,000 at m/z 200, and resolution for HCD spectra was set to 17,500 at m/z 200, and isolation width was 2 m/z. Normalized collision energy was 30 eV, and the underfill ratio, which specifies the minimum percentage of the target value likely to be reached at maximum fill time, was defined as 0.1%. The instrument was run with peptide recognition mode enabled. MS/MS spectra were searched in Tox-Prot (Jungo and Bairoch, 2005) (https://www.UniProt.org/program/Toxins) and *N. nomurai* genome database (Kim et al., 2019) (https://www.ncbi.nlm.nih.gov/genome/?term=Nemopilema+nomurai) with a mass tolerance for precursor ion of 20 ppm and MS/MS tolerance for 0.1 Da. Each identified protein should contain at least 1 unique peptide. Only ion scores >20 indicate identity or extensive homology ($p < 0.05$).

Statistical Analysis

The results were expressed as the mean ± SEM. The significant differences in the mean between various experimental groups were analyzed by an analysis of variance, followed by Tukey's test. $p < 0.05$ was considered statistically significant.

RESULTS

Isolation of High Proteinase Activity Fractions

The venomous sample used in the purification process was the supernatant of *N. nomurai* tentacle autolysis (NnTNV, **Figure 1A**). In Cnidaria, toxins may also exist in other tissues than nematocysts (Zhang et al., 2003; Xiao et al., 2011). In addition, during the tentacle autolysis, some nematocysts were discharged. So, NnTNV contained tentacle and nematocyst samples and showed significant proteinase activity measured as 314 U/mg (**Figure 1B**). Moreover, the operation of extracting nematocysts venom, which has been described in a previous research (Li et al., 2011), reduced the protein content by filtration, centrifugation, and ultrasonication. So, NnTNV is more suitable for multistep purification because it has significant activity, more sample volume, and higher protein concentration as shown in **Supplementary Table S1**.

The first fractionation step, ammonium sulfate fractional precipitation, separated the venomous sample into seven fractions by 20, 30, 40, 50, 60, 70, and 80% saturation. The protein concentration of each fraction is shown in **Supplementary Table S2**. According to SDS-PAGE, shown in **Figure 2A**, proteins in NnTNV could be preliminarily separated by solubility. Several proteins, such as the proteins above 97.4 kDa molecular weight in 20 and 30% saturation and proteins between 31.0 and 43.0 kDa molecular weight in 70 and 80% saturation were separated effectively. The proteins separated by 20, 40, 60, and 80% saturation showed significant proteinase activity with similar intensity (**Figure 2B**). It indicated that there were at least four different proteases contained in NnTNV. The fraction separated by 80% saturation showed the highest proteinase activity measured as 1,204 U/mg in mean value and more clear electrophoretic bands than other fractions, so it was selected for the next step. The fractions separated by 30, 50, and 70% saturation did not show proteinase activity (**Figure 2B**).

The second fractionation step was DEAE Sepharose Fast Flow chromatography. About 30 mg protein precipitation collected from 80% ammonium sulfate saturation was used in DEAE Sepharose Fast Flow chromatography. Elution peaks are shown in **Figure 3A**. The 80% saturation fraction was separated effectively by different ion intensities. Fractions eluted by 0 and 0.2 M NaCl contain more proteins judged by the peak shape. Fractions eluted by 0.1 and 0.2 M NaCl showed more clear electrophoretic bands (**Figure 3B**). The fraction eluted by 2 M NaCl did not show clear protein bands. Only the fraction eluted by 0.1 M NaCl did not show significant proteinase activity. Fractions eluted by 0 and 2 M NaCl showed similar activity intensity. The fraction eluted by 0.2 M NaCl showed the highest proteinase activity measured as 1065 U/mg, so it was selected for the next step. The protein content of this fraction was about 17.68 mg by calculating the collection volume (**Figure 3A**) and concentration (**Supplementary Table S3**). The ion intensity and proteinase activity did not show an obvious relationship (**Figure 3C**).

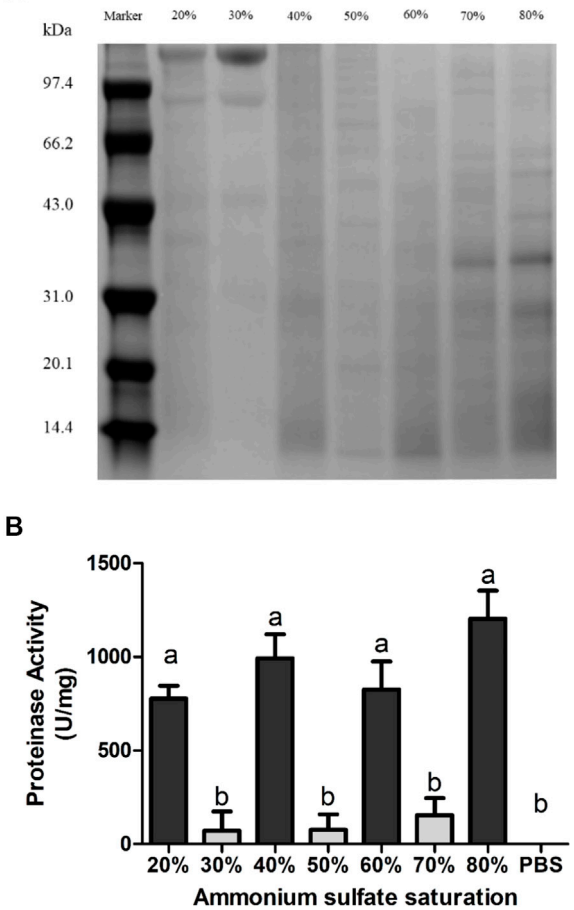

FIGURE 2 | Ammonium sulfate purification of venom from NnTNV. **(A)** Nonreducing SDS-PAGE of protein fractions in different ammonium sulfate saturations. The number and location of bands of each fraction were obviously different. Bands of fraction 80% were more clear than others. **(B)** Proteinase activity of different protein fractions. Four fractions showed significant proteinase activity, $p < 0.05$. Fraction 80% showed the highest activity.

The third fractionation step was Superdex chromatography. All collected elution sample of 0.2 M fraction was concentrated, filtered, and submitted onto a HiLoad 16/60 Superdex 75 column. The fraction eluted by 0.2 M NaCl was separated into four elution peaks as shown in **Figure 4A**. Elution peaks had mainly separated into peak A–B and peak C–D. Eluent was pooled into fractions A, B, C, and D. Calculating by collection volume (**Figure 4A**) and concentration (**Supplementary Table S4**), the protein content was 0.14 mg in A, 1.08 mg in B, 1.12 mg in C, and 1.63 mg in D. According to the SDS-PAGE, each fraction showed different electrophoretic bands distribution (**Figure 4B**). Fractions A and B had blurry bands above 66.2 kDa. Fraction C had clear

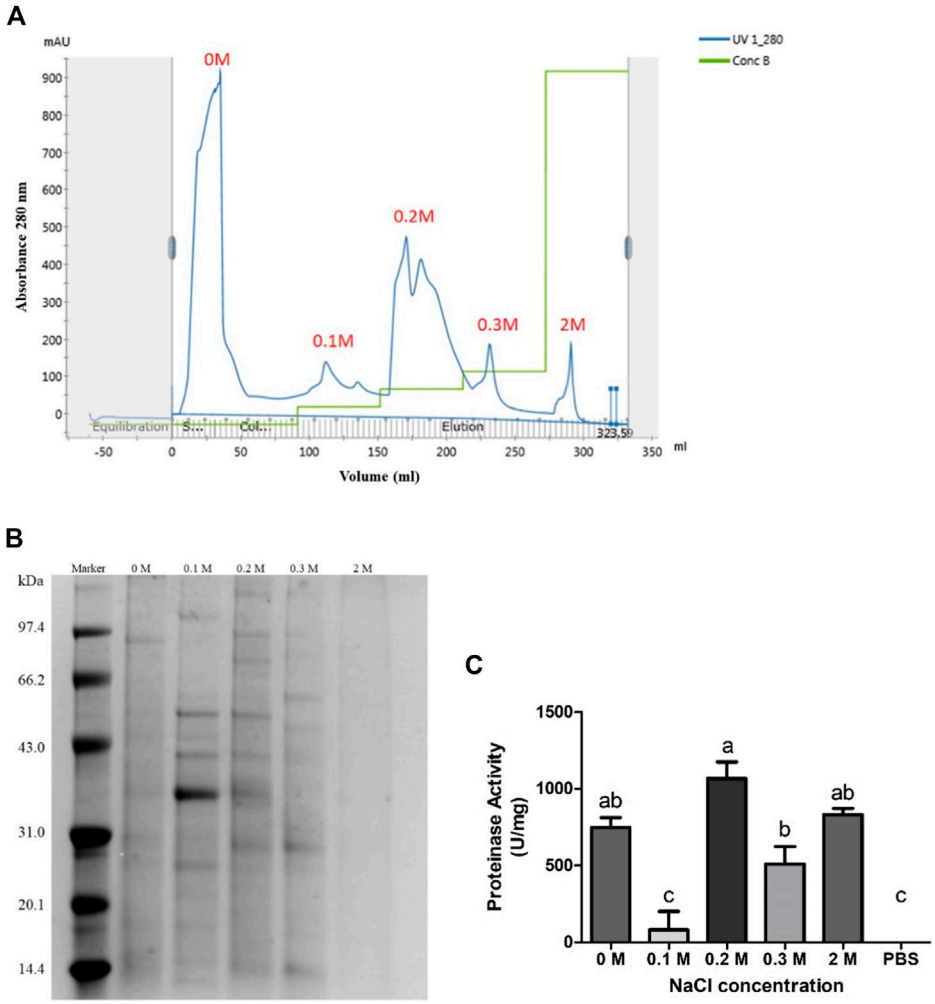

FIGURE 3 | DEAE Sepharose Fast Flow Chromatography purification of protein fraction in 80% ammonium sulfate saturation. **(A)** Elution peaks of protein fraction in 80% ammonium sulfate saturation purified by DEAE Sepharose Fast Flow chromatography. Five independent peaks were obtained. **(B)** Nonreducing SDS-PAGE of each fraction. Fraction 0.1 and 0.2 M showed more clear protein bands. **(C)** Proteinase activity of each fraction. Four fractions showed significant proteinase activity, $p < 0.05$. Fraction 0.2 M showed the highest activity.

bands between 20.1 and 97.4 kDa. Fraction D had clear bands below 43.0 kDa. Fraction B also had two blurry bands near 20.1 kDa. Although the fraction eluted by 0.2 M NaCl had the highest metalloproteinase activity in all DEAE Sepharose Fast Flow chromatography fractions, its elution peaks further separated by Superdex chromatography did not show significant proteinase activity to the negative control (PBS, 0 U/mg) as shown in **Figures 4C,D**.

Recover the Proteinase Activity of Deactivated Fractions

Deactivated fractions could recover the proteinase activity as shown in **Figure 5**. Mixture groups were made by mixing each fraction in equal volume and equal concentration. Three elution peak mixtures, "A + B," "C + D," and "A + B + C + D", showed significant activity, measured as 220–270 U/mg, to PBS (0 U/mg). The proteinase activity of other mixtures, measured as 110–180 U/mg, did not show significant differences both to three active groups and PBS.

LC-MS/MS Identification of Fractions C and D

According to the electrophoretic bands shown in **Figure 4B**, fractions C and D showed more clear bands and more obvious differences. Fractions A and B might be aggregated high molecular proteins. So, we selected fractions C and D to identify the protein components. The spectra obtained from LC-MS/MS were analyzed by the Tox-Prot database (all animal toxins database) and the *N. nomurai* genome database. The mass spectrometry proteomics data have been deposited to the ProteomeXchange Consortium *via* the PRIDE partner repository with the data set identifier PXD029333.

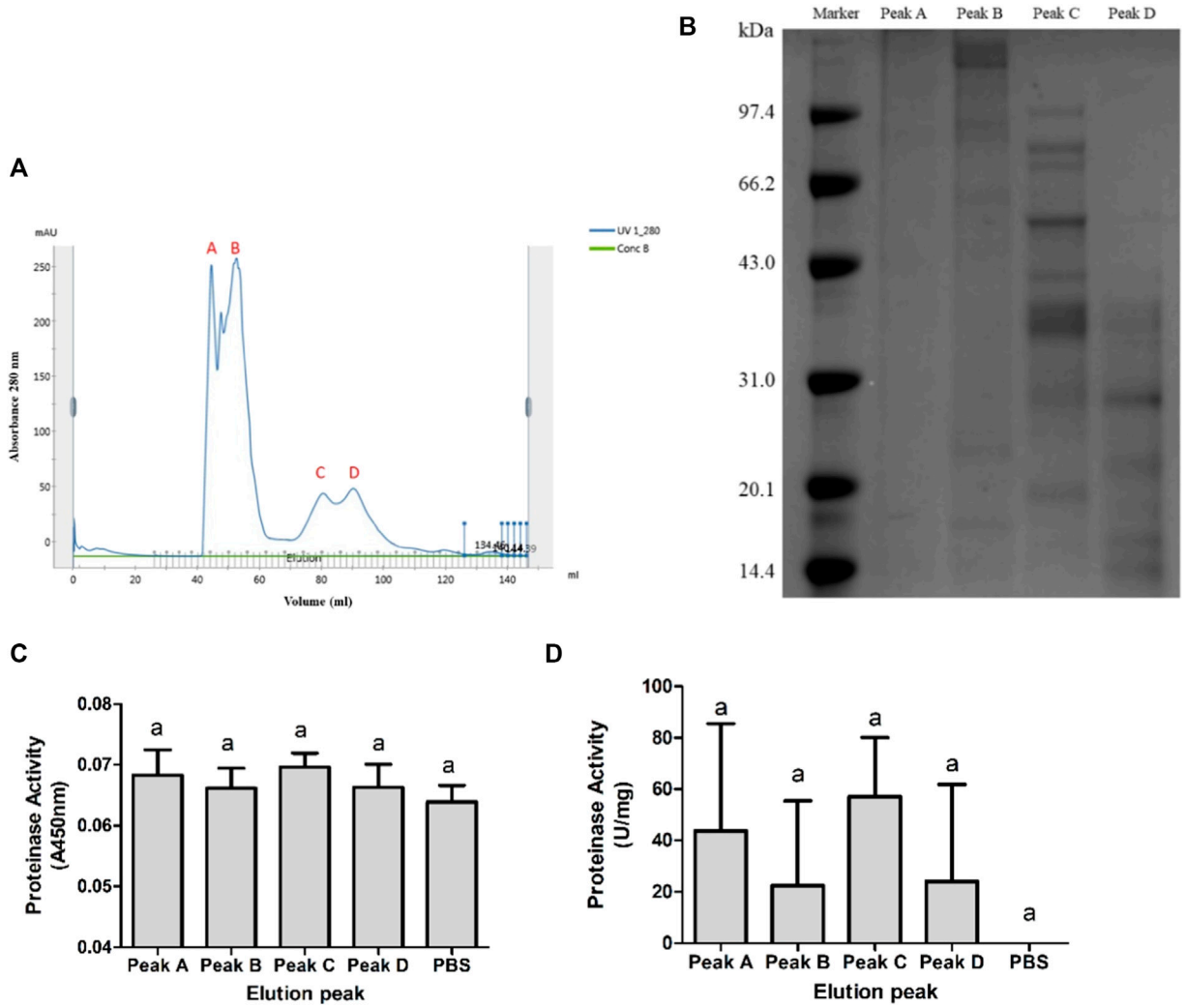

FIGURE 4 | Superdex chromatography purification of 0.2 M NaCl–eluted fraction. **(A)** Elution peaks of 0.2 M NaCl–eluted fraction purified by Superdex 75. Peaks A and B were well separated from C and D. But components in AB and CD were not entirely separated. **(B)** Nonreducing SDS-PAGE of each fraction. Protein bands of C and D were similar and more clear than those of A and B. **(C,D)** Proteinase activity of each fraction showed by A450 nm and U/mg. None of the four fractions showed significant proteinase activity, $p < 0.05$.

As seen in **Tables 1**, **2**, the results of the Tox-Prot analysis, a total of 41 peptides in fraction C were matched to 84 proteins which were classified as 41 protein groups (**Table 1**), and a total of 35 peptides in fraction D were matched to 71 proteins which were classified as 34 protein groups (**Table 2**). Some protein groups contain many high similarity proteins. Dermonecrotic toxin in fraction D was matched by three different peptides. The matched homologous toxins both in fractions C and D were venom allergen, dermonecrotic toxin, reticulocalbin, peroxiredoxin, serine protease, cysteine-rich venom protein, venom acid phosphatase, L-amino-acid oxidase, ion channel toxin, neurotoxin, etc. Most of these shared groups were matched by the same peptides. Protein toxins only matched in fraction C were phospholipase A_1, cystatin, zinc metalloproteinase, etc. Protein toxins only matched in fraction D were snake venom metalloprotease (SVMP) inhibitor, SVMP, hyaluronidase, etc.

The result of *N. nomurai* genome database analysis is shown in **Table 3**. Only two mitochondrion proteins, ATP synthase F0 subunit 8 and NADH dehydrogenase subunit 4L, were matched in fraction C.

DISCUSSION

As jellyfish stings pose a threat to humans in many marine activities in summer, especially swimming, the study of jellyfish sting mechanism is necessary for therapy researches. *N. nomurai* is a giant jellyfish widely distributed in the Yellow Sea and East China Sea, which blooms in summer in recent years (Sun

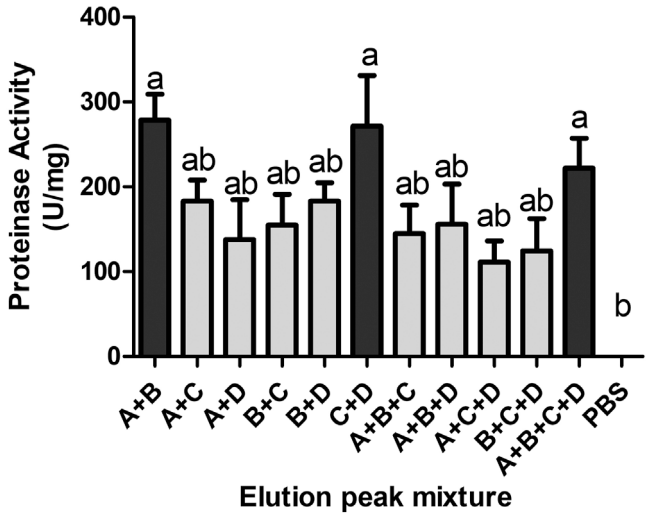

FIGURE 5 | Proteinase activity of different mixtures of the four elution peaks. Each group was an equal mixture of elution peaks in the same protein content. Three groups showed significant proteinase activity, $p < 0.05$.

et al., 2015a; Sun et al., 2015b). In *N. nomurai* venom, metalloproteinase is a major component (Li et al., 2014). NnVMPs showed azocasein hydrolysis activity and impacted the expression of many inflammatory factors (Li et al., 2019) and increased vascular permeability by directly degrading basement membrane components (Yue et al., 2021).

Metalloproteinases widely exist in venomous animals, including snakes, scorpions, spiders, jellyfish, etc. and play an important role in digestion and preying. Many different SVMPs are obtained by two or three steps of chromatography, such as CCSV-MPase (Cherifi et al., 2010), Atrase B (Sun and Bao, 2010), BmooMPα-II (de Queiroz et al., 2014), and CcD-II (Ami et al., 2017). Additionally, some metalloproteinases can be obtained by cDNA cloning and expression, such as rFIVa (Xu et al., 2006), Ahpfibrase (Zhang et al., 2010), and Jerdonitin (Zhu et al., 2010). Owing to the successful single protein purification, many SVMPs were studied in-depth in structures, functions, and mechanisms. SVMPs can be classified by their domain architecture into type P-I to P-III (Fox and Serrano, 2008). SVMPs are multifunction proteins, and they showed hemorrhagic, procoagulant, anticoagulant, and antiplatelet effects in envenomation cases (Fox and Serrano, 2005). Researches on the jellyfish venom purification are relatively difficult. Only a few toxins were highly purified from jellyfish venom, such as cytotoxin ClGp1, cytotoxin CcTX-1, neurotoxin CcNT, antioxidant protein SmP90 (Rottini et al., 1995; Yang et al., 2003; Helmholz et al., 2008; Lassen et al., 2011; Lassen et al., 2012; Li et al., 2012; Horiike et al., 2015), etc. Techniques most used in venom protein purification were activity-guided multidimensional chromatography, including size-exclude, ion-exchange, reversed-phase, and affinity chromatography. Lassen purified cytotoxin CcTX-1 and neurotoxin CcNT from *Cyanea capillata* in this program (Lassen et al., 2011; Lassen et al., 2012). Nevertheless, most jellyfish protein toxins could only be partially purified by multi-chromatography, such as a 95 kDa metalloproteinase from *R. pulmo* (barrel jellyfish) venom (Rastogi et al., 2017) and other hemolytic and lethal jellyfish toxins, such as SmTX from *S. meleagris* (Li et al., 2013) and NnLF from *N. nomurai* (Li et al., 2020). Due to the complex composition, it is not easy to get a single toxin component from jellyfish venom. In jellyfish venom, some different protein components have very similar physical properties such as molecule weight. In addition, toxins in jellyfish venom contained different subfamilies and may interact with other components. It was hard to efficiently isolate a single jellyfish toxin protein within two or three chromatography steps. In addition, the protein content in jellyfish nematocyst venom is too small an amount to do repeated chromatography, which makes it difficult to reveal the biological activity of a single toxin component. In this study, proteases from NnTNV were purified by ammonium sulfate precipitation, DEAE Sepharose Fast Flow, and Superdex 75 column chromatography successively. During the purification process, the proteinase activity of 80% saturation fraction and 0.2 M ion intensity fraction was increased from 314 U/mg to 1,204 U/mg and 1,065 U/mg, respectively. But none of the final fractions in Superdex chromatography showed significant proteinase activity to PBS (**Figures 4C,D**). However, when these fractions were mixed again by the same protein content, the mixed samples "A + B," "C + D," and "A + B + C + D" recovered the activity (**Figure 5**), which indicated that there was synergistic effect between the final fractions.

Synergistic effect is common in animal venom such as many snake toxins (Doley and Kini, 2009; Xiong and Huang, 2018). Currently, there is no universal method to study the synergistic effects of animal toxins. Laustsen proposed the Toxicity Score method to determine the presence of synergism in venom (Lauridsen et al., 2016). Venom synergistic effect is mainly revealed by the research of venom purification and molecular mechanisms. For example, SVMP may interact with

TABLE 1 | Toxins of NnTNV purification fraction C identified by LC-MS/MS analysis and Tox-Prot database.

Peptide sequence	Protein ID	Protein name	Cover percent (%)
AGATNGK	P84688	Toxin To7	8.33
	P84685	Toxin To6	8.24
ILKGGLK	C0HLS3	Delta-pseudomyrmecitoxin-Pp1a subunit B	21.21
VQIVR	A1BQQ5	Cysteine-rich venom protein Mr30	1.73
KM*LLEK	B1P1I3	U31-theraphotoxin-Cg1a	5.22
	B1P1I4	U31-theraphotoxin-Cg1b	5.22
TLQEK	B2D0J4	Venom dipeptidyl peptidase 4	0.65
LNPFR	B3EWX0	Short cationic peptide-6a	25
	B3EWX2	Short cationic peptide-6b	26.32
CLGIR	B5U2W0	Venom serine protease Bi-VSP	1.39
LICVR	B6V6L0	Conotoxin Im6.1	6.17
IVEVVK.D ! K.IVEVVK	C0HJH7	M-poneritoxin-Dq4a	21.43
	C0HJH6	M-poneritoxin-Dq4b/U1-poneritoxin-Dq4c/U1-poneritoxin-Dq4d	21.43
AAM*GTVRAK	C0HJT0	Potassium channel toxin alpha-KTx 2.19	24.32
	P0DL43	Potassium channel toxin alpha-KTx 2.14	24.32
LLM*QK	C0HLL3	Phospholipase A1	1.64
	P0CH47	Probable phospholipase A1 magnifin	1.48
EFADK	C0JB87	Dermonecrotic toxin SdSicTox-betaIIB1bxiii (Fragment)	1.82
	C0JB84	Dermonecrotic toxin SdSicTox-betaIIB1bx (Fragment)	1.82
	C0JB83	Dermonecrotic toxin SdSicTox-betaIIB1bix (Fragment)	1.82
	C0JB76	Dermonecrotic toxin SdSicTox-betaIIB1ai (Fragment)	1.82
	C0JB73	Dermonecrotic toxin SdSicTox-betaIIB1biii (Fragment)	1.82
	C0JB85	Dermonecrotic toxin SdSicTox-betaIIB1bxi (Fragment)	1.83
	C0JB80	Dermonecrotic toxin SdSicTox-betaIIB1bvi (Fragment)	1.82
	C0JB79	Dermonecrotic toxin SdSicTox-betaIIB1ai (Fragment)	1.82
	C0JB71	Dermonecrotic toxin SdSicTox-betaIIB1bi (Fragment)	1.2
	C0JB88	Dermonecrotic toxin SdSicTox-betaIIB1bxiv (Fragment)	1.83
	C0JB74	Dermonecrotic toxin SdSicTox-betaIIB1biv (Fragment)	1.82
	C0JB86	Dermonecrotic toxin SdSicTox-betaIIB1bxii (Fragment)	1.82
	C0JB82	Dermonecrotic toxin SdSicTox-betaIIB1bviii (Fragment)	1.82
	C0JB77	Dermonecrotic toxin SdSicTox-betaIIB1aii (Fragment)	1.82
	C0JB69	Dermonecrotic toxin SpaSicTox-betaIIA2 (Fragment)	1.82
	C0JB81	Dermonecrotic toxin SdSicTox-betaIIB1bvii (Fragment)	1.82
	C0JB72	Dermonecrotic toxin SdSicTox-betaIIB1bii (Fragment)	1.82
	C0JB78	Dermonecrotic toxin SdSicTox-betaIIB1aiii (Fragment)	1.83
	C0JB75	Dermonecrotic toxin SdSicTox-betaIIB1bv (Fragment)	1.82
IELTK	E3P6P2	Cystatin	3.55
	E3P6N9	Cystatin	3.55
	E3P6P0	Cystatin	3.55
	E3P6N3	AsCystatin	3.55
	E3P6N8	Cystatin	3.55
KTWSGTIIER	F8J2G5	Short neurotoxin 342	12.82
QGYISK	G0LXV8	Alpha-latrotoxin-Lh1a (Fragment)	0.44
	P23631	Alpha-latrotoxin-Lt1a	0.43
	P0DJE3	Alpha-latrotoxin-Lhe1a	0.42
IWDLK	H1ZZI8	Toxin Tpa7	6.10
IPILDGDGEATLK	I2C090	*Ophiophagus* venom factor	0.79
LSPEEQQK	J3S9D9	Reticulocalbin-2	2.61
LLDAAK	P0C1Q4	Mastoparan-1	42.86
QITMNDLPVGR	P0CV91	Peroxiredoxin-4 (Fragments)	30.56
ADLDLLR	P0DME8	Peptide Hp1239	10.45
VAACTNEIAGVK	P0DPT0	Phospholipase A1 VesT1.02	3.99
EEILR	P0DQF3	U-scoloptoxin(21)-Sm2a	7.25
EQITSRLK	P0DSJ9	U-myrmeciitoxin(01)-Mg5b	13.56
	P0DSJ8	U-myrmeciitoxin(01)-Mg5a	13.56
TRTSWDEDIMLIR	P26324	Thrombin-like enzyme ancrod	5.56
ILIHR	P43445	Short neurotoxin homolog	6.02
VSIGIK	P83108	Neurotoxin	17.14
QKNDKK	P86308	Tachykinin-like peptide-XI	46.15
ILGGIK	Q2XXP5	Cysteine-rich venom protein TEL1 (Fragment)	2.86
ESLEK	Q4JHE2	L-amino-acid oxidase	0.97
HM*LDVVSGTQK	Q5BLY5	Venom acid phosphatase Acph-1	2.84
EYLMK	Q5D7H4	Inactive hyaluronidase B	1.47
ELSIR	Q5Y4X2	U2-agatoxin-Ao1n	7.14

(Continued on following page)

TABLE 1 | (*Continued*) Toxins of NnTNV purification fraction C identified by LC-MS/MS analysis and Tox-Prot database.

Peptide sequence	Protein ID	Protein name	Cover percent (%)
VLFDK	Q68Y22	M-myrmeciitoxin-Mb2a	5.95
GAEIIR	Q6XLL6	Potassium channel toxin alpha-KTx 6.9	9.84
LPNKDR	Q7SYF1	Thrombin-like enzyme cerastocytin	2.34
MELIR	Q8AY79	Beta-fibrinogenase stejnefibrase-2	1.94
	Q8AY80	Alpha- and beta-fibrinogenase stejnefibrase-1	1.94
	Q91516	Venom plasminogen activator TSV-PA	1.94
KENGRK	Q8JIR2	Zinc metalloproteinase/disintegrin-like HR1a	0.99
	Q10749	Snake venom metalloproteinase–disintegrin-like mocarhagin	0.99
	Q4VM08	Zinc metalloproteinase–disintegrin-like VLAIP-A	0.97
	Q2UXQ5	Zinc metalloproteinase–disintegrin-like EoVMP2	0.98
	Q2UXR0	Zinc metalloproteinase–disintegrin-like Eoc1	0.98
	B8K1W0	Zinc metalloproteinase–disintegrin-like daborhagin-K	0.98
	Q7T046	Coagulation factor X–activating enzyme heavy chain	0.98
	Q7LZ61	Coagulation factor X–activating enzyme heavy chain	0.97
LVPIASK	Q98956	Cytotoxin 1b	8.64
	P86538	Cytotoxin 2a	11.67
LLNKR.S ! K.LLNKR	Q9BPF2	Conotoxin Vn-05	8.20
	Q68IP5	Conotoxin mr5.4b (Fragment)	9.26
VATGK	W4VS53	CRISP/Allergen/PR-1	1.23

phospholipase A_2 (Xiong et al., 2017). The enzyme activity of P-III metalloproteinase complex was regulated by its subunits (Doley and Kini, 2009). Although there has been no research in jellyfish metalloproteinase synergistic effect, unrevealed interaction of synergistic proteins may impact the bioactivity and purification studies.

As the final fractions were multicomponent, the protein components of fractions C and D were identified by LC-MS/MS to reveal the possible mechanism of proteinase activity regulation in *N. nomurai* venom. However, few jellyfish toxins are well understood. A large number of protein toxins were matched in snakes, spiders, scorpions, bees, and other organisms (**Table 1**, **Table 2**) by searching in Tox-Prot. The unique peptide count of most matched proteins was only one, but some peptides matched many similar proteins in different organisms, such as peptide KENGRK which was matched to eight different zinc metalloproteinases. It made the peptide sequence more probable to represent the matched protein group. This means even the unique peptide count and cover percent were not high, these matched toxins from other organisms also provided very important references. Similar to the chromatography and SDS-PAGE results, toxins matched in fractions C and D showing shared and different components. These different toxins contained in fractions C and D might contain the regulator of proteinase activity, such as phospholipase A1, P-III metalloproteinase, P-I metalloproteinase, and metalloproteinase inhibitor.

In fraction C, the matched toxin proteins which related to proteinase activity were zinc metalloproteinase and serine protease. The peptide sequence matched to zinc metalloproteinase was KENGRK. It matched eight similar P-III metalloproteinases from different snakes. They can produce proteolytic activity and hemorrhage activity (Howes et al., 2003; Morine et al., 2008). This kind of metalloproteinase has metalloproteinase domain, disintegrin domain, and cysteine-rich domain (Gowda et al., 1994; Siigur et al., 2001; Siigur et al., 2004; Trummal et al., 2005; Takeda et al., 2007; Chen et al., 2008). Sequence KENGRK is located in the cysteine-rich domain. The peptide sequences matched to serine protease were CLGIR, TRTSWDEDIMLIR, and LPNKDR. CLGIR matched venom serine protease Bi-VSP from *Bombus ignitus* (bumblebee). TRTSWDEDIMLIR matched thrombin-like enzyme ancrod from *Calloselasma rhodostoma* (Malayan pit viper). LPNKDR matched thrombin-like enzyme cerastocytin from *Cerastes cerastes* (horned desert viper). These serine proteases have fibrinogenolytic activity (Marrakchi et al., 1995; Marrakchi et al., 1997; Dekhil et al., 2003; Choo et al., 2010; Choo et al., 2012).

In fraction D, the matched toxin proteins which related to proteinase activity were SVMP, SVMP inhibitor, and serine protease. Serine protease was matched by peptide sequence TRTSWDEDIMLIR which was also identified in fraction C. The sequence LENVEKEDGGPK was matched to SVMP from *Crotalus molossus molossus* (Northern black-tailed rattlesnake). This kind of P-I metalloproteinase impairs hemostasis in the envenomed animal (Gutierrez et al., 1995; Farsky et al., 2000; Patino et al., 2010; Bernardes et al., 2013). The sequence QASQKWGR was matched to SVMP inhibitor 02D01 from *Echis ocellatus* (ocellated saw-scaled viper). This protein may inhibit metalloproteinase activity in the venom gland through abundant pEKW and poly-His-poly-Gly peptides. The inhibition may be disengaged by dilution or physiochemical change (Wagstaff et al., 2008).

These SVMP-like proteins in fractions C and D might be the important factors in regulating azocasein hydrolysis activity. Zinc metalloproteinases matched in fraction C were P-III metalloproteinase which contains metalloproteinase domain, disintegrin domain, and cysteine-rich domain (Gowda et al., 1994; Siigur et al., 2001; Siigur et al., 2004; Trummal et al., 2005; Takeda et al., 2007; Chen et al., 2008). Some of this kind of P-III metalloproteinase were confirmed that they can constitute complexes with C-type lectin homodimers light

TABLE 2 | Toxins of NnTNV purification fraction D identified by LC-MS/MS analysis and Tox-Prot database.

Peptide sequence	Protein ID	Protein name	Cover percent (%)
LSPEEQQK	J3S9D9	Reticulocalbin-2	4.25
QLHLK			
K.ILKGGLK.S	C0HLS3	Delta-pseudomyrmecitoxin-Pp1a subunit B	21.21
XIIGAPCRR	P0C7W7	Kappa-stichotoxin-Shd1a/kappa-stichotoxin-Shd1b	32.14
EEILR	P0DQF3	U-scoloptoxin(21)-Sm2a	7.25
RSEHEEQLMAK	P0DQF5	U-scoloptoxin(22)-Er1a	8.15
TRTSWDEDIMLIR	P26324	Thrombin-like enzyme ancrod	5.56
QASQKWGR	A8YPR6	Snake venom metalloprotease inhibitor 02D01	2.60
LNPFR	B3EWX0	Short cationic peptide-6a	25.00
	B3EWX2	Short cationic peptide-6b	26.32
SCAGMGQDCK	B6DD25	U13-lycotoxin-Ls1f	8.33
	B6DD28	U13-lycotoxin-Ls1b	8.33
	B6DD26	U13-lycotoxin-Ls1f	8.33
LDTVR	C0JB09	Dermonecrotic toxin LarSicTox-alphaIII1 (Fragment)	1.82
EFADK	C0JB80	Dermonecrotic toxin SdSicTox-betaIIB1bvi (Fragment)	1.82
	C0JB73	Dermonecrotic toxin SdSicTox-betaIIB1biii (Fragment)	1.82
	C0JB79	Dermonecrotic toxin SdSicTox-betaIIB1ai (Fragment)	1.82
	C0JB71	Dermonecrotic toxin SdSicTox-betaIIB1bi (Fragment)	1.82
	C0JB77	Dermonecrotic toxin SdSicTox-betaIIB1aii (Fragment)	1.82
	C0JB69	Dermonecrotic toxin SpaSicTox-betaIIA2 (Fragment)	1.82
	C0JB85	Dermonecrotic toxin SdSicTox-betaIIB1bxi (Fragment)	1.83
	C0JB88	Dermonecrotic toxin SdSicTox-betaIIB1bxiv (Fragment)	1.83
	C0JB84	Dermonecrotic toxin SdSicTox-betaIIB1bx (Fragment)	1.82
	C0JB83	Dermonecrotic toxin SdSicTox-betaIIB1bix (Fragment)	1.82
	C0JB87	Dermonecrotic toxin SdSicTox-betaIIB1bxiii (Fragment)	1.82
	C0JB76	Dermonecrotic toxin SdSicTox-betaIIB1ai (Fragment)	1.82
	C0JB86	Dermonecrotic toxin SdSicTox-betaIIB1bxii (Fragment)	1.82
	C0JB78	Dermonecrotic toxin SdSicTox-betaIIB1aiii (Fragment)	1.83
	C0JB82	Dermonecrotic toxin SdSicTox-betaIIB1bviii (Fragment)	1.82
	C0JB74	Dermonecrotic toxin SdSicTox-betaIIB1biv (Fragment)	1.82
	C0JB81	Dermonecrotic toxin SdSicTox-betaIIB1bvii (Fragment)	1.82
	C0JB75	Dermonecrotic toxin SdSicTox-betaIIB1bv (Fragment)	1.82
	C0JB72	Dermonecrotic toxin SdSicTox-betaIIB1bii (Fragment)	1.82
LTEALK	C0JB90	Dermonecrotic toxin SdSicTox-betaIIB2ii (Fragment)	2.19
	C0JB89	Dermonecrotic toxin SdSicTox-betaIIB2i (Fragment)	2.19
	C0JB91	Dermonecrotic toxin SaSicTox-betaIIB1 (Fragment)	2.19
KLDLR	D2Y2H8	U6-theraphotoxin-Hhn1a 4	5.15
	D2Y2H6	U6-theraphotoxin-Hhn1a 2	5.15
	D2Y2C1	U6-theraphotoxin-Hhn1a 1	5.15
	D2Y2H7	U6-theraphotoxin-Hhn1a 3	5.15
MIIFK	G3LU44	Translationally controlled tumor protein homolog	2.91
	M5B4R7	Translationally controlled tumor protein homolog	2.89
IWDLK	H1ZZI8	Toxin Tpa7	6.10
TGVEIK	P01393	Alpha-elapitoxin-Djk2a	8.33
QITMNDLPVGR	P0CV91	Peroxiredoxin-4 (Fragments)	30.56
ADLDLLR	P0DME8	Peptide Hp1239	10.45
EQITSRLK	P0DSJ8	U-myrmeciitoxin(01)-Mg5a	13.56
	P0DSJ9	U-myrmeciitoxin(01)-Mg5b	13.56
GLPEDAK	P0DUI0	Beta-toxin Ct13	8.64
NEILK	P10736	Venom allergen 5.01	2.20
LEILK	P81657	Venom allergen 5	2.48
	P0DMB9	Venom allergen 5	2.48
	P86870	Venom allergen 5	2.22
LVPIASK	P86538	Cytotoxin 2a	11.67
	Q98956	Cytotoxin 1b	8.64
ILGGIK	Q2XXP5	Cysteine-rich venom protein TEL1 (Fragment)	2.86
QEYGAERLR	Q3YEG6	Conotoxin LiC42	11.69
YENFNDFLK	Q4VDB5	Dermonecrotic toxin LgSicTox-alphaIA1	3.21
	P0CE80	Dermonecrotic toxin LiSicTox-alphaIA1a	2.94
	Q56JA9	Dermonecrotic toxin LsSicTox-alphaIA1	3.21
	P0CE82	Dermonecrotic toxin LiSicTox-alphaIA1bii (Fragment)	2.98
	P0CE81	Dermonecrotic toxin LiSicTox-alphaIA1bi	2.94
LNLIR	Q5BLY5	Venom acid phosphatase Acph-1	1.29
KVHEVK	Q6T627	L-amino-acid oxidase (Fragment)	10.00

(Continued on following page)

TABLE 2 | (*Continued*) Toxins of NnTNV purification fraction D identified by LC-MS/MS analysis and Tox-Prot database.

Peptide sequence	Protein ID	Protein name	Cover percent (%)
GAEVIR	Q6XLL5	Potassium channel toxin alpha-KTx 6.10	10.00
GAEIIR	Q6XLL6	Potassium channel toxin alpha-KTx 6.9	9.84
TIEELAK	Q75WG7	U13-hexatoxin-Mg1a	5.65
LENVEKEDGGPK	Q8JJ51	Snake venom metalloproteinase	2.90
LLNKR.S ! K.LLNKR	Q9BPF2	Conotoxin Vn-05	8.20
	Q68IP5	Conotoxin mr5.4b (Fragment)	9.26
DILDK.S ! K.DLLDK	R4J7Z9	Hyaluronidase	1.25
	F8J2D3	Phospholipase-B 81	0.90

TABLE 3 | Proteins of NnTNV purification fraction C identified by LC-MS/MS analysis and *N. nomurai* genome database.

Peptide sequence	CDS	Gene description	Cover percent (%)
LNEVR	YP_009421312.1	ATP synthase F0 subunit 8	7.46
LLNILK	YP_009421319.1	NADH dehydrogenase subunit 4 L	7.23

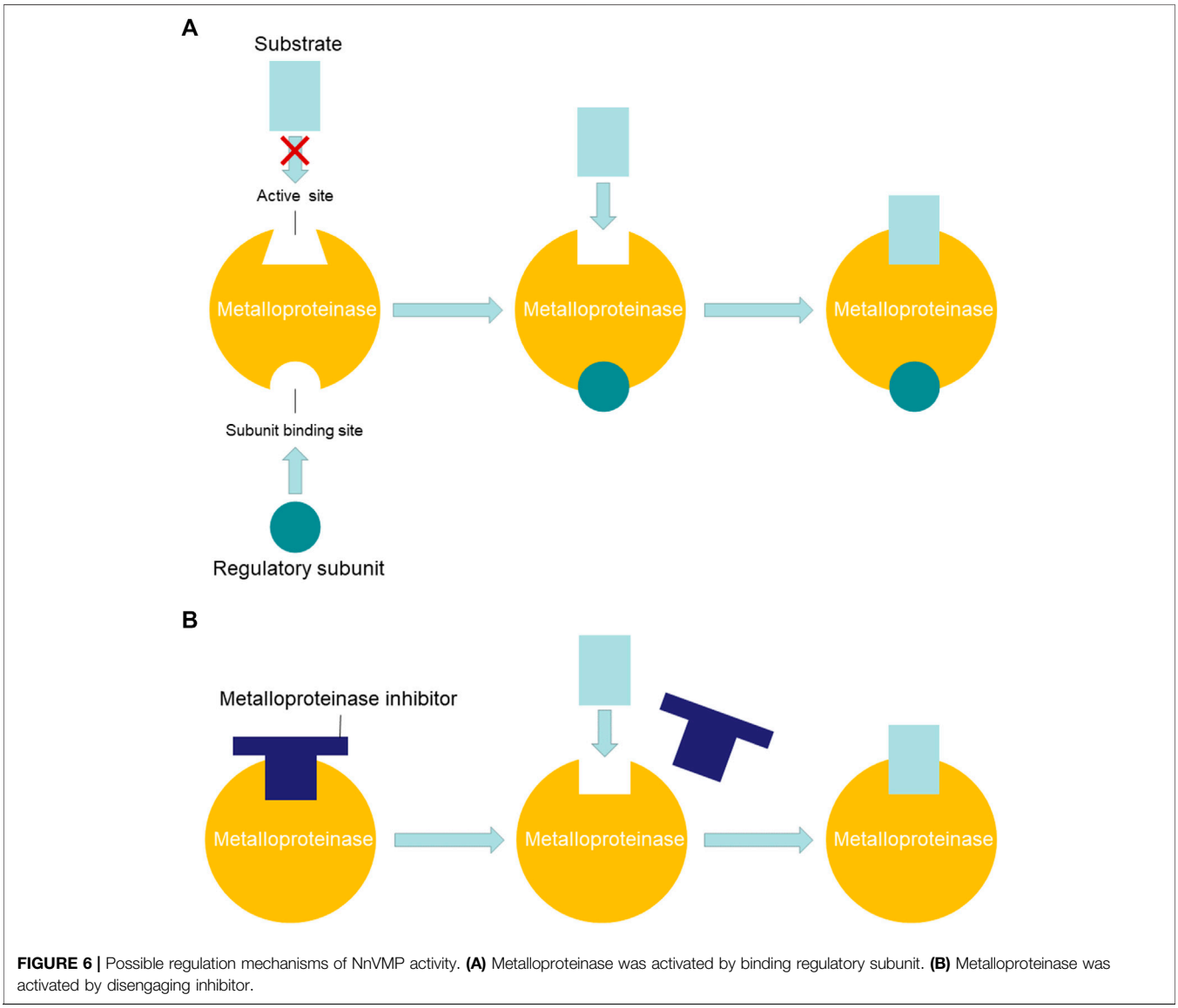

FIGURE 6 | Possible regulation mechanisms of NnVMP activity. **(A)** Metalloproteinase was activated by binding regulatory subunit. **(B)** Metalloproteinase was activated by disengaging inhibitor.

TABLE 4 | The nucleotide sequence of 21 amino acids in *Nemopilema nomurai*.

Amino acid	DNA sequence	mRNA sequence (codon)
M	ATG/ATA	AUG/AUA (I)
P	CCT	CCU
Q	CAA	CAA
L	TTA/TTG/CTA	UUA/UUG/CUA
D	GAT	GAU
I	ATT/ATA/ATC	AUU/AUA/AUC
V	GTT/GTA/GTC	GUU/GUA/GUC
T	ACA/ACT	ACA/ACU
F	TTT/TTC	UUU/UUC
N	AAT/AAC	AAU/AAC
Y	TAT/TAC	UAU/UAC
W	TGA	UGA (termination codon)
G	GGT/GGA	GGU/GGA
S	TCA/TCC/TCT/TCG/ AGT/AGC	UCA/UCC/UCU/UCG/ AGU/AGC
K	AAA/AAG	AAA/AAG
E	GAA/GAG	GAA/GAG
R	AGA	AGA
H	CAT	CAU
A	GCT/GCA	GCU/GCA
T	ACA	ACA
C	TGT	UGU

chains, such as RVV-X (Gowda et al., 1994; Takeda et al., 2007) and CA-1 (Yamada et al., 1996). RVV-X is a P-III metalloproteinase complex isolated from *Daboia siamensis* (Eastern Russel's viper) which can activate coagulation factor X by cleavage of Arg-|-Xaa bonds (Gowda et al., 1994; Takeda et al., 2007). The heavy chain (Protein ID, Q7LZ61) was matched in fraction C. In RVV-X complex, the heavy chain is the catalytic subunit of activating coagulation factor X, and the two light chains are regulatory subunits of binding the Gla domain of factor X (Takeya et al., 1992). Similar to RVV-X, this protein group can selectively hydrolyze factor X to Xa, but some of them were also confirmed having azocasein hydrolysis activity such as the protein zinc metalloproteinase–disintegrin-like bothropasin from *Bothrops jararaca* (Mandelbaum et al., 1982). However, the zinc metalloproteinase–disintegrin-like atrase B isolated from *Naja atra* (Chinese cobra) did not show hydrolysis activity to fibrin, azocasein, and BAEE (Cherifi et al., 2010). Therefore, it was speculated that a zinc metalloproteinase which can hydrolyze azocasein was contained in fraction C, and its activity could be activated by binding with regulatory subunits contained in fraction D. Differences from the C-type lectin subunits of RVV-X, the regulatory subunits in fraction D, might affect the active center of the zinc metalloproteinase, similar to allosteric regulation. According to **Table 2**, fraction D might contain similar proteins to P-I SVMP and SVMP inhibitor. This indicated that there might have been an interaction between them that could inhibit the metalloproteinase activity. The inhibition of SVMP inhibitor may be disengaged by dilution or physiochemical change (Wagstaff et al., 2008).

To sum up the regulation mechanism, inactivated fractions C and D would recover the metalloproteinase activity by binding regulator or disaggregating inhibitor. Fraction C contained a zinc metalloproteinase which could hydrolysis azocasein under the activation of regulatory subunits in fraction D (**Figure 6A**). In another explanation, the interacted metalloproteinase and inhibitor in fraction D would disengage to activate metalloproteinase activity when fractions C and D were mixed (**Figure 6B**).

The spectra in *N. nomurai* genome database were also searched. The whole-genome database was uploaded to NCBI by Hak-Min Kim's team (Kim et al., 2019). LC-MS/MS analysis did not match any toxins in this database. BLAST of SVMP, which was matched in fractions C and D, also had no significant similarity found. Although the nucleotide sequences of *N. nomurai* toxins were not obtained, some important peptide sequences were transformed into nucleotide sequence. The nucleotide sequence of 21 amino acids shown in **Table 4** was obtained from the two *N. nomurai* mitochondrion proteins listed in **Table 3**. Through the comparison of the protein sequence and nucleotide sequence of ATP synthase F0 subunit 8 and NADH dehydrogenase subunit 4 L in *N. nomurai*, two interesting differences were found. In *N. nomurai*, the isoleucine (Ile, I) codon AUA would translate to methionine (Met, M), and the termination codon UGA would translate to tryptophan (Try, W). This should be paid special attention in further expression works. Based on this nucleotide sequence table, three peptides, which were matched to zinc metalloproteinase, SVMP, and SVMP inhibitor, were transformed into nucleotide sequence as shown in **Figure 7**. These sequences may provide references for further studies interested in NnVMP.

It has been a problem for a long time that jellyfish venom purification has been limited by the complex protein components. As shown in each purification step, different proteins may have similar physical properties and are hard to be completely isolated by chromatography. Low protein content also limit sample reloading of chromatography. As a new revealed property of *N. nomurai* toxins, the synergistic effect of proteinase activity may impact further activity-guided chromatography studies. Although jellyfish venom purification is difficult, it might reveal more venom properties in the purification process and provide references for further studies.

In conclusion, the toxic protease components from NnTNV were isolated by ammonium sulfate precipitation, DEAE Sepharose Fast Flow, and Superdex 75 column chromatography successively. After the three purification steps, the main proteinase activity was lost, but it could be recovered by mixing again. This is the first time that the synergistic effect of jellyfish proteinase activity has been revealed. Through LC-MS/MS analysis, it has been shown that the proteinase activity might have been contributed by metalloproteinases and regulated by metalloproteinase subunit or metalloproteinase inhibitor. Three important peptide sequences were transformed into nucleotide sequences to provide more information on *N. nomurai* metalloproteinases. The results could help further research in jellyfish toxins purification and expression. The synergistic effect might be a new entry point in purifying *N. nomurai* metalloproteinases and regulators.

FIGURE 7 | Possible nucleotide sequence of three important peptides. The red and blue frames represent interchangeable bases. **(A)** The sequence of KENGRK. **(B)** The sequence of LENVEKEDGGPK. **(C)** The sequence of QASQKWGR.

DATA AVAILABILITY STATEMENT

The data sets presented in this study can be found in online repositories. The names of the repository/repositories and accession number(s) can be found below: ProteomeXchange with identifier PXD029333.

ETHICS STATEMENT

The animal study was reviewed and approved by the IOCAS Ethics Committee in March 2017, Ethics Application No. IOCAS/KLEMB/20170301.

AUTHOR CONTRIBUTIONS

RL, XY, and CY performed the experiments. HY, PL, and CY designed the experiments and interpreted the data. HY and CY wrote the manuscript. All authors read and discussed the manuscript.

FUNDING

This work was supported by the National Key R&D Program of China (2017YFE0111100-04, 2019YFC0312605), the National Natural Science Foundation of China (41776163, 41876164), and the Natural Science Foundation of Shandong Province (ZR2019QD012).

SUPPLEMENTARY MATERIAL

The Supplementary Material for this article can be found online at: https://www.frontiersin.org/articles/10.3389/fphar.2021.791847/full#supplementary-material

REFERENCES

Ami, A., Oussedik-Oumehdi, H., and Laraba-Djebari, F. (2017). Biochemical and Biological Characterization of a Dermonecrotic Metalloproteinase Isolated from Cerastes Cerastes Snake Venom. *J. Biochem. Mol. Toxicol.* 31, 9. doi:10.1002/jbt.21835

Bernardes, C. P., Menaldo, D. L., Camacho, E., Rosa, J. C., Escalante, T., Rucavado, A., et al. (2013). Proteomic Analysis of Bothrops Pirajai Snake Venom and Characterization of BpirMP, a New P-I Metalloproteinase. *J. Proteomics* 80, 250–267. doi:10.1016/j.jprot.2013.01.021

Bloom, D. A., Burnett, J. W., and Alderslade, P. (1998). Partial Purification of Box Jellyfish (Chironex Fleckeri) Nematocyst Venom Isolated at the Beachside. *Toxicon* 36, 1075–1085. doi:10.1016/s0041-0101(98)00096-8

Cegolon, L., Heymann, W. C., Lange, J. H., and Mastrangelo, G. (2013). Jellyfish Stings and Their Management: A Review. *Mar. Drugs* 11, 523–550. doi:10.3390/md11020523

Chen, H. S., Tsai, H. Y., Wang, Y. M., and Tsai, I. H. (2008). P-III Hemorrhagic Metalloproteinases from Russell's viper Venom: Cloning, Characterization, Phylogenetic and Functional Site Analyses. *Biochimie* 90, 1486–1498. doi:10.1016/j.biochi.2008.05.012

Chérifi, F., Rousselle, J. C., Namane, A., and Laraba-Djebari, F. (2010). CCSV-MPase, a Novel Procoagulant Metalloproteinase from Cerastes Cerastes Venom: Purification, Biochemical Characterization and Protein Identification. *Protein J.* 29, 466–474. doi:10.1007/s10930-010-9273-1

Choo, Y. M., Lee, K. S., Yoon, H. J., Kim, B. Y., Sohn, M. R., Roh, J. Y., et al. (2010). Dual Function of a Bee Venom Serine Protease: Prophenoloxidase-Activating Factor in Arthropods and Fibrin(ogen)olytic Enzyme in Mammals. *Plos One* 5, e10393. doi:10.1371/journal.pone.0010393

Choo, Y. M., Lee, K. S., Yoon, H. J., Qiu, Y., Wan, H., Sohn, M. R., et al. (2012). Antifibrinolytic Role of a Bee Venom Serine Protease Inhibitor that Acts as a Plasmin Inhibitor. *Plos One* 7, e32269. doi:10.1371/journal.pone.0032269

Chung, J. J., Ratnapala, L. A., Cooke, I. M., and Yanagihara, A. A. (2001). Partial Purification and Characterization of a Hemolysin (CAH1) from Hawaiian Box Jellyfish (Carybdea Alata) Venom. *Toxicon* 39, 981–990. doi:10.1016/s0041-0101(00)00237-3

De Queiroz, M. R., Mamede, C. C. N., Fonseca, K. C., De Morais, N. C. G., De Sousa, B. B., Santos, N. A., et al. (2014). Rapid Purification of a New P-I Class Metalloproteinase from Bothrops Moojeni Venom with Antiplatelet Activity. *Biomed. Res. Int.* 2014, 12. doi:10.1155/2014/352420

Dekhil, H., Wisner, A., Marrakchi, N., El Ayeb, M., Bon, C., and Karoui, H. (2003). Molecular Cloning and Expression of a Functional Snake Venom Serine Proteinase, with Platelet Aggregating Activity, from the Cerastes Cerastes viper. *Biochemistry* 42, 10609–10618. doi:10.1021/bi034790b

Doley, R., and Kini, R. M. (2009). Protein Complexes in Snake Venom. *Cell Mol Life Sci* 66, 2851–2871. doi:10.1007/s00018-009-0050-2

Farsky, S. H., Gonçalves, L. R., Gutiérrez, J. M., Correa, A. P., Rucavado, A., Gasque, P., et al. (2000). *Bothrops A* Snake Venom and its Metalloproteinase BaP-1 Activate the Complement System. Role in Leucocyte RecruitmentRole in Leucocyte Recruitment. *Mediators Inflamm.* 9, 213–221. doi:10.1080/09629350020025728

Fox, J. W., and Serrano, S. M. (2005). Structural Considerations of the Snake Venom Metalloproteinases, Key Members of the M12 Reprolysin Family of Metalloproteinases. *Toxicon* 45, 969–985. doi:10.1016/j.toxicon.2005.02.012

Fox, J. W., and Serrano, S. M. (2008). Insights into and Speculations about Snake Venom Metalloproteinase (SVMP) Synthesis, Folding and Disulfide Bond Formation and Their Contribution to Venom Complexity. *FEBS J.* 275, 3016–3030. doi:10.1111/j.1742-4658.2008.06466.x

Gowda, D. C., Jackson, C. M., Hensley, P., and Davidson, E. A. (1994). Factor X-Activating Glycoprotein of Russell's viper Venom. Polypeptide Composition and Characterization of the Carbohydrate Moieties. *J. Biol. Chem.* 269, 10644–10650. doi:10.1016/s0021-9258(17)34108-x

Gutiérrez, J., Romero, M., Díaz, C., Borkow, G., and Ovadia, M. (1995). Isolation and Characterization of a Metalloproteinase with Weak Hemorrhagic Activity from the Venom of the Snake *Bothrops asper* (Terciopelo). *Toxicon* 33, 19–29. doi:10.1016/0041-0101(94)00138-x

Helmholz, H., Naatz, S., Lassen, S., and Prange, A. (2008). Isolation of a Cytotoxic Glycoprotein from the Scyphozoa Cyanea Lamarckii by Lectin-Affinity Chromatography and Characterization of Molecule Interactions by Surface Plasmon Resonance. *J. Chromatogr. B Analyt Technol. Biomed. Life Sci.* 871, 60–66. doi:10.1016/j.jchromb.2008.06.040

Horiike, T., Nagai, H., and Kitani, S. (2015). Identification of Allergens in the Box Jellyfish Chironex Yamaguchii that Cause Sting Dermatitis. *Int. Arch. Allergy Immunol.* 167, 73–82. doi:10.1159/000434721

Howes, J. M., Wilkinson, M. C., Theakston, R. D., and Laing, G. D. (2003). The Purification and Partial Characterisation of Two Novel Metalloproteinases from the Venom of the West African Carpet viper, Echis Ocellatus. *Toxicon* 42, 21–27. doi:10.1016/s0041-0101(03)00096-5

Jungo, F., and Bairoch, A. (2005). Tox-Prot, the Toxin Protein Annotation Program of the Swiss-Prot Protein Knowledgebase. *Toxicon* 45, 293–301. doi:10.1016/j.toxicon.2004.10.018

Kawahara, M., Uye, S., Ohtsu, K., and Iizumi, H. (2006). Unusual Population Explosion of the Giant Jellyfish Nemopilema Nomurai (Scyphozoa: Rhizostomeae) in East Asian Waters. *Mar. Ecol. Prog. Ser.* 307, 161–173. doi:10.3354/meps307161

Kim, H. M., Weber, J. A., Lee, N., Park, S. G., Cho, Y. S., Bhak, Y., et al. (2019). The Genome of the Giant Nomura's Jellyfish Sheds Light on the Early Evolution of Active Predation. *BMC Biol.* 17, 28. doi:10.1186/s12915-019-0643-7

Laemmli, U. K. (1970). Cleavage of Structural Proteins during the Assembly of the Head of Bacteriophage T4. *Nature* 227, 680, 5.doi:10.1038/227680a0

Lassen, S., Helmholz, H., Ruhnau, C., and Prange, A. (2011). A Novel Proteinaceous Cytotoxin from the Northern Scyphozoa Cyanea Capillata (L.) with Structural Homology to Cubozoan Haemolysins. *Toxicon* 57, 721–729. doi:10.1016/j.toxicon.2011.02.004

Lassen, S., Wiebring, A., Helmholz, H., Ruhnau, C., and Prange, A. (2012). Isolation of a Nav Channel Blocking Polypeptide from Cyanea Capillata Medusae - a Neurotoxin Contained in Fishing Tentacle Isorhizas. *Toxicon* 59, 610–616. doi:10.1016/j.toxicon.2012.02.004

Lauridsen, L. P., Laustsen, A. H., Lomonte, B., and Gutiérrez, J. M. (2016). Toxicovenomics and Antivenom Profiling of the Eastern green Mamba Snake (Dendroaspis Angusticeps). *J. Proteomics* 136, 248–261. doi:10.1016/j.jprot.2016.02.003

Lee, H., Jung, E. S., Kang, C., Yoon, W. D., Kim, J. S., and Kim, E. (2011). Scyphozoan Jellyfish Venom Metalloproteinases and Their Role in the Cytotoxicity. *Toxicon* 58, 277–284. doi:10.1016/j.toxicon.2011.06.007

Li, R., Yu, H., Feng, J., Xing, R., Liu, S., Wang, L., et al. (2011). Two-Step Purification and *In Vitro* Characterization of a Hemolysin from the Venom of Jellyfish Cyanea Nozakii Kishinouye. *Int. J. Biol. Macromol* 49, 14–19. doi:10.1016/j.ijbiomac.2011.03.005

Li, R., Yu, H., Xing, R., Liu, S., Qing, Y., Li, K., et al. (2012). Isolation, Identification and Characterization of a Novel Antioxidant Protein from the Nematocyst of the Jellyfish Stomolophus meleagris. *Int. J. Biol. Macromol* 51, 274–278. doi:10.1016/j.ijbiomac.2012.05.015

Li, R., Yu, H., Xing, R., Liu, S., Qing, Y., Li, K., et al. (2013). Isolation and *In Vitro* Partial Characterization of Hemolytic Proteins from the Nematocyst Venom of the Jellyfish Stomolophus meleagris. *Toxicol. Vitro* 27, 1620–1625. doi:10.1016/j.tiv.2013.04.004

Li, R., Yu, H., Xue, W., Yue, Y., Liu, S., Xing, R., et al. (2014). Jellyfish Venomics and Venom Gland Transcriptomics Analysis of Stomolophus meleagris to Reveal the Toxins Associated with Sting. *J. Proteomics* 106, 17–29. doi:10.1016/j.jprot.2014.04.011

Li, R., Yu, H., Yue, Y., and Li, P. (2018). Combined Proteome and Toxicology Approach Reveals the Lethality of Venom Toxins from Jellyfish Cyanea Nozakii. *J. Proteome Res.* 17, 3904–3913. doi:10.1021/acs.jproteome.8b00568

Li, A., Yu, H., Li, R., Liu, S., Xing, R., and Li, P. (2019). Inhibitory Effect of Metalloproteinase Inhibitors on Skin Cell Inflammation Induced by Jellyfish Nemopilema Nomurai Nematocyst Venom. *Toxins (Basel)* 11, 12. doi:10.3390/toxins11030156

Li, R., Yu, H., Li, T., and Li, P. (2020). Comprehensive Proteome Reveals the Key Lethal Toxins in the Venom of Jellyfish Nemopilema Nomurai. *J. Proteome Res.* 19, 2491–2500. doi:10.1021/acs.jproteome.0c00277

Liumin, M., Ling-bo, L., Jian-zhong, L., and Jiansheng, C. J. (2011). Taxonomic Relationship between Nemopilema Nomurai(in the Yellow Sea of China and the East China Sea)and Stomolophus meleagris Based on the Analysis of 18 SrDNA Partial Sequences. *Mar. Fish.* 33, 131–137.

Mandelbaum, F. R., Reichel, A. P., and Assakura, M. T. (1982). Isolation and Characterization of a Proteolytic Enzyme from the Venom of the Snake

Bothrops jararaca (Jararaca). *Toxicon* 20, 955–972. doi:10.1016/0041-0101(82)90098-8

Marrakchi, N., Zingali, R. B., Karoui, H., Bon, C., and el Ayeb, M. (1995). Cerastocytin, A New Thrombin-Like Platelet Activator from the Venom of the Tunisian Viper Cerastes Cerastes. *Biochim. Biophys. Acta* 1244, 147–156. doi:10.1016/0304-4165(94)00216-k

Marrakchi, N., Barbouche, R., Guermazi, S., Bon, C., and el Ayeb, M. (1997). Procoagulant and Platelet-Aggregating Properties of Cerastocytin from Cerastes Cerastes Venom. *Toxicon* 35, 261–272. doi:10.1016/s0041-0101(96)00116-x

Morine, N., Matsuda, S., Terada, K., Eto, A., Ishida, I., and Oku, H. (2008). Neutralization of Hemorrhagic Snake Venom Metalloproteinase HR1a from Protobothrops Flavoviridis by Human Monoclonal Antibody. *Toxicon* 51, 345–352. doi:10.1016/j.toxicon.2007.10.009

Patiño, A. C., Pereañez, J. A., Núñez, V., Benjumea, D. M., Fernandez, M., Rucavado, A., et al. (2010). Isolation and Biological Characterization of Batx-I, a Weak Hemorrhagic and Fibrinogenolytic PI Metalloproteinase from Colombian *Bothrops A* Venom. *Toxicon* 56, 936–943. doi:10.1016/j.toxicon.2010.06.016

Rastogi, A., Sarkar, A., and Chakrabarty, D. (2017). Partial Purification and Identification of a Metalloproteinase with Anticoagulant Activity from Rhizostoma Pulmo (Barrel Jellyfish). *Toxicon* 132, 29–39. doi:10.1016/j.toxicon.2017.04.006

Rottini, G., Gusmani, L., Parovel, E., Avian, M., and Patriarca, P. (1995). Purification and Properties of a Cytolytic Toxin in Venom of the Jellyfish Carybdea Marsupialis. *Toxicon* 33, 315–326. doi:10.1016/0041-0101(94)00174-7

Sánchez-Rodríguez, J., Torrens, E., and Segura-Puertas, L. (2006). Partial Purification and Characterization of a Novel Neurotoxin and Three Cytolysins from Box Jellyfish (Carybdea Marsupialis) Nematocyst Venom. *Arch. Toxicol.* 80, 163–168. doi:10.1007/s00204-005-0023-7

Siigur, E., Tõnismägi, K., Trummal, K., Samel, M., Vija, H., Subbi, J., et al. (2001). Factor X Activator from Vipera Lebetina Snake Venom, Molecular Characterization and Substrate Specificity. *Biochim. Biophys. Acta* 1568, 90–98. doi:10.1016/s0304-4165(01)00206-9

Siigur, E., Aaspõllu, A., Trummal, K., Tõnismägi, K., Tammiste, I., Kalkkinen, N., et al. (2004). Factor X Activator from Vipera Lebetina Venom Is Synthesized from Different Genes. *Biochim. Biophys. Acta* 1702, 41–51. doi:10.1016/j.bbapap.2004.07.007

Sun, Q. Y., and Bao, J. (2010). Purification, Cloning and Characterization of a Metalloproteinase from Naja Atra Venom. *Toxicon* 56, 1459–1469. doi:10.1016/j.toxicon.2010.08.013

Sun, S., Sun, X.-X., and Jenkinson, I. R. (2015a). Preface: Giant Jellyfish Blooms in Chinese Waters. *Hydrobiologia* 754, 1–11. doi:10.1007/s10750-015-2320-3

Sun, S., Zhang, F., Li, C., Wang, S., Wang, M., Tao, Z., et al. (2015b). Breeding Places, Population Dynamics, and Distribution of the Giant Jellyfish Nemopilema Nomurai (Scyphozoa: Rhizostomeae) in the Yellow Sea and the East China Sea. *Hydrobiologia* 754, 59–74. doi:10.1007/s10750-015-2266-5

Takeda, S., Igarashi, T., and Mori, H. (2007). Crystal Structure of RVV-X: An Example of Evolutionary Gain of Specificity by ADAM Proteinases. *FEBS Lett.* 581, 5859–5864. doi:10.1016/j.febslet.2007.11.062

Takeya, H., Nishida, S., Miyata, T., Kawada, S., Saisaka, Y., Morita, T., et al. (1992). Coagulation Factor X Activating Enzyme from Russell's viper Venom (RVV-X). A Novel Metalloproteinase with Disintegrin (Platelet Aggregation Inhibitor)-like and C-type Lectin-like Domains. *J. Biol. Chem.* 267, 14109–14117. doi:10.1016/s0021-9258(19)49685-3

Trummal, K., Tõnismägi, K., Siigur, E., Aaspõllu, A., Lopp, A., Sillat, T., et al. (2005). A Novel Metalloprotease from Vipera Lebetina Venom Induces Human Endothelial Cell Apoptosis. *Toxicon* 46, 46–61. doi:10.1016/j.toxicon.2005.03.008

Wagstaff, S. C., Favreau, P., Cheneval, O., Laing, G. D., Wilkinson, M. C., Miller, R. L., et al. (2008). Molecular Characterisation of Endogenous Snake Venom Metalloproteinase Inhibitors. *Biochem. Biophys. Res. Commun.* 365, 650–656. doi:10.1016/j.bbrc.2007.11.027

Wang, W. J., Shih, C. H., and Huang, T. F. (2004). A Novel P-I Class Metalloproteinase with Broad Substrate-Cleaving Activity, Agkislysin, from Agkistrodon Acutus Venom. *Biochem. Biophys. Res. Commun.* 324, 224–230. doi:10.1016/j.bbrc.2004.09.031

Xiao, L., Liu, S., He, Q., Wang, Q., Ye, X., Liu, G., et al. (2011). The Acute Toxicity and Hematological Characterization of the Effects of Tentacle-Only Extract from the Jellyfish Cyanea Capillata. *Mar. Drugs* 9, 526–534. doi:10.3390/md9040526

Xiong, S., and Huang, C. (2018). Synergistic Strategies of Predominant Toxins in Snake Venoms. *Toxicol. Lett.* 287, 142–154. doi:10.1016/j.toxlet.2018.02.004

Xiong, S., Luo, Y., Zhong, L., Xiao, H., Pan, H., Liao, K., et al. (2017). Investigation of the Inhibitory Potential of Phospholipase A2 Inhibitor Gamma from *Sinonatrix A* to Snake Envenomation. *Toxicon* 137, 83–91. doi:10.1016/j.toxicon.2017.07.019

Xu, L. P., Jiang, W. J., Ma, T., Qiu, P. X., Hou, J., Huang, Y. J., et al. (2006). Expression, Purification and Molecular Modeling of Recombinant Fibrinogenase [IV], a Metalloproteinase from Deinakistrodon Acutus Venom. *Toxicon* 47, 241–248. doi:10.1016/j.toxicon.2005.11.005

Xu, Y., Ishizaka, J., Yamaguchi, H., Siswanto, E., and Wang, S. (2013). Relationships of Interannual Variability in SST and Phytoplankton Blooms with Giant Jellyfish (Nemopilema Nomurai) Outbreaks in the Yellow Sea and East China Sea. *J. Oceanogr* 69, 511–526. doi:10.1007/s10872-013-0189-1

Yamada, D., Sekiya, F., and Morita, T. (1996). Isolation and Characterization of Carinactivase, a Novel Prothrombin Activator in *Echis carinatus* Venom with a Unique Catalytic Mechanism. *J. Biol. Chem.* 271, 5200–5207. doi:10.1074/jbc.271.9.5200

Yang, Y., Cun, S., Peng, L., Xie, X., Wei, J., Yang, W., et al. (2003). cDNA Cloning, Identification and Characterization of a Novel Cystatin from the Tentacle of Cyanea Capillata. *Biochimie* 85, 1033–1039. doi:10.1016/s0300-9084(03)00132-9

Yang, S., Yang, F., Zhang, B., Lee, B. H., Li, B., Luo, L., et al. (2017). A Bimodal Activation Mechanism Underlies Scorpion Toxin-Induced Pain. *Sci. Adv.* 3, e1700810. doi:10.1126/sciadv.1700810

Yoon, W. D., Lee, H. E., Han, C., Chang, S.-J., and Lee, K. (2014). Abundance and Distribution of Nemopilema Nomurai (Scyphozoa, Rhizostomeae), in Korean Waters in 2005-2013. *Ocean Sci. J.* 49, 183–192. doi:10.1007/s12601-014-0018-5

Yu, H., Liu, X., Dong, X., Li, C., Xing, R., Liu, S., et al. (2005). Insecticidal Activity of Proteinous Venom from Tentacle of Jellyfish Rhopilema Esculentum Kishinouye. *Bioorg. Med. Chem. Lett.* 15, 4949–4952. doi:10.1016/j.bmcl.2005.08.015

Yue, Y., Yu, H., Li, R., Xing, R., Liu, S., Li, K., et al. (2017a). Functional Elucidation of Nemopilema Nomurai and Cyanea Nozakii Nematocyst Venoms' Lytic Activity Using Mass Spectrometry and Zymography. *Toxins (Basel)* 9, 18. doi:10.3390/toxins9020047

Yue, Y., Yu, H., Li, R., Xing, R., Liu, S., Li, K., et al. (2017b). Biochemical and Kinetic Evaluation of the Enzymatic Toxins from Two Stinging Scyphozoans Nemopilema Nomurai and Cyanea Nozakii. *Toxicon* 125, 1–12. doi:10.1016/j.toxicon.2016.11.005

Yue, Y., Yu, H., Li, R., and Li, P. (2021). Topical Exposure to Nemopilema Nomurai Venom Triggers Oedematogenic Effects: Enzymatic Contribution and Identification of Venom Metalloproteinase. *Toxins (Basel)* 13, 44. doi:10.3390/toxins13010044

Zhang, M., Fishman, Y., Sher, D., and Zlotkin, E. (2003). Hydralysin, a Novel Animal Group-Selective Paralytic and Cytolytic Protein from a Noncnidocystic Origin in hydra. *Biochemistry* 42, 8939–8944. doi:10.1021/bi0343929

Zhang, S. T., Lu, P., Qin, Y. F., Chen, S. J., and Guo, A. G. (2010). Cloning and Identification of a Novel P-II Class Snake Venom Metalloproteinase from Gloydius Halys. *Appl. Biochem. Biotechnol.* 162, 1391–1402. doi:10.1007/s12010-010-8911-6

Zhu, L., Yuan, C., Chen, Z., Wang, W., and Huang, M. (2010). Expression, Purification and Characterization of Recombinant Jerdonitin, a P-II Class Snake Venom Metalloproteinase Comprising Metalloproteinase and Disintegrin Domains. *Toxicon* 55, 375–380. doi:10.1016/j.toxicon.2009.08.016

Conflict of Interest: The authors declare that the research was conducted in the absence of any commercial or financial relationships that could be construed as a potential conflict of interest.

Publisher's Note: All claims expressed in this article are solely those of the authors and do not necessarily represent those of their affiliated organizations or those of the publisher, the editors, and the reviewers. Any product that may be evaluated in this article, or claim that may be made by its manufacturer, is not guaranteed or endorsed by the publisher.

frontiers in Pharmacology

ORIGINAL RESEARCH
published: 01 December 2021
doi: 10.3389/fphar.2021.763089

Toxic Peptide From *Palythoa caribaeorum* Acting on the TRPV1 Channel Prevents Pentylenetetrazol-Induced Epilepsy in Zebrafish Larvae

Xiufen Wang[1†], Qiwen Liao[1,2†], Hanbin Chen[1], Guiyi Gong[1], Shirley Weng In Siu[3], Qian Chen[1], Hiotong Kam[1], Carolina Oi Lam Ung[1], Kwok-Kuen Cheung[4], Gandhi Rádis-Baptista[5], Clarence Tsun Ting Wong[6] and Simon Ming-Yuen Lee[1]**

[1]State Key Laboratory of Quality Research in Chinese Medicine and Institute of Chinese Medical Sciences, University of Macau, Macau, China, [2]School of Life and Health Sciences, The Chinese University of Hong Kong, Shenzhen, China, [3]Department of Computer and Information Science, Faculty of Science and Technology, University of Macau, Macau, China, [4]Department of Rehabilitation Sciences, The Hong Kong Polytechnic University, Hong Kong, China, [5]Laboratory of Biochemistry and Biotechnology, Institute for Marine Sciences, Federal University of Ceará, Fortaleza, Brazil, [6]Department of Applied Biology and Chemical Technology, The Hong Kong Polytechnic University, Hong Kong, China

OPEN ACCESS

Edited by:
Heike Wulff,
University of California, Davis,
United States

Reviewed by:
Anselm Zdebik,
University College London,
United Kingdom
Jean-sebastien Rougier,
University of Bern, Switzerland

***Correspondence:**
Simon Ming-Yuen Lee
simonlee@um.edu.mo
Clarence Tsun Ting Wong
clarence-tt.wong@polyu.edu.hk

[†]These authors have contributed equally to this work

Specialty section:
This article was submitted to Pharmacology of Ion Channels and Channelopathies, a section of the journal Frontiers in Pharmacology

Received: 23 August 2021
Accepted: 08 November 2021
Published: 01 December 2021

Citation:
Wang X, Liao Q, Chen H, Gong G, Siu SWI, Chen Q, Kam H, Ung COL, Cheung K-K, Rádis-Baptista G, Wong CTT and Lee SM-Y (2021) Toxic Peptide From Palythoa caribaeorum Acting on the TRPV1 Channel Prevents Pentylenetetrazol-Induced Epilepsy in Zebrafish Larvae. Front. Pharmacol. 12:763089. doi: 10.3389/fphar.2021.763089

PcActx peptide, identified from the transcriptome of zoantharian *Palythoa caribaeorum,* was clustered into the phylogeny of analgesic polypeptides from sea anemone *Heteractis crispa* (known as APHC peptides). APHC peptides were considered as inhibitors of transient receptor potential cation channel subfamily V member 1 (TRPV1). TRPV1 is a calcium-permeable channel expressed in epileptic brain areas, serving as a potential target for preventing epileptic seizures. Through *in silico* and *in vitro* analysis, PcActx peptide was shown to be a potential TRPV1 channel blocker. *In vivo* studies showed that the linear and oxidized PcActx peptides caused concentration-dependent increases in mortality of zebrafish larvae. However, monotreatment with PcActx peptides below the maximum tolerated doses (MTD) did not affect locomotor behavior. Moreover, PcActx peptides (both linear and oxidized forms) could effectively reverse pentylenetetrazol (PTZ)-induced seizure-related behavior in zebrafish larvae and prevent overexpression of *c-fos* and *npas4a* at the mRNA level. The excessive production of ROS induced by PTZ was markedly attenuated by both linear and oxidized PcActx peptides. It was also verified that the oxidized PcActx peptide was more effective than the linear one. In particular, oxidized

Abbreviations: AEDs, antiepileptic drugs; AMPA, α-amino-3-hydroxy-5-methyl-4-isoxazolepropioniac acid; APHC, analgesic polypeptides from sea anemone Heteractis crispa; ASIC, acid-sensing ion channel; CaV, voltage-gated calcium channel; CNS, central nervous system; dpf, day post-fertilization; EAAT2, Excitatory amino acid transporter 2; GABA, γ-aminobutyric acid; Gabra1, GABAA receptor α 1; GAD1, glutamate decarboxylase 1; GAT 1, GABA transporter 1; GAT 1, GABA transporter 1; IER, immediate early response; iGluR, ionotropic glutamate receptors; KV, voltage-gated potassium channel; MD, molecular dynamics; mGluR, metabotropic glutamate receptor; MTD, maximum tolerated doses; MW, molecular weight; NaV, voltage-gated sodium channel; NMDA, N-methyl-D-aspartate; PTZ, pentylenetetrazol; RMSD, root-mean squared deviation; SCG, superior cervical ganglion; ShK, Stichodactyla toxin; TRP, transient receptor potential cation channel; TRPV1, transient receptor potential cation channel subfamily V member 1.

PcActx peptide notably modulated the mRNA expression of genes involved in calcium signaling and γ-aminobutyric acid (GABA)ergic-glutamatergic signaling, including *calb1, calb2*, *gabra1*, *grm1*, *gria1b*, *grin2b, gat1*, *slc1a2b, gad1b,* and *glsa*. Taken together, PcActx peptide, as a novel neuroactive peptide, exhibits prominent anti-epileptic activity, probably through modulating calcium signaling and GABAergic-glutamatergic signaling, and is a promising candidate for epilepsy management.

Keywords: zoantharian, PcActx peptide, transcriptomics analysis, TRPV1 channel, anti-epilepsy, zebrafish

INTRODUCTION

The Phylum Cnidaria, containing almost 13,000 species, is classified into five main classes: Anthozoa, Cubozoa, Hydrozoa, Scyphozoa, and Staurozoa (Kayal et al., 2013). The classes Myxozoa and Polypodiozoa are also recognized as cnidarians (Jimenez-Guri et al., 2007). Cnidocytes are specific to cnidarians, which convey venomous compounds to other organisms for defense or predation (Jouiaei et al., 2015). Phylum Cnidaria represents a large number of bioactive peptide toxins that could contribute to the development of drug therapies, owing to their selective and specific interaction with diverse kinds of ion channels, including voltage-gated potassium (K_V), calcium (Ca_V) and sodium (Na_V) channels, the acid-sensing ion (ASIC) channel, and the TRPV1 channel (Mouhat et al., 2004).

Of particular interest is Anthozoa which is currently categorized into 11 orders and almost 7,000 species (such as sea anemones, corals and zoanthids), comprising about 65% of all known cnidarian species. Most sources of the bioactive peptides of Anthozoa were identified from sea anemones. For example, Stichodactyla toxin (ShK) and its analogs, which were found in the sea anemone *Stichodactyla helianthus*, could specifically bind to the K_V1.3 ion channel, potentially serving as effective therapies for autoimmune diseases (Castaneda et al., 1995; Norton et al., 2015). An analog of ShK, named ShK-186 or dalazatide, is currently in human clinical trials (Tarcha et al., 2017). Another example is the peptide APETx2, derived from sea anemone *Anthopleura elegantissima* (Diochot et al., 2004). A previous report showed that it exerted analgesic effects in an inflammatory pain model through inhibition of the ASIC3 channel (Karczewski et al., 2010). Recently, understanding of the venom peptide components in anthozoan species other than sea anemones has allowed novel bioactive peptides with important pharmacological effects to be discovered. As a zoantharian, a subclass of Hexacorallia, *Palythoa caribaeorum* is in the sister clade of sea anemone (Kayal et al., 2017). Its mucus, traditionally used in folk medicine in northeastern Brazilian coastal regions, has properties that make it useful as an anesthetic, analgesic and anti-inflammatory agent, along with healing properties in the treatment of topical wounds (de Andrade Melo et al., 2012). It was reported that the venom of *P. caribaeorum* delays inactivation of the Na_V1.7 channel and inhibits Ca_V2.2 channel and K_V (I_A and I_{DR} currents) channels on superior cervical ganglion (SCG) neurons (Lazcano-Perez et al., 2016). In our previous studies, two peptides from *P. caribaeorum*, namely PcShK and PcKuz, were shown to act on the K_V ion channel and displayed neuroprotective and cardioprotective effects *in vitro* and *in vivo* (Liao et al., 2018a; Liao et al., 2018b).

APHC peptides from sea anemone *Heteractis crispa* were firstly reported as peptide antagonists of the TRPV1 channel (Andreev et al., 2008). APHC3 displayed the most potent inhibitory effect (71%) on capsaicin-induced TRPV1 activation (Nikolaev et al., 2017). *In vivo* studies showed that APHC peptides produced significant analgesic effects in different pain models (Andreev et al., 2008; Andreev et al., 2013). In addition, HCRG21, obtained from the sea anemone *H. crispa*, shares high structural homology with APHC peptides and fully inhibits the TRPV1 channel (Monastyrnaya et al., 2016).

The TRPV1 channel belongs to subfamily vanilloid of the transient receptor potential (TRP) cation channel (Montell et al., 2002). It is a tetrameric architecture, the subunits of which exhibit four-fold symmetry around a central ion-conducting pathway (Liao et al., 2013). Each subunit has six transmembrane domains (S1-S6), a hydrophobic pore located between S5 and S6, and cytosolic C- and N-terminal tails (Liao et al., 2013). The transmembrane domains S5, S6 and their linker form the central ion permeation pore, while S1-S4 and the cytosolic N- and C-terminals are considered to regulate channel gating (Vay et al., 2012). In addition, the TRPV1 channel allows Ca^{2+} to pass through the cell membrane via non-selectively hydrophobic pores (Ramsey et al., 2006). The TRPV1 channel was discovered in primary sensory neurons and non-neuronal cells (Caterina et al., 1997; Toth et al., 2005; Jeffry et al., 2009), and was activated by noxious heat (≥43°C) and inflammatory substances, such as N-arachidonoylethanolamide, as well as protons (low pH), which contribute to pain hypersensitivity (Liao et al., 2013). It can also be activated by capsaicin, oxidative stress, hydrogen peroxide, nitric oxide, and oxidized linoleic acid (Naziroglu, 2015).

Moreover, the TRPV1 channel has been confirmed to be expressed in dentate gyrus and the CA1 area of the hippocampus, which acts as an important site for epilepsy induction (Roberts et al., 2004; Toth et al., 2005). Epilepsy is pathologically characterized by an imbalance between excitatory glutamate transmission and inhibitory GABA impulses, and abnormal activation of ion channels (Na^+, K^+ and Ca^{2+}) (Jefferys, 2010). Reports showed that TRPV1 channel activation enhanced glutamate release and glutaminergic signaling (Gerdeman and Lovinger, 2001; Shoudai et al., 2010; Fawley et al., 2014), decreased GABA release (Gonzalez-Aparicio and Moratalla, 2014; von Ruden et al., 2015), and induced Ca^{2+}

accumulation (Naziroglu et al., 2014), which were confirmed to be responsible for synaptic efficacy and epilepsy. Overload of cytosolic Ca^{2+} causes severe mitochondrial dysfunction, and thereby increases the generation of ROS and release of apoptosis-related factors (like caspase 3 and 9) (Naziroglu et al., 2014; Ovey and Naziroglu, 2015). Meanwhile, ROS formation is recognized to further aggravate epileptic seizure via TRPV1 activation (Naziroglu, 2015). However, the TRPV1 channel blockers, capsazepine and 5′-iodoresiniferatoxin (IRTX), exhibited protective effects against epilepsy-induced Ca^{2+} influx and apoptosis via the TRPV1 channel in hippocampal and dorsal root ganglion (DRG) neurons (Ghazizadeh and Naziroglu, 2014; Naziroglu et al., 2015; Naziroglu and Ovey, 2015). The TRPV1 channel agonist capsaicin significantly increased the spontaneous excitatory synaptic transmission induced by glutamate, while it was reversed by treatment with both capsazepine and IRTX, indicating their modulation of glutamatergic systems (Starowicz et al., 2007; Bhaskaran and Smith, 2010). Taken together, a reduction of calcium accumulation and regulation of glutaminergic systems through inhibition of the TRPV1 channel can be exploited to induce neuronal protective effects against epileptic seizure.

We previously performed deep RNA-Seq of the whole transcriptome of *P. caribaeorum* which was deposited at DDBJ/EMBL/GenBank under the accession number of GESO00000000 associated with the BioProject PRJNA320984 (Liao et al., 2018b). A series of peptide precursors containing a Kunitz domain were identified, and some of these peptides are homologous with APHC peptides, which are defined as PcActx peptide in the present study. Since APHC peptides have been reported and confirmed as TRPV1 inhibitors, here we aimed to investigate the structure, bioactivity and mechanism of action of PcActx peptide identified from transcriptomics analysis of *P. caribaeorum*.

MATERIALS AND METHODS

Primary Structure Analysis

The peptide sequences, which the candidate peptide might be homologous, were obtained from the UniProtKB database. Phylogenetic analysis was conducted using the program MEGA, version 6 based on the maximum-likelihood method (Tamura et al., 2013), followed by sequence editing and alignment using the MUSCLE algorithm (Edgar, 2004a; b). The bootstrap method was used to validate the reliability of the phylogenetic tree.

Structural Modeling and Molecular Dynamics Simulation

Structures of APHC1 peptide (UniProt ID: B2G331), PcActx peptide and PcActx peptide dimer were homology modeled using the SWISS-MODEL server (Biasini et al., 2014). The GROMACS 5.1 simulation software (Pronk et al., 2013) was used to perform MD simulations with the CHARMM27 all-atom force field. The modeled peptide was firstly solvated with TIP3P water before subjected to equilibration in 300 K for 10 ns, with energy minimization in 5×10^7 steps. The production step is run for 100 ns, with a 2 fs timestep and van der Waals interaction cutoff of 1.2 nm. The thresholds 300 thermostat and 1.0 barostat were used to generate the NPT ensemble. Particle-meshed Ewald (PME) was carried out for long-range electrostatics. Structural alignment was performed to compare the equilibrated structures to the analgesic peptide APHC1 from sea anemone, which was similar to the PcActx peptide. Molecular visualization was achieved using the PyMOL program (version 1.8, Schrödinger, LLC).

Peptide Synthesis and Oxidative Folding

The linear PcActx peptide was synthesized by standard Fmoc solid phase chemistry (GL Biochem, Shanghai, China). All the Cys on the peptide used Cys (Trt) as protecting group. After the synthesis, complete cleavage and deprotection were performed using trifluoroacetic acid in water to remove all the protecting groups on the peptide. The precipitated peptide was obtained by the addition of chilled ether. The crude peptide was purified by RP-HPLC (Agilent Technologies, Santa Clara, CA, United States) using Kromasil 100-5 C18 column (5 μm, 4.6 mm × 150 mm) at a flow rate of 1 ml min^{-1}. The mixture of 0.1% trifluoroacetic in acetonitrile (mobile phase A) and water (mobile phase B) was used with the following gradient: 0–25 min, 25–50% A; 25–25.1 min, 50–100% A; 25.1–30 min, 100% A. The peptide was freeze-dried and retested by RP-HPLC to ensure its purity which was higher than 90% with the presence of one single peak. ESI-MS (Agilent Technologies) analysis was performed to confirm the molecular weight (MW) of the linear PcActx peptide. Operating conditions optimized for the detection of reaction mixture were the followings: Gas temperature: 300°C, Drying gas: 8 L min^{-1}, Nebulizer: 35 psig, Sheath gas temperature: 350°C, Sheath gas flow: 11 L min^{-1}, VCap: 3,500 V, Nozzle voltage: 1,000 V.

Oxidative folding was performed to achieve the oxidized PcActx peptide after synthesizing the linear form (Liao et al., 2019). Linear PcActx peptide was solubilized in sodium carbonate buffer (pH 8.0) at the final concentration of 100 μM, in the presence of reduced and oxidized glutathione of ratio 5:1 for 48 h at room temperature. Nitrogen gas was blown into the solution to protect the peptide against the air oxidation during the reaction. The oxidative reaction was terminated by acidification. Then, the oxidized peptide was purified and retested by RP-HPLC (Waters Corporation, Milford, MA, United States) using XBridge BEH300 C18 column (5 μm, 4.6 mm × 150 mm) at a flow rate of 1 ml min^{-1} with the gradient of 10–80% acetonitrile in 40 min. The ESI-MS analysis was performed to confirm the MW of the oxidized PcActx peptide.

Then the oxidized peptide was incubated in dd-H_2O for 48 h at 1 mM at room temperature. The mass identification of monomeric and dimeric peptides was conducted by ESI-MS. The linear and oxidized PcActx peptides were dissolved in dd-H_2O as a stock solution (10 mM) and stored at - 20 °C for bioactive assay.

Peptide-Protein Docking Analysis

The atomic coordinates of the TRPV1 channel were homology-modeled using the SWISS-MODEL server. The interactions between the PcActx peptide and TRPV1 channel and the interactions between the APHC1 peptide and TRPV1 channel were modeled using ZDOCK, which is a fast Fourier transform (FFT)-based, initial-stage rigid-body molecular docking algorithm (Pierce et al., 2011). The PyMOL program was used for molecular visualization (Humphrey et al., 1996).

Cell Culture and Fluorescent Calcium Measurement

The HEK293 cells (ATCC, Manassas, VA, United States) were maintained in DMEM medium (Gibco, Carlsbad, CA, United States) containing 10% (v/v) fetal bovine serum (FBS, Gibco), and 1% (v/v) penicillin-streptomycin (PS, Gibco), and incubated in a humidified atmosphere of 5% CO_2 at 37°C. HEK293 cells stably expressing human TRPV1 (HEK293-hTRPV1 cell) were generated using Lipo8000™ Transfection Reagent (Beyotime Company, Shanghai, China) according to manufacturer's protocol. Briefly, HEK293 cells were transfected with 2.5 μg of plasmid DNA encoding a human TRPV1 protein (NM_018727.5, IGE Biotechnology, Guangzhou, China). Cells were seeded on the 12-well plate and cultured overnight at 37°C. After pretreatment with PcActx peptide (1 and 0.5 μM) or capsazepine (0.25 μM, TRPV1 antagonist, MCE, NJ, United States) for 4 h, the cells were stained with 2 μM Fluo-4/AM (Invitrogen, San Diego, CA, United States) in dark at 37°C for 30 min in HEPES buffer (NaCl 140 mM, KCl 5 mM, HEPES 10 mM, $MgCl_2$ 2 mM, $CaCl_2$ 2 mM, glucose 10 mM, pH 7.4) and then washed with HEPES buffer three times. Subsequently, the cells were challenge with 10 nM capsaicin (TRPV1 agonist, Sigma-Aldrich, St. Louis, MO. United States) and the calcium levels were immediately detected using the cellSens imaging system of an IX73 microscope (Olympus Co., Tokyo, Japan). The excitation wavelength used was 494 nm and emission wavelength was measured at 516 nm.

Zebrafish Maintenance

AB wild-type zebrafish (*Danio rerio*) were manipulated under standard environmental conditions with a controlled temperature (28.5°C) and light (14 h/10 h light/dark cycle) (Westerfield, 2000). The embryos were collected after natural pairwise mating (3–12 months). Then, the embryos and larvae were raised in an incubator system maintained at 28.5°C in embryo medium.

Survival Rate Determination

Zebrafish larvae at 5-day post-fertilization (5-dpf) were exposed to different concentrations (linear form: 0–80 μM, oxidized form: 0–40 μM) of PcActx peptides for 24 h. The mortality of zebrafish was evaluated by determining the presence or absence of heartbeat. The survival rates, LC_{50} values and MTD values were calculated.

Locomotion Behavioral Test

Locomotion Assay on Normal Zebrafish

Zebrafish larvae (5-dpf) were exposed to PcActx peptides at different concentrations below the MTD (linear form: 5–20 μM, oxidized form: 2.5–10 μM) for 24 h. Then, they were transferred into a 96-well plate (1 fish/well). Zebrafish locomotion was measured for 60 min using a zebrafish tracking system (Viewpoint Life Sciences, Montreal, Canada). Six sessions (10 min each) of locomotion were recorded for each zebrafish larva. The total distance travelled by each zebrafish larva was simultaneously calculated for each recording session.

Locomotion Assay of PTZ-Induced Epileptic Zebrafish Model

Zebrafish larvae (5-dpf) received pretreatment with PcActx peptides at different concentrations for 24 h. Then, larvae were transferred to a 96-well plate (1 fish/well) and treated with 3.3 mM PTZ (Sigma-Aldrich) to induced epileptic seizure. Zebrafish locomotion recording was quickly initiated, and locomotion was measured for 30 min using a zebrafish tracking system (Viewpoint Life Sciences). Six sessions (5 min each) were recorded for each zebrafish larva. The total distance travelled, total distance travelled at high velocity (> 20 mm/s) and total duration of high velocity travel of each zebrafish were simultaneously calculated across sessions. The distance travelled at high velocity (>20 mm/s) was used to represent "fast" activity based on previously established protocols, which is rarely exceeded by control larvae (<5% of control activity) (Ellis et al., 2012).

Quantitative Real-Time PCR

Zebrafish larvae (5 dpf) were treated with PcActx peptides for 24 h prior to treatment of PTZ, which proceeded for an additional 30 min. Total RNA pools of zebrafish larvae were extracted from each group using TRIzol reagent (Life Technologies, Carlsbad, CA, United States) according to the standard protocol. cDNA was reverse-transcribed from isolated RNA using the Transcriptor First Strand cDNA Synthesis Kit (Roche Applied Science, Penzberg, Germany) following the manufacturer's protocol. RT-PCR was performed by using SYBR® Premix Ex Taq™ II (TaKaRa, Shiga, Japan) on the Real-Time PCR System (Agilent Technologies) according to the manufacturer's instructions. The mRNA expression was normalized to *ef1a*. The primer sequences used are listed in **Supplementary Table S1**.

ROS Detection

The concentrations of ROS were estimated using the fluorescent probe, CM-H_2DCFDA (Sigma-Aldrich). After treatment with different PcActx peptides for 24 h, zebrafish larvae were treated with PTZ (10 mM) and CM-H_2DCFA (10 μM) for 1.5 h at 28.5°C in the dark. Excess CM-H_2DCFA was subsequently washed out by embryo medium. Zebrafish larvae were observed by a Disk Scanning Unit (DSU) Confocal Imaging System (Olympus Co.). The microscopic images of zebrafish were obtained in FITC mode. The integrated intensity of ROS was quantified using ImageJ (NIH, Bethesda, MD, United States).

TABLE 1 | Primary sequences and physicochemical characteristics of the PcActx peptides.

Peptides	Primary sequence	MW (monoisotopic mass, Da)	p*I*	Net charge (z)
Linear PcActx	GPCKAAFPRWFYDTKTGKCSQFIYGGCDGNRNNFRT	4104.89	9.36	3.9
Oxidized PcActx	$GPC_3KAAFPRWFYDTKTGKCSQFIYGGC_{27}DGNRNNFRT$	4102.53	9.36	3.9

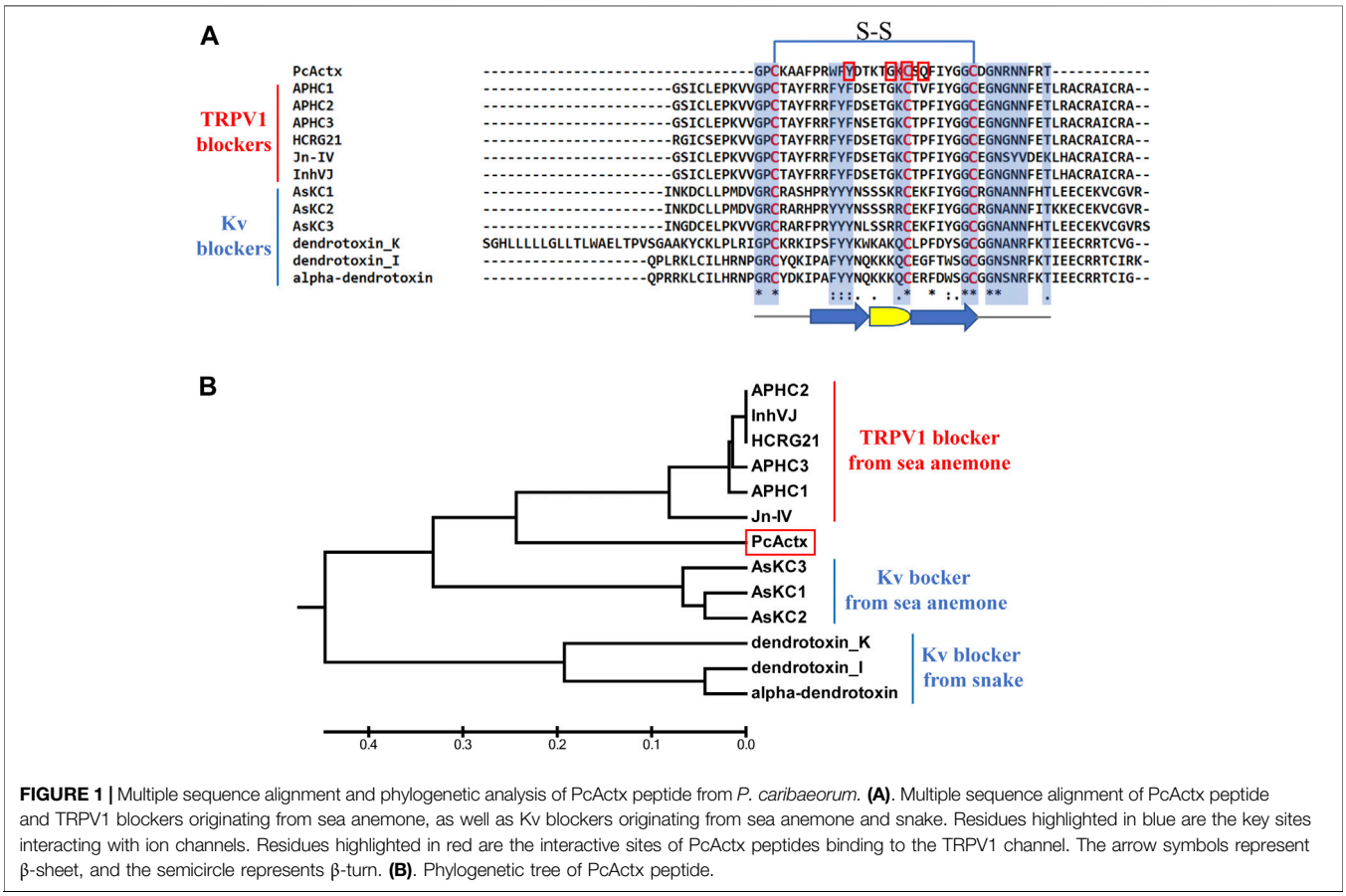

FIGURE 1 | Multiple sequence alignment and phylogenetic analysis of PcActx peptide from *P. caribaeorum*. **(A)**. Multiple sequence alignment of PcActx peptide and TRPV1 blockers originating from sea anemone, as well as Kv blockers originating from sea anemone and snake. Residues highlighted in blue are the key sites interacting with ion channels. Residues highlighted in red are the interactive sites of PcActx peptides binding to the TRPV1 channel. The arrow symbols represent β-sheet, and the semicircle represents β-turn. **(B)**. Phylogenetic tree of PcActx peptide.

Statistical Analysis

Statistical analyses were performed using GraphPad Prism software (version 8.0; GraphPad Software, Inc., San Diego, CA, United States). Data are expressed as means ± standard deviation (SD), and statistical significance was analyzed by one-way ANOVA followed by Dunnett's test for multiple comparisons. Differences between means were considered statistically significant when $p < 0.05$.

RESULTS

PcActx Peptide Sequence Clustering by APHC Peptide Phylogeny

The net charge values, p*I* values, MWs, and sequences of PcActx peptide are shown in **Table 1**. Multiple sequence alignment and phylogenetic analysis were employed to establish the structural relationships of PcActx peptide. As shown in the phylogenetic tree (**Figure 1B**), PcActx peptide was phylogenetically related to APHC and HCRG21 peptides isolated from sea anemone. Multiple sequence alignment analysis (**Figure 1A**) also revealed that PcActx peptide was homologous with APHC peptides. Moreover, the equilibrated PcActx structure well superposed spatially to APHC1 peptide, as shown in **Figure 2E**, giving a root-mean squared deviation (RMSD) value of 0.309 Å. However, APHC peptides contained six cysteine residues and formed three disulfide bridges (Andreev et al., 2008; Kozlov et al., 2009) while PcActx peptide had three cysteine residues and formed one disulfide bond (Cys 3-Cys 27, **Figure 1A**) with one free cysteine residue (Cys 19).

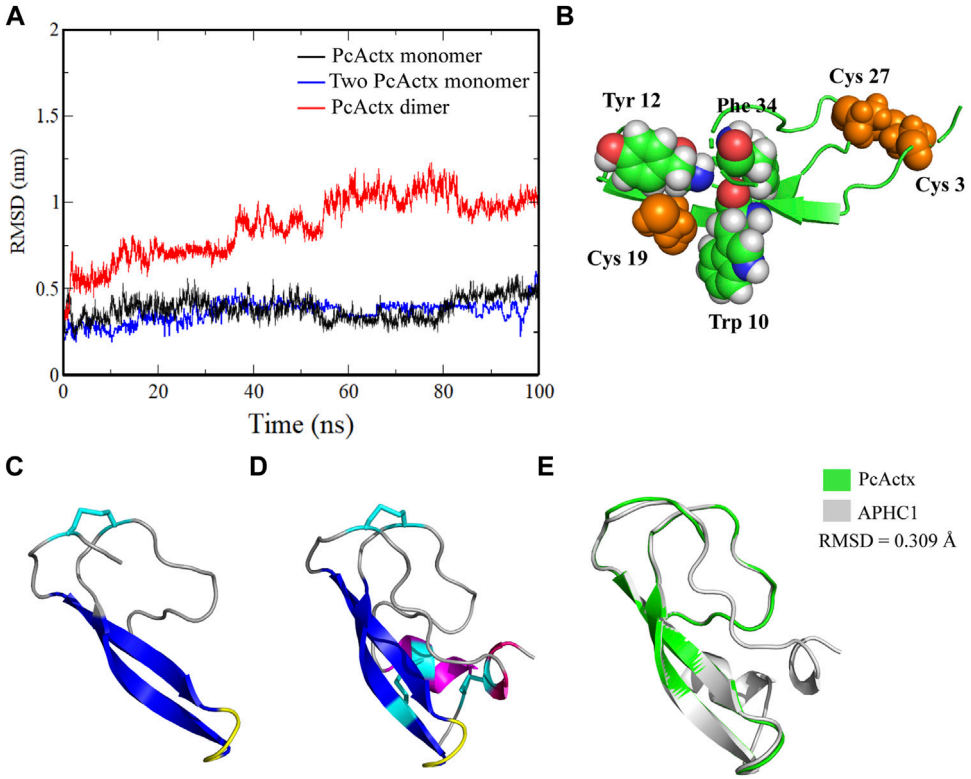

FIGURE 2 | MD simulation and structure comparison. **(A)**. MD simulation of PcActx peptide monomer and dimmer. **(B)**. Spatial structure of Cys 19 of PcActx peptide. Cys residues are shown as spheres in orange. Trp10, Tyr 12 and Phe 34 residues are shown as spheres in green. Other molecules are shown as cartoons in green. **(C,D).** Homology model structure of PcActx **(C)** and APHC1 **(D)** peptide. Molecules are shown as cartoons and colored based on the secondary structure: α-helix in purple, β-sheet in blue, β-turn in yellow, coil in gray, and disulfide bond in cyan. **(E).** Structure overlap of PcActx and APHC1. The structure of PcActx peptide is shown in green, and the structure of APHC1 peptide is shown in gray.

PcActx Peptide Functions as a Monomer Rather Than a Dimer

Since there is one single free cysteine in each PcActx peptide sequence, it is uncertain if the free cysteine residues may bound to each other to cause formation of dimer. The possibility of dimer formation was firstly determined by computational prediction. MD simulation was conducted to determine the stabilization of monomer and dimer forms of PcActx peptide. The RMSD values of PcActx peptide monomer reached a plateau at approximately 0.3 nm after 100 ns simulation (**Figure 2A** in black), indicating that the modeled PcActx peptide monomer is very stable. Similar result was also observed in the system of two PcActx peptide monomers (**Figure 2A** in blue). However, the dimer, formed by connection with an inter-chain disulfide bond at Cys 19 residues of the two peptides, significantly increased the RMSD values at about 1 nm (**Figure 2A** in red). One of the peptide chains in the dimer disrupted during the MD simulation, indicating the instability of the dimer structure. In addition, by looking at the structure (**Figure 2B**), the Cys 19 was frequently attracted by the neighbouring aromatic residues (Trp10, Tyr 12 and Phe 34), which was unfavorable to occurrence of dimerization in the Cys 19 residue.

Moreover, in addition to computational prediction, the feasibility of dimer formation of the PcActx peptide was further evaluated by a chemical experiment. Linear and oxidized PcActx peptides, the purity grade (>90%) and MWs (monoisotopic mass, 4104.89 and 4102.87 Da, respectively) were produced and analyzed by RP-HPLC and MS (**Figures 3A–D**). Then the oxidized peptide was incubated in dd-H_2O for 48 h, for checking if it might form dimer under experimental condition. After incubation for 48 h, no dimer mass was found in the solution as analyzed by ESI-MS (**Figure 3E**). Therefore, both computational and chemical experiments also suggest that the PcActx peptide tends to form a monomer rather than a dimer.

Computational Prediction and Biological Validation of PcActx Peptide as a Ligand of the TRPV1 Channel

Since PcActx peptide was phylogenetically close to APHC peptides, which were reported as TRPV1 inhibitors, we hypothesized that PcActx might also bind to the TRPV1 channel. The docking analysis of APHC1 peptide and PcActx peptide to TRPV1 channel were performed and compared. As depicted in **Figures 4A–D**, it seems that both APHC1 and PcActx could bind with two adjacent subunits of TRPV1 channel. As a positive control, APHC1 peptide interacted with S1, S5 and S5-P-

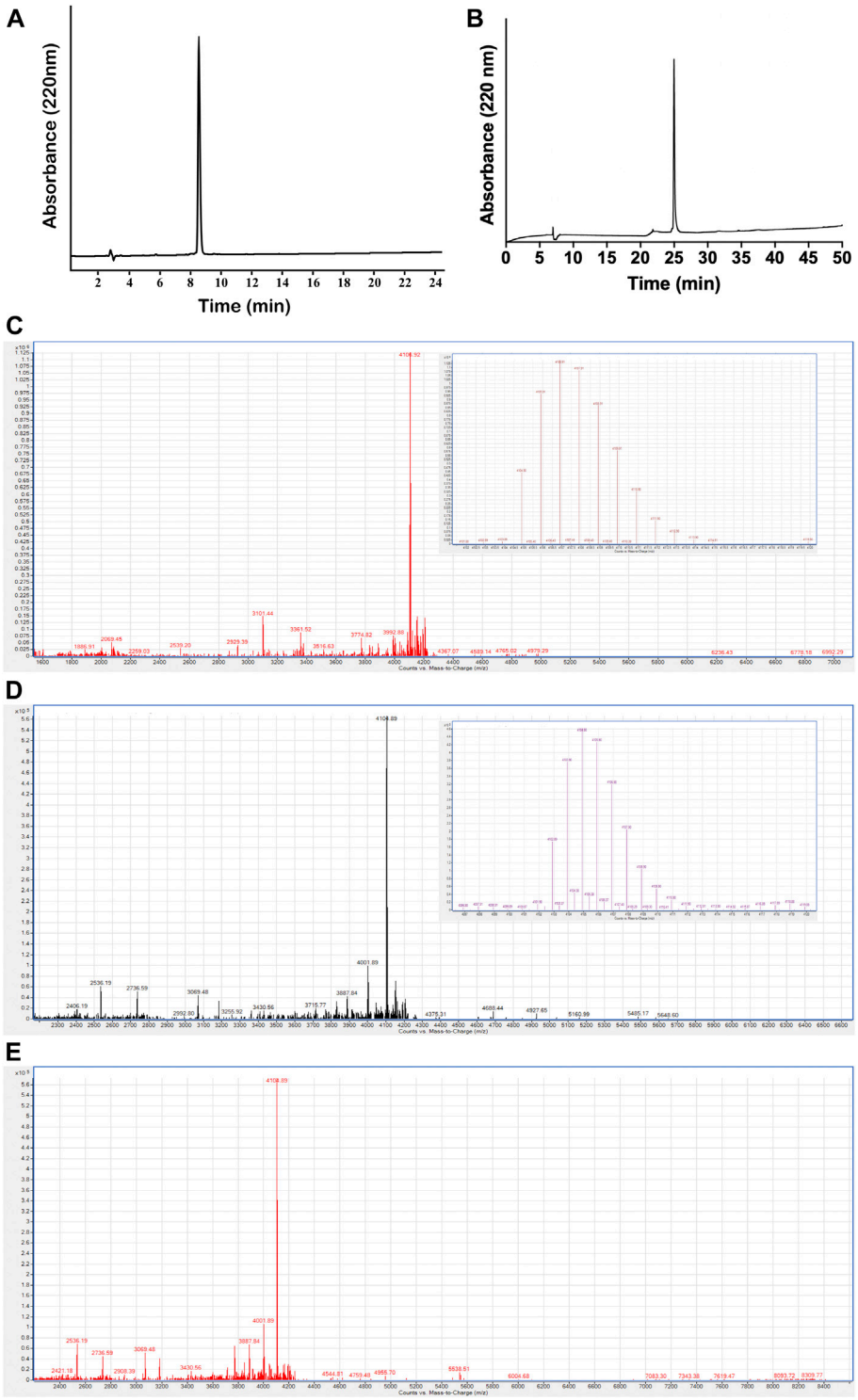

FIGURE 3 | Purification and characterization of PcActx peptides. **(A)**. Analytical RP-HPLC chromatograph for the final purified linear PcActx peptide with absorbance at 220 nm with purity ≥90%. **(B)**. Analytical RP-HPLC chromatograph for the final purified oxidized PcActx peptide with absorbance at 220 nm with purity ≥90%. **(C)**. ESI-MS analysis of linear PcActx peptide. Anal. calcd for $C_{182}H_{265}N_{53}O_{51}S_3$ $[M + H]^+$ 4104.89 Da (monoisotopic mass), found $[M + H]^+$ 4104.90 Da. **(D)**. ESI-MS analysis of oxidized PcActx peptide. Anal. calcd for $C_{182}H_{263}N_{53}O_{51}S_3$ $[M + H]^+$ 4102.87 Da (monoisotopic mass), found $[M + H]^+$ 4102.88 Da. **(E)**. ESI-MS analysis of oxidized PcActx peptide incubated in dd-H_2O for 48 h.

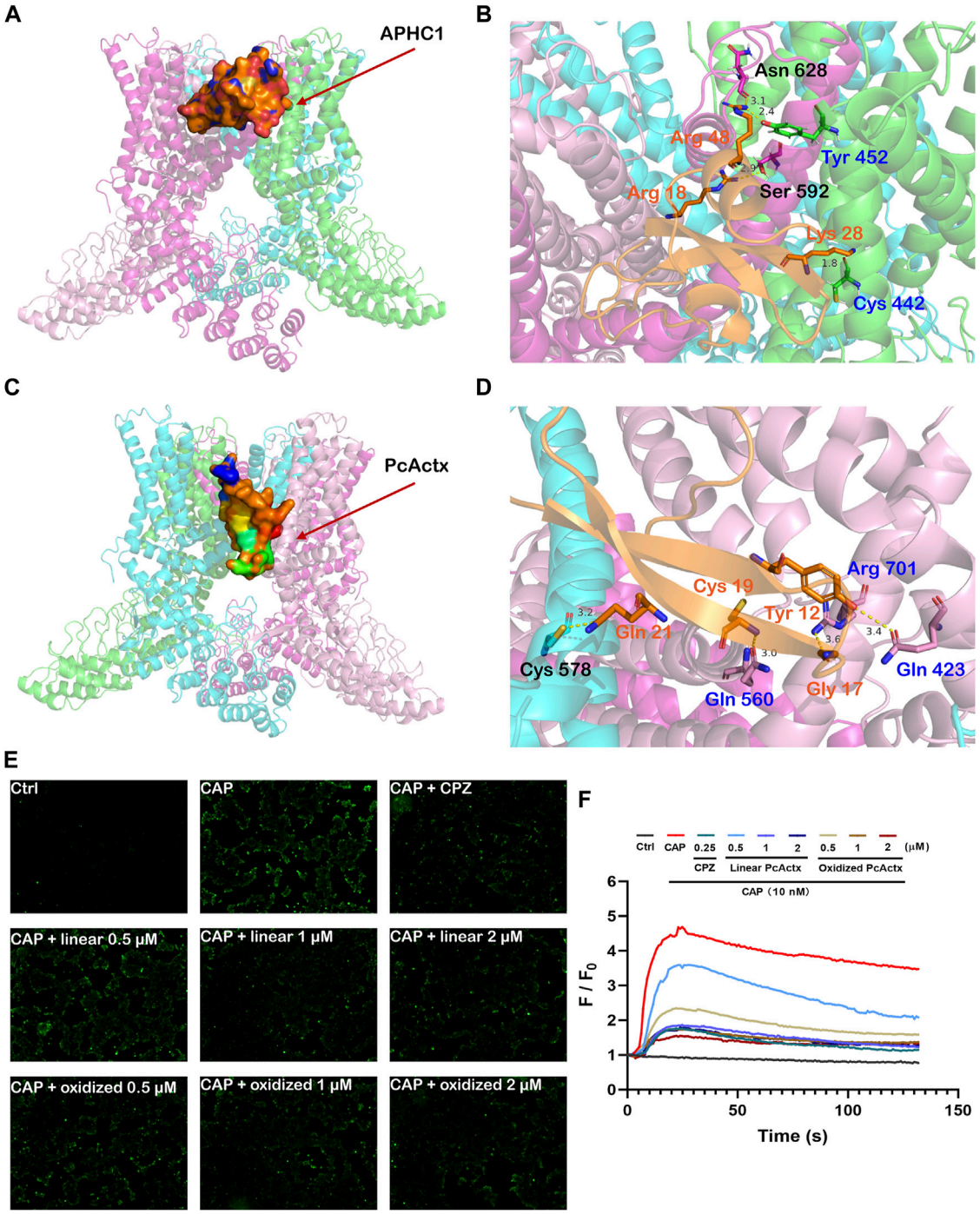

FIGURE 4 | Peptide-protein docking analysis and fluorescent calcium measurement. **(A)**. Side view of protein-peptide docking of the APHC1 peptide binding to the TRPV1 channel. The peptide is shown as a ribbon diagram colored in orange; the protein is shown as a cartoon. **(B)**. Interface residues between APHC1 peptide and the TRPV1 channel. APHC1 peptide is shown in orange cartoon. In α chain, the hydrogen bonds are formed by Arg 18 and Arg 48 of APHC1 peptide with residue Ser 592 and Asn 628, respectively. In β chain, the hydrogen bonds are formed by Lys 28 and Arg 48 of APHC1 peptide with residue Cys 442 and Try 453, respectively. **(C)**. Side view of protein-peptide docking of the PcActx peptide binding to the TRPV1 channel. The peptide is shown as a ribbon diagram colored in orange; the protein is shown as a cartoon. **(D)**. Interface residues between PcActx peptide and the TRPV1 channel. PcActx peptide is shown in orange cartoon. The hydrogen bonds are formed by Tyr12, Gly17, Cys19, and Gln21 of PcActx peptide with residue Gln423, Arg701, Gln560 in γ chain, and Cys578 in δ chain of TRPV1, respectively. **(E)**. Representative images of intracellular calcium concentration of HEK293-hTRPV1 cell (CAP: capsaicin; CPZ: capsazepine). **(F)**. Representative time-dependent response of Ca^{2+} fluorescence intensity in each group. Ca^{2+} responses were measured as changes in fluorescence intensity of the representative average plots (n = 5) before (F_0) and after capsaicin addition (F). **(E,F)** graphs represent a single representative experiment from a total of three independent experiments.

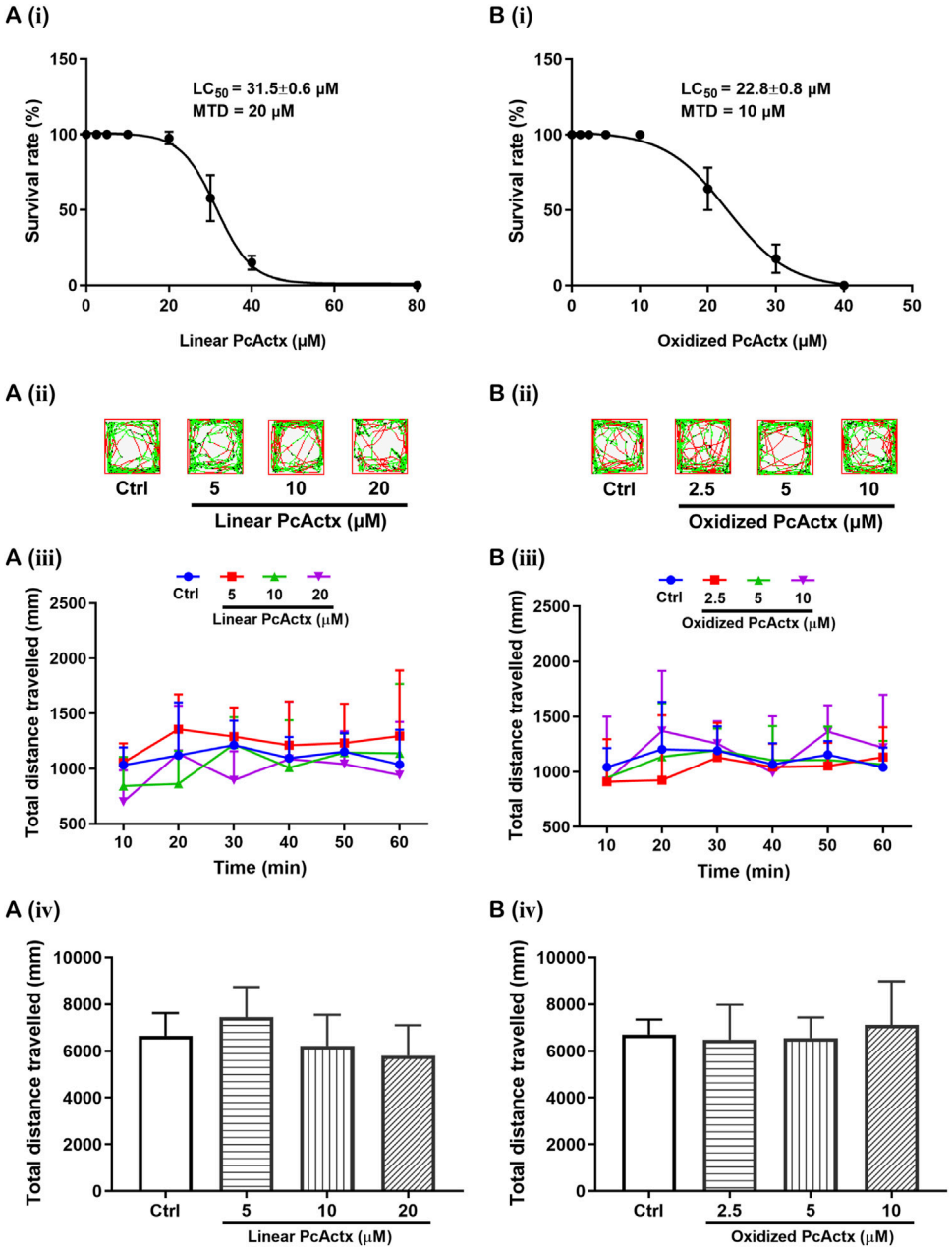

FIGURE 5 | Survival and behavioral toxicity of zebrafish larvae after 24 h exposure to PcActx peptides. **(A)** Linear PcActx peptide. **(B)**. Oxidized PcActx peptide. (i) Survival rates of zebrafish larvae. Data were expressed as means ± SD (n = 3). (ii). Representative patterns of locomotion behavior of zebrafish larvae. The swimming trajectory was recorded every 10 min and is represented by curves. The instantaneous velocity was detected and displayed in different colors (black, <2 mm/s; green, 2–8 mm/s; red, >8 mm/s). (iii). Changes in total distance travelled by period. (iv). Statistical analysis of total distance travelled. Data are expressed as means ± SD (n = 10–12).

S6 domains of the TRPV1 channel. Residues Arg 18 and Arg 48 of APHC1 peptide interacted with residues Ser 592 and Asn 628 in α chain with distances of 2.9 Å and 3.1 Å, respectively. Residues Lys 28 and Arg 48 of APHC1 peptide interacted with residues Cys 442 and Try 453 in β chain with distances of 1.8 Å and 2.4 Å, respectively. Meanwhile, PcActx peptide could interact with the pre-S1 helix, S4-S5 linker and TRP domain of the TRPV1 channel via four hydrogen bonds (**Figures 4C,D**). Residues Tyr 12, Gly 17, Cys 19 and Gln 21 were the interactive sites of PcActx peptide. In γ chain of the TRPV1 channel, Tyr12, Gly17 and Cys19 of the PcActx peptide interacted with Gln 423, Arg 701, and Gln 560 with distances of 3.6 Å, 3.4 Å and 3.0 Å, respectively. In δ chain of the TRPV1 channel, Gln 21 of the PcActx peptide interacted with Cys 578 with a distance of 3.2 Å. Therefore, both

APHC1 and PcActx could potentially bind with two adjacent subunits of TRPV1 channel, but they interacted with different structural domains, respectively.

Moreover, the effect of PcActx peptide on TRPV1 channel mediated calcium influx in cultured cell was determined to confirm the above computational prediction. As shown in **Figures 4E,F**, 10 nM capsaicin, the TRPV1 agonist, can obviously induce the calcium influx in HEK293-hTRPV1 cell at which HEK293 was engineered to express recombinant hTRPV1 protein. However, no obvious calcium response was observed when the non-expressing TRPV1-HEK293 cell were treated with capsaicin at dosages ranging from 10–2 mM (**Supplementary Figure S1**), indicating that capsaicin significantly induced TRPV1-dependent calcium influx. Similar to the TRPV1 channel antagonist capsazepine, linear PcActx pepetide could markedly abated the calcium accumulation at the concentration of 1 and 2 μM. Furthermore, treatment with 0.5 to 2 μM oxidized PcActx peptide also efficaciously inhibited the calcium response evoked by capsaicin (**Figures 4E,F**). Therefore, we believe that the PcActx peptide suppressed the capsaicin-induced calcium influx through the TRPV1 channel inactivation.

Survival Rates of Zebrafish Larvae After Exposure to PcActx Peptides

Survival rates of zebrafish larvae after 24 h exposure to PcActx peptides are shown in **Figure 5**. For linear PcActx peptide [**Figure 5A (i)**], the survival rate was maintained at about 100% when the animals were exposed to a concentration of 20 μM. However, treatment with 40 μM linear PcActx peptide for 24 h resulted in a reduction of survival rate to about 20%. For the oxidized PcActx peptide [**Figure 5B (i)**], survival decreased to low rates with concentrations lower than linear peptide, exhibiting a LC_{50} value of 22.8 μM compared to 31.5 μM. None of the zebrafish survived at the dosages of 40 μM or higher. In addition, the MTD values of linear and oxidized PcActx peptides were estimated as about 20 and 10 μM, respectively.

PcActx Peptides Did Not Interfere With the Normal Locomotor Behavior of Zebrafish Larvae

Locomotion tests were performed to investigate the behavioral regulating effect on zebrafish larvae after 24 h exposure to linear and oxidized forms of PcActx peptide, only at the indicated concentrations below their MTD. Treatment with linear PcActx peptide at dosages ranging from 5 to 20 μM could not significantly regulate the total distance travelled by zebrafish larvae [**Figure 5A (ii-iv)**]. Similar results were observed when zebrafish larvae were treated with 2.5– 10 μM of oxidized PcActx peptide [**Figure 5B (ii-iv)**]. These results demonstrated that neither the linear nor oxidized PcActx peptides interfered with the locomotor behavior of zebrafish larvae at the various indicated concentrations. Concentrations that did not cause death or obvious behavioral deficits in zebrafish larvae were selected for assessing the protective effects against PTZ-induced epileptic seizure.

PcActx Peptides Alleviated PTZ-Induced Hyperactivity in Zebrafish Larvae

PTZ, a non-competitive GABA antagonist, has been widely used to induce seizures for studying the effectiveness of novel antiepileptic drugs (AEDs) (Baraban et al., 2005; Ellis et al., 2012). PTZ-induced seizures elicited behavioral change, such as clonic-like convulsions (Baraban et al., 2005). As shown in **Figures 6**, **7**, 3.3 mM PTZ induced notable hyperactivity in zebrafish larvae, which clearly elevated the total distance travelled and total distance travelled at high velocity (>20 mm/s), and also prolonged the duration of high velocity travel. However, PTZ-induced seizure-related behaviors in zebrafish were efficaciously prevented by PcActx peptides. Linear PcActx peptide clearly decreased the total swimming distance at a concentration of 20 μM (**Figures 6B,C**). Obviously, the total distance travelled at high velocity was inhibited by pretreatment with 20 μM linear PcActx peptide (**Figures 6D,E**). Similarly, a reduction in the total duration of high velocity travel was also observed in the treatment group with 20 μM linear PcActx peptide (**Figures 6F,G**). The oxidized PcActx peptide exhibited a more pronounced effect than the linear version in terms of maintaining normal locomotor behavior (**Figure 7**). Oxidized PcActx peptide significantly decreased the total distance travelled at a dosage of 10 μM (**Figures 7B,C**), and dramatically reduced the total distance travelled at high velocity when the concentration was higher than 1.25 μM (**Figures 7D,E**). Quantitative analysis of the duration of high velocity travel also supported a protective effect of oxidized PcActx peptide on locomotor behavior (**Figures 7F,G**).

PcActx Peptides Prevented PTZ-Induced Up-Regulation of *c-fos* and *npas4a*

In addition to behavioral change, exposure to PTZ could result in an alteration in the expression of immediate early response (IER) genes. Both *c-fos* and *npas4a* are synaptic-activity-regulated genes that are known to be up-regulated by PTZ treatment (Baxendale et al., 2012; Torres-Hernandez et al., 2016). To further confirm the protective effect of PcActx peptides against PTZ-induced epileptic seizure, mRNA expression levels of *c-fos* and *npas4a* were determined by RT-PCR. As depicted in **Figure 8**, significant up-regulation of *c-fos* and *npas4a* was observed in the PTZ-treated groups, as compared to the control groups. Linear PcActx peptide was not able to suppress *c-fos* or *npas4a* expression until the concentration reached 20 μM (**Figure 8A**). Strikingly, both 5 and 10 μM oxidized PcActx peptide noticeably inhibited *c-fos* and *npas4a* expression (**Figure 8B**). Moreover, in the absence of PTZ treatment, the peptides did not induce significant changes in *c-fos* or *npas4a* expression, in parallel to the control groups.

PcActx Peptides Could Inhibit PTZ-Induced ROS Accumulation in Zebrafish

It is well known that oxidative stress can be a cause and consequence of epileptic seizures (Patel, 2004). Mitochondrial oxidative stress and dysfunction might contribute to seizure-related brain damage and can also render the brain more

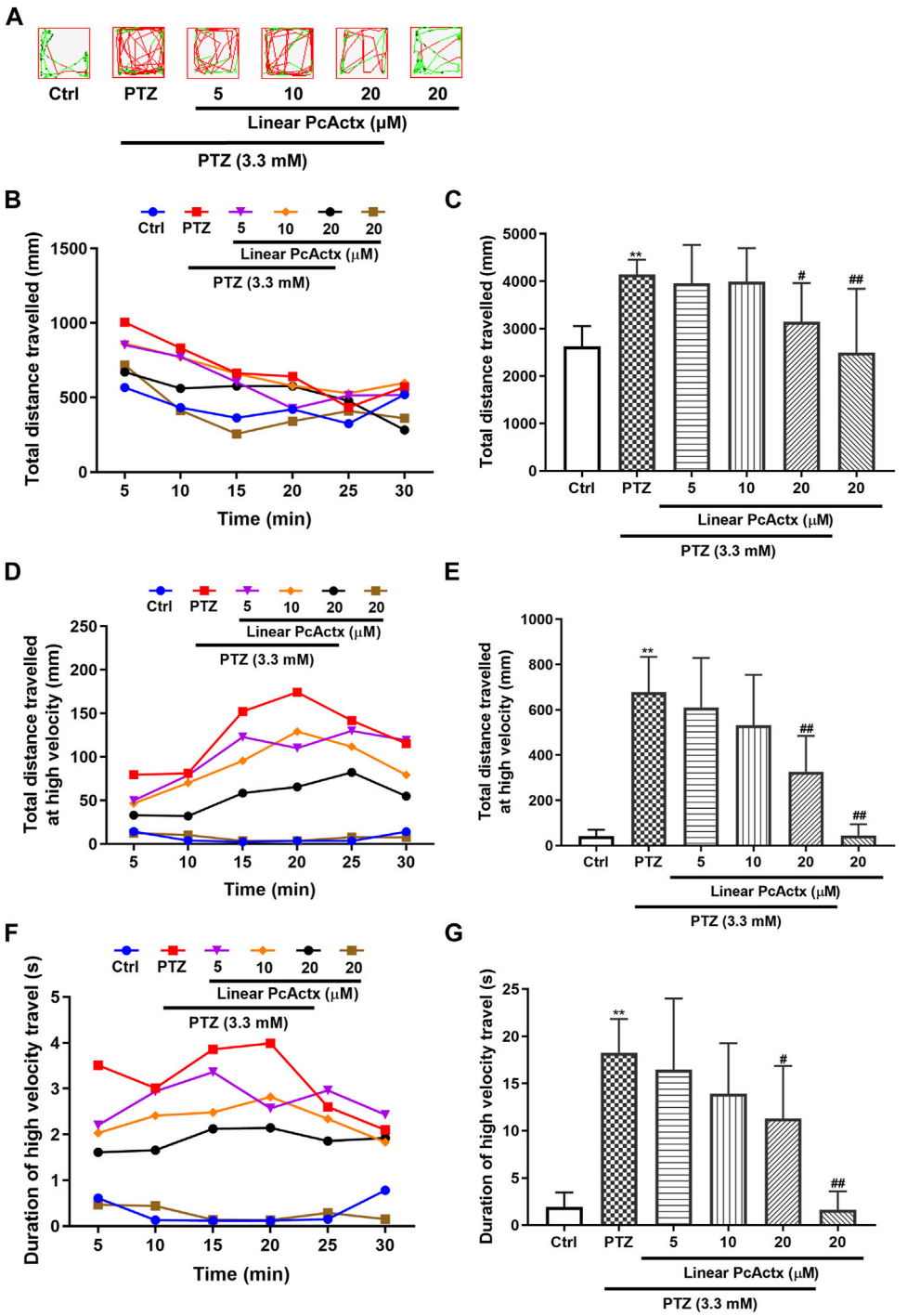

FIGURE 6 | Linear PcActx peptide alleviated PTZ-induced seizure-related behavior in zebrafish larvae. **(A)** Representative patterns of behavioral locomotion in zebrafish larvae. The swimming trajectory was recorded every 5 min and is represented by curves. The instantaneous velocity was detected and displayed in different colors (black, <2 mm/s; green, 2–20 mm/s; red, >20 mm/s). **(B)**. Changes in total distance travelled by period. **(C)**. Statistical analysis of total distance travelled. **(D)**. Changes in total distance travelled at high velocity by period (>20 cm/s). **(E)**. Statistical analysis of total distance travelled at high velocity (>20 cm/s). **(F)**. Changes in the duration of high velocity travel by period (>20 cm/s). **(G)**. Statistical analysis of the duration of high velocity travel (>20 cm/s). Data are expressed as means ± SD (n = 9–10). * $p < 0.05$ vs Ctrl group, ** $p < 0.01$ vs Ctrl group, # $p < 0.05$ vs PTZ group, ## $p < 0.01$ vs PTZ group.

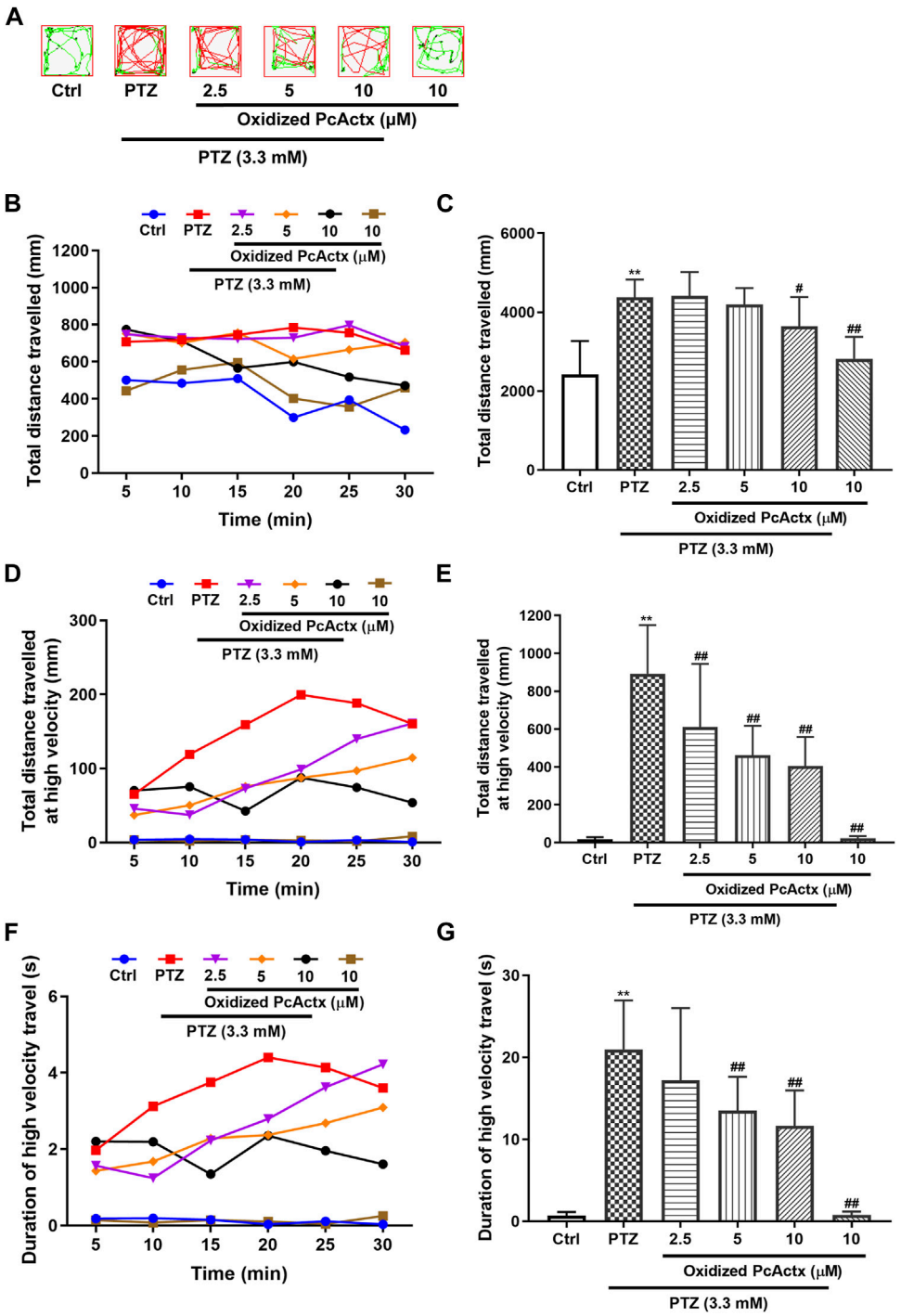

FIGURE 7 | Oxidized PcActx peptide inhibited PTZ-induced hyperactivity in zebrafish larvae. **(A)** Representative patterns of locomotion behavior in zebrafish larvae. The swimming trajectory was recorded every 5 min and is represented by curves. The instantaneous velocity was detected and displayed in different colors (black, <2 mm/s; green, 2–20 mm/s; red, >20 mm/s). **(B)**. Changes in total distance travelled by period. **(C)**. Statistical analysis of total distance travelled. **(D)**. Changes in total distance travelled at high velocity by period (>20 cm/s). **(E)**. Statistical analysis of total distance travelled at high velocity (>20 cm/s). **(F)**. Changes in duration of high velocity travel by period (> 20 cm/s). **(G)**. Statistical analysis of the duration of high velocity travel (>20 cm/s). Data are expressed as means ± SD (n = 9–10). * $p < 0.05$ vs Ctrl group, ** $p < 0.01$ vs Ctrl group, # $p < 0.05$ vs PTZ group, ## $p < 0.01$ vs PTZ group.

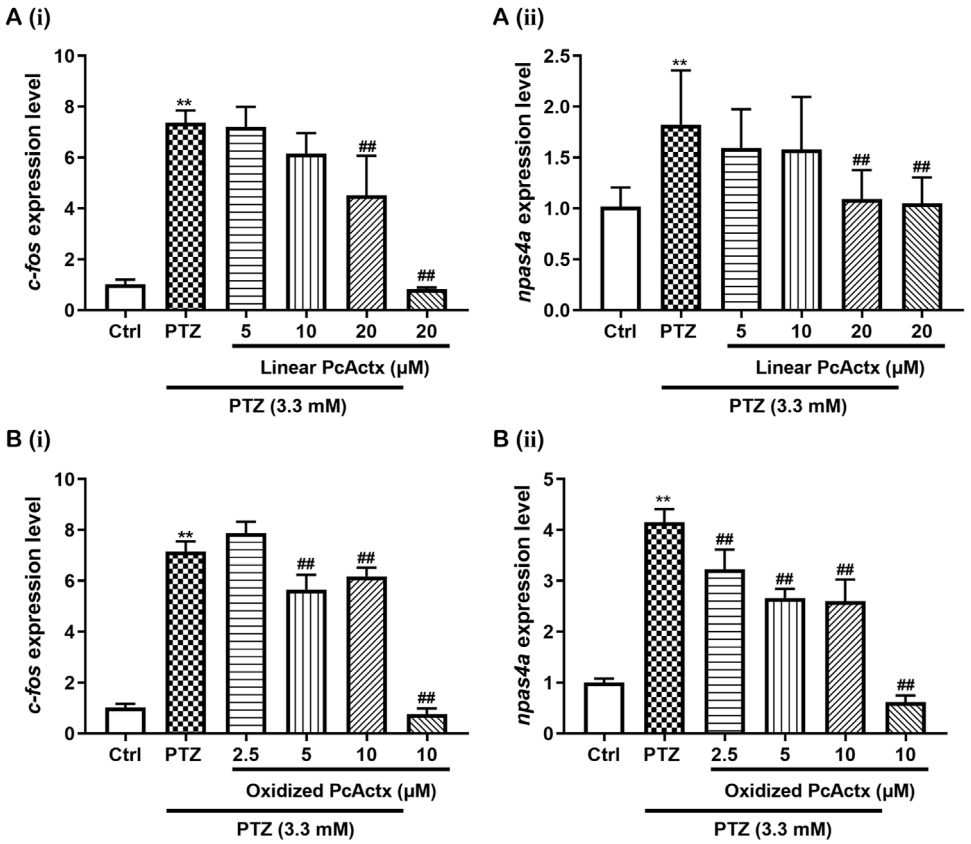

FIGURE 8 | PcActx peptides prevented IER gene expression in PTZ-induced seizures of zebrafish. **(A)** Linear PcActx peptide. **(B)**. Oxidized PcActx peptide. (i). *c-fos* expression level. (ii). *npas4a* expression level. Data are expressed as means ± SD (n = 4–6). * $p < 0.05$ vs Ctrl group, ** $p < 0.01$ vs Ctrl group, # $p < 0.05$ vs PTZ group, ## $p < 0.01$ vs PTZ group.

susceptible to epileptic seizures (Patel, 2004). As displayed in **Figure 9**, PTZ obviously increased the ROS level in zebrafish larvae. However, the excessive production of ROS triggered by PTZ was effectively decreased by linear PcActx peptide (**Figure 9A**). Moreover, oxidized PcActx peptide also dose-dependently attenuated PTZ-induced ROS accumulation in zebrafish larvae, especially at 5 and 10 μM (**Figure 9B**). Meanwhile, application of PcActx peptides alone, either in linear or oxidized form, did not induce abnormal generation of ROS when compared to the control group. The results regarding locomotion behavior, mRNA levels of *c-fos* and *npas4a*, and ROS production (**Supplementary Table S2**) all indicated that the protective activity of oxidized PcActx peptide was more potent than that of the linear form.

Oxidized PcActx Peptide Reduced the Expression Level of Several Genes Related to Calcium and GABAergic-Glutamatergic Signaling

In comparison with the control group (**Figure 10**), the PTZ-treated group showed a remarkable elevation in the mRNA expression of genes related to calcium signaling and glutamate-GABA metabolic signaling, including *calb1*, *calb2, gabra1, grm1, gria1b, grin1b, gat1, slc1a2b, gad1b,* and *glsa*. In contrast, oxidized PcActx peptide conspicuously modulated the abnormal expression levels of *calb1*, *calb2, gabra1, grm1, gria1b, grin1b, gat1, slc1a2b, gad1b,* and *glsa.* Furthermore, treatment with oxidized PcActx peptides alone (10 μM) also slightly reduced the expression of *calb2, grm1, gria1b, gad1b,* and *glsa*, even though no significant differences were observed in *gria1b, gad1b,* and *glsa* when compared to control group. These data provided clear evidence that the anti-epileptic activity of PcActx peptide may involve modulation of calcium signaling and GABAergic-glutamatergic signaling.

DISCUSSION

Improvements of transcriptomics and proteomics techniques, and widespread application thereof, led to significant advances in animal venom-peptide discovery. Several venom-derived drugs have been developed and approved for treatment of various diseases, owing to their extremely high specificity and potency for particular molecular targets (King, 2011; Robinson et al., 2017). For instance, ziconotide (Prialt®), a blocker of the Cav2.2

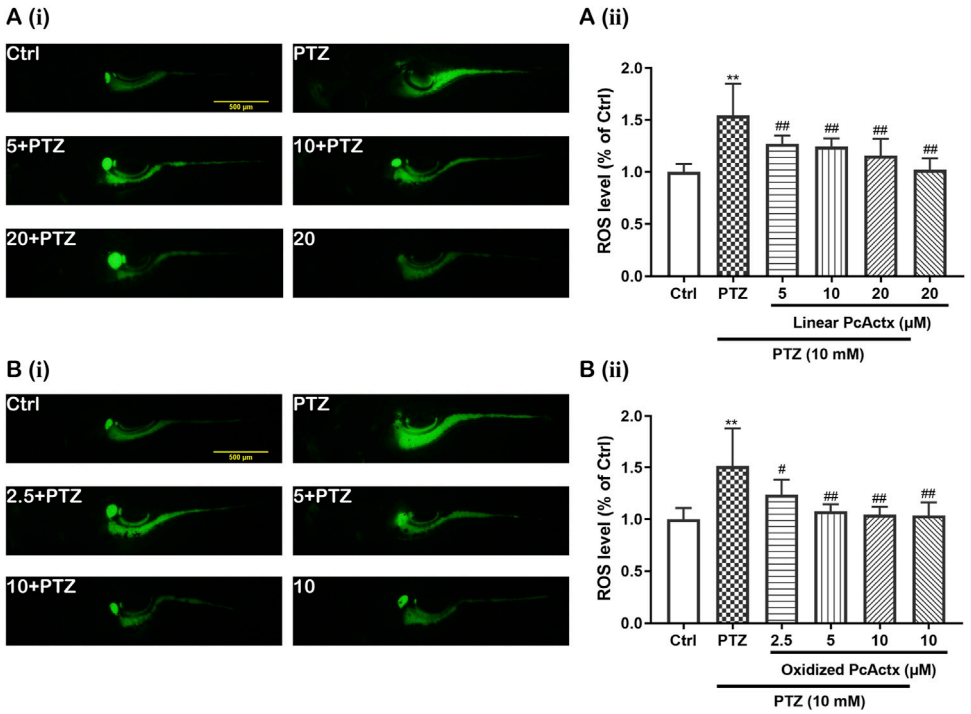

FIGURE 9 | PcActx peptides attenuated PTZ-induced accumulation of ROS in zebrafish larvae. **(A)**. Linear PcActx peptide. **(B)**. Oxidized PcActx peptide. (i). Representative micrographs of fluorescence. (ii). Statistical analysis of ROS production. Data are expressed as means ± SD (n = 6–8). * $p < 0.05$ vs Ctrl group, ** $p < 0.01$ vs Ctrl group, # $p < 0.05$ vs PTZ group, ## $p < 0.01$ vs PTZ group.

channel, is used to treat chronic pain. In addition, a number of animal venom-like proteins and peptides are currently in clinical trials (ShK-192, α-cobrotoxin) and preclinical studies (APETx2, Vicrostatin) (King, 2011; Robinson et al., 2017). Venom-peptides from cnidarians, especially sea anemones, have attracted growing interest in the context of the discovery and development of drug therapies, due to their potential for targeting various ion channels (Mouhat et al., 2004). However, proteinaceous (proteins and peptides) toxins originating from other species of Cnidaria, like the zoantharians, are largely underexploited. In the present study, we identified a novel neuropeptide through transcriptomics analysis of zoantharian *P. caribaeorum*, and investigated its anti-epileptic potential and underlying mechanism of action using a PTZ-induced seizure model of zebrafish larvae.

A novel peptide, named PcActx, was identified on the transcriptome of *P. caribaeorum*. Based on the maximum likelihood tree (**Figure 1B**), PcAcxt peptide was well clustered based on APHC and HCRG21 peptide phylogeny, where those peptides are TRPV1 channel inhibitors from the sea anemone *H. crispa*. The data obtained through molecular phylogenetic analysis and structural alignment showed that PcActx peptide shared a similar domain with APHC peptides (**Figures 1A**, **2E**). Unlike APHC peptides, PcActx peptide contains three cysteine residues and folds only one disulfide bond with one free cysteine residue. PcActx peptide functions as a monomer rather than a dimer, which might be due to the unique spatial structure of Cys 19 (**Figures 2A**,**B**, **3E**). A disulfide bridge forming between thiol groups in two cysteine residues is an important component of the secondary and tertiary structure of proteins and polypeptides for maintaining their structural stability and function (Thornton, 1981). *In silico* studies proved that cysteine-rich peptides, such as MCoTI-II and μ-Conotoxin PIIIA, showed different dynamic characteristics in terms of disulfide connectivity (Tietze et al., 2012; Zhang et al., 2016). *In vitro* and *in vivo* studies demonstrated that different disulfide bridge patterns in the same sequence resulted in different bioactivities. Tietze et al. (2012) reported that the ability of μ-Conotoxin PIIIA to block $Na_V1.4$-mediated ion currents varied depending on disulfide connectivity. Moreover, the unoxidized isomer cannot adopt an adequate conformation to block the Na_V channel. Meanwhile, the ribbon disulfide isomer of α-Conotoxin AuIB, a non-native structure, has approximately 10 times greater potency to block nicotinic acetylcholine receptors than the native peptide (Dutton et al., 2002). In addition, our previous study found that oxidized PpVα peptide with a single disulfide bridge was more efficacious than the linear form in epileptic and neurodegenerative models (Liao et al., 2019). Although the single free cysteine in the sequence might partly increase instability, other previous study also observed a peptide with a similar distinctive cysteine spacing pattern that remained biologically active; for example, Rattusin, an intestinal α-defensin-related peptide, contained five cysteine residues and exhibited salt-insensitive antibacterial properties (Patil et al., 2013). In this

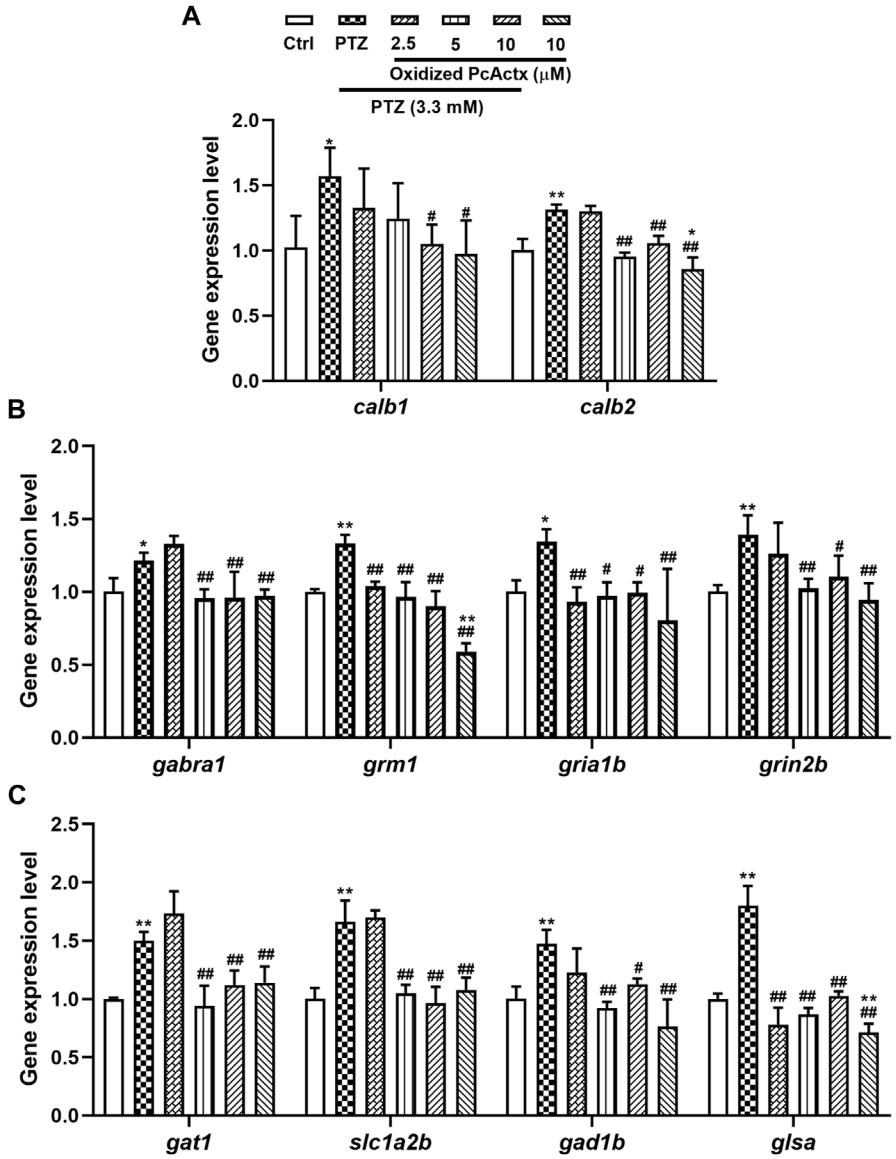

FIGURE 10 | Oxidized PcActx peptide could regulate calcium and glutamatergic-GABAergic signaling related genes in PTZ-stimulated epileptic zebrafish. **(A)** *calb1* and *calb2* expression levels. **(B)**. *gabra1, grm1, gria1b* and *grin2b* expression levels. **(C)**. *gat1, slc1a2b, gad1b* and *glsa* expression levels. Data are expressed as means ± SD (n = 4). * $p < 0.05$ vs Ctrl group, ** $p < 0.01$ vs Ctrl group, # $p < 0.05$ vs PTZ group, ## $p < 0.01$ vs PTZ group.

study, the anti-epileptic activities of linear and single disulfide bond oxidized PcActx peptides, which share the same primary amino acid sequence, were determined and compared.

Since PcActx peptide is homologous to APHC peptides that act on the TRPV1 channel, an interaction of PcActx peptide with the TRPV1 channel was expected. The peptide-protein docking analysis indicated that PcActx peptide has the potential to interact with the TRPV1 channel via four hydrogen bonds in pre-S1 helix, S4-S5 linker and TRP domain (**Figures 4C,D**). Furthermore, Fluorescent calcium measurement displayed that PcActx peptides conspicuously inhibited the capsaicin-induced calcium response via the TRPV1 channel inactivation (**Figures 4E,F**). The TRP domain, a unique structural feature of TRP channels, selectively interacts with the pre-S1 helix and S4-S5 linker via salt bridging and hydrogen bonding, which allosterically affects pore conformation (Liao et al., 2013). Moreover, cation-π interactions have been observed between the S4-S5 linker and S5 helix, thus achieving functional coupling (Liao et al., 2013). Covalent intra-subunit interactions have also been observed between the S4-S5 linker and S5-P-S6 pore region (Liao et al., 2013). Hence, interactions with these structures might affect TRPV1 channel activation.

In addition to its widely validated role in pain signal transduction, TRPV1 channel activation may also contribute to epileptogenesis. In an evaluation of the neuroprotective effect of PcActx peptides, PTZ, an anxiogenic epileptogenic

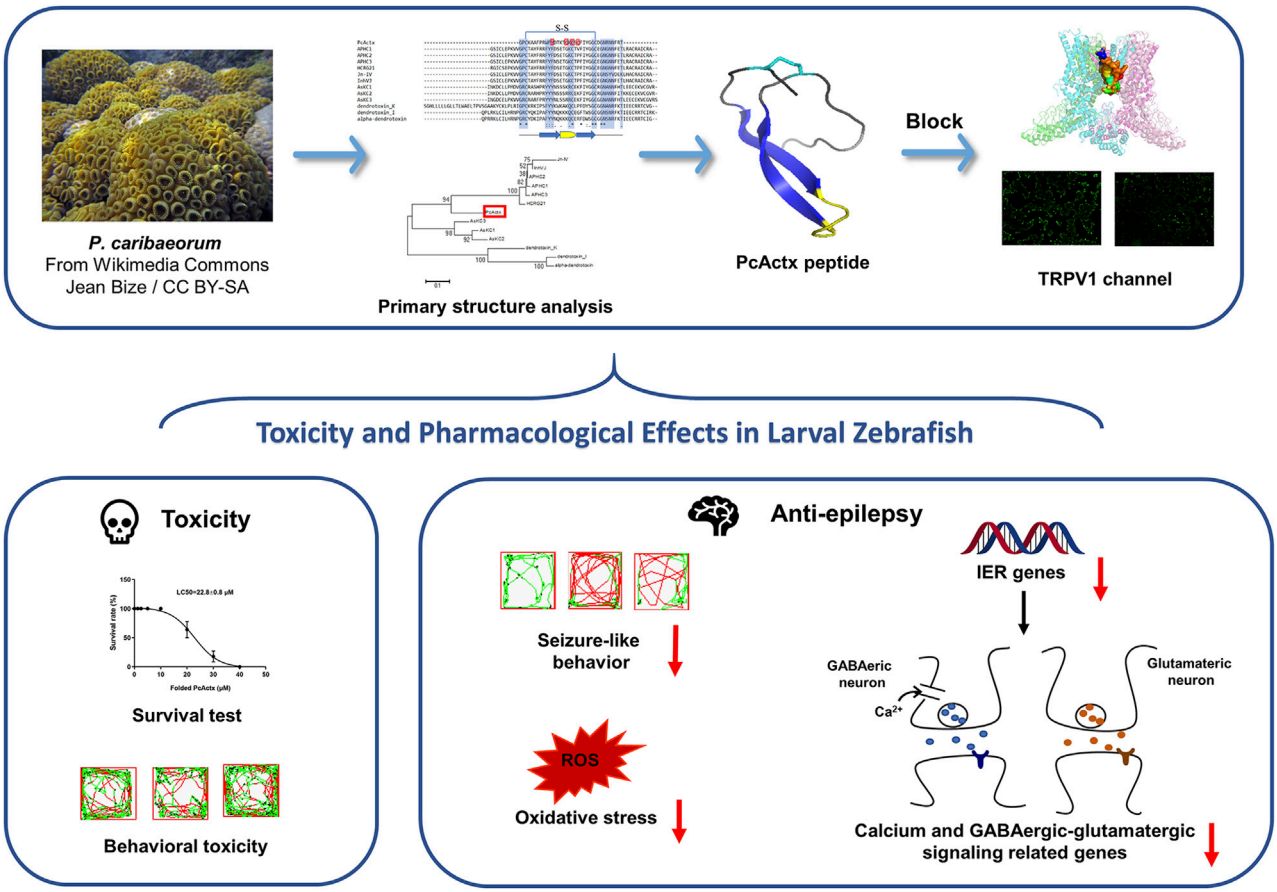

FIGURE 11 | A schematic diagram. PcActx peptide from transcriptome of zoantharian *P. caribaeorum* exhibits prominent anti-epileptic activity, probably through modulating calcium signaling and GABAergic-glutamatergic signaling.

compound, was widely utilized to induce an epileptic response in animal models. Zebrafish emerges as a successful experimental model for neurological disease due to its remarkable features, including low maintenance cost, high fecundity, rapid development and transparence (Hortopan et al., 2010; Barbalho et al., 2016). Due to the small size of zebrafish larvae, their behaviors could be further analyzed using a locomotion tracking system for the quantification of movement (Baraban et al., 2005). More importantly, zebrafish genes share approximately 70–80% homology to the human genome (Hortopan et al., 2010; Barbalho et al., 2016).

In the present study, PTZ provoked extremely abnormal behavioral changes (**Figures 6**, **7**) and IER gene overexpression (*c-fos* and *npas4a*, **Figure 8**) in zebrafish larvae. Both *c-fos* and *npas4a* are synaptic-activity-regulated genes, which can be up-regulated by PTZ stimulation (Baxendale et al., 2012; Torres-Hernandez et al., 2016). *c-fos* acts as the gold standard for measuring synaptic function in the central nervous system (CNS), which can be induce transiently in response to seizure onset (Baraban et al., 2005; Baxendale et al., 2012; Torres-Hernandez et al., 2016). The transcription factor *npas4a* regulate the development of inhibitory synapses through controlling the expression of a set of activity-dependent genes, thus maintaining the balance between excitatory and inhibitory synapses within neural circuits (Lin et al., 2008; Spiegel et al., 2014). Pre-treatment with PcActx peptides (both linear and oxidized isomers) significantly alleviated PTZ-induced seizure-related behaviors, including the total distance travelled, total distance travelled at high velocity (>20 mm/s) and duration of swimming at high velocity (**Figures 6**, **7**). Overexpression of *c-fos* and *npas4a* stimulated by PTZ was dramatically reduced by PcActx peptide treatment (**Figure 8**), suggesting that the PcActx peptides inhibited IER gene expression, thereby regulating the balance of synaptic excitatory and inhibitory activities.

ROS generation plays a critical role in epileptogenesis, serving as both contributor to and consequence of epilepsy (Patel, 2004). Similarly, ROS can be induced by activation of the TRPV1 channel via Ca^{2+} influx, and also mediates TRPV1 activation (Naziroglu, 2015). Our investigation showed obviously abnormal ROS production in PTZ-treated groups. However, PcActx peptides, as potential TRPV1 modulators, considerably decreased ROS accumulation (**Figure 9**), which manifested in PcActx peptide exerting favorable antioxidative properties against pathologic alterations induced by PTZ stimulation. Data regarding the anti-epileptic effects of linear and oxidized PcActx peptides are summarized in **Supplementary Table S2**.

We found that both linear and oxidized PcActx peptides could notably alleviate PTZ-induced epileptic seizure in zebrafish larvae, but the single disulfide oxidized PcActx peptide was more effective than the linear one. Our previous study also found that the oxidized form of PpVα peptide exhibited higher bioactivity than its linear counterpart, probably due to higher structural stability and binding affinity to the target receptor (Liao et al., 2019). Therefore, the oxidized PcActx peptide was subjected to further examination with respect to the upstream signaling pathways underlying its anti-epileptic activity.

Gene *calb1* and *calb2* encode intracellular calcium-binding proteins, which are called calbindin 1 and calbindin 2 (also known as calretinin) (Parmentier et al., 1991). The calbindins are involved in several cellular functions, such as signaling transduction and calcium homeostasis (Xu and Tang, 2018). Calretinin, expressed by GABAergic interneurons in the hippocampus, also functions as a modulator of neuronal excitability, which can regulate synaptic plasticity and transmission (Camp and Wijesinghe, 2009). The sensitivity of calretinin-positive interneurons is responsible for the impaired dendritic inhibition seen in epilepsy (Toth and Magloczky, 2014). The abnormal expression of calbindin-1 positive nerve cells might also participate in the process of epileptogenesis (Thom et al., 2000; Wittner et al., 2002). In the CNS, glutamate and GABA are the most important excitatory and inhibitory neurotransmitters, respectively, and are responsible for mediating the neuronal activity. Several proteins and/or genes are necessary in glutamate-GABA metabolic pathways and may be altered in epilepsy. Fast-inhibitory postsynaptic potential can be induced by the activation of $GABA_A$ receptor α 1 (Gabra1), which belongs to the $GABA_A$ receptor family (Kuriyama et al., 1993; Najm et al., 2001). Gene *grm1* encodes a metabotropic glutamate receptor (mGluR), which is a second-messenger coupled receptor involved in neuronal plasticity and epilepsy (Najm et al., 2001). N-methyl-D-aspartate (NMDA) receptors (encoded by the *grin* gene) and α-amino-3-hydroxy-5-methyl-4-isoxazolepropioniac acid (AMPA) receptors (encoded by the *gria* gene) are ionotropic glutamate receptors (iGluR), the activation of which leads to glutamate accumulation, overexcitement of synapses, and, ultimately, epilepsy (Najm et al., 2001; Rogawski and Loscher, 2004). GABA transporter 1 (GAT 1) is present in the cell membrane of neurons and astrocytes, and its primary function is to remove or reuptake GABA from the synaptic cleft, thereby inhibiting or terminating the synaptic actions of GABA (Meldrum and Rogawski, 2007; Scimemi, 2014). Excitatory amino acid transporter 2 (EAAT2) is encoded by the *slc1a2* gene and is responsible for over 90% of the glutamate reuptake in the forebrain (Holmseth et al., 2009), which is implicated in the regulation of synaptic activity and plasticity (Takahashi et al., 2015). Glutamate decarboxylase 1 (GAD1), encoded by *gad1*, is an enzyme that catalyzes the decarboxylation of glutamate to GABA, thus regulating the steady-state GABA concentration (Petroff, 2002). Glutaminase (encoded by the gene *glsa*) participates in the glutamate-glutamine cycle, where glutamate is formed from phosphate-activated glutaminase (Hertz and Zielke, 2004). In the present study, treatment with the oxidized PcActx peptide dramatically reduced the overexpression of *calb1, calb2, gabra1, grm1, gria1b, grin1b, gat1, slc1a2b, gad1b, and glsa*, the levels of which were increased by PTZ (**Figure 10**). Taken together, these results indicated that PcActx peptide exhibits prominent anti-epileptic activity, potentially involving modulation of calcium signaling and GABAergic-glutamatergic signaling.

In conclusion, PcActx peptide was characterized as a novel APHC homologue that seems to act on the TRPV1 channel. The bioactivity validation results comprehensively demonstrated that both linear and oxidized PcActx peptides not only effectively prevented PTZ-induced seizure-related behaviors, but also efficaciously suppressed the overexpression of *c-fos* and *npas4a*, as well as excessive ROS production, which are known biomarkers of neuronal injury. In particular, oxidized PcActx peptide clearly inhibited the mRNA expression levels of *calb1, calb2, gabra1, grm1, gria1b, grin2b gat1, slc1a2b, gad1b,* and *glsa*. Thus, PcActx peptide represents a promising therapeutic candidate for epilepsy management, the mechanism of action of which may involve regulation of calcium and GABAergic-glutamatergic signal pathways (**Figure 11**).

DATA AVAILABILITY STATEMENT

The original contributions presented in the study are included in the article/**Supplementary Material**, further inquiries can be directed to the corresponding authors.

ETHICS STATEMENT

The animal study was reviewed and approved by Animal Research Ethics Committee of the University of Macau.

AUTHOR CONTRIBUTIONS

Conceptualization, XW and QL; Methodology, XW, QL, GG, and SS; Investigation, XW, QL, HC, QC, and CW; Formal analysis, XW; Resources, CW and HK; Writing - Original Draft; XW; Writing - Reviewing and Editing, SS, CW, CU; K-KC, GR-B. and SM-YL; Supervision, SM-YL.

FUNDING

Research carried out at the University of Macau was funded by The Science and Technology Development Fund (FDCT) of Macau SAR (File no. 0058/2019/A1 and 0016/2019/AKP) and University of Macau (MYRG 2019-00105-ICMS).

SUPPLEMENTARY MATERIAL

The Supplementary Material for this article can be found online at: https://www.frontiersin.org/articles/10.3389/fphar.2021.763089/full#supplementary-material

REFERENCES

Andreev, Y. A., Kozlov, S. A., Korolkova, Y. V., Dyachenko, I. A., Bondarenko, D. A., Skobtsov, D. I., et al. (2013). Polypeptide Modulators of TRPV1 Produce Analgesia without Hyperthermia. *Mar. Drugs* 11 (12), 5100–5115. doi:10.3390/md11125100

Andreev, Y. A., Kozlov, S. A., Koshelev, S. G., Ivanova, E. A., Monastyrnaya, M. M., Kozlovskaya, E. P., et al. (2008). Analgesic Compound from Sea Anemone Heteractis Crispa Is the First Polypeptide Inhibitor of Vanilloid Receptor 1 (TRPV1). *J. Biol. Chem.* 283 (35), 23914–23921. doi:10.1074/jbc.M800776200

Baraban, S. C., Taylor, M. R., Castro, P. A., and Baier, H. (2005). Pentylenetetrazole Induced Changes in Zebrafish Behavior, Neural Activity and C-Fos Expression. *Neuroscience* 131 (3), 759–768. doi:10.1016/j.neuroscience.2004.11.031

Barbalho, P. G., Lopes-Cendes, I., and Maurer-Morelli, C. V. (2016). Indomethacin Treatment Prior to Pentylenetetrazole-Induced Seizures Downregulates the Expression of Il1b and Cox2 and Decreases Seizure-Like Behavior in Zebrafish Larvae. *BMC Neurosci.* 17, 12. doi:10.1186/s12868-016-0246-y

Baxendale, S., Holdsworth, C. J., Meza Santoscoy, P. L., Harrison, M. R., Fox, J., Parkin, C. A., et al. (2012). Identification of Compounds with Anti-Convulsant Properties in a Zebrafish Model of Epileptic Seizures. *Dis. Model. Mech.* 5 (6), 773–784. doi:10.1242/dmm.010090

Bhaskaran, M. D., and Smith, B. N. (2010). Effects of TRPV1 Activation on Synaptic Excitation in the Dentate Gyrus of a Mouse Model of Temporal Lobe Epilepsy. *Exp. Neurol.* 223 (2), 529–536. doi:10.1016/j.expneurol.2010.01.021

Biasini, M., Bienert, S., Waterhouse, A., Arnold, K., Studer, G., Schmidt, T., et al. (2014). SWISS-MODEL: Modelling Protein Tertiary and Quaternary Structure Using Evolutionary Information. *Nucleic Acids Res.* 42, W252–W258. Web Server issue. doi:10.1093/nar/gku340

Camp, A. J., and Wijesinghe, R. (2009). Calretinin: Modulator of Neuronal Excitability. *Int. J. Biochem. Cel Biol* 41 (11), 2118–2121. doi:10.1016/j.biocel.2009.05.007

Castañeda, O., Sotolongo, V., Amor, A. M., Stöcklin, R., Anderson, A. J., Harvey, A. L., et al. (1995). Characterization of a Potassium Channel Toxin from the Caribbean Sea Anemone Stichodactyla Helianthus. *Toxicon* 33 (5), 603–613. doi:10.1016/0041-0101(95)00013-c

Caterina, M. J., Schumacher, M. A., Tominaga, M., Rosen, T. A., Levine, J. D., and Julius, D. (1997). The Capsaicin Receptor: A Heat-Activated Ion Channel in the Pain Pathway. *Nature* 389 (6653), 816–824. doi:10.1038/39807

de Andrade Melo, L. F., da Camara, C. A. G., de Albuquerque Modesto, J. C., and Pérez, C. D. J. B. (2012). Toxicity against *Artemia S* of the Zoanthid Palythoa Caribaeorum (Cnidaria: Anthozoa) Used in Folk Medicine on the Coast of Pernambuco, Brazil. *Biotemas* 25 (3), 145–151. doi:10.5007/2175-7925.2012v25n3p145

Diochot, S., Baron, A., Rash, L. D., Deval, E., Escoubas, P., Scarzello, S., et al. (2004). A New Sea Anemone Peptide, APETx2, Inhibits ASIC3, a Major Acid-Sensitive Channel in Sensory Neurons. *EMBO J.* 23 (7), 1516–1525. doi:10.1038/sj.emboj.7600177

Dutton, J. L., Bansal, P. S., Hogg, R. C., Adams, D. J., Alewood, P. F., and Craik, D. J. (2002). A New Level of Conotoxin Diversity, a Non-native Disulfide Bond Connectivity in Alpha-Conotoxin AuIB Reduces Structural Definition but Increases Biological Activity. *J. Biol. Chem.* 277 (50), 48849–48857. doi:10.1074/jbc.M208842200

Edgar, R. C. (2004a). MUSCLE: a Multiple Sequence Alignment Method with Reduced Time and Space Complexity. *BMC Bioinformatics* 5, 113. doi:10.1186/1471-2105-5-113

Edgar, R. C. (2004b). MUSCLE: Multiple Sequence Alignment with High Accuracy and High Throughput. *Nucleic Acids Res.* 32 (5), 1792–1797. doi:10.1093/nar/gkh340

Ellis, L. D., Seibert, J., and Soanes, K. H. (2012). Distinct Models of Induced Hyperactivity in Zebrafish Larvae. *Brain Res.* 1449, 46–59. doi:10.1016/j.brainres.2012.02.022

Fawley, J. A., Hofmann, M. E., and Andresen, M. C. (2014). Cannabinoid 1 and Transient Receptor Potential Vanilloid 1 Receptors Discretely Modulate Evoked Glutamate Separately from Spontaneous Glutamate Transmission. *J. Neurosci.* 34 (24), 8324–8332. doi:10.1523/JNEUROSCI.0315-14.2014

Gerdeman, G., and Lovinger, D. M. (2001). CB1 Cannabinoid Receptor Inhibits Synaptic Release of Glutamate in Rat Dorsolateral Striatum. *J. Neurophysiol.* 85 (1), 468–471. doi:10.1152/jn.2001.85.1.468

Ghazizadeh, V., and Nazıroğlu, M. (2014). Electromagnetic Radiation (Wi-Fi) and Epilepsy Induce Calcium Entry and Apoptosis through Activation of TRPV1 Channel in hippocampus and Dorsal Root Ganglion of Rats. *Metab. Brain Dis.* 29 (3), 787–799. doi:10.1007/s11011-014-9549-9

González-Aparicio, R., and Moratalla, R. (2014). Oleoylethanolamide Reduces L-DOPA-Induced Dyskinesia via TRPV1 Receptor in a Mouse Model of Parkinson´s Disease. *Neurobiol. Dis.* 62, 416–425. doi:10.1016/j.nbd.2013.10.008

Hertz, L., and Zielke, H. R. (2004). Astrocytic Control of Glutamatergic Activity: Astrocytes as Stars of the Show. *Trends Neurosci.* 27 (12), 735–743. doi:10.1016/j.tins.2004.10.008

Holmseth, S., Scott, H. A., Real, K., Lehre, K. P., Leergaard, T. B., Bjaalie, J. G., et al. (2009). The Concentrations and Distributions of Three C-Terminal Variants of the GLT1 (EAAT2; Slc1a2) Glutamate Transporter Protein in Rat Brain Tissue Suggest Differential Regulation. *Neuroscience* 162 (4), 1055–1071. doi:10.1016/j.neuroscience.2009.03.048

Hortopan, G. A., Dinday, M. T., and Baraban, S. C. (2010). Zebrafish as a Model for Studying Genetic Aspects of Epilepsy. *Dis. Model. Mech.* 3 (3-4), 144–148. doi:10.1242/dmm.002139

Humphrey, W., Dalke, A., and Schulten, K. (1996). VMD: Visual Molecular Dynamics. *J. Mol. Graph* 14 (1), 3327–3838. doi:10.1016/0263-7855(96)00018-5

Jefferys, J. G. (2010). Advances in Understanding Basic Mechanisms of Epilepsy and Seizures. *Seizure* 19 (10), 638–646. doi:10.1016/j.seizure.2010.10.026

Jeffry, J. A., Yu, S. Q., Sikand, P., Parihar, A., Evans, M. S., and Premkumar, L. S. (2009). Selective Targeting of TRPV1 Expressing Sensory Nerve Terminals in the Spinal Cord for Long Lasting Analgesia. *PLoS One* 4 (9), e7021. doi:10.1371/journal.pone.0007021

Jiménez-Guri, E., Philippe, H., Okamura, B., and Holland, P. W. (2007). Buddenbrockia Is a Cnidarian Worm. *Science* 317 (5834), 116–118. doi:10.1126/science.1142024

Jouiaei, M., Sunagar, K., Federman Gross, A., Scheib, H., Alewood, P. F., Moran, Y., et al. (2015). Evolution of an Ancient Venom: Recognition of a Novel Family of Cnidarian Toxins and the Common Evolutionary Origin of Sodium and Potassium Neurotoxins in Sea Anemone. *Mol. Biol. Evol.* 32 (6), 1598–1610. doi:10.1093/molbev/msv050

Karczewski, J., Spencer, R. H., Garsky, V. M., Liang, A., Leitl, M. D., Cato, M. J., et al. (2010). Reversal of Acid-Induced and Inflammatory Pain by the Selective ASIC3 Inhibitor, APETx2. *Br. J. Pharmacol.* 161 (4), 950–960. doi:10.1111/j.1476-5381.2010.00918.x

Kayal, E., Roure, B., Philippe, H., Collins, A. G., and Lavrov, D. V. (2013). Cnidarian Phylogenetic Relationships as Revealed by Mitogenomics. *BMC Evol. Biol.* 13, 5. doi:10.1186/1471-2148-13-5

Kayal, E., Bastian, B., Pankey, M. S., Ohdera, A., Medina, M., Plachetzki, D. C., et al. (2017). Comprehensive Phylogenomic Analyses Resolve Cnidarian Relationships and the Origins of Key Organismal Traits. PeerJ Preprints.

King, G. F. (2011). Venoms as a Platform for Human Drugs: Translating Toxins into Therapeutics. *Expert Opin. Biol. Ther.* 11 (11), 1469–1484. doi:10.1517/14712598.2011.621940

Kozlov, S. A., Andreev, I. A., Murashev, A. N., Skobtsov, D. I., D'iachenko, I. A., and Grishin, E. V. (2009). New Polypeptide Components from the Heteractis Crispa Sea Anemone with Analgesic Activity. *Bioorg. Khim* 35 (6), 789–798. doi:10.1134/s1068162009060065

Kuriyama, K., Hirouchi, M., and Nakayasu, H. (1993). Structure and Function of Cerebral GABAA and GABAB Receptors. *Neurosci. Res.* 17 (2), 91–99. doi:10.1016/0168-0102(93)90087-7

Lazcano-Pérez, F., Castro, H., Arenas, I., García, D. E., González-Muñoz, R., and Arreguín-Espinosa, R. (2016). Activity of Palythoa Caribaeorum Venom on Voltage-Gated Ion Channels in Mammalian Superior Cervical Ganglion Neurons. *Toxins (Basel)* 8 (5), 135. doi:10.3390/toxins8050135

Liao, M., Cao, E., Julius, D., and Cheng, Y. (2013). Structure of the TRPV1 Ion Channel Determined by Electron Cryo-Microscopy. *Nature* 504 (7478), 107–112. doi:10.1038/nature12822

Liao, Q., Gong, G., Siu, S. W. I., Wong, C. T. T., Yu, H., Tse, Y. C., et al. (2018a). A Novel ShK-Like Toxic Peptide from the Transcriptome of the Cnidarian

Palythoa Caribaeorum Displays Neuroprotection and Cardioprotection in Zebrafish. *Toxins (Basel)* 10 (6), 238. doi:10.3390/toxins10060238

Liao, Q., Li, S., Siu, S. W. I., Morlighem, J. R. L., Wong, C. T. T., Wang, X., et al. (2019). Novel Neurotoxic Peptides from Protopalythoa Variabilis Virtually Interact with Voltage-Gated Sodium Channel and Display Anti-Epilepsy and Neuroprotective Activities in Zebrafish. *Arch. Toxicol.* 93 (1), 189–206. doi:10.1007/s00204-018-2334-5

Liao, Q., Li, S., Siu, S. W. I., Yang, B., Huang, C., Chan, J. Y., et al. (2018b). Novel Kunitz-Like Peptides Discovered in the Zoanthid Palythoa Caribaeorum through Transcriptome Sequencing. *J. Proteome Res.* 17 (2), 891–902. doi:10.1021/acs.jproteome.7b00686

Lin, Y., Bloodgood, B. L., Hauser, J. L., Lapan, A. D., Koon, A. C., Kim, T. K., et al. (2008). Activity-dependent Regulation of Inhibitory Synapse Development by Npas4. *Nature* 455 (7217), 1198–1204. doi:10.1038/nature07319

Meldrum, B. S., and Rogawski, M. A. (2007). Molecular Targets for Antiepileptic Drug Development. *Neurotherapeutics* 4 (1), 18–61. doi:10.1016/j.nurt.2006.11.010

Monastyrnaya, M., Peigneur, S., Zelepuga, E., Sintsova, O., Gladkikh, I., Leychenko, E., et al. (2016). Kunitz-Type Peptide HCRG21 from the Sea Anemone Heteractis Crispa Is a Full Antagonist of the TRPV1 Receptor. *Mar. Drugs* 14 (12), 229. doi:10.3390/md14120229

Montell, C., Birnbaumer, L., Flockerzi, V., Bindels, R. J., Bruford, E. A., Caterina, M. J., et al. (2002). A Unified Nomenclature for the Superfamily of TRP Cation Channels. *Mol. Cel* 9 (2), 229–231. doi:10.1016/s1097-2765(02)00448-3

Mouhat, S., Jouirou, B., Mosbah, A., De Waard, M., and Sabatier, J. M. (2004). Diversity of Folds in Animal Toxins Acting on Ion Channels. *Biochem. J.* 378 (Pt 3), 717–726. doi:10.1042/BJ20031860

Najm, I., Ying, Z., and Janigro, D. (2001). Mechanisms of Epileptogenesis. *Neurol. Clin.* 19 (2), 237–250. doi:10.1016/s0733-8619(05)70017-7

Nazıroğlu, M., Özkan, F. F., Hapil, S. R., Ghazizadeh, V., and Çiğ, B. (2015). Epilepsy but Not mobile Phone Frequency (900 MHz) Induces Apoptosis and Calcium Entry in hippocampus of Epileptic Rat: Involvement of TRPV1 Channels. *J. Membr. Biol.* 248 (1), 83–91. doi:10.1007/s00232-014-9744-y

Nazıroğlu, M., Senol, N., Ghazizadeh, V., and Yürüker, V. (2014). Neuroprotection Induced by N-Acetylcysteine and Selenium against Traumatic Brain Injury-Induced Apoptosis and Calcium Entry in hippocampus of Rat. *Cell Mol Neurobiol* 34 (6), 895–903. doi:10.1007/s10571-014-0069-2

Nazıroğlu, M., and Övey, İ. S. (2015). Involvement of Apoptosis and Calcium Accumulation through TRPV1 Channels in Neurobiology of Epilepsy. *Neuroscience* 293, 55–66. doi:10.1016/j.neuroscience.2015.02.041

Naziroglu, M. (2015). TRPV1 Channel: A Potential Drug Target for Treating Epilepsy. *Curr. Neuropharmacol* 13 (2), 239–247. doi:10.2174/1570159x13666150216222543

Nikolaev, M. V., Dorofeeva, N. A., Komarova, M. S., Korolkova, Y. V., Andreev, Y. A., Mosharova, I. V., et al. (2017). TRPV1 Activation Power Can Switch an Action Mode for its Polypeptide Ligands. *PLoS One* 12 (5), e0177077. doi:10.1371/journal.pone.0177077

Norton, R. S., Pennington, M. W., and Beeton, C. (2015). "CHAPTER 10. Case Study 2: Transforming a Toxin into a Therapeutic: The Sea Anemone Potassium Channel Blocker ShK Toxin for Treatment of Autoimmune Diseases," in *Venoms to Drugs: Venom as a Source for the Development of Human Therapeutics*. Editor G.F. King (Cambridge: Royal Soc Chemistry), 255–274. doi:10.1039/9781849737876-00255

Övey, İ. S., and Naziroğlu, M. (2015). Homocysteine and Cytosolic GSH Depletion Induce Apoptosis and Oxidative Toxicity through Cytosolic Calcium Overload in the hippocampus of Aged Mice: Involvement of TRPM2 and TRPV1 Channels. *Neuroscience* 284, 225–233. doi:10.1016/j.neuroscience.2014.09.078

Parmentier, M., Passage, E., Vassart, G., and Mattei, M. G. (1991). The Human Calbindin D28k (CALB1) and Calretinin (CALB2) Genes are Located at 8q21.3----q22.1 and 16q22----q23, Respectively, suggesting a Common Duplication with the Carbonic Anhydrase Isozyme loci. *Cytogenet. Cel Genet* 57 (1), 41–43. doi:10.1159/000133111

Patel, M. (2004). Mitochondrial Dysfunction and Oxidative Stress: Cause and Consequence of Epileptic Seizures. *Free Radic. Biol. Med.* 37 (12), 1951–1962. doi:10.1016/j.freeradbiomed.2004.08.021

Patil, A. A., Ouellette, A. J., Lu, W., and Zhang, G. (2013). Rattusin, an Intestinal α-Defensin-Related Peptide in Rats with a Unique Cysteine Spacing Pattern and Salt-Insensitive Antibacterial Activities. *Antimicrob. Agents Chemother.* 57 (4), 1823–1831. doi:10.1128/AAC.02237-12

Petroff, O. A. (2002). GABA and Glutamate in the Human Brain. *Neuroscientist* 8 (6), 562–573. doi:10.1177/1073858402238515

Pierce, B. G., Hourai, Y., and Weng, Z. (2011). Accelerating Protein Docking in ZDOCK Using an Advanced 3D Convolution Library. *PLoS One* 6 (9), e24657. doi:10.1371/journal.pone.0024657

Pronk, S., Páll, S., Schulz, R., Larsson, P., Bjelkmar, P., Apostolov, R., et al. (2013). GROMACS 4.5: A High-Throughput and Highly Parallel Open Source Molecular Simulation Toolkit. *Bioinformatics* 29 (7), 845–854. doi:10.1093/bioinformatics/btt055

Ramsey, I. S., Delling, M., and Clapham, D. E. (2006). An Introduction to TRP Channels. *Annu. Rev. Physiol.* 68, 619–647. doi:10.1146/annurev.physiol.68.040204.100431

Roberts, J. C., Davis, J. B., and Benham, C. D. (2004). [3H]Resiniferatoxin Autoradiography in the CNS of Wild-Type and TRPV1 Null Mice Defines TRPV1 (VR-1) Protein Distribution. *Brain Res.* 995 (2), 176–183. doi:10.1016/j.brainres.2003.10.001

Robinson, S. D., Undheim, E. A. B., Ueberheide, B., and King, G. F. (2017). Venom Peptides as Therapeutics: Advances, Challenges and the Future of Venom-Peptide Discovery. *Expert Rev. Proteomics* 14 (10), 931–939. doi:10.1080/14789450.2017.1377613

Rogawski, M. A., and Löscher, W. (2004). The Neurobiology of Antiepileptic Drugs for the Treatment of Nonepileptic Conditions. *Nat. Med.* 10 (7), 685–692. doi:10.1038/nrn143010.1038/nm1074

Scimemi, A. (2014). Structure, Function, and Plasticity of GABA Transporters. *Front Cel Neurosci* 8, 161. doi:10.3389/fncel.2014.00161

Shoudai, K., Peters, J. H., McDougall, S. J., Fawley, J. A., and Andresen, M. C. (2010). Thermally Active TRPV1 Tonically Drives Central Spontaneous Glutamate Release. *J. Neurosci.* 30 (43), 14470–14475. doi:10.1523/JNEUROSCI.2557-10.2010

Spiegel, I., Mardinly, A. R., Gabel, H. W., Bazinet, J. E., Couch, C. H., Tzeng, C. P., et al. (2014). Npas4 Regulates Excitatory-Inhibitory Balance Within Neural Circuits Through Cell-Type-Specific Gene Programs. *Cell* 157 (5), 1216–1229. doi:10.1016/j.cell.2014.03.058

Starowicz, K., Maione, S., Cristino, L., Palazzo, E., Marabese, I., Rossi, F., et al. (2007). Tonic Endovanilloid Facilitation of Glutamate Release in Brainstem Descending Antinociceptive Pathways. *J. Neurosci.* 27 (50), 13739–13749. doi:10.1523/JNEUROSCI.3258-07.2007

Takahashi, K., Foster, J. B., and Lin, C. L. (2015). Glutamate Transporter EAAT2: Regulation, Function, and Potential as a Therapeutic Target for Neurological and Psychiatric Disease. *Cell Mol Life Sci* 72 (18), 3489–3506. doi:10.1007/s00018-015-1937-8

Tamura, K., Stecher, G., Peterson, D., Filipski, A., and Kumar, S. (2013). MEGA6: Molecular Evolutionary Genetics Analysis Version 6.0. *Mol. Biol. Evol.* 30 (12), 2725–2729. doi:10.1093/molbev/mst197

Tarcha, E. J., Olsen, C. M., Probst, P., Peckham, D., Muñoz-Elías, E. J., Kruger, J. G., et al. (2017). Safety and Pharmacodynamics of Dalazatide, a Kv1.3 Channel Inhibitor, in the treatment of Plaque Psoriasis: A Randomized Phase 1b Trial. *PLoS One* 12 (7), e0180762. doi:10.1371/journal.pone.0180762

Thom, M., Holton, J. L., D'Arrigo, C., Griffin, B., Beckett, A., Sisodiya, S., et al. (2000). Microdysgenesis with Abnormal Cortical Myelinated Fibres in Temporal Lobe Epilepsy: A Histopathological Study with Calbindin D-28-K Immunohistochemistry. *Neuropathol. Appl. Neurobiol.* 26 (3), 251–257. doi:10.1046/j.1365-2990.2000.00229.x

Thornton, J. M. (1981). Disulphide Bridges in Globular Proteins. *J. Mol. Biol.* 151 (2), 261–287. doi:10.1016/0022-2836(81)90515-5

Tietze, A. A., Tietze, D., Ohlenschläger, O., Leipold, E., Ullrich, F., Kühl, T., et al. (2012). Structurally Diverse μ-Conotoxin PIIIA Isomers Block Sodium Channel NaV 1.4. *Angew. Chem. Int. Ed. Engl.* 51 (17), 4058–4061. doi:10.1002/anie.201107011

Torres-Hernández, B. A., Colón, L. R., Rosa-Falero, C., Torrado, A., Miscalichi, N., Ortíz, J. G., et al. (2016). Reversal of Pentylenetetrazole-Altered Swimming and Neural Activity-Regulated Gene Expression in Zebrafish Larvae by Valproic Acid and Valerian Extract. *Psychopharmacology (Berl)* 233 (13), 2533–2547. doi:10.1007/s00213-016-4304-z

Tóth, A., Boczán, J., Kedei, N., Lizanecz, E., Bagi, Z., Papp, Z., et al. (2005). Expression and Distribution of Vanilloid Receptor 1 (TRPV1) in the Adult Rat

Brain. *Brain Res. Mol. Brain Res.* 135 (1-2), 162–168. doi:10.1016/j.molbrainres.2004.12.003

Tóth, K., and Maglóczky, Z. (2014). The Vulnerability of Calretinin-Containing Hippocampal Interneurons to Temporal Lobe Epilepsy. *Front. Neuroanat.* 8, 100. doi:10.3389/fnana.2014.00100

Vay, L., Gu, C., and McNaughton, P. A. (2012). The Thermo-TRP Ion Channel Family: Properties and Therapeutic Implications. *Br. J. Pharmacol.* 165 (4), 787–801. doi:10.1111/j.1476-5381.2011.01601.x

von Rüden, E. L., Jafari, M., Bogdanovic, R. M., Wotjak, C. T., and Potschka, H. (2015). Analysis in Conditional Cannabinoid 1 Receptor-Knockout Mice Reveals Neuronal Subpopulation-Specific Effects on Epileptogenesis in the Kindling Paradigm. *Neurobiol. Dis.* 73, 334–347. doi:10.1016/j.nbd.2014.08.001

Westerfield, M. (2000). *The Zebrafish Book. A Guide for the Laboratory Use of Zebrafish (*Danio rerio*)*. 4th Edn. Eugene: University of Oregon Press.

Wittner, L., Eross, L., Szabó, Z., Tóth, S., Czirják, S., Halász, P., et al. (2002). Synaptic Reorganization Of Calbindin-Positive Neurons in the Human Hippocampal CA1 Region in Temporal Lobe Epilepsy. *Neuroscience* 115 (3), 961–978. doi:10.1016/s0306-4522(02)00264-6

Xu, J. H., and Tang, F. R. (2018). Voltage-Dependent Calcium Channels, Calcium Binding Proteins, and Their Interaction in the Pathological Process of Epilepsy. *Int. J. Mol. Sci.* 19 (9), 2735. doi:10.3390/ijms19092735

Zhang, Y., Schulten, K., Gruebele, M., Bansal, P. S., Wilson, D., and Daly, N. L. (2016). Disulfide Bridges: Bringing Together Frustrated Structure in a Bioactive Peptide. *Biophys. J.* 110 (8), 1744–1752. doi:10.1016/j.bpj.2016.03.027

Conflict of Interest: The authors declare that the research was conducted in the absence of any commercial or financial relationships that could be construed as a potential conflict of interest.

Publisher's Note: All claims expressed in this article are solely those of the authors and do not necessarily represent those of their affiliated organizations, or those of the publisher, the editors and the reviewers. Any product that may be evaluated in this article, or claim that may be made by its manufacturer, is not guaranteed or endorsed by the publisher.

frontiers in Pharmacology

ORIGINAL RESEARCH
published: 06 December 2021
doi: 10.3389/fphar.2021.778534

A Novel Spider Toxin Inhibits Fast Inactivation of the $Na_v1.9$ Channel by Binding to Domain III and Domain IV Voltage Sensors

Shuijiao Peng†, Minzhi Chen†, Zhen Xiao, Xin Xiao, Sen Luo, Songping Liang, Xi Zhou and Zhonghua Liu**

The National and Local Joint Engineering Laboratory of Animal Peptide Drug Development, College of Life Sciences, Hunan Normal University, Changsha, China

OPEN ACCESS

Edited by:
Jean-Marc Sabatier, Aix-Marseille Université, France

Reviewed by:
Peter Ruben, Simon Fraser University, Canada
Richard J Lewis, The University of Queensland, Australia

***Correspondence:**
Xi Zhou
xizh@hunnu.edu.cn
Zhonghua Liu
liuzh@hunnu.edu.cn

†These authors have contributed equally to this work

Specialty section:
This article was submitted to Pharmacology of Ion Channels and Channelopathies, a section of the journal Frontiers in Pharmacology

Received: *17 September 2021*
Accepted: *05 November 2021*
Published: *06 December 2021*

Citation:
Peng S, Chen M, Xiao Z, Xiao X, Luo S, Liang S, Zhou X and Liu Z (2021) A Novel Spider Toxin Inhibits Fast Inactivation of the $Na_v1.9$ Channel by Binding to Domain III and Domain IV Voltage Sensors. Front. Pharmacol. 12:778534. doi: 10.3389/fphar.2021.778534

Venomous animals have evolved to produce peptide toxins that modulate the activity of voltage-gated sodium (Na_v) channels. These specific modulators are powerful probes for investigating the structural and functional features of Na_v channels. Here, we report the isolation and characterization of δ-theraphotoxin-Gr4b (Gr4b), a novel peptide toxin from the venom of the spider *Grammostola rosea*. Gr4b contains 37-amino acid residues with six cysteines forming three disulfide bonds. Patch-clamp analysis confirmed that Gr4b markedly slows the fast inactivation of $Na_v1.9$ and inhibits the currents of $Na_v1.4$ and $Na_v1.7$, but does not affect $Na_v1.8$. It was also found that Gr4b significantly shifts the steady-state activation and inactivation curves of $Na_v1.9$ to the depolarization direction and increases the window current, which is consistent with the change in the ramp current. Furthermore, analysis of $Na_v1.9$/$Na_v1.8$ chimeric channels revealed that Gr4b preferentially binds to the voltage-sensor of domain III (DIII VSD) and has additional interactions with the DIV VSD. The site-directed mutagenesis analysis indicated that N1139 and L1143 in DIII S3-S4 linker participate in toxin binding. In sum, this study reports a novel spider peptide toxin that may slow the fast inactivation of $Na_v1.9$ by binding to the new neurotoxin receptor site-DIII VSD. Taken together, these findings provide insight into the functional role of the Na_v channel DIII VSD in fast inactivation and activation.

Keywords: $Na_v1.9$, fast inactivation, domain III voltage-sensor, spider peptide toxin, neurotoxin receptor site

INTRODUCTION

Voltage-gated sodium (Na_v) channels are important transmembrane proteins that play a vital role in the generation and propagation of action potentials in excitable cells, such as central and peripheral neurons, cardiac and skeletal muscle myocytes, and neuroendocrine cells (Goldin 2001; Catterall 2012; Mantegazza and Catterall 2012). Nine Na_v channels (denoted $Na_v1.1$–$Na_v1.9$) have been identified in human (Yu and Catterall 2003). The subtypes can be divided into two categories according to their sensitivity to TTX: TTX-sensitive ($Na_v1.1$–1.4, $Na_v1.6$, and $Na_v1.7$) or TTX-resistant ($Na_v1.5$, $Na_v1.8$, and $Na_v1.9$). Notably, these subtypes have different tissue-specific localization and functions. The $Na_v1.1$–$Na_v1.3$ subtypes are expressed primarily in the central nervous system (CNS); the $Na_v1.6$ subtypes are expressed in the central and peripheral nervo us system; the $Na_v1.7$–$Na_v1.9$ subtypes are mainly expressed in the peripheral nervous system (PNS);

$Na_v1.4$ is present in skeletal muscle; and $Na_v1.5$ is mainly expressed in cardiac muscle (Dib-Hajj et al., 1998; Goldin 2001; Renganathan et al., 2002; Fukuoka et al., 2008; Catterall 2012; Bennett et al., 2019). Structurally, Na_v channel consist of an approximately 260 kDa pore-forming α-subunit and one or more associated β-subunits of 30–40 kDa (Catterall 2012; Bennett et al., 2019). The α-subunit has four homologous domains (I–IV). Each domain consists of six transmembrane segments (S1–S6) that form a voltage-sensing domain (VSD) containing S1–S4 and a central pore-forming domain (PD) containing S5, two P-loop, and S6 (Catterall 2000). The 4–8 positively charged arginine or lysine residues at every third position in S4 act as gating charges, which are required for voltage-dependent activation (Numa and Noda 1986; Catterall et al., 2017). The gating charges move outward upon membrane depolarization and initiate the voltage-dependent activation and inactivation of Na_v channels (Jiang et al., 2020). These characteristics endow the various conformation transformations of Na_v channel via an electromechanical coupling mechanism to open and close the pore. The three major states are defined as resting, activation, and inactivation.

Inactivation, which is an intrinsic property of Na_v channels, is a complex process that includes two distinct modes: fast and slow. Fast inactivation involves an inactivation particle in the cytoplasmic linker between DIII and DIV binding to the intracellular side of the pore (Vassilev et al., 1988; Catterall 2012). In contrast, slow inactivation is when the pore domain undergoes conformational rearrangements during prolonged depolarization (Silva and Goldstein 2013). Na_v channels undergo fast inactivation on a millisecond timescale to interrupt Na^+ conductance, which was first described by Hodgkin and Huxley in 1952 (Hodgkin and Huxley 1952). The intracellular loop between DIII and DIV forms the fast inactivation gate in which the three hydrophobic amino acids, namely Ile, Phe, and Met (IFM motif), are the key sequence (West et al., 1992; Catterall 2012). The cryo-EM structure of eukaryotic Na_v channels shows a potential allosteric blocking mechanism for fast inactivation (Yan et al., 2017). The IFM motif plugs into the compact hydrophobic pocket formed by the S4–S5 linker of DIII and DIV and the intracellular ends of S5 and S6 of DIV (McPhee et al., 1994, 1995, 1998; Kellenberger et al., 1996; Smith and Goldin 1997; Jiang et al., 2020). Although the mechanism of the development of fast inactivation is unclear, we believe that the fast inactivation allosteric process requires voltage-sensing and electromechanical coupling, which may involve a contribution from one or more VSD to cause the conformational changes. Fluorescent labeling studies have shown that the VSDs in DI-DIII of the $Na_v1.4$ channel are activated by depolarization faster than in DIV, which is consistent with the time course of activation and fast inactivation (Cha et al., 1999; Chanda and Bezanilla 2002; Kubota et al., 2017). This suggests that the activation gate opening of the Na_v channel is in contact with the outward movement of voltage sensors in DI-DIII, whereas fast inactivation is initiated by subsequent movement of the voltage sensor in DIV. Moreover, the known α-scorpion toxins, which inhibit the outward movement of DIV VSD to prevent DIV activation, slow the fast inactivation of Na_v channels (Campos et al., 2008; Clairfeuille et al., 2019). These findings demonstrate that DIV initiates fast inactivation of Na_v channels. However, whether other domain VSDs participate in the development of fast inactivation remains unknown, although evidence to date suggests that is not the case.

Venomous animals (spiders, scorpions, cone snails, etc.) have evolved the ability to produce peptide toxins with high affinity to target Na_v channels for the capture of prey or enhanced defenses against predators (Stevens et al., 2011). These peptide toxins (also known as neuropeptide toxins) are useful pharmacological tools for exploring the physiological roles of Na_v channels and a potentially rich source for drug discovery. The interactions between these toxins and Na_v channels can occur in two different ways: by occluding pores (pore blockers) or altering gating kinetics (gating modifier toxins). At least three distinct binding sites of neuropeptide toxins have been identified (Stevens et al., 2011). Peptide toxins binding to site 1 use the first mechanism, e.g., some μ-conotoxins from cone snails are site 1 pore blockers. Site 1 is mainly localized in the extracellular loops between S5 and S6 of DI–DIV (Chau et al., 2011). Site 3 toxins, like α-toxins (from scorpion, spider and sea anemone), slow fast inactivation and bind to the S3–S4 extracellular loop in domain IV (Thomsen and Catterall 1989; Catterall et al., 2007). Site 4 peptide toxins (β-toxins) regulate activation kinetics by binding to the extracellular loop connecting the S3-S4 segments in DII (Catterall et al., 2007; Xiao et al., 2008; Song et al., 2011; Zhang et al., 2020). It is known that the central pore of Na_v channel-mediated ion flow and the DII VSD is associated with channel activation and the DIV VSD is responsible for fast inactivation of channels. Thus, these peptide toxins can serve as pharmacological tools to provide insight into the structural and functional features of Na_v channels.

In this study, we identified and characterized the spider peptide toxin Gr4b from the venom of the spider *Grammostola rosea*, which is a gating modifier and significantly inhibits fast inactivation of the $Na_v1.9$ channel. Like the previously described $Na_v1.9$ peptide toxin HpTx1 (Zhou et al., 2020), Gr4b also inhibits the currents of $Na_v1.4$ and $Na_v1.7$ but does not affect $Na_v1.8$. Interestingly, Gr4b displays a novel effect on $Na_v1.9$, which occurs mostly through binding to the DIII S3-S4 linker to slow fast inactivation. This is distinct from HpTx1 which only binds to the DIV S3-S4 linker. Thus, the results of our study provide direct evidence for the role of DIII VSD in Na_v channel fast inactivation and provide a new tool to probe the structural and functional features of Na_v channels.

MATERIALS AND METHODS

Venom Collection and Toxin Purification

As described in previous studies, the venom of the *Grammostola rosea* spider was collected by electrical stimulation. The collected venom was lyophilized and stored at −80°C. Subsequently, the venom was dissolved in 0.1% trifluoroacetic acid (TFA) in double-distilled water to a final concentration of 10 mg/ml immediately before being subjected to reversed-phase high-performance liquid chromatography (RP-HPLC) purification. First, reverse-phase HPLC purification was performed using a water HPLC system (Waters Alliance, 2695 HPLC system) with an Ultimate® XB-C18

column (10 × 250 mm, 5 μm, Welch Materials Inc., Shanghai, China) with a flow rate of 3 ml/min and a gradient of 10–55% A for more than 45 min (solvent A: 0.1% trifluoroacetic acid in acetonitrile, solvent B: 0.1% trifluoroacetic acid in water). The absorbance was measured at 215 nm. The fractions were collected, lyophilized, and then stored at −20°C until the next subdivision. Next, the target fraction containing Gr4b was subjected to a second round of RP-HPLC (Waters Alliance, 2695 HPLC system) using an analytic XB-C18 column, (300 Å, 4.6 mm × 250 mm, Welch Materials Inc., Shanghai, China) with a linear increasing acetonitrile gradient (acetonitrile at an increasing rate of 0.5% per minute and a flow rate of 1 ml/min) to obtain the purified Gr4b. The molecular weight of the peptide was confirmed by matrix assisted laser desorption/ionization-time of-flight mass-spectrometry (MALDI-TOF-TOF MS) spectrometry (AB SCIEX TOF/TOFTM 5800 system, Applied Biosystems, United States). The N-terminal amino acid sequence of the peptide was determined by automated Edman degradation in a PPSQ-53A protein sequencer (Shimadzu Corporation, Kyoto, Japan).

Plasmid Constructs and Mutagenesis

Rat $Na_v1.4$, human $Na_v1.7$ and rat $Na_v1.8$ cDNA clones were kindly gift from Dr. Theodore Cummins (Stark Neurosciences Research Institute, Indiana University School of Medicine, Indianapolis, IN, United States) and were subcloned into the pCMV or pCDNA3.1-blank vectors. Human $Na_v1.9$ was subcloned into the pEGFP-N1 vector. The C-terminal of $hNa_v1.9$ was linked to GFP to construct a fusion protein channel ($hNa_v1.9$-eGFP), which was as described in our previous studies (Zhou et al., 2017). Mutations were made using the site-directed mutation method or recombination-based cloning using GenBuilder™ Cloning Kit (GenScript, United States). Primers presented in **Supplementary Tables 1–4**. All mutations were verified by DNA sequencing.

Cell Culture and Transfection

ND7/23 and HEK293T cells were maintained at 37°C in a humidified 5% CO_2 incubator in Dulbecco's Modified Eagle's Medium (DMEM) supplemented with 10% fetal bovine serum, 100 μg/ml streptomycin, 100 U/ml penicillin, and 2 mM L-glutamine. The cells were trypsinized, diluted with 1 ml of culture medium, and seeded at a 1:5 ratio in 35 mm Petri dishes for culture. When grown to 80–90% confluence, the ND7/23 cells were transfected with $hNa_v1.9$-GFP or $hNa_v1.9$-GFP mutants using the X-tremeGENE HP DNA Transfection Reagent (Roche, Basel, Switzerland) according to the manufacturer's instructions. ND7/23 cells were used for $hNa_v1.9$-GFP chimeric channel expression and the conditions were as previously described (Zhou et al., 2017), the beta subunits (β1 and β3) are endogenously expressed in the cell lines used to study $Na_v1.9$ (Rogers et al., 2016). Transfections for the other plasmids were performed using Lipofectamine 2000 (Invitrogen, Carlsbad, CA, United States) following the manufacturer's instructions. Na_v channel plasmid (4 μg) plus 0.5 μg pEGFP-N1 (except for $hNa_v1.9$) plasmid were co-transfected into HEK293T or ND7/23 ($rNa_v1.8$ and $hNa_v1.9$ only) cells. The cells were seeded onto several 3.5 cm dishes at a 1:10 ratio at 4–6 h after transfection. Cells with green fluorescent protein (GFP) were selected for whole-cell patch-clamp analysis at 24–36 h post-transfection.

Electrophysiology Recordings

Whole-cell current recordings were performed using an EPC-10 USB patch-clamp amplifier operated by Patch Master software (HEKA Elektronik, Lambrecht, Germany). The recording pipettes were fabricated from borosilicate glass capillaries using a two-step vertical microelectrode PC-10 puller (Narishige Group, Tokyo, Japan), and the pipette resistance was controlled to be 2.0–3.0 MΩ. Voltage-clamp recordings were acquired with Patch Master software 2 × 73 (HEKA Elektronik) 4 min after establishing whole-cell configuration, and the currents elicited were sampled at 20 kHz and filtered at 5 kHz. After breaking in, the serial resistance was controlled below 5 MΩ, the voltage error was minimized by using 80% serial resistance compensation, and the compensation speed value was 10 μs. For recording Na_v channel currents, the external solution contained (mM): 150 NaCl, 2 KCl, 1.5 CaCl2, 1 MgCl2 and 10 HEPES (pH 7.4, adjusted with NaOH); the pipette solution contained (in mM): 35 NaCl, 105 CsF, 10 EGTA, 10 HEPES (pH 7.4, adjusted with CsOH). The osmotic pressure of the intracellular fluids and extracellular fluids is adjusted to 300–320 mOsm with sucrose. Before use, Gr4b was dissolved in ddH_2O to make a 250 μM stock solution at −20°C. TTX was dissolved in DMSO to make a 1 mM stock solution. TTX was added to bath solution to a final concentration of 1 μM when used to inhibit TTX-sensitive (TTX-S) Na_v channels. Unless otherwise indicated, all chemicals were products of Sigma-Aldrich (St. Louis, MO, United States). For electrophysiology experiments, the stock solution of Gr4b was diluted with fresh bath solution to a concentration of tenfold of the interested concentration, 30 μl of the concentrated peptide was diluted into the recording chamber (containing 270 μl bath solution) far from the recording pipet (the recording cell), and was mixed by repeatedly pipetting to achieve the specified final concentration.

Data Analysis

Data were analyzed using the PatchMaster v2x73 (HEKA Elektronik, Lambrecht, Germany), Igor Pro 6 (Wave Metrics, Lake Oswego, OR, United States), Office Excel 2010 (Microsoft Corporation, WA, United States), and GraphPad Prism 7 (GraphPad Software Inc., CA, United States). All data points are shown as mean ± standard error of the mean (SEM), and n was presented as the number of separate experimental cells. The Boltzmann function was used to fit steady-state activation and deactivation curves. Concentration-response curves were fitted using the Hill equation. One-way ANOVA was used to assess the difference between multiple groups. Significant levels were set at $p < 0.05$.

RESULTS

Toxin Purification and Identification

The venom of the spider *Grammostola rosea* contains several classes of peptide toxins that target ion channels (**Figure 1A**). For example, GpTx1 and PaurTx3 are potent inhibitors of the $Na_v1.7$ channel (Murray et al., 2015; Chen et al., 2020), HaTx1 and

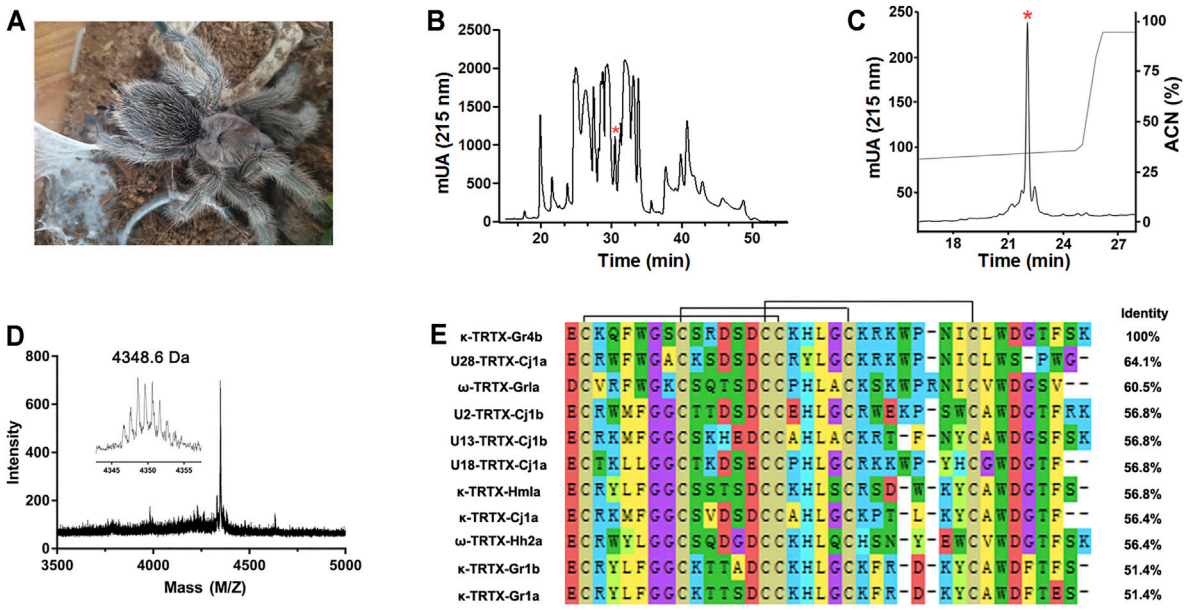

FIGURE 1 | Purification and identification of Gr4b. **(A)** The spider G. *Grammostola rosea*. **(B)** RP-HPLC profile of crude venom from spider *Grammostola rosea*. The asterisk indicated the peak containing Gr4b. **(C)** Gr4b was purified to homogeneity by analytical RP-HPLC. **(D)** MALDI-TOF MS spectrum showing a monoisotopic $M+H^+$ of 4348.6 Da. **(E)** Sequence alignment of Gr4b with similar toxins in NaSpTx family2; black lines show the disulfide linkage.

VsTx1 significantly inhibit the currents of the $K_v2.1$ channel (Chen et al., 2012; Bemporad et al., 2006), and GsMTx2/4 blocks mechanosensitive ion channels (Oswald et al., 2002). Due to poor heterologous expression in mammal cells, pharmacological studies of the $Na_v1.9$ channel have lagged. Previously, we succeeded in achieving functional expression of the $Na_v1.9$ channel in heterologous cells (Zhou et al., 2017). Using this system, we first identified a spider peptide toxin that activates the $Na_v1.9$ channel and produces pain in mice (Zhou et al., 2020). In order to identify more specific and novel peptide toxins for $Na_v1.9$, we used patch-clamp recording to screen animal peptide toxins for the ability to affect the $Na_v1.9$ channel. Crude venom was fractionated by RP-HPLC, as shown in **Figure 1B**. By screening the panel, venom fractions with significant $Na_v1.9$ regulation activity were identified; a fraction potently inhibited the fast inactivation of $Na_v1.9$ (**Figure 1B**). This fraction was further purified by RP-HPLC, and approximately 8 μg of purified peptide toxin was obtained from 1 mg crude spider venom (**Figure 1C**). The purity of this peak was confirmed by MALDI–TOF MS analysis which revealed a peptide toxin with a molecular weight of 4,348.6 Da, which was consistent with the calculated molecular mass (4,348.01 Da). (**Figure 1D**). N-terminal Edman sequencing and the venom gland transcriptome cDNA data determined a novel 37-residue peptide toxin named Gr4b (rational nomenclature: δ-theraphotoxin Gr4b) (Kimura et al., 2012), as shown in **Figure 1E**. Sequencing alignment showed that Gr4b shares highly sequence similarity with Family 2 Na_v-targeting spider toxins (NaSpTx), which comprise 42–44 residues and contained six residues and form a conserved cysteine pattern-inhibitor cystine knot (ICK) motif (Klint et al., 2012) (**Figure 1E**). NaSpTx Family 2 toxins have various ion channel activities that inhibit K_v, Ca_v, and Na_v channels (Klint et al., 2012). Interestingly, the members of the NaSpTx Family 2 Toxins JZTX-XI and Df1a display dual modulatory effects on specific Na_v channels, simultaneously inhibiting peak current and slowing fast inactivation (Liao et al., 2006; Klint et al., 2012; Tang et al., 2014; Cardoso et al., 2017).

Effect of Gr4b on Na_v Channel Subtypes

The $Na_v1.9$ current was evoked to −40 mV by a 100-ms depolarization potential from a holding potential of −120 mV in ND7/23 cells. A concentration of 250 nM Gr4b slowed the fast inactivation of $Na_v1.9$, leading to a large sustained current (**Figure 2A**). The half-maximum effective concentration (EC_{50}) of Gr4b was determined to be 25 ± 1.0 nM (**Figure 2B**). Next, we evaluated the effect of Gr4b on a range of Na_v channels expressed in HEK293T or ND7/23 cells. Interestingly, Gr4b inhibited $Na_v1.4$ and $Na_v1.7$ channels in HEK293T cells, with preference for $Na_v1.7$ (**Figures 2C–E**). As shown in **Figures 2D,E**, 250 nM Gr4b completely inhibited $Na_v1.7$ currents with a half-maximum inhibition concentration (IC_{50}) value of 27 ± 3.0 nM. It had substantially weaker effects on $Na_v1.4$, with an IC_{50} value of 411 ± 184 nM (**Figures 2C,E**). However, application of up to 2.5 μM Gr4b had no effect on $Na_v1.8$ subtype in ND7/23 cells (**Figure 2F**). Taken together, these results suggest that Gr4b has different actions on different Na_v channel subtypes.

Effect of Gr4b on Activation and Inactivation of $Na_v1.9$

A major effect of gating modifier toxins on Na_v channels is modification of the voltage dependence of channel activation and inactivation. Gr4b plays the role of a gating modifier toxin to slow fast inactivation of the $Na_v1.9$ channel. To clarify the mode of action of

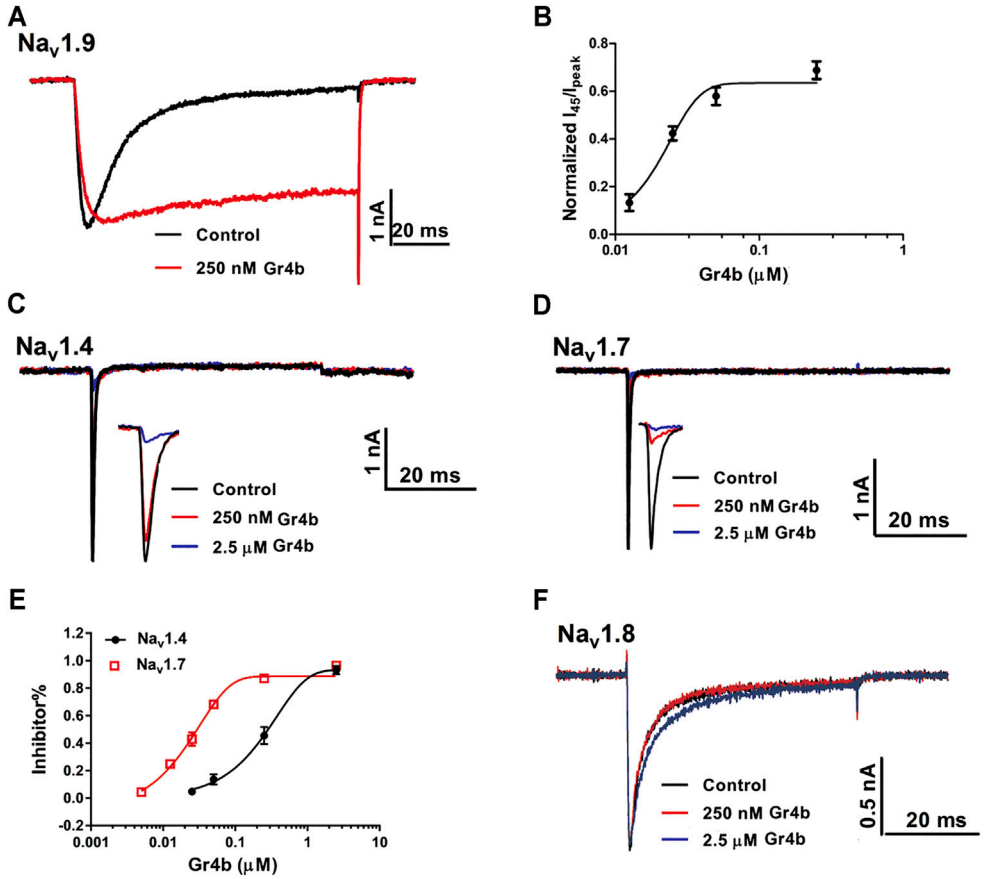

FIGURE 2 | Effect of Gr4b on Na_v channel subtypes. **(A)** Representative current traces showing that Gr4b slowed the fast inactivation of $Na_v1.9$ expressed in ND7/23 cells. The currents evoked by 100 ms depolarization to −40 mV from holding potentials of −120 mV. **(B)** The dose-response curves for the Gr4b-induced inhibition of the fast inactivation of $Na_v1.9$, EC_{50} of 25 ± 1 nM (n = 6). **(C,D)** Representative current traces show that Gr4b blocked the currents of $Na_v1.4$ and $Na_v1.7$. Currents were elicited by 50 ms depolarizing steps to −10 mV from a holding potential of −90 mV. **(E)** Dose-response curves for Gr4b inhibiting $Na_v1.4$ and $Na_v1.7$ currents. The IC_{50} values were 411 ± 184 nM and 27 ± 3 nM for $hNa_v1.4$ and $Na_v1.7$, respectively (n = 4–6). **(F)** Representative traces show that the $Na_v1.8$ currents are unaffected by Gr4b (n = 4). Representative current traces from ND7/23 cells expressing $Na_v1.8$ in the absence (black) and presence of 250 nM (red) or 2.5 μM (blue) Gr4b. Currents were elicited by 50 ms depolarizing steps to 10 mV from a holding potential of −90 mV.

Gr4b, we used the saturation concentration (250 nM) to analyze the effects of Gr4b on the voltage dependence of activation and inactivation properties of the $Na_v1.9$ channel. As shown in **Figure 3A**, Gr4b inhibited the fast inactivation currents at all tested voltages, but did not change the threshold of the initial activation voltage or the reversal potential of the $Na_v1.9$ current (**Figure 3B**). However, the peak of the current was significantly shifted by +10 mV (**Figure 3B**). In addition, Gr4b shifted the voltage dependence of the activation curve to a more positive potential by approximately 12.5 mV (Control: −51.3 ± 2.7 mV, Gr4b: −38.8 ± 2.9 mV, n = 8, $p < 0.0001$) (**Figure 3C** and **Table 1**). Furthermore, a remarkable change was observed in the slopes of the curves from 6.3 ± 0.3 mV in the control to 11.2 ± 0.4 mV in the presence of Gr4b (**Figure 3C** and **Table 1**, $p < 0.0001$), indicating that toxin binding might affect the cooperativity of the four voltage sensors of the $Na_v1.9$ channel. As shown in **Figure 3C** and **Table 1**, the steady-state inactivation curve was significantly shifted to a positive direction by approximately 37.1 mV in the presence of 250 nM Gr4b (Control: −53.7 ± 2.2 mV, Gr4b: −16.6 ± 2.7 mV, n = 6, $p < 0.0001$), whereas the slope of the curve was not changed (Control: 10.0 ± 0.8 mV, Gr4b: 11.3 ± 0.7 mV, n = 6). We also found that Gr4b introduced a non-inactivated component in the steady-state inactivation curve around the test potential. The β1 subunit is known to modulate the kinetics of fast inactivation (Vijayaragavan et al., 2001; Vijayaragavan et al., 2004). Because Gr4b affects inactivation kinetics, we tested whether overexpression of the β1 with $Na_v1.9$ altered the effect of the toxin. As shown in **Figures 3D,E** and **Table1**, Gr4b significantly inhibited the fast inactivation currents of $Na_v1.9$ co-expression with β1 in ND7/23 cells, and shifted the kinetics of fast inactivation and activation to positive potential, similar to that of the effect of toxin on $Na_v1.9$ expression in ND7/23 cells. The predicted window currents of the $Na_v1.9$ channel were obviously improved in the presence of 250 nM Gr4b (**Figure 3C**). Indeed, 250 nM Gr4b robustly increased the peak of the ramp current of $Na_v1.9$ currents in ND7/23 cells by 42.40% (Control: −404.0 ± 116.3 pA, Gr4b: −701.1 ± 236.6 pA, n = 5, $p < 0.05$) (**Figure 3F** and **Table 2**). Consistent with the effect of Gr4b on activation, the peak of the ramp current was observably shifted by 21.9 mV (Control: −47.4 ± 1.5 mV, Gr4b: −25.6 ± 3.4 mV, n = 5, $p <$

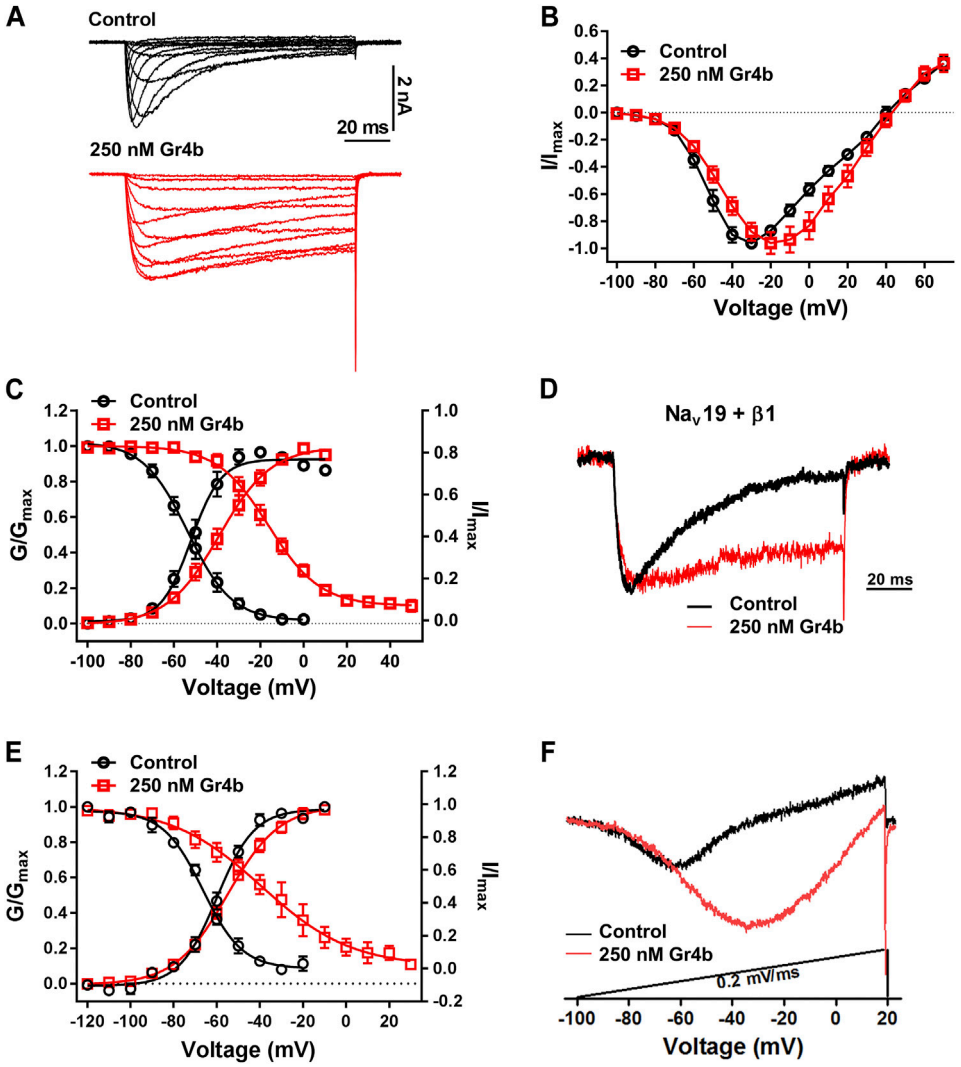

FIGURE 3 | Effect of Gr4b on activation and inactivation of $Na_v1.9$. **(A)** Representative current traces of $Na_v1.9$ tested by different voltages, in the absence (black) and presence of 250 nM Gr4b (red). **(B)** Current-voltage (I–V) curves for the $Na_v1.9$ channel in the absence (black) or presence (red) of 250 nM Gr4b (n = 8). **(C)** Voltage-dependent steady-state activation (G/G_{max}, n = 8) and fast inactivation (I/I_{max}, n = 6) of $Na_v1.9$ in the absence (black) or presence (red) of 250 nM Gr4b. Currents were elicited by a cluster of depolarizations from −100 mV to +70 mV (in 10 mV increments) from the holding potential of −120 mV for 50 ms. For simplicity, only part of the currents were shown. The voltage dependence of steady-state inactivation was estimated by using a standard double-pulse protocol, in which a 50 ms depolarizing test potential to −30 mV followed a 500 ms prepulse (ranged from −120 mV to +50 mV, in 10 mV increment). **(D)** Representative current traces showing that Gr4b slowed the fast inactivation of $Na_v1.9$ co-expressed with β1 in ND7/23 cells. The currents evoked by 100 ms depolarization to −40 mV from holding potentials of −120 mV. **(E)** Voltage-dependent steady-state activation (G/G_{max}, n = 5) and fast inactivation (I/I_{max}, n = 6) of $Na_v1.9$ co-expressed with β1 in the absence (black) or presence (red) of 250 nM Gr4b. **(F)** Compared with control treatment, 250 nM Gr4b significantly enhances the ramp currents of $Na_v1.9$ channels expressed in ND7/23 cells.

0.001), potentially increasing Na^+ influx (**Figure 3F** and **Table 2**). Based on these findings, Gr4b is clearly a gating modifier that alters the voltage dependence of activation and inactivation of the $Na_v1.9$ channel.

Kinetics of Dissociation of Gr4b From $Na_v1.9$

We further investigated the binding kinetics of toxin on the $Na_v1.9$ channel. As shown in **Figure 4A**, the time course for 250 nM Gr4b inducing the inhibited inactivation currents of $Na_v1.9$ was characterized by a slow onset of action, with a τ_{on} value of 42.8 ± 3.5 s (n = 3). Inhibition of fast inactivation by Gr4b slowed the reversible recovery upon perfusion bath solution washing, with a recovery of approximately 54.39% of the control current within 2.5 min (**Figure 4A**). These results indicate that Gr4b has a strong affinity for the $Na_v1.9$ channel.

Gating modifier toxins typically affect channel gating by regulating the voltage-sensor of the channel. In turn, the affinity of the toxins to the channel is also regulated by the stimulus voltage, e.g., the spider toxin ProTx-II inhibits the current of the $Na_v1.7$ channel with a significant voltage

TABLE 1 | The effects of Gr4b on activation and inactivation of $Na_v1.9$.

	Control						250 nM Gr4b					
	Voltage dependence of Activation (mV)			Voltage dependence of Inactivation (mV)			Voltage dependence of Activation (mV)			Voltage dependence of Inactivation (mV)		
	$V_{1/2}$	k	n	$V_{1/2}$	k	n	$V_{1/2}$	k	n	$V_{1/2}$	k	n
$Na_v1.9$	−51.3 ± 2.7	6.3 ± 0.3	8	−53.7 ± 2.2	10.0 ± 0.8	6	−38.8 ± 2.9****	11.2 ± 0.4****	8	−16.6 ± 2.7****	11.3 ± 0.7	6
$Na_v1.9 + \beta1$	−60.0 ± 1.3	9.3 ± 1.5	5	−63.2 ± 4.4	10.0 ± 0.9	5	−54.3 ± 0.9**	13.4 ± 1.9***	5	−38.9 ± 6.6*	23.1 ± 4.0*	5

*Data are presented as the mean ± SEM. **p < 0.01, ***p < 0.001, ****p < 0.0001. Parametric paired two-tailed t-test was used. n is presented as the number of the separate experimental cells.*

TABLE 2 | The effects of Gr4b on ramp current of $Na_v1.9$.

	Control				250 nM Gr4b			
	Voltage of the peak current (mV)	n	The peak current of ramp (pA)	n	Voltage of the peak current (mV)	n	The peak current of ramp (pA)	n
$Na_v1.9$	−47.4 ± 1.5	5	−404.0 ± 116.3	5	−25.6 ± 3.4***	5	−701.1 ± 236.6	5

*Data are presented as the mean ± SEM. *p < 0.05, ***p < 0.001, when compared with Control. Parametric paired two-tailed t-test was used. n is presented as the number of the separate experimental cells.*

dependence (Xiao et al., 2010). We previously reported that binding of the gating modifier toxins HNTX-III, HpTx1, and HWTX-IV was reversed by prolonged strong depolarizations that activate the voltage sensor (Xiao et al., 2008; Xiao et al., 2010; Zhou et al., 2020; Liu et al., 2013). Therefore, we examined whether prolonged strong depolarizations could reverse the inhibitory effect of Gr4b on $Na_v1.9$ using the protocol described in **Figure 4B**. As shown in **Figure 4B**, a progressively longer strong depolarization (up to 80 mV) led to an increase in the fraction of sodium current recovered from inhibition by Gr4b. A depolarization time lasting 1,028 ms resulted in complete recovery of the slowed inactivated current. These data indicate that Gr4b dissociated from $Na_v1.9$ in response to prolonged strong depolarizations. Furthermore, as shown in **Figure 4C**, the degree of dissociation is positively related to the depolarization time and the depolarization voltage, i.e., increased depolarization time and potential were correlated with increased dissociation. From the time course of dissociation of the toxin after strong depolarizations in the presence of 250 nM Gr4b, the dissociation time constant was fitted with a single exponential function and calculated to be 105.6 ± 36.3 ms, 240.0 ± 26.9 ms, and 473.5 ± 90.8 ms for 80 mV, 40 mV, and 20 mV (n = 4 each), respectively. These results suggest that the rate of Gr4b dissociation is voltage-dependent and that stronger depolarization is correlated with a higher rate of dissociation.

Gr4b Inhibits Fast Inactivation of $Na_v1.9$ via the VSD of DIII and DIV

Because Gr4b dissociation from $Na_v1.9$ is voltage-dependent, we hypothesized that the toxin may be bound to the VSD of the channel. Neurotoxins that act on Na_v channels can target six different sites in the channels, with site 3 (DIV VSD) being the

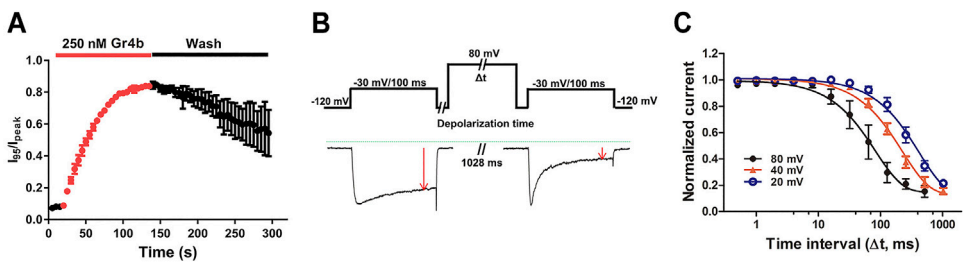

FIGURE 4 | Kinetics of dissociation of Gr4b from $Na_v1.9$. **(A)** Time course of the inhibition of fast inactivation by 250 nM Gr4b and the recovery upon washing with bath solution, in which the ratios of I_{95}/I_{peak} were plotted as a function of time, τ_{on} = 42.8 ± 3.5 s (n = 3). **(B)** Diagram showing the protocol for dissociation analysis (**upper**). Representative current showing in the presence of 0.25 μM Gr4b, progressively prolonged strong depolarization (to 80 mV) led to a greater degree of $Na_v1.9$ current recovery from Gr4b inhibition (**below**). **(C)** Time course of dissociation of 250 nM Gr4b from $Na_v1.9$ at 80 mV (τ = 105.6 ± 36.3 ms, n = 4), 40 mV (τ = 240.0 ± 26.9 ms, n = 4), and 20 mV (τ = 473.5 ± 90.8 ms, n = 4). Cells expressing $Na_v1.9$ were incubated in Gr4b for 110 s at a holding potential of −120 mV to allow binding. The rate of toxin dissociation was determined with the illustrated pulse paradigm by stepping to a depolarizing pulse of 80, 40, or 20 mV for 0–1,028 ms, returning to −120 mV for 100 ms to allow recovery from fast inactivation, and then assessing the effect of the depolarizing pulse with a 100 ms test pulse to −30 mV. Data are presented as the mean ± SEM.

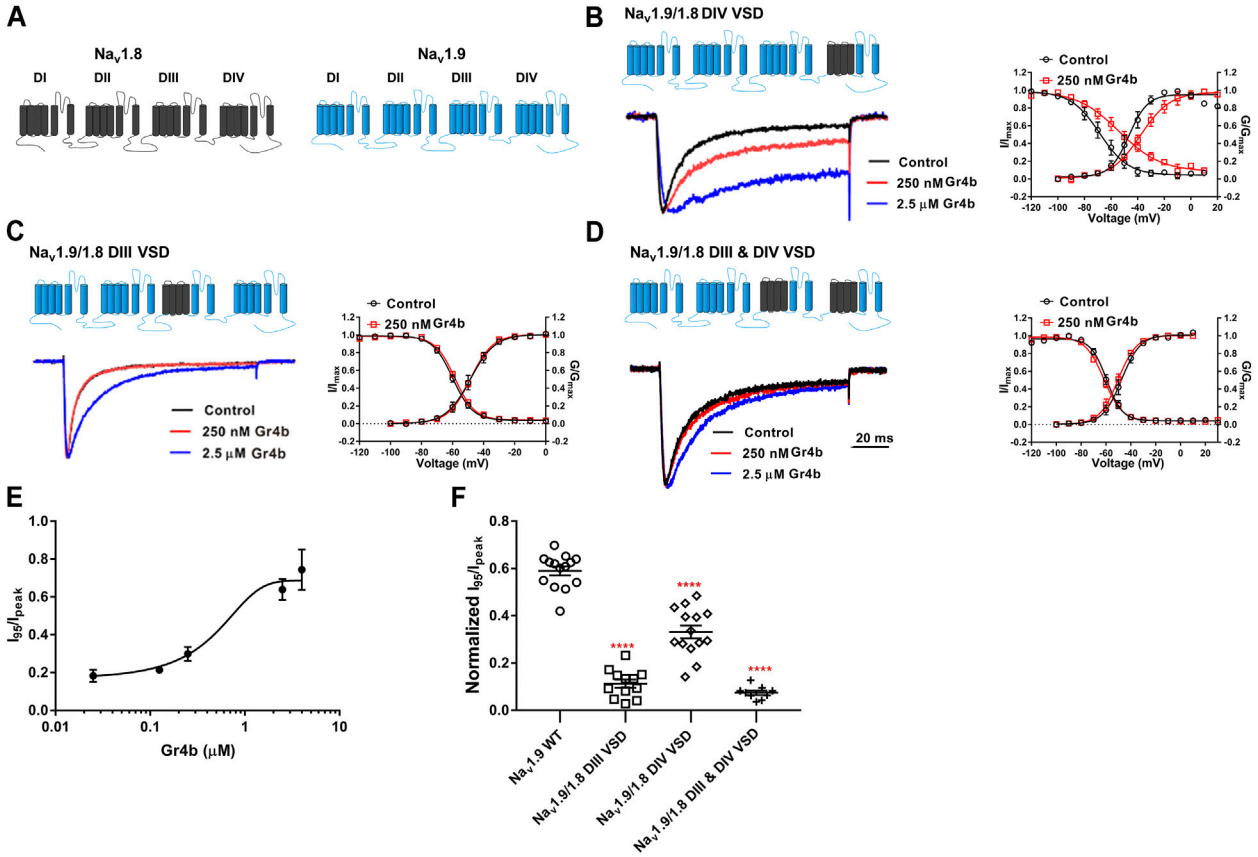

FIGURE 5 | DIII VSD and DIV VSD of $Na_v1.9$ is involved in interacting with Gr4b. **(A)**The topological structure of $Na_v1.9$ (blue) and r$Na_v1.8$ (grey), the numbers indicated the border of the transmembrane domains. **(B–D)** Representative normalized current traces, voltage-dependent steady-state activation and voltage-dependent steady-state inactivation show that the chimera channels (constructed as the cartoon illustrated) $Na_v1.9/1.8$ DIV VSD, $Na_v1.9/1.8$ DIII VSD, $Na_v1.9/1.8$ DIII & DIV VSD, in the absence (black), presence of 250 nM Gr4b (red) or 2.5 μM Gr4b (blue). **(E)** The dose-response curves for the Gr4b-induced inhibition of the fast inactivation of $Na_v1.9/1.8$ DIV VSD, EC_{50} of 1.5 ± 0.25 μM (n = 4). **(F)** The effect of Gr4b on the channel of WT and $Na_v1.9/1.8$ chimeras. Dot plots display the effect of 250 nM Gr4b on the persistent current (I_{95}/I_{peak}) (n = 14 for WT; n = 12 for $Na_v1.9/1.8$ DIII VSD, n = 14 for $Na_v1.9/1.8$ DIV VSD and n = 9 for $Na_v1.9/1.8$ DIII & DIV VSD). One-way ANOVA with Dunnett's Multiple Comparison Test and compared with WT, ****$p < 0.0001$.

hotspot for spider peptide toxins to inhibit fast inactivation (Stevens et al., 2011). One well-characterized example of a $Na_v1.9$ modulating peptide is HpTx1 from spider venom, which inhibits fast inactivation of the $Na_v1.9$ channel by binding to the DIV S3–S4 linker (Zhou et al., 2020). In the present study, the underlying mechanism of action of Gr4b on $Na_v1.9$ channels was similar to that described for HpTx1. To identify the critical region of $Na_v1.9$ for toxin-induced inhibition of fast inactivation, several chimeric channels were constructed. Since $Na_v1.8$ is resistant to Gr4b, a chimera strategy was used to screen the critical modules (VSD) responsible for the toxin's ability to reduce fast inactivation of $Na_v1.9$. Firstly, we made the chimera $Na_v1.9/1.8$ DIV VSD, in which the DIV VSD (DIV S1–S4) of $Na_v1.9$ was replaced with the corresponding domain of $Na_v1.8$. As shown in **Figure 5B**, compared with the wildtype (WT) channel, we observed that a Gr4b concentration of 250 nM reduced the efficacy of the $Na_v1.9/1.8$ DIV VSD chimeric channel (**Figures 5B,F**). But the steady-state activation curve was significantly shifted to a positive direction by approximately 8 mV in the presence of 250 nM Gr4b (Control: −45.8 ± 3.4 mV, Gr4b: −37.8 ± 3.5 mV, n = 3, $p < 0.05$) and the slope of the curve was also significantly changed (Control: 6.9 ± 0.6 mV, Gr4b: 10.7 ± 1.4 mV, n = 3, $p < 0.05$) (**Table 3**), that consistent with the effect of Gr4b on WT channel. Nevertheless, it still produced large inhibition of fast inactivation of the chimera channel at 2.5 μM, similar to that of WT-$Na_v1.9$. However, at this concentration, the toxin did not seem to affect $Na_v1.8$. Therefore, these results indicate that the channel DIV VSD might be involved in the Gr4b–$Na_v1.9$ interaction to inhibit fast inactivation and that additional binding areas may exist.

The DIII VSD of Na_v channels have been also shown to modulate channel inactivation (Hsu et al., 2017). Thus, we hypothesized that DIII VSD also is critical for Gr4b inhibition of fast inactivation of $Na_v1.9$. Thus we made the two chimeras $Na_v1.9/1.8$ DIII VSD and $Na_v1.9/1.8$ DIII & DIV VSD. The results showed that replacing these regions of $Na_v1.9$ abolished the effects of Gr4b on the channel. Even at high concentrations (2.5 μM), the chimeric channels were almost unaffected by Gr4b (**Figures 5C,D,F**). However, the EC_{50} of Gr4b was

TABLE 3 | The effects of 250 nM Gr4b on activation of $Na_v1.9$ mutants.

	Control						250 nM Gr4b					
	Voltage dependence of Activation (mV)			Voltage dependence of Inactivation (mV)			Voltage dependence of Activation (mV)			Voltage dependence of Inactivation (mV)		
	$V_{1/2}$	k	n	$V_{1/2}$	k	n	$V_{1/2}$	k	n	$V_{1/2}$	k	n
$Na_v1.9$	−51.3 ± 2.7	6.3 ± 0.3	8	−53.7 ± 2.2	10.0 ± 0.8	6	−38.8 ± 2.9****	11.2 ± 0.4****	8	−16.6 ± 2.7****	11.3 ± 0.7	6
$Na_v1.9$/1.8 DIII VSD	−48.6 ± 2.5	7.3 ± 0.5	5	−59.8 ± 1.3	6.3 ± 0.4	6	−48.4 ± 1.0	7.0 ± 0.4	5	−58.5 ± 1.0	6.4 ± 0.5	6
$Na_v1.9$/1.8 DIV VSD	−45.8 ± 3.4	6.9 ± 0.6	3	−67.9 ± 3.8	10.0 ± 0.4	6	−37.8 ± 3.5	10.7 ± 1.4	3	−54.7 ± 4.1**	13.7 ± 0.7**	6
$Na_v1.9$/1.8 DIII&DIV VSD	−47.7 ± 2.3	7.3 ± 0.4	3	−59.5 ± 1.6	6.0 ± 0.4	5	−50.6 ± 2.1*	7.3 ± 0.4	3	−61.7 ± 1.3	7.3 ± 0.6**	5
$Na_v1.9$/1.8 DIII S3-S4	−55.0 ± 2.4	6.3 ± 0.5	4	−66.0 ± 3.4	7.3 ± 0.5	4	−57.9 ± 2.2	7.4 ± 0.7*	4	−65.4 ± 3.9	7.5 ± 0.2	4

*Data are presented as the mean ± SEM. *p < 0.05, **p < 0.01, ***p < 0.001, ****p < 0.0001, when compared with Control. Parametric paired two-tailed t-test was used. n is presented as the number of the separate experimental cells.*

TABLE 4 | The effects of 250 nM Gr4b on activation of $Na_v1.9$ mutants.

	Control						250 nM Gr4b					
	Voltage dependence of Activation (mV)			Voltage dependence of Inactivation (mV)			Voltage dependence of Activation (mV)			Voltage dependence of Inactivation (mV)		
	$V_{1/2}$	k	n	$V_{1/2}$	k	n	$V_{1/2}$	k	n	$V_{1/2}$	k	n
$Na_v1.9$ N1139A	−51.5 ± 3.8	7.2 ± 1.0	5	−63.9 ± 3.0	9.5 ± 0.5	6	−43.8 ± 4.5**	12.9 ± 2.1*	5	−60.6 ± 2.8	11.9 ± 0.6*	6
$Na_v1.9$ N1139K	−51.1 ± 2.3	8.8 ± 0.9	8	−68.5 ± 3.9	9.6 ± 0.5	4	−52.1 ± 1.8	8.8 ± 0.7	8	−49.7 ± 13.0	19.6 ± 2.7*	4
$Na_v1.9$ L1140A	−52.1 ± 0.9	6.3 ± 0.2	5	−71.3 ± 2.8	10.5 ± 0.9	7	−42.6 ± 1.6**	13.2 ± 1.2**	5	−45.0 ± 7.1**	15.6 ± 0.8**	7
$Na_v1.9$M1141A	−54.7 ± 2.7	7.2 ± 0.5	5	−76.3 ± 2.7	9.9 ± 0.2	5	−55.5 ± 2.8	10.3 ± 2.0	5	−37.6 ± 7.1**	21.9 ± 1.0***	5
$Na_v1.9$ L1143A	−53.1 ± 1.8	6.7 ± 0.4	6	−68.3 ± 3.4	10.9 ± 0.3	5	−58.7 ± 1.8*	8.1 ± 5.0**	6	−63.5 ± 2.2*	10.3 ± 0.6	5
$Na_v1.9$ L1143V	−51.9 ± 2.2	7.2 ± 0.2	6	−79.9 ± 4.8	11.8 ± 0.4	4	−50.8 ± 3.9	11.4 ± 1.3*	6	−44.3 ± 3.8**	14.9 ± 1.8	4
$Na_v1.9$ S1145A	−49.1 ± 2.6	7.4 ± 0.4	7	−63.9 ± 2.5	8.8 ± 0.4	8	−37.8 ± 4.1**	15.0 ± 1.6**	7	−17.0 ± 5.0****	20.1 ± 2.1**	8

*Data are presented as the mean ± SEM. *p < 0.05, **p < 0.01, ***p < 0.001, ****p < 0.0001, when compared with Control. Parametric paired two-tailed t-test was used. n is presented as the number of the separate experimental cells.*

determined to be 1.5 ± 0.25 μM in $Na_v1.9$/1.8 DIV VSD channel (**Figure 5E**). These results suggest that the DIII VSD of the $Na_v1.9$ channel plays a key role in Gr4b-mediated inhibition of their fast inactivation currents. Furthermore, we observed that replacing DIII S3-S4 linker region of $Na_v1.9$ abolished the effects of Gr4b on the channel also (**Figures 6A,B,J**). To further elucidate the mechanism underlying Gr4b binding to $Na_v1.9$, amino acid residues in the S3–S4 linker of DIII were replaced by the alanine residues (**Figure 6A**). The results indicated that three component residues (namely N1139, L1143, and S1145) were critical for Gr4b binding to DIII S3-S4. Mutations in N1139 and L1143 significantly reduced sensitivity to Gr4b (**Figures 6B–J** and **Table 4**). In addition, a mutation of $Na_v1.9$ (S1145A) enhanced sensitivity to Gr4b (**Figures 6I,J** and **Table 4**). Taken together, these results suggest that Gr4b preferentially binds to the DIII VSD and has additional interactions with the DIV VSD, while two residues (N1139 and L1143) in the DIII S3-S4 linker may affect the interaction of $Na_v1.9$ with Gr4b.

DISCUSSION

Spider venoms comprise complex mixtures of various chemical substances, the majority of which are small, disulfide-rich peptides. These bioactive peptides are rich in Na_v channel modulators useful for predation and defense. Given their specificity and high affinity for Na_v channels, some of these peptides have become useful pharmacological tools for investigating the structure of the Na_v channel and studying the activation and inactivation processes that are a fundamental gating characteristic of Na_v channels. In this study, we screened the novel spider toxin Gr4b, which is a gating modifier that specifically delays fast inactivation of $Na_v1.9$. Gr4b belongs to NaSpTx Family 2 and contains a conserved ICK motif. Analyses to identify the site of action revealed that Gr4b preferentially interacts with the DIII VSD of the $Na_v1.9$ channel and, to a relatively lesser extent, with the DIV VSD. These results imply that, similar to the function of DIV VSD, DIII VSD may regulate fast inactivation.

Furthermore, structural and mutational studies revealed that the DIII S4–S5 linker is a docking receptor for the fast inactivation gate IFM. The IFM motif is responsible for fast inactivation via penetration of a compact hydrophobic pocket formed by the S4–S5 linker from DIV, the S4–S5 linker from DIII, and the intracellular ends of S5 and S6 from DIV (Yan et al., 2017; Jiang et al., 2020; Kellenberger et al., 1996; McPhee et al., 1994, 1995; Smith and Goldin 1997). Thus, the deactivation of voltage-gated sodium channels is closely

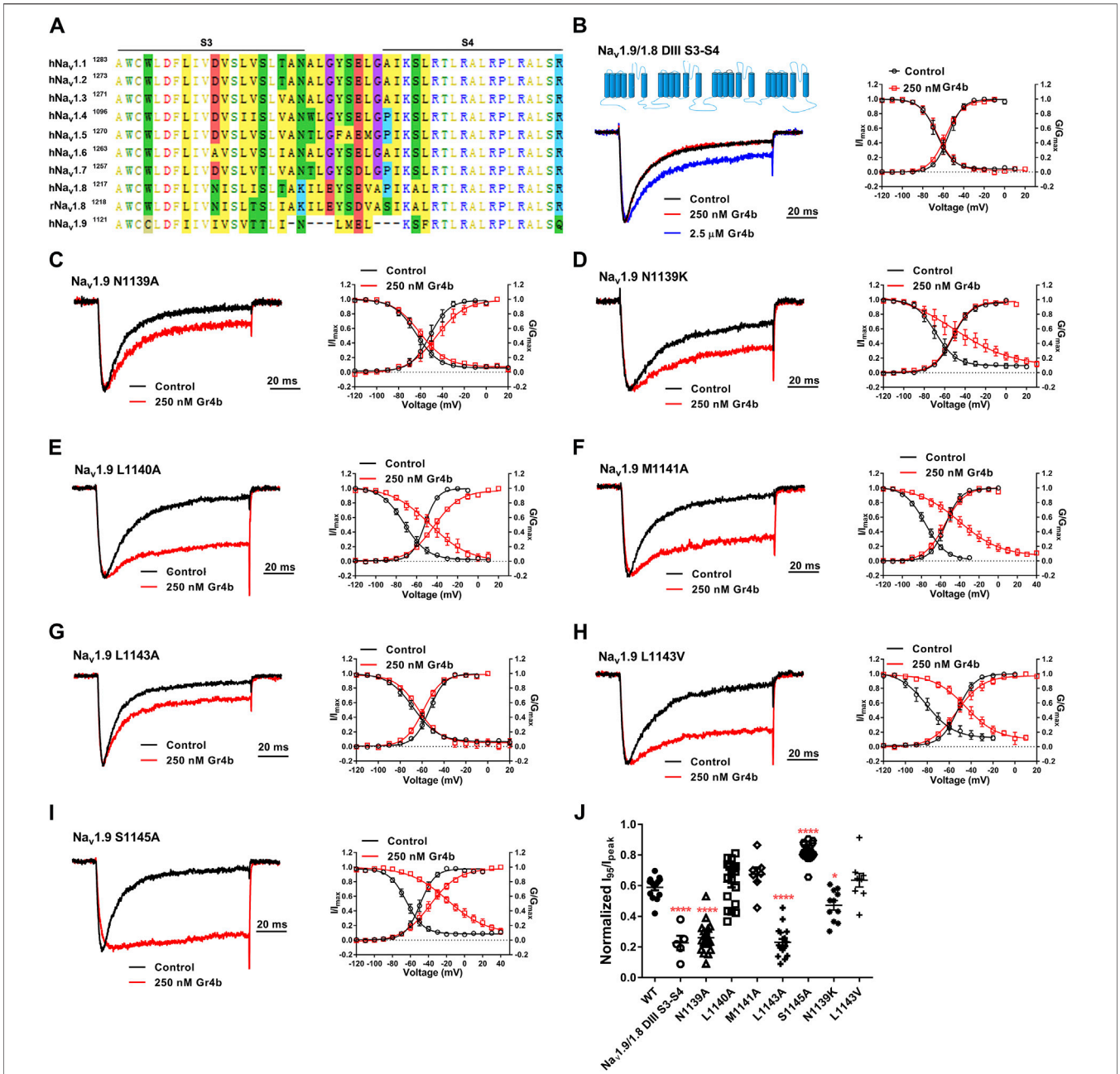

FIGURE 6 | DIII S3-S4 of $Na_v1.9$ is involved in interacting with Gr4b. **(A)** Sequence alignments corresponding to Na_v subtype domains III (DIII) S3-S4. **(B)** Representative normalized current traces, voltage-dependent steady-state activation and voltage-dependent steady-state inactivation show that the chimera channels (constructed as the cartoon illustrated) $Na_v1.9/1.8$ DIII S3-S4, in the absence (black), presence of 250 nM Gr4b (red) or 2.5 μM Gr4b (blue). **(C–I)** Representative traces, voltage-dependent steady-state activation and voltage-dependent steady-state inactivation show that the single point mutations of $Na_v1.9$, in the absence (black) and presence of 250 nM Gr4b (red). **(J)** Effects of Gr4b on WT and mutant $Na_v1.9$ channels. Dot plots display the effect of 250 nM Gr4b on the persistent current (n = 17 for N1139A, n = 11 for N1139K, n = 18 for L1140A and L1143A, n = 7 for M1141A, n = 9 for L1143V, n = 20 for S1145A and n = 5 for $Na_v1.9/1.8$ DIII S3-S4). One-way ANOVA with Dunnett's Multiple Comparison Test and compared with WT, $^*p < 0.05$, $^{****}p < 0.0001$.

related to DIII and DIV. However, based on the electromechanical coupling mechanism of the sodium channel, the motion of the S4 segment is coupled with the S4–S5 linker to the intracellular activation gate to open the pore. Thus, DIII S4-induced shifts of the DIII S4-S5 linker may be helpful for exposing the docking site of the fast inactivation gate IFM. Furthermore, we found that Gr4b binds to the DIII VSD of $Na_v1.9$ and impedes movement in depolarization, resulting in the suppression of fast inactivation. This conclusion is based on the following observations: (1) the effect of Gr4b on the $Na_v1.9$ channel is voltage-dependent and the relationships of the current-voltage curve and voltage-dependent steady-state

activation curve both shift in the direction of depolarization (**Figures 3B,C**); and (2) toxin dissociation from the $Na_v1.9$ channel was voltage-dependent and time-dependent, and the inhibition of fast inactivation was abolished during long-term depolarization (**Figure 4C**). Moreover, voltage-clamp fluorescent recordings to observe the $Na_v1.4$ VSDs revealed that DIII and DIV VSD immobilization is correlated with the onset of inactivation (Cha et al., 1999); some mutants in DIII VSD were shown to impair fast inactivation and cause channelopathies, e.g., a mutation of R1135H in DIII S4 of $Na_v1.4$ significantly enhanced entry into inactivation and prolonged recovery to cause hypokalemia periodic paralysis (Groome et al., 2014). Together, these findings suggest that the DIII VSD of the Na_v channel plays a prominent role in regulating inactivation.

The DIII VSD of the Na_v channel might be a neurotoxin binding site. To date, at least six different neurotoxin receptor sites have been identified on Na_v channels (Klint et al., 2012); however, there are no prior reports of neurotoxins binding to DIII VSD. In the present study, our results indicated that Gr4b preferentially binds to the DIII S3-S4 linker of the $Na_v1.9$ channel, and two residues (N1139 and L1143) in the DIII S3-S4 linker of $Na_v1.9$ might be involved in the interaction with Gr4b (**Figure 6**). Previously reported DIV VSD binding toxins, like the α-scorpion toxin LqqIV and spider toxins HpTx1 and Hm1a, have a common feature that shifts the steady-state inactivation curve to more positive potentials and produces a non-inactivated component in the steady-state inactivation curve (Bosmans and Tytgat 2007; Osteen et al., 2017; Zhou et al., 2020). In contrast, DIV VSD binding toxins do not change the steady-state activation curve but enhance the peak current. We found that Gr4b significantly shifts the activation curve to the depolarization direction and weakly suppresses the current of $Na_v1.9$ at voltages of −60 to −40 mV (**Figures 3B,C**). These effects distinguish this toxin from other DIV VSD binding toxins. Notably, these effects were limited to the channels where DIII VSD of $Na_v1.9$ exists (**Figures 5B–D**). The chimeric channels (19/18DIII VSD and 19/18DIII VSD & DIV VSD) abolished the effects of Gr4b, suggesting that the effect of Gr4b on channel activation depends on the toxins binding to DIII VSD. Taken together, our results suggest that the interaction of the toxin with $Na_v1.9$ DIII VSD affects fast inactivation of the channel as well as activation.

In summary, our study has revealed a novel spider peptide toxin that specifically interacts with the $Na_v1.9$ channel, as well as a novel Na_v channel neurotoxin binding to the site DIII VSD. The toxin binding to DIII VSD of $Na_v1.9$ affects both activation and fast inactivation, thereby providing pharmacological insight into the role of the DIII VSD in Na_v channel activation and fast inactivation.

DATA AVAILABILITY STATEMENT

The original contributions presented in the study are included in the article/**Supplementary Material**, further inquiries can be directed to the corresponding authors.

AUTHOR CONTRIBUTIONS

XZ, SP, and ZL designed the study and wrote the manuscript. XZ, SP, MC, ZX, XX, and SL performed the experiments and the data analysis. SL contributed to helpful discussion.

FUNDING

This work was supported by funding from the National Natural Science Foundation of China (Grant No. 31800655, 32071262, 31770832, 31570782, 31872718), the Science and Technology Innovation Program of Hunan Province (Grant No. 2020RC4023, 2021RC3092), the Hunan Provincial Natural Science Foundation of China (Grant No. 2020JJ5359), and the Scientific Research Foundation of Hunan Provincial Education Department (Grant No. 19C1159).

SUPPLEMENTARY MATERIAL

The Supplementary Material for this article can be found online at: https://www.frontiersin.org/articles/10.3389/fphar.2021.778534/full#supplementary-material

REFERENCES

Bemporad, D., Sands, Z. A., Wee, C. L., Grottesi, A., and Sansom, M. S. (2006). Vstx1, a Modifier of Kv Channel Gating, Localizes to the Interfacial Region of Lipid Bilayers. *Biochemistry* 45 (39), 11844–11855. doi:10.1021/bi061111z

Bennett, D. L., Clark, A. J., Huang, J., Waxman, S. G., and Dib-Hajj, S. D. (2019). The Role of Voltage-Gated Sodium Channels in Pain Signaling. *Physiol. Rev.* 99 (2), 1079–1151. doi:10.1152/physrev.00052.2017

Bosmans, F., and Tytgat, J. (2007). Voltage-gated Sodium Channel Modulation by Scorpion Alpha-Toxins. *Toxicon* 49 (2), 142–158. doi:10.1016/j.toxicon.2006.09.023

Campos, F. V., Chanda, B., Beirão, P. S., and Bezanilla, F. (2008). Alpha-scorpion Toxin Impairs a Conformational Change that Leads to Fast Inactivation of Muscle Sodium Channels. *J. Gen. Physiol.* 132 (2), 251–263. doi:10.1085/jgp.200809995

Cardoso, F. C., Dekan, Z., Smith, J. J., Deuis, J. R., Vetter, I., Herzig, V., et al. (2017). Modulatory Features of the Novel Spider Toxin μ-TRTX-Df1a Isolated from the Venom of the Spider Davus Fasciatus. *Br. J. Pharmacol.* 174 (15), 2528–2544. doi:10.1111/bph.13865

Catterall, W. A., Cestèle, S., Yarov-Yarovoy, V., Yu, F. H., Konoki, K., and Scheuer, T. (2007). Voltage-gated Ion Channels and Gating Modifier Toxins. *Toxicon* 49 (2), 124–141. doi:10.1016/j.toxicon.2006.09.022

Catterall, W. A. (2000). From Ionic Currents to Molecular Mechanisms: the Structure and Function of Voltage-Gated Sodium Channels. *Neuron* 26 (1), 13–25. doi:10.1016/s0896-6273(00)81133-2

Catterall, W. A. (2012). Voltage-gated Sodium Channels at 60: Structure, Function and Pathophysiology. *J. Physiol.* 590 (11), 2577–2589. doi:10.1113/jphysiol.2011.224204

Catterall, W. A., Wisedchaisri, G., and Zheng, N. (2017). The Chemical Basis for Electrical Signaling. *Nat. Chem. Biol.* 13 (5), 455–463. doi:10.1038/nchembio.2353

Cha, A., Ruben, P. C., George, A. L., Jr., Fujimoto, E., and Bezanilla, F. (1999). Voltage Sensors in Domains III and IV, but Not I and II, Are Immobilized by Na+ Channel Fast Inactivation. *Neuron* 22 (1), 73–87. doi:10.1016/s0896-6273(00)80680-7

Chanda, B., and Bezanilla, F. (2002). Tracking Voltage-dependent Conformational Changes in Skeletal Muscle Sodium Channel during Activation. *J. Gen. Physiol.* 120 (5), 629–645. doi:10.1085/jgp.20028679

Chau, R., Kalaitzis, J. A., and Neilan, B. A. (2011). On the Origins and Biosynthesis of Tetrodotoxin. *Aquat. Toxicol.* 104 (1-2), 61–72. doi:10.1016/j.aquatox.2011.04.001

Chen, M., Peng, S., Wang, L., Yang, L., Si, Y., Zhou, X., et al. (2020). Recombinant PaurTx-3, a Spider Toxin, Inhibits Sodium Channels and Decreases Membrane Excitability in DRG Neurons. *Biochem. Biophys. Res. Commun.* 533 (4), 958–964. doi:10.1016/j.bbrc.2020.09.103

Chen, R., Robinson, A., and Chung, S. H. (2012). Binding of Hanatoxin to the Voltage Sensor of Kv2.1. *Toxins (Basel)* 4 (12), 1552–1564. doi:10.3390/toxins4121552

Clairfeuille, T., Cloake, A., Infield, D. T., Llongueras, J. P., Arthur, C. P., Li, Z. R., et al. (2019). Structural Basis of α-scorpion Toxin Action on Nav Channels. *Science* 363 (6433), eaav8573. doi:10.1126/science.aav8573

Dib-Hajj, S. D., Tyrrell, L., Black, J. A., and Waxman, S. G. (1998). NaN, a Novel Voltage-Gated Na Channel, Is Expressed Preferentially in Peripheral Sensory Neurons and Down-Regulated after Axotomy. *Proc. Natl. Acad. Sci. U S A.* 95 (15), 8963–8968. doi:10.1073/pnas.95.15.8963

Fukuoka, T., Kobayashi, K., Yamanaka, H., Obata, K., Dai, Y., and Noguchi, K. (2008). Comparative Study of the Distribution of the Alpha-Subunits of Voltage-Gated Sodium Channels in normal and Axotomized Rat Dorsal Root Ganglion Neurons. *J. Comp. Neurol.* 510 (2), 188–206. doi:10.1002/cne.21786

Goldin, A. L. (2001). Resurgence of Sodium Channel Research. *Annu. Rev. Physiol.* 63, 871–894. doi:10.1146/annurev.physiol.63.1.871

Groome, J. R., Lehmann-Horn, F., Fan, C., Wolf, M., Winston, V., Merlini, L., et al. (2014). NaV1.4 Mutations Cause Hypokalaemic Periodic Paralysis by Disrupting IIIS4 Movement during Recovery. *Brain* 137 (Pt 4), 998–1008. doi:10.1093/brain/awu015

Hodgkin, A. L., and Huxley, A. F. (1952). The Dual Effect of Membrane Potential on Sodium Conductance in the Giant Axon of Loligo. *J. Physiol.* 116 (4), 497–506. doi:10.1113/jphysiol.1952.sp004719

Hsu, E. J., Zhu, W., Schubert, A. R., Voelker, T., Varga, Z., and Silva, J. R. (2017). Regulation of Na+ Channel Inactivation by the DIII and DIV Voltage-Sensing Domains. *J. Gen. Physiol.* 149 (3), 389–403. doi:10.1085/jgp.201611678

Jiang, D., Shi, H., Tonggu, L., Gamal El-Din, T. M., Lenaeus, M. J., Zhao, Y., et al. (2020). Structure of the Cardiac Sodium Channel. *Cell* 180 (1), 122. doi:10.1016/j.cell.2019.11.041

Kellenberger, S., Scheuer, T., and Catterall, W. A. (1996). Movement of the Na+ Channel Inactivation Gate during Inactivation. *J. Biol. Chem.* 271 (48), 30971–30979. doi:10.1074/jbc.271.48.30971

Kimura, T., Ono, S., and Kubo, T. (2012). Molecular Cloning and Sequence Analysis of the cDNAs Encoding Toxin-like Peptides from the Venom Glands of Tarantula Grammostola Rosea. *Int. J. Pept.* 2012, 731293. doi:10.1155/2012/731293

Klint, J. K., Senff, S., Rupasinghe, D. B., Er, S. Y., Herzig, V., Nicholson, G. M., et al. (2012). Spider-venom Peptides that Target Voltage-Gated Sodium Channels: Pharmacological Tools and Potential Therapeutic Leads. *Toxicon* 60 (4), 478–491. doi:10.1016/j.toxicon.2012.04.337

Kubota, T., Durek, T., Dang, B., Finol-Urdaneta, R. K., Craik, D. J., Kent, S. B., et al. (2017). Mapping of Voltage Sensor Positions in Resting and Inactivated Mammalian Sodium Channels by LRET. *Proc. Natl. Acad. Sci. U S A.* 114 (10), E1857–E1865. doi:10.1073/pnas.1700453114

Liao, Z., Yuan, C., Deng, M., Li, J., Chen, J., Yang, Y., et al. (2006). Solution Structure and Functional Characterization of Jingzhaotoxin-XI: a Novel Gating Modifier of Both Potassium and Sodium Channels. *Biochemistry* 45 (51), 15591–15600. doi:10.1021/bi061457+

Liu, Z., Cai, T., Zhu, Q., Deng, M., Li, J., Zhou, X., et al. (2013). Structure and Function of Hainantoxin-III, A Selective Antagonist of Neuronal Tetrodotoxin-Sensitive Voltage-Gated Sodium Channels Isolated from the Chinese Bird Spider Ornithoctonus Hainana. *J. Biol. Chem.* 288 (28), 20392–20403. doi:10.1074/jbc.M112.426627

Mantegazza, M., and Catterall, W. A. (2012). "Voltage-Gated Na(+) Channels: Structure, Function, and Pathophysiology," in *Jasper's Basic Mechanisms of the Epilepsies*. Editors J. L. Noebels, M. Avoli, M. A. Rogawski, R. W. Olsen, and A. V. Delgado-Escueta (Bethesda MD: National Center for Biotechnology Information (US)).

McPhee, J. C., Ragsdale, D. S., Scheuer, T., and Catterall, W. A. (1998). A Critical Role for the S4-S5 Intracellular Loop in Domain IV of the Sodium Channel Alpha-Subunit in Fast Inactivation. *J. Biol. Chem.* 273 (2), 1121–1129. doi:10.1074/jbc.273.2.1121

McPhee, J. C., Ragsdale, D. S., Scheuer, T., and Catterall, W. A. (1995). A Critical Role for Transmembrane Segment IVS6 of the Sodium Channel Alpha Subunit in Fast Inactivation. *J. Biol. Chem.* 270 (20), 12025–12034. doi:10.1074/jbc.270.20.12025

McPhee, J. C., Ragsdale, D. S., Scheuer, T., and Catterall, W. A. (1994). A Mutation in Segment IVS6 Disrupts Fast Inactivation of Sodium Channels. *Proc. Natl. Acad. Sci. U S A.* 91 (25), 12346–12350. doi:10.1073/pnas.91.25.12346

Murray, J. K., Ligutti, J., Liu, D., Zou, A., Poppe, L., Li, H., et al. (2015). Engineering Potent and Selective Analogues of GpTx-1, a Tarantula Venom Peptide Antagonist of the Na(V)1.7 Sodium Channel. *J. Med. Chem.* 58 (5), 2299–2314. doi:10.1021/jm501765v

Numa, S., and Noda, M. (1986). Molecular Structure of Sodium Channels. *Ann. N. Y Acad. Sci.* 479, 338–355. doi:10.1111/j.1749-6632.1986.tb15580.x

Osteen, J. D., Sampson, K., Iyer, V., Julius, D., and Bosmans, F. (2017). Pharmacology of the Nav1.1 Domain IV Voltage Sensor Reveals Coupling between Inactivation Gating Processes. *Proc. Natl. Acad. Sci. U S A.* 114 (26), 6836–6841. doi:10.1073/pnas.1621263114

Oswald, R. E., Suchyna, T. M., McFeeters, R., Gottlieb, P., and Sachs, F. (2002). Solution Structure of Peptide Toxins that Block Mechanosensitive Ion Channels. *J. Biol. Chem.* 277 (37), 34443–34450. doi:10.1074/jbc.M202715200

Renganathan, M., Dib-Hajj, S., and Waxman, S. G. (2002). Na(v)1.5 Underlies the 'third TTX-R Sodium Current' in Rat Small DRG Neurons. *Brain Res. Mol. Brain Res.* 106 (1-2), 70–82. doi:10.1016/s0169-328x(02)00411-4

Rogers, M., Zidar, N., Kikelj, D., and Kirby, R. W. (2016). Characterization of Endogenous Sodium Channels in the ND7-23 Neuroblastoma Cell Line: Implications for Use as a Heterologous Ion Channel Expression System Suitable for Automated Patch Clamp Screening. *Assay Drug Dev. Technol.* 14 (2), 109–130. doi:10.1089/adt.2016.704

Silva, J. R., and Goldstein, S. A. (2013). Voltage-sensor Movements Describe Slow Inactivation of Voltage-Gated Sodium Channels II: a Periodic Paralysis Mutation in Na(V)1.4 (L689I). *J. Gen. Physiol.* 141 (3), 323–334. doi:10.1085/jgp.201210910

Smith, M. R., and Goldin, A. L. (1997). Interaction between the Sodium Channel Inactivation Linker and Domain III S4-S5. *Biophys. J.* 73 (4), 1885–1895. doi:10.1016/S0006-3495(97)78219-5

Song, W., Du, Y., Liu, Z., Luo, N., Turkov, M., Gordon, D., et al. (2011). Substitutions in the Domain III Voltage-Sensing Module Enhance the Sensitivity of an Insect Sodium Channel to a Scorpion Beta-Toxin. *J. Biol. Chem.* 286 (18), 15781–15788. doi:10.1074/jbc.M110.217000

Stevens, M., Peigneur, S., and Tytgat, J. (2011). Neurotoxins and Their Binding Areas on Voltage-Gated Sodium Channels. *Front. Pharmacol.* 2, 71. doi:10.3389/fphar.2011.00071

Tang, C., Zhou, X., Huang, Y., Zhang, Y., Hu, Z., Wang, M., et al. (2014). The Tarantula Toxin Jingzhaotoxin-XI (κ-Theraphotoxin-Cj1a) Regulates the Activation and Inactivation of the Voltage-Gated Sodium Channel Nav1.5. *Toxicon* 92, 6–13. doi:10.1016/j.toxicon.2014.09.002

Thomsen, W. J., and Catterall, W. A. (1989). Localization of the Receptor Site for Alpha-Scorpion Toxins by Antibody Mapping: Implications for Sodium Channel Topology. *Proc. Natl. Acad. Sci. U S A.* 86 (24), 10161–10165. doi:10.1073/pnas.86.24.10161

Vassilev, P. M., Scheuer, T., and Catterall, W. A. (1988). Identification of an Intracellular Peptide Segment Involved in Sodium Channel Inactivation. *Science* 241 (4873), 1658–1661. doi:10.1126/science.2458625

Vijayaragavan, K., O'Leary, M. E., and Chahine, M. (2001). Gating Properties of Na(v)1.7 and Na(v)1.8 Peripheral Nerve Sodium Channels. *J. Neurosci.* 21 (20), 7909–7918. doi:10.1523/jneurosci.21-20-07909.2001

Vijayaragavan, K., Powell, A. J., Kinghorn, I. J., and Chahine, M. (2004). Role of Auxiliary Beta1-, Beta2-, and Beta3-Subunits and Their Interaction with Na(v) 1.8 Voltage-Gated Sodium Channel. *Biochem. Biophys. Res. Commun.* 319 (2), 531–540. doi:10.1016/j.bbrc.2004.05.026

West, J. W., Patton, D. E., Scheuer, T., Wang, Y., Goldin, A. L., and Catterall, W. A. (1992). A Cluster of Hydrophobic Amino Acid Residues Required for Fast Na(+)-Channel Inactivation. *Proc. Natl. Acad. Sci. U S A.* 89 (22), 10910–10914. doi:10.1073/pnas.89.22.10910

Xiao, Y., Bingham, J. P., Zhu, W., Moczydlowski, E., Liang, S., and Cummins, T. R. (2008). Tarantula Huwentoxin-IV Inhibits Neuronal Sodium Channels by Binding to Receptor Site 4 and Trapping the Domain Ii Voltage Sensor in the Closed Configuration. *J. Biol. Chem.* 283 (40), 27300–27313. doi:10.1074/jbc.M708447200

Xiao, Y., Blumenthal, K., Jackson, J. O., 2nd, Liang, S., and Cummins, T. R. (2010). The Tarantula Toxins ProTx-II and Huwentoxin-IV Differentially Interact with Human Nav1.7 Voltage Sensors to Inhibit Channel Activation and Inactivation. *Mol. Pharmacol.* 78 (6), 1124–1134. doi:10.1124/mol.110.066332

Yan, Z. Q., Zhou, L., Wang, J., Wu, Y., Zhao, G., Huang, W., et al. (2017). Structure of the Nav1.4-beta1 Complex from Electric Eel. *Cell* 170 (3), 470–482. e411. doi:10.1016/j.cell.2017.06.039

Yu, F. H., and Catterall, W. A. (2003). Overview of the Voltage-Gated Sodium Channel Family. *Genome Biol.* 4 (3), 207. doi:10.1186/gb-2003-4-3-207

Zhang, Q., Si, Y., Yang, L., Wang, L., Peng, S., Chen, Y., et al. (2020). Two Novel Peptide Toxins from the Spider Cyriopagopus Longipes Inhibit Tetrodotoxin-Sensitive Sodium Channels. *Toxins (Basel)* 12 (9), 529. doi:10.3390/toxins12090529

Zhou, X., Ma, T., Yang, L., Peng, S., Li, L., Wang, Z., et al. (2020). Spider Venom-Derived Peptide Induces Hyperalgesia in Nav1.7 Knockout Mice by Activating Nav1.9 Channels. *Nat. Commun.* 11 (1), 2293. doi:10.1038/s41467-020-16210-y

Zhou, X., Xiao, Z., Xu, Y., Zhang, Y., Tang, D., Wu, X., et al. (2017). Electrophysiological and Pharmacological Analyses of Nav1.9 Voltage-Gated Sodium Channel by Establishing a Heterologous Expression System. *Front. Pharmacol.* 8, 852. doi:10.3389/fphar.2017.00852

Conflict of Interest: The authors declare that the research was conducted in the absence of any commercial or financial relationships that could be construed as a potential conflict of interest.

Publisher's Note: All claims expressed in this article are solely those of the authors and do not necessarily represent those of their affiliated organizations, or those of the publisher, the editors and the reviewers. Any product that may be evaluated in this article, or claim that may be made by its manufacturer, is not guaranteed or endorsed by the publisher.

frontiers in Pharmacology

ORIGINAL RESEARCH
published: 08 December 2021
doi: 10.3389/fphar.2021.803397

Unique Pharmacological Properties of α-Conotoxin OmIA at α7 nAChRs

*Thao N.T. Ho, Nikita Abraham and Richard J. Lewis**

Centre for Pain Research, Institute for Molecular Bioscience, The University of Queensland, St Lucia, QLD, Australia

OmIA, isolated from *Conus omaria* venom, is a potent antagonist at α7 nAChRs. We determined the co-crystal structure of OmIA with *Lymnae stagnalis* acetylcholine binding protein (*Ls*-AChBP) that identified His5, Val10 and Asn11 as key determinants for the high potency of OmIA at α7 nAChRs. Remarkably, despite a competitive binding mode observed in the co-crystal structure, OmIA and analogues displayed functional insurmountable antagonism at α7 and α3β4 nAChRs, except OmIA analogues having long side chain at position 10 ([V10Q]OmIA and [V10L]OmIA), which were partial insurmountable antagonist at α7 nAChRs in the presence of type II positive allosteric modulators (PAMs). A "two-state, two-step" model was used to explain these observations, with [V10Q]OmIA and [V10L]OmIA co-existing in a fast reversible/surmountable as well as a tight binding/insurmountable state. OmIA and analogues also showed biphasic-inhibition at α7 nAChRs in the presence of PNU120596, with a preference for the high-affinity binding site following prolonged exposure. The molecular basis of binding and complex pharmacological profile of OmIA at α7 nAChRs presented in here expands on the potential of α-conotoxins to probe the pharmacological properties of nAChRs and may help guide the development novel α7 modulators.

Keywords: conotoxins, ligand-gated ion channels, α7 nAChR, pharmacology, AChBP, X-ray structrures

OPEN ACCESS

Edited by:
Jean-Marc Sabatier,
Aix-Marseille Université, France

Reviewed by:
Arik J. Hone,
The University of Utah, United States
Nathan Absalom,
The University of Sydney, Australia

****Correspondence:***
Richard J. Lewis
r.lewis@uq.edu.au

Specialty section:
This article was submitted to Pharmacology of Ion Channels and Channelopathies, a section of the journal Frontiers in Pharmacology

Received: *27 October 2021*
Accepted: *22 November 2021*
Published: *08 December 2021*

Citation:
Ho TNT, Abraham N and Lewis RJ (2021) Unique Pharmacological Properties of α-Conotoxin OmIA at α7 nAChRs. Front. Pharmacol. 12:803397. doi: 10.3389/fphar.2021.803397

INTRODUCTION

α-Conotoxins are among the smallest conopeptides from *Conus* venoms (12–20 amino acids (aa)). Classical α-conotoxins are characterised by a CC–X_m–C–X_n–C framework forming three possible disulfide connectivities: globular (I–III, II–IV), ribbon (I–IV, II–III) and bead (I–II, III–IV) (Azam and Mcintosh, 2009; Lewis et al., 2012; Ho et al., 2020) with the globular conformation generally the native bioactive isomer. α-conotoxins are further divided into several structural subgroups (*m*/*n*: 3/5, 5/5, 4/3, 4/4, 4/5, 4/6 and 4/7) based on the number of residues within the two loops (*m*, *n*) braced by the disulfide bonds. The pharmacological targets tend to correlate to the loop size, with α3/5-conotoxins active toward muscle nAChRs, while the 5/5, 4/3, 4/4, 4/5, 4/6 and the most common 4/7 subgroup mainly interacting with neuronal nAChRs (Abraham and Lewis, 2018; Jin et al., 2019). The exquisite potency and selectivity of these peptides have helped build our understanding of the pharmacology of nAChRs.

Abbreviations: nAChRs, nicotinic acetylcholine receptors; AChBP, acetylcholine binding protein; *Ls*, *Lymnaea Stagnalis*; Trt, trityl; Acm, S-acetamidomethyl; ACN, acetonitrile; MeOH, methanol; TFA, trifluoroacetic acid; Ub, Ubiquitin; IMAC, immobilized metal affinity chromatography purification; CD, circular diochroism; PNU120596, N-(5-Chloro-2,4-dimethoxyphenyl)-N′-(5-methyl-3-isoxazolyl)-urea; CI, confidence interval; PAMs, positive allosteric modulators; I_2, iodine; RP-HPLC, reverse phase- high performance liquid chromatography.

nAChRs are prototypical ligand-gated ion channels found in the central and peripheral nervous system, and recently in other biological systems such as in immune system, muscles, skin and lung (Taly and Charon, 2012). This family constitutes interesting therapeutic drug targets due to its association with the progression of CNS disorders (Gotti and Clementi, 2004; Hogg and Bertrand, 2004; Dani and Bertrand, 2007). Neuronal nAChRs are assembled as homopentamers of α7, α8 and α9 or heteropentamers of α2–α6 in complex with β2–β4 or α7 with β2 subunits or α9 with α10 subunits. Among different nAChRs subtypes, the homopentameric α7 nAChR is one of the most abundant nAChRs in the nervous system and also in many non-neuronal cells (Taly and Charon, 2012). It exhibits unique characteristics, including high permeability to Ca^{2+}, low agonist sensitivity in the resting state, inotropic/metabotropic dual action, rapid activation and fast desensitization. Agonist activation of α7 nAChRs is also sensitive to modulation by positive allosteric modulators (PAMs), with type I PAMs potentiating peak agonist responses and type II PAMs prolonging the opening times of nAChR by reducing receptor desensitization (Bertrand and Gopalakrishnan, 2007; Taly et al., 2009). These properties together with its involvement in pathologic conditions and the therapeutic potential of α7 ligands have made α7 nAChRs an important emerging drug targets (Lendvai et al., 2013; Dineley et al., 2015; Corradi and Bouzat, 2016).

OmIA, α-conotoxin purified from *Conus omaria,* is an α4/7-conotoxins that competitively antagonises α7 nAChRs (Talley et al., 2006). In this paper, we present the co-crystal structure of OmIA with *Lymnae stagnalis* (*Ls*)-acetylcholine binding protein (AChBP) that revealed three residues, His5, Val10 and Asn11, play essential roles in the activity of OmIA at α7 nAChRs. Interestingly, despite a competitive binding mode observed in the OmIA/*Ls*-AChBP complex, OmIA and analogues for the first time were found to display functional insurmountable antagonism at α7 and α3β4 nAChRs, with OmIA analogues having long side chains at position 10 acting as partial insurmountable antagonists at α7 nAChRs in the presence of type II PAMs. These studies provide with new insights into the pharmacological properties of α-conotoxins as well as the important α7 nAChR subtype.

MATERIALS AND METHODS

Peptide Synthesis by Two-step Oxidation

α-Conotoxin OmIA and its variants were assembled by solid-phase methodology on a Liberty PRIME peptide synthesizer (CEM, United States) using Fmoc chemistry and standard side chain protection, except for cysteine residues. Cys residues were orthogonally protected in pairs with acid-labile trityl (Trt) and acid-stable S-acetamidomethyl (Acm) respectively on Cys^{I}-Cys^{III} and Cys^{II}- Cys^{IV} for globular isomer. Peptide cleavage from resin and global side chain deprotection were done by treatment with scavenger mixture (trifluoroacetic acid (TFA)/water/triisopropylsilane, 95:2.5:2.5, v/v/v) for 30 min at 40°C on Razor system (CEM, United States). The cleaved peptides were precipitated with cold diethyl ether, centrifuged (1957x*g* x3), redissolved in 50% aqueous acetonitrile (ACN) and lyophilized.

Disulfide bonds were formed selectively via a directed two-step oxidation. Trt protecting groups of the first Cys pairs were removed after peptide cleavage from resin, while Acm groups on the second Cys pairs remained intact. The oxidation of peptides was carried out in a buffer of 90% acetic acid/10% methanol (MeOH) with peptides at final concentration of 2 mg/ml. The first disulfide bridge formation between free cysteines was performed upon the dropwise addition of iodine (I_2) (10 mg/ml dissolved in MeOH) while stirring until a pale yellow colour persisted. The solution containing partially oxidized peptide was then diluted with an equal volume of 50 mM HCl in 50% aqueous MeOH. Simultaneous removal of the Acm group and the second disulfide bridge formation were accomplished by the continued addition of I_2 (8 equivalents). The oxidation reaction was monitored via analytical high performance liquid chromatography (a linear gradient of 10–40% solvent B (90% ACN/0.05%TFA) over 30 min at a flow rate of 1 ml/min on a C18 column (Vydac 218 TP, Grace) and electrospray ionization-mass spectrometry. The oxidation reaction was quenched by the addition of ascorbic acid and diluted 20-fold with solvent A. Bicyclic peptide was purified by reverse phase- high performance liquid chromatography (RP-HPLC) on a C18 Vydac column (Vydac 218 TP, Grace) using a linear gradient of 5–45% solvent B over 40 min at a flow rate of 16 ml/min. The final product was collected and analyzed by analytical HPLC and matrix-assisted laser desorption/ionization-time of flight.

AChBPs Protein Expression and Purification

The over-expression of *Ls*-AChBP was performed as previously described (Abraham et al., 2016). Ubiquitin (Ub)-tagged AChBPs were used for radioligand binding assay. De-tagged *Ls*-AChBP was used for crystallization. Briefly, after immobilized metal affinity chromatography purification (IMAC), *Ls*-AChBPs were removed from Ub-tag by DUB enzyme (produced in-house). De-tagged *Ls*-AChBP was further purified by size exclusion chromatography to assess homogeneity and oligomerization state. The IMAC purified *Ls*-AChBP was analyzed on a calibrated analytical HiLoad 16/600 column and (GE Health care) for *Ls*-AChBP respectively using AKTA fast protein liquid chromatography system (GE Health care). The fractions containing the proteins were pooled and concentrated to the desired concentration using an Amicon centrifuge filter (30-kDa cut-off, Millipore).

Circular Dichroism Analysis

Circular dichroism (CD) analysis was used to study the secondary structure of peptides. CD spectra were obtained from Jasco J-810 spectropolarimeter (Jasco, Tokyo, Japan). Peptides were dissolved in 20 mM ammonium bicarbonate buffer pH 7.4 and 55% trifluoroethanol at a final concentration of 50 μM. All measurements were done at room temperature under a nitrogen atmosphere (15 ml/min) with a scanning speed at 10 min and a 4 s response time. Absorbance was measured in the far-UV region (185–260 nm) via a cell with a path length of 1 cm and the capacity of 400 μL. Interference due to solvent, cell, or spectropolarimeter optics was eliminated via the subtraction of CD spectra of the pure solvents from those of the peptide. CD

data in ellipticity was calculated to mean residue ellipticity [(θ)] using the equation: (θ) = θ/[10 × Np × (1,000 × Np × C) × l], where θ is the ellipticity in millidegrees, C is the peptide molar concentration (M) of the peptide, l is the cell path length (cm), and Np is the number of peptide residues.

Crystallization and Data Collection

Purified de-tagged *Ls*-AChBP and OmIA were mixed at a molar ratio of 1:2 at 4°C for 1 h before setting up crystallisation trials. Crystals were successfully grown at room temperature using the hanging drop method by mixing volumes of protein and reservoir solution at a ratio 2:1. The crystals for OmIA were grown at 0.2 M ammonium sulfate, 5% PEG4000 and 0.1 M sodium acetate trihydrate at pH 4.6. The crystals were cryo-protected with reservoir solution plus 20% (v/v) glycerol in liquid nitrogen.

Structure Determination and Refinement

Diffraction data were collected at the MX2 beam line of Australian Synchrotron, Melbourne. Diffraction data were indexed, integrated via XDS and Molfsm and scaled via AIMLESS (Collaborative Computational Project, Number 4, 1994; Battye et al., 2011). The structure was solved via molecular replacement using the PHASER (Mccoy et al., 2007) crystallographic software with LsIA/*Ls*-AChBP (PDB 2C9T) as search model. Refinement against experimental data was done using Phenix. refine and COOT until clear electron densities for OmIA were visible (Emsley and Cowtan, 2004; Afonine et al., 2012). NCS restraints and TLS restrains were then applied and the final structures validated with MOLPROBITY and PDB validation (Chen et al., 2010).

Homology Modelling

The homology modellings were performed via the project mode of the SWISSMODEL online server (Guex et al., 2009). Briefly, the homology models were generated via the alignment of the ligand binding domain of the nAChRs with the crystal structure of the OmIA with *Ls*-AChBP. The quality of alignment was manually adjusted. The resulting model was energy minimized using the GROSMACS force filed in the program DEEPVIEW and models were analyzed in PyMol.

Cell Culture

Cell culture was performed as previously described (Inserra et al., 2013). Briefly, SH-SY5Y neuroblastoma cells (a gift from Victor Diaz, Max Plank Institute for Experimental Medicine, Goettingen, Germany) were cultured at 37°C/5% (v/v) CO_2 in RPMI media containing 2 mM L-glutamine and 15% (v/v) FBS. Cells were passaged every 3–5 days using 0.25% trypsin/EDTA at a dilution of 1:5. Experiments were conducted over several months and spanned on average a minimum of 10–20 passages. Responses were not affected by cell passage number with consistent control responses recorded over the duration of experiments as responses.

FLIPR Assay

FLIPR assay was performed as previously described (Inserra et al., 2013). Briefly, cultured SH-SY5Y cells were plated at a density of 100,000 cells per well on black-walled 384-well imaging plates and cultured for 48 h to form a confluent monolayer. Growth media was removed and incubated for 30 min at 37°C with component A of the Calcium 4 assay kit. Intracellular increases in calcium in response to choline activating α7 nAChRs endogenously expressed by the SH-SY5Y cells. After incubation, the cells were transferred to the FLIPR (Molecular Devices). The changes in fluorescence correlated to intracellular calcium levels were measured using a cooled CCD camera with excitation 470–495 nm, emission 515–575 nm every 1s. Camera gain and intensity were adjusted for each plate of cells yielding a minimum of 1,500–2000 arbitrary fluorescence units (AFU) as a baseline fluorescence value. OmIA and analogues were added 10 min before applying choline for α7 nAChRs (30 μM). N-(5-Chloro-2,4-dimethoxyphenyl)-N′-(5-methyl-3-isoxazolyl)-urea (PNU120596) and TQS were also used (10 μM) to measure activity at the α7 subtype on the FLIPR platform. The channel kinetics are too fast to measure otherwise. All compounds were diluted with physiological salt solution [PSS (mM); 5.9 KCl, 1.5 $MgCl_2$, 1.2 NaH_2PO_4, 5.0 $NaHCO_3$, 140 NaCl, 11.5 glucose, 5 $CaCl_2$, 10 HEPES at pH 7.4]. FLIPR data was normalised to the maximum choline response in the SH-SY5Y cells to yield the %Fmax. A four-parameter Hill equation was fitted to the data using GraphPad Prism 9.0. For the examination of biphasic behaviours, a biphasic model was fitted to the data using GraphPad Prism 9.0. Experiments were performed in triplicates in three independent experiments. IC_{50} and EC_{50} values are reported as means ± S.E.M.

Binding Assays

The ability of VxXIIB variants to displace the binding of [^{3}H]-epibatidine to the recombinantly expressed *Ls*-AChBP was determined in competitive radioligand binding assays. Briefly, [^{3}H]-epibatidine (1 nM final concentration) and increasing concentrations of test ligand in a final volume of 100 ml were incubated in 96-well plates (Flexible PET Microplate, Perkin Elmer) precoated with 1 ng/ml of *Ls*-AChBP per well in binding buffer (phosphate buffered saline with 0.05% bovine serum albumin). The mixture was then removed and 100 ml of scintillant (Optiphase Supermix, Perkin Elmer) added to each well. Bound radioactivity was measured with a Wallac 1450 MicroBeta liquid scintillation counter (Perkin Elmer).

Data Analysis

Comparison of the IC_{50} values of each analogue with the wildtype α-conotoxin and comparison of agonist EC_{50} values in the presence of fixed concentration of antagonist with agonist EC_{50} values in the absence of antagonist were carried out by pairwise comparison using an extra sum-of-squares F test with $p < 0.05$ in GraphPad Prism 9.0. Statistical analysis for partial inhibition of the concentration-response curves, where a fixed concentration of agonist was added to an increasing concentration of antagonist, was determined as significant if 95% confidence interval (CI) of curve bottom values did not overlap 0%. Statistical analysis for insurmountable inhibition, where a fixed concentration of antagonist was added to an increasing concentration of agonist, was determined as significant if the 95% CI for the curve top values of the concentration-response did not overlap 100%.

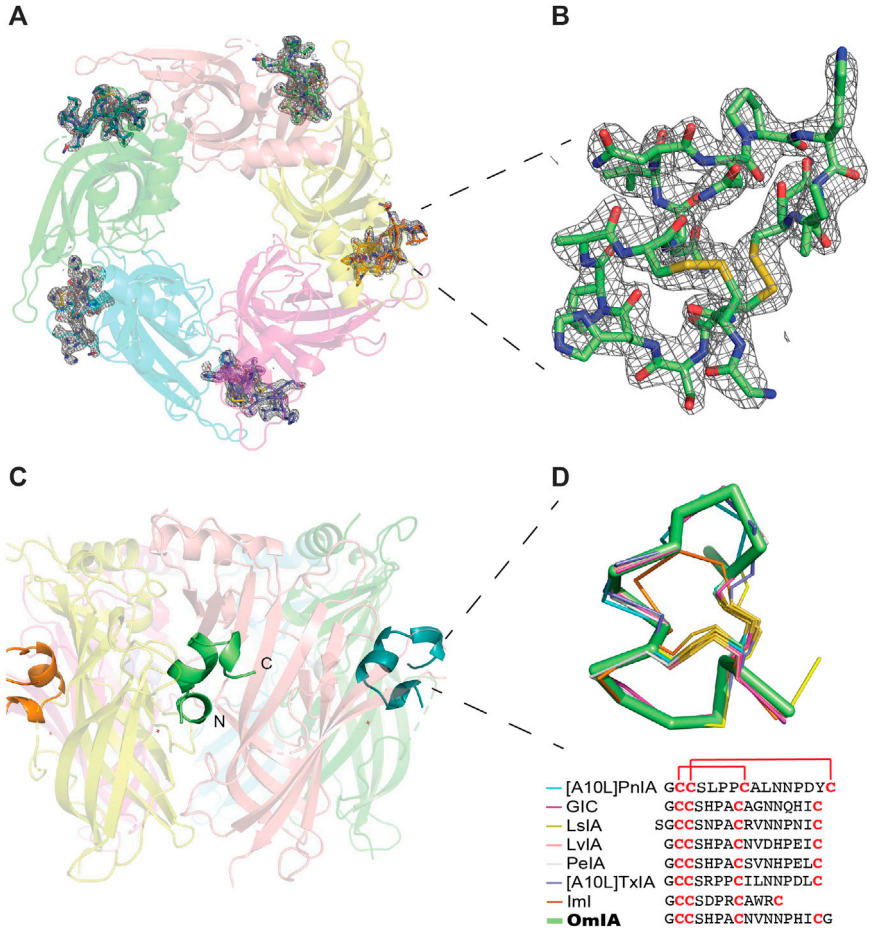

FIGURE 1 | OmIA/*Ls*-AChBP co-crystal structure. **(A)** OmIA co-crystal structure with *Ls*-AChBP shows OmIA similarly residing in each of the five binding pockets. **(B)** OmIA the Fo-Fc map for the ligand contoured to 1.0 σ is also shown. **(C)** The typical binding mode of α-conotoxins is presented by OmIA in which its N and C termini orientate towards the top and bottom of the ligand binding pocket, respectively, while the central helix enters more deeply into the ligand binding pocket. **(D)** Superimposition of OmIA with previously co-crystallised α-conotoxins shows all bind with a similar backbone orientation [[A10L]PnIA PDB 2BR7, GIC PDB 5CO5, LsIA PDB 5T90, LvIA PDB 5XGL, PeIA PDB 5JME, [A10L]TxIA PDB 2UZ6, Iml PDB 2C9T].

RESULTS

Crystal Structure of OmIA in Complex With *Ls*-AChBP

The structure of OmIA and *Ls*-AChBP was solved at 2.47 A˚ resolution (**Supplementary Table S1**). The diffraction data and electron density map were well defined, except certain residues on the flexible loops (mostly AChBP loop F: Thr156, Asn158, Ser159, Asp160) were excluded from the final model due to their ambiguous electron density. The crystals belonged to space-group $P42_12$ and had the following unit cell dimensions: a = 169.4 A˚, b = 169.4 A˚, c = 124.3 A˚. The structure was determined by molecular replacement with the structure LsIA/*Ls*-AChBP as the model and refined to a R_{free} value of 0.247.

A tight homopentameric ring assembly of subunits was observed for the OmIA/*Ls*-AChBP complex (**Figure 1A**), where OmIA occupied all five binding pockets located between two adjacent protomers. The N and C termini of bound OmIA orientated towards the top and bottom of the LBP, respectively, with the central helix abutting into the binding pocket. Structural superimposition with the HEPES/*Ls*-AChBP structure revealed that the C-loop of *Ls*-AChBP moved out a comparable distance (9.3 ± 0.4 A˚ from the Cys187 C_α atom) and had a similar backbone orientation to previously characterised co-crystal structures (**Figure 1A**). The backbone of bound co-crystallised OmIA also overlayed (RMSD = 1.53 ± 0.01 Å) the NMR solution structure of OmIA (PBD 2GCZ).

Structural Basis for Interactions Between α-Conotoxin OmIA and *Ls*-AChBP

Each of the five bound OmIA molecules interacted in a similar orientation (RMSD = 0.090 ± 0.005 Å) at the interface between two adjacent *Ls*-AChBP protomers that formed the principal and complementary binding sides (**Figure 2A**). Most interactions on the principal side were between His5 and Ala7 of OmIA and C-loop residues Tyr185–Tyr192, as

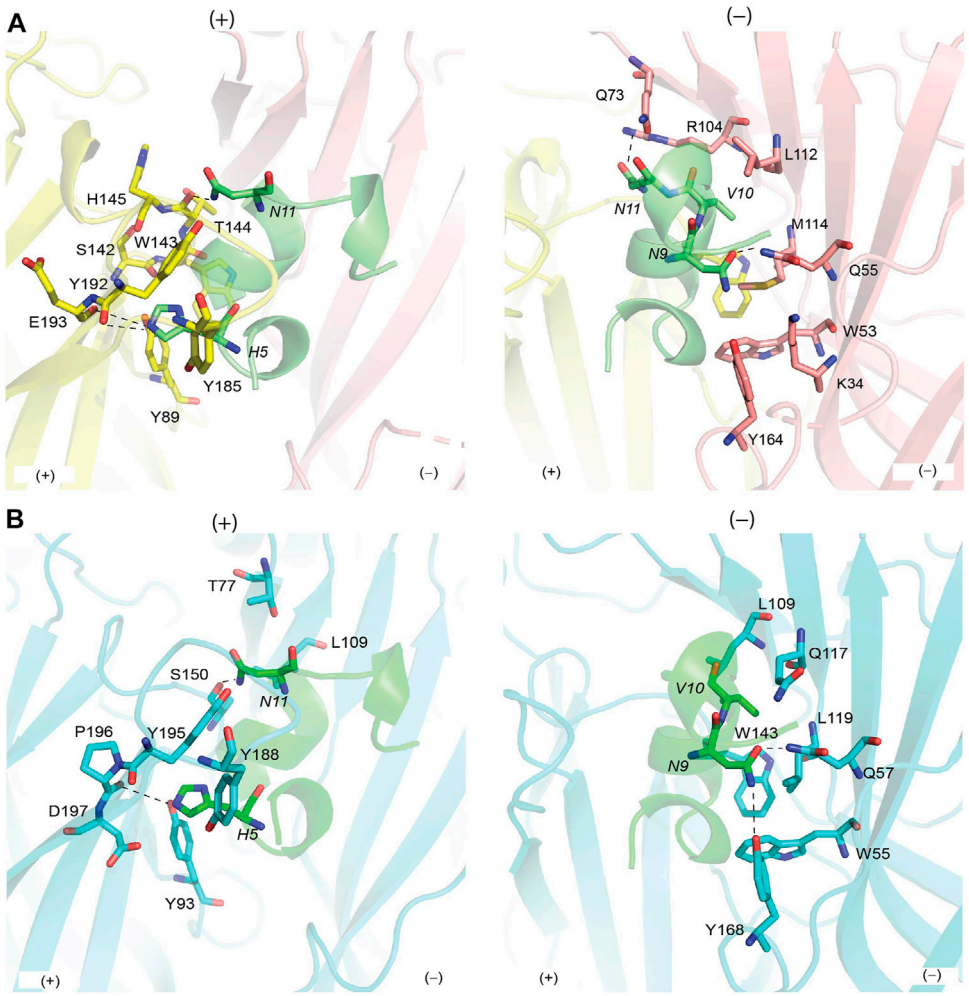

FIGURE 2 | Binding interface between OmIA with Ls-AChBP **(A)** and homology model of α7 nAChRs **(B)**. **(A)** His5 resides in the pocket consisting of conserved aromatic side-chain residues on the principal side of the *Ls*-AChBP, while hydrogen bond (dash line) is seen between Asn11 and backbone oxygen of Thr144. On the complementary side, Asn9 and Val10 show extensive contacts with the complementary side, with hydrogen bonds between Asn9/Gln55 and Asn9/Tyr164. (**B**) The binding surface of OmIA at α7 nAChRs is comparable to *Ls*-AChBP. Hydrogen bonds between Asn9/Gln57 (equivalent to *Ls*-AChBP_Gln55), Asn9/Tyr167 (equivalent to *Ls*-AChBP_Tyr164), Asn11/backbone Ser14450 (equivalent to *Ls*-AChBP_Thr144) remain intact in the α7 subtype. Residues of OmIA are in italics.

well as interactions between the disulfide bridge of OmIA and the vicinal disulfide Cys188-Cys189 of *Ls*-AChBP. His5 resided in a pocket formed by aromatic side-chain residues, specifically Tyr89, Tyr192 and Tyr185, and formed hydrogen bond with Tyr89 and the backbone oxygen of Glu193. Ala7 interacted with Ser142, Trp143, Thr144, His145 and Tyr192. On the complementary side, OmIA_Asn9 interacted with a surface comprising charged residue Lys34, polar residues Ser32, Gln55, Tyr164, and hydrophobic residue Met114, in which hydrogen bonds were seen between Asn9/Gln55 and Asn9/Tyr164 (**Figure 2A**). OmIA_Val10 interacted in a pocket formed by Thr144 on the principal side and Arg104, Leu112 and Met114 on the complementary side of *Ls*-AChBP. The surface interacting with OmIA_Asn11 in the co-crystal structure comprised mostly polar and charged residues from both the principal (Thr144, Glu149 and Tyr192) and complementary faces of each subunit interface (Gln73 and Arg104), where hydrogen backbone were seen between Asn11/Thr144 and Asn11/Gln73 (**Figure 2A**). Interactions between OmIA and *Ls*-AChBP are summarized in **Supplementary Table S2**.

Homology Model of OmIA Bound to α7 nAChRs

OmIA potently blocks human α7 nAChRs with an IC_{50} of 27 nM (Talley et al., 2006). Using the co-crystal structure of *Ls*-AChBP/OmIA as a template, a homology model of OmIA bound to α7 nAChRs was constructed (sequence alignment reported in **Supplementary Figure S1**). The OmIA/α7 complex revealed OmIA interacted similarly at α7 nAChR and *Ls*-AChBP. At the principal face, His5 formed π–π interactions with the conserved aromatic side chains of Tyr93, Tyr188 and Tyr195, as well as an interaction with negatively charged Asp197. A

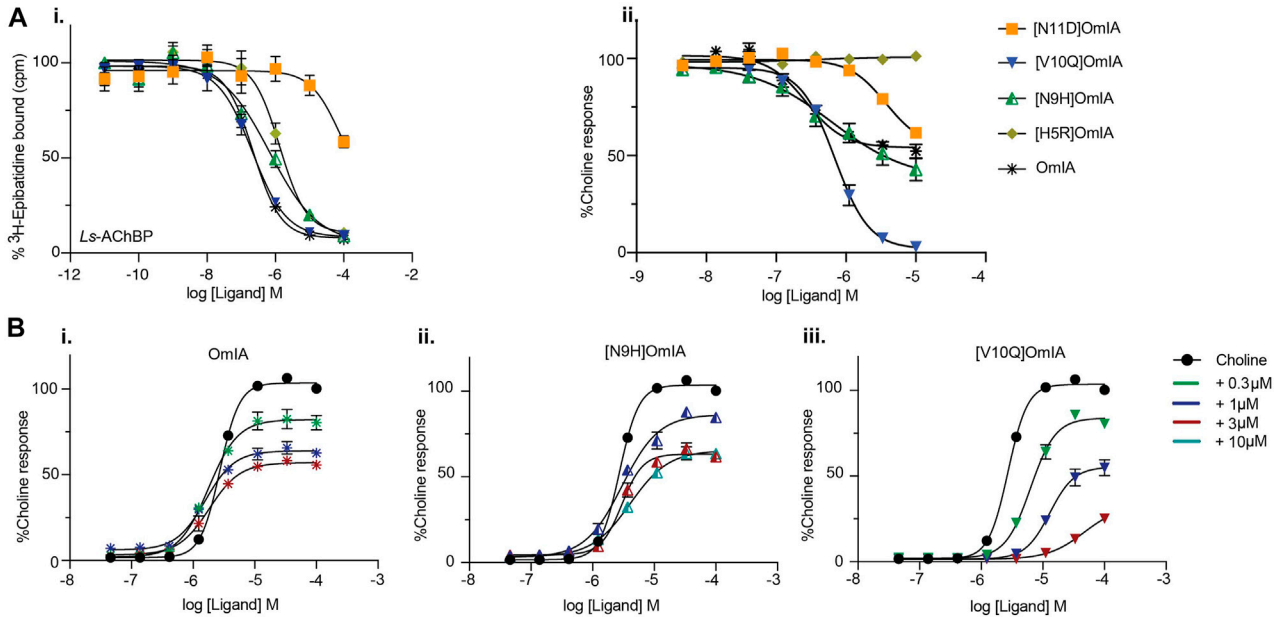

FIGURE 3 | Activity of OmIA and its analogues on Ls-AChBP **(A)** and α7 nAChRs with the addition of nAChR type II PAM PNU120596 **(B)**. **(A)** Displacement of (^{3}H)-epibatidine from *Ls*-AChBP (i) and the inhibition of choline activation of α7 nAChRs measured in a FLIPR Ca^{2+} influx assay on SH-SY5Y cells with the addition of nAChR type II PAM PNU-120596 (ii) by OmIA and its analogues. **(B)** Concentration-response curves for choline alone (black round) and in the presence of increasing concentrations of OmIA (i), [N9H]OmIA (ii), and [V10Q]OmIA (iii). Data represent mean ± SEM of triplicate data from three independent experiments.

TABLE 1 | IC_{50} values for displacement of (^{3}H)-epibatidine binding on *Ls*-AChBPs and the inhibition of choline activation at α7 nAChR in SH-SY5Y cells in the presence of PNU120596 by OmIA and its analogues. *Ratios were calculated between OmIA and its analogues. Data represent mean ± SEM of triplicate data from three independent experiments. [a]denotes significant difference in IC_{50} values to wildtype OmIA ($p < 0.05$). [b]denotes 95% CIs for curve bottom values non-overlapping 0%.

	[3H]-epibatidine binding, IC_{50} ± SEM (μM)		FLIPR SH-SY5Y, IC_{50} ± SEM (μM)	
	***Ls*-AChBP**	**Ratio***	**α7 nAChRs**	**Ratio***
OmIA	0.28 ± 0.07	1	0.27 ± 0.02	1[b]
[H5R]OmIA	1.00 ± 0.04	3.57[a]	>10	>10[a]
[N9H]OmIA	0.73 ± 0.05	2.61[a]	0.71 ± 0.19	2.63[a,b]
[V10Q]OmIA	0.22 ± 0.05	1	0.72 ± 0.10	2.67[a]
[N11D]OmIA	>10	>10[a]	3.80 ± 0.06	14.07[a]

hydrogen bond between His5 and the backbone oxygen of α7_Pro196 (equivalent to *Ls*-AChBP_Glu193) observed in the co-crystal structure also contributed to the docking pose at human α7 nAChRs (**Figure 2B**). On the complementary face, OmIA_Asn9 interacted with polar Gln57, hydrophobic Trp55, Tyr168, and Leu119 in the α7 subtype, similar to the interactions observed at *Ls*-AChBP. OmIA_Val10 interacted with Trp149 on the principal side and a hydrophobic triad comprising Leu109, Gln117 and Leu119 on the complementary side of the α7 nAChRs. OmIA_Asn11 interacted with a more hydrophobic surface comprising Ser150 on principal side and Thr77 and Leu109 on complementary side (**Figure 2B**). Based on these interactions, we synthesized [H5R]OmIA to evaluate whether the insertion of positively charged residue would disrupt the π–π interactions. Additionally, less favourable interactions with residues on the complementary side of α7 nAChRs were introduced in [N9H]OmIA, [V10Q]OmIA and [N11D]OmIA to assess their potential to disrupt contacts with α7 nAChRs (**Supplementary Table S3**). The CD spectroscopy profile for OmIA and analogues were consistent with that expected for an α–helical structure (**Supplementary Figure S2**).

Functional Characterisation of OmIA Analogues at *Ls*-AChBP and α7 nAChRs in the Presence of PNU120596

To validate the observations from the co-crystal structure of OmIA/*Ls*-AChBP, the binding of OmIA analogues were first examined on *Ls*-AChBP. [H5R]OmIA, [N9H]OmIA and [N11D] OmIA showed 3.6-, 2.6- and 10-fold reduced affinity for *Ls*-AChBP respectively, while the ability of [V10Q]OmIA to displace [^{3}H]-epibatidine at *Ls*-AChBP was unaffected, compared to OmIA (**Figure 3Ai** and **Table 1**). In contrast to results from binding studies, OmIA and [N9H]OmIA only partially (~ 50%)

TABLE 2 | Inhibition of choline activation of α7 nAChRs in SH-SY5Y cells by OmIA and analogues in the presence of PNU120596. Data represent mean ± SEM of triplicate data from three independent experiments. [b]denotes 95% CIs for curve top values non-overlapping 100%.[c] denotes significant difference in EC_{50} values to agonist alone ($p < 0.05$).

Peptide concentration		Choline EC_{50} ± SEM (μM)
Choline		3 ± 0.26
OmIA	0.3 μM	2 ± 0.28[b]
	1 μM	2 ± 0.32[b]
	3 μM	2 ± 0.63[b]
[N9H]OmIA	1 μM	3 ± 0.52[b]
	3 μM	3 ± 0.36[b]
	10 μM	5 ± 1.20[b]
[V10Q]OmIA	0.3 μM	6 ± 0.65
	1 μM	13 ± 0.44[b,c]
	3 μM	45 ± 4.80[b,c]

inhibited α7 nAChR responses to choline in SH-SY5Y cells, with 95% CI of the curve bottoms not overlapping 0%, while [V10Q]OmIA was a near full inhibitor in the presence of the type II PAM, PNU120596 (**Figure 3A**(ii) and **Table 1**). The inhibitory activity of all analogues decreased at α7 nAChRs, with [H5R]OmIA and [N11D]OmIA experiencing the largest drop in potency. Using a pairwise comparison of the IC_{50} values for binding affinity for *Ls*-AChBP and potency at human α7 nAChRs, all analogues were significantly ($p < 0.05$) different to wildtype OmIA.

To further characterise the partial inhibition observed in SH-SY5Y cells, a fixed concentration of OmIA and its analogues was preincubated with PNU120596 prior to the addition of increasing concentrations of choline. A decrease of the agonist's maximal response, where 95%CI of the curve top values did not overlap 100%, without a significant change in the agonist EC_{50} ($p > 0.05$), was observed for OmIA and [N9H]OmIA. The degree of maximal response depression increased as the concentration of OmIA and analogues increased, suggesting insurmountable antagonism by OmIA. In contrast, [V10Q]OmIA depressed the maximal response and caused a rightward shift in the EC_{50} for choline ($p < 0.05$), suggesting [V10Q]OmIA has a different

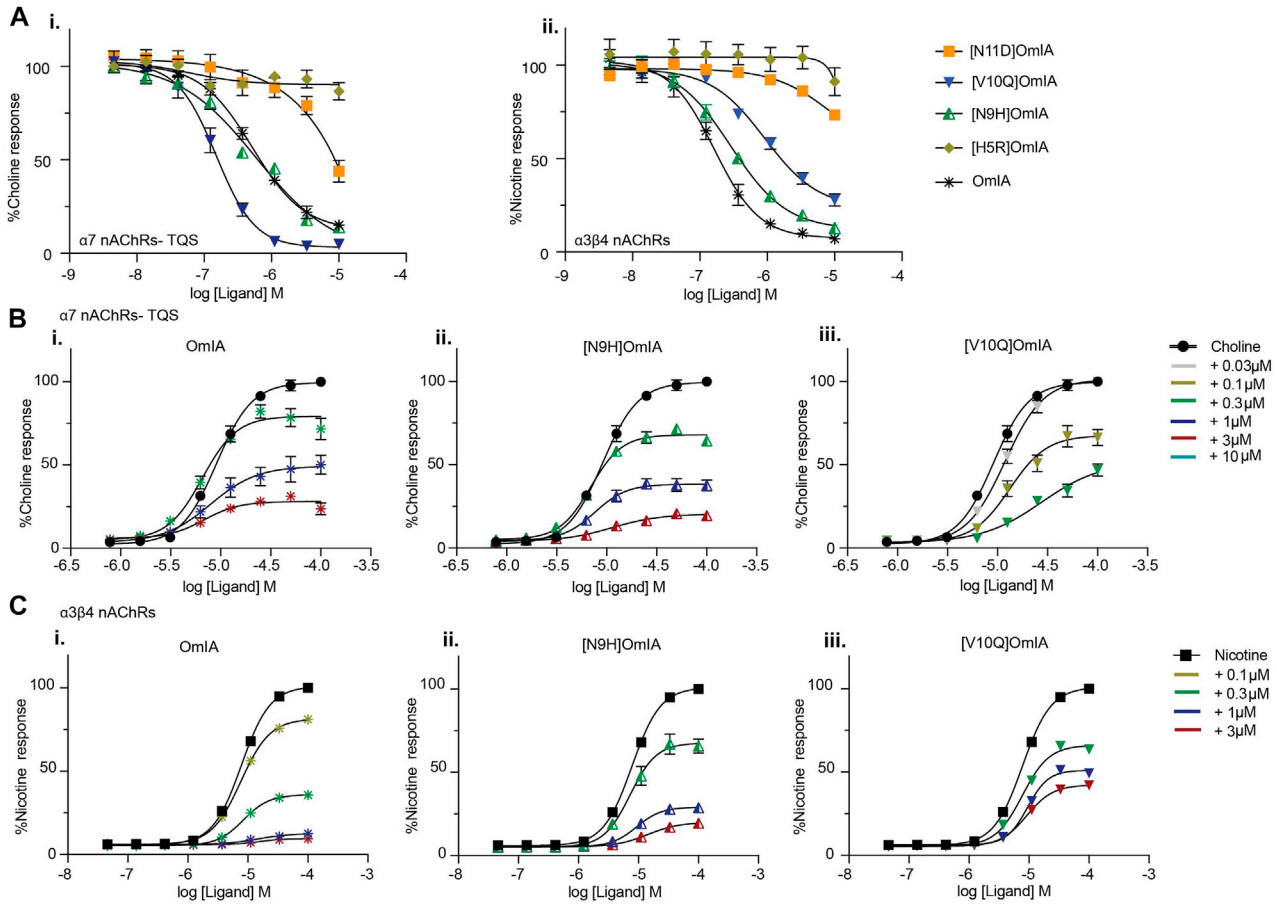

FIGURE 4 | Activity of OmIA and its analogues at α7 nAChRs in the presence of the type II PAM TQS, and at α3β4 nAChRs. **(A)** Inhibition of choline activation of α7 nAChR in the presence of TQS (i) and inhibition of nicotine activation of α3β4 nAChRs (ii) by OmIA and analogues using FLIPR Ca^{2+} influx assay results in SH-SY5Y cells Concentration-response curves for nicotine (filled square) and choline (filled circle) in the presence of varying concentrations of OmIA (i), [N9H]OmIA (ii) and [V10Q]OmIA (iii) at TQS-α7 nAChRs **(B)** and at α3β4 nAChRs **(C)**. Data represent mean ± SEM of triplicate data from three independent experiments.

TABLE 3 | IC_{50} values for the inhibition of choline activation of α7 nAChRs with the addition of nAChR type II PAM TQS and α3β4 nAChRs in SH-SY5Y cells by OmIA and its analogues. *Ratios were calculated between OmIA and its analogues. Data represent mean ± SEM of triplicate data from three independent experiments. [a]denotes significant difference in IC_{50} values to wildtype OmIA ($p < 0.05$). [b]denotes 95% CIs for curve bottom values non-overlapping 0%.

	FLIPR SH-SY5Y, IC_{50} ± SEM (μM)			
	TQS-α7 nAChRs (μM)	Ratio*	α3β4 nAChRs (μM)	Ratio*
OmIA	0.50 ± 0.09	1[b]	0.16 ± 0.03	1 [b]
[H5R]OmIA	>10	>10[a]	>10	>10
[N9H]OmIA	0.54 ± 0.09	1[b]	0.29 ± 0.04	1.69[b]
[V10Q]OmIA	0.14 ± 0.03	0.28[a]	0.92 ± 0.16	5.75[a,b]
[N11D]OmIA	>10	>10	>10	>10

TABLE 4 | Effect of OmIA and its analogues on choline concentration-activation curve at α7 nAChRs with the addition of nAChR type II PAM, TQS and on nicotine concentration-activation curve at α3β4 nAChRs in SH-SY5Y cells. [b]denotes 95% CIs for curve top values non-overlapping 100%. [c]denotes significant difference in EC_{50} values to agonist alone ($p < 0.05$). Data represent mean ± SEM of triplicate data from three independent experiments.

	Peptide concentration	Choline EC_{50} ± SEM (μM) at TQS-α7 nAChRs	Nicotine EC_{50} ± SEM (μM) at α3β4 nAChRs
Choline		9 ± 0.90	
Nicotine			8 ± 0.35
OmIA	0.1 μM		8 ± 1.40[b]
	0.3 μM	7 ± 0.62[b]	8 ± 0.50[b]
	1 μM	7 ± 0.29[b]	13 ± 3.40[b]
	3 μM	7 ± 0.53[b]	
[N9H]OmIA	0.3 μM	7 ± 0.12[b]	10 ± 0.67[b]
	1 μM	8 ± 0.72[b]	10 ± 1.50[b]
	3 μM	11 ± 1.10[b]	13 ± 0.23[b]
	10 μM		
[V10Q]OmIA	0.03 μM	12 ± 1.80	
	0.1 μM	14 ± 0.86[b,c]	
	0.3 μM	32 ± 11.70[b,c]	8 ± 0.74[b]
	1 μM		9 ± 0.39[b]
	3 μM		9 ± 1.10[b]

mechanism of action compared to OmIA and [N9H]OmIA (**Figure 3B** and **Table 2**).

Does Partial Inhibition by OmIA and Analogues Require PNU-120596?

To examine whether the partial inhibition produced by OmIA and analogues at α7 nAChRs only occurs in the presence of PNU120596, we examined their effects on α3β4 nAChR responses, and α7 nAChR responses in the presence of a different type II PAM, TQS, acting like PNU120596 to stabilize the open state of the α7 nAChRs (Halvard Grønlien et al., 2007). Interestingly, at both nAChR subtypes, at the highest concentration tested, OmIA and [N9H]OmiA had significant residual responses (~ 15%) (95% CI did not overlap 0%), albeit to a lesser extent than observed with PNU120596, except for (V10Q) OmIA (**Figure 4A**). While [N9H]OmIA retained wild-type potency, both [H5R]OmIA and [N11D]OmIA had reduced IC_{50} ($p < 0.05$), and [V10Q]OmIA had 3.6-fold increased potency at α3β4 nAChRs and 6-fold decreased potency at α7 nAChRs in the presence of TQS compared to wildtype ($p < 0.05$) (**Figure 4A** and **Table 3**). Similar to observations at α7 nAChRs in the presence of PNU120596, maximal α3β4 and TQS-α7 nAChR responses were significantly depressed without altering the EC_{50} for choline, except [V10Q]OmIA also showed an increased EC_{50} for choline at nAChRs in the presence of TQS ($p < 0.05$) (**Figures 4B,C** and **Table 4**).

Long Side Chain Amino Acids at Position 10 Differentially Effect OmIA Pharmacology

Given the differential pharmacological effects of [V10Q] OmIA compared to wildtype and other analogues, amino acids with different chemical properties were substituted at position 10 of OmIA, specifically [V10E]OmIA, [V10K] OmIA, [V10L]OmIA and [V10A]OmIA to examine the role of residue 10 in modulating OmIA pharmacology (**Supplementary Table S3**). The substitutions at position 10 made no change to the secondary structure compared to OmIA and decreased OmIA binding affinity at *Ls*-AChBP, with the largest reduction exhibited by [V10K]OmIA and [V10E]OmIA ($p < 0.05$, except for [V10L]OmIA (**Supplementary Figure S2**, **Figure 5A** and **Supplementary Table S4**).

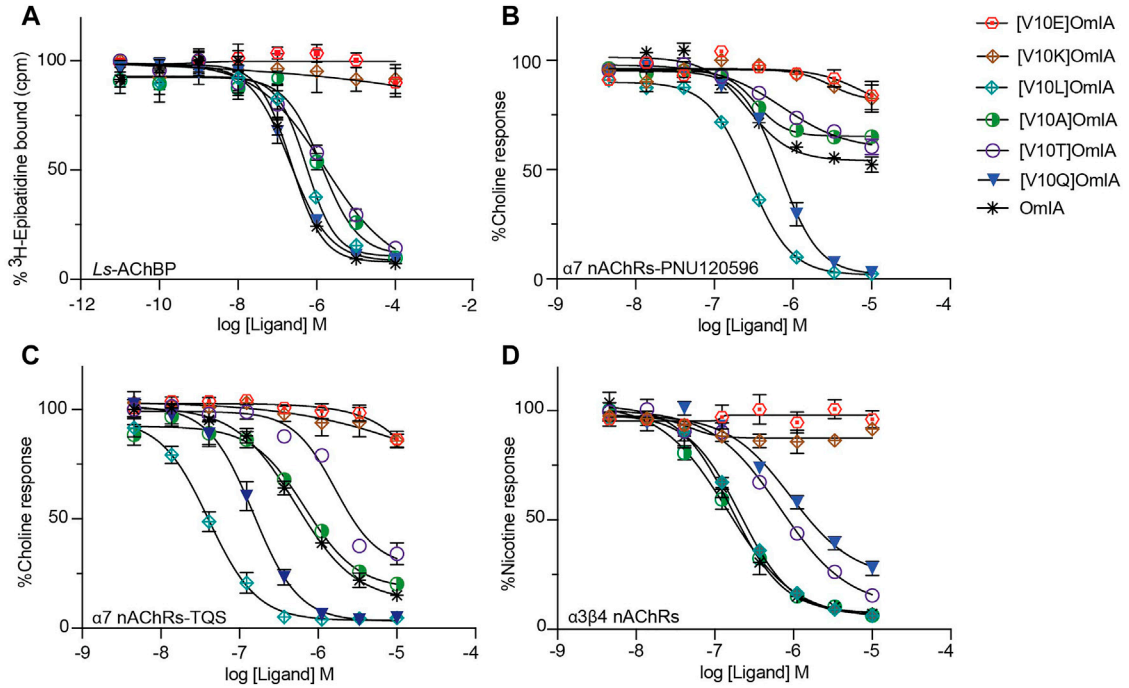

FIGURE 5 | Activity of OmIA and its analogues at position 10 at Ls-AChBP, α7 nAChRs with the addition of nAChR type II PAM PNU-120596, TQS and α3β4 nAChRs. **(A)** Displacement of [^{3}H]-epibatidine from *Ls*-AChBP. The inhibition of choline activation of α7 nAChRs with PNU-120596 **(B)**, TQS as PAMs **(C)** and inhibition of nicotine activation of α3β4 nAChRs **(D)** by OmIA and its analogues at position 10, measured in a FLIPR Ca^{2+} influx assay on SH-SY5Y cells. Data represent mean ± SEM of triplicate data from three independent experiments.

At nAChRs, the substitution of long charged side chain amino acid into position 10 abolished OmIA activity ($p < 0.05$) (**Figures 5B–D** and **Supplementary Table S4**). Meanwhile, at the highest concentration tested, [V10A]OmIA and [V10T]OmIA displayed residual response at both nAChR subtypes (95%CI nonoverlapping with 0%), with the most significant effect exhibited by [V10A]OmIA (65%) and [V10T]OmIA (60%) at PNU120596-α7 nAChRs (**Figure 5B**). While [V10A]OmIA retained its potency, [V10T]OmIA showed a decrease in activity with the highest loss of 10-fold observed at TQS-α7 nAChRs ($p < 0.05$) (**Figure 5C**). Replacement of Val10 in OmIA with a long hydrophobic amino acid (Leu) increased OmIA IC_{50} 10-fold at TQS-α7 nAChRs ($p < 0.05$) but slightly decreased OmIA activity at α3β4 nAChRs ($p > 0.05$).

All active OmIA analogues at position 10 also depressed the maximal response of agonist-activation curves at both nAChR subtypes significantly (**Supplementary Table S5** and **Figure 6**). However, similar to [V10Q]OmIA, only [V10L]OmIA both decreased PAMs-α7 maximal response and increased the EC_{50} of choline ($p < 0.05$).

OmIA and Analogues Displayed Biphasic Concentration-Inhibition Curves at PNU120596-α7 nAChRs

To further characterise the partial inhibition of OmIA and its analogues at PNU120596-α7 nAChRs, we compared full inhibitor dose-response curves at three incubation periods. Intriguingly, the dose-response relationship to OmIA and other analogues, except for [V10Q]OmIA and [V10L]OmIA, showed biphasic inhibition with clear high and low affinity binding sites (**Figure 7** and **Table 5**). With short preincubations, OmIA exhibits equal ratio between the high-affinity and low affinity site, while [N9H]OmIA, [V10A]OmIA and [V10T]OmIA preferred to bind to the low-affinity binding site. As the preincubation period increased from 3 to 30 min, there was an associated increase in the high affinity fraction (**Table 5**). OmIA, [N9H]OmIA and [V10Q]OmIA displayed a comparable antagonism to wildtype OmIA, while [V10A]OmIA and [V10T]OmIA showed the highest loss in potency ($p < 0.05$) (**Figure 7** and **Table 5**).

DISCUSSION

α-Conotoxins constitute the largest group of characterized *Conus* peptides that target nAChRs with high potency and selectivity and have contributed significantly to our understanding of nAChR pharmacology (Lewis and Garcia, 2003; Lewis et al., 2012). OmIA isolated from *Conus omaria* venom is an α4/7-conotoxin that exhibits high potency at α7 and α3β2 nAChRs. In this study, we present the co-crystal structure of OmIA with *Ls*-AChBP, and a new homology model of OmIA bound at α7 nAChRs, which revealed His5, Val10 and Asn11 were key contributors to OmIA binding at α7 nAChRs. Interestingly, OmIA and most analogues acted as functional insurmountable antagonists, while those with long side chain at position 10 were partial surmountable inhibitors at α7 nAChRs in the presence of

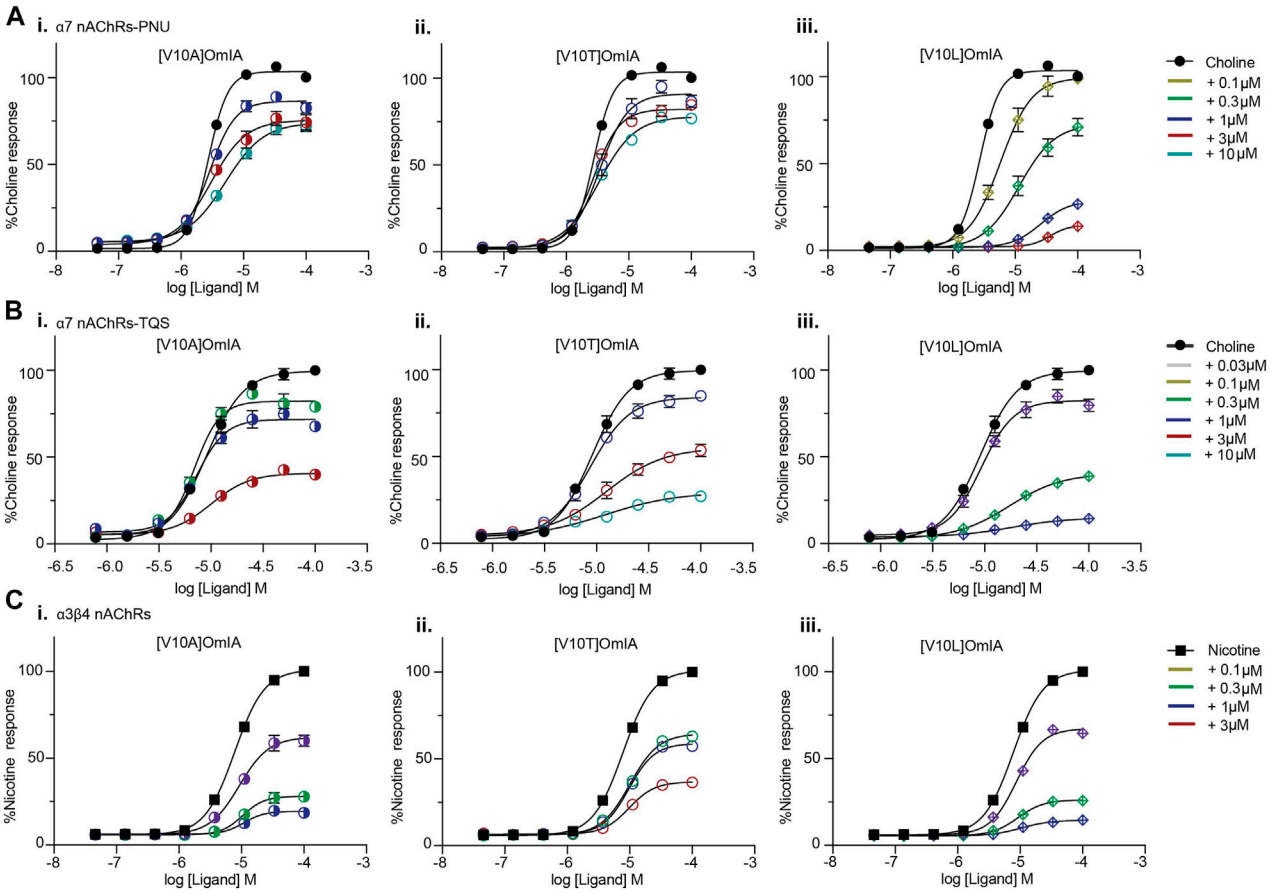

FIGURE 6 | Concentration-response curves for nicotine (black square) alone, choline alone (black round) in the presence of OmIA analogues at position 10 at α7 nAChRs with the addition of nAChR type II PAM, PNU120596 **(A)**, TQS **(B)** and at α3β4 nAChRs **(C)**. Data represent mean ± SEM of triplicate data from three independent experiments.

type II PAMs. OmIA and analogues also displayed biphasic inhibition at α7 nAChRs in the presence of PNU120596.

The co-crystal of OmIA with *Ls*-AChBP revealed a similar binding orientation to other α-conotoxins, including several overlapping pairwise interactions with these α-conotoxins (**Figure 1D**). However, differences in the residues interacting at the binding sites were also observed that likely underlie differences in α-conotoxin pharmacology and selectivity towards distinct nAChR subtypes (Celie et al., 2005; Hansen et al., 2005; Dutertre et al., 2007; Lin et al., 2016; Xu et al., 2017). From the co-crystal structure of OmIA/*Ls*-AChBP and OmIA docking to α7 nAChRs, we identified His5, Val10 and Asn11 as potential key residues for high potency at α7 nAChRs. In support, [H5R]OmIA showed a significant drop in potency, possibly arising from the disruption of the π-π interaction with Tyr93, Tyr188, Tyr195 as well as the loss in hydrogen bond between His5 and α7_Pro196 backbone (**Figure 2B**). Despite similarities in the interacting surface of OmIA, [A10L]TxIA, [A10L]PnIA and GIC (Celie et al., 2005; Dutertre et al., 2007; Lin et al., 2016), the H5R mutation in [L5R A10L]TxIA had no influence on potency at α7 nAChRs, while [H5A]GIC lost all activity α7 nAChRs, indicating that the role played by position 5 is highly variable across the different α-conotoxins. In the co-crystal structure, Val10_ OmIA was seen to occupy the previously characterised hydrophobic funnel Trp143 on the principal face and Leu112, Met114 on the complementary face of human α7 nAChRs that favoured interactions with hydrophobic residues (Celie et al., 2005; Dutertre et al., 2007; Hopping et al., 2014). Interestingly, while at PNU120596-α7 nAChRs the [V10Q]OmIA potency decreased but [V10L]OmIA potency remained unchanged, at TQS-α7 nAChRs, both the [V10L]OmIA and [V10Q]OmIA potency increased, suggesting differential effects can be modulated by different PAMs. Finally, [N11D]OmIA introduced a likely clash with the complementary hydrophobic interacting surface of α7 nAChRs, causing a significant drop in potency (**Supplementary Figure S2**). Interestingly, [N9H]OmIA introduced differential effects at α7 nAChRs in the presence of different PAMs, suggesting a novel role for position 9 in modulating OmIA activity (**Supplementary Figure S2**). Previously, position 9 was identified as important for the potency of a range of α-conotoxins (Halai et al., 2009; Azam et al., 2010; Hone et al., 2013; Hone et al., 2019). These studies suggest that further characterisation of the role played by these key positions in OmIA is warranted.

Surprisingly, OmIA and selected analogues displayed insurmountable antagonism of functional nAChR responses at α7

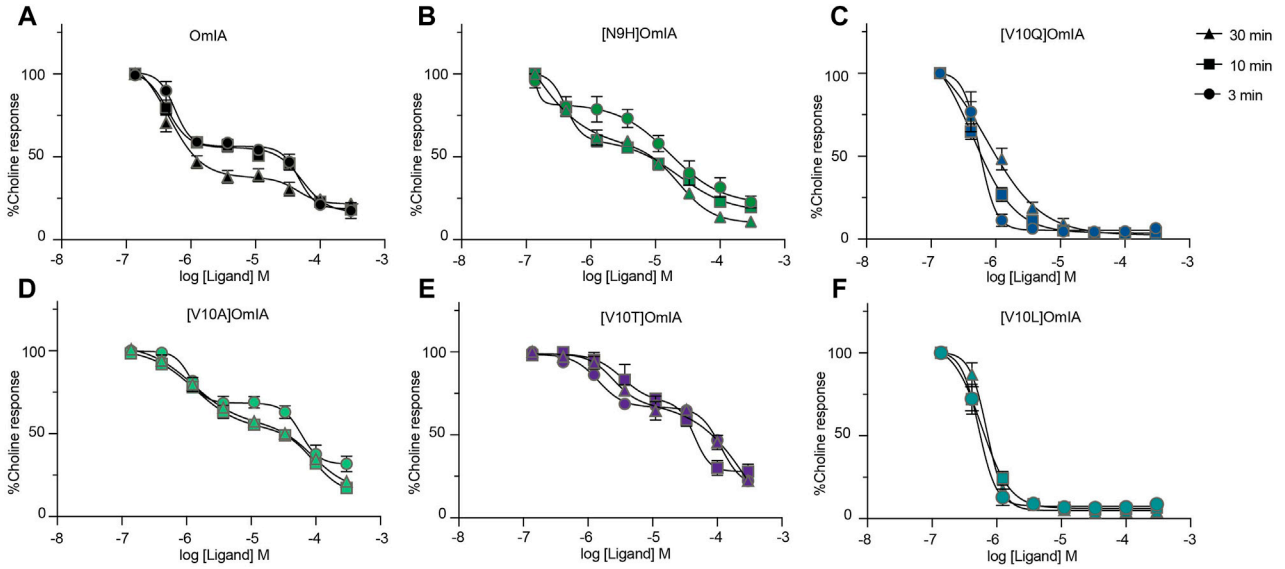

FIGURE 7 | OmIA and selected analogues show biphasic inhibition of α7 nAChRs in the presence of a type II PAM (PNU120596) pre-incubated at 3, 10 or 30 min. Data represent mean ± SEM of triplicate data from three independent experiments.

TABLE 5 | The IC_{50} (μM) of OmIA and analogues following inhibitor preincubations of 3, 10 or 30 min at PNU120596-modified α7 nAChRs. Data represent mean ± SEM of triplicate data from three independent experiments.

		OmIA	(N9H)OmIA	(V10Q)OmIA	(V10A)OmIA	(V10T)OmIA	(V10L)OmIA
IC_{50}_1 ± SEM	3 min	0.41 ± 0.04	0.24 ± 0.01	0.39 ± 0.11	1.1 ± 0.0[a]	1.7 ± 0.46[a]	0.47 ± 0.03
	10 min	0.61 ± 0.16	0.41 ± 0.01	0.50 ± 0.10	1.6 ± 0.77[a]	1.7 ± 0.17[a]	0.62 ± 0.11
	30 min	0.38 ± 0.06	0.41 ± 0.0	0.50 ± 0.19	1.5 ± 0.39[a]	2.8 ± 0.42[a]	0.69 ± 0.04
IC_{50}_2 ± SEM	3 min	50.0 ± 9.0	30.0 ± 7.0	NA	80.0 ± 3.0[a]	40.0 ± 1.0[a]	NA
	10 min	50.0 ± 1.0	20.0 ± 3.3[a]	NA	90.0 ± 1.0[a]	100.0 ± 3.0[a]	NA
	30 min	50.0 ± 4.1	10.0 ± 3.1[a]	NA	80.0 ± 16.0[a]	120.0 ± 3.5[a]	NA
Fraction 2 ± SEM	3 min	0.60 ± 0.02	0.39 ± 0.09	NA	0.37 ± 0.04	0.31 ± 0.05	NA
	10 min	0.51 ± 0.02	0.42 ± 0.02	NA	0.58 ± 0.04	0.46 ± 0.06	NA
	30 min	0.72 ± 0.02	0.54 ± 0.02	NA	0.57 ± 0.11	0.51 ± 0.02	NA

[a]*Denotes significant difference in IC_{50} values to wildtype OmIA* ($p < 0.05$).

nAChRs in the presence of type II PAMs and at α3β4 nAChRs. Insurmountable antagonism may arise through allosteric inhibition (Kenakin, 2017); however, OmIA binds at the orthosteric sites, consistent with a competitive interaction with the orthosteric agonists investigated. Alternatively, OmIA might stabilise nAChRs in a desensitized or a desensitized-like state without transitioning through the open state, resulting in decreased responsiveness of the receptor for a subsequent stimulus by agonists (Hurst et al., 2013). Antagonist stabilizing the desensitized state rather than the closed state of nAChRs was previously proposed for the competitive nAChR antagonist dihydro-β-erythroidine (DHβE) (Bertrand et al., 1992). In agreement with this proposal, the co-crystal complex of DHβE/AChBP revealed that DHβE induced closing of the nAChR_C-loop typical of agonist binding, and established a hydrogen-bonding network similar to agonists (Shahsavar et al., 2012). However, these features were not observed in the OmIA/*Ls*-AChBP complex, suggesting OmIA is unlikely to stabilise a desensitized state. Insurmountable antagonism could also be due to the presence of different receptor subpopulations (Kenakin, 2017). Despite SH-SY5Y cells expressing the β2 nAChR subunit, the presence of a novel heteromeric α7β2 nAChRs is not well documented. However, the possibility of this subpopulation potentially activated by choline analogues or subpopulations of α7 nAChRs in pharmacologically distinct activatable states that are not blocked by OmIA cannot be discounted (Vetter and Lewis, 2010) until effects on oocytes expressed homomeric α7 nAChRs and heteromeric α7β2 nAChRs are compared. Alternatively, the insurmountable action of OmIA may arise from non-equilibration interactions between antagonist and agonist since peak agonist responses are rapidly and transiently induced, while antagonist responses are slower to reverse (Vauquelin et al., 2001; Vauquelin et al., 2002; Charlton and Vauquelin, 2010; Kenakin, 2017). This effect could also be interpreted as "pseudo-irreversible" antagonism, as the antagonist-receptor complex could be considered irreversible within the time-frame of the agonist responses (Kenakin, 2017).

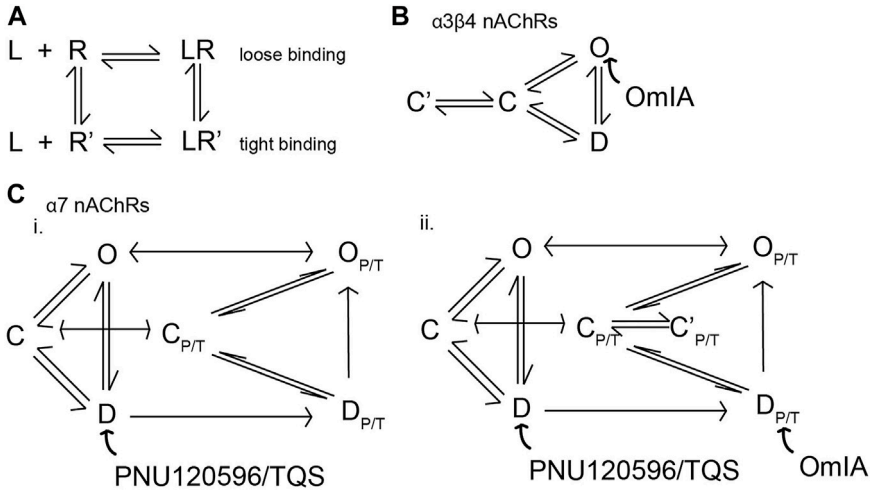

FIGURE 8 | Proposed model depicting conformational changes of nAChRs induced by the binding of OmIA. **(A)** Schematic representation of the potential mechanism of potential responsible for surmountable and insurmountable antagonism. When antagonists (L) bind to receptors (R), the antagonists-receptors may adopt two states: LR, a loose binding state accounting for the surmountable inhibition by the antagonists, and LR', a tight binding state accounting for the insurmountable inhibition by the antagonist. **(B)** The model of the activation of α3β4 nAChRs with three basic conformational states, resting or closed (C), inactivated or desensitized (D) and conducting or open state (O). OmIA bound to resting-state of nAChR, converting α3β4 nAChRs into close state. The OmIA-receptor complex may then convert into a tight binding state (C') that are slowly reversible and cannot be overcome during the short exposure of agonist, meaning that only part of the receptors can be liberated, and hence occupied and stimulated by the subsequence addition of agonist. This feature accounts for the insurmountable antagonism of OmIA and its analogues. **(C)** The PNU120596/TQS-bound channel exists in parallel ($C_{P/T}$, $D_{P/T}$, $O_{P/T}$) states (i). PNU120596/TQS predominantly binds to the desensitized state (D) that transforms the channel to a PNU120596/TQS-modified channels ($D_{P/T}$) which is energetically favourable to convert to a PNU120596/TQS-modified Open ($O_{P/T}$) (Szabo et al., 2014). OmIA and its (ii) binding to the $D_{P/T}$ and convert the receptor to the closed ($C_{P/T}$) state. Here, OmIA, [N9H]OmIA, [V10A]OmIA and [V10T]OmIA predominantly exists in the tight binding complex ($C'_{P/T}$), accounting for its fully surmountable inhibition. Meanwhile, [V10Q]OmIA and [V10L]OmIA complexes with receptors coexist in the loose binding state ($C_{P/T}$) and the tight binding state ($C'_{P/T}$), accounting for its partial surmountable inhibition.

Remarkably, [V10Q]OmIA and [V10L]OmIA not only displayed a depression in maximal response but also induced a right-ward shift to the concentration-response of choline at PNU120596/TQS-α7 nAChRs, characteristic of surmountable inhibition (Charlton and Vauquelin, 2010). This phenomenon could reflect the ability of the antagonist-receptor complexes to adopt two distinct states, a fast reversible state (for the surmountable inhibition) and a slowly reversing binding state (for insurmountable inhibition). In a "two-state, two-step" model explaining these observations (**Figure 8**), the antagonist (L) binds to the receptor to form a loose binding complex (L.R) which can convert into a tight binding complex (L.R*). The antagonist is fully surmountable if L.R predominates, partially insurmountable when L.R and L.R* coexist and fully insurmountable when all complexes are in the L.R* state (Kenakin, 1993; Vauquelin et al., 2001). Apparently, OmIA, [N9H]OmIA, [V10A]OmIA and [V10T]OmIA bind to PNU120596-α7 nAChRs in a tight binding state, resulting in fully insurmountable antagonism. In contrast, [V10L]OmIA and [V10Q]OmIA interact in both the LR (loose form) and LR* (tight form) states. Upon stimulation by agonist, a greater percentage of the pre-formed antagonist receptor complex could be free to be occupied by agonists, explaining for the rightward shift of agonist EC_{50} (**Figure 8**). Alternatively, [V10Q]OmIA and [V10L]OmIA might have faster off-rate that would allow a component of binding to be competitively inhibited.

Another unique feature identified in these studies is the ability of OmIA and [N9H]OmIA to display high affinity partial inhibition and a lower affinity inhibitory action at PNU120596-α7 nAChRs. Partial inhibition by OmIA and [N9H]OmIA may arise through OmIA being a partial agonist, however, OmIA and all analogues were unable to induce Ca^{2+} current (**Supplementary Figure S3**), or because OmIA interacts with two pharmacologically disctinct binding sites. Indeed, OmIA and its analogues displayed clearly distinct high and low affinity binding sites, with the low affinity binding state more rapidly occupied by OmIA and its analogues, while the high affinity binding site required longer incubation times to develop. This biphasic behavior of [V10Q]OmIA and [V10L]OmIA was not as apparent for other OmIA analogues, possibly due to their greater preference for high-affinity binding site over the low-affinity binding site.

The complex pharmacological profile of OmIA and analogues seen at PAM-α7 nAChRs, with different PAMs differentially enhancing this phenomenon at α7 nAChRs, suggests a direct involvement of type II PAMs in modulating this phenomenon. In contrast, at α3β4 nAChRs, any surmountable antagonism of [V10Q]OmIA and [V10L]OmIA or the biphasic behavior of OmIA are less apparent. The effect of PAMs on OmIA pharmacology may arise from enhanced channel gating and associated conformational changes in the orthosteric ligand binding site induced by PNU120596 and TQS (Barron et al., 2009) (**Supplementary Figure S4**). Long side chains at position 10 appear to change the way OmIA interacts with PAM-modified orthosteric binding site of α7 nAChRs, although in the absence of PAMs, [V10Q]OmIA docked similarly to OmIA at the α7 nAChR

(**Supplementary Figure S5**). Interestingly, substitution of long side chain at position 10 enhanced PnIA potency and shift it to an agonist at the [L247T]α7 nAChR, a mutant with prolonged desensitization reminiscent of the effect of type II PAMs on nAChR function (Hogg et al., 2003). Further studies are required to determine the extent different side chains at position 10 can stabilise different functional states of the receptor.

In summary, we report the crystal structure of OmIA with *Ls*-AChBP and a model of α-conotoxin OmIA complexed with α7 nAChRs that explains its high potency at α7 nAChRs. OmIA displayed functional insurmountable antagonism at human α7 nAChRs despite a binding to the othosteric site. OmIA pharmacology provides significant new insights into mechanisms of inhibition of α7 nAChRs, and the influence of type II PAMs on nAChR function. These results may facilitate the design of α-conotoxin analogues with novel features and potentially innovative therapeutic leads.

DATA AVAILABILITY STATEMENT

The datasets presented in this study can be found in online repositories. The names of the repository/repositories and accession number(s) can be found below: wwPDB Deposition; PDB ID 7N43.

AUTHOR CONTRIBUTIONS

TH: study design, structure determination, refinement, circular dichroism, functional experiments on FLIPR, radioligand binding studies, data analysis and interpretation, peptide synthesis, HPLC, mass spectrometry, circular dichroism, homology modeling, and prepared the first draft of the manuscript. NA: study design, data analysis and interpretation. RL: study design, data analysis, interpretation, manuscript writing, funding and facilities. All authors reviewed the manuscript.

FUNDING

A National Health and Medical Research Council of Australia Fellowship (APP1119056) and Program Grant (APP1072113), and an Australian Research Council Discovery Grant (DP200103087) provided research funding and support to RJL. TH was supported by a University of Queensland International scholarship (UQI).

ACKNOWLEDGMENTS

The authors thank Brett Collins and Gordon King for help with x-ray data collection, support from the staff and facilities of the University of Queensland Remote Operation Crystallization and X-ray (UQ ROCX) facility and the Australian Synchrotron.

SUPPLEMENTARY MATERIAL

The Supplementary Material for this article can be found online at: https://www.frontiersin.org/articles/10.3389/fphar.2021.803397/full#supplementary-material

REFERENCES

Abraham, N., and Lewis, R. J. (2018). Neuronal Nicotinic Acetylcholine Receptor Modulators from Cone Snails. *Mar. Drugs* 16, 208. doi:10.3390/md16060208

Abraham, N., Paul, B., Ragnarsson, L., and Lewis, R. J. (2016). *Escherichia coli* Protein Expression System for Acetylcholine Binding Proteins (AChBPs). *PLoS One* 11, e0157363. doi:10.1371/journal.pone.0157363

Afonine, P. V., Grosse-Kunstleve, R. W., Echols, N., Headd, J. J., Moriarty, N. W., Mustyakimov, M., et al. (2012). Towards Automated Crystallographic Structure Refinement with phenix.Refine. *Acta Crystallogr. D Biol. Crystallogr.* 68, 352–367. doi:10.1107/s0907444912001308

Azam, L., Maskos, U., Changeux, J. P., Dowell, C. D., Christensen, S., De Biasi, M., et al. (2010). α-Conotoxin BuIA[T5A;P6O]: a Novel Ligand that Discriminates between α6ß4 and α6ß2 Nicotinic Acetylcholine Receptors and Blocks Nicotine-Stimulated Norepinephrine Release. *Faseb J.* 24, 5113–5123. doi:10.1096/fj.10-166272

Azam, L., and Mcintosh, J. M. (2009). Alpha-conotoxins as Pharmacological Probes of Nicotinic Acetylcholine Receptors. *Acta Pharmacol. Sin.* 30, 771–783. doi:10.1038/aps.2009.47

Barron, S. C., Mclaughlin, J. T., See, J. A., Richards, V. L., and Rosenberg, R. L. (2009). An Allosteric Modulator of Alpha7 Nicotinic Receptors, N-(5-Chloro-2,4-dimethoxyphenyl)-N'-(5-methyl-3-isoxazolyl)-urea (PNU-120596), Causes Conformational Changes in the Extracellular Ligand Binding Domain Similar to Those Caused by Acetylcholine. *Mol. Pharmacol.* 76, 253–263. doi:10.1124/mol.109.056226

Battye, T. G., Kontogiannis, L., Johnson, O., Powell, H. R., and Leslie, A. G. (2011). iMOSFLM: a New Graphical Interface for Diffraction-Image Processing with MOSFLM. *Acta Crystallogr. D Biol. Crystallogr.* 67, 271–281. doi:10.1107/s0907444910048675

Bertrand, D., Devillers-Thiéry, A., Revah, F., Galzi, J. L., Hussy, N., Mulle, C., et al. (1992). Unconventional Pharmacology of a Neuronal Nicotinic Receptor Mutated in the Channel Domain. *Proc. Natl. Acad. Sci. U S A.* 89, 1261–1265. doi:10.1073/pnas.89.4.1261

Bertrand, D., and Gopalakrishnan, M. (2007). Allosteric Modulation of Nicotinic Acetylcholine Receptors. *Biochem. Pharmacol.* 74, 1155–1163. doi:10.1016/j.bcp.2007.07.011

Celie, P. H., Kasheverov, I. E., Mordvintsev, D. Y., Hogg, R. C., Van Nierop, P., Van Elk, R., et al. (2005). Crystal Structure of Nicotinic Acetylcholine Receptor Homolog AChBP in Complex with an Alpha-Conotoxin PnIA Variant. *Nat. Struct. Mol. Biol.* 12, 582–588. doi:10.1038/nsmb951

Charlton, S. J., and Vauquelin, G. (2010). Elusive Equilibrium: the challenge of Interpreting Receptor Pharmacology Using Calcium Assays. *Br. J. Pharmacol.* 161, 1250–1265. doi:10.1111/j.1476-5381.2010.00863.x

Chen, V. B., Arendall, W. B., 3rd, Headd, J. J., Keedy, D. A., Immormino, R. M., Kapral, G. J., et al. (2010). MolProbity: All-Atom Structure Validation for Macromolecular Crystallography. *Acta Crystallogr. D Biol. Crystallogr.* 66, 12–21. doi:10.1107/s0907444909042073

Collaborative Computational Project, Number 4 (1994). The CCP4 Suite: Programs for Protein Crystallography. *Acta Crystallogr. D. Biol. Crystallogr.* 50, 760–763. doi:10.1107/s0907444994003112

Corradi, J., and Bouzat, C. (2016). Understanding the Bases of Function and Modulation of α7 Nicotinic Receptors: Implications for Drug Discovery. *Mol. Pharmacol.* 90, 288–299. doi:10.1124/mol.116.104240

Dani, J. A., and Bertrand, D. (2007). Nicotinic Acetylcholine Receptors and Nicotinic Cholinergic Mechanisms of the central Nervous System. *Annu.*

Rev. Pharmacol. Toxicol. 47, 699–729. doi:10.1146/annurev.pharmtox.47.120505.105214

Dineley, K. T., Pandya, A. A., and Yakel, J. L. (2015). Nicotinic ACh Receptors as Therapeutic Targets in CNS Disorders. *Trends Pharmacol. Sci.* 36, 96–108. doi:10.1016/j.tips.2014.12.002

Dutertre, S., Ulens, C., Büttner, R., Fish, A., Van Elk, R., Kendel, Y., et al. (2007). AChBP-Targeted Alpha-Conotoxin Correlates Distinct Binding Orientations with nAChR Subtype Selectivity. *Embo J.* 26, 3858–3867. doi:10.1038/sj.emboj.7601785

Emsley, P., and Cowtan, K. (2004). Coot: Model-Building Tools for Molecular Graphics. *Acta Crystallogr. D Biol. Crystallogr.* 60, 2126–2132. doi:10.1107/s0907444904019158

Gotti, C., and Clementi, F. (2004). Neuronal Nicotinic Receptors: from Structure to Pathology. *Prog. Neurobiol.* 74, 363–396. doi:10.1016/j.pneurobio.2004.09.006

Guex, N., Peitsch, M. C., and Schwede, T. (2009). Automated Comparative Protein Structure Modeling with SWISS-MODEL and Swiss-PdbViewer: a Historical Perspective. *Electrophoresis* 30, S162–S173. doi:10.1002/elps.200900140

Halai, R., Clark, R. J., Nevin, S. T., Jensen, J. E., Adams, D. J., and Craik, D. J. (2009). Scanning Mutagenesis of α-Conotoxin Vc1.1 Reveals Residues Crucial for Activity at the α9α10 Nicotinic Acetylcholine Receptor. *J. Biol. Chem.* 284, 20275–20284. doi:10.1074/jbc.M109.015339

Halvard Grønlien, J., Håkerud, M., Ween, H., Thorin-Hagene, K., Briggs, C. A., Gopalakrishnan, M., et al. (2007). Distinct Profiles of α7 nAChR Positive Allosteric Modulation Revealed by Structurally Diverse Chemotypes. *Mol. Pharmacol.* 72, 715–724. doi:10.1124/mol.107.035410

Hansen, S. B., Sulzenbacher, G., Huxford, T., Marchot, P., Taylor, P., and Bourne, Y. (2005). Structures of *Aplysia* AChBP Complexes with Nicotinic Agonists and Antagonists Reveal Distinctive Binding Interfaces and Conformations. *Embo J.* 24, 3635–3646. doi:10.1038/sj.emboj.7600828

Ho, T. N. T., Abraham, N., and Lewis, R. J. (2020). Structure-function of Neuronal Nicotinic Acetylcholine Receptor Inhibitors Derived from Natural Toxins. *Front. Neurosci.* 14, 609005. doi:10.3389/fnins.2020.609005

Hogg, R. C., and Bertrand, D. (2004). Nicotinic Acetylcholine Receptors as Drug Targets. *Curr. Drug Targets CNS Neurol. Disord.* 3, 123–130. doi:10.2174/1568007043482507

Hogg, R. C., Hopping, G., Alewood, P. F., Adams, D. J., and Bertrand, D. (2003). Alpha-conotoxins PnIA and (A10L)PnIA Stabilize Different States of the Alpha7-L247t Nicotinic Acetylcholine Receptor. *J. Biol. Chem.* 278, 26908–26914. doi:10.1074/jbc.M212628200

Hone, A. J., Fisher, F., Christensen, S., Gajewiak, J., Larkin, D., Whiteaker, P., et al. (2019). PeIA-5466: A Novel Peptide Antagonist Containing Non-natural Amino Acids that Selectively Targets α3β2 Nicotinic Acetylcholine Receptors. *J. Med. Chem.* 62, 6262–6275. doi:10.1021/acs.jmedchem.9b00566

Hone, A. J., Ruiz, M., Scadden, M., Christensen, S., Gajewiak, J., Azam, L., et al. (2013). Positional Scanning Mutagenesis of α-conotoxin PeIA Identifies Critical Residues that Confer Potency and Selectivity for α6/α3β2β3 and α3β2 Nicotinic Acetylcholine Receptors. *J. Biol. Chem.* 288, 25428–25439. doi:10.1074/jbc.M113.482059

Hopping, G., Wang, C. I., Hogg, R. C., Nevin, S. T., Lewis, R. J., Adams, D. J., et al. (2014). Hydrophobic Residues at Position 10 of α-conotoxin PnIA Influence Subtype Selectivity between α7 and α3β2 Neuronal Nicotinic Acetylcholine Receptors. *Biochem. Pharmacol.* 91, 534–542. doi:10.1016/j.bcp.2014.07.025

Hurst, R., Rollema, H., and Bertrand, D. (2013). Nicotinic Acetylcholine Receptors: From Basic Science to Therapeutics. *Pharmacol. Ther.* 137, 22–54. doi:10.1016/j.pharmthera.2012.08.012

Inserra, M. C., Kompella, S. N., Vetter, I., Brust, A., Daly, N. L., Cuny, H., et al. (2013). Isolation and Characterization of α-conotoxin LsIA with Potent Activity at Nicotinic Acetylcholine Receptors. *Biochem. Pharmacol.* 86, 791–799. doi:10.1016/j.bcp.2013.07.016

Jin, A. H., Muttenthaler, M., Dutertre, S., Himaya, S. W. A., Kaas, Q., Craik, D. J., et al. (2019). Conotoxins: Chemistry and Biology. *Chem. Rev.* 119, 11510–11549. doi:10.1021/acs.chemrev.9b00207

Kenakin, T. P. (2017). "Chapter 4 - Drug Antagonism: Orthosteric Drug Effects," in *Pharmacology in Drug Discovery and Development*. Editor T. P. Kenakin. Second Edition (Academic Press), 65–100. doi:10.1016/b978-0-12-803752-2.00004-1

Kenakin, T. P. (1993). *Pharmacologic Analysis of Drug-Receptor Interaction*. New York: Raven.

Lendvai, B., Kassai, F., Szájli, A., and Némethy, Z. (2013). α7 Nicotinic Acetylcholine Receptors and Their Role in Cognition. *Brain Res. Bull.* 93, 86–96. doi:10.1016/j.brainresbull.2012.11.003

Lewis, R. J., Dutertre, S., Vetter, I., and Christie, M. J. (2012). *Conus* Venom Peptide Pharmacology. *Pharmacol. Rev.* 64, 259–298. doi:10.1124/pr.111.005322

Lewis, R. J., and Garcia, M. L. (2003). Therapeutic Potential of Venom Peptides. *Nat. Rev. Drug Discov.* 2, 790–802. doi:10.1038/nrd1197

Lin, B., Xu, M., Zhu, X., Wu, Y., Liu, X., Zhangsun, D., et al. (2016). From crystal Structure of α-conotoxin GIC in Complex with Ac-AChBP to Molecular Determinants of its High Selectivity for α3β2 nAChR. *Sci. Rep.* 6, 22349. doi:10.1038/srep22349

Mccoy, A. J., Grosse-Kunstleve, R. W., Adams, P. D., Winn, M. D., Storoni, L. C., and Read, R. J. (2007). Phaser Crystallographic Software. *J. Appl. Crystallogr.* 40, 658–674. doi:10.1107/s0021889807021206

Shahsavar, A., Kastrup, J. S., Nielsen, E. Ø., Kristensen, J. L., Gajhede, M., and Balle, T. (2012). Crystal Structure of *Lymnaea stagnalis* AChBP Complexed with the Potent nAChR Antagonist DHβE Suggests a Unique Mode of Antagonism. *PloS ONE* 7, e40757. doi:10.1371/journal.pone.0040757

Szabo, A. K., Pesti, K., Mike, A., and Vizi, E. S. (2014). Mode of Action of the Positive Modulator PNU-120596 on α7 Nicotinic Acetylcholine Receptors. *Neuropharmacology* 81, 42–54. doi:10.1016/j.neuropharm.2014.01.033

Talley, T. T., Olivera, B. M., Han, K.-H., Christensen, S. B., Dowell, C., Tsigelny, I., et al. (2006). α-Conotoxin OmIA Is a Potent Ligand for the Acetylcholine-Binding Protein as Well as α3β2 and α7 Nicotinic Acetylcholine Receptors. *J. Biol. Chem.* 281, 24678–24686. doi:10.1074/jbc.M602969200

Taly, A., and Charon, S. (2012). α7 Nicotinic Acetylcholine Receptors: a Therapeutic Target in the Structure Era. *Curr. Drug Targets* 13, 695–706. doi:10.2174/138945012800398919

Taly, A., Corringer, P. J., Guedin, D., Lestage, P., and Changeux, J. P. (2009). Nicotinic Receptors: Allosteric Transitions and Therapeutic Targets in the Nervous System. *Nat. Rev. Drug Discov.* 8, 733–750. doi:10.1038/nrd2927

Vauquelin, G., Fierens, F. L., Verheijen, I., and Vanderheyden, P. M. (2001). Distinctions between Non-peptide Angiotensin II AT1-Receptor Antagonists. *J. Renin Angiotensin Aldosterone Syst.* 2, S24–s31. doi:10.1177/14703203010020010401

Vauquelin, G., Van Liefde, I., and Vanderheyden, P. (2002). Models and Methods for Studying Insurmountable Antagonism. *Trends Pharmacol. Sci.* 23, 514–518. doi:10.1016/S0165-6147(02)02081-3

Vetter, I., and Lewis, R. J. (2010). Characterization of Endogenous Calcium Responses in Neuronal Cell Lines. *Biochem. Pharmacol.* 79, 908–920. doi:10.1016/j.bcp.2009.10.020

Xu, M., Zhu, X., Yu, J., Yu, J., Luo, S., and Wang, X. (2017). The crystal Structure of Ac-AChBP in Complex with α-conotoxin LvIA Reveals the Mechanism of its Selectivity towards Different nAChR Subtypes. *Protein Cell* 8, 675–685. doi:10.1007/s13238-017-0426-2

Conflict of Interest: The authors declare that the research was conducted in the absence of any commercial or financial relationships that could be construed as a potential conflict of interest.

Publisher's Note: All claims expressed in this article are solely those of the authors and do not necessarily represent those of their affiliated organizations, or those of the publisher, the editors, and the reviewers. Any product that may be evaluated in this article, or claim that may be made by its manufacturer, is not guaranteed or endorsed by the publisher.

frontiers in Pharmacology

ORIGINAL RESEARCH
published: 09 December 2021
doi: 10.3389/fphar.2021.788358

The Protective Effects of Cath-MH With Anti-Propionibacterium Acnes and Anti-Inflammation Functions on Acne Vulgaris

*Jiena Wu†, Ruiyin Guo†, Jinwei Chai, Weichen Xiong, Maolin Tian, Wancheng Lu and Xueqing Xu**

Guangdong Provincial Key Laboratory of New Drug Screening, School of Pharmaceutical Sciences, Southern Medical University, Guangzhou, China

Acne vulgaris is a common adolescent skin condition which is mainly caused by *Propionibacterium acnes* overcolonization and subsequent inflammation. Our previous studies have demonstrated that Cath-MH, an antimicrobial peptide from the skin of the frog *Microhyla heymonsivogt*, possesses potential antimicrobial, LPS-binding, and anti-septicemic properties. However, its protective effects and potential mechanisms against acne vulgaris are still unclear. In the present study, its anti-*P. acnes* effects were measured by two-fold broth dilution method, agglutination assay, scanning electron microscopy and confocal laser scanning microscopy experiments. Its treatment potential for acne vulgaris was further evaluated in mice ear inoculated by *P. acnes*. In addition, the binding ability between Cath-MH and LTA was measured by the Circular Dichroism and antibacterial assay. Moreover, the anti-inflammatory efficiency of Cath-MH was evaluated in LTA- and LPS-induced RAW 264.7 macrophage cells. Cath-MH was found to kill *P. acnes* with a MIC value of about 1.56 μM by membrane disruption mechanism. It also exhibited agglutination activity against *P. acnes*. Cath-MH was able to bind LTA as well as LPS, inhibit LTA/LPS-stimulated TLR2/4 expression, and subsequently decreased the inflammatory response in RAW 264.7 cells. As expected, Cath-MH alleviated the formation of edema and the infiltration of inflammatory cells in acne mouse model with concurrent suppression of *P. acnes* growth and inflammatory cytokines expression *in vivo*. The potent *P. acnes* inhibition activity combined with powerful anti-inflammatory effect of Cath-MH indicates its potential as a novel therapeutic option for acne vulgaris.

Keywords: acne vulgaris, antimicrobial peptide, Microhyla heymonsivogt, Cath-MH, inflammation, lipoteichoic acid, lipopolysaccharide

OPEN ACCESS

Edited by:
Zhijian Cao,
Wuhan University, China

Reviewed by:
Francesco Merlino,
University of Naples Federico II, Italy
Marc Christophe Karam,
University of Balamand, Lebanon

****Correspondence:***
Xueqing Xu
xu2003@smu.edu.cn

†These authors have contributed equally to this work and share first authorship

Specialty section:
This article was submitted to Translational Pharmacology, a section of the journal Frontiers in Pharmacology

Received: *02 October 2021*
Accepted: *08 November 2021*
Published: *09 December 2021*

Citation:
Wu J, Guo R, Chai J, Xiong W, Tian M, Lu W and Xu X (2021) The Protective Effects of Cath-MH With Anti-Propionibacterium Acnes and Anti-Inflammation Functions on Acne Vulgaris. Front. Pharmacol. 12:788358. doi: 10.3389/fphar.2021.788358

INTRODUCTION

Acne vulgaris is one of the most familiar chronic inflammatory skin conditions which affects 80–85% of adolescents globally (Cong et al., 2019; Habeshian and Cohen, 2020). Although acne vulgaris is common, its etiology is still not fully understood and is believed to be multifactorial. As an opportunistic pathogen in acne vulgaris, *Propionibacterium acnes* overcolonization of the pilosebaceous follicle is considered as one of the central factors of acne vulgaris, which induces the secretion of lipase, hyaluronidase as well as proteases and activation of immune cells, thus

initiating inflammation (Tanghetti, 2013; Cong et al., 2019). Besides skin pathogenic bacteria and inflammation, two other factors involved in this chronic inflammatory skin disease are the increased sebum production and follicular hyperkeratinization (Dréno, 2017). Commonly used anti-acne drugs include benzoyl peroxide, retinoids, salicylic acid, isotretinoin, antibiotics and hormonal agents. However, almost all of them have certain drawbacks like causing skin irritation, dry skin, immune hypersensitivity, organ damage, and photosensitivity (Lee et al., 2014). Specially, the long-term use of antibiotics may even induce bacterial resistance, which makes some antibiotics become ineffective for acne vulgaris (Nakase et al., 2014; Cong et al., 2019). Therefore, it is essential to develop alternative therapeutic agents with fewer adverse effects and high efficacy (Habeshian and Cohen, 2020).

Antimicrobial peptides (AMPs) are the important effectors of the innate immune system in the skin and provide the first line of defense against invading microorganisms (Woodburn et al., 2019), (Mansour et al., 2014). Typically, AMPs which are generally amphipathic and cationic can electrostatically interact with the anionic bacterial membrane and cause membranolysis (Wimley, 2010). In addition to the well-known antimicrobial properties, AMPs also have other effects like anti-inflammation, lipopolysaccharide (LPS) or/and lipoteichoic acid (LTA) binding, bacterial agglutination and so on (Heinbockel et al., 2013; Xu and Lai, 2015; Zeng et al., 2018; Ye et al., 2020). For example, cathelicidin-PY has both antimicrobial and anti-inflammatory activities, FM-CATH can not only trigger the agglutination of bacteria but also bind to LPS and LTA, and LL-37 can modulates the immune responses (Wei et al., 2013; Hancock et al., 2016; Wu et al., 2021). Compared with conventional antibiotics, AMPs are able to modulate host immune responses and less likely to cause microbial resistance in the short term due to the distinct modes of action (Zelezetsky et al., 2006). Thus, AMPs can be potential candidate for treating acne vulgaris and some of them are reported to show treatment potential for acne vulgaris by direct killing bacteria and inhibiting Toll-like receptor 2 (TLR2)-induced NF-κB activation (Marta Guarna et al., 2006).

We previously identified and characterized a novel AMP, Cath-MH, from the skin of the frog *Microhyla heymonsivogt*, which possesses single α-helical structure in membrane-mimetic environments. Cath-MH can kill fungi and bacteria, bind LPS, and inhibit LPS- as well as cecal ligation and puncture-induced sepsis through its antimicrobial, LPS-neutralizing, coagulation suppressing effects as well as suppression of MAPK signaling (Chai et al., 2021). Taking into account the bioactivities of Cath-MH, our present study is conducted to assess the anti-*P. acnes* and anti-inflammatory properties of Cath-MH *in vitro* and *in vivo*. Our results suggest that Cath-MH might be an excellent therapeutic agent for acne vulgaris.

MATERIALS AND METHODS

Animals and Ethics Statement

All six-week-old BALB/c mice were obtained from the Laboratory Animal Center of Southern Medical University, and were reared in the SPF facility at Southern Medical University. The animal experiments were carried out in the light of the approval and guidelines of Animal Care and Use Committee of Southern Medical University. All procedures in this study strictly complied with the Animal Welfare Act and principles stated in the Guide for the Care and Use of Laboratory Animals, National Research Council, 1996.

Peptide Synthesis

Cath-MH (APCKLGCKIKKVKQKIKQKLKAKVNAVKTVIGK ISEHLG) and FITC-labeled Cath-MH were synthesized by GL Biochem Ltd. (Shanghai, China), and then were further purified and identified as described in our previous report (Chai et al., 2021).

P. acnes Proliferation Inhibition Analysis

Minimum inhibitory concentration (MIC) and minimum bactericidal concentration (MBC) of Cath-MH against *P. acnes* ATCC 6919 and ATCC 11827 were determined using two-fold broth dilution method as previously described by us (Ye et al., 2020). Specifically, two strains *P. acnes* ATCC 6919 and ATCC 11827 acquired from Guangdong Institute of Microbiology were grown in brain heart infusion (BHI) broth (HKM, China) under MGC Anaeropack systems (Mitsubishi, Gas Chemical, Japan) which provides anaerobic conditions. A two-fold serial dilution of peptide was added to 96-well plate (Costar, Corning, United States) at final concentrations of 0.78, 1.56, 3.13, 6.25, 12.5, 25, and 50 μM before an equal volume of bacteria in fresh BHI broth (the microbial loading was 10^6 CFU/ml) was loaded. After 72 h incubation at 37°C, the absorbance measurement of *P. acnes* suspension solution was done at 600 nm with microplate reader (Infinite M1000 Pro, Tecan Company, Switzerland). As a positive control, clindamycin (Sigma, United States) was used. MIC was defined as the minimum concentration inhibiting visible growth. To determine the minimum concentration of Cath-MH causing bacterial death, MBC was then determined following the MIC assay. 10 μl of sample which exhibited no evident growth after 72 h incubation was inoculated onto BHI agar plates. These plates were placed at 37°C for another 72 h under an anaerobic atmosphere. The MBC was defined as the peptide concentration at which there was no colony growth (Andrä et al., 2005).

Bacterial Killing Kinetic Assay

The bacterial killing kinetics of Cath-MH against *P. acnes* ATCC 6919 were carried out according to our previous method with minor modification (Ye et al., 2020). Briefly, Cath-MH at final concentration of 1× MIC was mixed with an equal volume of bacteria in fresh BHI broth under an anaerobic atmosphere. Duplicate samples were withdrawn at various timepoints (0, 15, 30, 60, 90, 120, 150, and 180 min) and spread on BHI agar plates. The 0 timepoint represents the sample withdrawn immediately after mixing. Viable colonies were counted after incubation of the plates for 72 h at 37°C under anaerobic conditions. Clindamycin at 1× MIC value and sterile saline were applied as the positive and negative control, respectively.

Bacterial Agglutination Test

The bacterial agglutination assay was done according to the method previously reported by us (Wu et al., 2021). In brief, *P. acnes* ATCC 6919 at exponential phase were harvested, washed twice and diluted to 2.0×10^8 CFU/ml of density with fresh BHI broth and incubated with BSA, Cath-MH (2× MICs), or Cath-MH (2× MICs) plus equal volume of 0.2 mg/ml LPS (L2880, *Escherichia coli* O55:B5, Sigma, United States) or 0.2 mg/ml LTA (L2512, *Staphylococcus aureus*, Sigma, United States) at 37°C for 30 min. The mixture was dropped on a glass slide and dyed with a Gram staining kit (Solarbio Technology, Beijing), and the results were observed under an oil microscope (Nikon Corporation, Japan).

Circular Dichroism Measurement

The Circular Dichroism (CD) measurement was performed to study the interaction of Cath-MH with LTA or LPS. In brief, Cath-MH was prepared in H_2O or 30 mM SDS solution. Then, LTA or LPS (0.2 mg/ml) was loaded to the peptide solution (50 μM) for 1 h at room temperature, respectively. Binding of Cath-MH to LTA or LPS was studied by monitoring the change in its secondary structure. CD measurement was then carried out with Jasco-810 spectropolarimeter (Jasco, Japan). CD data were presented as the mean residue ellipticity (θ) of three consecutive scans per sample in $deg{\cdot}cm^2{\cdot}dmol^{-1}$.

LTA Binding Assay

LTA binding of Cath-MH was further confirmed by measuring the inhibitory effects of LTA on the antimicrobial activity of Cath-MH against *P. acnes* ATCC 6919. In detail, LTA at concentrations (0, 0.0625, 0.125, 0.25, and 0.5 mg/ml) dissolved in sterile saline was mixed with 0.5, 1, and 2× MICs of Cath-MH for 30 min. Then, an equal volume of 10^6 CFU/ml bacterial suspension in fresh BHI broth was added to the above mixture before coated on BHI agar plates. After anaerobic incubation for 72 h, the number of colonies were calculated. All experiments were repeated three times.

Membrane Permeability and Morphology Alteration Analysis

To ensure the underlying mechanism of action of Cath-MH against *P. acnes* ATCC 6919, confocal laser scanning microscopy (CLSM) and scanning electron microscopy (SEM) experiments were performed for determination of the membrane permeability and morphological changes of *P. acnes*. Briefly, *P. acnes* ATCC 6919 at logarithmic growth phase were diluted to 10^6 CFU/ml and incubated with Cath-MH (2× MICs) for 30 min at 37°C. SYTO9 and PI staining (LIVE/DEAD® BacLight kit, Invitrogen, USA) was added to the bacterial suspensions, followed by incubation for 30 min at room temperature in the dark. CLSM (Leica TCS SP5, Leica Microsystems, Germany) was used to detect SYTO9 and PI with the excitation/emission spectrum of 480 and 635 nm, respectively. For SEM observation, bacterial suspensions at logarithmic growth phase were incubated with Cath-MH (2× MICs) for 30 min at 37°C. Then, *P. acnes* were harvested by centrifugation, sequentially fixed with 4 and 2.5% glutaraldehyde solution at room temperature for 4 h and 2.5% at 4°C overnight, respectively. After three times of wash with PBS, bacteria were dehydrated sequentially with 30, 50, 70, 85, 90, and 100% ethanol solution, followed by tert-Butyl alcohol, and dried in a freeze dryer (Quorum, UK). After gold coating, bacterial morphology was visualized by JSM-840 instrument (Hitachi, Japan) at the magnification of ×50,000.

Cytotoxic Analysis

The cytotoxicity of Cath-MH on RAW 264.7 cells was measured by the MTT method as reported previously by us (Zeng et al., 2020). In short, RAW 264.7 cells at a density of 5,000 cells per well were plated in 96-well plates and grown with medium DMEM in the presence or absence of continuous concentrations of Cath-MH (2.5, 5, 10, 20, and 40 μM) at 37°C for 24 h before MTT was added in the dark and the culture was continued for another 4 h. The supernatant was discarded and DMSO was loaded before the absorbance at 490 nm as measured. The experiment was repeated at least three times.

Membrane Binding Assays

Membrane binding assays were undertaken with FITC-labeled Cath-MH. In short, RAW 264.7 murine macrophage cells in the logarithmic phase of growth were prepared in PBS at a density of 1×10^5 cells/ml and incubation with FITC-labeled Cath-MH (0, 2, 4, 8, and 16 μM) at 37°C for 30 min. The unbound peptide was washed out with PBS containing 1% BSA in advance. Cell fluorescence intensity was detected with a FACscan flow cytometer (Becton Dickinson, United States), representing the ability to bind to cell membranes. Cells without peptide treatment were regarded as the negative control.

NO and Pro-Inflammatory Cytokine Measurement

RAW 264.7 murine macrophage cells at the density of 1×10^5 cells per well were added into 24-well plates and grown for 12 h for adherence. The cells were pretreated with Cath-MH (0, 1, 2, 4, and 8 μM) for 1 h and then co-incubated with LTA (10 μg/ml) or LPS (100 ng/ml) for 24 h. Then, the culture supernatants were used for analysis of NO production by Griess reagent (Beyotime Biotechnology, China) and IL-1β, IL-6, and TNF-α levels using enzyme linked immunosorbent assay (ELISA) (Thermo Fisher Scientific, United States) in light of the manufacturer's manuals.

Quantitative Real-Time PCR

RAW 264.7 murine macrophage cells at the density of 1×10^6 cells per well were added into 6-well plates and cultured for 12 h for adherence. The cells were pretreated with Cath-MH (0, 1, 2, 4, and 8 μM) for 1 h and then stimulated with LTA (10 μg/ml) or LPS (100 ng/ml) for 6 h at 37°C in 5% CO_2. Cells were subsequently harvested to measure the mRNA levels of iNOS, IL-1β, IL-6, TNF-α, TLR2, and TLR4 by qRT-PCR as reported previously by Zeng (Zeng et al., 2018). GAPDH gene was applied as a control to standardize the amount of the sample mRNA.

TABLE 1 | Anti-*P. acnes* activity of Cath-MH.

Microorganisms	MIC (μM)		MBC (μM)	
	Cath-MH	Clindamycin	Cath-MH	Clindamycin
P. acnes ATCC 6919	1.56	3.39	1.56	6.77
P. acnes ATCC 11827	1.56	3.39	1.56	13.54

Forty amplification cycles were required to complete exponential amplification.

Western Blot Analysis

RAW 264.7 murine macrophage cells were plated in 6-well plates at the density of 1×10^6 cells/well and grown for 12 h for adherence. The cells were pretreated with Cath-MH (0, 1, 2, 4, and 8 μM) for 1 h and then stimulated with LTA (10 μg/ml) or LPS (100 ng/ml) at 37°C for 30 min in 5% CO_2. After that, the cells were lysed with RIPA lysis buffer (Beyotime Biotechnology, China) and proteins were extracted using commercial kit (Cayman Chemical, United States) in light of the manufacturer's recommendations. Primary antibodies of phospho-ERK/ERK, phospho-JNK/JNK, phosphor-p38/p38, NF-κB p65, Lamin A/C and GAPDH (1: 1,500, Cell Signaling Technology, United States) and horseradish peroxidase conjugated secondary antibodies (1: 2,000, Cell Signaling Technology, United States) were applied in western blot analysis. All experiments were repeated three times.

In vivo Anti-Acne Analysis

The *in vivo* anti-acne effect of Cath-MH was evaluated using the procedure described previously by us (Ye et al., 2020). Six-week-old BALB/c mice weighing about 22 g were randomly subdivided into four groups ($n = 6$). Approximately 25 μl of *P. acnes* (5×10^8 CFU/ml) was intradermally administrated into the left ears of mice and the control mice received an equivalent volume of PBS. Clindamycin (10 μg) and Cath-MH (50 μg) were mixed in 50 mg of sterile vaseline and then were painted onto the ear surfaces, respectively. The ear thickness was measured at 24 h with a micro-caliper (Mitutoyo, Japan) after *P. acnes* injection. Afterwards, mice were sacrificed and ears were sampled for bacterial cell counts, histopathological assay, ELISA, qRT-PCR, and western blot detection.

Statistical Analysis

qRT-PCR data were calculated with the $2^{-\Delta\Delta CT}$ method. All data were expressed as mean ± SEM. Statistical analysis were carried out using one-way ANOVA. $^*p < 0.05$, $^{**}p < 0.01$, and $^{***}p < 0.001$ were considered statistically significant as compared to control.

RESULTS

Anti-*P. acnes* Activity

The effect of Cath-MH on *P. acnes* was determined using MIC and MBC assays. As shown in **Table 1**, both MIC and MBC values of Cath-MH against *P. acnes* ATCC 6919 and ATCC 11827 were about 1.56 μM. However, the MICs of clindamycin against two stains were about 3.39 μM. Moreover, its MBCs against *P. acnes* ATCC 6919 and ATCC 11827 were approximately 6.77 and 13.54 μM, respectively. Therefore, Cath-MH has more potent anti-*P. acnes* activity than the positive control clindamycin.

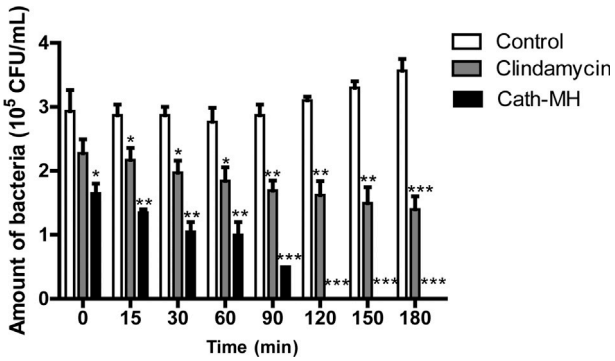

FIGURE 1 | Killing kinetics of Cath-MH against *P. acnes* ATCC 6919. Bacteria were treated with Cath-MH at their 1× MIC of concentration for different time. Clindamycin was used as the positive control. Data are represented as mean ± SEM ($n = 3$) $^*p < 0.05$, $^{**}p < 0.01$, and $^{***}p < 0.001$ were considered statistically significant as compared to the corresponding control groups incubated with sterile saline for different time.

To further explore the anti-*P. acnes* activity of Cath-MH, its bacterial killing kinetics against *P. acnes* ATCC 6919 was evaluated. As seen in **Figure 1**, Cath-MH (1× MIC) exhibited potent bactericidal activity within 120 min of incubation. However, under same circumstances, clindamycin (1× MIC) showed much slower killing kinetic, which could not completely kill bacteria in 180 min.

P. acnes Agglutination and LTA/LPS Binding Activities

Cath-MH can agglutinate *E. coli* ATCC 25922 (Chai et al., 2021). Therefore, we measured its agglutination activity against *P. acnes* ATCC 6919. As shown in **Figure 2A**, Cath-MH displayed a high agglutinating activity after incubation with *P. acnes* for 30 min (panel b) when compared with the control treated with BSA (panel a). However, this agglutination was abolished by 0.2 mg/ml LPS (panel c) and 0.2 mg/ml LTA (panel d), respectively, indicating that Cath-MH could bind LPS and LTA.

The LTA/LPS-binding ability of Cath-MH was further supported by CD spectroscopy and antimicrobial assay. As presented in **Figure 2B**, in the presence of LTA or LPS, Cath-MH showed

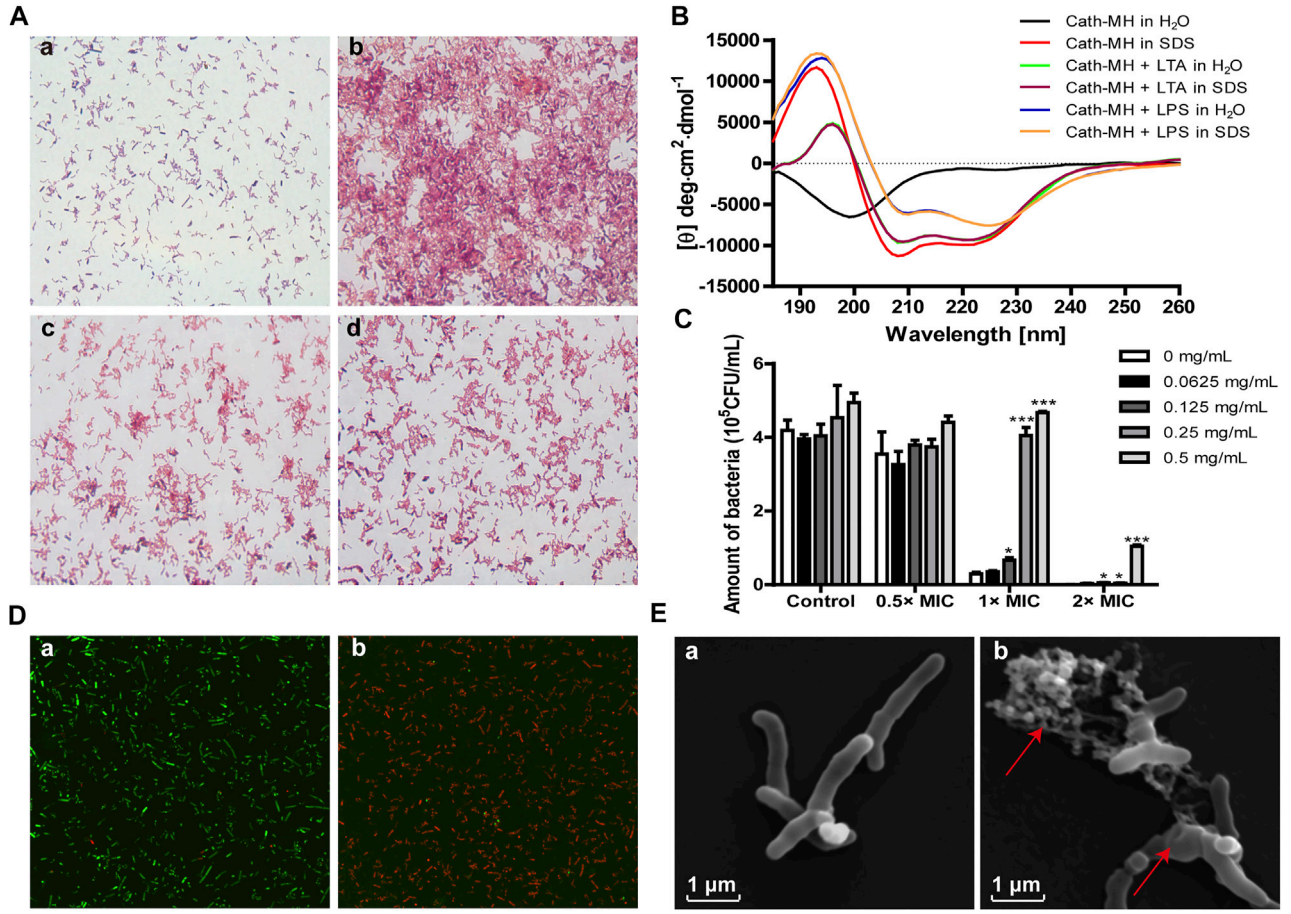

FIGURE 2 | Anti-*P. acnes* mechanism of Cath-MH. **(A)** Agglutination of *P. acnes* ATCC 6919 by Cath-MH. *P. acnes* were incubated with BSA (a), Cath-MH (2× MICs) (b), and Cath-MH (2× MICs) plus equal volume of 0.2 mg/ml LPS (c) or 0.2 mg/ml LTA (d) for 30 min before being stained with Gram staining kit. **(B)** CD spectra of 50 μM Cath-MH in different solutions. **(C)** Suppression of LTA on the anti-*P. acnes* activity of Cath-MH. Cath-MH at the concentrations of 0.5×, 1× and 2× MICs were mixed with indicated concentrations of LTA for 30 min and then incubated with *P. acnes* for 72 h before its MIC was measured. **(D)** CLSM observation. *P. acnes* treated with sterile saline (a), or Cath-MH (2× MICs, b) for 30 min, respectively. **(E)** SEM observation. *P. acnes* treated with sterile saline (a), or Cath-MH (2× MICs, b) for 30 min, respectively. Data are expressed as mean ± SEM (n = 3). *$p < 0.05$, ***$p < 0.001$ were considered statistically significant compared with the control group without LTA.

obviously different CD spectra which were similar to peptide dissolved in SDS solution. Furtherly, the suppression effects of increasing concentrations of LTA on antimicrobial activities of Cath-MH at 0.5, 1, and 2× MICs against *P. acnes* were examined. As expected, LTA alone did not change the proliferation of *P. acnes*. However, the anti-*P. acnes* activities of Cath-MH at 1× and 2× MICs were significantly decreased after incubation with LTA at concentrations ranging from 0.0625 mg/ml to 0.5 mg/ml for 30 min. Moreover, this inhibitory effect depended on the concentration of LTA (**Figure 2C**).

Effects on the Cell Membrane of *P. acnes*

AMP generally starts their killing bacteria process promptly once their attraction and attachment to microbial surfaces (Vineeth Kumar and Sanil, 2017). CLSM was carried to ensure the permeabilization of bacteria caused by Cath-MH. The results showed the Cath-MH-treated group with intense red fluorescence, which confirmed the majority of *P. acnes* with damaged membranes, while the untreated group showed intense green fluorescence which indicated with intact cell membrane (**Figure 2D**). To better understand the mechanism of action of Cath-MH against *P. acnes*, SEM was used. As shown in **Figure 2E**, after Cath-MH treatment, *P. acnes* had changed in morphology including obviously wrinkling and cell contents releasing (areas indicated by arrow) compared to the control group. Altogether, these data demonstrated that the Cath-MH treatment could effectively destroy the bacterial cell membrane and then kill bacteria, like most AMPs.

Suppression of Inflammatory Factor and TLR2/4 Expression Induced by LTA/LPS

Some AMPs can bind to their targets on the surface of macrophages, and then set off cellular signaling pathway and regulate the secretion of pro-inflammatory factors (Wang et al., 2011; Wei et al., 2015; Magrone et al., 2018; Zeng et al., 2018;

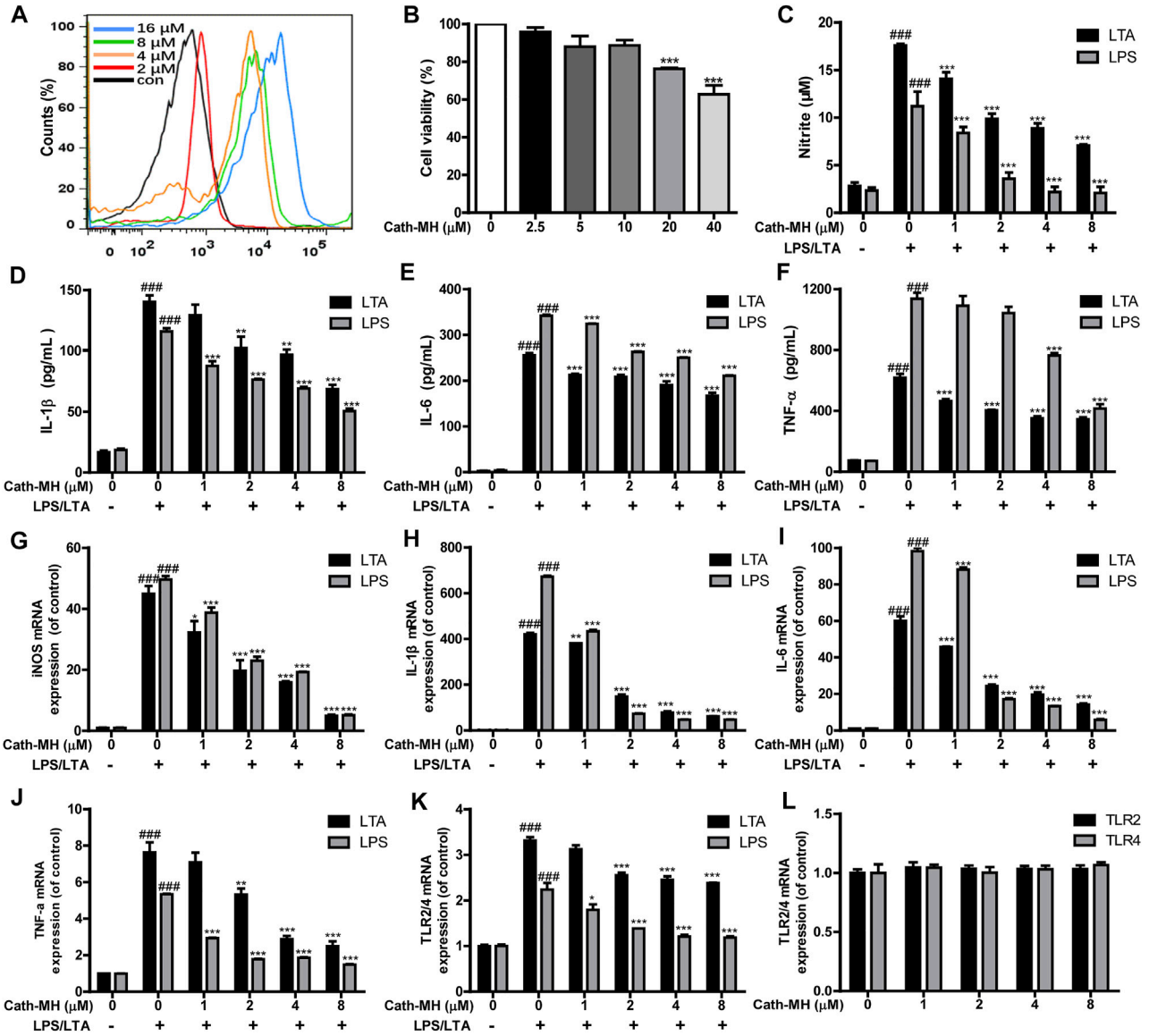

FIGURE 3 | Suppression effects of Cath-MH on inflammatory cytokine and TLR2/4 expression stimulated by LTA or LPS. **(A)** Flow cytometry analysis of interaction between FITC-labeled Cath-MH and RAW 264.7 cells. **(B)** Cytotoxicity of Cath-MH towards RAW 264.7 cells. **(C–F)** Effects of Cath-MH on nitrite **(C)**, IL-1β **(D)**, IL-6 **(E)**, and TNF-α **(F)** levels stimulated by LTA or LPS. **(G–J)** Effects of Cath-MH on the mRNA levels of iNOS **(G)**, IL-1β **(H)**, IL-6 **(I)**, and TNF-α **(J)**. **(K,L)** Effects of Cath-MH on the mRNA levels of TLR2/4 induced by LTA/LPS **(K)** or without LTA/LPS stimulation **(L)**. Data are reported as mean ± SEM ($n = 3$). $^{###}p < 0.001$, significantly different compared with the control group without LTA/LPS and Cath-MH; $^{*}p < 0.05$, $^{**}p < 0.01$, $^{***}p < 0.001$ were significantly different compared with the control group with LTA/LPS but without Cath-MH treatment.

Kasus-Jacobi et al., 2020; Chai et al., 2021). Therefore, the binding of Cath-MH to RAW 264.7 cells were evaluated with flow cytometry. As displayed in **Figure 3A**, Cath-MH could concentration-dependently bind to RAW 264.7 cells after co-incubation for 30 min. To define whether Cath-MH can affect the release of inflammatory factors in RAW 264.7 cells stimulated by LTA/LPS, we tested firstly its effect on the viability of RAW 264.7 cells. As shown in **Figure 3B**, Cath-MH at the concentrations of less than and equal to 10 μM had no cytotoxicity toward RAW 264.7 cells. Thus, we further investigated whether Cath-MH at the concentration of lower than 10 μM could inhibit the generation of inflammatory factors induced by LPS/LTA. As shown in **Figures 3C–J**, both 100 ng/ml LPS and 10 μg/ml LTA significantly increased the protein and mRNA contents of NO, IL-1β, IL-6, and TNF-α in the cell culture supernatants in comparison with the control without any treatment. However, the enhanced expressions induced by LPS/LTA were markedly reversed by Cath-MH in concentration-dependent manner. LTA/LPS as the TLR2/4 agonist can induce the TLR2/4-mediated inflammatory response and the expression elevation of TLR2/4 at mRNA and protein levels, respectively (Kwak et al., 2015). Therefore,

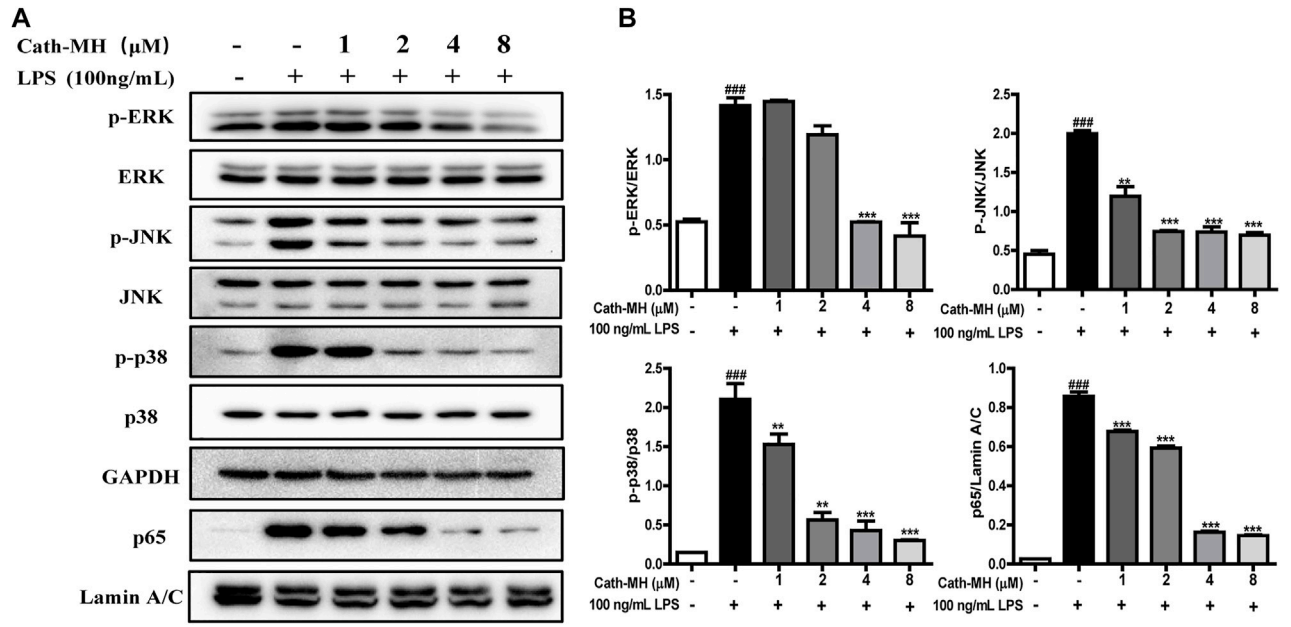

FIGURE 4 | Effects of Cath-MH on inflammatory response pathways in LPS-activated RAW 264.7 cells. **(A)** Western blot of ERK, JNK, p38, and NF-κB p65 in LPS-stimulated RAW 264.7 cells. GAPDH were served as the internal control and Lamin A/C served as the nuclear control. **(B)** Ratios of phosphorylated ERK, JNK, p38 to corresponding total protein and NF-κB p65 to Lamin A/C, respectively. Band densities were analyzed using ImageJ software (NIH Image, United States). Data are reported as mean ± SEM (n = 3). $^{###}p < 0.001$ significantly different compared with the control group without LPS and Cath-MH; $^{**}p < 0.01$, $^{***}p < 0.001$, significantly different compared to the control group with LPS but without Cath-MH treatment.

we examined whether or not the suppressive effects of Cath-MH on LTA/LPS-induced cytokine production was correlated to TLR2/4 expression. The results showed that, with Cath-MH pre-treatment, TLR2/4 mRNA expression induced by LTA/LPS was downregulated (**Figure 3K**). However, without LTA/LPS stimulation, Cath-MH did not change TLR2/4 mRNA expression (**Figure 3L**), suggesting that the effect of Cath-MH on inflammatory factor expressions is associated with its suppression of TLR2/4 mRNA expression stimulated by LTA/LPS.

Inhibition of LPS-Activated Inflammatory Response Pathways

It has been well known that MAPK/NF-κB signaling pathways play a vital role in pro-inflammatory process by regulating the expression of inflammatory factors including IL-1β, IL-6, and TNF-α. Therefore, we evaluated the effects of Cath-MH on MAPK/NF-κB signaling pathways in LPS-stimulated RAW 264.7 cells using western blot. As presented in **Figure 4**, LPS (100 ng/ml) significantly increased the expression of phosphorylated ERK, JNK, p38, and the nuclear translocation of NF-κB p65 when compared to the control group. However, this upregulation induced by LPS was significantly repressed by Cath-MH in a dose-dependent manner.

Anti-Acne Effects *In Vivo*

The *in vivo* anti-acne activity of Cath-MH was explored using acne mouse model. As shown in **Figure 5**, following *P. acnes* injection, the ears of mice became red and swollen. However, like clindamycin, Cath-MH obviously relieved *P. acnes*-induced ear redness and swelling (**Figures 5A,B**). Moreover, as shown in **Figure 5C**, both Cath-MH and clindamycin substantially decreased the number of *P. acnes* colonized in the ear when compared with the model group only injected by *P. acnes* suspensions. To explore its effects on inflammation induced by *P. acnes,* histopathological analysis and cytokine expression measurement were also performed. As shown in **Figure 5D,** the infiltration of inflammatory cell and ear swelling were obviously increased in the ear injection of *P. acnes* when compared with the control sample. Nevertheless, it was significantly decreased after Cath-MH or clindamycin treatment. Consistently, following 24 h injection of *P. acnes*, both protein and mRNA expressions of TNF-α, IL-1β and IL-6 were all significantly upregulated. Yet, their upregulations were markedly reversed after treatment with Cath-MH or clindamycin (**Figures 5E,F**). To further clear the protective mechanism of Cath-MH in acne vulgaris mice, MAPK/NF-κB signaling pathways were investigated by western blotting (**Figures 5G,H**). Consistent with their effects on cytokine expression *in vitro*, injection of *P. acnes* significantly upregulated the expression of phosphorylated ERK, JNK, p38 and p65 translocated in nucleus of ear tissues when compared with vehicle. However, treatment with Cath-MH and clindamycin successfully suppressed these increases but had no influence on total ERK, JNK, and p38 expression. Together, these data demonstrated that the Cath-MH treatment can effectively improve acne vulgaris in mice.

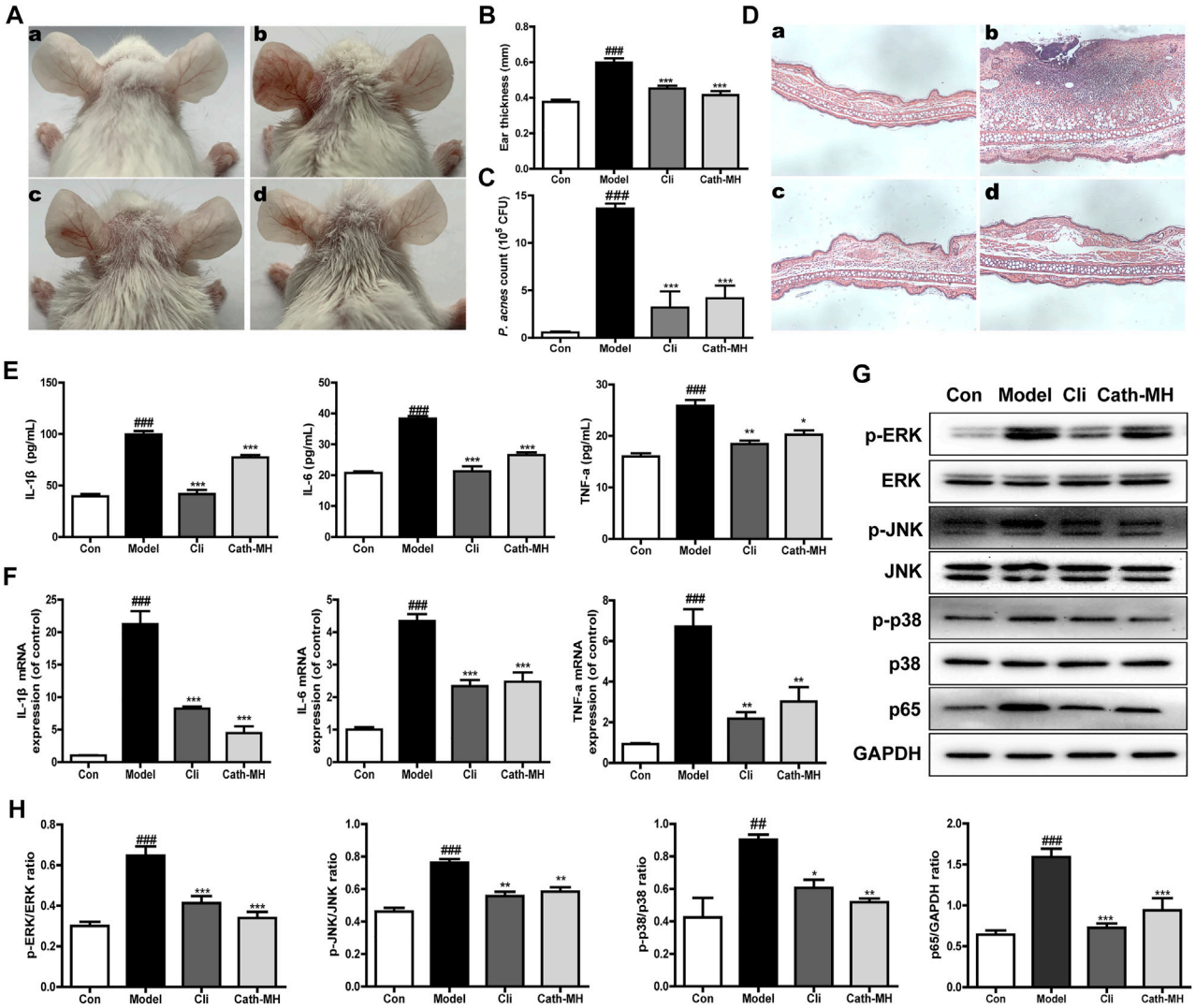

FIGURE 5 | Effects of Cath-MH on acne vulgaris in mice. **(A)** Representative ear photographs after *P. acnes* exposure for 24 h. **(B)** Statistical analysis of mice ear thickness. **(C)** Statistical analysis of the counts of *P. acnes* in mice ear. **(D)** Histopathological analysis of mouse ear. **(E,F)** The protein and mRNA levels of IL-1β, IL-6, and TNF-α in mouse ear. **(G)** Western blot of ERK, JNK, p38, and NF-κB p65 in mouse ear. **(H)** Ratio of phosphorylated ERK, JNK, p38, and NF-κB p65 to total protein. In **(A)** and **(D)**, panels a–d represent images captured from the mouse ear administrated by sterile saline (a), *P. acnes* (b), 10 μg of clindamycin (c) and 50 μg of Cath-MH (d) after injection of *P. acnes*, respectively. In column and WB graphs, con, model, cil and Cath-MH represent the statistical data in control, model, clindamycin- and Cath-MH-treated groups which are presented as the mean ± SEM ($n = 5$). $^{###}p < 0.001$ significantly different compared to the control group; $^{*}p < 0.05$, $^{**}p < 0.01$, $^{***}p < 0.001$ significantly different compared to the model group.

DISCUSSION

Acne vulgaris is a chronic inflammatory conditions of the skin, concerning colonization of *P. acnes*, and subsequent activation of immune cells (Vowels et al., 1995), then ensuing excessive secretion of pro-inflammatory cytokines such as IL-1β, IL-6 and TNF-α which in turn results in inflammatory cascade and tissue injury (Vowels et al., 1995; Dréno, 2017). Therefore, it is generally considered as promising treatment for acne vulgaris to inhibit colonization of *P. acnes* and harmful inflammatory response (Cong et al., 2019; Habeshian and Cohen, 2020). Several AMPs such as Esc-1GN, LZ1, and Cathelicidin-BF are reported to show potent treatment potential for Acne vulgaris because of their suppressive effects on *P. acnes* and inflammation (Wang et al., 2011; Zhang et al., 2013; Ye et al., 2020). In our study, the overwhelming evidences have confirmed that Cath-MH can kill and agglutinate *P. acnes*, bind LTA/LPS, and suppress inflammation induced by *P. acnes in vitro* and *in vivo*. Furtherly, Cath-MH can more strongly and quickly inhibit the growth of the tested *P. acnes in vitro* than clindamycin which is an antibiotic frequently used to treat acne vulgaris (**Figure 1**; **Table 1**). Secondly, agglutination of *P. acnes by* Cath-MH prevents dissemination of the infection focus and facilitates the infection clearance by the host innate cells

(**Figure 2A**). Thirdly, it makes less likely to induce bacterial resistance that Cath-MH directly kills *P. acnes* by the membrane disruption mechanism (**Figures 2D,E**) (Yeaman and Yount, 2003). Finally, Cath-MH is relatively low cytotoxicity to mammal cells and high stability *in vitro* and *in vivo* (Chai et al., 2021). Taken together, these findings suggest that Cath-MH with anti-*P. acnes* and anti-inflammatory activity is an excellent candidate drug molecule against acne.

The engagements of TLR4 by LPS and TLR2 by LTA trigger the activation of downstream intracellular NF-κB/MAPK signaling pathways, consequently causing the generation of pro-inflammatory mediators such as TNF-α, IL-1β and IL-6 (Wu et al., 2017). Human LL-37 and chicken CATH-2 have been reported to suppress TLR2/4 activation by directly interaction with the outer membrane-derived lipoproteins and LPS (Coorens et al., 2017). In addition, cationic peptide P5 suppresses TLR2-to-NF-κB signaling by binding to LTA, thereby inhibiting the production of inflammatory factors (Ryu et al., 2015). Considering that Cath-MH can bind to LPS (Chai et al., 2021) as well as LTA (**Figures 2A–C**), we conjectured that Cath-MH has anti-inflammatory effects related to TLR2/4. Macrophages as crucial immune cells are involved in the regulation of many chronic inflammatory diseases including Acne vulgaris through the secretion of a great deal of pro-inflammatory cytokines and chemokines (Kim, 2005; Navegantes et al., 2017), and are extensively used as an *in vitro* inflammation model assessing the potential protection of a drug (Lee et al., 2020; Nguyen et al., 2020). Thus, in this study, we used RAW 264.7 murine macrophage cells to identify the anti-inflammation effects and underlying mechanism of Cath-MH (Zhao et al., 2017). In agreement with our assumption, Cath-MH is found to significantly inhibit the TLR2/TLR4 expression, inflammatory factor secretion and MAPK/NF-κB pathway activation in RAW 264.7 cells stimulated by LPS/LTA (**Figures 3**, **4**). Cath-MH also produces similar effects in mouse ears with exposure to *P. acnes* (**Figure 5**). It has been described that both *P. acnes* and its important component, LTA, can induce not only TLR2/4 expression but also pro-inflammatory cytokine release associated with TLR2/4 signaling pathways *in vitro* and *in vivo* (Jugeau et al., 2005; Kwak et al., 2015; Dréno, 2017; Suvanprakorn et al., 2019). Therefore, Cath-MH may have anti-inflammatory effects by binding LPS/LTA and blocking TLR2/4-mediated MAPK/NF-κB signaling pathways in macrophage cells and acne mouse models.

Some AMPs like Hc-CATH and HPA_3NT_3 have been reported to, respectively, bind TLR4 or TLR2, accordingly suppressing the activation of TLR2/4-mediated signaling pathways (Ni et al., 2014; Ryu et al., 2014; Wei et al., 2015). As shown in **Figure 3A**, Cath-MH can bind directly to the surface of RAW 264.7 cells. Additionally, Cath-MH can also reduce carrageenan-stimulated inflammation in mouse paw in the absence of LPS and LTA (Data not shown). Thus, it is possible that Cath-MH bind its receptors on the membranes of macrophages, consequently inhibiting the activation of MAPK/NF-κB pathways and the transcription of NO and other inflammatory cytokines *in vitro* and *in vivo*. Therefore, further study is necessary to explore its anti-inflammatory mechanism of Cath-MH. Finally, our previous studies have showed that Cath-MH reduces the LPS-induced inflammation in sepsis (Chai et al., 2021). In the present study, Cath-MH attenuates LTA- and *P. acnes*-induced inflammation, which extends the scope of inflammatory agonists antagonized by Cath-MH and help to clarify its anti-inflammation mechanism.

In conclusion, we demonstrate that Cath-MH exerts direct antimicrobial effects against *P. acnes* by aggregation of bacterial cells and disruption of the bacterial cell membrane. Cath-MH also binds to LTA/LPS, inhibits LTA/LPS-stimulated TLR2/4 expression, and subsequently reduces the production of the inflammatory cytokines through blocking MAPK/NF-κB signaling pathways *in vitro*. Consistently, Cath-MH displays both anti-*P. acnes* and anti-inflammatory effects in *P. acnes*-stimulated mouse model via inhibition of *P. acnes* proliferation, inflammatory cytokines expression as well as MAPK/NF-κB signaling activation. Taken together, these findings indicate that Cath-MH can potentially serve as an effective therapeutic agent for the treatment of acne vulgaris.

DATA AVAILABILITY STATEMENT

The raw data supporting the conclusion of this article will be made available by the authors, without undue reservation.

ETHICS STATEMENT

The animal study was reviewed and approved by the Animal Care and Use Committee of Southern Medical University.

AUTHOR CONTRIBUTIONS

JW, RG, JC, WX, MT, and WL performed experiments and analyzed data; XX designed experiments, supervised the study, evaluated the data and revised the manuscript for publication. All authors contributed to the manuscript and have given approval to the final version of the manuscript.

FUNDING

This research was funded by National Natural Science Foundation of China, grant numbers 31772476, 31861143050, and 31911530077.

REFERENCES

Andrä, J., Lohner, K., Blondelle, S. E., Jerala, R., Moriyon, I., Koch, M. H., et al. (2005). Enhancement of Endotoxin Neutralization by Coupling of a C12-Alkyl Chain to a Lactoferricin-Derived Peptide. *Biochem. J.* 385, 135–143. doi:10.1042/BJ20041270

Chai, J., Chen, X., Ye, T., Zeng, B., Zeng, Q., Wu, J., et al. (2021). Characterization and Functional Analysis of cathelicidin-MH, a Novel Frog-Derived Peptide with Anti-septicemic Properties. *Elife* 10, 1. doi:10.7554/eLife.64411

Cong, T.-X., Hao, D., Wen, X., Li, X.-H., He, G., and Jiang, X. (2019). From Pathogenesis of Acne Vulgaris to Anti-acne Agents. *Arch. Dermatol. Res.* 311, 337–349. doi:10.1007/s00403-019-01908-x

Coorens, M., Schneider, V. A. F., de Groot, A. M., van Dijk, A., Meijerink, M., Wells, J. M., et al. (2017). Cathelicidins Inhibit Escherichia Coli-Induced TLR2 and TLR4 Activation in a Viability-dependent Manner. *J. Immunol.* 199, 1418–1428. doi:10.4049/jimmunol.1602164

Dréno, B. (2017). What Is New in the Pathophysiology of Acne, an Overview. *J. Eur. Acad. Dermatol. Venereol.* 31, 8–12. doi:10.1111/jdv.14374

Habeshian, K. A., and Cohen, B. A. (2020). Current Issues in the Treatment of Acne Vulgaris. *Pediatrics* 145, S225. doi:10.1542/PEDS.2019-2056L

Hancock, R. E., Haney, E. F., and Gill, E. E. (2016). The Immunology of Host Defence Peptides: Beyond Antimicrobial Activity. *Nat. Rev. Immunol.* 16, 321–334. doi:10.1038/nri.2016.29

Heinbockel, L., Sánchez-Gómez, S., Martinez de Tejada, G., Dömming, S., Brandenburg, J., Kaconis, Y., et al. (2013). Preclinical Investigations Reveal the Broad-Spectrum Neutralizing Activity of Peptide Pep19-2.5 on Bacterial Pathogenicity Factors. *Antimicrob. Agents Chemother.* 57, 1480–1487. doi:10.1128/AAC.02066-12

Jugeau, S., Tenaud, I., Knol, A. C., Jarrousse, V., Quereux, G., Khammari, A., et al. (2005). Induction of Toll-like Receptors by Propionibacterium Acnes. *Br. J. Dermatol.* 153, 1105–1113. doi:10.1111/j.1365-2133.2005.06933.x

Kasus-Jacobi, A., Land, C. A., Stock, A. J., Washburn, J. L., and Pereira, H. A. (2020). Antimicrobial Peptides Derived from the Immune Defense Protein CAP37 Inhibit TLR4 Activation by S100A9. *Invest. Ophthalmol. Vis. Sci.* 61, 16. doi:10.1167/iovs.61.4.16

Kim, J. (2005). Review of the Innate Immune Response in Acne Vulgaris: Activation of Toll-like Receptor 2 in Acne Triggers Inflammatory Cytokine Responses. *Dermatology* 211, 193–198. doi:10.1159/000087011

Kwak, M. S., Lim, M., Lee, Y. J., Lee, H. S., Kim, Y. H., Youn, J. H., et al. (2015). HMGB1 Binds to Lipoteichoic Acid and Enhances TNF-α and IL-6 Production through HMGB1-Mediated Transfer of Lipoteichoic Acid to CD14 and TLR2. *J. Innate Immun.* 7, 405–416. doi:10.1159/000369972

Lee, J.-H., Eom, S.-H., Lee, E.-H., Jung, Y.-J., Kim, H.-J., Jo, M.-R., et al. (2014). *In Vitro* antibacterial and Synergistic Effect of Phlorotannins Isolated from Edible Brown Seaweed *Eisenia bicyclis* against Acne-Related Bacteria. *ALGAE* 29, 47–55. doi:10.4490/algae.2014.29.1.047

Lee, S. G., Brownmiller, C. R., Lee, S. O., and Kang, H. W. (2020). Anti-inflammatory and Antioxidant Effects of Anthocyanins of trifolium Pratense (Red clover) in Lipopolysaccharide-Stimulated raw-267.4 Macrophages. *Nutrients* 12, 1. doi:10.3390/nu12041089

Magrone, T., Russo, M. A., and Jirillo, E. (2018). Antimicrobial Peptides: Phylogenic Sources and Biological Activities. First of Two Parts. *Curr. Pharm. Des.* 24, 1043–1053. doi:10.2174/1381612824666180403123736

Mansour, S. C., Pena, O. M., and Hancock, R. E. (2014). Host Defense Peptides: Front-Line Immunomodulators. *Trends Immunol.* 35, 443–450. doi:10.1016/j.it.2014.07.004

Marta Guarna, M., Coulson, R., and Rubinchik, E. (2006). Anti-inflammatory Activity of Cationic Peptides: Application to the Treatment of Acne Vulgaris. *FEMS Microbiol. Lett.* 257, 1–6. doi:10.1111/j.1574-6968.2006.00156.x

Nakase, K., Nakaminami, H., Takenaka, Y., Hayashi, N., Kawashima, M., and Noguchi, N. (2014). Relationship between the Severity of Acne Vulgaris and Antimicrobial Resistance of Bacteria Isolated from Acne Lesions in a Hospital in Japan. *J. Med. Microbiol.* 63, 721–728. doi:10.1099/jmm.0.067611-0

Navegantes, K. C., de Souza Gomes, R., Pereira, P. A. T., Czaikoski, P. G., Azevedo, C. H. M., and Monteiro, M. C. (2017). Immune Modulation of Some Autoimmune Diseases: The Critical Role of Macrophages and Neutrophils in the Innate and Adaptive Immunity. *J. Transl. Med.* 15, 36. doi:10.1186/s12967-017-1141-8

Nguyen, T., Chen, X., Chai, J., Li, R., Han, X., Chen, X., et al. (2020). Antipyretic, Anti-inflammatory and Analgesic Activities of *Periplaneta americana* Extract and Underlying Mechanisms. *Biomed. Pharmacother.* 123, 109753. doi:10.1016/j.biopha.2019.109753

Ni, W., Zhang, Q., Liu, G., Wang, F., Yuan, H., Guo, Y., et al. (2014). *Escherichia coli* Maltose-Binding Protein Activates Mouse Peritoneal Macrophages and Induces M1 Polarization via TLR2/4 *In Vivo* and *In Vitro*. *Int. Immunopharmacol.* 21, 171–180. doi:10.1016/j.intimp.2014.04.025

Ryu, S., Han, H. M., Song, P. I., Armstrong, C. A., and Park, Y. (2015). Suppression of Propionibacterium Acnes Infection and the Associated Inflammatory Response by the Antimicrobial Peptide P5 in Mice. *PLoS One* 10, e0132619. doi:10.1371/journal.pone.0132619

Ryu, S., Park, Y., Kim, B., Cho, S. M., Lee, J., Lee, H. H., et al. (2014). Inhibitory and Anti-inflammatory Effects of the Helicobacter Pylori-Derived Antimicrobial Peptide HPA3NT3 against Propionibacterium Acnes in the Skin. *Br. J. Dermatol.* 171, 1358–1367. doi:10.1111/bjd.13480

Suvanprakorn, P., Tongyen, T., Prakhongcheep, O., Laoratthaphong, P., and Chanvorachote, P. (2019). Establishment of an Anti-acne Vulgaris Evaluation Method Based on TLR2 and TLR4-Mediated Interleukin-8 Production. *In Vivo* 33, 1929–1934. doi:10.21873/invivo.11687

Tanghetti, E. A. (2013). The Role of Inflammation in the Pathology of Acne. *J. Clin. Aesthet. Dermatol.* 6, 27–35.

Vineeth Kumar, T. V., and Sanil, G. (2017). A Review of the Mechanism of Action of Amphibian Antimicrobial Peptides Focusing on Peptide-Membrane Interaction and Membrane Curvature. *Curr. Protein Pept. Sci.* 18, 1263–1272. doi:10.2174/1389203718666170710114932

Vowels, B. R., Yang, S., and Leyden, J. J. (1995). Induction of Proinflammatory Cytokines by a Soluble Factor of Propionibacterium Acnes: Implications for Chronic Inflammatory Acne. *Infect. Immun.* 63, 3158–3165. doi:10.1128/IAI.63.8.3158-3165.1995

Wang, Y., Zhang, Z., Chen, L., Guang, H., Li, Z., Yang, H., et al. (2011). Cathelicidin-BF, a Snake Cathelicidin-Derived Antimicrobial Peptide, Could Be an Excellent Therapeutic Agent for Acne Vulgaris. *PLoS One* 6, e22120. doi:10.1371/journal.pone.0022120

Wei, L., Gao, J., Zhang, S., Wu, S., Xie, Z., Ling, G., et al. (2015). Identification and Characterization of the First Cathelicidin from Sea Snakes with Potent Antimicrobial and Anti-inflammatory Activity and Special Mechanism. *J. Biol. Chem.* 290, 16633–16652. doi:10.1074/jbc.M115.642645

Wei, L., Yang, J., He, X., Mo, G., Hong, J., Yan, X., et al. (2013). Structure and Function of a Potent Lipopolysaccharide-Binding Antimicrobial and Anti-inflammatory Peptide. *J. Med. Chem.* 56, 3546–3556. doi:10.1021/jm4004158

Wimley, W. C. (2010). Describing the Mechanism of Antimicrobial Peptide Action with the Interfacial Activity Model. *ACS Chem. Biol.* 5, 905–917. doi:10.1021/cb1001558

Woodburn, K. W., Jaynes, J. M., and Clemens, L. E. (2019). Evaluation of the Antimicrobial Peptide, RP557, for the Broad-Spectrum Treatment of Wound Pathogens and Biofilm. *Front. Microbiol.* 10, 1688. doi:10.3389/fmicb.2019.01688

Wu, B. C., Lee, A. H., and Hancock, R. E. W. (2017). Mechanisms of the Innate Defense Regulator Peptide-1002 Anti-inflammatory Activity in a Sterile Inflammation Mouse Model. *J. Immunol.* 199, 3592–3603. doi:10.4049/jimmunol.1700985

Wu, J., Zhang, H., Chen, X., Chai, J., Hu, Y., Xiong, W., et al. (2021). FM-CATH, A Novel Cathelicidin from Fejervarya Multistriata, Shows Therapeutic Potential for Treatment of CLP-Induced Sepsis. *Front. Pharmacol.* 12, 1. doi:10.3389/fphar.2021.731056

Xu, X., and Lai, R. (2015). The Chemistry and Biological Activities of Peptides from Amphibian Skin Secretions. *Chem. Rev.* 115, 1760–1846. doi:10.1021/cr4006704

Ye, T., Wu, J., Xu, Z., Chai, J., Zeng, Q., Zeng, B., et al. (2020). Esc-1GN Shows Therapeutic Potentials for Acne Vulgaris and Inflammatory Pain. *J. Pept. Sci.* 26, e3269. doi:10.1002/psc.3269

Yeaman, M. R., and Yount, N. Y. (2003). Mechanisms of Antimicrobial Peptide Action and Resistance. *Pharmacol. Rev.* 55, 27–55. doi:10.1124/pr.55.1.2

Zelezetsky, I., Pontillo, A., Puzzi, L., Antcheva, N., Segat, L., Pacor, S., et al. (2006). Evolution of the Primate Cathelicidin. Correlation between Structural

Variations and Antimicrobial Activity. *J. Biol. Chem.* 281, 19861–19871. doi:10.1074/jbc.M511108200

Zeng, B., Chai, J., Deng, Z., Ye, T., Chen, W., Li, D., et al. (2018). Functional Characterization of a Novel Lipopolysaccharide-Binding Antimicrobial and Anti-inflammatory Peptide *In Vitro* and *In Vivo*. *J. Med. Chem.* 61, 10709–10723. doi:10.1021/acs.jmedchem.8b01358

Zeng, Q., Lu, W., Deng, Z., Wu, J., Guo, R., and Xu, X. (2020). Tablysin-15 Inhibits Osteoclastogenesis and LPS-Induced Bone Loss via Attenuating the Integrin αvβ3 Pathway. *Chem. Biol. Interact.* 327, 109179. doi:10.1016/j.cbi.2020.109179

Zhang, Z., Mu, L., Tang, J., Duan, Z., Wang, F., Wei, L., et al. (2013). A Small Peptide with Therapeutic Potential for Inflammatory Acne Vulgaris. *PLoS One* 8, e72923. doi:10.1371/journal.pone.0072923

Zhao, G., Jiang, K., Wu, H., Qiu, C., Deng, G., and Peng, X. (2017). Polydatin Reduces *Staphylococcus aureus* Lipoteichoic Acid-Induced Injury by Attenuating Reactive Oxygen Species Generation and TLR2-Nfkb Signalling. *J. Cell. Mol. Med.* 21, 2796–2808. doi:10.1111/jcmm.13194

Conflict of Interest: The authors declare that the research was conducted in the absence of any commercial or financial relationships that could be construed as a potential conflict of interest.

Publisher's Note: All claims expressed in this article are solely those of the authors and do not necessarily represent those of their affiliated organizations, or those of the publisher, the editors and the reviewers. Any product that may be evaluated in this article, or claim that may be made by its manufacturer, is not guaranteed or endorsed by the publisher.

frontiers in Pharmacology

ORIGINAL RESEARCH
published: 24 December 2021
doi: 10.3389/fphar.2021.795455

Voltage-Gated Sodium Channel Modulation by a New Spider Toxin Ssp1a Isolated From an Australian Theraphosid

*Yashad Dongol[1], Phil M. Choi[1], David T. Wilson[2], Norelle L. Daly[2], Fernanda C. Cardoso[1] and Richard J. Lewis[1]**

[1]Centre for Pain Research, Institute for Molecular Bioscience, The University of Queensland, Brisbane, QLD, Australia, [2]Centre for Molecular Therapeutics, Australian Institute of Tropical Health and Medicine, James Cook University, Cairns, QLD, Australia

Given the important role of voltage-gated sodium (Na_V) channel-modulating spider toxins in elucidating the function, pharmacology, and mechanism of action of therapeutically relevant Na_V channels, we screened the venom from Australian theraphosid species against the human pain target $hNa_V1.7$. Using assay-guided fractionation, we isolated a 33-residue inhibitor cystine knot (ICK) peptide (Ssp1a) belonging to the NaSpTx1 family. Recombinant Ssp1a (rSsp1a) inhibited neuronal hNa_V subtypes with a rank order of potency $hNa_V1.7 > 1.6 > 1.2 > 1.3 > 1.1$. rSsp1a inhibited $hNa_V1.7$, $hNa_V1.2$ and $hNa_V1.3$ without significantly altering the voltage-dependence of activation, inactivation, or delay in recovery from inactivation. However, rSsp1a demonstrated voltage-dependent inhibition at $hNa_V1.7$ and rSsp1a-bound $hNa_V1.7$ opened at extreme depolarizations, suggesting rSsp1a likely interacted with voltage-sensing domain II (VSD II) of $hNa_V1.7$ to trap the channel in its resting state. Nuclear magnetic resonance spectroscopy revealed key structural features of Ssp1a, including an amphipathic surface with hydrophobic and charged patches shown by docking studies to comprise the interacting surface. This study provides the basis for future structure-function studies to guide the development of subtype selective inhibitors.

Keywords: ICK peptide, Ssp1a, spider toxin, venom peptide, voltage-gated sodium channel

OPEN ACCESS

Edited by:
Jean-Marc Sabatier, Aix-Marseille Université, France

Reviewed by:
Peter Ruben, Simon Fraser University, Canada
Theodore R. Cummins, Indiana University-Purdue University Indianapolis, United States

****Correspondence:***
Richard J. Lewis
r.lewis@uq.edu.au

Specialty section:
This article was submitted to Pharmacology of Ion Channels and Channelopathies, a section of the journal Frontiers in Pharmacology

Received: *15 October 2021*
Accepted: *22 November 2021*
Published: *24 December 2021*

Citation:
Dongol Y, Choi PM, Wilson DT, Daly NL, Cardoso FC and Lewis RJ (2021) Voltage-Gated Sodium Channel Modulation by a New Spider Toxin Ssp1a Isolated From an Australian Theraphosid. Front. Pharmacol. 12:795455. doi: 10.3389/fphar.2021.795455

INTRODUCTION

Voltage-gated sodium (Na_V) channels are crucial for signalling in electrically excitable cells including nerve, heart and skeletal muscle (Ahern et al., 2016). Accordingly, Na_V channel dysfunction is associated with various diseases including pain (Cox et al., 2006; Vetter et al., 2017; Cardoso and Lewis, 2018; Bennett et al., 2019), migraine (Kahlig et al., 2008), epilepsy (Kaplan et al., 2016), multiple sclerosis (Waxman, 2006), cardiac arrythmia (Tarradas et al., 2013; Jeevaratnam et al., 2016) and myopathies (Cannon, 2010; Jurkat-Rott et al., 2010), supporting their therapeutic potential (Bagal et al., 2015; Kwong and Carr, 2015). Na_V channels comprise a single polypeptide chain arranged into four non-homologous domains, DI–DIV, which comes together to form the pore-forming α-subunit (de Lera Ruiz and Kraus, 2015). Humans have nine α-subunit isoforms $hNa_V1.1$–1.9, each with distinct tissue localization, channel kinetics and physiological functions (Deuis et al., 2017b; Wu et al., 2018). Additional β-subunits associate with the α-subunit to regulate Na^+ current kinetics and channel expression at the cell surface (Patino and Isom, 2010). These non-

homologous domains and the channel pore provide key interaction sites for neurotoxins that either block the pore or modify channel gating (Stevens et al., 2011; Wu et al., 2018; Shen et al., 2019). Peptidic gating modifier toxins (GMTs) such as spider toxins preferentially target the extracellular face of domain II (neurotoxin receptor site 4) and domain IV (neurotoxin receptor site 3). In contrast, domains I and III are preferentially occupied by β-subunits, as observed in a recent cryo-EM structure of $hNa_V1.7$-β1-β2 complexed with pore blockers and spider venom GMTs (Shen et al., 2019).

Spider venoms are a rich source of Na_V GMTs, with 12 families (NaSpTx1–12) defined based on intercysteine spacing and conserved amino acids (Klint et al., 2012). These spider toxins possess an inhibitor cystine knot (ICK) scaffold that provides structural, thermal, proteolytic and pH stability. By targeting voltage-sensing domains (VSD) II and IV, these spider toxins can affect channel activation or inactivation, respectively (Cardoso and Lewis, 2019; Dongol et al., 2019). Interestingly, some spider toxins appear to bind to both VSD II (Site 4) and VSD IV (Site 3), consistent with a more complex mode of action (Cardoso et al., 2017). Recently, the spider toxin Hm1a was used to investigate the role of $Na_V1.1$ in chronic visceral pain and mechanical hypersensitivity (Osteen et al., 2016) but many more provide new molecular tools to help define the role and molecular pharmacology of Na_V channels. Increasingly, structure-function studies of these spider toxins are providing valuable new opportunities to rationally design potential drug leads with improved selectivity and potency (Xiao et al., 2010; Rong et al., 2011; Xiao et al., 2011; Cai et al., 2015; Wingerd et al., 2017; Xu et al., 2019; Jiang et al., 2021), especially NaSpTx1–3 family toxins ProTx-II (Flinspach et al., 2017), Pn3a (Deuis et al., 2017a; Mueller et al., 2019), HnTx-IV (Liu et al., 2014b), HwTx-IV (Liu et al., 2014a), and Ca2a (Zhang et al., 2018). In this study, we report the discovery of Ssp1a from an Australian theraphosid *Selenotypus* species and investigate its mode of action and selectivity across $hNa_V1.1$–1.8. We conclude that Ssp1a is a gating modifier toxin that traps VSD II of Na_V channels in the closed (down) state without significantly altering the voltage-dependence of activation and inactivation.

MATERIALS AND METHODS

Cell Culture

Cell culture reagents were from Life Technologies Corporation, CA, United States, unless otherwise stated. The human neuroblastoma cell line SHSY5Y was cultured in Roswell Park Memorial Institute (RPMI) medium supplemented with 15% fetal bovine serum (FBS) and 2 mM L-glutamine. Human embryonic kidney 293 (HEK293) cells stably expressing recombinant $hNa_V1.1$–1.7 and the β1 auxiliary subunit (Scottish Biomedical Drug Discovery, Glasgow, United Kingdom) was cultured in Minimal Essential medium (MEM) (Sigma-Aldrich, MO, United States) supplemented with 10% v/v FBS-New Zealand origin (Assay Matrix), 2 mM L-glutamine and selection antibiotics as per manufacturer's recommendation. Chinese hamster ovary (CHO) cells stably expressing $hNa_V1.8$/β3 (ChanTest, Cleveland, United States) were cultured in MEM containing 10% v/v FBS and selection antibiotics as per manufacturer's recommendation. All cells were maintained at 37°C in a humidified 5% CO_2 incubator and sub-cultured every 3–4 days in a ratio of 1:5 using 0.25% trypsin/EDTA (Invitrogen).

$hNa_V1.7$ Screening

The crude venom of a female *Selenotypus* species was screened against $hNa_V1.7$ in SH-SY5Y cells using a Fluorescent Imaging Plate Reader ($FLIPR^{Tetra}$, Molecular Devices, CA, United States) as previously described (Cardoso et al., 2015; Cardoso et al., 2021). Briefly, SH-SY5Y cells were plated at 40,000 cells per well in 384-well flat clear-bottom black plates (Corning, NY, United States) and cultured at 37°C in a humidified 5% CO_2 incubator for 48 h before commencing assays. Cells were loaded with 20 µL per well of Calcium 4 dye (Molecular Devices) reconstituted in assay buffer containing (in mM) 140 NaCl, 11.5 glucose, 5.9 KCl, 1.4 $MgCl_2$, 1.2 NaH_2PO_4, 5 $NaHCO_3$, 1.8 $CaCl_2$, and 10 HEPES pH 7.4 and incubated for 30 min at 37°C in a humidified 5% CO_2 incubator. Fluorescence responses were excited at 470–495 nm and emission recorded at 515–575 nm for 10 s to set the baseline, 600 s after addition of 250, 25 or 2.5 µg/ml venom, and for a further 300 s after addition of 4 µM veratridine and 30 nM scorpion toxin OD1.

Venom Peptide Purification

Venom obtained from a female *Selenotypus* species (1 mg) was dissolved in 100 µL Milli-Q water containing 0.05% trifluoroacetic acid (TFA) (Auspep, VIC, Australia) and 5% acetonitrile (ACN) (Sigma-Aldrich, MO, United States). The sample was then centrifuged at 20,000 × *g* for 10 min to remove particulates. Venom was fractionated *via* reversed-phase high performance liquid chromatography (RP-HPLC) using a C18 column (Vydac 4.6 mm × 250 mm, 5 µm, Grace Discovery Sciences, United States) with a gradient of solvent B (90% ACN, 0.045% TFA in MilliQ water) in solvent A (0.05% TFA in MilliQ water). Fractionation started with isocratic elution at 5% solvent B for 5 min, followed by a gradient of 5–20% B from 5 to 10 min then a gradient of 20–40% solvent B over 40 min. The flow rate throughout was 0.7 ml/min, and 0.7 ml fractions were collected and lyophilized before storage at −20°C. The activity of each fraction on $hNa_V1.7$ expressed in SHSY5Y cells was measured using FLIPR. The peptide mass of the most potent fraction was determined using a Triple TOF 5600 LC/MS/MS mass spectrometer (SCIEX, Framingham, MA, United States) using a C18 column (Zorbax 2.1 mm × 100 mm, 1.8 µm, Agilent) with a gradient of solvent B (0.1% formic acid in ACN) in solvent A (0.1% formic acid in ACN) at 60°C and flow rate 0.2 ml/min. N-terminal sequencing was outsourced to the Australian Proteome Analysis Facility. Briefly, peptides were reduced using dithiothreitol (25 mM) and incubated at 56°C for 30 min. The samples were then alkylated using iodoacetamide (55 mM) at room temperature for 30 min. The samples were purified *via* RP-HPLC using a Zorbax 300SB-C18 column (3 × 150 mm) (Agilent, CA, United States). 90% of the collected sample was loaded onto a pre-cycled Biobrene-treated disc and the sample was subjected to 38–42 cycles of Edman

degradation using an ABI 494 Procise Protein Sequencing System (Applied Biosystems).

Recombinant Production of Ssp1a

Recombinant Ssp1a (rSsp1a) was expressed in *E. coli* using the protocols previously described (Klint et al., 2013; Cardoso et al., 2015). Briefly, GeneArt Gene Synthesis (Life Technologies) was used to design a pLicC vector comprising Ssp1a gene, MalE signal sequence, maltose binding protein (MBP) tag, His_6 affinity tag and a tobacco etch virus (TEV) protease recognition and cleavage sequence including other features necessary for periplasmic expression of Ssp1a in *E. coli*. The plasmid was transformed into BL21 (λDE3) competent *E. coli* cells and cultured in Luria-Bertani (LB) medium at 37°C, 120 rpm until optical density at 600 nm (OD_{600}) reached 0.8–1.0. The expression of Ssp1a was induced at 16°C with 500 μM IPTG (isopropyl *β*-D-1-thiogalactopyranoside) and 120 rpm overnight. Cells were harvested at 6,000 rpm for 10 min at 4°C. The pellet was resuspended in TN buffer (Tris 25 mM, NaCl 150 mM, pH 8.0) and lysed in a constant pressure cell disruptor at 25 kPa. The lysate was centrifuged at 15,000 rpm, 4°C for 45 min and the supernatant containing the fusion protein was collected. The lysate supernatant was applied to Ni-NTA resin (Hispur NiNTA, Thermo Scientific) prewashed and equilibrated with TN buffer to capture the His-tagged fusion protein in the resin followed by washing with TN buffer containing 15 mM imidazole. The fusion protein was eluted by TN buffer containing 500 mM imidazole. The eluate was then desalted and concentrated in TN buffer using an Amicon centrifuge filter (30 kDa cut-off, Millipore). The fusion protein was cleaved by employing TEV protease at a final concentration of 0.02 mg/ml. The reducing environment required for TEV protease was maintained by using redox pair of glutathione (0.6 mM/0.4 mM GSH/GSSG). The effect of incubation temperature and time on TEV protease activity was monitored *via* gel (SDS-PAGE) analysis to determine the optimum temperature and time for TEV cleavage. The mixture of fusion protein, TEV protease and glutathione redox pair was incubated overnight at room temperature with gentle shaking at 100 rpm. The post-cleavage sample was filtered through a centrifuge filter to isolate the recombinant peptide. The filtrate which contained the peptide was applied on to a C18 column (30Å, 5 μm, 4.6 × 250 mm, Vydac 218TP, Grace) equilibrated with 5% solvent B (90% ACN, 0.05% TFA in MilliQ water) for RP-HPLC purification. A RP-HPLC fractionation was performed on Agilent 1,100 series using following gradient profile of solvent B in solvent A (0.05% TFA in MilliQ water): 5% solvent B over 0–5 min, 5–10% solvent B over 5–10 min, 10–50% solvent B over 10–40 min, 50–80% solvent B over 40–45 min, wash at 80% solvent B over 45–50 min, 80–5% solvent B over 50–55 min and a final wash with 5% solvent B over 55–65 min at a flow rate of 1 ml/min. Peak fractions were collected, analysed for the mass and purity, lyophilized, quantitated, and stored at −20°C until use. Matrix-assisted laser desorption/ionization time-of-flight mass spectrometry (MALDI-TOF-MS) was used to verify the mass of the recombinant peptide. The lyophilized fractions were reconstituted in Milli-Q water, mixed well with CHCA (α-cyano-4-hydroxycinnamic acid, 7 mg/ml in 50% ACN) matrix in a 1:1 (v/v) ratio and spotted on the MALDI plate. After drying out at room temperature, the plate was processed on a SCIEX 5800 MALDI-TOF/TOF and the spectra and data of monoisotopic $[M + H]^+$ ions for rSsp1a acquired in positive reflectron mode.

Automated Whole Cell Patch Clamp Electrophysiology

The HEK293 cells stably expressing $hNa_V1.1–1.7/\beta1$ and CHO cells stably expressing $hNa_V1.8/\beta3$ were prepared following manufacturer's guidelines. After 48 h of incubation to achieve ~80% confluency, cells were detached using Detachin (Genlantis) and resuspended to 5×10^6 cells/mL in serum free media (CHO-cell SFM (Life Technologies), 25 mM HEPES and 100 U/mL penicillin/streptomycin). As $hNa_V1.8$ expression in CHO cells is tetracycline inducible, the cells were further cultured for 24 h at 27°C in the presence of tetracycline (1 μg/ml). The electrophysiology experiments were conducted using the automated whole-cell patch clamp technology (QPatch 16X; Sophion Bioscience A/S, Ballerup, Denmark) as previously described (Cardoso et al., 2015; Cardoso et al., 2017) using QPlates with single patch hole/well for $hNa_V1.1–1.7$ and 10 patch hole/well for $hNa_V1.8$. The extracellular solution comprised (in mM) 1 $CaCl_2$, 1 $MgCl_2$, 5 HEPES, 3 KCl, 140 NaCl and 20 TEA-Cl with pH adjusted to 7.3 with NaOH. The intracellular solution comprised (in mM) 140 CsF, 1 EGTA, 5 CsOH, 10 HEPES and 10 NaCl with pH adjusted to 7.3 with CsOH. The osmolarity of both solutions was adjusted to 320 mOsm with sucrose. Compounds were prepared in extracellular solution containing 0.1% bovine serum albumin (Sigma-Aldrich). For experiments to record the outward Na^+ currents in larger depolarization, modified solutions were used. The modified extracellular solutions contained (in mM) 105 NaCl, 5 CsCl, 35 choline chloride, 2 KCl, 10 HEPES, 1 $MgCl_2$, 1 $CaCl_2$, and 20 TEA-Cl with pH adjusted to 7.3. Similarly, the modified intracellular solutions contained (in mM) 108 NaCl, 35 CsF, 1 EGTA, 2 KCl and 10 HEPES, with pH adjusted to 7.3. Data was filtered at 3–8 kHz and sampled at 25 kHz. The mean seal resistance was 658 MΩ (95% confidence interval: 557–759 MΩ) while series resistance (Rs) was maintained below 10 MΩ with a mean for the last measured series resistance of 7 MΩ (95% confidence interval: 6.7–7.5 MΩ) with no compensation except for current-voltage experiments on $hNa_V1.2$ and $hNa_V1.7$, where fast Rs was compensated by 70%.

To obtain potency estimates at $hNa_V1.1–1.7$, cells were maintained at a holding potential −80 mV and Na^+ currents were elicited by 20 ms voltage step to 0 mV from a −120 mV conditioning pulse applied for 200 ms. Increasing concentrations of the peptide were incubated with the cells at holding potential for 5 min for native Ssp1a and 2 min for rSsp1a before the voltage protocol was applied. For CHO cells expressing $hNa_V1.8$, cells were maintained at a holding potential of −90 mV and Na^+ currents were elicited by 50 ms voltage step to +10 mV from a −90 mV conditioning pulse applied for 150 ms. For voltage-dependent inhibition of $hNa_V1.7$, an IC_{70} concentration of

rSsp1a was used and Na^+ currents elicited by stepping cells to 0 and 50 mV for 20 ms from a −120 mV conditioning pulse applied for 200 ms.

The voltage protocols to determine voltage-dependence of activation and fast inactivation were combined, with cells held at −90 mV for 150 ms followed by step pulses from −110 mV to +75 mV in 5 mV increments to elicit the Na^+ currents and determine voltage-dependence of activation. Each step pulse was maintained for 500 ms followed by a 10 ms pulse of −20 mV to elicit the Na^+ currents to determine the voltage-dependence of steady-state fast inactivation. The cells were returned to −90 mV at 6 s intervals. Conductance-voltage curves were obtained by calculating the conductance (G) at each voltage (V) using equation $G = I/(V–V_{rev})$, where I, V and V_{rev} represent the current value, membrane potential and reversal potential, respectively. For on-rate experiments, cells were maintained at a holding potential −80 mV and Na^+ currents elicited by 20 ms voltage steps to 0 mV from a −120 mV conditioning pulse applied for 200 ms at 10 s interval for 300 s after addition of rSsp1a at 1x, 3x and 10x its IC_{50} at each hNa_V subtype analysed. The time constants for current block (Tau, τ_{on}) at three concentrations were used to determine the actual on-rate (k_{on}) for rSsp1a at hNa_V subtypes tested. The τ_{on} were used to determine k_{obs}, where $k_{obs} = 1/\tau_{on}$. The calculated k_{obs} were plotted against their corresponding concentration to obtain a linear curve-fit where the slope of the curve represented the actual k_{on} (Dowling and Charlton, 2006; Pierre, 2011). For off-rate experiments, cells expressing $hNa_V1.2$, $hNa_V1.3$ and $hNa_V1.7$ were maintained at the holding potential −80 mV and Na^+ currents elicited by 20 ms voltage steps to 0 mV from a −120 mV conditioning pulse applied for 60 ms. Off-rates were determined using ~ IC_{50} values of rSsp1a (250 nM, 500 and 130 nM, respectively) incubated for 5 min and Na^+ currents measured every 3 min for 30 min during rSsp1a washout. The off-rate (k_{off}) and dissociation constant (K_d) values at three hNa_V subtypes were calculated using $k_{off} = 1/\tau_{off}\,(s^{-1})$ and $K_d = k_{off}/k_{on}$ (nM). Recovery from fast inactivation was examined using a two-pulse protocol where cells were conditioned at −120 mV for 200 ms were depolarized to 0 mV for 50 ms to inactivate the channels, followed by a step to −120 mV of variable duration (1–130 ms) to promote recovery, and a 50 ms test pulse to 0 mV to assess the availability of channels. To assess the effect of larger depolarizations on rSsp1a-bound $hNa_V1.7$, cells were maintained at a holding potential of −90 mV and Na^+ currents were recorded from a series of step depolarizations from −60 mV to +160 mV at 10 mV increment for 50 ms.

Nuclear Magnetic Resonance Structure Determination of rSsp1a

Lyophilized peptide (500–1,000 µg) was resuspended in 90% H_2O:10%D_2O. 2D ^1H–^1H TOCSY, ^1H–^1H NOESY, ^1H–^1H DQF-COSY, ^1H-^{15}N HSQC, and ^1H-^{13}C HSQC spectra were acquired at 290 K, 298 and 305 K using a 600 MHz AVANCE III NMR spectrometer (Bruker, Karlsruhe, Germany) equipped with a cryogenically cooled probe. All spectra were recorded with an interscan delay of 1 s. NOESY spectra were acquired with mixing times of 200–250 ms, and TOCSY spectra were acquired with isotropic mixing periods of 80 ms. Two-dimensional spectra were collected over 4,096 data points in the f2 dimension and 512 increments in the f1 dimension over a spectral width of 12 ppm. Standard Bruker pulse sequences were used with an excitation sculpting scheme for solvent suppression. NMR assignments were made using established protocols (Wüthrich, 1983), and the secondary shifts derived by subtracting the random coil αH shift from the experimental αH shifts (Wishart et al., 1995). The three-dimensional structure of rSsp1a was determined using CYANA based on an automated assignment protocol for the non-intra-residue NOESY cross-peaks (Güntert, 2004). Torsion-angle restraints from TALOS+ were used in the structure calculations. One-dimensional and TOCSY spectra were recorded at 290 K, 298 and 305 K and referenced to internal 4,4-dimethyl-4-silapentane-1-sulfonic acid (DSS). The amide protons assigned at the different temperatures were used to calculate temperature coefficients based on Cierpicki and Otlewski, 2001 (Cierpicki and Otlewski, 2001). Hydrogen bond restraints were inferred from the analysis of the temperature coefficients and preliminary structures. Residues with temperature coefficients more positive than −4.6 ppb/K indicate involvement in hydrogen bonds (Cierpicki and Otlewski, 2001), with restraints for eight hydrogen bonds included in the structure calculations based on analysis of preliminary structures. Final structures were visualized using MOLMOL (Koradi et al., 1996).

Molecular Docking

The recently solved structure of $Na_VAb/Na_V1.7$ VS2A chimera (Wisedchaisri et al., 2021) VSD II and our NMR structure of rSsp1a were uploaded in HADDOCK2.2 Easy interface (Van Zundert et al., 2016) with structure and restraint definitions. We defined the active residues (W5, F6, P11, Y20, K25, W28, R30, Y31, and L33) for rSsp1a based on homology to related NaSpTx1 spider toxins HwTx-IV (Minassian et al., 2013) and GpTx-1 (Murray et al., 2015), while active residues on $hNa_V1.7$ DII were defined based on the previously published channel mutation data (Xiao et al., 2010; Xiao et al., 2011; Cai et al., 2015; Zeng et al., 2018; Xu et al., 2019). The docking results were displayed as a cluster of water-refined models which were downloaded and visualized using Pymol 2.4.1 (DeLano, 2002).

Data Analysis

The experimental data were analysed using QPatch Assay software v5.6.4 and GraphPad Prism 7.0 days using four-parameter Hill equation [Y = Bottom + (Top–Bottom)/(1 + 10^(Log IC_{50}-X)*Hillslope)] to fit concentration response curves by non-linear regression analysis, Boltzmann function [$I(V) = I_{Vmin} + (I_{Vmax}–I_{Vmin})/(1.0 + \exp(–(V–V_{50}/V_{slope})$] for voltage-dependence of activation and inactivation, plateau followed by one-phase decay for on-rate, simple linear regression for actual on-rate determination, exponential growth equation for off-rate, one-phase decay for recovery from inactivation, one-way ordinary ANOVA (multiple comparisons) and Student's *t*-test. Data are presented as mean ± standard error of mean (SEM) with number of

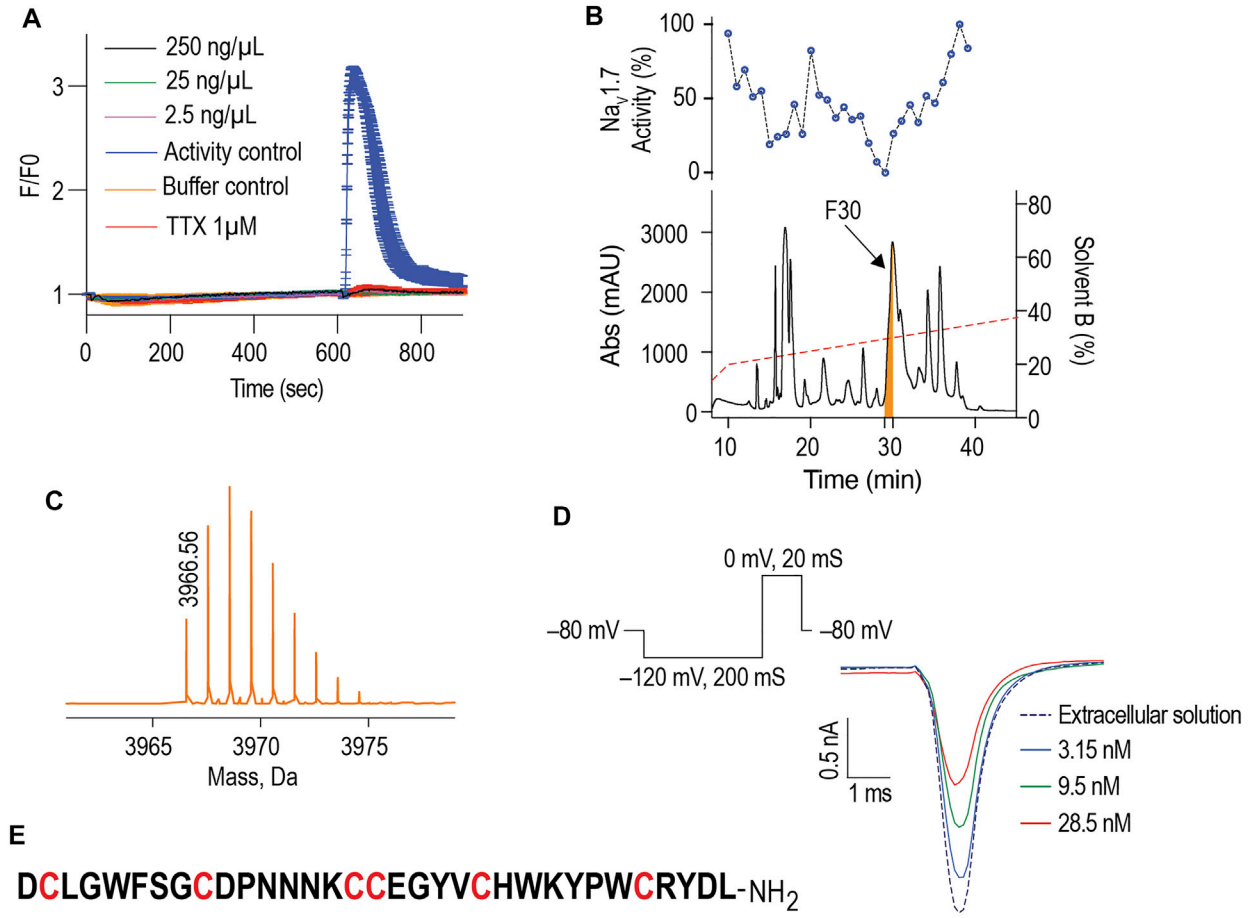

F

NaSpTx1		Loop 1	Loop 2	Loop 3	Loop 4	C-term	%ID	%Sim
Ssp1a	33 aa	DCLGWFSGCDPNNNKCCEGYVCHWKYPWCRYDL*	-	-
CcoTx-1	33 aa	DCLGWFKSCDPKNDKCCKNYTCSRRDRWCKYDL*	61	72
GpTx-1	34 aa	DCLGFMRKCIPDNDKCCRPNLVCSRTHKWCKYVF*	44	58
HnTx-IV	35 aa	ECLGFGKGCNPSNDQCCKSSNLVCSRKHRWCKYEI*	43	74
HwTx-IV	35 aa	ECLEIFKACNPSNDQCCKSSKLVCSRKTRWCKYQI*	40	62
HnTx-I	33 aa	ECKGFGKSCVPGKNECCSNYACNSRDKWCKVLL*	39	57
HnTx-III	33 aa	GCKGFGDSCTPGKNECCPNYACSSKHKWCKVYL*	39	51

FIGURE 1 | Isolation of the Australian tarantula peptide Ssp1a. **(A)** The crude venom of *Selenotypus* species was screened against hNa$_V$1.7 at 250, 25 and 2.5 ng/ml measuring calcium influx into SH-SY5Y cells on a FLIPR^{Tetra}. Tetrodotoxin (TTX) at 1 µM fully inhibited these veratridine (4 µM) + OD1 (30 nM) activated responses. **(B)** The crude venom was fractionated by RP-HPLC in C18 column using a gradient from 20 to 40% solvent B (dashed line) and 1-min fractions screened against hNa$_V$1.7 to identify fraction 30 has the most prominent activity. **(C)** Reconstructed mass from Triple TOF LC/MS/MS spectra of fraction 30 revealed a single monoisotopic mass of 3,966.56 Da. **(D)** The inhibitory activity of fraction 30 against hNa$_V$1.7 was confirmed by whole cell patch-clamp electrophysiology using HEK293 cells expressing hNa$_V$1.7/β1 subunits on a QPatch 16X. Data are representative traces of n = 3. **(E)** N-terminal sequencing revealed the primary amino acids sequence of Ssp1a supporting the predicted monoisotopic mass of 3,966.60 Da with the C-terminal residue predicted to be leucine based on C-terminal tail homology. **(F)** Sequence alignment of Ssp1a with selected NaSpTx1 family toxins. Yellow highlights cysteines, green hydrophobic residues, cyan positively charged residues, red negatively charged residues, and bolded letters aromatic residues. The * indicates C-terminal amide.

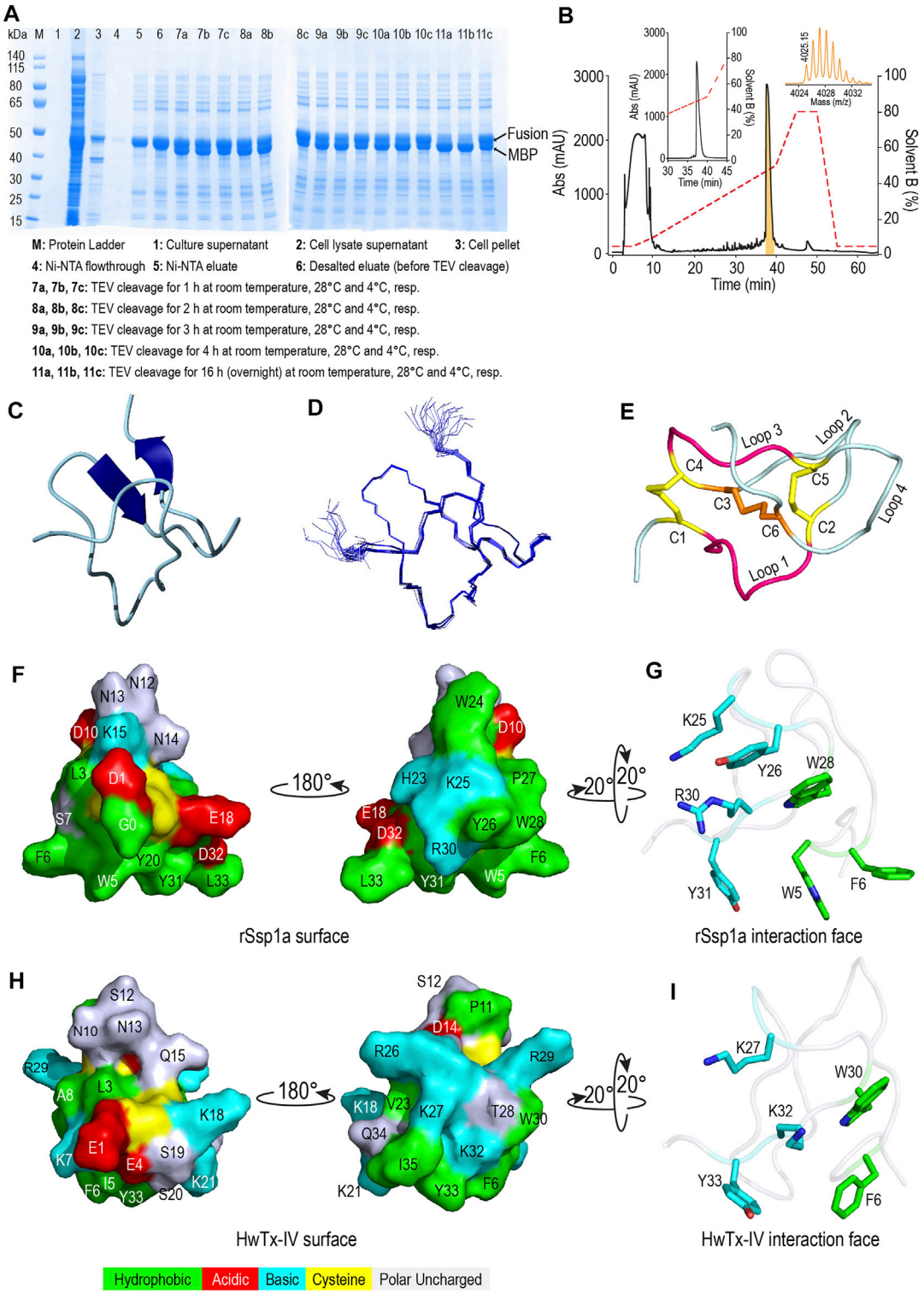

FIGURE 2 | Recombinant production and structural characterization of rSsp1a. **(A)** SDS-PAGE analysis of the samples from various steps in recombinant expression of rSsp1a. **(B)** Analytical RP-HPLC (left inset) of rSsp1a obtained after semi-preparative RP-HPLC. The right inset shows the MALDI-TOF/TOF mass spectra of the purified rSsp1a. **(C,D)** NMR structure of rSsp1a showing a region of β-sheet connected by a β-hairpin at the C-terminus **(C)** and overlay of twenty lowest energy structures of rSsp1a **(D)**. **(E)** rSsp1a displaying an ICK motif. A ring structure made up of two disulfide bridges (yellow) and the intervening peptide backbone (pink) is penetrated by a third disulfide bridge (orange) to form a pseudo-knot. **(F,H)** Amphipathic surface profile of rSsp1a and HwTx-IV (PDB: 2M4X (Minassian et al., 2013)), respectively showing patches of hydrophobic residues (green) and charged residues (red: acidic residues and cyan: basic residues). **(G,I)** The interaction face of rSsp1a and HwTx-IV aligned to WCK/R motif characteristic to NaSpTx1 and 3 family toxins and showing important polar basic and polar hydrophobic residues (cyan) and hydrophobic residues (green).

independent experiments stated and $p < 0.05$ is considered statistically significant.

RESULTS

Isolation of Ssp1a Spider Venom Peptide

$hNa_V1.7$-specific calcium responses generated in SH-SY5Y cells using combination of veratridine and scorpion toxin OD1 provide a robust method to screen the $hNa_V1.7$ blockers (Vetter et al., 2012). In these $FLIPR^{Tetra}$ calcium assays, crude venom from the Australian Theraphosidae *Selenotypus* sp. inhibited $hNa_V1.7$ at concentrations down to 2.5 ng/ml (**Figure 1A**). Screening the RP-HPLC fractions of *Selenotypus* sp. crude venom across $hNa_V1.7$ revealed several fractions with inhibitory activity, especially fraction 30 (**Figure 1B**). MS analysis revealed fraction 30 contained a dominant peptide with a monoisotopic mass of 3,966.56 Da (**Figure 1C**). The $Na_V1.7$ inhibitory activity of fraction 30 was confirmed using HEK293 cells recombinantly expressing $hNa_V1.7/\beta1$ and automated whole cell patch-clamp electrophysiology in QPatch 16X (**Figure 1D**). The N-terminal sequencing revealed fraction 30 contained a 33-residue peptide with six cysteine residues typical for spider inhibitor cystine knot (ICK) peptides (**Figure 1E**). The C-terminal residue of Ssp1a was predicted to be either leucine or isoleucine from its monoisotopic mass, with leucine chosen considering C-terminal homology to related NaSpTx1 toxins. The sequence homology, amino acid residue number and intercysteine spacing categorised Ssp1a in the NaSpTx1 family (Klint et al., 2012), confirmed from its pairwise alignment with related NaSpTx1 family spider ICK peptides (**Figure 1F**).

Recombinant Production and Structural Characterization of Ssp1a

Recombinant Ssp1a (rSsp1a) was expressed in the periplasm of BL21 (λDE3) *E. coli* strain as a fusion protein which was purified using Ni-NTA affinity chromatography followed by TEV protease cleavage to release the Gly-Ssp1a (rSsp1a). This N-terminal Gly residue is a remnant of TEV protease specific sequence (ENLYFQG) where TEV protease specifically cleaves between Q and G. The samples from each significant step of the expression protocol were analysed by SDS-PAGE to guide optimisation. The time and temperature kinetics of TEV cleavage was optimal at room temperature and 28°C for 16 h (**Figure 2A**), indicating the convenience to carry out the cleavage reaction at room temperature and also modified the previously used TEV cleavage temperature (30°C) in our lab at which 50% of the fusion protein was cleaved (Cardoso et al., 2015). Nickel affinity-purified rSsp1a eluted as a single peak at ~ 50% solvent B from the C18 column, reflecting the relatively hydrophobic nature of this peptide (**Figure 2B**). The yield of rSsp1a after final RP-HPLC purification was 0.31 mg/L. The protonated monoisotopic mass ($[M + H]^+$) of rSsp1a determined by MALDI-TOF/TOF was 4,025.99 m/z (**Figure 2B**, inset), consistent with the calculated monoisotopic mass (M, 4,024.61 Da) for native Ssp1a with an N-terminal Gly residue and C-terminal acid.

Structure of rSsp1a

The structure of rSsp1a (PDB: 7SKC; BMRB: 30961) was determined using 2D NMR (**Figure 2C**), with an ensemble of 20 lowest-energy structures (**Figure 2D**) chosen to represent its structure (**Supplementary Table S1**). Ssp1a comprised a region of β-sheet connected by a β-hairpin at the C-terminus (**Figure 2C**) as the major element of secondary structure. This secondary structure, along with the disulfide connectivity (C1–C4, C2–C5, and C3–C6) and topology, constitute an ICK motif typical for spider ICK peptides targeting the Na_V channels (Klint et al., 2012). The ICK motif was formed by disulfide bridges C1–C4 and C2–C5 along with their intervening peptide backbone forming a ring through which the third disulfide bridge C3–C6 penetrates to form a pseudo-knot (**Figure 2E**). The hydropathicity/hydrophilicity analysis performed using Kyte and Doolittle hydropathy scale (Kyte and Doolittle, 1982; Gasteiger et al., 2005) revealed an amphipathic surface with uncharged hydrophobic amino acids contributing 26.5%, acidic and basic amino acids contributing 11.8% each, and polar uncharged (neutral) amino acids contributing 50% of the peptide (**Figure 2F**), like other Na_V-targeting spider ICK peptides (Bosmans and Swartz, 2010), exemplified by HwTx-IV (**Figure 2H**). The surface arrangement of basic residues H23, K25 and R30 surrounded by hydrophobic residues W5, F6, Y26, W28 and Y31 (**Figure 2G**) on rSsp1a is predicted to represent the activity face of the peptide (**Figure 2G**), similarly to activity face defined for HwTx-IV (**Figure 2I**). π-Stacking between the aromatic rings of Y26 and W28 was also observed.

rSsp1a Inhibits hNa_V Channel Subtypes

We determined the inhibitory potency of rSsp1a across $hNa_V1.1$–1.7 stably expressed in HEK 293 cells and on $hNa_V1.8$ stably expressed in CHO cells using automated whole-cell patch clamp electrophysiology (**Figures 3A,B**). rSsp1a inhibited hNa_V current at nanomolar concentrations, with a rank order of potency at TTX-S neuronal $hNa_V1.7 > 1.6 > 1.2 > 1.3 > 1.1$. rSsp1a also blocked ~60% $hNa_V1.5$ current at 3 μM concentration, whereas it was weakly active at $hNa_V1.4$ and $hNa_V1.8$ at 3 and 9 μM, respectively. **Figure 3C** shows the representative current traces of $hNa_V1.1$–1.8 channels after addition of negative control (extracellular solution), rSsp1a and the positive control TTX (1 μM for $hNa_V1.1$–1.4, $hNa_V1.6$ and $hNa_V1.7$; 50 μM for $hNa_V1.5$; and 1 mM for $hNa_V1.8$).

Effect of rSsp1a on Activation, Inactivation, and Recovery From Inactivation of $hNa_V1.2$, $hNa_V1.3$ and $hNa_V1.7$

The inhibition of therapeutically relevant $hNa_V1.2$, $hNa_V1.3$ and $hNa_V1.7$ by rSsp1a at nanomolar potency supported our broader aim to extend the structure–function and rational

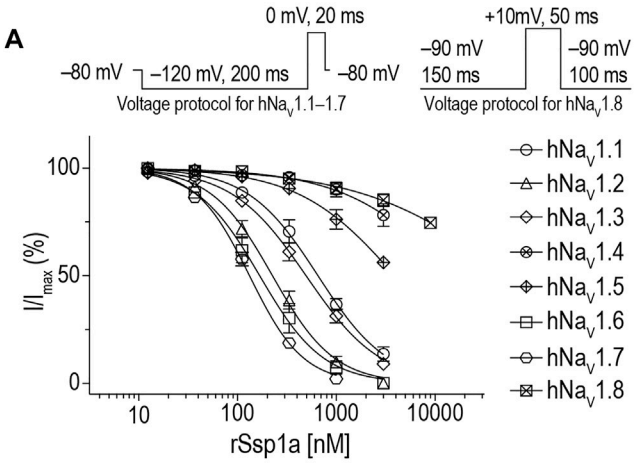

B

hNa_V subtypes	Mean IC_{50} ± SEM (nM)
$hNa_V1.1$	674 ± 104 (n=4)
$hNa_V1.2$	239 ± 26 (n=7)
$hNa_V1.3$	547 ± 70 (n=12)
$hNa_V1.4$	> 3000 (n=4)
$hNa_V1.5$	> 3000 (n=5)
$hNa_V1.6$	191 ± 40 (n=6)
$hNa_V1.7$	134 ± 9 (n=7)
$hNa_V1.8$	> 9000 (n=7)

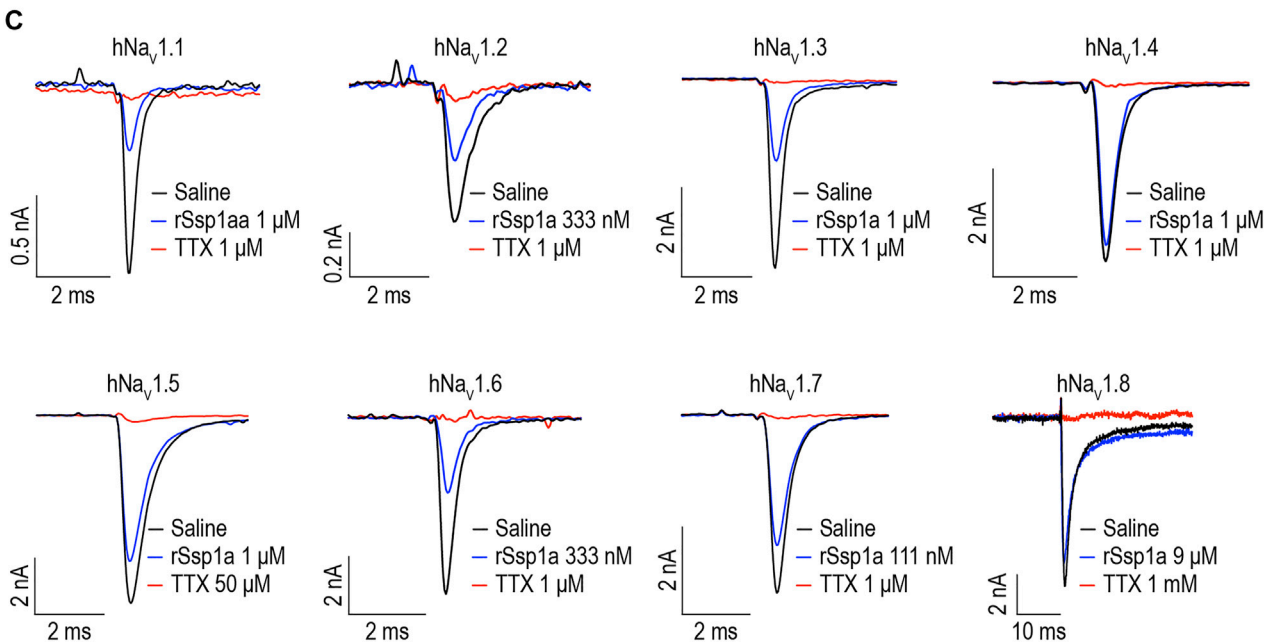

FIGURE 3 | rSsp1a inhibition of hNa_V subtypes. **(A)** Dose-response profile of $hNa_V1.1$–1.8 on automated-patch clamp electrophysiology platform (QPatch 16X). Voltage protocols used for dose-response assay on $hNa_V1.1$–1.7 and $hNa_V1.8$ are shown above the dose-response curve. **(B)** The mean IC_{50} ± SEM dose of rSsp1a observed at $hNa_V1.1$–1.8 using electrophysiology assay. **(C)** Current traces of positive control (TTX, 1 µM for $hNa_V1.1$–1.4, $hNa_V1.6$ and $hNa_V1.7$; 50 µM for $hNa_V1.5$; and 1 mM for $hNa_V1.8$), negative control (extracellular solution) and rSsp1a at varying concentration at $hNa_V1.1$–1.8. CHO-cells expressing $hNa_V1.8$ was used to obtain the dose-response curve on automated-patch clamp electrophysiology platform, otherwise HEK293 cells stably expressing $hNa_V1.1$–1.7 were used to obtain the dose-response curve. Averaged data are shown as mean ± SEM (n = 4–12).

design of NaSpTx beyond $hNa_V1.7$ up to $hNa_V1.2$ and $hNa_V1.3$. To begin with, the basic pharmacology experiments to characterize the rSsp1a mode of action on channel gating were performed. As Na_V-modulatory spider ICK peptides typically interact with VSD II associated with channel activation and/or VSD IV associated with channel inactivation (Dongol et al., 2019), rSsp1a effect on channel activation and inactivation was evaluated. At sub-saturating concentrations, rSsp1a had little or no significant effect on the voltage-dependence of steady-state activation and inactivation or the reversal potential on $hNa_V1.2$, $hNa_V1.3$ and $hNa_V1.7$ (**Table 1**; **Figures 4A–D**). There was also no significant effect on the slope factor for voltage-dependence of activation at $hNa_V1.2$ and $hNa_V1.7$; however, at $hNa_V1.3$ rSsp1a decreased the slope ($k = 5.8 \pm 0.4$ mV) compared to the control ($k = 4 \pm 0.2$ mV). On the other hand, for voltage-dependence of inactivation, the slope factor at $hNa_V1.3$ remained unchanged whereas the steepness decreased by

TABLE 1 | Effect of rSsp1a on voltage dependence of activation and steady-state inactivation. Data are shown as mean ± SEM (n = 3–4), with statistical significance determined using the Student's t-test (unpaired).

		Activation (mean ± SEM)			Inactivation (mean ± SEM)		
		V_{50} (mV)	k (mV)	*n*	V_{50} (mV)	k (mV)	*n*
$hNa_V1.2$	Extracellular solution	–24.5 ± 0.8	4.8 ± 0.3	4	–62.2 ± 0.5	–6.4 ± 0.5	4
	250 nM rSsp1a	–23 ± 2.1[a]	5.3 ± 1.7[a]	4	–61.8 ± 0.8[a]	–9.9 ± 1.2[b]	4
$hNa_V1.3$	Extracellular solution	–28 ± 0.3	4 ± 0.2	3	–67.8 ± 0.8	–5.4 ± 0.4	3
	500 nM rSsp1a	–24 ± 1.3[b]	5.8 ± 0.4[b]	3	–69.4 ± 0.4[a]	–5.6 ± 0.4[a]	3
$hNa_V1.7$	Extracellular solution	–22.3 ± 2	4.4 ± 1.4	3	–64.3 ± 1.1	–9 ± 2.4	3
	130 nM rSsp1a	–24 ± 0.2[a]	4.9 ± 0.8[a]	3	–66.3 ± 1.2[a]	–11.5 ± 2.2[a]	3

[a]*Statistically insignificant (p > 0.05) compared to control (extracellular solution).*
[b]*Statistically significant (p < 0.05) compared to control (extracellular solution).*

3.5 mV for $hNa_V1.2$ (−6.4 ± 0.5 mV, control Vs −9.9 ± 1.2 mV, 250 nM rSsp1a) and by 2.5 mV for $hNa_V1.7$ (−9 ± 2.4 mV, control vs. −11.5 ± 2.2, 130 nM rSsp1a). rSsp1a also had no significant effect on recovery from fast inactivation at $hNa_V1.7$ (τ value: control, 2.4 ± 0.1 ms vs. 130 nM rSsp1a, 2.1 ± 0.1 ms, n = 6) but accelerated recovery from fast inactivation at the $hNa_V1.2$ by 1.2 mS (τ value: control, 3.4 ± 0.5 ms vs. 250 nM rSsp1a, 2.2 ± 0.4 ms, n = 4–6) and at $hNa_V1.3$ by 2.7 ms (τ value: control, 4.7 ± 0.8 ms vs. 250 nM rSsp1a, 2.0 ± 0.2 ms, n = 3–5) (**Figures 5A–D**).

On-Rate and Off-Rate Effect of rSsp1a at $hNa_V1.2$, $hNa_V1.3$ and $hNa_V1.7$

As binding kinetics are an important consideration in drug development, we investigated the on- and off-rate for the inhibitory effects of rSsp1a at $hNa_V1.2$, $hNa_V1.3$ and $hNa_V1.7$. rSsp1a on-rates were determined at an ~ $IC_{50\ (2\ min)}$ (250 nM for $hNa_V1.2$, 500 nM for $hNa_V1.3$, 130 nM for $hNa_V1.7$), 3x IC_{50}, and 10x IC_{50} concentrations (**Figures 6A–D**; **Table 2**). Off-rates at $hNa_V1.2$, $hNa_V1.3$ and $hNa_V1.7$ revealed rSsp1a binding was slowly reversible and incomplete, with ~25% of $hNa_V1.2$, ~50% of $hNa_V1.3$ and ~40% of $hNa_V1.7$ channels recovering from block after a 30-min washout (**Figures 6E–H**). K_d was determined from the on-rate and reversible binding component at each hNa_V subtype, which revealed an ~ 2-fold higher affinity of rSsp1a at $hNa_V1.7$ (22.5 nM) and $hNa_V1.2$ (19.5 nM) than at $hNa_V1.3$ (37.0 nM) (**Table 2**).

rSsp1a is a Gating Modifier

Gating modifiers can allow an outward current at high depolarizing potentials (Xiao et al., 2008; Liu et al., 2013; Cai et al., 2015). To investigate this phenomena, we depolarized cells from a holding potential of −90 mV to −60 mV to +160 mV for 50 ms using a modified extracellular and intracellular solutions to shift the reversal potential to 0 mV and enhance the amplitude of outward currents at strong depolarizing potentials as described by Xiao et al. (2008) (**Figures 7A,B**). Despite using a saturating concentration of rSsp1a (2 μM) to completely block the inward current at moderate depolarizing potentials, we observed a gradual increase in the outward current with increasing depolarizing potentials at ≥ 50 mV. The outward current observed for rSsp1a-bound $hNa_V1.7$ at +160 mV was ~21% compared to the current produced before rSsp1a application. This inferred that the rSsp1a-bound $hNa_V1.7$ channels could be opened under strong depolarizing conditions. Further, rSsp1a (255 nM) inhibited ~60% of $hNa_V1.7$ channels at depolarisation to 0 mV compared to ~40% at depolarisation to +50 mV (**Figure 7C**) confirming the toxin caused voltage-dependent inhibition of $hNa_V1.7$.

Molecular Docking of rSsp1a and $hNa_V1.7$

Mode of action studies suggest rSsp1a traps the VSD II of hNa_V channels in the resting conformation. Fortunately, the resting state of VSD II of $Na_V1.7$ trapped by m3-HwTx-IV was recently solved (Wisedchaisri et al., 2021), allowing predictive docking of rSsp1a. Despite several studies suggesting membrane partitioning of spider toxin contributes to high-affinity toxin-channel interactions (Xu et al., 2019; Henriques et al., 2016; Milescu et al., 2007), the resolved structure of m3-HwTx-IV–Na_VAb/$Na_V1.7$ VS2A we used for rSsp1a docking lacked a defined membrane-lipid environment and m3-HwTx-IV was allowed to interact directly with Na_VAb/$Na_V1.7$ VS2A chimera (Wisedchaisri et al., 2021). HADDOCK2.2 was used to generate a molecular docking pose by defining rSsp1a active residues based on alanine scan data of closely related HwTx-IV (Minassian et al., 2013) and GpTx-1 (Murray et al., 2015) and published $Na_V1.7$ channel mutational data (Xu et al., 2019; Xiao et al., 2010; Zeng et al., 2018; Cai et al., 2015; Xiao et al., 2011). The docking pose revealed that rSsp1a thrust itself to occupy the aqueous cleft formed in between S1–S2 and S3–S4 loop provisioning a strong salt bridge between K25–E753 (2.8 Å), R30–E818 (2.7 Å) and R30–D816 (2.7 Å), with further electrostatic interaction between Y26–E811 (2.0 Å) (**Figure 8A**). The hydrophobic stretch LFLA in the S3–S4 loop interacted with hydrophobic patch in rSsp1a comprising W5, F6, Y20, Y31, and W28 in a space filling model (**Figure 8B**). This binding mode is expected to further restrict the upward movement of S4 upon depolarization and thus trap VSD II in the resting state. Similar docking features were demonstrated by the closely related m3-HwTx-IV bound to the resting state VSD II in a recently captured cryo-EM structure, where the authors highlighted deep toxin penetration, stronger ionic interactions, and hydrophobic interactions at the S3–S4 loop that were important in locking the VSD II in the resting state (Wisedchaisri et al., 2021).

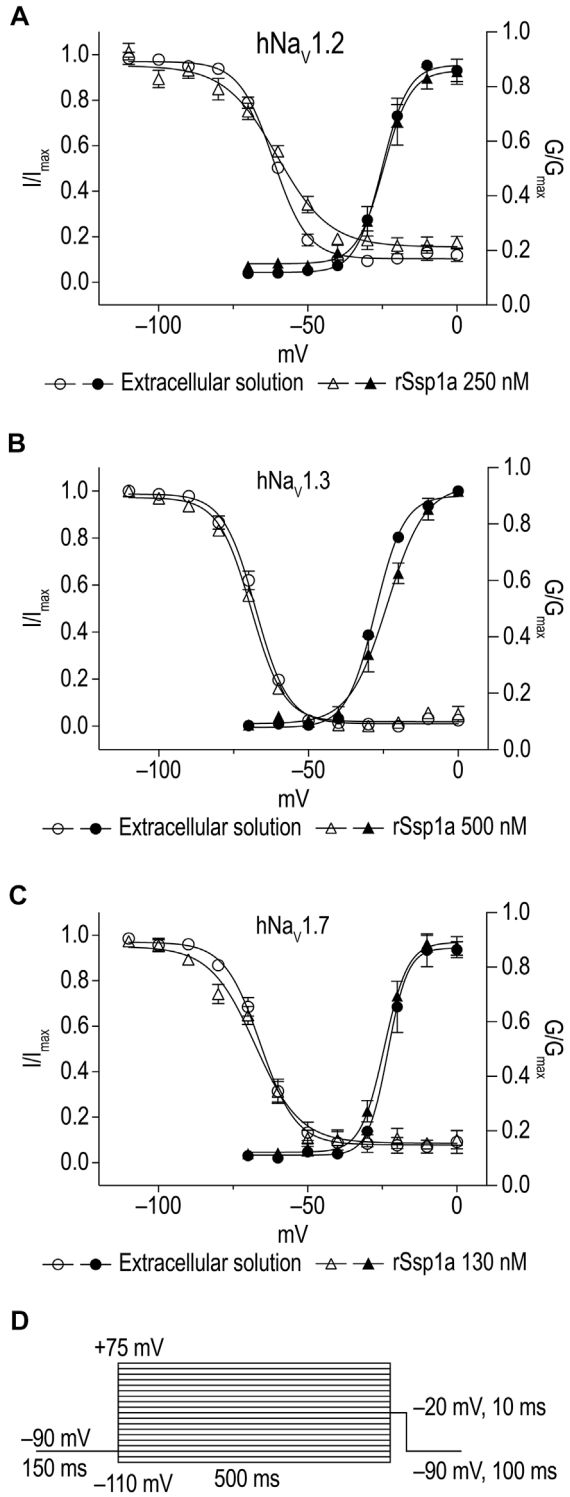

FIGURE 4 | Current-voltage relationship of rSsp1a at $hNa_V1.2$, $hNa_V1.3$ and $hNa_V1.7$. **(A–C)** show the voltage-dependence of activation and inactivation plotted as a function of G/G_{max} and I/I_{max}. The corresponding I-V curves are shown in the **Supplementary Figure S1**. rSsp1a had little to no significant effects on the voltage-dependence of activation and steady-state inactivation. Data are represented as mean ± SEM (n = 3–4). **(D)** Voltage protocol used to determine the voltage-dependence of activation and inactivation.

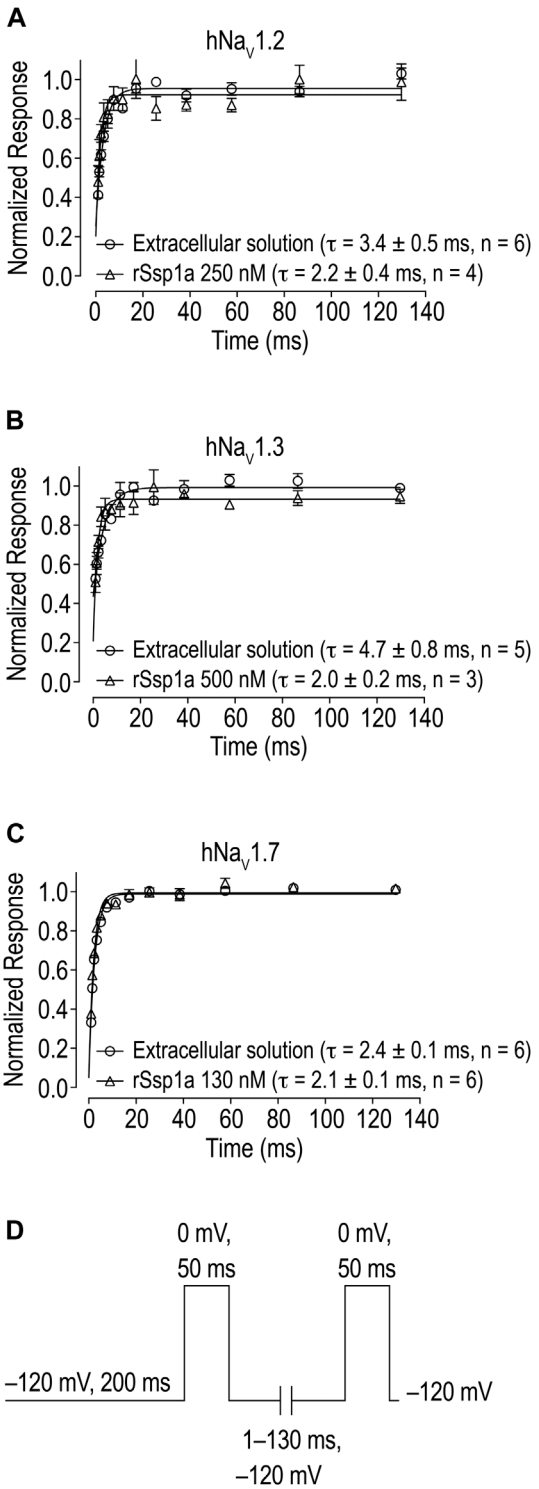

FIGURE 5 | Effect of rSsp1a on the rate of recovery from inactivation. **(A–C)** rSsp1a does not delay the recovery rate from inactivation of $hNa_V1.2$, $hNa_V1.3$ and $hNa_V1.7$, respectively. Data are shown as mean ± SEM, n = 3–6. **(D)** Voltage protocol used to determine the rate of recovery from inactivation.

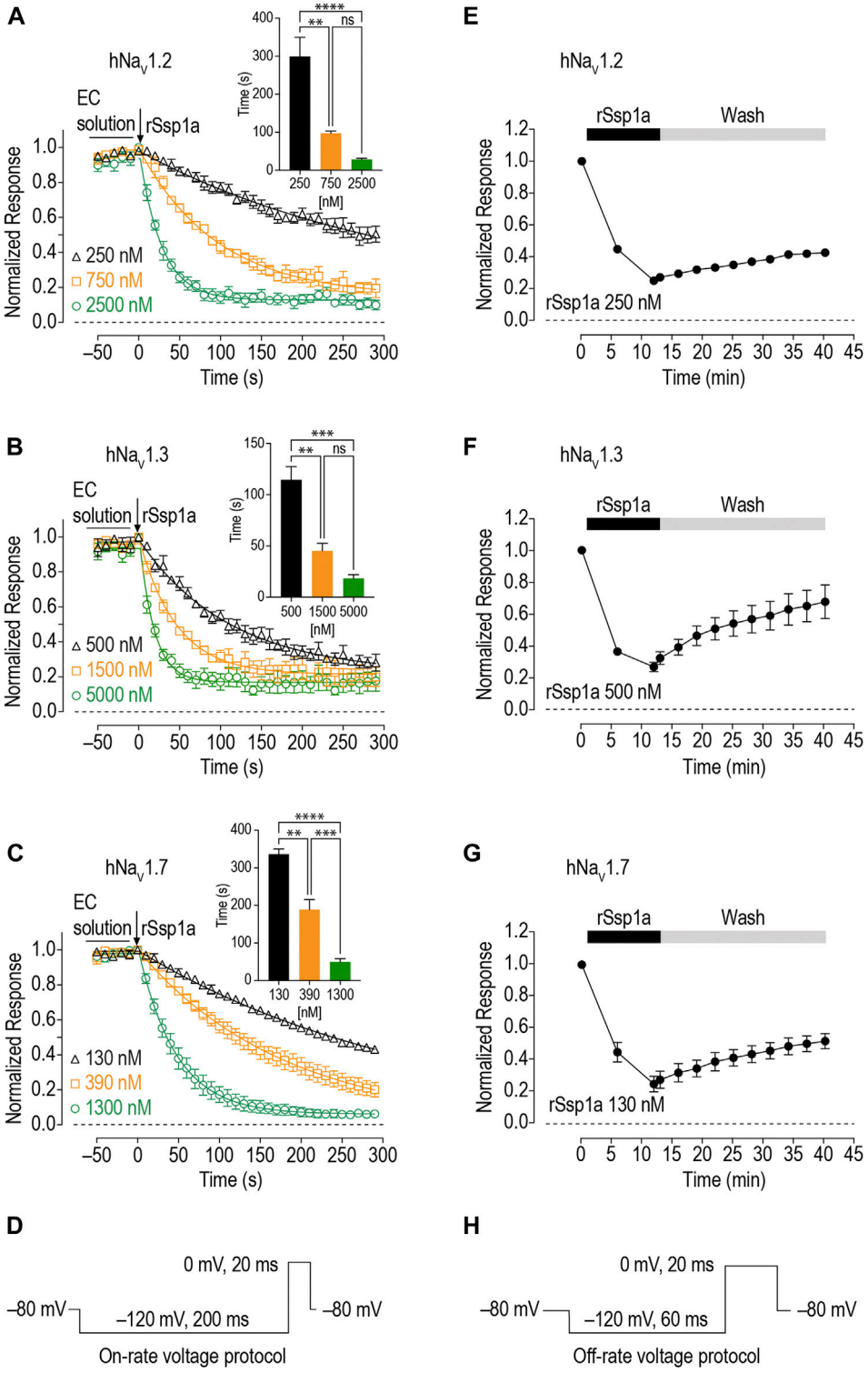

FIGURE 6 | On-rate and off-rates for rSsp1a binding at $hNa_V1.2$, $hNa_V1.3$ and $hNa_V1.7$. **(A–C)** On-rates for different concentrations of rSsp1a at $hNa_V1.2$ (n = 4–6), $hNa_V1.3$ (n = 3–4) and $hNa_V1.7$ (n = 3–5), respectively. The Na^+ currents were measured immediately after rSsp1a addition at 10 s interval for 300 s. The bar diagram for each plot compares the statistical significance of on-rate time constant between the rSsp1a concentrations. EC solution refers to extracellular solution. **(E–G)** Off-rate effects of 250 nM, 500 and 130 nM rSsp1a at $hNa_V1.2$ (n = 6), $hNa_V1.3$ (n = 6) and $hNa_V1.7$ (n = 4), respectively. Cells were incubated for 5 min with rSsp1a at an ~ IC_{50} concentrations and Na^+ currents measured during washes with extracellular solution every 3 min for 30 min. Data are shown as mean ± SEM. **, ***, and ****, and ns refer p values at < 0.01, < 0.001, < 0.0001, and > 0.05, respectively. **(D,H)** Voltage protocols used for on-rate and off-rate experiments.

TABLE 2 | Association and dissociation kinetics of rSsp1a at $hNa_V1.2$, $hNa_V1.3$ and $hNa_V1.7$. Data are shown as mean ± SEM (n = 3–6), while derived mean values were used to calculate K_d. Statistical significance was determined using a one-way ANOVA with multiple comparisons.

	rSsp1a (nM)	τ_{on} (s)[a]	k_{obs} (s^{-1})	k_{on} (nM^{-1} s^{-1})	k_{off} (s^{-1})	K_d (nM)
hNaV1.2	250	299 ± 50	$3.76 \pm 0.64 \times 10^{-3}$[b]	$1.53 \pm 0.18 \times 10^{-5}$	$2.98 \pm 0.41 \times 10^{-4}$[#]	19.5
	750	97 ± 6	$1.05 \pm 0.07 \times 10^{-2}$[c]			
	2,500	28 ± 3	$3.80 \pm 0.45 \times 10^{-2}$[d]			
hNaV1.3	500	115 ± 13	$8.97 \pm 1.07 \times 10^{-3}$[e]	$1.12 \pm 0.21 \times 10^{-5}$	$4.13 \pm 0.46 \times 10^{-4}$[#]	37.0
	1,500	45 ± 7	$2.36 \pm 0.42 \times 10^{-2}$[f]			
	5,000	18 ± 4	$6.04 \pm 1.04 \times 10^{-2}$[g]			
hNaV1.7	130	336 ± 14	$2.98 \pm 0.13 \times 10^{-3}$[h]	$1.75 \pm 0.29 \times 10^{-5}$	$3.93 \pm 0.82 \times 10^{-4}$[#]	22.5
	390	189 ± 27	$5.58 \pm 0.68 \times 10^{-3}$[i]			
	1,300	50 ± 9	$2.27 \pm 0.35 \times 10^{-2}$[j]			

*$k_{obs} = 1/\tau_{on}$, where k_{obs} is observed k_{on}; $k_{off} = 1/\tau_{off}$; $K_d = k_{off}/k_{on}$; k_{on} is derived by plotting k_{obs} at three concentrations against their respective concentration to obtain a linear curve-fit ($y = mx + c$), where the slope (m) represented the actual k_{on}. [a] refer **Figures 6A–C** for corresponding p values; [b and c, e and f, h and i, #] not significantly different ($p > 0.05$); [c and d] significantly different ($p < 0.001$); [b and d] significantly different ($p < 0.0001$); [f and g] significantly different ($p < 0.05$); [e and g, i and j, h and j] significantly different ($p < 0.01$).*

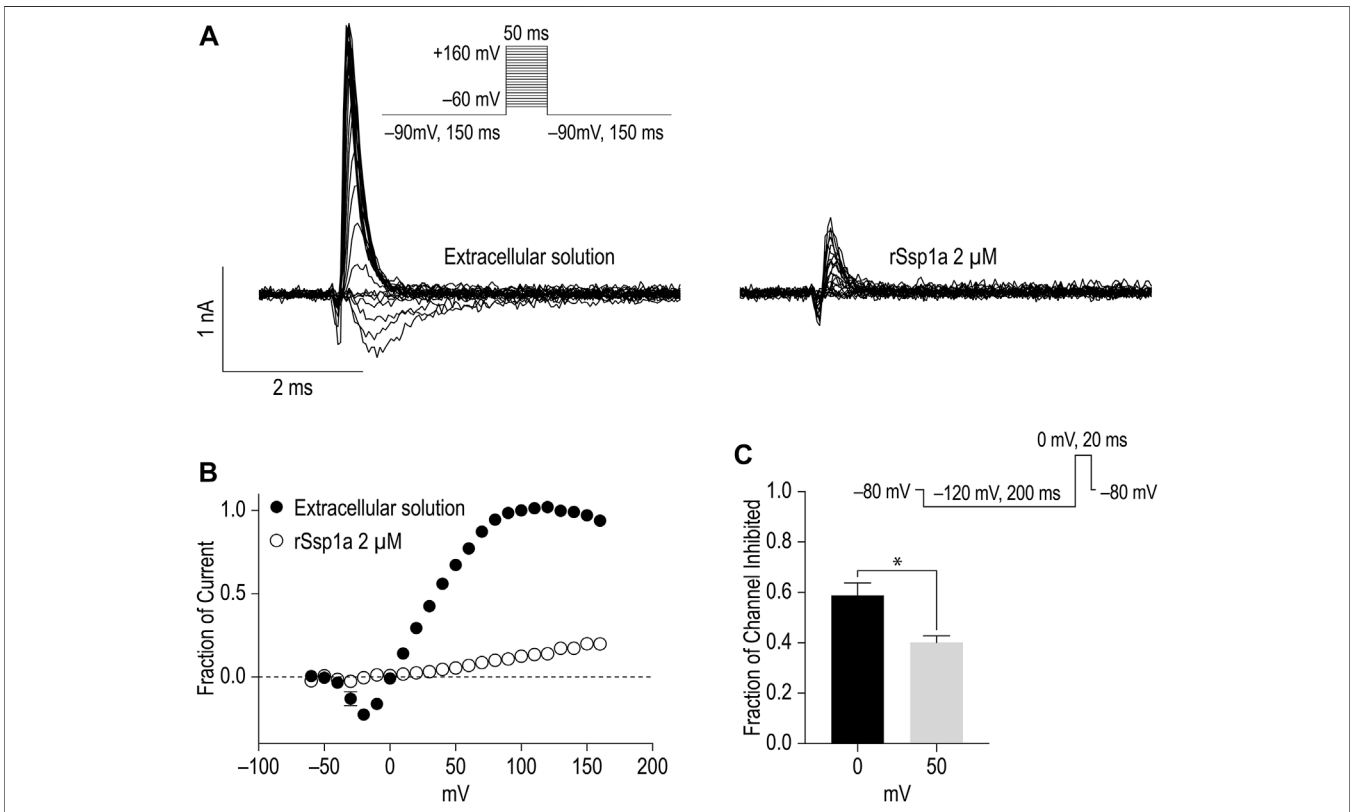

FIGURE 7 | Voltage-dependent inhibition of $hNa_V1.7$ by rSsp1a. **(A)** A current-voltage assay of $hNa_V1.7$ at strong depolarizing potential ranging from –60 to +160 mV. The $hNa_V1.7$ currents were recorded before (left) and after (right) application of toxin. **(B)** Current-voltage plot of peak current amplitude obtained before and after application of 2 µM rSsp1a (n = 5). Current amplitudes were normalized against the amplitude at –100 mV before rSsp1a application. **(C)** Voltage dependent inhibition of $hNa_V1.7$ at 0 and 50 mV test pulse by 255 nM (IC_{70}) rSsp1a (n = 4). The statistical significance was tested using Student's t-test. Data are shown as mean ± SEM. *$p < 0.05$.

DISCUSSION

The advances in analytical and high-throughput technologies have overcome the hindrances of discovering and characterizing bioactive compounds from the smaller species such as spiders that produce miniscule amounts of venom (Escoubas et al., 2006; Pineda et al., 2014; Dongol et al., 2019). Pioneering work in the 1980s to elucidate the Na_V-modulating effect of crude venom from *Phoneutria nigriventer* (Fontana and Vital-Brazil, 1985) and µ-agatoxins from *Agelenopsis aperta* (Adams et al., 1989)

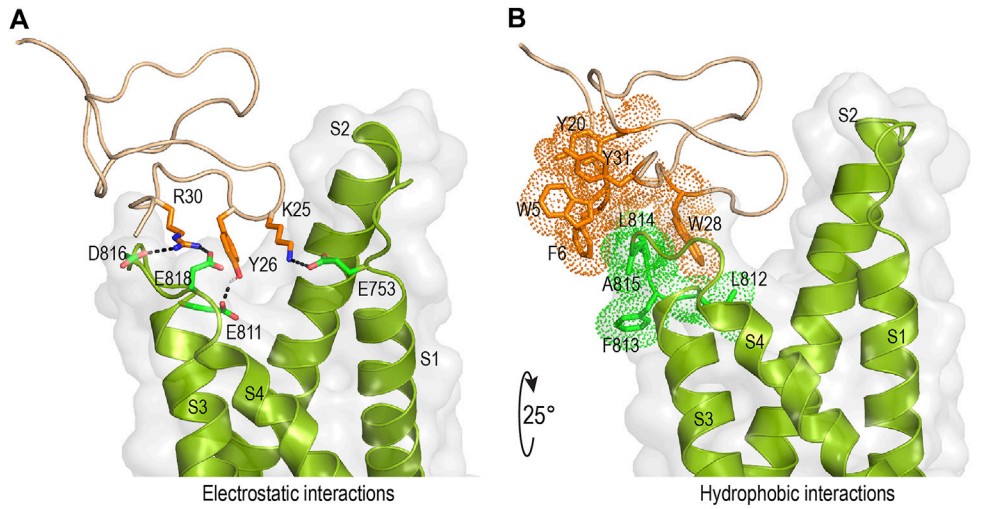

FIGURE 8 | Molecular interaction of rSsp1a at hNa$_V$1.7 VSD II. **(A,B)** Molecular docking results of rSsp1a at hNa$_V$1.7 VSD II illustrating electrostatic and hydrophobic interactions. HADDOCK2.2 Easy interface (Van Zundert et al., 2016) was used to dock rSsp1a at recently solved resting structure of Na$_V$Ab/Na$_V$1.7-VS2A chimera (PDB 7K48) (Wisedchaisri et al., 2021) and the results were visualized using Pymol 2.4.1 (DeLano, 2002).

commenced the era of spider-venom toxin research. Initially these toxins served as a resource of novel ligands for ion channels and receptors to probe their structure–function (Escoubas et al., 2000; Stevens et al., 2011; Kalia et al., 2015; Wu et al., 2018) and later provided a novel library of potential drug leads (Saez et al., 2010; Pineda et al., 2014; Cardoso and Lewis, 2019; Saez and Herzig, 2019). Of the estimated >10 million bioactive peptides in the venom of spider species, < 0.01% have been described (Wilson, 2016), the majority of which targeted ion channels, importantly Na$_V$s and Ca$_v$s that are potential therapeutic targets (Smith et al., 2015). Building on this opportunity, we discovered and characterized a new Na$_V$-modulatory toxin from the venom of an Australian theraphosid *Selenotypus* species with potential as a therapeutic lead.

Isolation and Production of Ssp1a

Using hNa$_V$1.7-guided fractionation of venom from a *Selenotypus* species, we isolated a new peptide, Ssp1a. Native Ssp1a is 33-residue long, C-terminal amidated venom peptide belonging to the NaSpTx1 family defined by conserved WCK/R motif, strongly conserved proline in loop 2, and intercysteine connectivity (C1–C4, C2–C5 and C3–C6) generating an anti-parallel β-sheet within a cystine knot (Klint et al., 2012). The closest homolog of Ssp1a with sequence identity 76% is a 32-residue μ-TRTX-Se1a isolated from *Selenocosmia effera* (Klint et al., 2015), which remains uncharacterized. Further, Ssp1a has a completely characterized homolog, HwTx-IV, that shares the same Na$_V$-inhibitory mechanism and has 40% sequence identity with Ssp1a (**Figure 1F**). Thus, Ssp1a characterization might represent several closer uncharacterized homologs. A previously described bacterial expression system (Klint et al., 2013) efficiently produced the rSsp1a with a non-native N-terminal glycine TEV protease cleavage remnant and without C-terminal amidation. The periplasm expressed linear rSsp1a was folded under the redox environment provided by a GSH/GSSG redox pair. Nickel affinity chromatography and RP-HPLC separation techniques were used to purify rSsp1a as a single major product with the predicted mass (**Figures 2A,B**).

Structure of rSsp1a

The 2D NMR analysis of this cysteine-rich rSsp1a confirmed that the peptide adopted a typical ICK fold (**Figures 2C–E**) which is the most prominent among the structural motifs, including disulfide-directed β-hairpin (DDH), Kunitz-type, colipase-like and helical arthropod-neuropeptide-derived (HAND), adopted by spider venom cysteine-rich peptides (Langenegger et al., 2019; Pineda et al., 2020). rSsp1a displayed an amphipathic surface comprising hydrophobic and charged patches (**Figure 2F**) often contributing to the interacting surface of ICK peptides (**Figure 2H**) (Lee and MacKinnon, 2004; Henriques et al., 2016; Lawrence et al., 2019). This surface typically includes functional residues (Y33 and K32) adjacent to hydrophobic residues (W30 and F6) that form the high affinity interface as shown for HwTx-IV (**Figure 2I**). Interestingly, rSsp1a surface displayed a cluster of K25, Y26 and R30 adjacent to a hydrophobic patch comprising W5, F6, Y26, Y31 and W28, that appears to facilitate charge-charge interactions (**Figure 2G**), as supported by docking study discussed below.

Pharmacology of rSsp1a

Whole-cell automated patch clamp electrophysiology revealed rSsp1a was inactive at hNa$_V$1.4 and hNa$_V$1.5, as well as at hNa$_V$1.8 but dose-dependently inhibited neuronal hNa$_V$1.7 > 1.6 > 1.2 > 1.3 > 1.1 (**Figures 3A,B**). The related HwTx-IV was similarly potent (IC$_{50}$ 41–190 nM) at these five subtypes but had an altered rank order hNa$_V$1.1 > 1.2 > 1.6 > 1.7 > 1.3 (Gonçalves et al., 2018). Interestingly, the rank order of potency of the

$Na_V1.7$ potency-optimized m3-HwTx-IV ($hNa_V1.7$ > 1.6 > 1.3 > 1.1 > 1.2) was more similar to rSsp1a despite its enhanced potency (IC_{50} 3.3–11.9 nM) (Rahnama et al., 2017), while the most closely related CcoTx-1 had a different potency rank [$hNa_V1.2$ (~70 nM) > 1.1 (~1,000 nM) > 1.7 (~5,120 nM >> 1.3 and 1.6] in FLIPR assays (Sousa et al., 2017). These results exemplify that achieving improved subtype-selectivity can be challenging; however, lack of effect of these toxins on $hNa_V1.4$ (muscle isoform) and $hNa_V1.5$ (cardiac isoform) should simplify further development (Gonçalves et al., 2018).

The high potency of rSsp1a at $hNa_V1.7$ indicates potential to inhibit pain signalling (Yang et al., 2004; Cox et al., 2006; Fertleman et al., 2006; Faber et al., 2012; Vetter et al., 2017). $hNa_V1.7$ is a compelling target for pain therapeutics as silencing its activity completely caused pain insensitivity without any serious side effects except anosmia (Cox et al., 2006; Liu et al., 2014b; Tanaka et al., 2015; Deuis et al., 2017a; Flinspach et al., 2017; Zhang et al., 2018; Cardoso and Lewis, 2019; Mueller et al., 2019). rSsp1a potently inhibited $hNa_V1.6$ (IC_{50} 191 nM) which plays a role in a variety of pain models, including oxaliplatin-induced cold allodynia (Sittl et al., 2012; Deuis et al., 2013), spinal nerve ligation induced mechanical pain (Xie et al., 2015), painful diabetic neuropathy (Ren et al., 2012) and trigeminal neuralgia (Tanaka et al., 2016), as well as in epilepsy (Blanchard et al., 2015; de Kovel et al., 2014; O'Brien and Meisler, 2013; Veeramah et al., 2012). However, the high expression of $hNa_V1.6$ in peripheral motor neurons contributing to saltatory conduction of action potential may limit the utility of rSsp1a as a systemic analgesic lead (Rahnama et al., 2017; Gonçalves et al., 2018), although $Na_V1.6$-selective blockers such as Xen901 (Bialer et al., 2018) and GS967 (Baker et al., 2018) have shown promise in treating epileptogenic disorders. The third most potently inhibited subtype $hNa_V1.2$, localized in the central nervous system, is associated with epileptogenic channelopathies and might serve as an important therapeutic target for epilepsy-related disorders (Menezes et al., 2020). Similarly, rSsp1a also targeted $hNa_V1.3$ suggesting potential to reverse pain phenotypes in animal models of neuropathic and inflammatory pain (Black et al., 1999; Kim et al., 2001; Hains et al., 2004; Hong et al., 2004; Garry et al., 2005; Lindia et al., 2005; Black et al., 2008; Chen et al., 2014; Tan et al., 2015; Xu et al., 2016) where it might be re-expressed in injured or affected sensory nerve (Waxman et al., 1994; Wang et al., 2011; Bennett et al., 2019). Lastly, the nanomolar inhibition of $hNa_V1.1$ by rSsp1a suggest it may prove useful in reducing visceral pain and mechanical hypersensitivity (Osteen et al., 2016; Salvatierra et al., 2018).

Further pharmacological characterization was carried out on $hNa_V1.7$, $hNa_V1.3$ and $hNa_V1.2$ that were most potently targeted by rSsp1a. rSsp1a reduced channel conductance with small effects on voltage-dependence of activation and inactivation at all three subtypes (**Figure 4**; **Table 1**), reminiscent of the inhibitory spider toxins HwTx-IV (Xiao et al., 2008; Xiao et al., 2010), HnTx-III (Liu et al., 2013) and HnTx-IV (Cai et al., 2015) from the NaSpTx1 family. Earlier studies suggesting HwTx-IV traps VSD II S4 in the closed (resting) state (Xiao et al., 2008; Xiao et al., 2010; Xiao et al., 2011) were confirmed by $hNa_V1.7$ channel mutations (Cai et al., 2015; Liu et al., 2013; Xiao et al., 2008) and the recent cryo-EM structure analysis of the $Na_VAb/Na_V1.7$-VS2A–m3-HwTx-IV complex (Wisedchaisri et al., 2021). Gating modifier spider ICK peptides can modulate the channel conductance by targeting neurotoxin Site 3 (domain IV) and Site 4 (domain II) in either the 1) down state of DII S4 (closed channel), 2) up state of DII S4 (open channel), and 3) down state of DIV S4 (open channel) (Dongol et al., 2019). Recently, the spider ICK peptide Tsp1a was reported to stabilize the inactivated state of the channel in the up state of DIV S4 (closed channel) (Jiang et al., 2021). Although rSsp1a's effect on channel activation and inactivation at the three subtypes tested was independent of membrane potential, the extent of inhibition was voltage dependent (**Figure 7C**) and at saturating concentrations of rSsp1a, inward currents were fully inhibited at moderate depolarizations, while depolarizations above +50 mV partially restored current (**Figures 7A,B**). This phenomena is not observed with pore blockers, such as TTX (Xiao et al., 2008; Liu et al., 2013), indicating that rSsp1a is a gating modifier like HwTx-IV (Xiao et al., 2008), HnTx-IV (Cai et al., 2015), and HnTx-III (Liu et al., 2013) which trap VSD II in the closed state. Interestingly, rSsp1a did not alter the $hNa_V1.7$ recovery from fast inactivation but slightly enhanced recovery from inactivation for $hNa_V1.2$ and $hNa_V1.3$ (**Figure 5**). On-rates were concentration-dependent, with rSsp1a binding to $hNa_V1.2$ and $hNa_V1.7$ at slower rate than to $hNa_V1.3$ (**Figures 6A–C**; **Table 2**). Off-rates at $hNa_V1.2$, $hNa_V1.7$ and $hNa_V1.3$ were slow and incomplete (**Figures 6E–G**) and the toxin had comparatively higher affinity for $hNa_V1.7$ and $hNa_V1.2$ than for $hNa_V1.3$.

Molecular Docking of rSsp1a at $hNa_V1.7$

rSsp1a, HwTx-IV, HnTx-IV, and HnTx-III from the NaSpTx1 family share similar mechanisms of action and are expected to bind at overlapping sites on Na_V channels. Mutational (Xiao et al., 2008; Liu et al., 2013; Cai et al., 2015) and recent cryo-EM structures of $Na_V1.7$ with bound HwTx-IV (Shen et al., 2019) or m3-HwTx-IV (Wisedchaisri et al., 2021) suggest rSsp1a might also bind to VSD II in the closed state. This was supported by docking studies that revealed rSsp1a bound to $Na_V1.7$ similarly to m3-HwTx-IV to make important electrostatic and hydrophobic interactions with the S1–S2 and S3–S4 loop that would allow it to trap VSD II in the resting state (Wisedchaisri et al., 2021). Specifically, predicted functional residues K25 and R30 formed salt bridges with the acidic E753, D816 and E818, while Y26 H-bonded with E811 (**Figure 8A**). Docking suggests Y31 plays a lesser role in rSsp1a, whereas the equivalent Y33 in HwTx-IV is functionally critical (**Figures 2G,I**) (Minassian et al., 2013). The Y26 equivalent in HwTx-IV (T28) showed differential activity at hNa_V subtypes, as T28A-HwTx-IV had reduced potency (6-fold) at $hNa_V1.2$ but similar potency at $hNa_V1.7$ (Minassian et al., 2013). In contrast, the equivalent H27 in GpTx-1 was key to $hNa_V1.7$ inhibition, with H27A-GpTx-1

showing a 10-fold potency reduction at this subtype (Murray et al., 2015). Comparison of the surfaces of rSsp1a and HwTx-IV (**Figures 2F–I**) revealed that the interacting face of these toxins comprises hydrophobic and basic residues distributed around the WCK/R motif. However, with 20% basic residues in HwTx-IV compared to 12% in rSsp1a, HwTx-IV contributes more basic residues to the binding face than rSsp1a, affecting charge distribution, hydrophobicity and toxin-membrane interaction (Henriques et al., 2016; Agwa et al., 2017; Lawrence et al., 2019). The low sequence identity of rSsp1a (40%) compared to HwTx-IV is expected to provide new opportunities to optimize its potency and/or hNa_V subtype selectivity.

Channel mutational (Xu et al., 2019; Xiao et al., 2010; Zeng et al., 2018; Cai et al., 2015; Xiao et al., 2011) and recent structural evidence (Xiao et al., 2011; Cai et al., 2015) have revealed that acidic residues in the VSD II S1–S2 loop (E753) and S3–S4 loop (E811, D816 and E818) provide the key toxin–channel interactions (Wisedchaisri et al., 2021). In addition to these charge interactions, hydrophobic interactions are also important in forming stable and high affinity toxin–channel complex. Accordingly, in the rSsp1a–$hNa_V1.7$ VSD II docking, we observed the rSsp1a aromatic patch (W5, F6, Y20, W28, and Y31) contributed hydrophobic interactions with $hNa_V1.7$ VSD II S3–S4 (L812, F813, L814, and A815) (**Figure 8A**). A similar set of interactions was also observed in the m3-HwTx-IV–Na_VAb/$Na_V1.7$ VS2A complex (Wisedchaisri et al., 2021) where I5, F6, W30 and W33 interacted with the LFLA stretch in the S3–S4 loop to inhibit upward movement of voltage sensor S4 upon membrane depolarization.

CONCLUDING REMARKS

We characterized a new spider toxin Ssp1a which potently inhibited neuronal Na_V-channels with little effect on the voltage-dependence of activation and inactivation or delay in recovery from inactivation. These and docking data indicate Ssp1a traps VSD II of hNa_V channel in the resting state. Ssp1a is distantly related to well-characterized HwTx-IV (40% sequence identity) though each share the conserved WCK/R motif. Extending its pharmacological characterization to structure–function studies at $hNa_V1.2$, $hNa_V1.3$ and $hNa_V1.7$ will help guide the development of potent and subtype selective inhibitors as well as provide new insights into the structure–function details to NaSpTx1 homologs more closely related to Ssp1a.

DATA AVAILABILITY STATEMENT

The original contributions presented in the study are included in the article/**Supplementary Material**, further inquiries can be directed to the corresponding author. The dataset generated/analyzed for rSsp1a structure can be found in the Protein Data Bank (PDB code 7SKC; PDB DOI: 10.2210/pdb7skc/pdb) and Biological Magnetic Resonance Data Bank (BMRB Code: 30961).

AUTHOR CONTRIBUTIONS

YD, PMC, FCC, and DTW performed experiments; YD, FCC, and NLD analysed data, and YD and RJL interpreted the data. YD wrote the first draft of the manuscript, FCC and RJL contributed to PhD supervision, and RJL conceived and directed the study. All authors edited and approved drafts of the manuscript.

FUNDING

This work was supported by the Australian National Health and Medical Research Council (NHMRC) Program Grant APP1072113 and Principal Research Fellowship APP1119056 (to RJL), and an NHMRC Ideas Grant APP1188959 (to RJL and FCC). YD was supported by a UQ Research Training Scholarship. The James Cook University NMR facility was partially funded by the Australian Research Council (LE120100015, LE160100218).

ACKNOWLEDGMENTS

The authors thank Alun Jones from IMB Mass Spectrometry Facility for helping with mass spectrometric analysis, and Jennifer Deuis and Irina Vetter from Vetter lab for providing CHO cells stably expressing $hNa_V1.8/\beta3$ and help in QPatch experiments. We thank Tianjiao Zhao and Md. Mahadhi Hasan for help and advice.

SUPPLEMENTARY MATERIAL

The Supplementary Material for this article can be found online at: https://www.frontiersin.org/articles/10.3389/fphar.2021.795455/full#supplementary-material

REFERENCES

Adams, M. E., Herold, E. E., and Venema, V. J. (1989). Two Classes of Channel-specific Toxins from Funnel Web Spider Venom. *J. Comp. Physiol. A.* 164, 333–342. doi:10.1007/BF00612993

Agwa, A. J., Lawrence, N., Deplazes, E., Cheneval, O., Chen, R. M., Craik, D. J., et al. (2017). Spider Peptide Toxin HwTx-IV Engineered to Bind to Lipid Membranes Has an Increased Inhibitory Potency at Human Voltage-Gated Sodium Channel hNaV1.7. *Biochim. Biophys. Acta Biomembr* 1859, 835–844. doi:10.1016/j.bbamem.2017.01.020

Ahern, C. A., Payandeh, J., Bosmans, F., and Chanda, B. (2016). The Hitchhiker's Guide to the Voltage-Gated Sodium Channel Galaxy. *J. Gen. Physiol.* 147, 1–24. doi:10.1085/jgp.201511492

Bagal, S. K., Marron, B. E., Owen, R. M., Storer, R. I., and Swain, N. A. (2015). Voltage Gated Sodium Channels as Drug Discovery Targets. *Channels (Austin)* 9, 360–366. doi:10.1080/19336950.2015.1079674

Baker, E. M., Thompson, C. H., Hawkins, N. A., Wagnon, J. L., Wengert, E. R., Patel, M. K., et al. (2018). The Novel Sodium Channel Modulator GS-458967 (GS967) Is an Effective Treatment in a Mouse Model of SCN8A Encephalopathy. *Epilepsia* 59, 1166–1176. doi:10.1111/epi.14196

Bennett, D. L., Clark, A. J., Huang, J., Waxman, S. G., and Dib-Hajj, S. D. (2019). The Role of Voltage-gated Sodium Channels in Pain Signaling. *Physiol. Rev.* 99, 1079–1151. doi:10.1152/physrev.00052.2017

Bialer, M., Johannessen, S. I., Koepp, M. J., Levy, R. H., Perucca, E., Tomson, T., et al. (2018). Progress Report on New Antiepileptic Drugs: A Summary of the Fourteenth Eilat Conference on New Antiepileptic Drugs and Devices (EILAT XIV). I. Drugs in Preclinical and Early Clinical Development. *Epilepsia* 59, 1811–1841. doi:10.1111/epi.14557

Black, J. A., Cummins, T. R., Plumpton, C., Chen, Y. H., Hormuzdiar, W., Clare, J. J., et al. (1999). Upregulation of a Silent Sodium Channel after Peripheral, but Not Central, Nerve Injury in DRG Neurons. *J. Neurophysiol.* 82, 2776–2785. doi:10.1152/jn.1999.82.5.2776

Black, J. A., Nikolajsen, L., Kroner, K., Jensen, T. S., and Waxman, S. G. (2008). Multiple Sodium Channel Isoforms and Mitogen-Activated Protein Kinases Are Present in Painful Human Neuromas. *Ann. Neurol.* 64, 644–653. doi:10.1002/ana.21527

Blanchard, M. G., Willemsen, M. H., Walker, J. B., Dib-Hajj, S. D., Waxman, S. G., Jongmans, M. C., et al. (2015). *De Novo* Gain-of-function and Loss-Of-Function Mutations of *SCN8A* in Patients with Intellectual Disabilities and Epilepsy. *J. Med. Genet.* 52, 330–337. doi:10.1136/jmedgenet-2014-102813

Bosmans, F., and Swartz, K. J. (2010). Targeting Voltage Sensors in Sodium Channels with Spider Toxins. *Trends Pharmacol. Sci.* 31, 175–182. doi:10.1016/j.tips.2009.12.007

Cai, T., Luo, J., Meng, E., Ding, J., Liang, S., Wang, S., et al. (2015). Mapping the Interaction Site for the Tarantula Toxin Hainantoxin-IV (β-TRTX-Hn2a) in the Voltage Sensor Module of Domain II of Voltage-Gated Sodium Channels. *Peptides* 68, 148–156. doi:10.1016/j.peptides.2014.09.005

Cannon, S. C. (2010). Voltage-sensor Mutations in Channelopathies of Skeletal Muscle. *J. Physiol.* 588, 1887–1895. doi:10.1113/jphysiol.2010.186874

Cardoso, F. C., Castro, J., Grundy, L., Schober, G., Garcia-Caraballo, S., Zhao, T., et al. (2021). A Spider-venom Peptide with Multitarget Activity on Sodium and Calcium Channels Alleviates Chronic Visceral Pain in a Model of Irritable Bowel Syndrome. *Pain* 162, 569–581. doi:10.1097/j.pain.0000000000002041

Cardoso, F. C., Dekan, Z., Rosengren, K. J., Erickson, A., Vetter, I., Deuis, J. R., et al. (2015). Identification and Characterization of ProTx-III [μ-TRTX-Tp1a], a New Voltage-Gated Sodium Channel Inhibitor from Venom of the Tarantula *Thrixopelma pruriens*. *Mol. Pharmacol.* 88, 291–303. doi:10.1124/mol.115.098178

Cardoso, F. C., Dekan, Z., Smith, J. J., Deuis, J. R., Vetter, I., Herzig, V., et al. (2017). Modulatory Features of the Novel Spider Toxin μ-TRTX-Df1a Isolated from the Venom of the Spider *Davus fasciatus*. *Br. J. Pharmacol.* 174, 2528–2544. doi:10.1111/bph.13865

Cardoso, F. C., and Lewis, R. J. (2018). Sodium Channels and Pain: from Toxins to Therapies. *Br. J. Pharmacol.* 175, 2138–2157. doi:10.1111/bph.139610.1111/bph.13962

Cardoso, F. C., and Lewis, R. J. (2019). Structure-function and Therapeutic Potential of Spider Venom-derived Cysteine Knot Peptides Targeting Sodium Channels. *Front. Pharmacol.* 10, 366. doi:10.3389/fphar.2019.00366

Chen, H. P., Zhou, W., Kang, L. M., Yan, H., Zhang, L., Xu, B. H., et al. (2014). Intrathecal miR-96 Inhibits Nav1.3 Expression and Alleviates Neuropathic Pain in Rat Following Chronic Construction Injury. *Neurochem. Res.* 39, 76–83. doi:10.1007/s11064-013-1192-z

Cierpicki, T., and Otlewski, J. (2001). Amide Proton Temperature Coefficients as Hydrogen Bond Indicators in Proteins. *J. Biomol. NMR* 21, 249–261. doi:10.1023/a:1012911329730

Cox, J. J., Reimann, F., Nicholas, A. K., Thornton, G., Roberts, E., Springell, K., et al. (2006). An *SCN9A* Channelopathy Causes Congenital Inability to Experience Pain. *Nature* 444, 894–898. doi:10.1038/nature05413

de Kovel, C. G., Meisler, M. H., Brilstra, E. H., van Berkestijn, F. M., van 't Slot, R., van Lieshout, S., et al. (2014). Characterization of a *De Novo SCN8A* Mutation in a Patient with Epileptic Encephalopathy. *Epilepsy Res.*. 108: 1511–151. doi:10.1016/j.eplepsyres.2014.08.020

de Lera Ruiz, M., and Kraus, R. L. (2015). Voltage-gated Sodium Channels: Structure, Function, Pharmacology, and Clinical Indications. *J. Med. Chem.* 58, 7093–7118. doi:10.1021/jm501981g

DeLano, W. (2002). *The PyMOL Molecular Graphics System*. San Carlos, CA, USA: DeLano Scientific.

Deuis, J. R., Dekan, Z., Wingerd, J. S., Smith, J. J., Munasinghe, N. R., Bhola, R. F., et al. (2017a). Pharmacological Characterisation of the Highly NaV1.7 Selective Spider Venom Peptide Pn3a. *Sci. Rep.* 7, 40883. doi:10.1038/srep40883

Deuis, J. R., Mueller, A., Israel, M. R., and Vetter, I. (2017b). The Pharmacology of Voltage-Gated Sodium Channel Activators. *Neuropharmacology* 127, 87–108. doi:10.1016/j.neuropharm.2017.04.014

Deuis, J. R., Zimmermann, K., Romanovsky, A. A., Possani, L. D., Cabot, P. J., Lewis, R. J., et al. (2013). An Animal Model of Oxaliplatin-Induced Cold Allodynia Reveals a Crucial Role for Nav1.6 in Peripheral Pain Pathways. *Pain* 154, 1749–1757. doi:10.1016/j.pain.2013.05.032

Dongol, Y., Cardoso, F. C., and Lewis, R. J. (2019). Spider Knottin Pharmacology at Voltage-gated Sodium Channels and Their Potential to Modulate Pain Pathways. *Toxins (Basel)* 11, 626. doi:10.3390/toxins11110626

Dowling, M. R., and Charlton, S. J. (2006). Quantifying the Association and Dissociation Rates of Unlabelled Antagonists at the Muscarinic M3 Receptor. *Br. J. Pharmacol.* 148, 927–937. doi:10.1038/sj.bjp.0706819

Escoubas, P., Diochot, S., and Corzo, G. (2000). Structure and Pharmacology of Spider Venom Neurotoxins. *Biochimie* 82, 893–907. doi:10.1016/S0300-9084(00)01166-4

Escoubas, P., Sollod, B., and King, G. F. (2006). Venom Landscapes: Mining the Complexity of Spider Venoms via a Combined cDNA and Mass Spectrometric Approach. *Toxicon* 47, 650–663. doi:10.1016/j.toxicon.2006.01.018

Faber, C. G., Hoeijmakers, J. G., Ahn, H. S., Cheng, X., Han, C., Choi, J. S., et al. (2012). Gain of Function Nav1.7 Mutations in Idiopathic Small Fiber Neuropathy. *Ann. Neurol.* 71, 26–39. doi:10.1002/ana.22485

Fertleman, C. R., Baker, M. D., Parker, K. A., Moffatt, S., Elmslie, F. V., Abrahamsen, B., et al. (2006). *SCN9A* Mutations in Paroxysmal Extreme Pain Disorder: Allelic Variants Underlie Distinct Channel Defects and Phenotypes. *Neuron* 52, 767–774. doi:10.1016/j.neuron.2006.10.006

Flinspach, M., Xu, Q., Piekarz, A. D., Fellows, R., Hagan, R., Gibbs, A., et al. (2017). Insensitivity to Pain Induced by a Potent Selective Closed-State Nav1.7 Inhibitor. *Sci. Rep.* 7, 39662. doi:10.1038/srep39662

Fontana, M. D., Vital-Brazil, O., and Vital-Brasil, O. (1985). Mode of Action of *Phoneutria nigriventer* Spider Venom at the Isolated Phrenic Nerve-Diaphragm of the Rat. *Braz. J. Med. Biol. Res.* 18, 557–565.

Garry, E. M., Delaney, A., Anderson, H. A., Sirinathsinghji, E. C., Clapp, R. H., Martin, W. J., et al. (2005). Varicella Zoster Virus Induces Neuropathic Changes in Rat Dorsal Root Ganglia and Behavioral Reflex Sensitisation that Is Attenuated by Gabapentin or Sodium Channel Blocking Drugs. *Pain* 118, 97–111. doi:10.1016/j.pain.2005.08.003

Gasteiger, E., Hoogland, C., Gattiker, A., Duvaud, S. e., Wilkins, M. R., Appel, R. D., et al. (2005). "Protein Identification and Analysis Tools on the ExPASy Server," in *The Proteomics Protocols Handbook.Springer Protocols Handbooks*. Editor J. M. Walker (Totowa, New Jersey: Humana Press), 571–607. doi:10.1385/1-59259-890-0:571

Gonçalves, T. C., Boukaiba, R., Molgó, J., Amar, M., Partiseti, M., Servent, D., et al. (2018). Direct Evidence for High Affinity Blockade of NaV1.6 Channel Subtype by Huwentoxin-IV Spider Peptide, Using Multiscale Functional Approaches. *Neuropharmacology* 133, 404–414. doi:10.1016/j.neuropharm.2018.02.016

Güntert, P. (2004). "Automated NMR Structure Calculation with CYANA," in *Protein NMR Techniques*. Editor A. K. Downing (Totowa, New Jersey: Humana Press), 353–378.

Hains, B. C., Saab, C. Y., Klein, J. P., Craner, M. J., and Waxman, S. G. (2004). Altered Sodium Channel Expression in Second-Order Spinal Sensory Neurons Contributes to Pain after Peripheral Nerve Injury. *J. Neurosci.* 24, 4832–4839. doi:10.1523/jneurosci.0300-04.2004

Henriques, S. T., Deplazes, E., Lawrence, N., Cheneval, O., Chaousis, S., Inserra, M., et al. (2016). Interaction of Tarantula Venom Peptide ProTx-II with Lipid Membranes Is a Prerequisite for its Inhibition of Human Voltage-gated Sodium Channel NaV1.7. *J. Biol. Chem.* 291, 17049–17065. doi:10.1074/jbc.M116.729095

Hong, S., Morrow, T. J., Paulson, P. E., Isom, L. L., and Wiley, J. W. (2004). Early Painful Diabetic Neuropathy Is Associated with Differential Changes in Tetrodotoxin-sensitive and -resistant Sodium Channels in Dorsal Root Ganglion Neurons in the Rat. *J. Biol. Chem.* 279, 29341–29350. doi:10.1074/jbc.M404167200

Jeevaratnam, K., Guzadhur, L., Goh, Y. M., Grace, A. A., and Huang, C. L. (2016). Sodium Channel Haploinsufficiency and Structural Change in Ventricular Arrhythmogenesis. *Acta Physiol. (Oxf)* 216, 186–202. doi:10.1111/apha.12577

Jiang, Y., Castro, J., Blomster, L. V., Agwa, A. J., Maddern, J., Schober, G., et al. (2021). Pharmacological Inhibition of the Voltage-gated Sodium Channel NaV1.7 Alleviates Chronic Visceral Pain in a Rodent Model of Irritable Bowel Syndrome. *ACS Pharmacol. Transl. Sci.* 4, 1362–1378. doi:10.1021/acsptsci.1c00072

Jurkat-Rott, K., Holzherr, B., Fauler, M., and Lehmann-Horn, F. (2010). Sodium Channelopathies of Skeletal Muscle Result from Gain or Loss of Function. *Pflugers Arch.* 460, 239–248. doi:10.1007/s00424-010-0814-4

Kahlig, K. M., Rhodes, T. H., Pusch, M., Freilinger, T., Pereira-Monteiro, J. M., Ferrari, M. D., et al. (2008). Divergent Sodium Channel Defects in Familial Hemiplegic Migraine. *Proc. Natl. Acad. Sci. U. S. A.* 105, 9799–9804. doi:10.1073/pnas.0711717105

Kalia, J., Milescu, M., Salvatierra, J., Wagner, J., Klint, J. K., King, G. F., et al. (2015). From Foe to Friend: Using Animal Toxins to Investigate Ion Channel Function. *J. Mol. Biol.* 427, 158–175. doi:10.1016/j.jmb.2014.07.027

Kaplan, D. I., Isom, L. L., and Petrou, S. (2016). Role of Sodium Channels in Epilepsy. *Cold Spring Harb. Perspect. Med.* 6, a022814. doi:10.1101/cshperspect.a022814

Kim, C. H., Oh, Y., Chung, J. M., and Chung, K. (2001). The Changes in Expression of Three Subtypes of TTX Sensitive Sodium Channels in Sensory Neurons after Spinal Nerve Ligation. *Brain Res. Mol. Brain Res.* 95, 153–161. doi:10.1016/s0169-328x(01)00226-1

Klint, J. K., Senff, S., Rupasinghe, D. B., Er, S. Y., Herzig, V., Nicholson, G. M., et al. (2012). Spider-venom Peptides that Target Voltage-gated Sodium Channels: Pharmacological Tools and Potential Therapeutic Leads. *Toxicon* 60, 478–491. doi:10.1016/j.toxicon.2012.04.337

Klint, J. K., Senff, S., Saez, N. J., Seshadri, R., Lau, H. Y., Bende, N. S., et al. (2013). Production of Recombinant Disulfide-rich Venom Peptides for Structural and Functional Analysis via Expression in the Periplasm of *E. coli*. *PLoS One* 8, e63865. doi:10.1371/journal.pone.0063865

Klint, J. K., Smith, J. J., Vetter, I., Rupasinghe, D. B., Er, S. Y., Senff, S., et al. (2015). Seven Novel Modulators of the Analgesic Target NaV 1.7 Uncovered Using a High-Throughput Venom-based Discovery Approach. *Br. J. Pharmacol.* 172, 2445–2458. doi:10.1111/bph.13081

Koradi, R., Billeter, M., and Wüthrich, K. (1996). MOLMOL: a Program for Display and Analysis of Macromolecular Structures. *J. Mol. Graph.* 14, 51–32. doi:10.1016/0263-7855(96)00009-4

Kwong, K., and Carr, M. J. (2015). Voltage-gated Sodium Channels. *Curr. Opin. Pharmacol.* 22, 131–139. doi:10.1016/j.coph.2015.04.007

Kyte, J., and Doolittle, R. F. (1982). A Simple Method for Displaying the Hydropathic Character of a Protein. *J. Mol. Biol.* 157, 105–132. doi:10.1016/0022-2836(82)90515-0

Langenegger, N., Nentwig, W., and Kuhn-Nentwig, L. (2019). Spider Venom: Components, Modes of Action, and Novel Strategies in Transcriptomic and Proteomic Analyses. *Toxins (Basel)* 11, 611. doi:10.3390/toxins11100611

Lawrence, N., Wu, B., Ligutti, J., Cheneval, O., Agwa, A. J., Benfield, A. H., et al. (2019). Peptide-membrane Interactions Affect the Inhibitory Potency and Selectivity of Spider Toxins ProTx-II and GpTx-1. *ACS Chem. Biol.* 14, 118–130. doi:10.1021/acschembio.8b00989

Lee, S. Y., and MacKinnon, R. (2004). A Membrane-access Mechanism of Ion Channel Inhibition by Voltage Sensor Toxins from Spider Venom. *Nature* 430, 232–235. doi:10.1038/nature02632

Lindia, J. A., Köhler, M. G., Martin, W. J., and Abbadie, C. (2005). Relationship between Sodium Channel NaV1.3 Expression and Neuropathic Pain Behavior in Rats. *Pain* 117, 145–153. doi:10.1016/j.pain.2005.05.027

Liu, Y., Tang, J., Zhang, Y., Xun, X., Tang, D., Peng, D., et al. (2014b). Synthesis and Analgesic Effects of μ-TRTX-Hhn1b on Models of Inflammatory and Neuropathic Pain. *Toxins (Basel)* 6, 2363–2378. doi:10.3390/toxins6082363

Liu, Y., Wu, Z., Tang, D., Xun, X., Liu, L., Li, X., et al. (2014a). Analgesic Effects of Huwentoxin-IV on Animal Models of Inflammatory and Neuropathic Pain. *Protein Pept. Lett.* 21, 153–158. doi:10.2174/09298665113206660119

Liu, Z., Cai, T., Zhu, Q., Deng, M., Li, J., Zhou, X., et al. (2013). Structure and Function of Hainantoxin-III, a Selective Antagonist of Neuronal Tetrodotoxin-sensitive Voltage-gated Sodium Channels Isolated from the Chinese Bird Spider *Ornithoctonus hainana*. *J. Biol. Chem.* 288, 20392–20403. doi:10.1074/jbc.M112.426627

Menezes, L. F. S., Sabiá Júnior, E. F., Tibery, D. V., Carneiro, L. D. A., and Schwartz, E. F. (2020). Epilepsy-related Voltage-gated Sodium Channelopathies: A Review. *Front. Pharmacol.* 11, 1276. doi:10.3389/fphar.2020.01276

Milescu, M., Vobecky, J., Roh, S. H., Kim, S. H., Jung, H. J., Kim, J. I., et al. (2007). Tarantula Toxins Interact with Voltage Sensors within Lipid Membranes. *J. Gen. Physiol.* 130, 497–511. doi:10.1085/jgp.200709869

Minassian, N. A., Gibbs, A., Shih, A. Y., Liu, Y., Neff, R. A., Sutton, S. W., et al. (2013). Analysis of the Structural and Molecular Basis of Voltage-sensitive Sodium Channel Inhibition by the Spider Toxin Huwentoxin-IV (μ-TRTX-Hh2a). *J. Biol. Chem.* 288, 22707–22720. doi:10.1074/jbc.M113.461392

Mueller, A., Starobova, H., Morgan, M., Dekan, Z., Cheneval, O., Schroeder, C. I., et al. (2019). Antiallodynic Effects of the Selective NaV1.7 Inhibitor Pn3a in a Mouse Model of Acute Postsurgical Pain: Evidence for Analgesic Synergy with Opioids and Baclofen. *Pain* 160, 1766–1780. doi:10.1097/j.pain.0000000000001567

Murray, J. K., Ligutti, J., Liu, D., Zou, A., Poppe, L., Li, H., et al. (2015). Engineering Potent and Selective Analogues of GpTx-1, a Tarantula Venom Peptide Antagonist of the NaV-1.7 Sodium Channel. *J. Med. Chem.* 58, 2299–2314. doi:10.1021/jm501765v

O'Brien, J. E., and Meisler, M. H. (2013). Sodium Channel *SCN8A* (Nav1.6): Properties and De Novo Mutations in Epileptic Encephalopathy and Intellectual Disability. *Front. Genet.* 4, 213. doi:10.3389/fgene.2013.00213

Osteen, J. D., Herzig, V., Gilchrist, J., Emrick, J. J., Zhang, C., Wang, X., et al. (2016). Selective Spider Toxins Reveal a Role for the Nav1.1 Channel in Mechanical Pain. *Nature* 534, 494–499. doi:10.1038/nature17976

Patino, G. A., and Isom, L. L. (2010). Electrophysiology and beyond: Multiple Roles of Na+ Channel β Subunits in Development and Disease. *Neurosci. Lett.* 486, 53–59. doi:10.1016/j.neulet.2010.06.050

Pierre, N. (2011). Determination of Association (K_{on}) and Dissociation (K_{off}) Rates of Spiperone on the Dopamine D2 Receptor Using a Platform for GPCR Applications. *Am. Lab.*, 2–4. https://www.americanlaboratory.com/913-Technical-Articles/35225-Determination-of-Association-kon-and-Dissociation-koff-Rates-of-Spiperone-on-the-Dopamine-D2-Receptor-Using-a-Platform-for-GPCR-Applications/.

Pineda, S. S., Chin, Y. K., Undheim, E. A. B., Senff, S., Mobli, M., Dauly, C., et al. (2020). Structural Venomics Reveals Evolution of a Complex Venom by Duplication and Diversification of an Ancient Peptide-encoding Gene. *Proc. Natl. Acad. Sci. U. S. A.* 117, 11399–11408. doi:10.1073/pnas.1914536117

Pineda, S. S., Undheim, E. A., Rupasinghe, D. B., Ikonomopoulou, M. P., and King, G. F. (2014). Spider Venomics: Implications for Drug Discovery. *Future Med. Chem.* 6, 1699–1714. doi:10.4155/fmc.14.103

Rahnama, S., Deuis, J. R., Cardoso, F. C., Ramanujam, V., Lewis, R. J., Rash, L. D., et al. (2017). The Structure, Dynamics and Selectivity Profile of a NaV1.7 Potency-optimised Huwentoxin-IV Variant. *PLoS One* 12, e0173551. doi:10.1371/journal.pone.0173551

Ren, Y. S., Qian, N. S., Tang, Y., Liao, Y. H., Yang, Y. L., Dou, K. F., et al. (2012). Sodium Channel Nav1.6 Is Up-regulated in the Dorsal Root Ganglia in a Mouse Model of Type 2 Diabetes. *Brain Res. Bull.* 87, 244–249. doi:10.1016/j.brainresbull.2011.10.015

Rong, M., Chen, J., Tao, H., Wu, Y., Jiang, P., Lu, M., et al. (2011). Molecular Basis of the Tarantula Toxin Jingzhaotoxin-III (β-TRTX-Cj1α) Interacting with Voltage Sensors in Sodium Channel Subtype Nav1.5. *FASEB J.* 25, 3177–3185. doi:10.1096/fj.10-178848

Saez, N. J., and Herzig, V. (2019). Versatile Spider Venom Peptides and Their Medical and Agricultural Applications. *Toxicon* 158, 109–126. doi:10.1016/j.toxicon.2018.11.298

Saez, N. J., Senff, S., Jensen, J. E., Er, S. Y., Herzig, V., Rash, L. D., et al. (2010). Spider-venom Peptides as Therapeutics. *Toxins (Basel)* 2, 2851–2871. doi:10.3390/toxins2122851

Salvatierra, J., Castro, J., Erickson, A., Li, Q., Braz, J., Gilchrist, J., et al. (2018). NaV1.1 Inhibition Can Reduce Visceral Hypersensitivity. *JCI Insight* 3, e121000. doi:10.1172/jci.insight.121000

Shen, H., Liu, D., Wu, K., Lei, J., and Yan, N. (2019). Structures of Human Nav1.7 Channel in Complex with Auxiliary Subunits and Animal Toxins. *Science* 363, 1303–1308. doi:10.1126/science.aaw2493

Sittl, R., Lampert, A., Huth, T., Schuy, E. T., Link, A. S., Fleckenstein, J., et al. (2012). Anticancer Drug Oxaliplatin Induces Acute Cooling-Aggravated Neuropathy via Sodium Channel Subtype NaV1.6-resurgent and Persistent Current. *Proc. Natl. Acad. Sci. U. S. A.* 109, 6704–6709. doi:10.1073/pnas.1118058109

Smith, J. J., Lau, C. H. Y., Herzig, V., Ikonomopoulou, M. P., Rash, L. D., and King, G. F. (2015). "Chapter 8. Therapeutic Applications of Spider-Venom Peptides," in *Venoms to Drugs: Venom as a Source for the Development of Human Therapeutics*. Editor G. F. King (Cambridge, United Kingdom: The Royal Society of Chemistry), 221–244. doi:10.1039/9781849737876-00221

Sousa, S. R., Wingerd, J. S., Brust, A., Bladen, C., Ragnarsson, L., Herzig, V., et al. (2017). Discovery and Mode of Action of a Novel Analgesic β-toxin from the African Spider *Ceratogyrus darlingi*. *PLoS One* 12, e0182848. doi:10.1371/journal.pone.0182848

Stevens, M., Peigneur, S., and Tytgat, J. (2011). Neurotoxins and Their Binding Areas on Voltage-gated Sodium Channels. *Front. Pharmacol.* 2, 71. doi:10.3389/fphar.2011.00071

Tan, A. M., Samad, O. A., Dib-Hajj, S. D., and Waxman, S. G. (2015). Virus-Mediated Knockdown of Nav1.3 in Dorsal Root Ganglia of STZ-induced Diabetic Rats Alleviates Tactile Allodynia. *Mol. Med.* 21, 544–552. doi:10.2119/molmed.2015.00063

Tanaka, B. S., Zhao, P., Dib-Hajj, F. B., Morisset, V., Tate, S., Waxman, S. G., et al. (2016). A Gain-Of-Function Mutation in Nav1.6 in a Case of Trigeminal Neuralgia. *Mol. Med.* 22, 338–348. doi:10.2119/molmed.2016.00131

Tanaka, K., Sekino, S., Ikegami, M., Ikeda, H., and Kamei, J. (2015). Antihyperalgesic Effects of ProTx-II, a Nav1.7 Antagonist, and A803467, a Nav1.8 Antagonist, in Diabetic Mice. *J. Exp. Pharmacol.* 7, 11–16. doi:10.2147/JEP.S79973

Tarradas, A., Selga, E., Beltran-Alvarez, P., Pérez-Serra, A., Riuró, H., Picó, F., et al. (2013). A Novel Missense Mutation, I890T, in the Pore Region of Cardiac Sodium Channel Causes Brugada Syndrome. *PLoS One* 8, e53220. doi:10.1371/journal.pone.0053220

Van Zundert, G. C. P., Rodrigues, J. P. G. L. M., Trellet, M., Schmitz, C., Kastritis, P. L., Karaca, E., et al. (2016). The HADDOCK2.2 Web Server: User-friendly Integrative Modeling of Biomolecular Complexes. *J. Mol. Biol.* 428, 720–725. doi:10.1016/j.jmb.2015.09.014

Veeramah, K. R., O'Brien, J. E., Meisler, M. H., Cheng, X., Dib-Hajj, S. D., Waxman, S. G., et al. (2012). *De Novo* pathogenic *SCN8A* Mutation Identified by Whole-genome Sequencing of a Family Quartet Affected by Infantile Epileptic Encephalopathy and SUDEP. *Am. J. Hum. Genet.* 90, 502–510. doi:10.1016/j.ajhg.2012.01.006

Vetter, I., Deuis, J. R., Mueller, A., Israel, M. R., Starobova, H., Zhang, A., et al. (2017). NaV1.7 as a Pain Target - from Gene to Pharmacology. *Pharmacol. Ther.* 172, 73–100. doi:10.1016/j.pharmthera.2016.11.015

Vetter, I., Mozar, C. A., Durek, T., Wingerd, J. S., Alewood, P. F., Christie, M. J., et al. (2012). Characterisation of Nav Types Endogenously Expressed in Human SH-SY5Y Neuroblastoma Cells. *Biochem. Pharmacol.* 83, 1562–1571. doi:10.1016/j.bcp.2012.02.022

Wang, W., Gu, J., Li, Y. Q., and Tao, Y. X. (2011). Are Voltage-gated Sodium Channels on the Dorsal Root Ganglion Involved in the Development of Neuropathic Pain?. *Mol. Pain* 7, 16. doi:10.1186/1744-8069-7-16

Waxman, S. G. (2006). Axonal Conduction and Injury in Multiple Sclerosis: the Role of Sodium Channels. *Nat. Rev. Neurosci.* 7, 932–941. doi:10.1038/nrn2023

Waxman, S. G., Kocsis, J. D., and Black, J. A. (1994). Type III Sodium Channel mRNA Is Expressed in Embryonic but Not Adult Spinal Sensory Neurons, and Is Reexpressed Following Axotomy. *J. Neurophysiol.* 72, 466–470. doi:10.1152/jn.1994.72.1.466

Wilson, D. T. (2016). "The Venom of Australian Spiders," in *Spider Venoms. Toxinology, 21-46*. Editors P. Gopalakrishnakone, G. Corzo, M. de Lima, and E. Diego-Garcia (Dordrecht: Springer). doi:10.1007/978-94-007-6389-0_21

Wingerd, J. S., Mozar, C. A., Ussing, C. A., Murali, S. S., Chin, Y. K., Cristofori-Armstrong, B., et al. (2017). The Tarantula Toxin β/δ-TRTX-Pre1a Highlights the Importance of the S1-S2 Voltage-sensor Region for Sodium Channel Subtype Selectivity. *Sci. Rep.* 7, 974. doi:10.1038/s41598-017-01129-0

Wisedchaisri, G., Tonggu, L., Gamal El-Din, T. M., McCord, E., Zheng, N., and Catterall, W. A. (2021). Structural Basis for High-affinity Trapping of the NaV1.7 Channel in its Resting State by Tarantula Toxin. *Mol. Cel* 81, 38–e4. doi:10.1016/j.molcel.2020.10.039

Wishart, D. S., Bigam, C. G., Holm, A., Hodges, R. S., and Sykes, B. D. (1995). 1H, 13C and 15N Random Coil NMR Chemical Shifts of the Common Amino Acids. I. Investigations of Nearest-neighbor Effects. *J. Biomol. NMR* 5, 67–81. doi:10.1007/BF00227471

Wu, Y., Ma, H., Zhang, F., Zhang, C., Zou, X., and Cao, Z. (2018). Selective Voltage-gated Sodium Channel Peptide Toxins from Animal Venom: Pharmacological Probes and Analgesic Drug Development. *ACS Chem. Neurosci.* 9, 187–197. doi:10.1021/acschemneuro.7b00406

Wüthrich, K. (1983). Sequential Individual Resonance Assignments in the 1H-NMR Spectra of Polypeptides and Proteins. *Biopolymers* 22, 131–138. doi:10.1002/bip.360220121

Xiao, Y., Bingham, J. P., Zhu, W., Moczydlowski, E., Liang, S., and Cummins, T. R. (2008). Tarantula Huwentoxin-IV Inhibits Neuronal Sodium Channels by Binding to Receptor Site 4 and Trapping the Domain II Voltage Sensor in the Closed Configuration. *J. Biol. Chem.* 283, 27300–27313. doi:10.1074/jbc.M708447200

Xiao, Y., Jackson, J. O., Liang, S., and Cummins, T. R. (2011). Common Molecular Determinants of Tarantula Huwentoxin-IV Inhibition of Na+ Channel Voltage Sensors in Domains II and IV. *J. Biol. Chem.* 286, 27301–27310. doi:10.1074/jbc.M70844720010.1074/jbc.M111.246876

Xiao, Y., Blumenthal, K., Jackson, J. O., Liang, S., and Cummins, T. R. (2010). The Tarantula Toxins ProTx-II and Huwentoxin-IV Differentially Interact with Human Nav1.7 Voltage Sensors to Inhibit Channel Activation and Inactivation. *Mol. Pharmacol.* 78, 1124–1134. doi:10.1124/mol.110.066332

Xie, W., Strong, J. A., and Zhang, J. M. (2015). Local Knockdown of the NaV1.6 Sodium Channel Reduces Pain Behaviors, Sensory Neuron Excitability, and Sympathetic Sprouting in Rat Models of Neuropathic Pain. *Neuroscience* 291, 317–330. doi:10.1016/j.neuroscience.2015.02.010

Xu, H., Li, T., Rohou, A., Arthur, C. P., Tzakoniati, F., Wong, E., et al. (2019). Structural Basis of Nav1.7 Inhibition by a Gating-Modifier Spider Toxin. *Cell* 176, 702–e14. doi:10.1016/j.cell.2018.12.018

Xu, W., Zhang, J., Wang, Y., Wang, L., and Wang, X. (2016). Changes in the Expression of Voltage-gated Sodium Channels Nav1.3, Nav1.7, Nav1.8, and Nav1.9 in Rat Trigeminal Ganglia Following Chronic Constriction Injury. *Neuroreport* 27, 929–934. doi:10.1097/wnr.0000000000000632

Yang, Y., Wang, Y., Li, S., Xu, Z., Li, H., Ma, L., et al. (2004). Mutations in *SCN9A*, Encoding a Sodium Channel Alpha Subunit, in Patients with Primary Erythermalgia. *J. Med. Genet.* 41, 171–174. doi:10.1136/jmg.2003.012153

Zeng, X., Li, P., Chen, B., Huang, J., Lai, R., Liu, J., et al. (2018). Selective Closed-state Nav1.7 Blocker JZTX-34 Exhibits Analgesic Effects against Pain. *Toxins (Basel)* 10, E64. doi:10.3390/toxins10020064

Zhang, Y., Peng, D., Huang, B., Yang, Q., Zhang, Q., Chen, M., et al. (2018). Discovery of a Novel Nav1.7 Inhibitor from *Cyriopagopus albostriatus* Venom with Potent Analgesic Efficacy. *Front. Pharmacol.* 9, 1158. doi:10.3389/fphar.2018.01158

Conflict of Interest: The authors declare that the research was conducted in the absence of any commercial or financial relationships that could be construed as a potential conflict of interest.

frontiers in Pharmacology

BRIEF RESEARCH REPORT
published: 04 January 2022
doi: 10.3389/fphar.2021.809595

Inhibition of *Clostridioides difficile* Toxins TcdA and TcdB by Ambroxol

Sebastian Heber[1], *Lara Barthold*[1], *Jan Baier*[1], *Panagiotis Papatheodorou*[1], *Giorgio Fois*[2], *Manfred Frick*[2], *Holger Barth*[1]* *and Stephan Fischer*[1]*

[1]*Institute of Pharmacology and Toxicology, Ulm University Medical Center, Ulm, Germany,* [2]*Institute of General Physiology, Ulm University, Ulm, Germany*

Clostridioides (C.) difficile produces the exotoxins TcdA and TcdB, which are the predominant virulence factors causing *C. difficile* associated disease (CDAD). TcdA and TcdB bind to target cells and are internalized via receptor-mediated endocytosis. Translocation of the toxins' enzyme subunits from early endosomes into the cytosol depends on acidification of endosomal vesicles, which is a prerequisite for the formation of transmembrane channels. The enzyme subunits of the toxins translocate into the cytosol via these channels where they are released after auto-proteolytic cleavage. Once in the cytosol, both toxins target small GTPases of the Rho/Ras-family and inactivate them by mono-glucosylation. This in turn interferes with actin-dependent processes and ultimately leads to the breakdown of the intestinal epithelial barrier and inflammation. So far, therapeutic approaches to treat CDAD are insufficient, since conventional antibiotic therapy does not target the bacterial protein toxins, which are the causative agents for the clinical symptoms. Thus, directly targeting the exotoxins represents a promising approach for the treatment of CDAD. Lately, it was shown that ambroxol (Ax) prevents acidification of intracellular organelles. Therefore, we investigated the effect of Ax on the cytotoxic activities of TcdA and TcdB. Ax significantly reduced toxin-induced morphological changes as well as the glucosylation of Rac1 upon intoxication with TcdA and TcdB. Most surprisingly, Ax, independent of its effects on endosomal acidification, decreased the toxins' intracellular enzyme activity, which is mediated by a catalytic glucosyltransferase domain. Considering its undoubted safety profile, Ax might be taken into account as therapeutic option in the context of CDAD.

Keywords: bacterial AB-type protein toxins, ambroxol, *C. difficile* toxins TcdA and TcdB, glucosyltransferase inhibitor, *C. difficile* infections

OPEN ACCESS

Edited by:
Patrick Michael McNutt, Wake Forest School of Medicine, United States

Reviewed by:
Joel D. A. Tyndall, University of Otago, New Zealand
Martin Diener, University of Giessen, Germany

***Correspondence:**
Holger Barth
holger.barth@uni-ulm.de
Stephan Fischer
stephan-1.fischer@uni-ulm.de

Specialty section:
This article was submitted to Pharmacology of Ion Channels and Channelopathies, a section of the journal Frontiers in Pharmacology

Received: *05 November 2021*
Accepted: *10 December 2021*
Published: *04 January 2022*

Citation:
Heber S, Barthold L, Baier J, Papatheodorou P, Fois G, Frick M, Barth H and Fischer S (2022) Inhibition of Clostridioides difficile *Toxins TcdA and TcdB by Ambroxol. Front. Pharmacol. 12:809595. doi: 10.3389/fphar.2021.809595*

INTRODUCTION

The gram-positive enterobacterium *Clostridioides (C.) difficile* is the major cause of (nosocomial) hospital-acquired diarrhea and of severe forms of pseudomembranous colitis. Infections with *C. difficile* (CDI) are accountable for up to one-fourth of all cases of antibiotic-associated diarrhea, which has made *C. difficile* an important and emerging enteropathogen (Larson et al., 1978; Bauer et al., 2011). The incidence and the severity of CDIs has increased significantly in recent years, leading to outbreaks of infections in hospitals worldwide (Cartmill et al., 1994). In 2011–2012, the European Center for Disease Control and Prevention assumed that more than 150,000 new CDI cases emerged annually, with an incidence of about 30 cases (per 100,000 population), resulting in more than 8,000 deaths per year (Cassini et al., 2016). Similar rates were also found for the

United States of America. Here, CDIs were accountable for more than 220,000 cases among hospitalized patients in 2017, with estimated attributable health care costs of about $1B and more than 12,000 estimated deaths (Lessa et al., 2015; Kordus et al., 2021). All of this led the national public healthcare agency of the United States, the Centers for Disease Control and Prevention, to classify the threat level for *C. difficile* as urgent.

The major virulence factors of *C. difficile* are the two secreted protein toxins A (TcdA) and B (TcdB). The presence of the toxins is sufficient to fully develop the emergence of the characteristic clinical symptoms (Lyras et al., 2009; Kuehne et al., 2010). Both toxins display a high sequence homology and an overall comparable multimodal structure (von Eichel-Streiber et al., 1992). They belong to the group of clostridial glucosyltransferases and are subdivided into at least four distinct domains (Jank and Aktories, 2008; Belyi and Aktories, 2010). The enzymatically active glucosyltransferase domain (GTD) is located at the N-terminal part of the toxins whereas the two middle parts are responsible for toxin processing and translocation into the host cell cytosol. The C-terminal domain mediates the binding of the toxins to their cell surface receptors. Recently, progress has been made in identifying the responsible protein receptors. TcdA and TcdB use different cell surface receptors (Kordus et al., 2021). For TcdA, sulfated glycosaminoglycans and low-density lipoprotein receptor were determined as important host factors responsible for binding and uptake of the toxin (Tao et al., 2019). For TcdB, at least three possible receptors were determined including the Wnt receptor Frizzled (Tao et al., 2016), the chondroitin sulfate proteoglycan 4 (Yuan et al., 2015), and poliovirus receptor-like 3 (LaFrance et al., 2015).

TcdA and TcdB are released from *C. difficile* into the surrounding host tissue where they enter target cells via receptor-mediated endocytosis in a specific toxin-receptor complex (Florin and Thelestam, 1983; Frisch et al., 2003). The acidic milieu in early endosomes leads to conformational changes within the toxins' structure that enables the insertion of hydrophobic regions inside the translocation domain and subsequent pore formation in endosomal membranes (Henriques et al., 1987; Qa'Dan et al., 2000; Barth et al., 2001). With the help of the transmembrane pores, the GTD translocates from the endosomal lumen to the cytosolic side of the endosomes where an autoproteolytic cleavage, which requires inositol hexakisphosphate ($InsP_6$), mediates the release of the GTD into the cytosol (Pfeifer et al., 2003; Reineke et al., 2007). Once in the cytosol, the GTD glucosylates small GTPases of the Rho/Ras-superfamily. TcdA and TcdB covalently transfer a glucose moiety from the co-substrate UDP-glucose to the GTPases, which results in inactivation of signal transduction (Just et al., 1995a; Just et al., 1995b), reorganization of the actin cytoskeleton and cell rounding. The most well defined proteins of the Rho-family are RhoA, Rac1, and Cdc42, all together important key regulators of actin based processes. Both toxins mono-glucosylate Rho proteins by transferring a glucose-residue onto the highly conserved effector domain amino acids threonine 37 in case of RhoA and threonine 35 in case of Rac1 and Cdc42 (Just et al., 1995a). *In vivo*, these actions of the toxins are the reason for gut barrier disruption and the development of the clinical symptoms.

As acidification of endosomal vesicles is essential for the successful translocation of the toxins into the cytosol, we investigated the effects of the licensed muco-lytic drug ambroxol (Ax) on TcdA and TcdB in the context of the present study. Ax contains a lipophilic organic ring system linked to a secondary amine via a short spacer allowing it to cross membranes by diffusion. Ax is a weak base and is predicted to enrich in acidic compartments by protonation where it leads to pH neutralization (Fois et al., 2015). In particular, acidification of endosomal vesicles is essential for the successful translocation of the toxins into the cytosol, which has been demonstrated using bafilomycin A1 (BafA1), an inhibitor of the vacuolar H^+-ATPase (Barth et al., 2001). Ax protected cells from native TcdA and/or TcdB and, unexpectedly, directly inhibited the glucosyltransferase activity.

MATERIALS AND METHODS

Toxins and Reagents

The native toxins TcdA and TcdB from *C. difficile* VPI 10463 were purified as described earlier (von Eichel-Streiber et al., 1987). *N*-Ethylmaleimide was ordered from Sigma Aldrich, United States. Castanospermine was purchased from Santa Cruz Biotechnology, United States. α-Defensin-5 was ordered from PeptaNova, Germany. Ax was generously provided by Dr. Birgit Jung, Böhringer-Ingelheim Pharma GmbH & Co., KG, Biberach, Germany.

Cell Culture and Cytotoxicity Assays

Cells were cultured in saturated humidity at 37°C, 5% CO_2 and reseeded three times per week. Vero cells were cultured using MEM with additions of 10% fetal calf serum (both GIBCO Life Technologies, United States), 1 mM sodium pyruvate, 1 mM L-glutamine, 0.1 mM non-essential amino acids, 100 U/ml penicillin and 100 µg/ml streptomycin. HCT116 cells were cultured under the same conditions using DMEM with 10% fetal calf serum (both GIBCO Life Technologies, United States), 1% sodium pyruvate and 100 U/ml penicillin and 100 µg/ml streptomycin. For imaging, either an Axiovert 40CFL microscope (Zeiss, Germany) with a ProgRes C10 CCD camera (Jenoptik, Germany) or a Leica DMi1 microscope with a Leica MC170 HD camera (both Leica, Germany) was used. Images were processed using ImageJ software (Schneider et al., 2012). For cytotoxicity assays, the respective growth medium of the cells was removed and the toxins in the presence or absence of the single test substances were added to the cells in serum-free medium. Afterwards, the cells were further incubated at 37°C until the respective time points.

Probing the Intracellular Rac1 Glucosylation Status in Intact Vero Cells After Treatment With TcdB

3×10^4 Vero cells per well were seeded in a 24-well plate 2 days prior intoxication. Intoxication was performed as described in the

previous paragraph in serum-free medium. Cells were mechanically harvested using a cell scraper in PBS supplemented with 1× cOmplete™ protease inhibitor (Roche, Germany). After one freeze/thaw cycle, the cell lysate was transferred to SDS-PAGE followed by Rac1 immunoblotting. Mouse anti-non-glucosylated Rac1 antibody (1:500, BD Biosciences, #610650, United States) was used for determination of the glucosylation status, which was normalized to Hsp90 signal (1:1,000, Santa Cruz Biotechnology, #13119, United States).

Immunofluorescence Microscopy

4×10^4 Vero cells per well were seeded 1 day prior imaging in 8-well µ-slides (ibidi GmbH, Germany). Intoxication was performed as mentioned. Cells were fixed with 4% PFA for 20 min, permeabilized with 0.4% Triton-X100 in PBS for 5 min, treated with 100 mM glycine, 0.1% Tween20 in PBS for 2 min and blocked with blocking buffer (5% skim milk powder, 0.1% Tween®20) for 30 min at 37°C. The cells were washed, immunostained with a specific antibody only recognizing non-glucosylated Rac1 (1:100) in blocking buffer and washed again. For fluorescence analysis, a fluorescently-labeled goat anti-mouse-568 secondary antibody (1:750, Invitrogen, A11004, United States) and phalloidin-FITC (1:100, Sigma Aldrich, P5282, United States) was used for 30 min followed by Hoechst33342 staining (1:5,000, 5 min, both in blocking buffer). iMic Digital Microscope and Live Acquisition 2.6 software (both FEI Munich GmbH, Thermo Fisher Scientific, United States) were used for imaging. Images were processed using ImageJ software.

Precipitation Studies With TcdB

TcdB stock solution was centrifuged at 14,000 rpm for 20 min at 4°C to remove preformed aggregates. 50 ng of TcdB were incubated in the presence and absence of the respective inhibitors for 30 min at 37°C in a total volume of 35 µl. Aggregated protein was collected as a pellet by centrifugation as mentioned above. 30 µl supernatant were collected and the remaining pellet was resuspended in a total volume of 60 µl PBS. 30 µl of each fraction were subjected for separation to an 8% SDS-polyacrylamide gel and detected by immunoblotting against TcdB. Anti-TcdB-antibody (1:1,000, Abcam, ab270452, United Kingdom) was used for signal detection.

Analysis of TcdB Binding to Vero Cells

3×10^4 Vero cells per well were seeded in a 24-well plate 2 days prior to analysis. The cells were pre-cooled on ice for 30 min to prevent endocytosis. Ice-cold intoxication medium (serum-free) was used to allow binding of TcdB to the cells for 1 h. After two washing steps with PBS to remove non-bound proteins, cells were harvested by addition of 100 µl pre-heated (95°C) 2.5× Laemmli buffer. Next, cells were scraped off, heated for 10 min at 95°C, and cell lysates were transferred to SDS-PAGE followed by immunoblotting against TcdB (1:1,000, Abcam, ab270452, United Kingdom). Hsp90 was detected as loading control as described above.

In Vitro Glucosylation of Rac1 by TcdB

20 µg total protein from a whole cell lysate (as source for Rac1) in combination with TcdB (10 nM) was used for *in vitro* glucosylation. The reaction was performed in glucosylation buffer (50 mM HEPES, 100 mM KCl, 2 mM $MgCl_2$, 1 mM $MnCl_2$, 100 mg/L BSA, pH 7.5) for 1 h at 37°C in a total volume of 20 µl. Reaction was stopped by adding 5 µl 5× Laemmli buffer and 10 min heating of the samples at 95°C. The glucosylation status of Rac1 was determined by immunoblotting as described above. Hsp90 was detected as loading control.

In Vitro Enzyme Activity of the Enzyme Component C2I of the Binary *Clostridium (C.) botulinum* C2 Toxin

C2I (1 ng) was supplemented with ADP-ribosylation buffer, whole cell lysate (40 µg) as source for actin, two different concentrations of Ax (100 and 1,000 µM) and 10 µM biotin-labelled NAD^+ (R&D Systems, #6573/131U, United States) for 30 min at 37°C. Afterwards, reaction was stopped by adding 5× Laemmli buffer and heating at 95°C for 10 min. Then, SDS-PAGE and immunoblotting was performed and biotinylated actin was detected by the enhanced chemiluminescence reaction (ECL) using a peroxidase-coupled streptavidin antibody (Merck, #11089153001, Germany).

Expression and Purification of Recombinant Rac1

Rac1 was expressed as a recombinant GST-tagged protein in *E. coli* BL21 transformed with the pGEX-4T-2-GST_Rac1 plasmid. Purification was performed as described earlier for other GST-tagged proteins (Barth et al., 1998).

In Vitro Cysteine Protease Activity of TcdB

TcdB (2 µg) was incubated for 1 h at 37°C with 1 mM inositol hexakisphosphate (Santa Cruz Biotechnology, United States) in 20 µl to allow for autoproteolytic cleavage. Reactions were buffered using 20 mM Tris and 150 mM NaCl with pH 7.4 and stopped by addition of 5 µl 5× Laemmli buffer and 10 min heating at 95°C. For analysis, samples were transferred to SDS-PAGE and subsequent Coomassie staining of the gel.

Hydrolase and Glucosyltransferase Activity of TcdB

UDP-Glo™ Glycosyltransferase Assay with UDP-glucose as cosubstrate (Promega, V6991, United States) was used to monitor hydrolase and glucosyltransferase activity. The assay was performed as described by the manufacturer. In short, reactions were performed for 1 h at 37°C in a total volume of 40 µl of glucosylation buffer. 50 nM (for hydrolase activity) and 200 pM (for glucosyltransferase activity) TcdB was used and for both reactions, 100 µM of UDP-glucose was added. For measuring the glucosyltransferase activity, 5 µM recombinant Rac1 was added as substrate. Thereafter, the preparations were

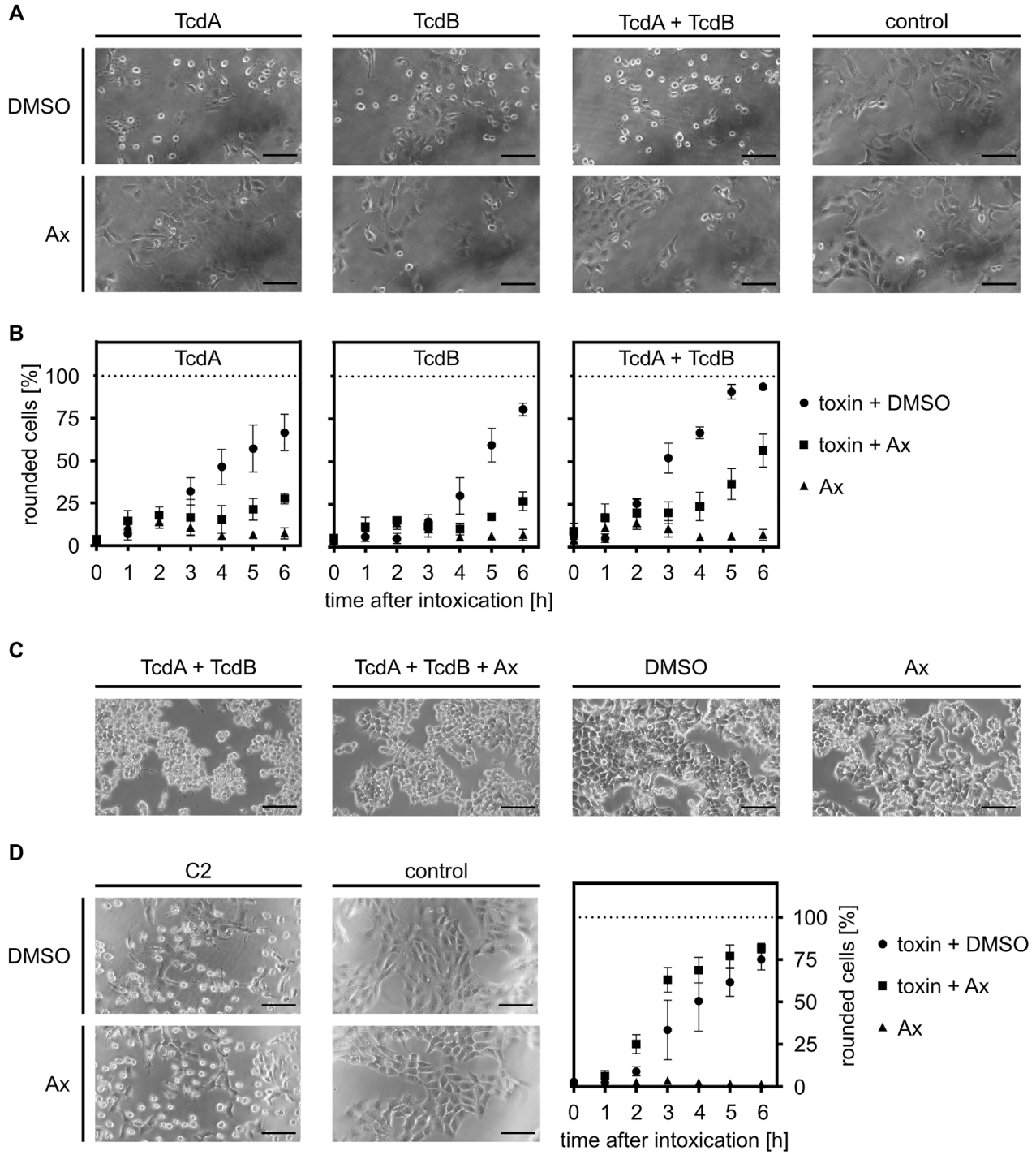

FIGURE 1 | Ax protects cells from intoxication with TcdA, TcdB and the combination of both toxins. **(A)** Vero cells were intoxicated with 10 pM TcdA, 10 pM TcdB or the combination of both (each 10 pM) in the presence or absence of Ax (150 μM) or DMSO as solvent control. Representative pictures after 5 h are depicted ($n = 3$). **(B)** At indicated time points, pictures were taken and the amount of rounded Vero cells was determined. Depicted is the ratio of rounded cells compared to total cell number. Values are given as mean ± standard deviation (SD) of three technical replicates. Biological replicates showed comparable inhibitions of intoxication ($n = 3$). **(C)** HCT116 cells were treated as in **(A)**. 100 pM of the toxins were used. Images depict representative cells after 4 h incubation. **(D)** Vero cells were incubated with C2 toxin (C2I: 1 nM, C2IIa: 1.66 nM) in the presence or absence of Ax (150 μM) or DMSO as solvent control. Pictures were taken 5 h after intoxication. Intoxication kinetics are depicted as mentioned for **(B)**. Scale bars correspond to 100 μm.

split into three times 10 µl and transferred to a 96-well half-area microplate (Greiner, #675075, Austria). Reactions were stopped by addition of 10 µl UDP Detection Reagent. Content was mixed by shaking at 1,000 rpm for 30 s. Luminescence signal was recorded within 1 h after addition of UDP Detection Reagent using a Tecan infinite M1000Pro plate reader (Tecan Trading AG, Switzerland) with an integration time of 750 ms.

Statistics

All experiments were performed at least three times as independent replicates. Each replicate was carried out at minimum in duplicate. For statistical analysis, ordinary one-way ANOVA was performed with Dunnett's multiple comparison test (GraphPad, Version 6). Resulting p values were indicated as follows: ns, not significant; $^{*}p < 0.05$; $^{**}p < 0.01$.

RESULTS

Ax Protects Vero and HCT116 Cells From *C. difficile* TcdA and TcdB

In the first set of experiments, the effect of Ax on intoxication of cells with TcdA or TcdB was investigated in the well-established cell-rounding assay with Vero cells. These cells are very sensitive towards both toxins and display a clear and robust response in terms of rounding (**Figure 1A**). When applied concomitantly, i.e., without any pre-incubation period, the number of round cells challenged with either TcdA or TcdB and Ax (150 µM) was significantly lowered compared to cells treated only with the toxins, indicating that Ax reduces the intoxication of the cells. Moreover, Ax protected cells from the intoxication by the medically relevant combination of TcdA and TcdB (**Figure 1A**). The quantitative analysis of the toxin-induced changes in cell morphology over time revealed protection of cells by Ax even after 6 h (**Figure 1B**). This result was morphologically confirmed in the physiologically and medically more relevant human colon cancer cell line HCT116 (**Figure 1C**). For both cell lines, Ax alone did not cause any substantial changes in cell morphology (**Figures 1A, C**) or cell viability (**Supplementary Figure S1**). Interestingly, the binary actin ADP-ribosylating C2 toxin from *C. botulinum* was not affected by Ax (**Figure 1D**), demonstrating a selective mode of action of Ax against TcdA and TcdB. Moreover, since C2 toxin also requires acidic endosomes for its cellular uptake, this result suggests another mechanism underlying the inhibitory effect of Ax towards TcdA/TcdB. Even at comparatively high concentrations of TcdB, a significant and clear reduction in TcdB-induced cell rounding was observed (**Supplementary Figure S2**). Because TcdB was more cytotoxic than TcdA in earlier studies (Just and Gerhard, 2004) and considered as the major virulence factor of *C. difficile* (Carter et al., 2015), all further experiments investigating the underlying molecular mechanism were performed with TcdB.

Less Rac1 is Glucosylated in Intact Cells by TcdB in the Presence of Ax

To further elucidate the protective effect of increasing concentrations of Ax against TcdB, the glucosylation status of intracellular Rac1 was analyzed in more detail by immunoblotting with an antibody that specifically recognizes non-glucosylated Rac1 (Genth et al., 2006; Egerer et al., 2007; Fischer et al., 2020; Korbmacher et al., 2020). This experiment revealed that less Rac1 was glucosylated in intact cells in the presence of 150 µM of Ax after incubation with TcdB (**Figure 2A**). The results were confirmed by an alternative, immunofluorescence microscopy-based approach, where the glucosylation status of Rac1 was analyzed with the same antibody in cells displaying their native morphology (**Figure 2B**). Treatment of Vero cells with TcdB resulted in an almost complete glucosylation of intracellular Rac1, as indicated by the virtually entire disappearance of the non-glucosylated Rac1 signal. Also, the F-actin structure is highly impaired, as illustrated by the typical rounding of the cells. In the presence of Ax, non-glucosylated Rac1 as well as F-actin were more comparable to the untreated control cells.

Investigation of the Underlying Molecular Mechanism of TcdB-Neutralization by Ax

From the observation that less Rac1 was glucosylated by TcdB in intact cells in the presence of Ax, it cannot be distinguished whether Ax directly inhibits the enzyme activity of the GTD or prevents the transport of the GTD into the host cell cytosol, or both. Therefore, we investigated the effect of Ax on the individual steps of TcdB uptake into cells. First, the capability of Ax to directly precipitate and thereby sequester TcdB was investigated. To this end, TcdB was incubated with or without Ax and centrifuged to obtain potential toxin-aggregates as described earlier (Korbmacher et al., 2020). As depicted in **Figure 3A**, TcdB was present in the supernatant fraction after incubation with Ax (i), indicating that Ax does not form insoluble aggregates with TcdB. In contrast, incubation of TcdB with α-defensin-5, a peptide for which we demonstrated earlier that it precipitates TcdB (Korbmacher et al., 2020), resulted in an almost quantitative TcdB precipitation demonstrating that this assay works under the chosen conditions (ii). Next, the influence of Ax on the binding of TcdB to cultured cells was investigated. Therefore, cells were cooled down to 4°C to reduce endocytosis to a minimum and incubated with TcdB in the presence and absence of Ax. Subsequently, cells were washed and bound TcdB was analyzed via immunoblotting. Here, the amount of cell-bound TcdB was slightly reduced in the presence of Ax (**Figure 3B**). However, this modest reduction might not fully explain the strong inhibition of TcdB intoxication of cells by Ax. Therefore, further steps of toxin uptake were examined, such as the intracellular processing of TcdB. It was tested whether Ax has an effect on the cysteine protease domain (CPD) of TcdB *in vitro* by analyzing the intrinsic autoproteolysis of the toxin in the presence of $InsP_6$. As a result, it was clearly visible that Ax did not affect $InsP_6$-induced autocatalytic processing of TcdB indicating that the CPD-related activity of TcdB is not affected by Ax (**Figure 3C**). Noteworthy, *N*-ethylmaleimide (NEM), an established CPD inhibitor (Egerer et al., 2007), prevented the autocatalytic processing of TcdB in the same experiment.

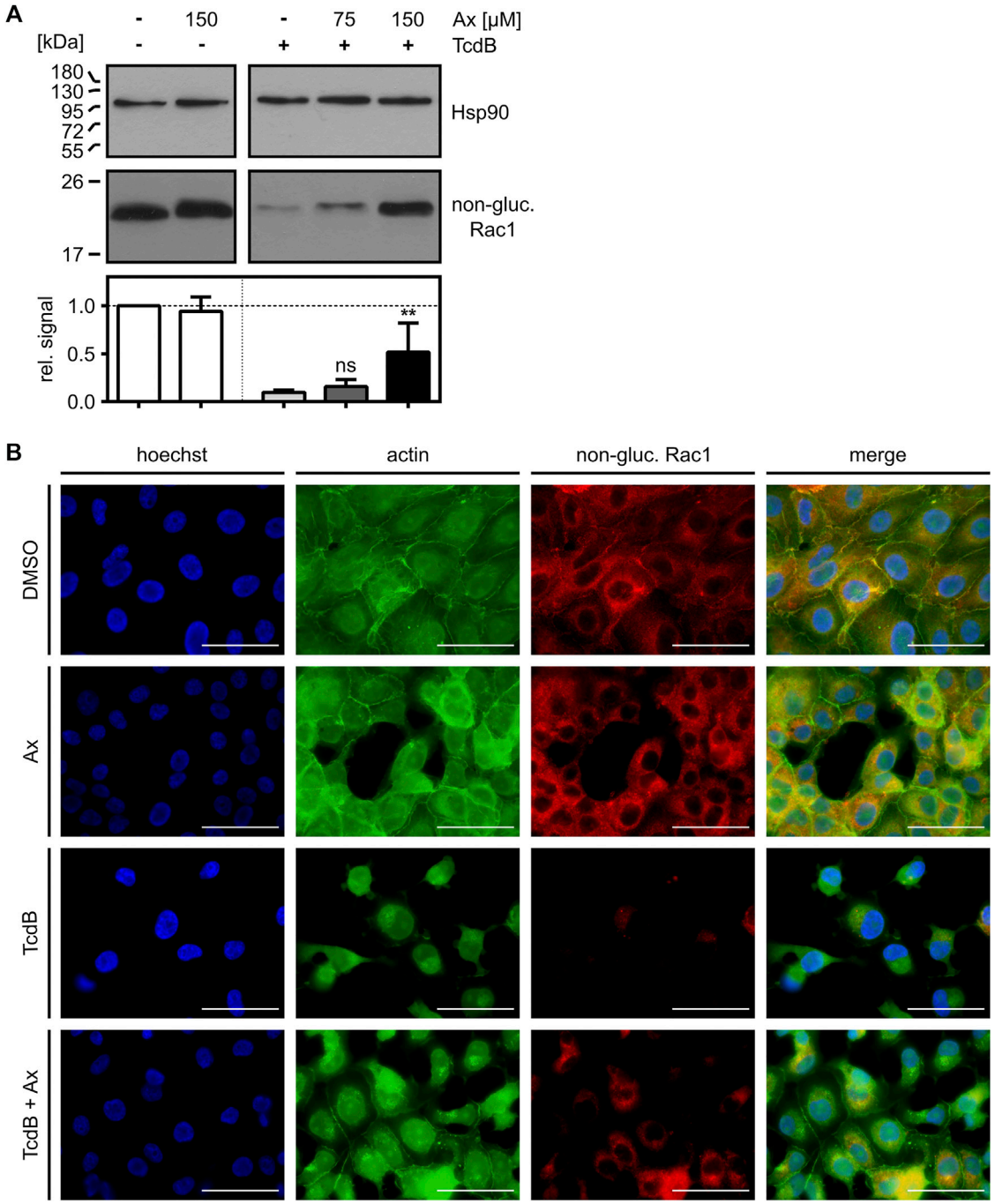

FIGURE 2 | Ax prevents TcdB-induced intracellular Rac1 glucosylation. **(A)** Vero cells were intoxicated with TcdB (10 pM) in the presence or absence of increasing concentrations of Ax or DMSO as solvent control. After 5 h, cells were harvested, lysed and transferred to Western blotting. Non-glucosylated Rac1 signal was normalized to Hsp90 loading control. Relative signal intensities are given as mean ± SD (n = 4). Ordinary one-way ANOVA was performed with Dunnett's multiple comparison test against toxin-only control. Asterisks indicate significance levels for toxin containing samples, with ns (not significant), *$p < 0.05$ and **$p < 0.01$. **(B)** Vero cells were treated with TcdB (10 pM), Ax (150 μM) and DMSO as solvent control. After 5 h, cells were fixated and immunofluorescence staining was performed. Nuclei (blue), actin cytoskeleton (green) and non-glucosylated Rac1 (red) were stained. Representative images of the individual channels and the merge of all three are depicted. Scale bars correspond to 50 μm.

Effect of Ax on the GTD of TcdB *In Vitro*

Finally, the effects of Ax on the intracellular glucosylation activity of TcdB were investigated in more detail. For this purpose, the glucosylation of Rac1 by TcdB was analyzed *in vitro* by incubating TcdB with whole cell lysate (as a source for Rac1) in the presence and absence of increasing concentrations of Ax. Here, a clear

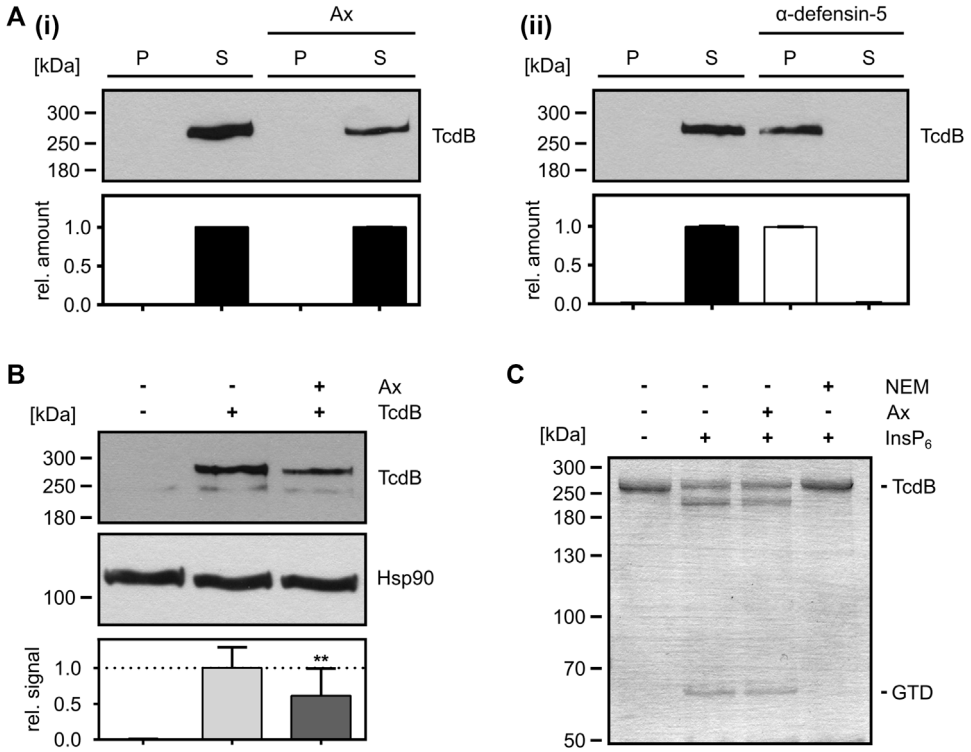

FIGURE 3 | Mode-of-inhibition of Ax as inhibitor of TcdB. **(A)** TcdB (50 ng) was incubated in the presence or absence of Ax (1 mM, **i**) and α-defensin-5 (6 μM, **ii**) for 30 min at 37°C. Samples were centrifuged, separated into supernatant (S) and pellet (P) fraction and analyzed by Western blotting. Relative signals within the two fractions are compared as relative amount of the sample (S + P). Relative amounts are given as mean ± SD (n = 3). **(B)** Precooled Vero cells were treated with TcdB (500 pM) to allow for toxin binding. Binding of TcdB was analyzed in the presence of Ax (150 μM) or DMSO as solvent control. Cells were washed, harvested and bound TcdB was analyzed by Western blotting. Relative signal intensities are given as mean ± SD (n = 3). A representative Western blot is depicted. Ordinary one-way ANOVA was performed with Dunnett's multiple comparison test against toxin-only control. Asterisks indicate significance levels for toxin containing samples, with ns (not significant), *$p < 0.05$ and **$p < 0.01$. **(C)** *In vitro* cysteine protease activity of TcdB (2 μg) was analyzed in the presence of $InsP_6$ (1 mM) to induce cysteine-protease activity. Ax (1 mM) or NEM (1 mM) were added. Cysteine protease activity was analyzed after 1 h at 37°C by SDS-PAGE and subsequent Coomassie staining. After successful cleavage, GTD (~63 kDa) is released from full length TcdB (~270 kDa). One representative SDS-PAGE is depicted.

concentration-dependent inhibition of the enzyme activity of TcdB by Ax was observed (**Figure 4A**). As expected from our earlier result that C2 toxin is not affected by Ax in the cell rounding assay (**Figure 1D**), no effect by Ax was detected on the enzyme activity of the ADP-ribosyltransferase C2I (**Figure 4B**), suggesting that Ax is a specific inhibitor of glucosyltransferases such as TcdA and TcdB. To get further insights into the underlying inhibitory mode of action of Ax, the glucosyltransferase and glucosylhydrolase activities of TcdB were analyzed. Ax was not only able to reduce the glucosyltransferase activity (**Figure 4C**) but also the glucosylhydrolase activity (**Figure 4D**). For both activities, similar IC_{50} values were determined for Ax and compared with castanospermine, a well-established glucosidase inhibitor (Jank et al., 2008). Noteworthy, the addition of Ax to either the glucosylation buffer or the culture medium did not result in any changes in the respective pH values (**Supplementary Figure S3**).

DISCUSSION

Infections with the human-pathogenic bacterium *C. difficile* persist to be a major challenge for healthcare systems in Western countries. CDI come along with a wide range of gastrointestinal diseases characteristically in hospitalized patients treated with broad-spectrum antibiotics, which reduces the abundance of the protective host microbiota in the gastrointestinal tract (Theriot et al., 2016). Although there are therapeutic options with some specific antibiotics such as vancomycin, fidaxomicin or metronidazole against CDI (Louie et al., 2011; Tart, 2013), pharmacological inhibitors against the produced toxins, which are the major virulence factors in this context, are urgently needed in addition to antibacterial drugs to neutralize the toxins TcdA and TcdB. In this study, the commonly used muco-lytic drug Ax was identified as a potent inhibitor of TcdA and TcdB, as well as their physiologically more relevant combination, in cell models.

Ax has mucociliary as well as mucokinetic effects and is used worldwide to treat acute and chronic respiratory diseases (Gupta, 2010). Recent studies revealed therapeutic effects of Ax also against Parkinson's disease (McNeill et al., 2014) and against various viruses like rhinovirus (Yamaya et al., 2014) and SARS-CoV-2 (Carpinteiro et al., 2021), in part due to the ability of Ax to accumulate in acidic vesicles such as late endosomes and lysosomes, where it neutralizes intravesicular pH levels. This

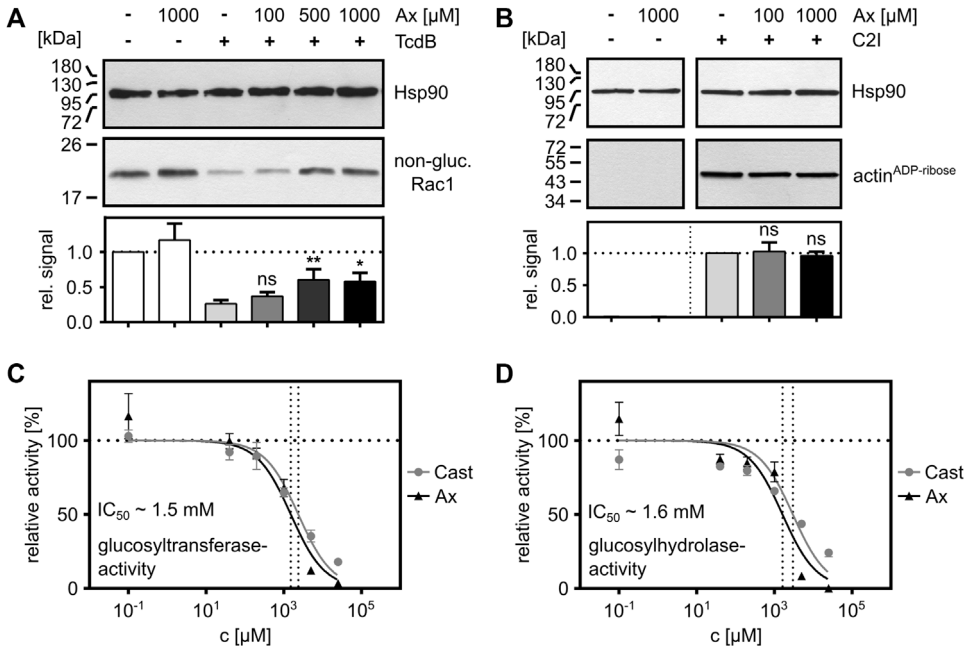

FIGURE 4 | Ax inhibits the enzyme activity of TcdB *in vitro*. **(A)** Whole cell lysate (20 µg) as source for Rac1 was supplemented with TcdB (10 nM) in the presence or absence of Ax (150 µM) or DMSO (solvent control) for 2 h at 37°C. Afterwards, samples were subjected to SDS-PAGE followed by Western blotting. Non-glucosylated Rac1 signals are normalized to Hsp90 loading control. Relative signals to toxin control are given as mean ± SD ($n = 4$). A representative Western blot image is depicted. Ordinary one-way ANOVA was performed with Dunnett's multiple comparison test against toxin-only control. Asterisks indicate significance levels for toxin containing samples, with ns (not significant), $^*p < 0.05$ and $^{**}p < 0.01$. **(B)** C2I (1 ng) was incubated with whole cell lysate (40 µg) with two different concentrations of Ax (100 µM, 1,000 µM) and DMSO as solvent control for 30 min at 37°C. ADP-ribosylated and thereby biotin-labeled actin (actin$^{ADP\text{-}ribose}$) signals are normalized to Hsp90 loading control. Relative signals to toxin control are given as mean ± SD ($n = 3$). A representative Western blot is depicted. Ordinary one-way ANOVA was performed with Dunnett's multiple comparison test against C2I-only control. Asterisks indicate significance levels for toxin containing samples, with ns (not significant). **(C)** TcdB (200 pM) and recombinant Rac1 (5 µM) were incubated with increasing concentrations of Ax and castanospermine (Cast) to analyze glucosyltransferase activity of TcdB by UDP-Glo™ glycosyltransferase assay. Nonlinear fit was applied with Graphpad Prism via log(inhibitor) vs. normalized response function. The estimated IC_{50} value for Ax (~1.5 mM) is displayed in the graph. **(D)** TcdB (50 nM) was incubated with increasing concentrations of Ax and castanospermine (Cast) to analyze glucosylhydrolase activity of TcdB by UDP-Glo™ glycosyltransferase assay. Nonlinear fit was applied with Graphpad Prism via log(inhibitor) vs. normalized response function. The estimated IC_{50} value for Ax (~1.6 mM) is displayed in the graph.

property makes Ax an attractive candidate to examine its inhibitory potential against bacterial toxins that essentially require the acidification of endosomes for their uptake into human cells.

Many bacterial protein toxins rely on acidification of early endosomes to translocate from endosomal vesicles into the cytosol of their target cells. Prominent examples are anthrax toxin (Ménard et al., 1996; Young and Collier, 2007), *C. botulinum* C2 toxin (Barth et al., 2000) or diphtheria toxin (Madshus et al., 1991), but also the toxins TcdA and TcdB from *C. difficile* (Aktories et al., 2017). Given that inhibition of vacuolar H^+-ATPase with BafA1 reliably inhibits intoxication of cells by all bacterial toxins that exploit acidic endosomes (Umata et al., 1990; Barth et al., 2001; Gerhard et al., 2013), we initially challenged cells with the native *C. difficile* toxins TcdA and/or TcdB, or with C2 toxin in the presence and absence of Ax.

Intoxication of eukaryotic cells by those toxins is characterized by high specificity and efficiency and a clear change in cell morphology (rounding up). Thus, analysis of cell rounding represents an ideal endpoint to monitor intoxication processes. It was surprising that Ax was capable of inhibiting TcdA, TcdB and their combination, whereas C2 toxin was not affected. This fact argued against a universal inhibitory mechanism of Ax against bacterial toxins that are internalized via acidic endosomes. However, the role of Ax-induced neutralization of acidic endosomal pH could not be fully elucidated, and why the intoxication of cells by C2 toxin is not inhibited by Ax. One possible explanation might be that the pH of the endosomes is still acidic enough for the C2 toxin to deliver its enzyme subunit C2I into the cytosol. For C2 toxin, a pH value below pH 5.5 is described to be sufficient for successful translocation of the enzyme component C2I into the cytosol (Blöcker et al., 2003). The endosomal pH for successful translocation of TcdB however is described to be below pH 4 (Lanis et al., 2010). Yet this still needs to be clarified in the future.

In the present study, the detailed effect of Ax on clostridial glucosylating toxins was investigated for TcdB. The time- and concentration-dependent reduction of TcdB-cytotoxicity by Ax was confirmed using different methods relying on changes in cell morphology and intracellular substrate modification (immunoblot analyses and fluorescence microscopy). Internalization of TcdB is a multi-modal process. To unravel

the underlying molecular mode of inhibition, individual steps during the intoxication process were evaluated more extensively. First of all, it was examined whether Ax is able to form biologically inactive aggregates with TcdB, similar to what has been observed with α-defensins, which also act as bacterial toxin-inhibitors (Giesemann et al., 2008; Korbmacher et al., 2020). Since there was no obvious aggregation of TcdB, binding of TcdB to the cell surface was studied. In our opinion, the reduction observed here was not sufficient to fully explain the strong inhibition of TcdB by Ax, so the following step was to analyze the toxins' intramolecular autoprotease activity. In general, not the full-length toxin but only the GTD reaches the cytosol of target cells (Pfeifer et al., 2003). After translocation across the endosomal membrane, TcdB is autoproteolytically cleaved in the presence of intracellular $InsP_6$ (Reineke et al., 2007). However, we could exclude an effect of Ax on this step, which occurs immediately before substrate modification. Most interestingly, Ax had a marked effect on the glucosylation levels of Rac1 when treated with TcdB. In the presence of Ax, a clear inhibition of the glucosyltransferase activity with IC_{50} values in the low millimolar range was obtained. At comparable concentrations, Ax also inhibited glucosylhydrolase activity of TcdB in the absence of its natural substrate Rac1, indicating neither an influence on the GTD-Rac1 interaction nor a direct interaction between Ax and Rac1. In our hands, Ax was as potent as castanospermine, an already known inhibitor of the enzyme domain of TcdB (Jank et al., 2008). Hydrolase activities are known for several bacterial toxins, such as for various ADP-ribosyltransferases. In this case, the enzymatically active ADP-ribosyltransferases catalyze the attachment of an ADP-ribose residue to specific target proteins of the host through glycosidic bonds. However, in the absence of the target substrate, ADP-ribosyltransferases possess NAD glycohydrolase activity, resulting in the cleavage of intracellular NAD into ADP-ribose and nicotinamide (Deng and Barbieri, 2008). For TcdA and TcdB, similar activities were found (Ciesla and Bobak, 1998). Both toxins are able to cleave intracellular UDP-glucose (UDP-Glc) into glucose and UDP. In the presence of their target substrates, the toxins glucosylate GTPases at a key threonine. In the absence of an appropriate acceptor protein, though, they hydrolyze the nucleotide-sugar UDP-Glc to UDP and free glucose (Bhattacharyya et al., 2002; Reinert et al., 2005).

Ax is a small molecule that acts as a radical scavenger and that is composed of a primary aromatic and a secondary amine. It has been used in medical applications for almost four decades and underwent a broad range of toxicity studies revealing a low toxicity and a favorable safety profile (Cazan et al., 2018). Typically, Ax is administered in different pharmaceutic formulations with an absolute bioavailability of about 79% (Malerba and Ragnoli, 2008). Depending on the formulation and the doses applied, peak plasma concentrations of Ax greater than 150 ng/ml (around 360 μM) can be achieved (Rojpibulstit et al., 2003). Thus, concentrations used in this study are plausible and Ax alone did not show any adverse side effects on different mammalian cell lines. Also for TcdB, concentrations are below those reported in literature. For mild forms of CDI, stool TcdB-concentrations around 1.3 ng/ml (~5 pM) were reported, whereas for severe forms of CDI, stool toxin concentration achieved levels up to 111 ng/ml (~410 pM) (Ryder et al., 2010). Nevertheless, in our attempts, a TcdB concentration up to 500 pM was inhibited by Ax.

Taken together, we identified the licensed drug Ax as a novel potent inhibitor of the clinically important toxins TcdA and TcdB in living cells and *in vitro*. Prompted by the results from this study, it will be interesting to investigate whether Ax also inhibits these toxins *in vivo* and whether Ax is able to neutralize further bacterial toxins of the glucosyltransferase family.

DATA AVAILABILITY STATEMENT

The original contributions presented in the study are included in the article/**Supplementary Material**, further inquiries can be directed to the corresponding authors.

AUTHOR CONTRIBUTIONS

SF, PP, MF and HB designed research. SH, LB and JB performed experiments. SF, SH, PP and HB analyzed data. SH, JB, MF, GF and PP proof-read the manuscript. SF and HB supervised the study and wrote the manuscript.

FUNDING

The work was financially supported by the Deutsche Forschungsgemeinschaft (BA 2087/8-1, project number 450938962 to HB) and the Medical Faculty Ulm (Baustein 3.2 to SF). SH is a participant of "The International PhD Program in Molecular Medicine" of the International Graduate School in Molecular Medicine Ulm (IGradU). LB and JB are members of the "*Promotionsprogramm Experimentelle Medizin*" of IGradU.

ACKNOWLEDGMENTS

Barbara Moepps and Michael Meister (Institute of Pharmacology and Toxicology, University of Ulm Medical Center, Ulm, Germany) are thanked for providing the pGEX-4T-2-GST_Rac1 plasmid. Furthermore, the authors would like to thank Klaus Aktories (Institute of Experimental and Clinical Pharmacology and Toxicology, Albert Ludwig University of Freiburg, Freiburg, Germany) for providing toxins.

SUPPLEMENTARY MATERIAL

The Supplementary Material for this article can be found online at: https://www.frontiersin.org/articles/10.3389/fphar.2021.809595/full#supplementary-material

REFERENCES

Aktories, K., Schwan, C., and Jank, T. (2017). *Clostridium difficile* Toxin Biology. *Annu. Rev. Microbiol.* 71, 281–307. doi:10.1146/annurev-micro-090816-093458

Barth, H., Blocker, D., Behlke, J., Bergsma-Schutter, W., Brisson, A., Benz, R., et al. (2000). Cellular Uptake of *Clostridium botulinum* C2 Toxin Requires Oligomerization and Acidification. *J. Biol. Chem.* 275, 18704–18711. doi:10.1074/jbc.M000596200

Barth, H., Hofmann, F., Olenik, C., Just, I., and Aktories, K. (1998). The N-Terminal Part of the Enzyme Component (C2I) of the Binary *Clostridium botulinum* C2 Toxin Interacts with the Binding Component C2II and Functions as a Carrier System for a Rho ADP-Ribosylating C3-Like Fusion Toxin. *Infect. Immun.* 66, 1364–1369. doi:10.1128/IAI.66.4.1364-1369.1998

Barth, H., Pfeifer, G., Hofmann, F., Maier, E., Benz, R., and Aktories, K. (2001). Low pH-Induced Formation of Ion Channels by *Clostridium difficile* Toxin B in Target Cells. *J. Biol. Chem.* 276, 10670–10676. doi:10.1074/jbc.M009445200

Bauer, M. P., Notermans, D. W., van Benthem, B. H., Brazier, J. S., Wilcox, M. H., Rupnik, M., et al. (2011). *Clostridium difficile* Infection in Europe: A Hospital-Based Survey. *Lancet* 377, 63–73. doi:10.1016/S0140-6736(10)61266-4

Belyi, Y., and Aktories, K. (2010). Bacterial Toxin and Effector Glycosyltransferases. *Biochim. Biophys. Acta* 1800, 134–143. doi:10.1016/j.bbagen.2009.07.022

Bhattacharyya, S., Kerzmann, A., and Feig, A. L. (2002). Fluorescent Analogs of UDP-Glucose and Their Use in Characterizing Substrate Binding by Toxin A from *Clostridium difficile*. *Eur. J. Biochem.* 269, 3425–3432. doi:10.1046/j.1432-1033.2002.03013.x

Blöcker, D., Pohlmann, K., Haug, G., Bachmeyer, C., Benz, R., Aktories, K., et al. (2003). Clostridium Botulinum C2 Toxin: Low pH-Induced Pore Formation is Required for Translocation of the Enzyme Component C2I into the Cytosol of Host Cells. *J. Biol. Chem.* 278, 37360–37367. doi:10.1074/jbc.M305849200

Carpinteiro, A., Gripp, B., Hoffmann, M., Pöhlmann, S., Hoertel, N., Edwards, M. J., et al. (2021). Inhibition of Acid Sphingomyelinase by Ambroxol Prevents SARS-CoV-2 Entry Into Epithelial Cells. *J. Biol. Chem.* 296, 100701. doi:10.1016/j.jbc.2021.100701

Carter, G. P., Chakravorty, A., Pham Nguyen, T. A., Mileto, S., Schreiber, F., Li, L., et al. (2015). Defining the Roles of TcdA and TcdB in Localized Gastrointestinal Disease, Systemic Organ Damage, and the Host Response during *Clostridium difficile* Infections. *mBio* 6, e00551. doi:10.1128/mBio.00551-15

Cartmill, T. D., Panigrahi, H., Worsley, M. A., McCann, D. C., Nice, C. N., and Keith, E. (1994). Management and Control of a Large Outbreak of Diarrhoea Due to *Clostridium difficile*. *J. Hosp. Infect.* 27, 1–15. doi:10.1016/0195-6701(94)90063-9

Cassini, A., Plachouras, D., Eckmanns, T., Abu Sin, M., Blank, H. P., Ducomble, T., et al. (2016). Burden of Six Healthcare-Associated Infections on European Population Health: Estimating Incidence-Based Disability-Adjusted Life Years through a Population Prevalence-Based Modelling Study. *Plos Med.* 13, e1002150. doi:10.1371/journal.pmed.1002150

Cazan, D., Klimek, L., Sperl, A., Plomer, M., and Kölsch, S. (2018). Safety of Ambroxol in the Treatment of Airway Diseases in Adult Patients. *Expert Opin. Drug Saf.* 17, 1211–1224. doi:10.1080/14740338.2018.1533954

Ciesla, W. P., and Bobak, D. A. (1998). *Clostridium difficile* Toxins A and B are Cation-Dependent UDP-Glucose Hydrolases with Differing Catalytic Activities. *J. Biol. Chem.* 273, 16021–16026. doi:10.1074/jbc.273.26.16021

Deng, Q., and Barbieri, J. T. (2008). Molecular Mechanisms of the Cytotoxicity of ADP-Ribosylating Toxins. *Annu. Rev. Microbiol.* 62, 271–288. doi:10.1146/annurev.micro.62.081307.162848

Egerer, M., Giesemann, T., Jank, T., Satchell, K. J., and Aktories, K. (2007). Auto-Catalytic Cleavage of *Clostridium difficile* Toxins A and B Depends on Cysteine Protease Activity. *J. Biol. Chem.* 282, 25314–25321. doi:10.1074/jbc.M703062200

Fischer, S., Ückert, A. K., Landenberger, M., Papatheodorou, P., Hoffmann-Richter, C., Mittler, A. K., et al. (2020). Human Peptide α-defensin-1 Interferes with *Clostridioides difficile* Toxins TcdA, TcdB, and CDT. *FASEB j.* 34, 6244–6261. doi:10.1096/fj.201902816R

Florin, I., and Thelestam, M. (1983). Internalization of *Clostridium difficile* Cytotoxin Into Cultured Human Lung Fibroblasts. *Biochim. Biophys. Acta* 763, 383–392. doi:10.1016/0167-4889(83)90100-3

Fois, G., Hobi, N., Felder, E., Ziegler, A., Miklavc, P., Walther, P., et al. (2015). A New Role for an Old Drug: Ambroxol Triggers Lysosomal Exocytosis via pH-dependent Ca^{2+} Release from Acidic Ca^{2+} Stores. *Cell Calcium* 58, 628–637. doi:10.1016/j.ceca.2015.10.002

Frisch, C., Gerhard, R., Aktories, K., Hofmann, F., and Just, I. (2003). The Complete Receptor-Binding Domain of *Clostridium difficile* Toxin A Is Required for Endocytosis. *Biochem. Biophys. Res. Commun.* 300, 706–711. doi:10.1016/S0006-291X(02)02919-4

Genth, H., Huelsenbeck, J., Hartmann, B., Hofmann, F., Just, I., and Gerhard, R. (2006). Cellular Stability of Rho-GTPases Glucosylated by *Clostridium difficile* Toxin B. *FEBS Lett.* 580, 3565–3569. doi:10.1016/j.febslet.2006.04.100

Gerhard, R., Frenzel, E., Goy, S., and Olling, A. (2013). Cellular Uptake of *Clostridium difficile* TcdA and Truncated TcdA Lacking the Receptor Binding Domain. *J. Med. Microbiol.* 62, 1414–1422. doi:10.1099/jmm.0.057828-0

Giesemann, T., Guttenberg, G., and Aktories, K. (2008). Human Alpha-Defensins Inhibit *Clostridium difficile* Toxin B. *Gastroenterol.* 134, 2049–2058. doi:10.1053/j.gastro.2008.03.008

Gupta, P. R. (2010). Ambroxol - Resurgence of an Old Molecule as an Anti-inflammatory Agent in Chronic Obstructive Airway Diseases. *Lung India* 27, 46–48. doi:10.4103/0970-2113.63603

Henriques, B., Florin, I., and Thelestam, M. (1987). Cellular Internalisation of *Clostridium difficile* Toxin A. *Microb. Pathog.* 2, 455–463. doi:10.1016/0882-4010(87)90052-0

Jank, T., and Aktories, K. (2008). Structure and Mode of Action of Clostridial Glucosylating Toxins: The ABCD Model. *Trends Microbiol.* 16, 222–229. doi:10.1016/j.tim.2008.01.011

Jank, T., Ziegler, M. O., Schulz, G. E., and Aktories, K. (2008). Inhibition of the Glucosyltransferase Activity of Clostridial Rho/Ras-Glucosylating Toxins by Castanospermine. *FEBS Lett.* 582, 2277–2282. doi:10.1016/j.febslet.2008.05.025

Just, I., and Gerhard, R. (2004). Large Clostridial Cytotoxins. *Rev. Physiol. Biochem. Pharmacol.* 152, 23–47. doi:10.1007/s10254-004-0033-5

Just, I., Selzer, J., Wilm, M., von Eichel-Streiber, C., Mann, M., and Aktories, K. (1995a). Glucosylation of Rho Proteins by *Clostridium difficile* Toxin B. *Nature* 375, 500–503. doi:10.1038/375500a0

Just, I., Wilm, M., Selzer, J., Rex, G., von Eichel-Streiber, C., Mann, M., et al. (1995b). The Enterotoxin from *Clostridium difficile* (ToxA) Monoglucosylates the Rho Proteins. *J. Biol. Chem.* 270, 13932–13936. doi:10.1074/jbc.270.23.13932

Korbmacher, M., Fischer, S., Landenberger, M., Papatheodorou, P., Aktories, K., and Barth, H. (2020). Human α-Defensin-5 Efficiently Neutralizes Clostridioides Difficile Toxins TcdA, TcdB, and CDT. *Front. Pharmacol.* 11, 1204. doi:10.3389/fphar.2020.01204

Kordus, S. L., Thomas, A. K., and Lacy, D. B. (2021). Clostridioides Difficile Toxins: Mechanisms of Action and Antitoxin Therapeutics. *Nat. Rev. Microbiol.* [Epub ahead of print]. doi:10.1038/s41579-021-00660-2

Kuehne, S. A., Cartman, S. T., Heap, J. T., Kelly, M. L., Cockayne, A., and Minton, N. P. (2010). The Role of Toxin A and Toxin B in *Clostridium difficile* Infection. *Nature* 467, 711–713. doi:10.1038/nature09397

LaFrance, M. E., Farrow, M. A., Chandrasekaran, R., Sheng, J., Rubin, D. H., and Lacy, D. B. (2015). Identification of an Epithelial Cell Receptor Responsible for *Clostridium difficile* TcdB-Induced Cytotoxicity. *Proc. Natl. Acad. Sci. U S A.* 112, 7073–7078. doi:10.1073/pnas.1500791112

Lanis, J. M., Barua, S., and Ballard, J. D. (2010). Variations in TcdB Activity and the Hypervirulence of Emerging Strains of *Clostridium difficile*. *PLoS Pathog.* 6, e1001061. doi:10.1371/journal.ppat.1001061

Larson, H. E., Price, A. B., Honour, P., and Borriello, S. P. (1978). *Clostridium difficile* and the Aetiology of Pseudomembranous Colitis. *Lancet* 1, 1063–1066. doi:10.1016/S0140-6736(78)90912-1

Lessa, F. C., Mu, Y., Bamberg, W. M., Beldavs, Z. G., Dumyati, G. K., Dunn, J. R., et al. (2015). Burden of *Clostridium difficile* Infection in the United States. *N. Engl. J. Med.* 372, 825–834. doi:10.1056/NEJMoa1408913

Louie, T. J., Miller, M. A., Mullane, K. M., Weiss, K., Lentnek, A., Golan, Y., et al. (2011). Fidaxomicin Versus Vancomycin for *Clostridium difficile* Infection. *N. Engl. J. Med.* 364, 422–431. doi:10.1056/NEJMoa0910812

Lyras, D., O'Connor, J. R., Howarth, P. M., Sambol, S. P., Carter, G. P., Phumoonna, T., et al. (2009). Toxin B is Essential for Virulence of *Clostridium difficile*. *Nature* 458, 1176–1179. doi:10.1038/nature07822

Madshus, I. H., Stenmark, H., Sandvig, K., and Olsnes, S. (1991). Entry of Diphtheria Toxin-Protein A Chimeras Into Cells. *J. Biol. Chem.* 266, 17446–17453. doi:10.1016/S0021-9258(19)47393-6

Malerba, M., and Ragnoli, B. (2008). Ambroxol in the 21st century: Pharmacological and Clinical Update. *Expert Opin. Drug Metab. Toxicol.* 4, 1119–1129. doi:10.1517/17425255.4.8.1119

McNeill, A., Magalhaes, J., Shen, C., Chau, K. Y., Hughes, D., Mehta, A., et al. (2014). Ambroxol Improves Lysosomal Biochemistry in Glucocerebrosidase Mutation-Linked Parkinson Disease Cells. *Brain* 137, 1481–1495. doi:10.1093/brain/awu020

Ménard, A., Altendorf, K., Breves, D., Mock, M., and Montecucco, C. (1996). The Vacuolar ATPase Proton Pump is Required for the Cytotoxicity of Bacillus Anthracis Lethal Toxin. *FEBS Lett.* 386 (2–3), 161–164. doi:10.1016/0014-5793(96)00422-x

Pfeifer, G., Schirmer, J., Leemhuis, J., Busch, C., Meyer, D. K., Aktories, K., et al. (2003). Cellular Uptake of *Clostridium difficile* Toxin B. Translocation of the N-Terminal Catalytic Domain into the Cytosol of Eukaryotic Cells. *J. Biol. Chem.* 278, 44535–44541. doi:10.1074/jbc.M307540200

Qa'Dan, M., Spyres, L. M., and Ballard, J. D. (2000). pH-Induced Conformational Changes in *Clostridium difficile* Toxin B. *Infect. Immun.* 68, 2470–2474. doi:10.1128/iai.68.5.2470-2474.2000

Reineke, J., Tenzer, S., Rupnik, M., Koschinski, A., Hasselmayer, O., Schrattenholz, A., et al. (2007). Autocatalytic Cleavage of *Clostridium difficile* Toxin B. *Nature* 446, 415–419. doi:10.1038/nature05622

Reinert, D. J., Jank, T., Aktories, K., and Schulz, G. E. (2005). Structural Basis for the Function of *Clostridium difficile* Toxin B. *J. Mol. Biol.* 351, 973–981. doi:10.1016/j.jmb.2005.06.071

Rojpibulstit, M., Kasiwong, S., Juthong, S., Phadoongsombat, N., and Faroongsarng, D. (2003). Ambroxol Lozenge Bioavailability. *Clin. Drug Invest.* 23, 273–280. doi:10.2165/00044011-200323040-00007

Ryder, A. B., Huang, Y., Li, H., Zheng, M., Wang, X., Stratton, C. W., et al. (2010). Assessment of *Clostridium difficile* Infections by Quantitative Detection of tcdB Toxin by Use of a Real-Time Cell Analysis System. *J. Clin. Microbiol.* 48, 4129–4134. doi:10.1128/JCM.01104-10

Schneider, C. A., Rasband, W. S., and Eliceiri, K. W. (2012). NIH Image to ImageJ: 25 Years of Image Analysis. *Nat. Methods* 9, 671–675. doi:10.1038/nmeth.2089

Tao, L., Tian, S., Zhang, J., Liu, Z., Robinson-McCarthy, L., Miyashita, S. I., et al. (2019). Sulfated Glycosaminoglycans and Low-Density Lipoprotein Receptor Contribute to *Clostridium difficile* Toxin A Entry into Cells. *Nat. Microbiol.* 4, 1760–1769. doi:10.1038/s41564-019-0464-z

Tao, L., Zhang, J., Meraner, P., Tovaglieri, A., Wu, X., Gerhard, R., et al. (2016). Frizzled Proteins Are Colonic Epithelial Receptors for *C. difficile* Toxin B. *Nature* 538, 350–355. doi:10.1038/nature19799

Tart, S. B. (2013). The Role of Vancomycin and Metronidazole for the Treatment of Clostridium Difficile-Associated Diarrhea. *J. Pharm. Pract.* 26, 488–490. doi:10.1177/0897190013499525

Theriot, C. M., Bowman, A. A., and Young, V. B. (2016). Antibiotic-Induced Alterations of the Gut Microbiota Alter Secondary Bile Acid Production and Allow for *Clostridium difficile* Spore Germination and Outgrowth in the Large Intestine. *mSphere* 1, e00045–15. doi:10.1128/mSphere.00045-15

Umata, T., Moriyama, Y., Futai, M., and Mekada, E. (1990). The Cytotoxic Action of Diphtheria Toxin and its Degradation in Intact Vero Cells are Inhibited by Bafilomycin A1, a Specific Inhibitor of Vacuolar-type H(+)-ATPase. *J. Biol. Chem.* 265, 21940–21945. doi:10.1016/S0021-9258(18)45829-2

von Eichel-Streiber, C., Harperath, U., Bosse, D., and Hadding, U. (1987). Purification of Two High Molecular Weight Toxins of *Clostridium difficile* Which are Antigenically Related. *Microb. Pathog.* 2, 307–318. doi:10.1016/0882-4010(87)90073-8

von Eichel-Streiber, C., Laufenberg-Feldmann, R., Sartingen, S., Schulze, J., and Sauerborn, M. (1992). Comparative Sequence Analysis of the *Clostridium difficile* Toxins A and B. *Mol. Gen. Genet.* 233, 260–268. doi:10.1007/bf00587587

Yamaya, M., Nishimura, H., Nadine, L. K., Ota, C., Kubo, H., and Nagatomi, R. (2014). Ambroxol Inhibits Rhinovirus Infection in Primary Cultures of Human Tracheal Epithelial Cells. *Arch. Pharm. Res.* 37, 520–529. doi:10.1007/s12272-013-0210-7

Young, J. A., and Collier, R. J. (2007). Anthrax Toxin: Receptor Binding, Internalization, Pore Formation, and Translocation. *Annu. Rev. Biochem.* 76, 243–265. doi:10.1146/annurev.biochem.75.103004.142728

Yuan, P., Zhang, H., Cai, C., Zhu, S., Zhou, Y., Yang, X., et al. (2015). Chondroitin Sulfate Proteoglycan 4 Functions as the Cellular Receptor for *Clostridium difficile* Toxin B. *Cell Res.* 25, 157–168. doi:10.1038/cr.2014.169

Conflict of Interest: The authors declare that the research was conducted in the absence of any commercial or financial relationships that could be construed as a potential conflict of interest.

Publisher's Note: All claims expressed in this article are solely those of the authors and do not necessarily represent those of their affiliated organizations, or those of the publisher, the editors and the reviewers. Any product that may be evaluated in this article, or claim that may be made by its manufacturer, is not guaranteed or endorsed by the publisher.

frontiers in Pharmacology

ORIGINAL RESEARCH
published: 10 January 2022
doi: 10.3389/fphar.2021.788874

Scorpion Venom Antimicrobial Peptides Induce Caspase-1 Dependant Pyroptotic Cell Death

Ranwa A. Elrayess[1,2], Mahmoud E. Mohallal[2], Yomn M. Mobarak[3], Hala M. Ebaid[2], Sarah Haywood-Small[1], Keith Miller[1], Peter N. Strong[1] and Mohamed A. Abdel-Rahman[2]**

[1]Biomolecular Sciences Research Centre, Sheffield Hallam University, Sheffield, United Kingdom, [2]Zoology Department, Faculty of Science, Suez Canal University, Ismailia, Egypt, [3]Zoology Department, Faculty of Science, Suez University, Suez, Egypt

Within the last decade, several peptides have been identified according to their ability to inhibit the growth of microbial pathogens. These antimicrobial peptides (AMPs) are a part of the innate immune system of all living organisms. Many studies on their effects on prokaryotic microorganisms have been reported; some of these peptides have cytotoxic properties although the molecular mechanisms underlying their activity on eukaryotic cells remain poorly understood. Smp24 and Smp43 are novel cationic AMPs which were identified from the venom of the Egyptian scorpion *Scorpio maurus palmatus*. Smp24 and Smp43 showed potent activity against both Gram-positive and Gram-negative bacteria as well as fungi. Here we describe cytotoxicity of these peptides towards two acute leukaemia cell lines (myeloid (KG1-a) and lymphoid (CCRF-CEM) leukaemia cell lines) and three non-tumour cell lines $CD34^+$ (hematopoietic stem progenitor from cord blood), HRECs (human renal epithelial cells) and HaCaT (human skin keratinocytes). Smp24 and Smp43 (4–256 μg/ml) decreased the viability of all cell lines, although HaCaT cells were markedly less sensitive. With the exception HaCaT cells, the caspase-1 gene was uniquely up-regulated in all cell lines studied. However, all cell lines showed an increase in downstream interleukin-1β (IL-1β) expression. Transmission electron microscope studies revealed the formation of cell membrane blebs and the appearance of autolysosomes and lipid droplets in all cell lines; KG1-a leukemia cells also showed the unique appearance of glycogen deposits. Our results reveal a novel mechanism of action for scorpion venom AMPs, activating a cascade of events leading to cell death through a programmed pyroptotic mechanism.

Keywords: Antimicrobial peptides, scorpio maurus palmatus, Smp24, Smp43, cell death, pyroptosis, caspase-1, IL-1b

OPEN ACCESS

Edited by:
Zhijian Cao,
Wuhan University, China

Reviewed by:
Zhonghua Liu,
Hunan Normal University, China
Yang Xiang,
Nanchang University, China

****Correspondence:***
Peter N. Strong
p.strong@shu.ac.uk
Mohamed A. Abdel-Rahman
mohamed_hassanain@science.suez.edu.eg

Specialty section:
This article was submitted to Pharmacology of Ion Channels and Channelopathies, a section of the journal Frontiers in Pharmacology

Received: *03 October 2021*
Accepted: *13 December 2021*
Published: *10 January 2022*

Citation:
Elrayess RA, Mohallal ME, Mobarak YM, Ebaid HM, Haywood-Small S, Miller K, Strong PN and Abdel-Rahman MA (2022) Scorpion Venom Antimicrobial Peptides Induce Caspase-1 Dependant Pyroptotic Cell Death. Front. Pharmacol. 12:788874. doi: 10.3389/fphar.2021.788874

INTRODUCTION

Antimicrobial peptides (AMPs) are found throughout the animal kingdom and represent an ancient host defence mechanism of the innate immune system (Zasloff, 2002; Lai and Gallo, 2009; Bahar and Ren, 2013). They are increasingly recognized as a potential source of new broad-spectrum antibiotics, to combat the steady and alarming rise in the resistance of pathogenic microorganisms to conventional drugs (Guilhelmelli et al., 2013; Nuti et al., 2017). AMPs have also been shown to selectively target several types of tumour cells, with the prospect of being able to develop these peptides as novel anti-cancer drugs (Deslouches and Di 2017).

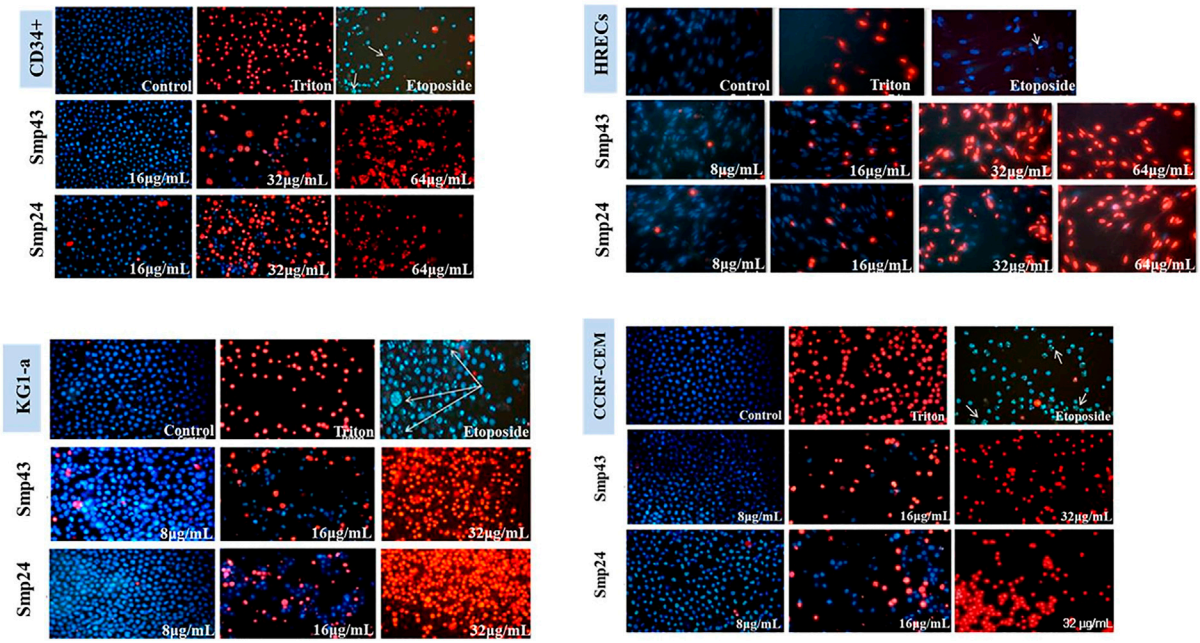

FIGURE 1 | Changes in nuclear morphology of the non-tumour (CD34$^+$ and HRECs) and tumour (KG1-a and CCRF-CEM) cell lines treated with different concentrations of Smp24 or Smp43 (8–256 μg/ml) showed significant increase in PI stain uptake in a concentration dependant manner (20X).

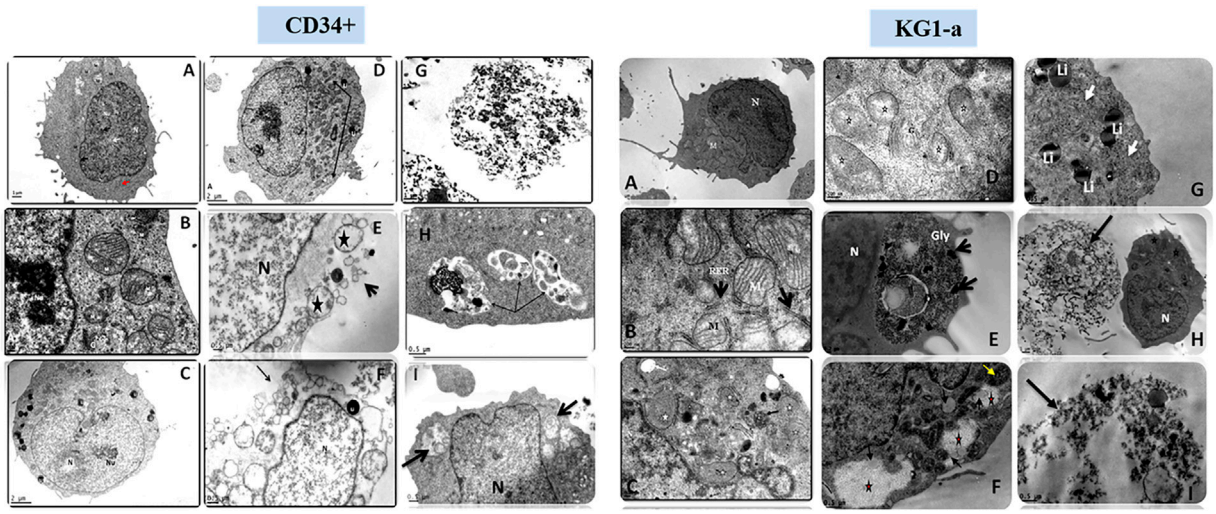

FIGURE 2 | Transmission electron micrograph of CD34$^+$ and KG1-a cells showing the effects of Smp24 and Smp43 treatment on their cell components. CD34$^+$, **(A,B)**, control untreated cells showing normal ultrastructure of the cell. **(C,D)** cells treated with 1/2 LC_{50} concentration of Smp43 and Smp24, respectively, showing obvious increase in cell size, mitochondria were with inconspicuous cristae (star, arrow) and many lipid droplets (Li). **(E–I)** cells treated with LC_{50} concentration of Smp24 and Smp43. Most of cells were completely lysed **(G)** while other cells **(E,F)** showed ruptured cell membrane (arrow), karyolysis nucleus (N) and many lucent vacuoles (star). Autolysosomes were also noted (arrow) in the cytoplasm **(H,I)**. KG1-a, control untreated cells showing normal ultrastructure of the cell. **(C,D)**, cells treated with 1/2 LC_{50} concentration of Smp43 and Smp24, respectively, showing mitochondria were with inconspicuous cristae (star) and appearance of lucent vacuoles (White arrow) and multivesicular body (black arrow). **(E–I)** cells treated with LC_{50} concentration of Smp24 and Smp43. Most of cells were completely lysed **(H,I)** while other cells **(G)** showed deposition of lipid droplets (Li), and deposition of glycogen granules **(E,F)** inside lysosomes (Gly, star) deposits of dense pigments (arrow).

The attractiveness of AMPs in antimicrobial therapy lies in their mechanism of action as membrane disruptive agents, against which microbes have little natural resistance. AMPs are predominantly cationic, amphipathic molecules. Their selectivity arises from a primary electrostatic interaction of their charged surface with negatively charged prokaryotic

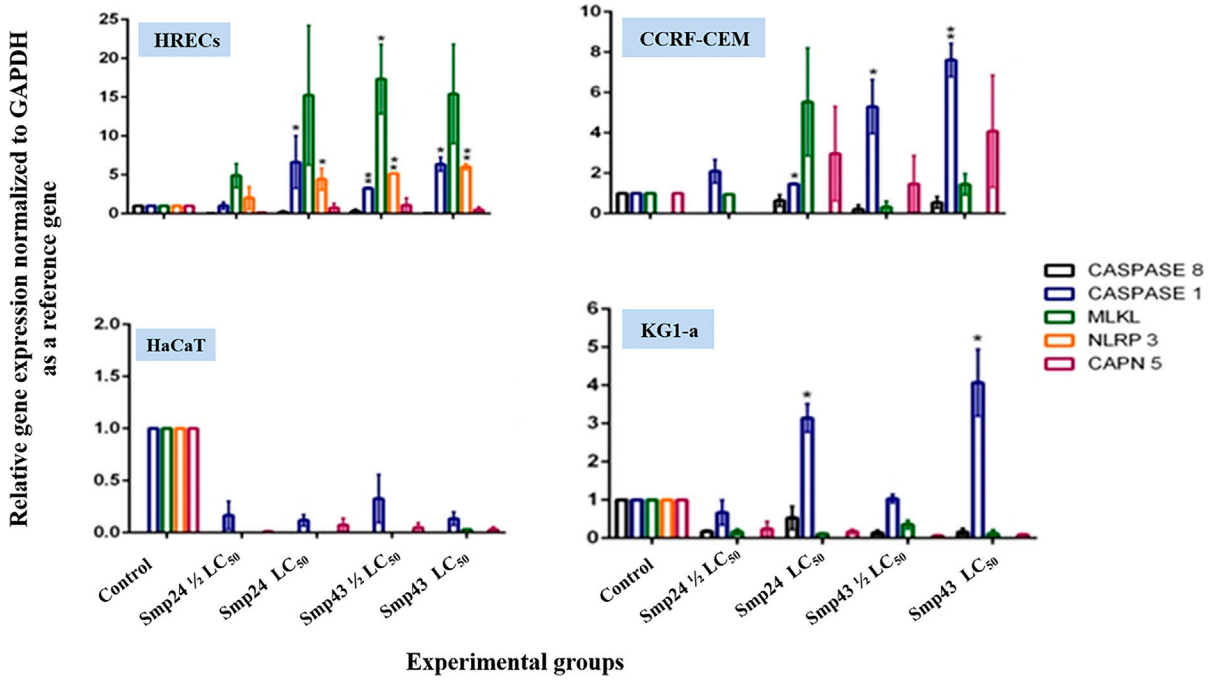

FIGURE 3 | Charts showing relative genes expressions quantified by a qRT-PCR after treating non-tumour (HRECs and HaCaT) and tumour (CCRF-CEM and KG1-a) cell lines, with Smp24 and Smp43. All gene expressions were normalized to the expression of the housekeeping gene, GAPDH. The data represented as mean ± SE. The statistical significance (*$p \leq 0.05$, **$p \leq 0.001$) was determined by comparison with the control using student t-test.

membranes (Huang, 2000; Zasloff, 2002). Although healthy eukaryotic cells have a zwitterionic external membrane, cancer cells are characterized by the transbilayer movement of phosphatidylserine to the outer membrane leaflet, thereby endowing tumour cell membranes, analogously to prokaryotic cell membranes, with a negative charge (for a review, see Sharma and Kanwar, 2018). The appearance of phosphatidylserine on the outer membrane leaflet regulates malignant transformation by primarily suppressing anti-tumour immune responses (Utsugi et al., 1991; Fadok et al., 2000).

Clearly, the development of AMPs as anti-cancer agents (Schweizer, 2009; Wang and Wang, 2016; Crusca et al., 2018; Lei et al., 2019), will depend on developing selectivity by creating a sufficient distinction (effective therapeutic index) between their cytotoxic effects on target tumour cell membranes with respect to the membranes of normal cells. Understanding the cytotoxic mechanism by which AMPs exert their action is therefore crucial to the development of these potentially very attractive agents, as therapeutic drugs.

Abdel-Rahman et al. (2013) identified two novel amphipathic cationic AMPs (Smp43 and Smp24) through cDNA sequencing of the venom gland of the Egyptian scorpion *Scorpio maurus palmatus*. Both peptides showed a potent activity against both Gram-positive and Gram-negative bacteria as well as fungi. Both peptides formed pores in model prokaryotic and eukaryotic phospholipid membranes, although their detailed mechanism of action differed and the same peptide was shown to act by different mechanisms according to the cell membrane composition of the host cell (Harrison et al., 2016b; Heath et al., 2018). Both peptides had cytotoxic effects on various cancer cell lines (liver, myeloid and lymphoid leukaemia). In contrast, keratinocytes were markedly less sensitive and although Smp24 was cytotoxic to erythrocytes, Smp 43 was non-haemolytic at all concentrations tested (Harrison et al., 2016b; Elrayess et al., 2019).

Cell death can occur in both a controlled and uncontrolled manner (for a recent review, see Darcy, 2019). The loss of cell membrane integrity has conventionally been associated with the process of necrosis, an uncontrolled form of cell death induced by external injury such as hypoxia or inflammation which often involves the up-regulation of pro-inflammatory molecules, resulting in rupture of the cell membrane. In contrast, apoptosis is a programmed, tightly controlled form of cell death that crucially, does not involve damage to the cell membrane. It is now recognised that, in conjunction with cell death programmes that do not disrupt cell membranes, some forms of necrosis are not passive and can also be programmed by the cell in a process known as pyroptosis (Hersh et al., 1999; Bergsbaken et al., 2009; Frank and Vince, 2019). Pyroptosis is a lytic, inflammatory type of necrotic cell death, characterized by cell swelling and the release of inflammatory factors. It is highly regulated. The expression of caspase-1 is a primary marker of pyroptosis and results from the activation of the pro-enzyme by pattern recognition receptors of inflammasome complexes. Gastrodermin-D (GSDMT) is a key substrate of caspase-1 and the enzyme catalyses the release of an N-terminal fragment

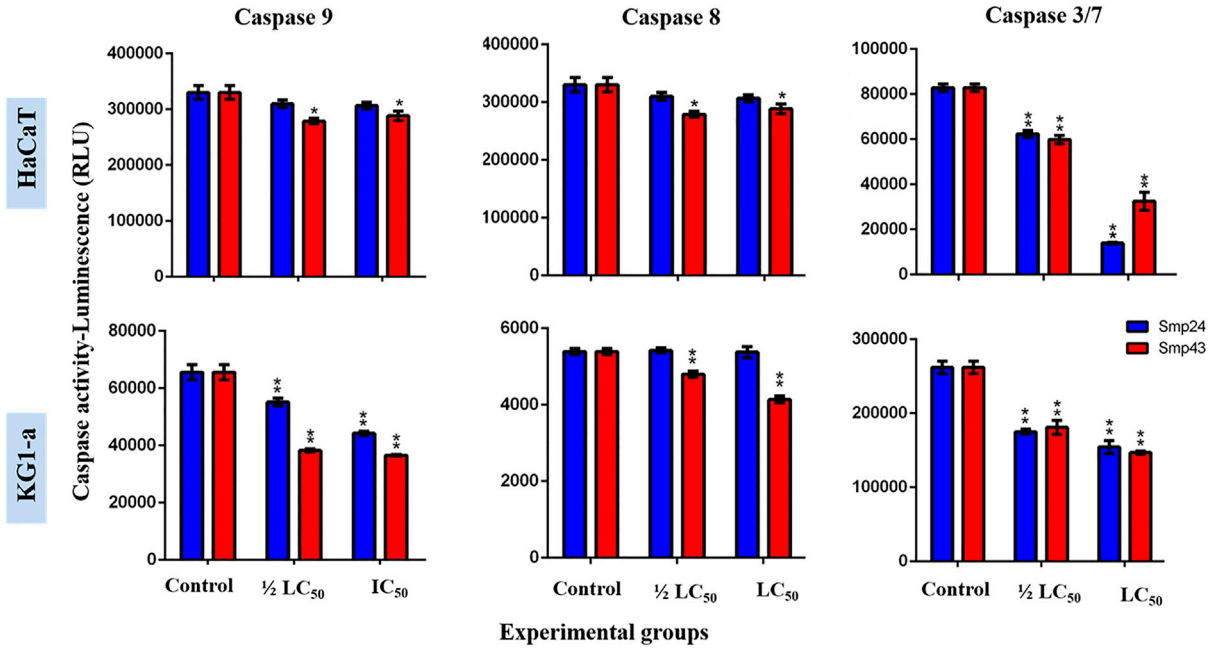

FIGURE 4 | Charts showing the effect of Smp24 and Smp43 (1/2 LC_{50} and LC_{50}) on the activity of caspase 8, 9 and 3/7 of representative non-tumour (HaCaT) and tumour (KG1-a) cell lines. The results showed no significant increase in caspases activities. The data represented as mean ± SE. The statistical significance (*$p \leq 0.05$, **$p \leq 0.001$) was determined by comparison with the control using student t-test.

(GSDMT-cNT) which causes cells to swell until they rupture. Caspase-1 also processes inflammatory cytokines such as interleukin-1β (IL-1β) and interleukin-18, which can be released by channels formed by GSDMD-cNT. Both the activation of caspase-1 and the increased expression of IL-1β are key pyroptotic markers, in clear distinction from activation by caspases 3/7 and 8/9, which are hallmarks of apoptosis.

Pyroptosis is increasingly recognised to play an important role in cancer (for recent reviews, see Xia et al., 2019; Fang et al., 2020). Intriguingly, pyroptosis may play dual but opposite roles in both promoting and inhibiting tumorigenesis. On the one hand, the many inflammatory mediators released in pyroptosis are closely related to tumorigenesis and the resistance to chemotherapeutic drugs. In contrast, triggering the pyroptosis of tumour cells can offer a novel way of inhibiting tumour cell expression.

Some AMPs can exploit both differences in membrane charge and cell stability to specifically target certain cancer cells (Rathinakumar et al., 2009; Mahlapuu et al., 2016; Wang et al., 2017), suggesting that these peptides are potential new anti-cancer agents and encouraging further development of other classes of AMPs in this area. When examining the effects of Smp24 and Smp43 in morphological studies (Elrayess et al., 2019), we found suggestive evidence of pyroptosis. Here we have studied these preliminary observations in greater detail and suggest that Smp24 and Smp43 exert pyroptotic effects in both cancer and non-cancer cells, with the release of inflammatory cytokines. The pyroptotic effects in cancer cells are mediated by the activation of caspase-1, whereas the release of IL-1β in normal cells appears to be both dependent and independent of caspase-1.

MATERIALS AND METHODS

Peptides and Materials

Smp24 (IWSFLIKAATKLLPSLFGGGKKDS) and Smp43 (GVWDWIKKTAGKIWNSEPVKALKSQALNAAKNFVAEKIG ATPS) were synthesized (>90% pure) using solid-phase chemistry and were purchased from Think Peptides (Oxford, United Kingdom). DMEM media was obtained from Lonza (Cologne, Germany). Epithelial growth media was obtained from Innoprot (Deria, Spain). 96-well white microplates were obtained from Fisher Scientific (Loughborough United Kingdom). PCR primers were obtained from Applied Bioscience (Warrington, United Kingdom). Interleukin 1B antibody was obtained from Santa Cruz (Heidelberg, Germany). Fluorescent IRDye 800 CW goat anti-rabbit secondary antibody was obtained from LICOR (Cambridge, United Kingdom). Caspase activity (caspases 3/7,8 and 9) was measured using a Caspase-Glo® Assay kit obtained from Promega (Southampton, United Kingdom). Caspase-1 inhibitor (Z-WEHD-FMK) was obtained from R&D systems (Abingdon, United Kingdom). All other reagents were the highest grade available and were obtained from Sigma (Gillingham, United Kingdom).

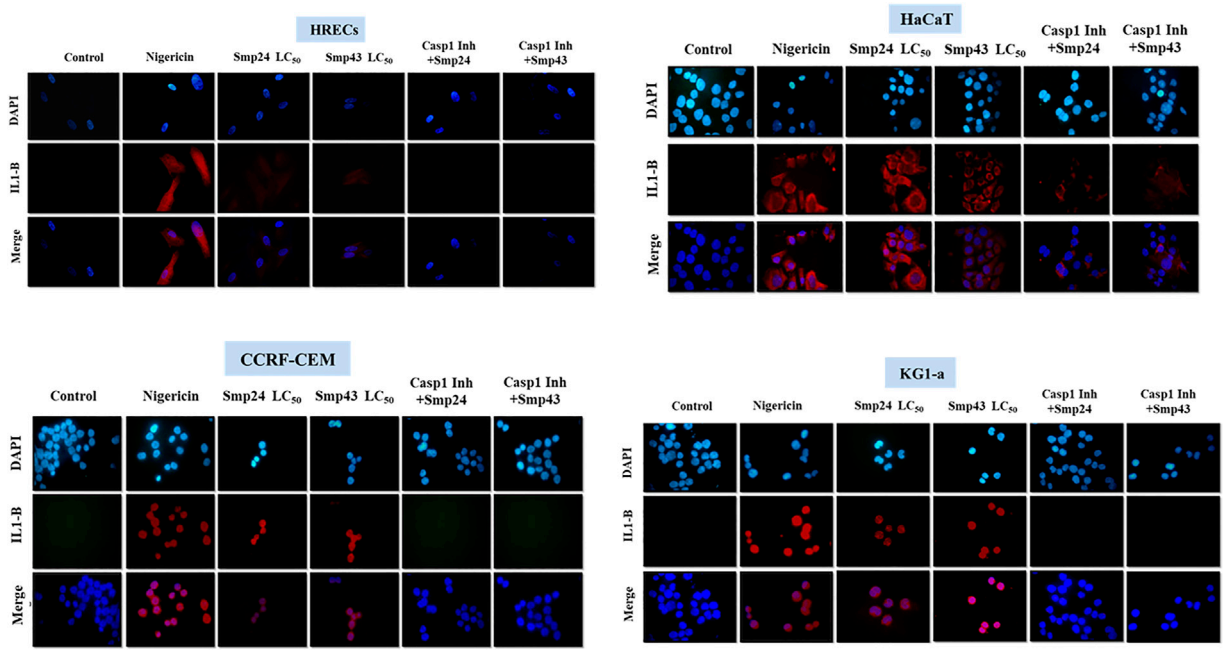

FIGURE 5 | Intracellular IL-1B localization was visualized using fluorescence microscopy after treatment of non-tumour (HRECs and HaCaT) and tumour (CCRF-CEM and KG1-a) cell lines with Smp42 and Smp43 (LC_{50} concentrations). Cells were stained with antibody against IL-1B followed by Alexa Fluor 647 donkey anti-rabbit (red colour) and countered with a Nuclear DNA dye, DAPI (blue colour) (X50).

Cell Lines and Culture Conditions

Non-tumour haematopoietic progenitor stem cells ($CD34^+$) were obtained from Stem Cell Technologies (Grenoble, France). Primary human renal epithelial cells (HRECS) were obtained from Innoprot. Immortalized human skin keratinocytes (HaCaT) were obtained from Cell Lines Service (Eppelheim, Germany). Human lymphoid leukaemia cells (CCRF-CEM, acute lymphoblastic leukaemia, ATCC: CCL-119) and human myeloid leukaemia cells (KG1-a, acute mylogenous leukaemia, ATCC: CCL-243) were obtained from the ATCC (Teddington, United Kingdom). MycoAlert^{TM} *mycoplasma* detection kits were obtained from Lonza (Cologne, Germany).

Suspended cells ($CD34^+$, CCRF-CEM and KG1-a) were seeded in T75 cm^2 flasks in RMPI 1640 medium supplemented with 10% (v/v) foetal bovine serum (FBS), 1.5 mM L-glutamine and 100 µg/ml penicillin/streptomycin. HaCaT cells were seeded in T75 cm^2 flasks in DMEM medium supplemented with 10% FBS, 1.5 mM L-glutamine and 100 µg/ml penicillin/streptomycin. HRECs were seeded in T75 cm^2 flasks in epithelial cell media containing 2% FBS, 1% epithelial cell growth supplement (EPICGS) and 1% penicillin/streptomycin. Cells were incubated at 37°C with 5% CO_2 and tested regularly for *mycoplasma* contamination; all cells were negative throughout the study.

Hoechst 33342 and Propidium Iodide (PI) Staining

Nuclear morphology was assessed by fluorescence microscopy following Hoechst 33342 and propidium iodide (PI) double staining. Cells were seeded in 96 well plates (2.5×10^4 cells/well) and treated with peptides at different concentrations. Triton X-100 (10%) was used as positive control for necrosis while etoposide was used as positive control for apoptosis. Water was used as a negative control. Following treatments, double stain (10 µL) was added to all samples which were then incubated in the dark (30 min) and examined using a fluorescence microscope (Olympus BX60, Japan).

Transmission Electron Microscopy

Cells were seeded in 6 well plates at 0.5×10^6 cells/well and treated with different concentrations of Smp24 or Smp43 and water as vehicle control for 24 h. The treated cells were then harvested and centrifuged at 5000 RPM at 4°C (5 min). The supernatant was removed, and the cells were washed twice in 100 µL cold 0.1M PBS. The cells were fixed by adding 100 µL of 3% Glutaraldehyde in 0.1 M Sodium Phosphate Buffer, PBS (3 h at RT). The cells were then washed twice with cold 0.1M PBS each for 15 min. Then, they were fixed again by 1% aqueous osmium tetraoxide for 1 h. The cells were washed twice with 0.1 M PBS followed by ascending series of ethanol for dehydration (75%, 95%, and then twice in 100% each step 15 min). Cells were then placed in propylene oxide (two changes, 15 min each). Infiltration was accomplished by placing the cells in propylene oxide/Araldite resin (1:1) overnight at RT on a rotating mixer. Cells were then left in full strength Araldite resin (6 h, RT on a rotating mixer), after which they were embedded in fresh Araldite resin (48–72 h at 60°C). Semi-thin 0.5 µm sections were cut (Reichert Ultracut E ultramicrotome) and stained with 1% toludine blue in 1% borax.

Ultrathin sections (70–90 nm thick) were similarly cut but stained with 3% aqueous uranyl acetate (25 min) followed by Reynold's lead citrate (5 min). Sections were examined using a FEI Tecnai Transmission Electron Microscope (Gothenburg, Sweden) at an accelerating voltage of 80 Kv. Electron micrographs were taken using a Gatan digital camera (Abingdon, United Kingdom).

Reverse Transcription Polymerase Chain Reaction

Reverse transcription polymerase chain reaction (qRT-PCR) analysis was used to analyze the gene expression of, *Casp1*, *Casp8*, *Capn5*, *MLKL*, *NLRP3*, and *GAPDH* (housekeeping gene) on cells treated with either Smp24 or Smp43. Water was used as a vehicle control. Full gene names, functions and primer details are shown in **Supplementary Table S1**.

Caspase Activity

Cells were seeded into white 96-well plates at 2.5×10^4 cells/well and treated with different concentrations of Smp24 and Smp43 (37°C, 24 h). Following treatments, 100 µL of Caspase-Glo® (8, 9, 3/7) reagent was added to the cells, which were incubated (RT, 1 h) after initial mixing (1–2 min using a plate shaker at 300–500 rpm). Luminescence was measured using a Wallac Victor 2 1420 detector (Marshall Scientific, United Kingdom). Experiments were performed in triplicate in three independent repeats.

Detection of Interleukin-1β (IL-1β) by Dot Blotting

Media from cell lines, treated with either Smp24 or Smp43 for 24 h (at respective LC_{50} concentrations, Elrayess et al., 2019) were concentrated and stored at −80°C until used. Media (2 µL) were spotted on the middle of nitrocellulose membranes placed in individual wells of a 6-well plate and left to dry. 1 ml blocking solution (TBS-T) (0.15M NaCl, 0.05% Tween-20, 25 mM Tris pH 7.5) was added and the plate incubated (1 h, RT with shaking). After removing the blocking solution, IL-1β rabbit antibody (500 µL, 1:200 diluted in blocking solution) was added to each well and incubated overnight (4°C with shaking). After washing the membranes (TBS-T, RT, 10 min × 3 times with shaking), goat anti-rabbit secondary antibody was added (1:10000 dilution) and incubated (1 h, RT with shaking in the dark). Membranes were finally washed (TBS-T, RT, 10 min with shaking x3) before being scanned. The experiment was performed in duplicate in three independent repeats.

Immunocytochemical Detection of IL-1β

Adherent cells were seeded on cover slips (6 well plates, 5×10^5 cells/well). Plates coated with poly-Lysine were used for suspended cells. Cells were treated (at respective LC_{50} concentrations for 24 h, with or without a caspase-1 inhibitor (Z-WEHD-FMK) before incubation with either Smp24 or Smp43 for 24 h at their respective LC_{50} concentrations (Elrayess et al., 2019). Cover slips were then washed (PBS x2), fixed (4% paraformaldehyde, 15min, RT) and washed again (PBS x2). Cells were permeabilized (100% ice cold methanol/acetone (1: 1), 15 min, RT), blocked (5% bovine serum albumin in TBS-T, 1 h, RT with shaking) and incubated overnight with IL-1B antibody (1 µL/ml, 4°C with shaking). Cells were washed (TBS-T, RT, 10 min x 3 with shaking) and then incubated in the dark with Alexa fluor-488 goat anti-rabbit IgG (1 µL/ml, RT, 1 h with shaking). Cover slips were finally washed (TBS-T, 10 min, RT x3 with shaking) before mounting onto a glass slide in the presence of DAPI. Slides were examined using a fluorescence microscope (Olympus, BX60, United Kingdom) and images were captured (Micropublisher 5.0 RTV). Experiments were performed in triplicate with three independent repeats. Nigericin was used as positive control for maximum IL-1β release.

Statistical Analysis

Data were analysed (unpaired student-*t* test) using Prism 6 software (Graph Pad). Means and standard errors were calculated and results were considered statistically significant when $p \leq 0.05$ and highly significant when at $p \leq 0.001$.

RESULTS

Previous results have demonstrated that Smp24 and Smp43 disrupted the integrity of cell membranes as evidenced by the release of cytoplasmic lactate dehydrogenase in a range of tumour and non-tumour cell lines as well as primary cells[18]. To examine this cytotoxic event in more detail, all cell lines were double stained with Hoechst 33342 dye and propidium iodide (PI) after treatment with either Smp24 or Smp43. All cell lines showed a concentration-dependent increase in PI uptake as evidenced by red-stained nuclei, as compared with controls which were stained blue with Hoechst 33342 dye (**Figure 1**; **Supplementary Figure S1**). Triton X-100 (10%) was used as positive control for necrotic cell death (100% PI uptake) and etoposide was used as positive control for apoptotic cell death. All treated cells had homogeneously dispersed chromatin, indistinguishable from controls and there was no evidence of highly condensed chromatin or small, dispersed apoptotic bodies, typical of an apoptotic process. These results suggest that the cytotoxic effects of Smp24 and Smp43 are due to a lytic mechanism.

Scanning EM studies of cells treated with either Smp24 or Smp43 revealed the loss of cell membrane microvilli and filopodia. The presence of pores in many cell membranes was also evident (Elrayess et al., 2019). In addition, transmission EM studies identified the existence of vacuolized cytoplasm and the complete absence of intracellular organelles in many cells (**Figure 2**; **Supplementary Figure S2**). Compelling evidence of intracellular damage in other cells was widespread, e.g., inconspicuous mitochondrial cristae, the dilatation and fragmentation of cisternae in endoplasmic reticula and the shedding of microvesicles. The presence of autophagosomes, lipid droplets, myelinamellar structures and multivesicular bodies were seen in all cells examined. In summary, the

demonstration of membrane blebbing producing apoptotic-like cell body protrusions, the formation of membrane pores and evidence of cell swelling prior to cell lysis, strongly suggests that Smp24 and Smp43 are causing a pyroptotic response in all the cells examined here.

The relative expression of various target genes after treating cells with either Smp24 or Smp43 (at concentrations ranging from 0.5-2 LC_{50}) was examined by qRT-PCR analysis. The *Casp1* gene was significantly ($p \leq 0.05$) up-regulated in all cells except primary epithelial cells (**Figure 3**). In contrast, *Casp8* was significantly down-regulated ($p \leq 0.05$) across all cells studied. *NLRP3* also showed significant up-regulation ($p \leq 0.05$) in non-tumour cells but not in the tumour cell lines. *MLKL* and *CAPN5* gene expression were unaltered.

At concentrations (1/2 LC_{50} and LC_{50}) of either Smp24 or Smp43, no significant increase in either initiator caspase enzymatic activity (caspase-8 and 9) or executioner caspase enzymatic activity (caspase-3/7) was detected, as compared to their controls ($p \leq 0.05$) (**Figure 4**; **Supplementary Figure S3**).

The pro-inflammatory cytokine IL-1β was detected by dot blot analysis in the culture supernatants of all cells treated with either Smp24 or Smp43 (**Supplementary Figure S4**). Nigericin was used as a positive control to induce the expression of IL-1β. Immunofluorescence microscopy showed that IL-1β was present in the cytoplasm of both tumour and non-tumour cells all cells treated with either Smp24 or Smp43 (**Figure 5**). IL-1β was absent from all cells pre-treated with the synthetic peptide caspase-1 inhibitor, Z-WEHD-FMK, with the exception of HaCaT cells, which still showed presence of the cytokine.

DISCUSSION

AMPs play an important role in the defence system of all organisms against diverse microbial infections. Smp24 and Smp43 are novel cationic AMPs characterized from the venom gland of the Egyptian scorpion *Scorpio maurus palmatus* (Abdel-Rahman et al., 2013). Both peptides showed potent antibacterial and antifungal activities (Harrison et al., 2016a,b), as well as cytotoxic effects in both tumour and non-tumour cell lines at higher concentrations (Elrayess et al., 2019), although tumour cells were markedly more sensitive to the effects of Smp peptides than either stem cells or primary epithelial cells. In previous studies we have shown that Smp24 may be favoured over Smp43 for potential development as an anti-microbial agent (Harrison et al., 2016a,b). In contrast, toxicity studies on leukemia cell lines have demonstrated that Smp43 may have higher potential as an anti-cancer agent (El-Rayess et al., 2019).

Although the classical pyroptosis pathway is caspase-1 dependent, non-classical pathways also exist that are independent of caspase-1 activation. With the exception of HaCaT cells, all cell lines, treated with either Smp24 or Smp43, revealed an up-regulation of *Casp1* and a down-regulation of *Casp8.* The Nod-like receptor, *NLRP3* was up-regulated in $CD34^+$ and HRECs cell lines treated with both peptides, suggesting that they induce caspase-1-dependent pyroptotic cell death via an NLRP3 inflammasome complex. In contrast, leukaemia cell lines (CCRF-CEM and KG-1a) probably activate caspase-1 through different inflammasome complexes. Although morphological evidence suggests that HaCaT cells undergo pyroptotic death on treatment with both Smp24 and Smp43, these must do so by non-classical pathways.

Other AMPs induce pyroptosis by both classical and non-classical pathways. For example, the human a-defensin HNP-1 AMP induces pyroptosis *via* NLRP3 inflammasome activation of caspase-1 (Chen et al., 2014), whereas *Tityus serrulatus* scorpion venom induced pyroptosis by a caspase-1 independent pathway, probably through Toll-like receptors (Zoccal et al., 2016).

In support of a pyroptotic mechanism, pro-inflammatory cytokine IL-1β was detected (either extracellularly or in the cytoplasm) of all cells treated with either Smp24 or Smp43, independent of whether cytokine release was a consequence of caspase-1 activation or not. The role of caspase-1 in triggering the activation of IL-1β was confirmed by immunofluorescence, using a caspase-1 inhibitor. The mechanism by which Smp24 and Smp43 stimulate the expression of IL-1β in HaCaT cells is presently not understood, although Caspase-4 or the NF-κB signalling pathway are attractive candidates.

Cytochemical evidence from the uptake of propidium iodide into cells treated with either Smp24 or Smp43 suggests that these peptides induce membrane rupture and cause cell death in a necrotic manner. Similar results have been observed using other DNA-binding dyes; temporin, isolated from the skin secretions of the Chinese brown frog and sclopendrasin, isolated from centipede secretions, both stimulate ethidium bromide uptake into various cancer cell lines (Hsu et al., 2011; Wang et al., 2013; Chen et al., 2014; Lee et al., 2015). Experiments with propidium iodide also support our earlier studies demonstrating the cytotoxic effects of Smp24 and Smp43 through LDH release and the loss of intracellular ATP (Elrayess et al., 2019). Membrane disintegration was also directly observed in this earlier study in scanning electron micrographs, with observation of pore formation, cell swelling and the presence of autolysosomes, all strongly suggesting that Smp24 and Smp43 causing a pyroptotic, rather than an apoptotic response. Morphological evidence for various classes of AMPs causing pyroptotic cell death in diverse tumour cell lines has been provided by several groups (Lehmann et al., 2006; Suttmann et al., 2008; Chang et al., 2011; Wang et al., 2013; Lu et al., 2016).

The present transmission electron microscopy studies also suggest that ultrastructural changes induced by Smp24 and Smp43 are a consequence of pyroptosis. Many cells showed an obvious increase in cell size and appearance of blebs in the cell membrane, in conjunction with shedding of microvesicles from the cell membranes and the formation of multivesicular bodies. Bleb formation has been suggested to be due to the formation of caspase-1-dependent membrane pores, with the consequent disruption of cellular ionic gradients and an increase in osmotic pressure, leading to water influx and cell swelling (Fink and Cookson 2006; Bergsbaken et al., 2009). Bubble-like protrusions (pyroptotic bodies) have also been observed by others (Chen et al., 2016). The shedding of microvesicles is an attractive mechanism for the release of IL-1β after caspase-1 activation (MacKenzie et al., 2001), although multiple other mechanisms

have also been proposed, for example the involvement of secretory lysosomes and secretory autophagy and autolysosomes/autophagosomes have also reported in the present study (Bianco et al., 2005; Qu et al., 2007; Monteleone et al., 2015).

The appearance of glycogen deposits was uniquely seen in KG1-a leukaemia cells. Glycogen accumulation may also be the result of caspase-1 activation since the enzyme also regulates glycolysis and lipid metabolism (Ghukasyan and Heikal, 2014). The deposition of lipid droplets in cells treated with either Smp24 or Smp43 suggests that lipid metabolism is impaired; caspase-1 activation has been demonstrated to inhibit the clearance of triglyceride (Kotas et al., 2013) and stimulate lipid biogenesis by activating sterol regulatory element binding proteins, which are key regulators of cellular lipid levels (Gurcel et al., 2006; Im et al., 2011).

The observed karyolysis in the nuclei of all cells treated with either Smp24 or Smp43 could be attributed to the activation of nuclear endonucleases in injured cells (Williams et al., 2000), as caspase-1 can also stimulate endonuclease activity (Fink and Cookson, 2006).

Although Smp24 and Smp43 both convincingly stimulate pyroptosis, there are subtle differences in their mechanism of action, dependent on the cell line studied. This should not be surprising as we have already shown that the two peptides cause membrane degradation (albeit in bacteria) in different ways (Harrison et al., 2016a,b; Heath et al., 2018). Smp24 and Smp43 both stimulate the release of the inflammatory mediator IL-1β in all cell lines tested (with the sole exception of HaCaT cells), by a caspase-1 dependent pathway. KG1-a leukemic cells are also unique in showing glycogen deposits.

The high metabolic turnover of proteins in a cancer cell causes developmental deficiencies in their cytoskeleton with respect to normal cells (Lei et al., 2019). Cancer cells are also associated with an anomalous high density of acidic, negatively charged phospholipids on their outer membrane leaflet, more akin to prokaryotic membranes. Although AMPs have been shown to act by a variety of diverse mechanisms, both within the membrane and in the cytoplasm and cell nucleus (Graf and Wilson, 2019; Haney et al., 2019; Zasloff, 2019), all AMPs, as positively charged amphipathic molecules are initially targeted to the cell membrane through electrostatic interactions. Some AMPs can exploit both differences in membrane charge and cell stability to specifically target certain cancer cells (Rathinakumar et al., 2009; Mahlapuu et al., 2016; Wang et al., 2017), suggesting that these peptides are potential new anti-cancer agents and encouraging the further development of other classes of AMPs in this area.

Can we identify any distinguishing features that separate the effects of Smp24 and Smp43 between cancer and non-cancer cell lines from this study? Non-cancerous keratinocytes (HaCaT cells) are markedly less sensitive to the peptides as well as uniquely stimulating the release of IL-1β by a caspase-1 independent mechanism. In contrast, the leukaemia cell line KG1-a was unique in creating glycogen deposits. Although this is the first step, clearly the mechanism by which the peptides initially trigger inflammasome activation is probably key to understanding these differences and perhaps developing AMPs which are cancer-cell specific.

DATA AVAILABILITY STATEMENT

The raw data supporting the conclusion of this article will be made available by the authors, without undue reservation.

AUTHOR CONTRIBUTIONS

RE carried out the experiments, analyzed the data and wrote the initial draft of the manuscript. MA-R, PS, KM, and SH-S designed and supervised the entire project, participated in analyzing the data and wrote the final draft of the manuscript. MM, YM and HE reviewed the manuscript. All authors read and approved the final manuscript.

ACKNOWLEDGMENTS

RE acknowledges the support of the Egyptian Ministry of Higher Education through a Scholarship to study at Sheffield Hallam University (Channel Scheme between Suez Canal University, Egypt and Sheffield Hallam University, United Kingdom). PS and KM acknowledge support from the Biomolecular Research Centre, Department of Biosciences and Chemistry, Sheffield Hallam University, United Kingdom.

SUPPLEMENTARY MATERIAL

The Supplementary Material for this article can be found online at: https://www.frontiersin.org/articles/10.3389/fphar.2021.788874/full#supplementary-material

REFERENCES

Abdel-Rahman, M. A., Quintero-Hernandez, V., and Possani, L. D. (2013). Venom Proteomic and Venomous Glands Transcriptomic Analysis of the Egyptian Scorpion *Scorpio Maurus Palmatus* (Arachnida: Scorpionidae). *Toxicon* 74, 193–207. doi:10.1016/j.toxicon.2013.08.064

Bahar, A. A., and Ren, D. (2013). Antimicrobial Peptides. *Pharmaceuticals (Basel)* 6, 1543–1575. doi:10.3390/ph6121543

Bergsbaken, T., Fink, S. L., and Cookson, B. T. (2009). Pyroptosis: Host Cell Death and Inflammation. *Nat. Rev. Microbiol.* 7, 99–109. doi:10.1038/nrmicro2070

Bianco, F., Pravettoni, E., Colombo, A., Schenk, U., Möller, T., Matteoli, M., et al. (2005). Astrocyte-derived ATP Induces Vesicle Shedding and IL-1 Beta Release from Microglia. *J. Immunol.* 174, 7268–7277. doi:10.4049/jimmunol.174.11.7268

Chang, W. T., Pan, C. Y., Rajanbabu, V., Cheng, C. W., and Chen, J. Y. (2011). Tilapia (*Oreochromis mossambicus*) Antimicrobial Peptide, Hepcidin 1-5, Shows Antitumor Activity in Cancer Cells. *Peptides* 32, 342–352. doi:10.1016/j.peptides.2010.11.003

Chen, Q., Jin, Y., Zhang, K., Li, H., Chen, W., Meng, G., et al. (2014). Alarmin HNP-1 Promotes Pyroptosis and IL-1β Release through Different Roles of NLRP3 Inflammasome via P2X7 in LPS-Primed

Macrophages. *Innate Immun.* 20 (3), 290–300. doi:10.1177/1753425913490575

Chen, X., He, W. T., Hu, L., Li, J., Fang, Y., Wang, X., et al. (2016). Pyroptosis Is Driven by Non-selective Gasdermin-D Pore and its Morphology Is Different from MLKL Channel-Mediated Necroptosis. *Cell Res* 26, 1007–1020. doi:10.1038/cr.2016.100

Crusca, E., Jr, Basso, L. G. M., Altei, W. F., and Marchetto, R. (2018). Biophysical Characterization and Antitumor Activity of Synthetic Pantinin Peptides from Scorpion's Venom. *Biochim. Biophys. Acta Biomembr* 1860 (11), 2155–2165. doi:10.1016/j.bbamem.2018.08.012

Darcy, M. (2019). Cell Death. A Review of the Major Forms of Apoptosis, Necrosis and Autophagy. *Cell Biol. Inter.* 43 (3), 11137.

Deslouches, B., and Di, Y. P. (2017). Antimicrobial Peptides with Selective Antitumor Mechanisms: Prospect for Anticancer Applications. *Oncotarget* 8 (28), 46635–46651. doi:10.18632/oncotarget.16743

Elrayess, R. A., Mohallal, M. E., EL-Shahat, Y. M., Ebaid, H. M., Miller, K., Strong, P. N., et al. (2019). Cytotoxic Effects of Smp24 and Smp43 Scorpion Venom Antimicrobial Peptides on Tumour and Non-tumour Cell Lines. *Int. J. Pept. Res. Ther.* 26 (3), 1409–1415. doi:10.1007/s10989-019-09932-1

Fadok, V. A., Bratton, D. L., Rose, D. M., Pearson, A., Ezekewitz, R. A., and Henson, P. M. (2000). A Receptor for Phosphatidylserine-specific Clearance of Apoptotic Cells. *Nature* 405, 85–90. doi:10.1038/35011084

Fang, Y., Tian, S., Pan, Y., Li, W., Wang, Q., Tang, Y., et al. (2020). Pyroptosis: A New Frontier in Cancer. *Biomed. Pharmacother.* 121, 109595. doi:10.1016/j.biopha.2019.109595

Fink, S. L., and Cookson, B. T. (2006). Caspase-1-dependent Pore Formation during Pyroptosis Leads to Osmotic Lysis of Infected Host Macrophages. *Cell Microbiol* 8 (11), 1812–1825. doi:10.1111/j.1462-5822.2006.00751.x

Frank, D., and Vince, J. E. (2019). Pyroptosis versus Necroptosis: Similarities, Differences, and Crosstalk. *Cell Death Differ* 26 (1), 99–114. doi:10.1038/s41418-018-0212-6

Ghukasyan, V. V., and Heikal, A. A. (2014). *Natural Biomarkers for Cellular Metabolism: Biology, Techniques, and Applications*. 1st ed. Boca Raton, Florida: CRC Press.

Graf, M., and Wilson, D. N. (2019). Intracellular Antimicrobial Peptides Targeting the Protein Synthesis Machinery. *Adv. Exp. Med. Biol.* 1117, 73–89. doi:10.1007/978-981-13-3588-4_6

Guilhelmelli, F., Vilela, N., Albuquerque, P., Derengowski, Lda. S., Silva-Pereira, I., and Kyaw, C. M. (2013). Antibiotic Development Challenges: the Various Mechanisms of Action of Antimicrobial Peptides and of Bacterial Resistance. *Front. Microbiol.* 4, 353. doi:10.3389/fmicb.2013.00353

Gurcel, L., Abrami, L., Girardin, S., Tschopp, J., van der Goot, F. G., and Goot, V. (2006). Caspase-1 Activation of Lipid Metabolic Pathways in Response to Bacterial Pore-Forming Toxins Promotes Cell Survival. *Cell Survival* 126 (6), 1135–1145. doi:10.1016/j.cell.2006.07.033

Haney, E. F., Straus, S. K., and Hancock, R. E. W. (2019). Reassessing the Host Defense Peptide Landscape. *Front. Chem.* 7, 43. doi:10.3389/fchem.2019.00043

Harrison, P. L., Abdel-Rahman, M. A., Strong, P. N., Tawfik, M. M., and Miller, K. (2016a). Characterisation of Three Alpha-Helical Antimicrobial Peptides from the Venom of Scorpio Maurus Palmatus. *Toxicon* 117, 30–36. doi:10.1016/j.toxicon.2016.03.014

Harrison, P. L., Heath, G. R., Johnson, B. R. G., Abdel-Rahman, M. A., Strong, P. N., Evans, S. D., et al. (2016b). Phospholipid Dependent Mechanism of Smp24, an α-helical Antimicrobial Peptide from Scorpion Venom. *Biochim. Biophys. Acta* 1858, 2737–2744. doi:10.1016/j.bbamem.2016.07.018

Heath, G. R., Harrison, P. L., Strong, P. N., Evans, S. D., and Miller, K. (2018). Visualization of Diffusion Limited Antimicrobial Peptide Attack on Supported Lipid Membranes. *Soft Matter* 14 (29), 6146–6154. doi:10.1039/c8sm00707a

Hersh, D., Monack, D. M., Smith, M. R., Ghori, N., Falkow, S., and Zychlinsky, A. (1999). The Salmonella Invasin SipB Induces Macrophage Apoptosis by Binding to Caspase-1. *Proc. Natl. Acad. Sci. U S A.* 96, 2396–2401. doi:10.1073/pnas.96.5.2396

Hsu, J. C., Lin, L. C., Tzen, J. T., and Chen, J. Y. (2011). Characteristics of the Antitumor Activities in Tumor Cells and Modulation of the Inflammatory Response in RAW264.7 Cells of a Novel Antimicrobial Peptide, Chrysophsin-1, from the Red Sea Bream (Chrysophrys Major). *Peptides* 32, 900–910. doi:10.1016/j.peptides.2011.02.013

Huang, H. W. (2000). Action of Antimicrobial Peptides: Two-State Model. *Biochemistry* 39, 8347–8352. doi:10.1021/bi000946l

Im, S. S., Yousef, L., Blaschitz, C., Liu, J. Z., Edwards, R. A., Young, S. G., et al. (2011). Linking Lipid Metabolism to the Innate Immune Response in Macrophages through Sterol Regulatory Element Binding Protein-1a. *Cell Metab* 13, 540–549. doi:10.1016/j.cmet.2011.04.001

Kotas, M. E., Jurczak, M. J., Annicelli, C., Gillum, M. P., Cline, G. W., Shulman, G. I., et al. (2013). Role of Caspase-1 in Regulation of Triglyceride Metabolism. *Proc. Natl. Acad. Sci. U S A.* 110 (2), 4810–4815. doi:10.1073/pnas.1301996110

Lai, Y., and Gallo, R. (2009). AMPed up Immunity: How Antimicrobial Peptides Have Multiple Roles in Immune Defense. *Trends Immunol.* 30 (3), 131–141.

Lee, J. H., Kim, I. W., Kim, S. H., Kim, M. A., Yun, E. Y., Nam, S. H., et al. (2015). Anticancer Activity of the Antimicrobial Peptide Scolopendrasin VII Derived from the Centipede, Scolopendra Subspinipes Mutilans. *J. Microbiol. Biotechnol.* 25 (8), 1275–1280. doi:10.4014/jmb.1503.03091

Lehmann, J., Retz, M., Sidhu, S. S., Suttmann, H., Sell, M., Paulsen, F., et al. (2006). Antitumor Activity of the Antimicrobial Peptide Magainin II against Bladder Cancer Cell Lines. *Eur. Urol.* 50, 141–147. doi:10.1016/j.eururo.2005.12.043

Lei, J., Sun, L., Huang, S., Zhu, C., Li, P., He, J., et al. (2019). The Antimicrobial Peptides and Their Potential Clinical Applications. *Am. J. Transl. Res.* 11, 3919–3931.

Lu, Y., Zhang, T. F., Shi, Y., Zhou, H. W., Chen, Q., Wei, B. Y., et al. (2016). PFR Peptide, One of the Antimicrobial Peptides Identified from the Derivatives of Lactoferrin, Induces Necrosis in Leukemia Cells. *Sci. Rep.* 6, 20823–23. doi:10.1038/srep20823

MacKenzie, A., Wilson, H. L., Kiss-Toth, E., Dower, S. K., North, R. A., and Surprenant, A. (2001). Rapid Secretion of Interleukin-1beta by Microvesicle Shedding. *Immunity* 15 (5), 825–835. doi:10.1016/s1074-7613(01)00229-1

Mahlapuu, M., Håkansson, J., Ringstad, L., and Björn, C. (2016). Antimicrobial Peptides: an Emerging Category of Therapeutic Agents. *Front Cel Infect Microbiol* 6, 194. doi:10.3389/fcimb.2016.00194

Monteleone, M., Stow, J. L., and Schroder, K. (2015). Mechanisms of Unconventional Secretion of IL-1 Family Cytokines. *Cytokine* 74 (2), 213–218. doi:10.1016/j.cyto.2015.03.022

Nuti, R., Goud, N. S., Saraswati, A. P., Alvala, R., and Alvala, M. (2017). Antimicrobial Peptides: A Promising Therapeutic Strategy in Tackling Antimicrobial Resistance. *Curr. Med. Chem.* 24 (38), 4303–4314. doi:10.2174/0929867324666170815102441

Qu, Y., Franchi, L., Nunez, G., and Dubyak, G. R. (2007). Nonclassical IL-1 Beta Secretion Stimulated by P2X7 Receptors Is Dependent on Inflammasome Activation and Correlated with Exosome Release in Murine Macrophages. *J. Immunol.* 179, 1913–1925. doi:10.4049/jimmunol.179.3.1913

Rathinakumar, R., Walkenhorst, W. F., and Wimley, W. C. (2009). Broad-spectrum Antimicrobial Peptides by Rational Combinatorial Design and High-Throughput Screening: the Importance of Interfacial Activity. *J. Am. Chem. Soc.* 131, 7609–7617. doi:10.1021/ja8093247

Schweizer, F. (2009). Cationic Amphiphilic Peptides with Cancer-Selective Toxicity. *Eur. J. Pharmacol.* 625, 190–194. doi:10.1016/j.ejphar.2009.08.043

Sharma, B., and KanwarPhosphatidylserine, S. S. (2018). Phosphatidylserine: A Cancer Cell Targeting Biomarker. *Semin. Cancer Biol.* 52 (Pt1), 17–25. doi:10.1016/j.semcancer.2017.08.012

Suttmann, H., Retz, M., Paulsen, F., Harder, J., Zwergel, U., Kamradt, J., et al. (2008). Antimicrobial Peptides of the Cecropin-Family Show Potent Antitumor Activity against Bladder Cancer Cells. *BMC Urol.* 8, 5. doi:10.1186/1471-2490-8-5

Utsugi, T., Schroit, A. J., Connor, J., Bucana, C. D., and Fidler, I. J. (1991). Elevated Expression of Phosphatidylserine in the Outer Membrane Leaflet of Human Tumor Cells and Recognition by Activated Human Blood Monocytes. *Cancer Res.* 51, 3062–3066.

Wang, C., Tian, L. L., Li, S., Li, H. B., Zhou, Y., Wang, H., et al. (2013). Rapid Cytotoxicity of Antimicrobial Peptide Tempoprin-1CEa in Breast Cancer Cells through Membrane Destruction and Intracellular Calcium Mechanism. *PLoS ONE* 8 (4), e60462. doi:10.1371/journal.pone.0060462

Wang, D. M., Jiao, X., Plotnikoff, N. P., Griffin, N., Qi, R. Q., Gao, X. H., et al. (2017). Killing Effect of Methionine Enkephalin on Melanoma *In Vivo* and *In Vitro*. *Oncol. Rep.* 38, 2132–2140. doi:10.3892/or.2017.5918

Wang, X., and Wang, G. (2016). Insights into Antimicrobial Peptides from Spiders and Scorpions. *Protein Pept. Lett.* 23 (8), 707–721. doi:10.2174/0929866523666160511151320

Williams, P. L., James, R. C., and Roberts, S. R. (2000). *Principles of Toxicology. Environmental and Industrial Applications*. 2ed. New York: Wiley-Interscience Publication, 111–432.

Xia, X., Wang, X., Cheng, Z., Qin, W., Lei, L., Jiang, J., et al. (2019). The Role of Pyroptosis in Cancer: Pro-cancer or Pro-"host". *Cell Death Dis* 10, 650. doi:10.1038/s41419-019-1883-8

Zasloff, M. (2002). Antimicrobial Peptides of Multicellular Organisms. *Nature* 415 (6870), 389–395. doi:10.1038/415389a

Zasloff, M. (2019). Antimicrobial Peptides of Multicellular Organisms: My Perspective. *Adv. Exp. Med. Biol.* 1117, 3–6. doi:10.1007/978-981-13-3588-4_1

Zoccal, K. F., Sorgi, C. A., Hori, J. I., Paula-Silva, F. W., Arantes, E. C., Serezani, C. H., et al. (2016). Opposing Roles of LTB4 and PGE2 in Regulating the Inflammasome-dependent Scorpion Venom-Induced Mortality. *Nat. Commun.* 7, 10760. doi:10.1038/ncomms10760

Conflict of Interest: The authors declare that the research was conducted in the absence of any commercial or financial relationships that could be construed as a potential conflict of interest.

The handling editor declared a past collaboration with one of the authors MA-R.

frontiers in Pharmacology

ORIGINAL RESEARCH
published: 12 January 2022
doi: 10.3389/fphar.2021.812295

Action of Varespladib (LY-315920), a Phospholipase A_2 Inhibitor, on the Enzymatic, Coagulant and Haemorrhagic Activities of *Lachesis muta rhombeata* (South-American Bushmaster) Venom

*Pamella G. Gutierres[1], Diego R. Pereira[1], Nataly L. Vieira[1], Lilian F. Arantes[2], Nelson J. Silva Jr.[3], Kristian A. Torres-Bonilla[4], Stephen Hyslop[4], Karen Morais-Zani[5], Rosa M. B. Nogueira[1], Edward G. Rowan[6] and Rafael S. Floriano[1]**

[1]Laboratory of Toxinology and Cardiovascular Research, University of Western São Paulo, Presidente Prudente, Brazil, [2]Graduate Program in Zootechnics, Rural Federal University of Pernambuco, Recife, Brazil, [3]Graduate Program in Environmental Sciences and Health, School of Medical, Pharmaceutical and Biomedical Sciences, Pontifical Catholic University of Goiás, Goiânia, Brazil, [4]Department of Pharmacology, Faculty of Medical Sciences, State University of Campinas, Campinas, Brazil, [5]Laboratory of Herpetology, Butantan Institute, São Paulo, Brazil, [6]Strathclyde Institute of Pharmacy and Biomedical Sciences, University of Strathclyde, Glasgow, United Kingdom

OPEN ACCESS

Edited by:
Delavar Shahbazzadeh,
Pasteur Institute of Iran (PII), Iran

Reviewed by:
Manuela Berto Pucca,
Federal University of Roraima, Brazil
Kamran Pooshang Bagheri,
Pasteur Institute of Iran (PII), Iran
Roghieh Mirzazadeh,
Pasteur Institute of Iran (PII), Iran

***Correspondence:**
Rafael S. Floriano
rafael@unoeste.br

Specialty section:
This article was submitted to Translational Pharmacology, a section of the journal Frontiers in Pharmacology

Received: 10 November 2021
Accepted: 09 December 2021
Published: 12 January 2022

Citation:
Gutierres PG, Pereira DR, Vieira NL, Arantes LF, Silva Jr. NJ, Torres-Bonilla KA, Hyslop S, Morais-Zani K, Nogueira RMB, Rowan EG and Floriano RS (2022) Action of Varespladib (LY-315920), a Phospholipase A_2 Inhibitor, on the Enzymatic, Coagulant and Haemorrhagic Activities of Lachesis muta rhombeata (South-American Bushmaster) Venom. Front. Pharmacol. 12:812295. doi: 10.3389/fphar.2021.812295

Varespladib (VPL) was primarily developed to treat inflammatory disturbances associated with high levels of serum phospholipase A_2 (PLA_2). VPL has also demonstrated to be a potential antivenom support agent to prevent PLA_2-dependent effects produced by snake venoms. In this study, we examined the action of VPL on the coagulant, haemorrhagic and enzymatic activities of *Lachesis muta rhombeata* (South-American bushmaster) venom. Conventional colorimetric enzymatic assays were performed for PLA_2, caseinolytic and esterasic activities; *in vitro* coagulant activities for prothrombin time (PT) and activated partial thromboplastin time (aPTT) were performed in rat citrated plasma through a quick timer coagulometer, whereas the dimensions of haemorrhagic haloes obtained after i.d. injections of venom in Wistar rats were determined using ImageJ software. Venom (1 mg/ml) exhibited accentuated enzymatic activities for proteases and PLA_2 *in vitro*, with VPL abolishing the PLA_2 activity from 0.01 mM; VPL did not affect caseinolytic and esterasic activities at any tested concentrations (0.001–1 mM). In rat citrated plasma *in vitro*, VPL (1 mM) alone efficiently prevented the venom (1 mg/ml)-induced procoagulant disorder associated to extrinsic (PT) pathway, whereas its association with a commercial antivenom successfully prevented changes in both intrinsic (aPTT) and extrinsic (PT) pathways; commercial antivenom by itself failed to avoid the procoagulant disorders by this venom. Venom (0.5 mg/kg)-induced hemorrhagic activity was slightly reduced by VPL (1 mM) alone or combined with antivenom (antivenom:venom ratio 1:3 'v/w') in rats, with antivenom alone producing no protective action on this parameter. In

conclusion, VPL does not inhibit other major enzymatic groups of *L. m. rhombeata* venom, with its high PLA_2 antagonize activity efficaciously preventing the venom-induced coagulation disturbances.

Keywords: Viperidae snake, phospholipase A2 (PLA2), coagulating activity, haemorrhage, varespladib, antivenom, neutralization

INTRODUCTION

Snakes of *Lachesis* genus are represented by three species found in Central America (*L. stenophrys*, *L. melanocephala*, and *L. acrochorda*) and one in South America (*L. muta*), with the latter being recognized as two subspecies distributed in the Amazon river basin (=*L. muta muta*) and Atlantic rainforest (=*L. muta rhombeata*) in Brazil (Costa and Bérnils, 2018; Nogueira et al., 2019; Diniz-Sousa et al., 2020). Together, these snakes are responsible by the second most frequent cases of snakebites in Americas, being exceeded only by *Bothrops* snakes (Magalhães et al., 2019; Diniz-Sousa et al., 2020).

Envenomation by *Lachesis* spp. is characterized by intense local pain, oedema and necrosis (Damico et al., 2006; Ferreira et al., 2009; Damico et al., 2012), systemic myotoxicity (Fuly et al., 2000; Fuly et al., 2003; Damico et al., 2006), renal failure (Damico et al., 2007), haemorrhage and coagulopathy (Sánchez et al., 1987; Sánchez et al., 1991; Sánchez et al., 1995; Fuly et al., 1997; Rucavado et al., 1999; Estêvão-Costa et al., 2000; Torres-Huaco et al., 2013), including severe cardiovascular disorders (Diniz and Oliveira, 1992; Giovanni-De-Simone et al., 1997; Dias et al., 2016a; Dias et al., 2016b). Such effects have been associated predominantly with the presence of phospholipases A_2 (PLA_2) (Cordeiro et al., 2015; Diniz-Sousa et al., 2018), metalloproteases (Cordeiro et al., 2018) and serine proteases (Wiezel et al., 2019), including biologically active peptides (Graham et al., 2005; Soares et al., 2005; Sanz et al., 2008; Pla et al., 2013; Pinheiro-Júnior et al., 2018), in these venoms.

Polyvalent antivenom (=anti-*Bothrops*/*Lachesis* serum) therapies comprise the main therapeutic options to treat the systemic envenomation by *Lachesis* snakes (Madrigal et al., 2017; Solano et al., 2018). Recently, several studies have demonstrated the value of varespladib, a PLA_2 inhibitor drug (Lewin et al., 2016; Salvador et al., 2019), concerning its suppressive action on the biological effects of Elapidae and Viperidae venoms (Bittenbinder et al., 2018; Lewin et al., 2018; Wang et al., 2018; Zinenko et al., 2020; Gutiérrez et al., 2020a), including their toxins (Bryan-Quirós et al., 2019; Salvador et al., 2021). However, there are not reports about the action of varespladib, as a stand-alone therapy and/or combined with antivenoms, on the toxic effects caused by *Lachesis* venoms. In the present study, we have investigated the efficiency of this drug on some aspects of the envenomation by *Lachesis muta rhombeata* venom using *in vitro* and *in vivo* approaches for enzymatic, coagulant and haemorrhagic activities of this venom. We have also assessed an eventual synergic mechanism of action by varespladib when combined with a commercial antivenom used to treat envenomations by *Lachesis* in Brazil.

MATERIALS AND METHODS

Reagents

Varespladib (LY-315920) was obtained from Sigma-Aldrich Chemical Co. (St. Louis, MO, United States) and anti-*Bothrops*/*Lachesis* serum was from Butantan Institute (São Paulo, SP, Brazil); varespladib was dissolved in DMSO prior to use, whereas the antivenom was provided ready for injection and maintained under refrigeration. Azocasein (A2765), Nα-Benzoyl-DL-arginine 4-nitroanilide hydrochloride (B4875) and 4-nitro-3-octanoyloxy-benzoic acid (N1646) substrates were also from Sigma-Aldrich Chemical Co. (St. Louis, MO, United States). *Lachesis m. rhombeata* venom was provided by Center for Biological Studies and Research of the Pontifical Catholic University of Goiás (PUC Goiás, Goiânia, GO, Brazil) through Dr Nelson J. Silva Jr. A lyophilized pool of venom obtained from one female adult snake was stored at −20°C and dissolved in ultrapure water prior to use.

Animals

Wistar rats (300–350 g; 2–3 months old) obtained from Central Bioterium of the University of Western São Paulo (UNOESTE, Presidente Prudente, SP, Brazil) were housed in plastic cages (3 animals/cage) with a wood-shaving substrate, at 23 ± 1°C on a 12-h light/dark cycle with lights on at 6 a.m. The animals had free access to food and water. The experimental procedures were approved by an institutional Committee for Ethics in Animal Use (CEUA/UNOESTE, Protocol No. 6713/2021) and were done according to the general ethical guidelines for animal use established by the Brazilian Society of Laboratory Animal Science (SBCAL) and Brazilian Federal Law No. 11.794 of October 8, 2008, in conjunction with the guidelines for animal experiments established by the Brazilian National Council for Animal Experimentation (CONCEA).

Phospholipase A_2 (PLA_2) Activity

PLA_2 activity was assayed essentially as described elsewhere (Carregari et al., 2013). The standard assay mixture contained 200 µl of buffer (10 mM Tris-HCl, 10 mM $CaCl_2$ and 100 mM NaCl, pH 8.0), 20 µl of substrate (3 mM 4-nitro-3-octanoyloxy-benzoic acid) and 20 µl of sample [venom alone (1 mg/ml) or venom (1 mg/ml) pre-incubated (for 30 min at 37°C) with varespladib (0.001–1 mM)] in a final volume of 240 µl. After adding sample, the mixture was incubated for 30 min at 37°C, with one unit of enzymatic activity being defined as an increase in absorbance of 0.001/min at 425 nm. All assays were done in triplicate with readings at 60-s intervals using a SpectraMax 340

multiwell plate reader (Molecular Devices, San Jose, CA, United States).

Caseinolytic Activity

Caseinolytic activity was determined through colorimetric assay in a SpectraMax 340 multiwell plate reader (Molecular Devices, San Jose, CA, United States) using Azocasein as substrate, essentially as described elsewhere (Torres-Bonilla et al., 2020). The standard assay mixture contained 90 µl of substrate (212 mM Azocasein), 10 µl of reaction buffer (0.05 M Tris-HCl, 1 mM $CaCl_2$, pH 8.0) and 10 µl of sample [venom alone (1 mg/ml) or venom (1 mg/ml) pre-incubated (for 30 min at 37°C) with varespladib (0.001–1 mM)] in a final volume of 110 µl. The mixture was incubated for 90 min at 37°C and then the reaction was terminated adding 200 µl of TCA 5% for 5 min at room temperature; the mixture was centrifuged (5 min at 8.000 g) and 150 µl of supernatant was transferred to the multiwell plate containing the same volume of NaOH (0.5 M). Finally, the absorbance was read at 440 nm via endpoint mode, with one activity unit being defined as an increase of absorbance of 0.001/min.

Esterase Activity

Esterase activity was assayed essentially as described by (Erlanger et al., 1961) and adapted by (Torres-Bonilla et al., 2020). The standard assay mixture contained 200 µl of substrate (100 mM Nα-Benzoyl-DL-arginine 4-nitroanilide hydrochloride), 50 µl of reaction buffer (10 mM Tris-HCl, 10 mM $CaCl_2$, 100 mM NaCl, pH 8.0), 15 µl of ultrapure water and 5 µl of sample [venom alone (1 mg/ml) or venom (1 mg/ml) pre-incubated (for 30 min at 37°C) with varespladib (0.001–1 mM)] in a final volume of 270 µl. The mixture was incubated for 30 min at 37°C in a multiwell plate and then read under an absorbance at $\lambda = 410$ nm via endpoint mode, with one activity unit being defined as an increase of absorbance of 0.001/min.

Coagulant Activity

Coagulant activity was performed using Labtest® commercial kits (Labtest Diagnóstica S.A., Lagoa Santa, MG, Brasil) performed in a quick timer Coagmaster 4.0 (Wama Diagnóstica Produtos para Laboratórios, São Carlos, SP, Brazil). Wistar rats were anesthetized by a non-lethal dose (1.8 mg/kg, i.p.) of thiopental (Cristália®, São Paulo, SP, Brazil) and, subsequently, subjected to intracardiac puncture in order to obtain blood samples using BD Vacutainer® Citrate Tubes with 3.2% buffered sodium citrate solution at an anticoagulant:blood ratio of 1:10 (v/v); after this procedure, the animals were euthanased in saturated atmosphere with CO_2. Blood samples were centrifuged (2,500 g, 4°C, 15 min) in order to obtain citrated platelet-poor plasma used in the prothrombin time (PT) and activated partial thromboplastin clotting time (aPTT) assays at 37°C; for each assay, 190 µl of platelet-poor plasma was incubated at 37°C with 10 µl of sample [1 – saline solution, 2 – varespladib (1 mM) or 3 – antivenom (antivenom: venom ratio 1:3 'v/w'), 4 – *L. m. rhombeata* venom (1 mg/ml), 5 – *L. m. rhombeata* venom + VPL, 6 – *L. m. rhombeata* venom + antivenom, 7 – and *L. m. rhombeata* venom + VPL + antivenom]. Antivenom:venom ratio was based on the manufacturer's stated neutralizing capacity for the antivenom, where 1 ml of antivenom neutralizes 3 mg of *L. muta* venom (Instituto Butantan, São Paulo, SP, Brazil). The minimum effective dose of varespladib (1 mM) was confirmed in pilot experiments. Protocols: 1 – *L. m. rhombeata* venom was pre-incubated with VPL and/or antivenom for 30 min at 37°C before PT- and aPTT-required clot formation recording; 2 – *L. m. rhombeata* venom was directly exposed to VPL and/or antivenom and followed by immediate PT- and aPTT-required clot formation recording.

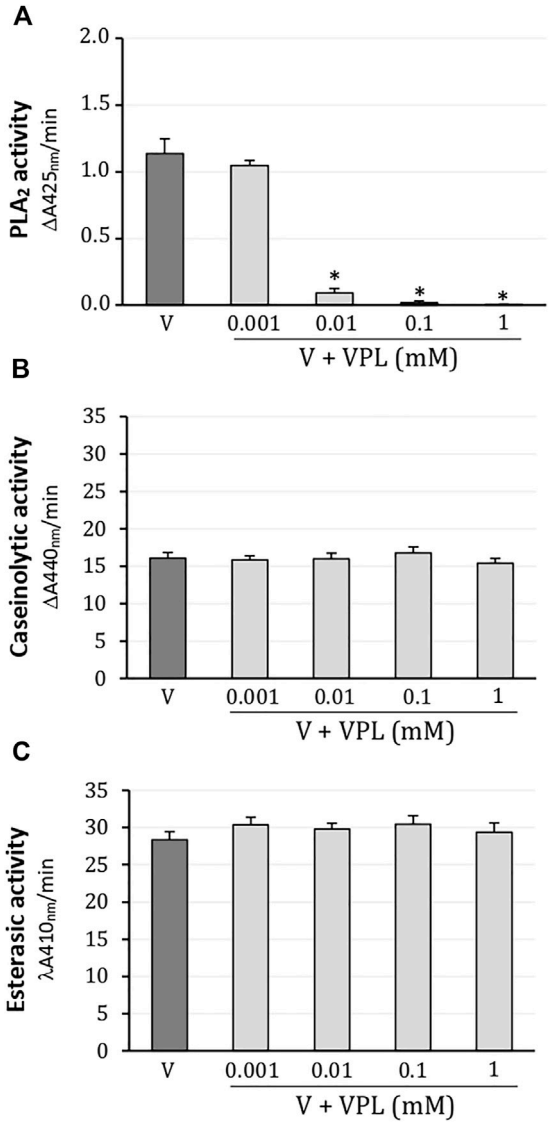

FIGURE 1 | Action of varespladib on the major enzymatic activities of *L. m. rhombeata* venom. **(A)** Varespladib abolished the PLA_2 activity at low concentrations. Unaffected **(B)** caseinolytic and **(C)** esterasic activities by varespladib at any tested concentration. Bars represent the mean ± SDM ($n = 5$). *$p < 0.05$ compared to venom alone.

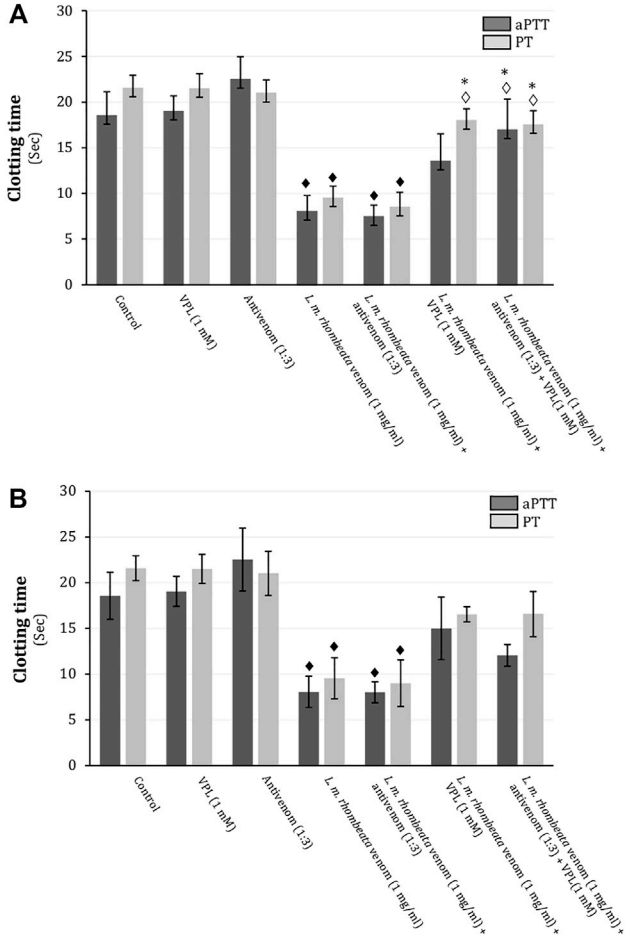

FIGURE 2 | Action of varespladib on the procoagulant activity of *L. m. rhombeata* venom in rat citrated plasma *in vitro*. **(A)** Antivenom did not prevent the venom-induced procoagulant action applying the pre-incubation protocol, whereas varespladib alone avoided the procoagulant action for PT and its association with antivenom successfully prevented both intrinsic and extrinsic disorders. **(B)** Antivenom did not prevent the venom-induced procoagulant action applying the direct exposure protocol, whereas varespladib alone or combined with antivenom produced minor protective action on both coagulant pathways even combined with antivenom. Bars represent the mean ± SDM ($n = 6$). $^{\blacklozenge}p < 0.05$ compared to control, $^{\lozenge}p < 0.05$ compared to venom alone and $^{*}p < 0.05$ compared to antivenom alone.

Haemorrhagic Activity

Hemorrhagic activity was performed according to (Theakston and Reid, 1983). Male Wistar rats were anesthetized with sodium thiopental (1.8 mg/kg, i.p.) and their dorsal region was trichotomized in order to set the injection sites. Initially, some doses of *L. m. rhombeata* venom (0.01, 0.05, 0.1, 0.5 and 1 mg/kg) were tested in order to find the minimum haemorrhagic dose (0.5 mg/kg), which was used to investigate the neutralizing action of antivenom (antivenom:venom ratio of 1:3 'v/w') and varespladib (1 mM). Protocol: after injection of venom (i.d.), the animals were subsequently treated with antivenom and/or varespladib via an intraperitoneal injection, followed by monitoring period of 24 h. Control sites were injected with 0.9% NaCl, DMSO (varespladib solvent) or antivenom. After 24 h, the rats were euthanized in saturated atmosphere with CO_2, the dorsal skin was removed and the subcutaneous hemorrhagic halos in the inner surface were measured through ImageJ software (National Institute of Health, Bethesda, Maryland, United States).

Statistical Analysis

All results (enzymatic, coagulant and haemorrhagic) were expressed as the mean ± SDM and statistical comparisons were done using Student's t test or ANOVA followed by the Tukey–Kramer test, with $p < 0.05$ indicating significance. Data were analyzed using SAS University Edition software (SAS Institute Inc., Cary, NC, United States).

RESULTS

Inhibitory Action of Varespladib on the Main Enzymatic Groups of *L. m. rhombeata* Venom

In colorimetric assays, *L. m. rhombeata* (1 mg/ml) exhibited moderate enzymatic activity for PLA_2 which was promptly abolished from 0.01 mM of varespladib; the lowest concentration of varespladib (0.001 mM) did not produce inhibitory effect on the PLA_2 activity of this venom (**Figure 1A**). Caseinolytic (**Figure 1B**) and esterasic (**Figure 1C**) activities were not affected by any of these concentrations of varespladib tested on artificial substrates (0.001–1 mM).

Inhibitory Action of Varespladib on the Coagulant Effect of *L. m. rhombeata* Venom in Rat Citrated Plasma

In rat citrated plasma, *L. m. rhombeata* venom (1 mg/ml) exhibited procoagulant action on the aPPT (intrinsic pathway) and PT (extrinsic pathway), decreasing in approximately 56.5 and 55.7% these times, respectively ($p < 0.05$ compared to basal values for both, $n = 6$) (**Figures 2A,B**). *L. m. rhombeata* venom (1 mg/ml)-induced procoagulant action (aPTT and PT) was not prevented by pre-incubating venom with antivenom (antivenom:venom ratio of 1:3 'v/w') alone for 30 min at 37°C before clotting assay; however, varespladib (1 mM) alone significantly prevented the venom-induced procoagulant action for PT, with approximately 16.4% of decreasing being verified ($p < 0.05$ compared to venom alone, $n = 6$), and it partially avoided the venom-induced procoagulant action for aPTT, being observed approximately 26.9% of decreasing; the combination of both agents successfully contributed to avoid both intrinsic and extrinsic disorders in rat citrated plasma, resulting in 8.4 and 18.6% of decreasing for PT and aPTT, respectively ($p < 0.05$ compared to venom alone, $n = 6$) (**Figure 2A**). In assays

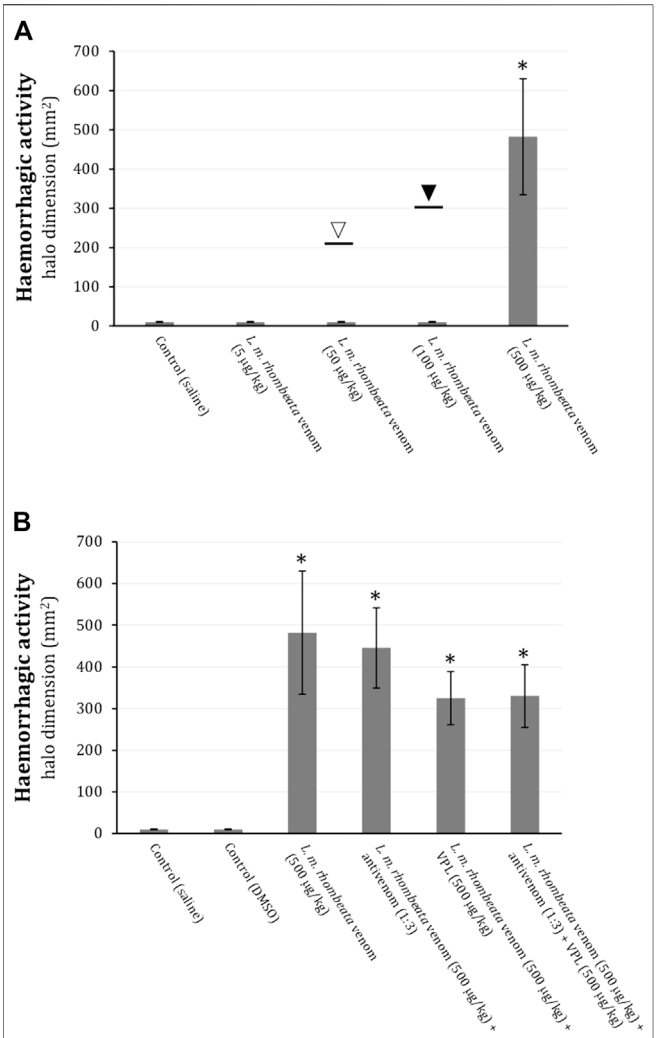

FIGURE 3 | Action of varespladib on the haemorrhagic activity of *L. m. rhombeata* venom in rats. **(A)** *L. m rhombeata* venom produced intense subcutaneous haemorrhage at a dose of 500 µg of venom/kg, with the lowest doses (5, 50, and 100 µg/kg) being ineffective to produce haemorrhage; the opened and filled arrows indicate the haemorrhagic dimension caused in single animals envenomed with 50 and 100 µg of venom/kg, respectively. **(B)** Antivenom did not prevent the venom-induced subcutaneous haemorrhage, with varespladib alone or combined with antivenom producing discreet reduction of this alteration. Bars represent the mean ± SDM ($n = 6$). *$p < 0.05$ compared to control (saline).

performed immediately after the exposure *L. m. rhombeata* venom (1 mg/ml) to antivenom (antivenom:venom ratio of 1: 3 'v/w') and/or varespladib (1 mM), both of agents slightly delayed the *L. m. rhombeata* venom (1 mg/ml)-induced procoagulant action for PT and aPTT; under this experimental condition, varespladib alone or combined with antivenom were more effective in avoiding only the venom-induced procoagulant action for PT, with approximately 23.3% of decreasing being verified using both agents (**Figure 2B**).

Inhibitory Action of Varespladib on the *L. m. rhombeata* Venom-Induced Subcutaneous Haemorrhage in Rat

L. m. rhombeata venom at low doses (5, 50 and 100 µg/kg) did not produce subcutaneous haemorrhagic action in rats, however, with exceptionally one animal exhibiting ~213 mm^2 of haemorrhagic halo for 50 µg of venom/kg (opened arrow) and another one ~301 mm^2 for 100 µg of venom/kg (filled arrow); the higher dose of this venom (500 µg/kg) induced pronounced haemorrhagic halo formation ($p < 0.05$ compared to control saline, n = 6) (**Figure 3A**). Antivenom (antivenom:venom ratio of 1:3 'v/w') administered (i.p) immediately after intradermic injections of *L. m. rhombeata* venom (500 µg/kg) was not able to prevent the venom-induced subcutaneous haemorrhage; varespladib (1 mM) alone or associated with antivenom (antivenom:venom ratio of 1:3 'v/w') exhibited a mild protective effect on the venom-induced subcutaneous haemorrhage (**Figure 3B**).

DISCUSSION

Envenomations by Viperidae snakes comprise a serious public health problem in Latin America (Chippaux, 2017; Ochoa-Avilés et al., 2020; Gutiérrez et al., 2020b). In Brazil, these snakes are represented by three main genera, i.e., *Bothrops*, *Crotalus* and *Lachesis* (Viperidae–Crotalinae), being responsible for more than 20,000 cases of snakebites per year in this country, as reported by Notifiable Diseases Information System of the Brazilian Ministry of Health (SINAN, Brasília, DF, Brazil). *Lachesis* snakes found in South America (*L. muta muta* and *L. m. rhombeata*) occasionally cause severe human envenomations (Magalhães et al., 2019; Diniz-Sousa et al., 2020), which are characterized by pronounced local and systemic disorders, e.g., necrosis (Damico et al., 2006; Ferreira et al., 2009; Damico et al., 2012), haemorrhage, coagulopathy (Sánchez et al., 1987; Sánchez et al., 1991; Sánchez et al., 1995; Fuly et al., 1997; Rucavado et al., 1999; Estêvão-Costa et al., 2000; Torres-Huaco et al., 2013) and hypotension (Dias et al., 2016a; Dias et al., 2016b), strongly associated with a variety of enzymatically active proteins such as snake venom metalloproteases, serine proteases, PLA_2, C-type lectins and L-amino acid oxidases (Weinberg et al., 2004; Junqueira-de-Azevedo et al., 2006; Bregge-Silva et al., 2012; Madrigal et al., 2012; Cordeiro et al., 2018; Diniz-Sousa et al., 2018; Wiezel et al., 2019) present in these venoms.

In recent years, the PLA_2 antagonistic activity of varespladib (Lewin et al., 2016; Salvador et al., 2019; Salvador et al., 2021), a synthetic drug developed to treat disturbances of inflammatory cascades associated with high levels of secreted PLA_2 (Varespladib, 2011), has been experimentally explored as an useful therapeutic alternative to complement antivenom therapies applied in envenomations by Elapidae and Viperidae snakes, with potential even to replace them in special situations in which these antivenoms are not available. Varespladib has high efficacy to suppress the systemic effects caused by several venoms from Elapidae (Lewin et al., 2016; Bittenbinder et al., 2018; Lewin et al., 2018; Wang et al.,

2018; Oliveira et al., 2020; Gutiérrez et al., 2020a; Dashevsky et al., 2021; Kazandjian et al., 2021; Silva-Carvalho et al., 2021) and Viperidae (Lewin et al., 2016; Wang et al., 2018; Youngman et al., 2020; Zinenko et al., 2020; Gutiérrez et al., 2020a; Liu et al., 2021) snakes. However, there is no report associating the efficacy of varespladib with toxicological aspects of *Lachesis* venoms.

Based on this premise, we have unprecedentedly investigated the action of varespladib on the enzymatic, coagulant and haemorrhagic activities of *Lachesis muta rhombeata* venom to determine its efficiency as a single pharmacological tool or combined with a commercial antivenom used in Brazil. In summary, we have demonstrated that varespladib used as a single pharmacological tool abolishes the PLA_2 activity of *L. m. rhombeata* venom at low concentrations, without affecting the catalytic activity for proteases (metalloprotease and serino protease) of the venom, indicating a very specific inhibitory activity; its high PLA_2 antagonistic activity was reflected on the venom-induced procoagulant action, mostly interfering on the extrinsic pathway disorders produced by venom in rat citrated serum (pre-incubation protocol), whereas the drug did not prevent the haemorrhagic activity induced by *L. m. rhombeata* venom in rats. The association of varespladib with a commercial antivenom used in Brazil to treat envenomations by *Lachesis* spp. did not produce important synergic actions on the procoagulant (direct incubation protocol) and haemorrhagic effects induced by *L. m. rhombeata* venom; such interaction resulted in a major prevention of the venom-induced intrinsic and extrinsic coagulant disorders seen under pre-incubation protocol.

Although the procoagulant action of Viperidae venoms has been mostly associated with the presence of serine proteases in these venoms (Gutiérrez et al., 2021), varespladib can partially prevent the procoagulant action of *L. m. rhombeata* venom, indicating an eventual role of PLA_2 in these processes. Accordingly, varespladib also contributes to prevent coagulating disorders induced by other groups of snake venoms, e.g., *Bothrops* (Viperidae-Crotalinae), *Daboia*, *Echis*, *Oxyuranus*, *Naja*, *Pseudechis* and *Bitis* spp., which exhibit high PLA_2 activity (Bittenbinder et al., 2018; Xie et al., 2020; Youngman et al., 2020; Zdenek et al., 2020). On the other hand, varespladib does not affect the *L. m. rhombeata* venom-induced subcutaneous haemorrhage in rats, reflecting its disability in antagonizing the metalloproteases of this venom, since local and systemic haemorrhagic actions produced by Viperidae venoms are mainly mediated by this family of toxins (Escalante et al., 2011; Seo et al., 2017). In addition, although an Asp49 PLA_2 (LmrTX) with anticoagulant activity has been already isolated from *L. m. rhombeata* venom (Damico et al., 2012), it does not appear to contribute expressively with the subcutaneous haemorrhage induced in rats, as reported in this study.

L. m. rhombeata venom has been an important object of study for structural characterization of toxins such as metalloproteases (Cordeiro et al., 2018), serine proteases (Aguiar et al., 1996; Wiezel et al., 2019), C-type lectins (Wiezel et al., 2019), basic and acid PLA_2 (Damico et al., 2012; Cordeiro et al., 2015; Diniz-Sousa et al., 2018), phospholipase B and hialuronidase (Wiezel et al., 2015), including bradykinin-potentiating peptides (BPPs) (Pinheiro-Júnior et al., 2018). As previously commented, these toxins are responsible by developing the main toxicological aspects of the envenomation by *Lachesis*. However, the factual involvement of PLA_2 toxins on the effects produced by *Lachesis* venoms have been poorly investigated, with a few reports describing their inhibitory action of platelet aggregation (Cordeiro et al., 2015), anticoagulant and antithrombotic activities (Damico et al., 2012), and cytotoxicity on C2C12 myotubes (Diniz-Sousa et al., 2018).

In Brazil, envenomations by *L. m. muta* and *L. m. rhombeata* are treated with anti-*Bothrops*/*Lachesis* serums, with their rescue action being dependent on early i.v. administration (Pla et al., 2013; Madrigal et al., 2017; Solano et al., 2018). There are some negative factors that resulting in deaths by accidents involving *Lachesis* snakes in Brazil: 1) limited availability of antivenoms, 2) difficulties in accessing health services in certain regions of the country, and 3) lack of a specific anti-*Lachesis* serum. Consequently, other types of antivenoms, e.g., anti-*Bothrops* serum and anti-*Bothrops*/*Crotalus* serum, have been inaccurately recommended to treat envenomations by *L. muta* in the absence of anti-*Bothrops*/*Lachesis* serum (Magalhães et al., 2019; Muniz et al., 2021). These challenges involving the treatment of envenomations by *Lachesis* snakes strengthen the search for therapeutically useful adjuncts, with varespladib rising as a plausible tool.

In conclusion, varespladib abolishes efficiently the PLA_2 activity of *L. m. rhombeata* venom at low concentrations and does not affect other majority enzymatic groups of this venom, e.g., metalloproteases and serine proteases. Varespladib alone might partially prevent the procoagulant effect of *L. m. rhombeata* venom, with its combination with antivenom avoiding alterations in both intrinsic and extrinsic pathways. Varespladib does not reduce the subcutaneous haemorrhage formation induced by *L. m. rhombeata* venom in rats due to the lack of inhibitory action on the proteases of the venom. The association of varespladib with a recommended polyvalent antivenom does not produce synergic action on the venom-induced haemorrhagic action but it helps to prevent the venom-induced coagulation disorders.

DATA AVAILABILITY STATEMENT

The original contributions presented in the study are included in the Article/Supplementary Material, further inquiries can be directed to the corresponding author.

ETHICS STATEMENT

The animal study was reviewed and approved by the Committee for Ethics in Animal Use of University of Western São Paulo (CEUA/UNOESTE, Protocol No. 6713/2021).

AUTHOR CONTRIBUTIONS

RMBN and RSF contributed to conception and design of the study. PGG, DRP, and NLV organized the database. LFA performed the statistical analysis. PGG, DRP, and KAT-B wrote the first draft of the manuscript. NJSJ and SH wrote

sections of the manuscript. KM-Z, EGR, and RSF contributed to manuscript revision, read, and approved the submitted version.

FUNDING

This work was funded by institutional resources from University of Western São Paulo (UNOESTE, Presidente Prudente, SP, Brazil) and Fundação de Amparo à Pesquisa do Estado de São Paulo (FAPESP, São Paulo, SP, Brazil, Grant No. 2020/04287-6 and 2021/14375-2). PGG was also supported by a studentship from FAPESP (Grant No. 2020/11268-8). NJSJ and SH are supported by a research fellowship from Conselho Nacional de Desenvolvimento Científico e Tecnológico (CNPq, Brasília, DF, Brazil, Grant Nos. 309320/2016-0 and 310547/2014-8, respectively).

REFERENCES

Aguiar, A. S., Alves, C. R., Melgarejo, A., and Giovanni-De-Simone, S. (1996). Purification and Partial Characterization of a Thrombin-Like/gyroxin Enzyme from Bushmaster (Lachesis muta Rhombeata) Venom. *Toxicon* 34 (5), 555–565. doi:10.1016/0041-0101(95)00159-X

Bittenbinder, M. A., Zdenek, C. N., Op den Brouw, B., Youngman, N. J., Dobson, J. S., Naude, A., et al. (2018). Coagulotoxic Cobras: Clinical Implications of Strong Anticoagulant Actions of African Spitting *Naja* Venoms that Are Not Neutralised by Antivenom but Are by LY315920 (Varespladib). *Toxins (Basel)* 10 (12), E516. doi:10.3390/toxins10120516

Bregge-Silva, C., Nonato, M. C., de Albuquerque, S., Ho, P. L., Junqueira de Azevedo, I. L., Vasconcelos Diniz, M. R., et al. (2012). Isolation and Biochemical, Functional and Structural Characterization of a Novel L-Amino Acid Oxidase from *Lachesis muta* Snake Venom. *Toxicon* 60 (7), 1263–1276. doi:10.1016/j.toxicon.2012.08.008

Bryan-Quirós, W., Fernández, J., Gutiérrez, J. M., Lewin, M. R., and Lomonte, B. (2019). Neutralizing Properties of LY315920 toward Snake Venom Group I and II Myotoxic Phospholipases A_2. *Toxicon* 157, 1–7. doi:10.1016/j.toxicon.2018.11.292

Chippaux, J. P. (2017). Snakebite Envenomation Turns Again into a Neglected Tropical Disease!. *J. Venom. Anim. Toxins Incl. Trop. Dis.* 23, 38–42. doi:10.1186/s40409-017-0127-6

Carregari, V. C., Stuani Floriano, R., Rodrigues-Simioni, L., Winck, F. V., Baldasso, P. A., Ponce-Soto, L. A., et al. (2013). Biochemical, Pharmacological, and Structural Characterization of New Basic PLA2 Bbil-TX from Bothriopsis Bilineata Snake Venom. *Biomed. Res. Int.* 2013, 612649. doi:10.1155/2013/612649

Cordeiro, F. A., Coutinho, B. M., Wiezel, G. A., de Castro Figueiredo Bordon, K., Bregge-Silva, C., Rosa-Garzon, N. G., et al. (2018). Purification and Enzymatic Characterization of a Novel Metalloprotease from Lachesis muta Rhombeata Snake Venom. *J. Venom. Anim. Toxins Incl. Trop. Dis.* 24, 32. doi:10.1186/s40409-018-0171-x

Cordeiro, F. A., Perini, T. G., Bregge-Silva, C., Cremonez, C. M., Rodrigues, R. S., Boldrini-França, J., et al. (2015). A New Phospholipase A_2 from Lachesis muta Rhombeata: Purification, Biochemical and Comparative Characterization with Crotoxin B. *Protein Pept. Lett.* 22 (9), 816–827. doi:10.2174/0929866522666150706112431

Costa, H. C., and Bérnils, R. S. (2018). Répteis Do Brasil e suas Unidades Federativas: Lista de espécies. *Herpetologia Brasileira* 8, 11–57.

Damico, D. C., Bueno, L. G., Rodrigues-Simioni, L., Marangoni, S., da Cruz-Höfling, M. A., and Novello, J. C. (2006). Functional Characterization of a Basic D49 Phospholipase A_2 (LmTX-I) from the Venom of the Snake Lachesis muta Muta (Bushmaster). *Toxicon* 47 (7), 759–765. doi:10.1016/j.toxicon.2006.02.007

Damico, D. C., Nascimento, J. M., Lomonte, B., Ponce-Soto, L. A., Joazeiro, P. P., Novello, J. C., et al. (2007). Cytotoxicity of Lachesis muta Muta Snake (Bushmaster) Venom and its Purified Basic Phospholipase A_2 (LmTX-I) in Cultured Cells. *Toxicon* 49 (5), 678–692. doi:10.1016/j.toxicon.2006.11.014

Damico, D. C., Vassequi-Silva, T., Torres-Huaco, F. D., Nery-Diez, A. C., de Souza, R. C., Da Silva, S. L., et al. (2012). LmrTX, a Basic PLA_2 (D49) Purified from Lachesis muta Rhombeata Snake Venom with Enzymatic-Related Antithrombotic and Anticoagulant Activity. *Toxicon* 60 (5), 773–781. doi:10.1016/j.toxicon.2012.06.010

Dashevsky, D., Bénard-Valle, M., Neri-Castro, E., Youngman, N. J., Zdenek, C. N., Alagón, A., et al. (2021). Anticoagulant Micrurus Venoms: Targets and Neutralization. *Toxicol. Lett.* 337, 91–97. doi:10.1016/j.toxlet.2020.11.010

Dias, L., Rodrigues, M. A., Inoue, B. R., Rodrigues, R. L., Rennó, A. L., de Souza, V. B., et al. (2016a). Pharmacological Analysis of Hemodynamic Responses to Lachesis muta (South American Bushmaster) Snake Venom in Anesthetized Rats. *Toxicon* 123, 25–44. doi:10.1016/j.toxicon.2016.10.002

Dias, L., Rodrigues, M. A., Rennó, A. L., Stroka, A., Inoue, B. R., Panunto, P. C., et al. (2016b). Hemodynamic Responses to Lachesis muta (South American Bushmaster) Snake Venom in Anesthetized Rats. *Toxicon* 123, 1–14. doi:10.1016/j.toxicon.2016.10.001

Diniz, M. R., and Oliveira, E. B. (1992). Purification and Properties of a Kininogenin from the Venom of Lachesis muta (Bushmaster). *Toxicon* 30 (3), 247–258. doi:10.1016/0041-0101(92)90867-5

Diniz-Sousa, R., Caldeira, C. A. S., Kayano, A. M., Paloschi, M. V., Pimenta, D. C., Simões-Silva, R., et al. (2018). Identification of the Molecular Determinants of the Antibacterial Activity of LmutTX, a Lys49 Phospholipase A_2 Homologue Isolated from Lachesis muta muta Snake Venom (Linnaeus, 1766). *Basic Clin. Pharmacol. Toxicol.* 122 (4), 413–423. doi:10.1111/bcpt.12921

Diniz-Sousa, R., Moraes, J. D. N., Rodrigues-da-Silva, T. M., Oliveira, C. S., and Caldeira, C. A. D. S. (2020). A Brief Review on the Natural History, Venomics and the Medical Importance of Bushmaster (Lachesis) Pit viper Snakes. *Toxicon X* 7 (7), 100053. doi:10.1016/j.toxcx.2020.100053

Erlanger, B. F., Kokowsky, N., and Cohen, W. (1961). The Preparation and Properties of Two New Chromogenic Substrates of Trypsin. *Arch. Biochem. Biophys.* 95 (2), 271–278. doi:10.1016/0003-9861(61)90145-x

Escalante, T., Rucavado, A., Fox, J. W., and Gutiérrez, J. M. (2011). Key Events in Microvascular Damage Induced by Snake Venom Hemorrhagic Metalloproteinases. *J. Proteomics* 74 (9), 1781–1794. doi:10.1016/j.jprot.2011.03.026

Estêvão-Costa, M. I., Diniz, C. R., Magalhães, A., Markland, F. S., and Sanchez, E. F. (2000). Action of Metalloproteinases Mutalysin I and II on Several Components of the Hemostatic and Fibrinolytic Systems. *Thromb. Res.* 99 (4), 363–376. doi:10.1016/s0049-3848(00)00259-0

Ferreira, T., Camargo, E. A., Ribela, M. T., Damico, D. C., Marangoni, S., Antunes, E., et al. (2009). Inflammatory Oedema Induced by Lachesis muta muta (Surucucu) Venom and LmTX-I in the Rat Paw and Dorsal Skin. *Toxicon* 53 (1), 69–77. doi:10.1016/j.toxicon.2008.10.016

Fuly, A. L., Calil-Elias, S., Martinez, A. M., Melo, P. A., and Guimarães, J. A. (2003). Myotoxicity Induced by an Acidic Asp-49 Phospholipase A(2) Isolated from Lachesis muta Snake Venom. Comparison with Lysophosphatidylcholine. *Int. J. Biochem. Cell Biol.* 35 (10), 1470–1481. doi:10.1016/s1357-2725(03)00129-8

Fuly, A. L., Calil-Elias, S., Zingali, R. B., Guimarães, J. A., and Melo, P. A. (2000). Myotoxic Activity of an Acidic Phospholipase A_2 Isolated from Lachesis muta (Bushmaster) Snake Venom. *Toxicon* 38 (7), 961–972. doi:10.1016/s0041-0101(99)00208-1

Fuly, A. L., Machado, O. L., Alves, E. W., and Carlini, C. R. (1997). Mechanism of Inhibitory Action on Platelet Activation of a Phospholipase A_2 Isolated from Lachesis muta (Bushmaster) Snake Venom. *Thromb. Haemost.* 78 (5), 1372–1380. doi:10.1055/s-0038-1665414

Giovanni-De-Simone, S., Aguiar, A. S., Gimenez, A. R., Novellino, K., and de Moura, R. S. (1997). Purification, Properties, and N-Terminal Amino Acid Sequence of a Kallikrein-like Enzyme from the Venom of Lachesis muta Rhombeata (Bushmaster). *J. Protein Chem.* 16 (8), 809–818. doi:10.1023/a:1026372018547

Graham, R. L., Graham, C., McClean, S., Chen, T., O'Rourke, M., Hirst, D., et al. (2005). Identification and Functional Analysis of a Novel Bradykinin Inhibitory Peptide in the Venoms of New World Crotalinae Pit Vipers. *Biochem. Biophys. Res. Commun.* 338 (3), 1587–1592. doi:10.1016/j.bbrc.2005.10.130

Gutiérrez, J. M., Albulescu, L-O., Clare, R. H., Casewell, N. R., Abd El-Aziz, T. M., Escalante, T., et al. (2021). The Search for Natural and Synthetic Inhibitors that Would Complement Antivenoms as Therapeutics for Snakebite Envenoming. *Toxins (Basel)* 13 (7), 451. doi:10.3390/toxins13070451

Gutiérrez, J. M., Lewin, M. R., Williams, D. J., and Lomonte, B. (2020a). Varespladib (LY315920) and Methyl Varespladib (LY333013) Abrogate or Delay Lethality Induced by Presynaptically Acting Neurotoxic Snake Venoms. *Toxins (Basel)* 12 (2), 131. doi:10.3390/toxins12020131

Gutiérrez, J. M., Castillo, L., de Naves, K. M. D., Masís, J., and Alape-Girón, A. (2020b). Epidemiology of Snakebites in El Salvador (2014-2019). *Toxicon* 186, 26–28. doi:10.1016/j.toxicon.2020.07.027

Junqueira-de-Azevedo, I. L., Ching, A. T., Carvalho, E., Faria, F., Nishiyama, M. Y., Jr, Ho, P. L., et al. (2006). Lachesis muta (Viperidae) cDNAs Reveal Diverging Pit viper Molecules and Scaffolds Typical of Cobra (Elapidae) Venoms: Implications for Snake Toxin Repertoire Evolution. *Genetics* 173, 877–889. doi:10.1534/genetics.106.056515

Kazandjian, T. D., Arrahman, A., Still, K. B. M., Somsen, G. W., Vonk, F. J., Casewell, N. R., et al. (2021). Anticoagulant Activity of *Naja nigricollis* Venom Is Mediated by Phospholipase A_2 Toxins and Inhibited by Varespladib. *Toxins (Basel)* 13, 302. doi:10.3390/toxins13050302

Lewin, M., Samuel, S., Merkel, J., and Bickler, P. (2016). Varespladib (LY315920) Appears to Be a Potent, Broad-Spectrum, Inhibitor of Snake Venom Phospholipase A_2 and a Possible Pre-referral Treatment for Envenomation. *Toxins (Basel)* 8 (9), 248. doi:10.3390/toxins8090248

Lewin, M. R., Gilliam, L. L., Gilliam, J., Samuel, S. P., Bulfone, T. C., Bickler, P. E., et al. (2018). Delayed LY333013 (Oral) and LY315920 (Intravenous) Reverse Severe Neurotoxicity and rescue Juvenile Pigs from Lethal Doses of Micrurus fulvius (Eastern Coral Snake) Venom. *Toxins (Basel)* 10 (11), E479. doi:10.3390/toxins10110479

Liu, C. C., Wu, C. J., Hsiao, Y. C., Yang, Y. H., Liu, K. L., Huang, G. J., et al. (2021). Snake Venom Proteome of Protobothrops Mucrosquamatus in Taiwan: Delaying Venom-Induced Lethality in a Rodent Model by Inhibition of Phospholipase A_2 Activity with Varespladib. *J. Proteomics* 234, 104084. doi:10.1016/j.jprot.2020.104084

Madrigal, M., Pla, D., Sanz, L., Barboza, E., Arroyo-Portilla, C., Corrêa-Netto, C., et al. (2017). Cross-reactivity, Antivenomics, and Neutralization of Toxic Activities of Lachesis Venoms by Polyspecific and Monospecific Antivenoms. *Plos Negl. Trop. Dis.* 11 (8), e0005793. doi:10.1371/journal.pntd.0005793

Madrigal, M., Sanz, L., Flores-Díaz, M., Sasa, M., Núñez, V., Alape-Girón, A., et al. (2012). Snake Venomics across Genus Lachesis. Ontogenetic Changes in the Venom Composition of Lachesis Stenophrys and Comparative Proteomics of the Venoms of Adult Lachesis Melanocephala and Lachesis Acrochorda. *J. Proteomics* 77, 280–297. doi:10.1016/j.jprot.2012.09.003

Magalhães, S. F. V., Peixoto, H. M., Moura, N., Monteiro, W. M., and de Oliveira, M. R. F. (2019). Snakebite Envenomation in the Brazilian Amazon: a Descriptive Study. *Trans. R. Soc. Trop. Med. Hyg.* 113, 143–151. doi:10.1093/trstmh/try121

Muniz, E. G., Noronha, M. D. D. N., Saraiva, M. D. G. G., Monteiro, W. M., and Oliveira, S. S. (2021). Neutralization of Hemostatic Disorders Induced by Lachesis muta Venom using Brazilian Antivenoms. *Toxicon* 191, 44–47. doi:10.1016/j.toxicon.2020.12.013

Nogueira, C. C., Argôlo, A. J. S., Arzamendia, V., Azevedo, J. A., Barbo, F. E., Bérnils, R. S., et al. (2019). Atlas of Brazilian Snakes: Verified point-locality Maps to Mitigate the Wallacean Shortfall in a Megadiverse Snake Fauna. *South. Am. J. Herpetol.* 14 (1), 1–274. doi:10.2994/sajh-d-19-00120.1

Ochoa-Avilés, A., Heredia-Andino, O. S., Escandón, S. A., Celorio-Carvajal, C. A., Arias-Peláez, M. C., Zaruma-Torres, F., et al. (2020). Viperidae Snakebites in Ecuador: a Review of Epidemiological and Ecological Aspects. *Toxicon X* 7, 100051. doi:10.1016/j.toxcx.2020.100051

Oliveira, I. C. F., Gutiérrez, J. M., Lewin, M. R., and Oshima-Franco, Y. (2020). Varespladib (LY315920) Inhibits Neuromuscular Blockade Induced by Oxyuranus Scutellatus Venom in a Nerve-Muscle Preparation. *Toxicon* 187, 101–104. doi:10.1016/j.toxicon.2020.08.023

Pinheiro-Júnior, E. L., Boldrini-França, J., de Campos Araújo, L. M. P., Santos-Filho, N. A., Bendhack, L. M., Cilli, E. M., et al. (2018). LmrBPP9: A Synthetic Bradykinin-Potentiating Peptide from Lachesis muta Rhombeata Venom that Inhibits the Angiotensin-Converting Enzyme Activity *in vitro* and Reduces the Blood Pressure of Hypertensive Rats. *Peptides* 102, 1–7. doi:10.1016/j.peptides.2018.01.015

Pla, D., Sanz, L., Molina-Sánchez, P., Zorita, V., Madrigal, M., Flores-Díaz, M., et al. (2013). Snake Venomics of Lachesis muta Rhombeata and Genus-wide Antivenomics Assessment of the Paraspecific Immunoreactivity of Two Antivenoms Evidence the High Compositional and Immunological Conservation across Lachesis. *J. Proteomics* 89, 112–123. doi:10.1016/j.jprot.2013.05.028

Rucavado, A., Flores-Sánchez, E., Franceschi, A., Magalhaes, A., and Gutiérrez, J. M. (1999). Characterization of the Local Tissue Damage Induced by LHF-II, a Metalloproteinase with Weak Hemorrhagic Activity Isolated from Lachesis muta muta Snake Venom. *Toxicon* 37 (9), 1297–1312. doi:10.1016/s0041-0101(98)00268-2

Salvador, G. H. M., Borges, R. J., Lomonte, B., Lewin, M. R., and Fontes, M. R. M. (2021). The Synthetic Varespladib Molecule Is a Multi-Functional Inhibitor for PLA2 and PLA2-like Ophidic Toxins. *Biochim. Biophys. Acta Gen. Subj* 1865 (7), 129913. doi:10.1016/j.bbagen.2021.129913

Salvador, G. H. M., Gomes, A. A. S., Bryan-Quirós, W., Fernández, J., Lewin, M. R., Gutiérrez, J. M., et al. (2019). Structural Basis for Phospholipase A2-like Toxin Inhibition by the Synthetic Compound Varespladib (LY315920). *Sci. Rep.* 9 (1), 17203. doi:10.1038/s41598-019-53755-5

Sánchez, E. F., Costa, M. I., Chavez-Olortegui, C., Assakura, M. T., Mandelbaum, F. R., and Diniz, C. R. (1995). Characterization of a Hemorrhagic Factor, LHF-I, Isolated from the Bushmaster Snake (Lachesis muta muta) Venom. *Toxicon* 33 (12), 1653–1667. doi:10.1016/0041-0101(95)00097-6

Sánchez, E. F., Magalhës, A., Mandelbaum, F. R., and Diniz, C. R. (1991). Purification and Characterization of the Hemorrhagic Factor II from the Venom of the Bushmaster Snake *(Lachesis muta muta)*. *Biochim. Biophys. Acta* 1074 (3), 347–356. doi:10.1016/0304-4165(91)90084-t

Sánchez, E. F., Magalhães, A., and Diniz, C. R. (1987). Purification of a Hemorrhagic Factor (LHF-I) from the Venom of the Bushmaster Snake, Lachesis muta muta. *Toxicon* 25 (6), 611–619. doi:10.1016/0041-0101(87)90107-3

Sanz, L., Escolano, J., Ferretti, M., Biscoglio, M. J., Rivera, E., Crescenti, E. J., et al. (2008). Snake Venomics of the South and Central American Bushmasters. Comparison of the Toxin Composition of Lachesis muta Gathered from Proteomic versus Transcriptomic Analysis. *J. Proteomics* 71 (1), 46–60. doi:10.1016/j.jprot.2007.10.004

Seo, T., Sakon, T., Nakazawa, S., Nishioka, A., Watanabe, K., Matsumoto, K., et al. (2017). Haemorrhagic Snake Venom Metalloproteases and Human ADAMs Cleave LRP5/6, Which Disrupts Cell-Cell Adhesions *in vitro* and Induces Haemorrhage *in vivo*. *FEBS J.* 284 (11), 1657–1671. doi:10.1111/febs.14066

Silva-Carvalho, R., Gaspar, M. Z., Quadros, L. H. B., Lobo, L. G. G., Rogério, L. M., Santos, N. T. S., et al. (2021). *In Vivo* treatment with Varespladib, a Phospholipase A_2 Inhibitor, Prevents the Peripheral Neurotoxicity and Systemic Disorders Induced by *Micrurus corallinus* (Coral Snake) Venom in Rats. *Toxicol. Lett.* 356, 54–63. doi:10.1016/j.toxlet.2021.11.003

Soares, M. R., Oliveira-Carvalho, A. L., Wermelinger, L. S., Zingali, R. B., Ho, P. L., Junqueira-de-Azevedo, I. L., et al. (2005). Identification of Novel Bradykinin-Potentiating Peptides and C-type Natriuretic Peptide from Lachesis muta Venom. *Toxicon* 46 (1), 31–38. doi:10.1016/j.toxicon.2005.03.006

Solano, G., Gómez, A., Corrales, G., Chacón, D., Estrada, R., and León, G. (2018). Contributions of the Snake Venoms of Bothrops asper, Crotalus Simus and Lachesis Stenophrys to the Paraspecificity of the Central American Polyspecific Antivenom (PoliVal-ICP). *Toxicon* 144, 1–6. doi:10.1016/j.toxicon.2018.01.016

Theakston, R. D., and Reid, H. A. (1983). Development of Simple Standard Assay Procedures for the Characterization of Snake Venom. *Bull World Health Organ.* 61 (6), 949–956.

Torres-Bonilla, K. A., Panunto, P. C., Pereira, B. B., Zambrano, D. F., Herrán-Medina, J., Bernal, M. H., et al. (2020). Toxinological Characterization of Venom from Leptodeira annulata (Banded Cat-Eyed Snake; Dipsadidae, Imantodini). *Biochimie* 174, 171–188. doi:10.1016/j.biochi.2020.04.006

Torres-Huaco, F. D., Werneck, C. C., Vicente, C. P., Vassequi-Silva, T., Nery-Diez, A. C., Mendes, C. B., et al. (2013). Rapid Purification and Procoagulant and Platelet Aggregating Activities of Rhombeobin: a Thrombin-like/gyroxin-like Enzyme from Lachesis muta Rhombeata Snake Venom. *Biomed. Res. Int.* 2013, 903292. doi:10.1155/2013/903292

Varespladib (2011). Varespladib. *Am. J. Cardiovasc. Drugs* 11:137–43. doi:10.2165/11533650-000000000-00000

Wang, Y., Zhang, J., Zhang, D., Xiao, H., Xiong, S., and Huang, C. (2018). Exploration of the Inhibitory Potential of Varespladib for Snakebite Envenomation. *Molecules* 23 (2), E391. doi:10.3390/molecules23020391

Weinberg, M. L., Felicori, L. F., Bello, C. A., Magalhães, H. P., Almeida, A. P., Magalhães, A., et al. (2004). Biochemical Properties of a Bushmaster Snake Venom Serine Proteinase (LV-Ka), and its Kinin Releasing Activity Evaluated in Rat Mesenteric Arterial Rings. *J. Pharmacol. Sci.* 96, 333–342. doi:10.1254/jphs.fpj04005x

Wiezel, G. A., Bordon, K. C., Silva, R. R., Gomes, M. S., Cabral, H., Rodrigues, V. M., et al. (2019). Subproteome of Lachesis muta Rhombeata Venom and Preliminary Studies on LmrSP-4, a Novel Snake Venom Serine Proteinase. *J. Venom. Anim. Toxins Incl. Trop. Dis.* 25, e147018. doi:10.1590/1678-9199-JVATITD-1470-18

Wiezel, G. A., dos Santos, P. K., Cordeiro, F. A., Bordon, K. C., Selistre-de-Araújo, H. S., Ueberheide, B., et al. (2015). Identification of Hyaluronidase and Phospholipase B in Lachesis muta Rhombeata Venom. *Toxicon* 107 (Pt B), 359–368. doi:10.1016/j.toxicon.2015.08.029

Xie, C., Albulescu, L. O., Still, K. B. M., Slagboom, J., Zhao, Y., Jiang, Z., et al. (2020). Varespladib Inhibits the Phospholipase A_2 and Coagulopathic Activities of Venom Components from Hemotoxic Snakes. *Biomedicines* 8 (6), 165. doi:10.3390/biomedicines8060165

Youngman, N. J., Walker, A., Naude, A., Coster, K., Sundman, E., and Fry, B. G. (2020). Varespladib (LY315920) Neutralises Phospholipase A_2 Mediated Prothrombinase-Inhibition Induced by Bitis Snake Venoms. *Comp. Biochem. Physiol. C Toxicol. Pharmacol.* 236, 108818. doi:10.1016/j.cbpc.2020.108818

Zdenek, C. N., Youngman, N. J., Hay, C., Dobson, J., Dunstan, N., Allen, L., et al. (2020). Anticoagulant Activity of Black Snake (Elapidae: Pseudechis) Venoms: Mechanisms, Potency, and Antivenom Efficacy. *Toxicol. Lett.* 330, 176–184. doi:10.1016/j.toxlet.2020.05.014

Zinenko, O., Tovstukha, I., and Korniyenko, Y. (2020). PLA_2 Inhibitor Varespladib as an Alternative to the Antivenom Treatment for Bites from Nikolsky's viper Vipera berus Nikolskii. *Toxins (Basel)* 12 (6), 356. doi:10.3390/toxins12060356

Conflict of Interest: The authors declare that the research was conducted in the absence of any commercial or financial relationships that could be construed as a potential conflict of interest.

Publisher's Note: All claims expressed in this article are solely those of the authors and do not necessarily represent those of their affiliated organizations, or those of the publisher, the editors and the reviewers. Any product that may be evaluated in this article, or claim that may be made by its manufacturer, is not guaranteed or endorsed by the publisher.

frontiers in Pharmacology

MINI REVIEW
published: 14 January 2022
doi: 10.3389/fphar.2021.810821

The Arsenal of Bioactive Molecules in the Skin Secretion of Urodele Amphibians

Ana L. A. N. Barros[1,2], Abdelaaty Hamed[3,4], Mariela Marani[5], Daniel C. Moreira[1], Peter Eaton[6,7], Alexandra Plácido[6,8], Massuo J. Kato[3] and José Roberto S. A. Leite[1,2,8]**

[1]Núcleo de Pesquisa em Morfologia e Imunologia Aplicada, NuPMIA, Faculdade de Medicina, Universidade de Brasília, Brasília, Brazil, [2]Programa de Pós-graduação em Medicina Tropical, PPGMT, Núcleo de Medicina Tropical, NMT, Faculdade de Medicina, UnB, Brasília, Brazil, [3]Instituto de Química, IQ, Universidade de São Paulo, São Paulo, Brazil, [4]Chemistry Department, Faculty of Science, Al-Azhar University, Nasr City-Cairo, Egypt, [5]IPEEC-CONICET, Consejo Nacional de Investigaciones Científicas y Técnicas, Puerto Madryn, Argentina, [6]LAQV/REQUIMTE, Departamento de Química e Bioquímica, Faculdade de Ciências da Universidade do Porto, Porto, Portugal, [7]Joseph Banks Laboratories, The Bridge, School of Chemistry, University of Lincoln, Lincoln, United Kingdom, [8]Bioprospectum, Lda, UPTEC, Porto, Portugal

Urodele amphibians (~768 spp.), salamanders and newts, are a rich source of molecules with bioactive properties, especially those isolated from their skin secretions. These include pharmacological attributes, such as antimicrobial, antioxidant, vasoactive, immune system modulation, and dermal wound healing activities. Considering the high demand for new compounds to guide the discovery of new drugs to treat conventional and novel diseases, this review summarizes the characteristics of molecules identified in the skin of urodele amphibians. We describe urodele-derived peptides and alkaloids, with emphasis on their biological activities, which can be considered new scaffolds for the pharmaceutical industry. Although much more attention has been given to anurans, bioactive molecules produced by urodeles have the potential to be used for biotechnological purposes and stand as viable alternatives for the development of therapeutic agents.

Keywords: amphibians, urodela, bioactive molecules, peptides, alkaloids

OPEN ACCESS

Edited by:
Jean-Marc Sabatier, Aix-Marseille Université, France

Reviewed by:
Sarah Woodley, Duquesne University, United States
Elvira Brunelli, University of Calabria, Italy

****Correspondence:***
José Roberto S. A. Leite
jrsaleite@gmail.com
jrleite@pq.cnpq.br
Massuo J. Kato
majokato@iq.usp.br

Specialty section:
This article was submitted to Translational Pharmacology, a section of the journal Frontiers in Pharmacology

Received: *08 November 2021*
Accepted: *24 December 2021*
Published: *14 January 2022*

Citation:
Barros ALAN, Hamed A, Marani M, Moreira DC, Eaton P, Plácido A, Kato MJ and Leite JRSA (2022) The Arsenal of Bioactive Molecules in the Skin Secretion of Urodele Amphibians. Front. Pharmacol. 12:810821. doi: 10.3389/fphar.2021.810821

INTRODUCTION

The skin of amphibians exerts a broad spectrum of functions, which are fundamental for their homeostasis and interaction with the environment. Different multicellular skin glands produce compounds involved in both vital processes and defense strategies (Clarke, 1997; Heiss et al., 2009). Mucous glands produce a slippery mucus film, made basically of mucopolysaccharides and mucoproteoglycans, which minimize underwater friction and also make the animal slippery to predators. Other functions of the mucus include the prevention of water loss and the maintenance of a moist surface for skin gas exchange when the animal leaves the water. Granular glands are classified into different types depending on their histological characteristics and, on the other hand, synthesize and release compounds (e.g., amines, peptides and alkaloids) that participate in several defense mechanisms against potential aggressors, which can be either large predators or pathogenic microorganisms (Bucciarelli et al., 2016; Demori et al., 2019). In the first case, the compounds might irritate mucous membranes, cause an unpleasant sensation (e.g., pain or distastefulness), or even be highly toxic and lethal for their aggressors. In the second case, antimicrobial substances, in association with the commensal microbiota, prevent the colonization or infection by fungi, bacteria, and viruses (Brunetti et al., 2021).

The skin secretions of amphibians have been historically used as ethno-pharmaceutical drugs in a variety of cultures. Extensive research on this topic has accumulated over the years and many of the molecules secreted by amphibians have been isolated and characterized to date. These were found to influence different processes in living systems, acting, for example, as myotropic, immunomodulatory, antibiotic, anti-inflammatory, and antioxidant compounds. For this reason, the skin of amphibians has been recognized as a storehouse of bioactive molecules with pharmacological potential. In this context, "bioactivity" refers to the ability of a molecule to exert a given effect in an organism that can be explored for biotechnological applications (e.g., food or pharmaceutical industries), regardless of its original (evolutionary) function in its source. Indeed, amphibian-derived bioactive molecules currently stand as possible substitutes for conventional drugs or as drug leads for the development of therapeutic agents. Among amphibian orders, much more attention has been given to anurans than to that given to caecilians and urodeles in the research of bioactive molecules.

The Urodela order comprises salamanders and newts currently distributed in North and Central America, Europe, Asia, and North Africa, with some species occurring in South America (Baitchman and Herman, 2015). The order is divided into Salamandroidea and Cryptobranchoidea suborders (Jia and Gao, 2016). Salamandroidea differs from its sister clade Cryptobranchoidea regarding anatomic characteristics as bones jaw and ribs, and internal fertilization, and includes the genus *Amphiuma*, *Ambystoma*, *Plethodon*, *Salamandra*, *Tylotriton*, and *Taricha* (Anderson, 2012; Jia and Gao, 2016). Like anurans, bioactive molecules produced by urodeles have the potential to be used for biotechnological purposes, which make this group of amphibians a promising alternative to develop products with application in human health (Afolabi et al., 2018). In this mini review, we provide a brief appraisal of molecules isolated from the skin of urodele amphibians with an overview of their biological activities, with emphasis on peptides and alkaloids.

ALKALOIDS

Alkaloids have been isolated from phylogenetically diverse organisms, including microorganisms (Zhang et al., 2012; Casciaro et al., 2019), plants (Lelario et al., 2019; Petruczynik et al., 2019), and animals (Dumbacher et al., 2000; Jones et al., 2012; Santos et al., 2012; Saporito et al., 2012; Cushnie et al., 2014; Jeckel et al., 2015; Ligabue-Braun and Carlini, 2015; Knepper et al., 2019). Alkaloids have been shown to possess important biological activities as a defense mechanism against microorganisms and predators (De Luca and Laflamme, 2001; Zhang et al., 2021). They are generally derived from dietary sources of these animals (Macfoy et al., 2005), but certain alkaloids, such as samandarins of salamanders, are synthesized *de novo* from cholesterol (Habermehl and Haaf, 1968; Daly et al., 2005).

The search for alkaloids in amphibians of the Urodela order was pioneered by Zalesky in 1866, who isolated an alkaloid named samandarine from fire salamander (*Salamandra salamandra*) secretion. Then, Schöpf and Habermehl described a series of steroidal alkaloids and elucidated their absolute configurations (Weitz and Wolfel, 1962; Habermehl, 1967; Knepper et al., 2019). To date, the alkaloids characterized from the skin secretion of fire salamanders include samanine (**1**), samandinine (**2**), samandenone (**3**), samandarone (**4**), samandarine (**5**), samandaridine (**6**), cycloneosamandione (**7**), *O*-Acetyl-samandarine (**8**) and isocycloneosamandaridine (**9**) (Habermehl, 1964; Habermehl, 1967; Habermehl and Vogel, 1969; Habermehl, 1971; Daly et al., 2005), samanone (**10**) and *O*-(*S*)-3-hydroxybutanoylsamandarine (**11**) (Knepper et al., 2019) (**Figure 1**). A study of toxins using gas chromatography/mass spectrometry confirmed the presence of samandarine and/or samandarone steroidal alkaloids in all species of *Salamandra* as well as in representatives of *Lyciasalamandra* group. Other salamandrids, such as *Calotriton, Euproctus, Lissotriton*, and *Triturus*, also present low concentrations of samandarone (Vences et al., 2014), evidencing the widespread of alkaloids in the skin secretion of this group of animals.

Antibiotic resistance has become one of the major concerns for global health systems and the worldwide emergence of microbial resistance to available antibiotic drugs has led to an exhaustive search for new molecules with antimicrobial properties, and those from urodeles are valid alternatives. The alkaloids from the secretion of *S. salamandra* were able to inhibit the growth of fungi (*Geotrichum candidum*) and bacteria (*Bacillus subtilis*) (Habermehl and Preusser, 1969). Samandarone completely inhibited the growth of fungi (*Phycomyces blakesleeanus*) at a minimum effective concentration of 3×10^{-6} M. Samandarone and salamandarine from *S. maculosa* inhibit the growth of *Escherichia coli, Proteus mirabilis, Bacillus subtilis, Phycomyces blakesleeanus, Saccharomyces cerevisiae, Geotrichum candidum,* and *Trichoderma viride* in agar-diffusion tests. Samandarone presented the widest zones of inhibition for all the strains and also inhibited the growth of *Penicillium expansum*. Samandarone, samandarine, and samandaridine completely inhibited the growth of *Saccharomyces cerevisiae* at a minimum effective concentration of 1.5×10^{-6} M (Preusser et al., 1975). Although the performance of alkaloids as antibiotics against a variety of microorganisms stand out, their toxicity in major groups of vertebrates have also been documented discouraging its pharmacological use (von Byern et al., 2017). Indeed, alkaloids from urodele amphibians are known to be neurotoxins towards vertebrates (Phisalix, 1900; Mebs and Pogoda, 2005; Erjavec et al., 2017; Preißler et al., 2019).

PEPTIDES

Peptides form another group of molecules with antibiotic activity produced by the skin of salamanders and newts, but with presumed (and in some cases, proven) low toxicity (Peters et al., 2010). Among these, antimicrobial peptides (AMPs) are found in several species (Jenssen et al., 2006). In general, antimicrobial peptides have between 12 and 100 amino acid residues, are cationic, amphipathic and have a range of typical

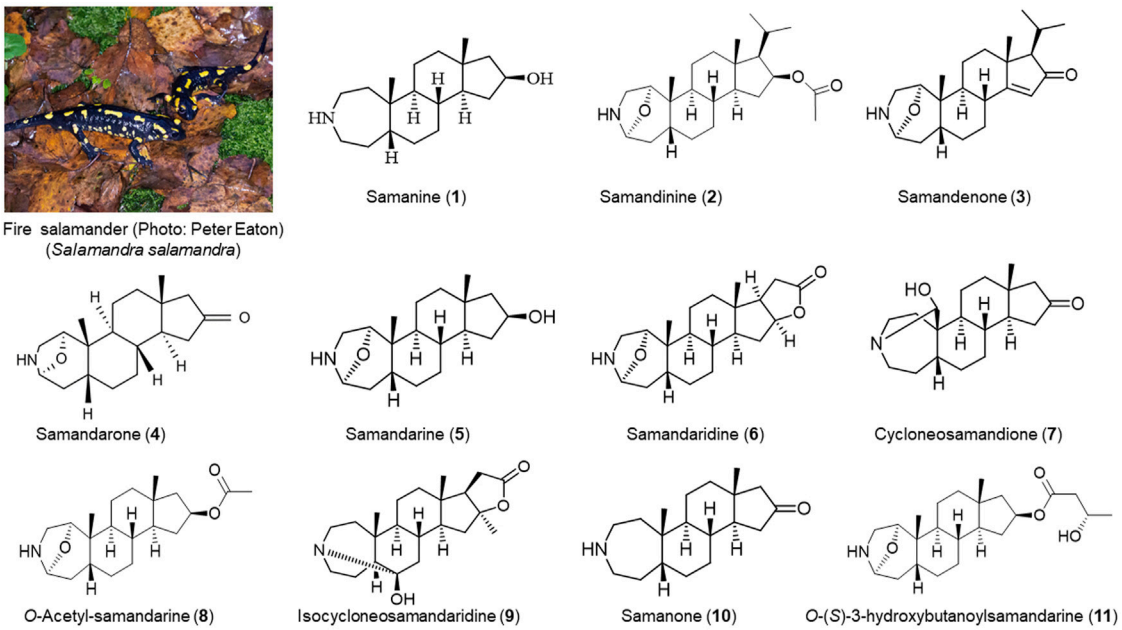

FIGURE 1 | Alkaloids identified in the skin secretion of fire salamander (*Salamandra salamandra*). **(1)**: (Habermehl, 1967; Habermehl and Haaf, 1968; Habermehl and Preusser, 1969; Habermehl, 1971); **(2)** (Habermehl and Vogel, 1969); **(3**,**4**,**5**,**6**, and **7)**: (Habermehl, 1964, Habermehl, 1967; Habermehl and Haaf, 1968; Habermehl and Preusser, 1969; Habermehl, 1971); **(8)** (Habermehl, 1964); **(9)** (Daly et al., 2005); **(10**,**11)** (Knepper et al., 2019).

TABLE 1 | Primary structure of peptides isolated from urodele amphibians.

Source	Name	Structure	Molecular Mass	Biological activity	Reference
Andrias davidianus	Andricin 01	AIGHCLGATL	955.1 Da	Antibacterial	Pei and Jiang, (2017)
Andrias davidianus	Andricin B	GLTRLPSVIK	-	Antibacterial Antifungal	Pei et al. (2018)
Plethodon cinereus	F15	-	13.75 kDa	Antibacterial	Fredericks and Dankert, (2000)
Cynops fudingens	CFBD-1	FAVWGCADYRGYCRAACFAFEYSLGPKGCTEGYVCCVPNTF	4,251.37 Da	Antibacterial	Meng et al. (2013)
Salamandra salamandra	Salamandrin-I	FAVWGCADYRGY-NH2	1,406.6 Da	Antioxidant	Plácido et al. (2020)
Cynops pyrrhogaster	NVRP-1	HSDAVFTDNYSRLLGKTALKNYLDGALKKE	3,000 Da	Muscle relaxant	Teranishi et al. (2004)
	NVRP-2	HSDAVFTDNYSRLLAKTALKNYLDGALKKE			
	NVRP-3	HSDAVFTDNYSRLLGKIALKNYLDEALKKE			
	NVRP-4	HSDAVFTDNYSRLLGKTALKNYLDSALKKE			
Tylototriton verrucosus	Tylotoin	KCVRQNNKRVCK	1,473.80 Da	Wound healing	Mu et al. (2014)

secondary structures, as α-helices, β-sheets, and extended and flexible loops (Nguyen et al., 2011; Gao et al., 2017). The development of resistance by microorganisms to AMPs is considered relatively unlikely, mainly because they target the cell membrane directly. It has also been claimed that they have a poorly mutable structure, and present a wide range of epitopes, which makes their recognition difficult (Yeaman and Yount, 2003; Shen et al., 2018). Therefore, AMPs have been considered as alternative candidates for the development of new antimicrobial agents either alone (Nicola et al., 2019) or in combination with conventional antibiotics (Choi and Lee, 2012; Nuding et al., 2014).

In amphibians of the Urodela order, peptides with potential biological activities were isolated particularly from the skin secretion, although also from different parts of the animals (**Table 1**) (Pei et al., 2018). The peptide andricin 01 was isolated from the skin secretion of giant Chinese salamander *Andrias davidianus*. Andricin 01 showed antimicrobial activity against Gram-negative and Gram-positive bacteria however, it did not show cytotoxic activity to human hepatocytes or renal

cells, and no hemolytic activity was observed (Pei and Jiang, 2017).

The 13.75 kDa peptide F15 was isolated from the skin of the red-backed salamander *Plethodon cinereus*. In a colony counting assay, F15 reduced *S. aureus* by 90% in 2 h, thus showing strong antibacterial activity against Gram-positive bacteria (Fredericks and Dankert, 2000). Another work identified CFBD-1 in the skin of the newt *Cynops fudingens*, a peptide of the β-defensin class, consisting of 41 amino acids, with a molecular mass of 4251.37 Da. This defensin was shown to be active mainly against the Gram-positive bacteria *S. aureus*, similarly to the previously described F15 peptide, with a minimum inhibitory concentration (MIC) of 65 μg/ml (Meng et al., 2013).

As a first approximation, numerous colleagues determined the antimicrobial activity of the total crude extract or the protein fraction of the skin secretion of several urodels. A study performed with the analysis of the total number of peptides isolated from the skin of salamander larvae and adults of the *Ambystoma tigrinum* species revealed antibacterial activity against *Bacillus dendrobatidis*, *Staphylococcus aureus,* and *Klebsiella* sp. (Sheafor et al., 2008). Studies with the crude extract of the cutaneous secretions of the species *Lissotriton vulgaris* and *Triturus ivanbureschi* showed that these secretions present a total of 18 and 20 protein fractions, respectively. These extracts showed antimicrobial activity for several bacteria, *Escherichia coli* and *Enterococcus faecalis*, and fungi, *Candida albicans*, strains, and hemolytic activity for human and rabbit red blood cells (Mert et al., 2018). The antimicrobial activity may be is a result of the action of active peptides (Pukala et al., 2006). In addition, they also showed high cytotoxic effects for cancer cell lines, with the highest anti-cancer activity of both secretion samples (*L.vulgaris* and *T. ivanbureschi*) being for the MDA-MB-231 breast cancer cell line (Mert et al., 2018). These preliminary findings highlight the importance of further research on the skin secretions of these animals, to characterize the molecules responsible for the antibiotic activities.

In addition to AMPs, other peptides isolated from urodeles can also have diverse pharmacological properties, such as antioxidant, and immunomodulatory activities (Coorens et al., 2017; Holthausen et al., 2017; Lee et al., 2019; Woodhams et al., 2020). Some examples of the last one is the neutralization of endotoxins, chemotaxis, and wound healing activities (Mangoni and Casciaro, 2020).

Reactive oxygen species (ROS) are necessary for the normal biochemical processes of cells (Litescu et al., 2011). However, in excessive amounts, when oxidative stress occurs, they can damage some structures, like DNA, proteins, and lipids (Duarte and Lunec, 2005). This process is related to cardiovascular disorders, diabetes, neurodegenerative diseases, cancer, chronic inflammatory diseases (Llesuy et al., 2001).

Synthetic chemical antioxidants often have low stability, cytotoxic, and carcinogenic effects, which led to search for natural antioxidants with low cytotoxicity (Gürlek et al., 2020). Salamandrin-I is a recently described molecule that showed relevant antioxidant activity. This molecule was the first peptide identified in the skin of the European fire salamander (*S. salamandra*). The peptide neutralizes the free radicals DPPH and ABTS at nontoxic concentrations for microglial cells and human red blood cells (Plácido et al., 2020). The discovery of this peptide paves the way for further investigation of other antioxidant peptides in the skin secretion of urodeles.

The medication currently available for wound healing is costly, has low activity, and produces hyperplastic scars necessitating the search for new drugs (Hardwicke et al., 2008). The amphibian peptides have shown potential as alternative treatment (Cao et al., 2018). The peptide tylotoin identified from the salamander *Tylototriton verrucosus* skin has shown to be effective in assay with dermal wounds in mice. It showed a similar wound healing capacity as the epidermal growth factor. The peptide has been shown to promote increased motility and proliferation of keratinocytes, vascular endothelial cells, and fibroblasts, resulting in accelerated re-epithelialization and formation of granulation tissue at the wound site. Tylotoin promotes the release of transforming growth factor β1 (TGF-β1) and Interleukin 6 (IL-6), which are essential in the wound healing response (Mu et al., 2014).

In general, due to its distinct biochemical and therapeutic properties, peptides are under development to disrupt protein-protein interactions and target or inhibit intracellular molecules such as proteinaceous receptors (Lee et al., 2019). Moreover, numerous peptide molecules were described to interact with microbial membranes through different mechanisms, destabilizing them, making peptides a unique class of pharmaceutical compounds (Vineeth Kumar and Sanil, 2017). The field of peptide drug discovery has evolved from both computational-aided rational design and combinatorial chemistry to the discovery of new molecules as stepping stones to new drug design, involving academic groups and private companies (de la Torre and Albericio, 2020; Al Shaer et al., 2020; Sampaio de Oliveira et al., 2020). With a high level of dynamism several peptide drugs are approved for clinical use in the United States, Europe, and Japan, and near 400 peptides are already in clinical development (Lee et al., 2019). The urodel peptides deserve more attention to clarify their structural features and mechanism of action.

OTHER MOLECULES

In addition to the alkaloids and peptides, other compounds have been described from salamanders and newts. CCK-TV is a molecule of the cholecystokinin class, a gastrointestinal hormone, identified from salamander skin *Tylototriton verrucosus*. CCK-TV showed potential for inducing muscle contraction isolated smooth striatum from the porcine gallbladder in concentrations range of 5.0×10^{-11} to 2.0×10^{-6} M (Jiang et al., 2015).

Dermal secretion analysis of salamander *Plethodon cinereus*, shows the presence of three fatty acids with antibacterial activity. The inhibition test showed that myristoleic acid, linolenic acid, and palmitoleic acid, inhibited the growth of *Bacillus cereus* in 24 h, at concentrations of 27, 7, and 6.9 μg, respectively, with halos of inhibition around 8.0–6.5 mm in diameter (Rickrode et al., 1986).

Another class of bioactive molecules found in amphibian skin are biogenic amines. Amines, such as putrescine, histamine, tryptamine, and phenylethylamine, are low molecular weight bases found in living organisms or as breakdown products of the fermentation process (Erspamer, 1971; Jovaisiene et al., 2017). Studies reported the presence of high concentrations of tryptamine and serotonin in the skin of salamander species (Erspamer, 1971; Roseghini et al., 1976; Luddecke et al., 2018).

CONCLUSION

Understanding the Earth's biodiversity is important for describing genetic diversity and prospecting for bioactive molecules from diverse organisms. Skin secretion of amphibians of order Urodela are a unique source of alkaloids, peptides, biogenic amines and other compounds with diverse structures and functions to be considered as bioactive compounds. The studies compile in this review shows that steroidal alkaloids and peptides from Urodela skin secretions are considered the first line of defense against pathogens, however diverse limitations of the studies performed as difficulties to obtain toxins or to synthetize it by artificial methods made that the full capacity of these unique molecules as antimicrobials has not been properly studied and most of the studies described are still preliminary. In the case of peptides, the availability of synthetic methodology has provided access to explore the structures of analogues while in case of complex molecules, the partial or total synthesis can be more challenging specially when only putative compounds are inferred from the mass spectrometric data and the number of chiral centers and the number of possible diastereoisomers makes the task even more complex.

Despite considerable knowledge on alkaloids from urodeles, studies of secretions in terms as-of-yet unidentified antimicrobial components are needed to improve the current understanding of the complex toxin system of their skin (Luddecke et al., 2018). Urodele-derived molecules are underexplored therapeutic alternatives to conventional antibiotics used to treat fungal and bacterial infections.

AUTHOR CONTRIBUTIONS

ALANB: Data curation; Methodology; Writing-original draft; Conceptualization. AH: Data curation; Methodology; Writing-original draft; Conceptualization. MM: Data curation; Methodology; Writing-original draft; Conceptualization. DCM: Data curation; Methodology; Writing-original draft; Conceptualization. PE: Data curation; Methodology; Writing-original draft; Funding acquisition; Conceptualization. AP: Data curation; Methodology; Writing-original draft; Funding acquisition; Conceptualization. MJK: Data curation; Methodology; Writing-original draft; Funding acquisition; Conceptualization. JRSAL: Data curation; Methodology; Writing-original draft; Funding acquisition; Conceptualization.

FUNDING

This study is part of the project VIDA-FROG, which is funded by Fundação para a Ciência e a Tecnologia (FCT, Portugal), grant number PTDC/BII-BIO/31158/2017, and Fundação de Amparo à Pesquisa do Estado de São Paulo (FAPESP, Brazil), grant number 2018/07999-7. A.P. is a recipient of a post-doctoral grant from the same project (FCT, PTDC/BII-BIO/31158/2017). This study was financed in part by the Coordenação de Aperfeiçoamento de Pessoal de Nível Superior (CAPES, Brazil) - Finance Code 001.

ACKNOWLEDGMENTS

MM thanks the support of Consejo Nacional de Investigaciones Científicas y Técnicas (Puerto Madryn, Argentina).

REFERENCES

Afolabi, L. T., Saeed, F., Hashim, H., and Petinrin, O. O. (2018). Ensemble Learning Method for the Prediction of New Bioactive Molecules. *PLoS One* 13 (1), e0189538. doi:10.1371/journal.pone.0189538

Al Shaer, D., Al Musaimi, O., Albericio, F., and de la Torre, B. G. (2020). 2019 FDA TIDES (Peptides and Oligonucleotides) Harvest. *Pharmaceuticals (Basel)* 13 (3). doi:10.3390/ph13030040

Anderson, J. S. (2012). Fossils, Molecules, Divergence Times, and the Origin of Salamandroidea. *Proc. Natl. Acad. Sci. U S A.* 109 (15), 5557–5558. doi:10.1073/pnas.1202491109

Baitchman, E. J., and Herman, T. A. (2015). "Caudata (Urodela)," in *Fowler's Zoo and Wild Animal Medicine*. Editors R. E. Miller and M. E. Fowler (St. Louis: W.B. Saunders), 8, 13–20. doi:10.1016/b978-1-4557-7397-8.00002-5

Brunetti, A. E., Bunk, B., Lyra, M. L., Fuzo, C. A., Marani, M. M., Spröer, C., et al. (2021). Molecular Basis of a Bacterial-Amphibian Symbiosis Revealed by Comparative Genomics, Modeling, and Functional Testing. *ISME J.* doi:10.1038/s41396-021-01121-7

Bucciarelli, G. M., Green, D. B., Shaffer, H. B., and Kats, L. B. (2016). Individual Fluctuations in Toxin Levels Affect Breeding Site Fidelity in a Chemically Defended Amphibian. *Proc. Biol. Sci.* 283 (1831). doi:10.1098/rspb.2016.0468

Cao, X., Wang, Y., Wu, C., Li, X., Fu, Z., Yang, M., et al. (2018). Cathelicidin-OA1, a Novel Antioxidant Peptide Identified from an Amphibian, Accelerates Skin Wound Healing. *Sci. Rep.* 8 (1), 943. doi:10.1038/s41598-018-19486-9

Casciaro, B., Calcaterra, A., Cappiello, F., Mori, M., Loffredo, M. R., Ghirga, F., et al. (2019). Nigritanine as a New Potential Antimicrobial Alkaloid for the Treatment of Staphylococcus Aureus-Induced Infections. *Toxins (Basel)* 11 (9). doi:10.3390/toxins11090511

Choi, H., and Lee, D. G. (2012). Synergistic Effect of Antimicrobial Peptide Arenicin-1 in Combination with Antibiotics against Pathogenic Bacteria. *Res. Microbiol.* 163 (6-7), 479–486. doi:10.1016/j.resmic.2012.06.001

Clarke, B. T. (1997). The Natural History of Amphibian Skin Secretions, Their normal Functioning and Potential Medical Applications. *Biol. Rev. Camb Philos. Soc.* 72 (3), 365–379. doi:10.1017/s0006323197005045

Coorens, M., Scheenstra, M. R., Veldhuizen, E. J., and Haagsman, H. P. (2017). Interspecies Cathelicidin Comparison Reveals Divergence in Antimicrobial Activity, TLR Modulation, Chemokine Induction and Regulation of Phagocytosis. *Sci. Rep.* 7, 40874. doi:10.1038/srep40874

Cushnie, T. P., Cushnie, B., and Lamb, A. J. (2014). Alkaloids: an Overview of Their Antibacterial, Antibiotic-Enhancing and Antivirulence Activities. *Int. J. Antimicrob. Agents* 44 (5), 377–386. doi:10.1016/j.ijantimicag.2014.06.001

Daly, J. W., Spande, T. F., and Garraffo, H. M. (2005). Alkaloids from Amphibian Skin: a Tabulation of over Eight-Hundred Compounds. *J. Nat. Prod.* 68 (10), 1556–1575. doi:10.1021/np0580560

De Luca, V., and Laflamme, P. (2001). The Expanding Universe of Alkaloid Biosynthesis. *Curr. Opin. Plant Biol.* 4 (3), 225–233. doi:10.1016/s1369-5266(00)00165-5

Demori, I., Rashed, Z. E., Corradino, V., Catalano, A., Rovegno, L., Queirolo, L., et al. (2019). Peptides for Skin Protection and Healing in Amphibians. *Molecules* 24 (2). doi:10.3390/molecules24020347

Duarte, T. L., and Lunec, J. (2005). Review: When Is an Antioxidant Not an Antioxidant? A Review of Novel Actions and Reactions of Vitamin C. *Free Radic. Res.* 39 (7), 671–686. doi:10.1080/10715760500104025

Dumbacher, J. P., Spande, T. F., and Daly, J. W. (2000). Batrachotoxin Alkaloids from Passerine Birds: A Second Toxic Bird Genus (Ifrita Kowaldi) from New Guinea. *Proc. Natl. Acad. Sci. U S A.* 97 (24), 12970–12975. doi:10.1073/pnas.200346897

Erjavec, V., Lukanc, B., and Žel, J. (2017). Intoxication of a Dog with Alkaloids of the Fire Salamander. *Medycyna Weterynaryjna* 73, 186–188. doi:10.21521/mw.5648

Erspamer, V. (1971). Biogenic Amines and Active Polypeptides of the Amphibian Skin. *Annu. Rev. Pharmacol.* 11, 327–350. doi:10.1146/annurev.pa.11.040171.001551

Fredericks, L. P., and Dankert, J. R. (2000). Antibacterial and Hemolytic Activity of the Skin of the Terrestrial Salamander, *Plethodon cinereus*. *J. Exp. Zool* 287, 3402–3459. doi:10.1002/1097-010X(20001001)287:53.0.COdoi:10.1002/1097-010x(20001001)287:5<340:aid-jez2>3.0.co;2-9

Gao, Y., Wu, D., Wang, L., Lin, C., Ma, C., Xi, X., et al. (2017). Targeted Modification of a Novel Amphibian Antimicrobial Peptide from Phyllomedusa tarsius to Enhance its Activity against MRSA and Microbial Biofilm. *Front. Microbiol.* 8, 628. doi:10.3389/fmicb.2017.00628

Gürlek, C., Yarkent, Ç., Köse, A., Tuğcu, B., Gebeloğlu, I. K., Öncel, S. Ş., et al. (2020). Screening of Antioxidant and Cytotoxic Activities of Several Microalgal Extracts with Pharmaceutical Potential. *Health Technol.* 10 (1), 111–117. doi:10.1007/s12553-019-00388-3

Habermehl, G., and Haaf, A. (1968). Cholesterol as the First Step in the Biosynthesis of the Salamander Alkaloids. *Chem. Ber* 101 (1), 198–200. doi:10.1002/cber.19681010126

Habermehl, G., and Vogel, G. (1969). Samandinine, a Minor Alkaloid from Salamandra Maculosa Laur. *Toxicon* 7 (2), 163–164. doi:10.1016/0041-0101(69)90080-4

Habermehl, G. (1967). "Chapter 9 the Steroid Alkaloids: The Salamandra Group," in *The Alkaloids: Chemistry and Physiology*. Editor R. H. F. Manske (Academic Press), 427–439. doi:10.1016/s1876-0813(08)60205-5

Habermehl, G. (1964). O-Acetyl-samandarin im Gift von Salamandra Maculosa. *Justus Liebigs Ann. Chem.* 679 (1), 164–167. doi:10.1002/jlac.19646790123

Habermehl, G., and Preusser, H.-J. (1969). Hemmung des Wachstums von Pilzen und Bakterien durch das Hautdrüsensekret von Salamandra maculosa. *Z. für Naturforschung B* 24(12), 1599–1601. doi: doi:doi:10.1515/znb-1969-1220

Habermehl, G. (1971). "Toxicology, Pharmacology, Chemistry, and Biochemistry of Salamander Venom," in *Venomous Animals and Their Venoms*. Editors W. BÜCherl and E. E. Buckley (Academic Press), 569–584. doi:10.1016/b978-0-12-138902-4.50029-5

Hardwicke, J., Schmaljohann, D., Boyce, D., and Thomas, D. (2008). Epidermal Growth Factor Therapy and Wound Healing-Ppast, Present and Future Perspectives. *Surgeon* 6 (3), 172–177. doi:10.1016/S1479-666X(08)80114-X

Heiss, E., Natchev, N., Rabanser, A., Weisgram, J., and Hilgers, H. (2009). Three Types of Cutaneous Glands in the Skin of the Salamandrid *Pleurodeles waltl*. A Histological and Ultrastructural Study. *J. Morphol.* 270 (7), 892–902. doi:10.1002/jmor.10728

Holthausen, D. J., Lee, S. H., Kumar, V. T., Bouvier, N. M., Krammer, F., Ellebedy, A. H., et al. (2017). An Amphibian Host Defense Peptide Is Virucidal for Human H1 Hemagglutinin-Bearing Influenza Viruses. *Immunity* 46 (4), 587–595. doi:10.1016/j.immuni.2017.03.018

Jeckel, A. M., Grant, T., and Saporito, R. A. (2015). Sequestered and Synthesized Chemical Defenses in the Poison Frog *Melanophryniscus moreirae*. *J. Chem. Ecol.* 41 (5), 505–512. doi:10.1007/s10886-015-0578-6

Jenssen, H., Hamill, P., and Hancock, R. E. (2006). Peptide Antimicrobial Agents. *Clin. Microbiol. Rev.* 19 (3), 491–511. doi:10.1128/CMR.00056-05

Jia, J., and Gao, K. Q. (2016). A New Basal Salamandroid (Amphibia, Urodela) from the Late Jurassic of Qinglong, Hebei Province, China. *PLoS One* 11 (5), e0153834. doi:10.1371/journal.pone.0153834

Jiang, W. B., Hakim, M., Luo, L., Li, B. W., Yang, S. L., Song, Y. Z., et al. (2015). Purification and Characterization of Cholecystokinin from the Skin of Salamander *Tylototriton verrucosus*. *Dongwuxue Yanjiu* 36 (3), 174–177.

Jones, T. H., Adams, R. M., Spande, T. F., Garraffo, H. M., Kaneko, T., and Schultz, T. R. (2012). Histrionicotoxin Alkaloids Finally Detected in an Ant. *J. Nat. Prod.* 75 (11), 1930–1936. doi:10.1021/np300485v

Jovaišienė, J., Bakutis, B., Baliukonienė, V., Matusevičius, P., Lipiński, K., Antoszkiewicz, Z., et al. (2017). Biogenic Amines and Mycotoxins Concentrations in Baled Silage from Organic and Conventional Farms. *Arq. Bras. Med. Vet. Zootec.* 69, 269–277. doi:10.1590/1678-4162-9130

Karış, M., Şener, D., Yalçın, H. T., Nalbantsoy, A., and Göçmen, B. (2018). Major Biological Activities and Protein Profiles of Skin Secretions of *Lissotriton vulgaris* and Triturus Ivanbureschi. *Turkish J. Biochem.* 43 (6), 605–612. doi:10.1515/tjb-2017-0306

Knepper, J., Lüddecke, T., Preissler, K., Vences, M., and Schulz, S. (2019). Isolation and Identification of Alkaloids from Poisons of Fire Salamanders (*Salamandra salamandra*). *J. Nat. Prod.* 82 (5), 1319–1324. doi:10.1021/acs.jnatprod.9b00065

Lee, A. C., Harris, J. L., Khanna, K. K., and Hong, J. H. (2019). A Comprehensive Review on Current Advances in Peptide Drug Development and Design. *Int. J. Mol. Sci.* 20 (10). doi:10.3390/ijms20102383

Lelario, F., De Maria, S., Rivelli, A. R., Russo, D., Milella, L., Bufo, S. A., et al. (2019). A Complete Survey of Glycoalkaloids Using LC-FTICR-MS and IRMPD in a Commercial Variety and a Local Landrace of Eggplant (Solanum Melongena L.) and Their Anticholinesterase and Antioxidant Activities. *Toxins (Basel)* 11 (4). doi:10.3390/toxins11040230

Ligabue-Braun, R., and Carlini, C. R. (2015). Poisonous Birds: A Timely Review. *Toxicon* 99, 102–108. doi:10.1016/j.toxicon.2015.03.020

Litescu, S. C., Eremia, S., Diaconu, M., Tache, A., and Radu, G. (2011). *Biosensors Applications on Assessment of Reactive Oxygen Species and Antioxidants*.

Llesuy, S., Evelson, P., Campos, A. M., and Lissi, E. (2001). Methodologies for Evaluation of Total Antioxidant Activities in Complex Mixtures. A Critical Review. *Biol. Res.* 34, 51–73. doi:10.4067/s0716-97602001000200009

Lüddecke, T., Schulz, S., Steinfartz, S., and Vences, M. (2018). A Salamander's Toxic Arsenal: Review of Skin Poison Diversity and Function in True Salamanders, Genus Salamandra. *Naturwissenschaften* 105 (9-10), 56. doi:10.1007/s00114-018-1579-4

Macfoy, C., Danosus, D., Sandit, R., Jones, T. H., Garraffo, H. M., Spande, T. F., et al. (2005). Alkaloids of Anuran Skin: Antimicrobial Function. *Z. Naturforsch C J. Biosci.* 60 (11-12), 932–937. doi:10.1515/znc-2005-11-1218

Makarova, M., Rycek, L., Hajicek, J., Baidilov, D., and Hudlicky, T. (2019). Tetrodotoxin: History, Biology, and Synthesis. *Angew. Chem. Int. Ed. Engl.* 58 (51), 18338–18387. doi:10.1002/anie.201901564

Mangoni, M. L., and Casciaro, B. (2020). Development of Antimicrobial Peptides from Amphibians. *Antibiotics (Basel)* 9 (11). doi:10.3390/antibiotics9110772

Mebs, D., and Pogoda, W. (2005). Variability of Alkaloids in the Skin Secretion of the European Fire Salamander (Salamandra Salamadra Terrestris). *Toxicon* 45 (5), 603–606. doi:10.1016/j.toxicon.2005.01.001

Meng, P., Yang, S., Shen, C., Jiang, K., Rong, M., and Lai, R. (2013). The First Salamander Defensin Antimicrobial Peptide. *PLoS One* 8 (12), e83044. doi:10.1371/journal.pone.0083044

Mookherjee, N., and Hancock, R. E. (2007). Cationic Host Defence Peptides: Innate Immune Regulatory Peptides as a Novel Approach for Treating Infections. *Cell Mol Life Sci* 64 (7-8), 922–933. doi:10.1007/s00018-007-6475-6

Mu, L., Tang, J., Liu, H., Shen, C., Rong, M., Zhang, Z., et al. (2014). A Potential Wound-Healing-Promoting Peptide from Salamander Skin. *FASEB J.* 28 (9), 3919–3929. doi:10.1096/fj.13-248476

Nguyen, L. T., Haney, E. F., and Vogel, H. J. (2011). The Expanding Scope of Antimicrobial Peptide Structures and Their Modes of Action. *Trends Biotechnol.* 29 (9), 464–472. doi:10.1016/j.tibtech.2011.05.001

Nicola, A. M., Albuquerque, P., Paes, H. C., Fernandes, L., Costa, F. F., Kioshima, E. S., et al. (2019). Antifungal Drugs: New Insights in Research & Development. *Pharmacol. Ther.* 195, 21–38. doi:10.1016/j.pharmthera.2018.10.008

Nuding, S., Frasch, T., Schaller, M., Stange, E. F., and Zabel, L. T. (2014). Synergistic Effects of Antimicrobial Peptides and Antibiotics against *Clostridium difficile*. *Antimicrob. Agents Chemother.* 58 (10), 5719–5725. doi:10.1128/AAC.02542-14

Pei, J., and Jiang, L. (2017). Antimicrobial Peptide from Mucus of *Andrias davidianus*: Screening and Purification by Magnetic Cell Membrane Separation Technique. *Int. J. Antimicrob. Agents* 50 (1), 41–46. doi:10.1016/j.ijantimicag.2017.02.013

Pei, J., Feng, Z., Ren, T., Sun, H., Han, H., Jin, W., et al. (2018). *Purification, Characterization and Application of a Novel Antimicrobial Peptide from* Andrias davidianus *Blood*, 1472–765X. (Electronic)).

Peters, B. M., Shirtliff, M. E., and Jabra-Rizk, M. A. (2010). Antimicrobial Peptides: Primeval Molecules or Future Drugs. *Plos Pathog.* 6 (10), e1001067. doi:10.1371/journal.ppat.1001067

Petruczynik, A., Plech, T., Tuzimski, T., Misiurek, J., Kaproń, B., Misiurek, D., et al. (2019). Determination of Selected Isoquinoline Alkaloids from Mahonia Aquifolia; Meconopsis Cambrica; Corydalis Lutea; Dicentra Spectabilis; Fumaria Officinalis; Macleaya Cordata Extracts by HPLC-DAD and Comparison of Their Cytotoxic Activity. *Toxins* 11 (10), 575. doi:10.3390/toxins11100575

Phisalix, M. (1900). *Recherches embryologiques, histologiques et physiologiques sur les glandes à venin de la salamandre terrestre*. Pariséditeurs: Librairie C. Reinwald, Schleicher frères.

Plácido, A., Bueno, J., Barbosa, E. A., Moreira, D. C., Dias, J. D. N., Cabral, W. F., et al. (2020). The Antioxidant Peptide Salamandrin-I: First Bioactive Peptide Identified from Skin Secretion of Salamandra Genus (*Salamandra salamandra*). *Biomolecules* 10 (4). doi:10.3390/biom10040512

Preißler, K., Gippner, S., Lüddecke, T., Krause, E. T., Schulz, S., Vences, M., et al. (2019). More Yellow More Toxic? Sex rather Than Alkaloid Content Is Correlated with Yellow Coloration in the Fire Salamander. *J. Zool* 308 (4), 293–300. doi:10.1111/jzo.12676

Preusser, H. J., Habermehl, G., Sablofski, M., and Schmall-Haury, D. (1975). Antimicrobial Activity of Alkaloids from Amphibian Venoms and Effects on the Ultrastructure of Yeast Cells. *Toxicon* 13 (4), 285–289. doi:10.1016/0041-0101(75)90135-X

Pukala, T. L., Bowie, J. H., Maselli, V. M., Musgrave, I. F., and Tyler, M. J. (2006). Host-defence Peptides from the Glandular Secretions of Amphibians: Structure and Activity. *Nat. Prod. Rep.* 23 (3), 368–393. doi:10.1039/b512118n

Rickrode, T. E., Mueller, C. F., and Taylor, D. (1986). Identification and Antibiotic Activity of Fatty Acids in Dermal Secretions of *Plethodon cinereus*. *Am. Midland Naturalist* 115 (1), 198–200. doi:10.2307/2425850

Roseghini, M., Erspamer, V., and Endean, R. (1976). Indole-, Imidazole- and Phenyl-Alkylamines in the Skin of One Hundred Amphibian Species from Australia and Papua New Guinea. *Comp. Biochem. Physiol. C Comp. Pharmacol.* 54 (1), 31–43. doi:10.1016/0306-4492(76)90022-8

Sampaio de Oliveira, K. B., Leite, M. L., Rodrigues, G. R., Duque, H. M., da Costa, R. A., Cunha, V. A., et al. (2020). Strategies for Recombinant Production of Antimicrobial Peptides with Pharmacological Potential. *Expert Rev. Clin. Pharmacol.* 13 (4), 367–390. doi:10.1080/17512433.2020.1764347

Santos, I. J. M., Melo Coutinho, H. D., Ferreira Matias, E. F., Martins da Costa, J. G., Nóbrega Alves, R. R., and de Oliveira Almeida, W. (2012). Antimicrobial Activity of Natural Products from the Skins of the Semiarid Living Lizards *Ameiva ameiva* (Linnaeus, 1758) and Tropidurus Hispidus (Spix, 1825). *J. Arid Environments* 76, 138–141. doi:10.1016/j.jaridenv.2011.08.005

Saporito, R. A., Donnelly, M. A., Spande, T. F., and Garraffo, H. M. (2012). A Review of Chemical Ecology in Poison Frogs. *Chemoecology* 22 (3), 159–168. doi:10.1007/s00049-011-0088-0

Sheafor, B., Davidson, E. W., Parr, L., and Rollins-Smith, L. (2008). Antimicrobial Peptide Defenses in the Salamander, *Ambystoma tigrinum*, against Emerging Amphibian Pathogens. *J. Wildl. Dis.* 44 (2), 226–236. doi:10.7589/0090-3558-44.2.226

Shen, W., He, P., Xiao, C., and Chen, X. (2018). From Antimicrobial Peptides to Antimicrobial Poly(α-Amino Acid)s. *Adv. Healthc. Mater.* 7 (20), e1800354. doi:10.1002/adhm.201800354

Teranishi, H., Muneoka, Y., Takao, T., Shimonishi, Y., and Kojima, M. (2004). Isolation and Characterization of Four VIP-Related Peptides from Red-Bellied Newt, *Cynops pyrrhogaster*. *Regul. Pept.* 123 (1-3), 173–179. doi:10.1016/j.regpep.2004.04.024

Vences, M., Sanchez, E., Hauswaldt, J. S., Eikelmann, D., Rodríguez, A., Carranza, S., et al. (2014). Nuclear and Mitochondrial Multilocus Phylogeny and Survey of Alkaloid Content in True Salamanders of the Genus Salamandra (Salamandridae). *Mol. Phylogenet. Evol.* 73, 208–216. doi:10.1016/j.ympev.2013.12.009

Vineeth Kumar, T. V., and Sanil, G. (2017). A Review of the Mechanism of Action of Amphibian Antimicrobial Peptides Focusing on Peptide-Membrane Interaction and Membrane Curvature. *Curr. Protein Pept. Sci.* 18 (12), 1263–1272. doi:10.2174/1389203718666170710114932

von Byern, J., Mebs, D., Heiss, E., Dicke, U., Wetjen, O., Bakkegard, K., et al. (2017). Salamanders on the Bench - A Biocompatibility Study of Salamander Skin Secretions in Cell Cultures. *Toxicon* 135, 24–32. doi:10.1016/j.toxicon.2017.05.021

Weitz, G., and Wölfel, E. (1962). The Structure of Salamander Alkaloids. I. On the Structure of Samandarine-Hydrobromide. *Acta Cryst.* 15(5), 484–491. doi:10.1107/S0365110X6200119X

Woodhams, D. C., Rollins-Smith, L. A., Reinert, L. K., Lam, B. A., Harris, R. N., Briggs, C. J., et al. (2020). Probiotics Modulate a Novel Amphibian Skin Defense Peptide that Is Antifungal and Facilitates Growth of Antifungal Bacteria. *Microb. Ecol.* 79 (1), 192–202. doi:10.1007/s00248-019-01385-9

Yeaman, M. R., and Yount, N. Y. (2003). Mechanisms of Antimicrobial Peptide Action and Resistance. *Pharmacol. Rev.* 55 (1), 27–55. doi:10.1124/pr.55.1.2

Zhang, J., Morris-Natschke, S. L., Ma, D., Shang, X. F., Yang, C. J., Liu, Y. Q., et al. (2021). Biologically Active Indolizidine Alkaloids. *Med. Res. Rev.* 41 (2), 928–960. doi:10.1002/med.21747

Zhang, Y., Han, T., Ming, Q., Wu, L., Rahman, K., and Qin, L. (2012). Alkaloids Produced by Endophytic Fungi: A Review. *Nat. Prod. Commun.* 7 (7), 963–968. doi:10.1177/1934578X1200700742

Conflict of Interest: The authors declare that the research was conducted in the absence of any commercial or financial relationships that could be construed as a potential conflict of interest.

Publisher's Note: All claims expressed in this article are solely those of the authors and do not necessarily represent those of their affiliated organizations, or those of the publisher, the editors and the reviewers. Any product that may be evaluated in this article, or claim that may be made by its manufacturer, is not guaranteed or endorsed by the publisher.

frontiers in Pharmacology

OPINION
published: 03 February 2022
doi: 10.3389/fphar.2022.830384

Rodent Lethality Models Are Problematic for Evaluating Antivenoms for Human Envenoming

Anjana Silva[1,2,3], *Wayne C. Hodgson*[2], *Theo Tasoulis*[4] *and Geoffrey K. Isbister*[3,4]*

[1]Department of Parasitology, Faculty of Medicine and Allied Sciences, Rajarata University of Sri Lanka, Saliyapura, Sri Lanka, [2]Monash Venom Group, Faculty of Medicine, Nursing and Health Sciences, Monash University, Clayton, VIC, Australia, [3]South Asian Clinical Toxicology Research Collaboration, University of Peradeniya, Peradeniya, Sri Lanka, [4]Clinical Toxicology Research Group, University of Newcastle, Newcastle, NSW, Australia

Keywords: lethality, snake venom, antivenom, LD50, ED50, rodent, mouse

INTRODUCTION

Snakebite is a major public health problem in the tropics, being closely associated with agricultural economy, poverty and underdevelopment. The neglected nature of the condition over a long period of time has meant that our current understanding of the epidemiology, clinical effects, pathophysiology and the treatment of snakebite has many gaps (Isbister and Silva, 2018). Knowledge of the pathophysiology is essential to understanding the clinical effects of snake envenoming and, more importantly, the response to antivenom.

Snake venoms are a complex mix of different toxins with varying pharmacological properties (Tasoulis and Isbister, 2017). The effects of snake venoms on natural prey species are likely to be different to the effects on non-prey species, such as humans (Richards et al., 2012). Animal models have been important tools for understanding the effects of snake venoms on humans. The action of the whole venom and isolated toxins, and their response to antivenoms, are tested in living laboratory animals, such as rats, mice, and rabbits (*in-vivo*) and tissues isolated from laboratory animals, such as rats, mice, rabbits, frogs, and chickens (*in-vitro*) (Silva and Isbister, 2020). Despite the biochemical and functional complexity of snake venoms observed in animal models, bites by medically important snakes commonly result in a narrow range of acute effects in human envenoming, including local tissue necrosis, venom-induced consumption coagulopathy (VICC), neuromuscular paralysis, acute kidney injury (AKI) and myotoxicity. It is important that animal models used for testing snake toxins, venoms and antivenoms, to better represent human envenoming, mirror the observed clinical effects of human envenoming.

Neutralisation of rodent lethality from snake venoms *in-vivo* has been recommended to manufacturers and regulatory bodies as an essential pre-clinical test of antivenoms by the World Health Organisation (WHO). Mouse lethality prevention assays are considered the "gold standard test" until alternative tests become accepted (World Health Organisation, 2010; Calvete et al., 2018). The WHO further states that the suffering of test animals due to the venom effects until death, or during the 24 or 48 observation period, in the lethality studies outweighed by the larger benefits to humans (World Health Organisation, 2010).

Why Rodent Lethality Models Are Problematic for Evaluating Antivenoms for Human Envenoming?

The majority of snake venoms that cause paralysis in envenomed humans contain pre-synaptic neurotoxins, which cause paralysis that is, not reversible with antivenom (Silva et al., 2017, 2018). The other major group of snake neurotoxins are the post-synaptically acting α-neurotoxins. These toxins are present in venoms from a range of snakes, including many species that do not result in

OPEN ACCESS

Edited by:
Jing-Lin Wang,
Beijing Institute of Microbiology and Epidemiology, China

Reviewed by:
Dexter Tagwireyi,
University of Zimbabwe, Zimbabwe

***Correspondence:**
Geoffrey K. Isbister
geoff.isbister@gmail.com

Specialty section:
This article was submitted to Pharmacology of Ion Channels and Channelopathies, a section of the journal Frontiers in Pharmacology

Received: *07 December 2021*
Accepted: *17 January 2022*
Published: *03 February 2022*

Citation:
Silva A, Hodgson WC, Tasoulis T and Isbister GK (2022) Rodent Lethality Models Are Problematic for Evaluating Antivenoms for Human Envenoming. Front. Pharmacol. 13:830384. doi: 10.3389/fphar.2022.830384

paralysis in humans (Barber et al., 2013; Youngman et al., 2021). The proportion of α-neurotoxins in snake venoms is known to be associated with the prey selectivity of the venoms (Harris et al., 2020), which further suggests that these particular toxins are animal-specific. The two major types of α-neurotoxins, i.e., long-chain (LαNTx) and short-chain (SαNTx), bind to the same region of the α-subunit of the nAChR, resulting in inhibition of neurotransmission at the skeletal neuromuscular junction. Current knowledge about the relevance of snake venom α-neurotoxins in human envenoming and paralysis is largely based on projections from data generated from rodent, avian, and amphibian pharmacological models (Silva et al., 2017). However, using skeletal muscle from several animals, including rodents, non-human primates and humans, a largely neglected study, dating back to 1985, showed that human nAChR have an exceptionally low affinity for SαNTx compared to LαNTx, while both groups bind with high affinity to mouse nAChRs (Ishikawa et al., 1985). Consistent with these observations, in a functional study using human and rat nAChR, we recently demonstrated that the human nAChR is more resistant to snake SαNTx compared to the rat nAChR, as evidenced by marked differences in the speed of the reversibility of toxin-mediated inhibition of the human nAChR (Silva et al., 2018). The experiments, with and without various mutations of the human and rat nAChR, showed that this species difference is due to the absence of large aromatic amino acid residues at positions 187 and 189 in loop C of the α subunit of the human nAChR. This is in contrast to rats, mice, and nAChRs in other animals commonly used for *in-vitro* testing, including *Torpedo californica*, which possess large aromatic amino acid residues at equivalent positions. However, no such difference was observed between the effects of LαNTx on rat and human nAChRs.

Inhibition of the nAChR only requires the binding of one α-neurotoxin molecule to one of the two ACh binding sites on the receptor. Theoretically, paralysis could develop in humans following a snakebite if the concentration of α-neurotoxins at the neuromuscular junction is such that the nAChRs are inhibited and α-neurotoxin-receptor binding could be sustained, without being rapidly reversed naturally. However, sustaining sufficient α-neurotoxin concentrations at the neuromuscular junction to maintain inhibition of the nAChR depends on the relative abundance of the α-neurotoxins in the particular snake venom as well as the amount of venom injected during the snakebite. This means that snakes injecting large amounts of venom when biting humans, and/or having a higher relative abundance of LαNTx in their venoms, such as some species of cobras (*Naja*) or the king cobra (*Ophiophagus hannah*), can potentially cause post-synaptic neurotoxic paralysis in humans. Snakes containing only SαNTx or only small amounts of LαNTx, will not cause paralysis in humans. SαNTxs are unlikely to be clinically important, except in unique situations such as Philippine cobra (*Naja philippinensis*) envenomings in which there is such a large venom load, human paralysis can still occur, despite a higher relative abundance of SαNTx (~45%) (Tan et al., 2019). Therefore, assays heavily influenced by the effects of α-neurotoxins in any animal except humans are not representative of paralysis in humans and are problematic for antivenom development. In agreement with this, recent studies have demonstrated that the outcome of rodent lethality assays are heavily influenced by the α-neurotoxin activity of snake venoms, when α-neurotoxins are present in the venoms (Petras et al., 2011; Pruksaphon et al., 2020).

Rodent lethality prevention assays have shown results comparable to human envenoming in some viperine venoms lacking α-neurotoxins, such as carpet vipers (*Echis* sp.) and south American Bushmasters (*Lachecis* sp.) (Gutiérrez et al., 1988; Bard et al., 1994; Diniz-Sousa et al., 2020). Although α-neurotoxins are mostly found in elapids and colubrids, they are present even in some viperid venoms that do not cause neurotoxicity in humans, such as Puff adders (Wang et al., 2020; Youngman et al., 2021) hence the utility of these assays remains narrow.

There are other examples in which animal models do not represent human envenoming. Plasma from several large animals, including rats, were shown to be resistant to concentrations of procoagulant toxins several orders of magnitude greater compared to humans, from viperids such as *Daboia russelii*, *Echis carinatus*, *Callocellasma rhodostoma* and elapids such as *Pseudonaja textillis*, (Maduwage KP. et al., 2016). This means, in order to replicate VICC in rodent models, the animals need to be exposed to very high venom concentrations, which would lead to the death of animals from the primary and secondary effects of venom that are not relevant to humans (i.e., neurotoxicity). In a recent study, acute kidney injury was not able to be replicated in rats with sub-lethal doses of *D. russelii* venom suggesting it to be a poor model for venom-induced acute kidney injury (Wijewickrama et al., 2018). VICC, AKI and thrombocytopaenia only occurred with experimental venom doses that were unrealistically higher than what is observed in actual human envenomings, making it difficult to match the real-life envenoming scenarios in humans (Tan et al., 2012; Romanelli et al., 2021; Thomazini et al., 2021; Yamamoto et al., 2021).

DISCUSSION

Among the WHO approved list of essential quality control parameters for routine quality control testing of antivenoms, the sole parameter that is used to assess the pharmacological/therapeutic efficacy of antivenom is the lethality neutralisation test (World Health Organisation, 2017; Patra et al., 2021). The WHO guidelines for the production, control and regulation of snake antivenom immunoglobulins, published in 2017, states that "Despite reservations about the physiological relevance of these animal (murine) models to human envenoming and the harm that these *in vivo* assays cause to the animals, they are used by both manufacturers and regulatory authorities worldwide for determining venom lethality (LD_{50}) and antivenom neutralizing capacity (ED_{50}) as these are currently the only validated means of assessing venom toxicity and antivenom neutralizing potency" (World Health Organisation, 2017). Further, it states "Non-sentient or *in vitro* assays as alternatives to the standard venom LD_{50} and antivenom ED_{50} *in vivo* tests have been promoted. Unfortunately, such systems have not been developed to the point where they can fully replace

the above-mentioned preclinical assays." Further, the WHO report states that "in the absence of effective alternatives, the continued use of experimental animals is still justified by the considerable benefits to human health of these preclinical assays" (World Health Organisation, 2017).

The fundamental assumption behind testing venoms, toxins and antivenoms, using rodent lethality models in relation to human envenoming, is that the "toxins possessing the highest rodent lethality are the most medically important toxins in human envenoming" (Lauridsen et al., 2016; Calvete et al., 2018; Silva and Isbister, 2020). This assumption requires evidence that there is a clear relationship between the outcome of rodent lethality tests and clinical toxicity in human envenoming, in venom doses comparable with bites in human envenomings. However, due to the reasons highlighted above, we argue that the relevance of the death or survival of an animal observed in rodent lethality studies, lethality prevention studies or rescue models, to an envenomed human with snakebite is highly questionable. It is not an appropriate model for characterisation of medically important venoms and pre-clinical testing of snake antivenoms. Rodent lethality-based assays cause enormous suffering to the test animals, so the minimal value of these lethality models does not outweigh the suffering of test animals.

The venom composition of snakes varies enormously resulting in different envenoming syndromes in envenomed humans with different clinical outcomes. Reducing the complexity of the effects of snake venoms in humans to a single parameter, the lethality of an experimental animal, is a gross oversimplification. Efficacy assays need to be based on the ability of the antibodies in antivenoms to bind with the venom toxins *in-vitro* and to neutralise or prevent the clinically relevant effects of snake toxins in human envenoming (Maduwage K. et al., 2016). The efficacy of antivenoms in neutralising the clinically most-important systemic effects of envenoming such as neuromuscular paralysis, VICC and myotoxicity could be successfully tested using *in-vitro* functional assays such as neuromuscular preparations that test the neutralisation of clinically relevant pre-synaptic neurotoxins and post-synaptic toxins by antivenom (Silva et al., 2016b; 2016a) and *in-vitro* procoagulant activity neutralisation assays that test the ability of antivenoms to neutralise the procoagulant effects of venoms on human plasma (Maduwage K. et al., 2016). Although the *in-vitro* procoagulant assays are relatively simple to conduct, the *in-vitro* neurotoxicity assays require organ-bath systems and sufficient technical expertise. More ethically appropriate alternative tests such as embryonated egg models have also been introduced, but need validation across a range of snake venoms as well as the relevance to envenoming syndromes in humans (Sells, 2003; Verity et al., 2021).

Rodent lethality models are relatively simple to conduct hence not resource-intensive. They are easy to interpret and are affordable for developing settings (1). While acknowledging the long history and simplicity of rodent LD_{50} and ED_{50} assays, we emphasise that they measure toxic effects that are not necessarily relevant in humans. They do not sufficiently represent envenoming syndromes in humans and have considerable ethical issues. The lack of alternative models does not justify the use of irrelevant and ethically questionable rodent lethality tests.

AUTHOR CONTRIBUTIONS

Conceived the work: AS, GI, and WH; Drafted the article: AS, Critically revised the manuscript: GI, WH, and TT; Acquired funding: GI.

FUNDING

GI received National Health and Medical Research Council (NHMRC) Centers for Research Excellence Grant ID: 1110343 and NHMRC Senior Research Fellowship Grant ID: 1154503.

REFERENCES

Barber, C. M., Isbister, G. K., and Hodgson, W. C. (2013). Alpha Neurotoxins. *Toxicon* 66, 47–58. doi:10.1016/j.toxicon.2013.01.019

Bard, R., Lima, J. C. R. d., Sa Neto, R. P. d., Oliveira, S. G. d., and Santos, M. C. d. (1994). Ineficácia Do antiveneno botrópico na neutralização da atividade coagulante Do veneno de *Lachesis muta* muta: relato de caso e comprovação experimental. *Rev. Inst. Med. Trop. S. Paulo* 36, 77–81. doi:10.1590/s0036-46651994000100012

Calvete, J. J., Rodríguez, Y., Quesada-Bernat, S., and Pla, D. (2018). Toxin-resolved Antivenomics-Guided Assessment of the Immunorecognition Landscape of Antivenoms. *Toxicon* 148, 107–122. doi:10.1016/j.toxicon.2018.04.015

Diniz-Sousa, R., Moraes, J. D. N., Rodrigues-da-Silva, T. M., Oliveira, C. S., and Caldeira, C. A. D. S. (2020). A Brief Review on the Natural History, Venomics and the Medical Importance of Bushmaster (Lachesis) Pit viper Snakes. *Toxicon X* 7, 100053. doi:10.1016/j.toxcx.2020.100053

Gutiérrez, J. M., Chaves, F., Rojas, E., Elizondo, J., Avila, C., and Cerdas, L. (1988). Production of Monovalent Anti-Bothrops asper Antivenom: Development of Immune Response in Horses and Neutralizing Ability. *Rev. Biol. Trop.* 36, 511–517.

Harris, R. J., Zdenek, C. N., Harrich, D., Frank, N., and Fry, B. G. (2020). An Appetite for Destruction: Detecting Prey-Selective Binding of α-Neurotoxins in the Venom of Afro-Asian Elapids. *Toxins (Basel)* 12, 1–12. doi:10.3390/toxins12030205

Isbister, G. K., and Silva, A. (2018). Addressing the Global challenge of Snake Envenoming. *Lancet* 392, 619–620. doi:10.1016/S0140-6736(18)31328-X

Ishikawa, Y., Kano, M., Tamiya, N., and Shimada, Y. (1985). Acetylcholine Receptors of Human Skeletal Muscle: a Species Difference Detected by Snake Neurotoxins. *Brain Res.* 346, 82–88. doi:10.1016/0006-8993(85)91097-2

Lauridsen, L. P., Laustsen, A. H., Lomonte, B., and Gutiérrez, J. M. (2016). Toxicovenomics and Antivenom Profiling of the Eastern green Mamba Snake (Dendroaspis Angusticeps). *J. Proteomics* 136, 248–261. doi:10.1016/j.jprot.2016.02.003

Maduwage, K., Silva, A., O'Leary, M. A., Hodgson, W. C., and Isbister, G. K. (2016b). Efficacy of Indian Polyvalent Snake Antivenoms against Sri Lankan Snake Venoms: Lethality Studies or Clinically Focussed *In Vitro* Studies. *Sci. Rep.* 6, 26778. doi:10.1038/srep26778

Maduwage, K. P., Scorgie, F. E., Lincz, L. F., O'Leary, M. A., and Isbister, G. K. (2016a). Procoagulant Snake Venoms Have Differential Effects in Animal Plasmas: Implications for Antivenom Testing in Animal Models. *Thromb. Res.* 137, 174–177. doi:10.1016/j.thromres.2015.12.002

Patra, A., Herrera, M., Gutiérrez, J. M., and Mukherjee, A. K. (2021). The Application of Laboratory-Based Analytical Tools and Techniques for the Quality Assessment and Improvement of Commercial Antivenoms Used in the Treatment of Snakebite Envenomation. *Drug Test. Anal.* 13, 1471–1489. doi:10.1002/dta.3108

Petras, D., Sanz, L., Segura, A., Herrera, M., Villalta, M., Solano, D., et al. (2011). Snake Venomics of African Spitting Cobras: Toxin Composition and Assessment of Congeneric Cross-Reactivity of the Pan-African EchiTAb-Plus-ICP Antivenom by Antivenomics and Neutralization Approaches. *J. Proteome Res.* 10, 1266–1280. doi:10.1021/pr101040f

Pruksaphon, K., Tan, K. Y., Tan, C. H., Simsiriwong, P., Gutiérrez, J. M., and Ratanabanangkoon, K. (2020). An *In Vitro* α-neurotoxin-nAChR Binding Assay Correlates with Lethality and *In Vivo* Neutralization of a Large Number of Elapid Neurotoxic Snake Venoms from Four Continents. *Plos Negl. Trop. Dis.* 14, e0008581–21. doi:10.1371/journal.pntd.0008581

Richards, D. P., Barlow, a., and Wüster, W. (2012). Venom Lethality and Diet: Differential Responses of Natural Prey and Model Organisms to the Venom of the Saw-Scaled Vipers (Echis). *Toxicon* 59, 110–116. doi:10.1016/j.toxicon.2011.10.015

Romanelli, M. A., Soeiro, P. A., Silva, R. C. D., Taveira-da-Silva, R., Melo, P. A., and Lara, L. S. (2021). Revisiting the Acute Kidney Injury in Wistar Rats Experimentally Envenomated Wity Bothrops Jararacussu Venom. *Toxicon* 199, 117–126. doi:10.1016/j.toxicon.2021.06.004

Sells, P. G. (2003). Animal Experimentation in Snake Venom Research and *In Vitro* Alternatives. *Toxicon* 42, 115–133. doi:10.1016/S0041-0101(03)00125-9

Silva, A., Cristofori-Armstrong, B., Rash, L. D., Hodgson, W. C., and Isbister, G. K. (2018). Defining the Role of post-synaptic α-neurotoxins in Paralysis Due to Snake Envenoming in Humans. *Cell. Mol. Life Sci.* 75, 4465–4478. doi:10.1007/s00018-018-2893-x

Silva, A., Hodgson, W. C., and Isbister, G. K. (2017). Antivenom for Neuromuscular Paralysis Resulting from Snake Envenoming. *Toxins (Basel)* 9, E143. doi:10.3390/toxins9040143

Silva, A., Hodgson, W. C., and Isbister, G. K. (2016a). Cross-Neutralisation of *In Vitro* Neurotoxicity of Asian and Australian Snake Neurotoxins and Venoms by Different Antivenoms. *Toxins (Basel)* 8, 302. doi:10.3390/toxins8100302

Silva, A., and Isbister, G. K. (2020). Current Research into Snake Antivenoms, Their Mechanisms of Action and Applications. *Biochem. Soc. Trans.* 48, 537–546. doi:10.1042/BST20190739

Silva, A., Johnston, C., Kuruppu, S., Kneisz, D., Maduwage, K., Kleifeld, O., et al. (2016b). Clinical and Pharmacological Investigation of Myotoxicity in Sri Lankan Russell's Viper (*Daboia russelii*) Envenoming. *Plos Negl. Trop. Dis.* 10, e0005172. doi:10.1371/journal.pntd.0005172

Tan, C. H., Tan, N. H., Sim, S. M., Fung, S. Y., Jayalakshmi, P., and Gnanathasan, C. A. (2012). Nephrotoxicity of Hump-Nosed Pit viper (Hypnale Hypnale) Venom in Mice Is Preventable by the Paraspecific Hemato Polyvalent Antivenom (HPA). *Toxicon* 60, 1259–1262. doi:10.1016/j.toxicon.2012.08.012

Tan, C. H., Wong, K. Y., Chong, H. P., Tan, N. H., and Tan, K. Y. (2019). Proteomic Insights into Short Neurotoxin-Driven, Highly Neurotoxic Venom of Philippine Cobra (Naja Philippinensis) and Toxicity Correlation of Cobra Envenomation in Asia. *J. Proteomics* 206, 103418. doi:10.1016/j.jprot.2019.103418

Tasoulis, T., and Isbister, G. (2017). A Review and Database of Snake Venom Proteomes. *Toxins (Basel)* 9, 290. doi:10.3390/toxins9090290

Thomazini, C. M., Sachetto, A. T. A., de Albuquerque, C. Z., de Moura Mattaraia, V. G., de Oliveira, A. K., Serrano, S. M. T., et al. (2021). Involvement of von Willebrand factor and botrocetin in the thrombocytopenia induced by *Bothrops jararaca* snake venom. *Plos Negl. Trop. Dis.* 15, e0009715. doi:10.1371/journal.pntd.0009715

Verity, E. E., Stewart, K., Vandenberg, K., Ong, C., and Rockman, S. (2021). Potency Testing of Venoms and Antivenoms in Embryonated Eggs: An Ethical Alternative to Animal Testing. *Toxins* 13, 233–313. doi:10.3390/toxins13040233

Wang, C. R., Bubner, E. R., Jovcevski, B., Mittal, P., and Pukala, T. L. (2020). Interrogating the Higher Order Structures of Snake Venom Proteins Using an Integrated Mass Spectrometric Approach. *J Proteomics* 216, 103680. doi:10.1016/j.jprot.2020.103680

Wijewickrama, E. S., Kurukulasooriya, I., Gunatilake, M., Priyani, A. A., Gnanathasan, A., Gawarammana, I., et al. (2018). Determination of the Sub-lethal Nephrotoxic Dose of Russell's viper (*Daboia russelii*) Venom in Wistar Rats. *Toxicon* 152, 43–45. doi:10.1016/j.toxicon.2018.07.023

World Health Organisation (2017). *Guidelines for the Production , Control and Regulation of Snake Antivenom immunoglobulinsNo. 964)*. in *Replacement of Annex 2 of WHO Technical Report Series*. Geneva, Switzerland.

World Health Organisation (2010). *WHO Guidelines for the Production Control and Regulation of Snake Antivenom Immunoglobulins*. Geneva, Switzerland.

Yamamoto, A., Ito, T., and Hifumi, T. (2021). Attempt to Develop Rat Disseminated Intravascular Coagulation Model Using Yamakagashi (Rhabdophis Tigrinus) Venom Injection. *Toxins (Basel)* 13, 160. doi:10.3390/toxins13020160

Youngman, N. J., Harris, R. J., Huynh, T. M., Coster, K., Sundman, E., Braun, R., et al. (2021). Widespread and Differential Neurotoxicity in Venoms from the Bitis Genus of Viperid Snakes. *Neurotox. Res.* 39, 697–704. doi:10.1007/s12640-021-00330-4

Conflict of Interest: The authors declare that the research was conducted in the absence of any commercial or financial relationships that could be construed as a potential conflict of interest.

Publisher's Note: All claims expressed in this article are solely those of the authors and do not necessarily represent those of their affiliated organizations, or those of the publisher, the editors and the reviewers. Any product that may be evaluated in this article, or claim that may be made by its manufacturer, is not guaranteed or endorsed by the publisher.

frontiers in Pharmacology

ORIGINAL RESEARCH
published: 11 February 2022
doi: 10.3389/fphar.2022.810611

The Pore-Forming Subunit C2IIa of the Binary *Clostridium botulinum* C2 Toxin Reduces the Chemotactic Translocation of Human Polymorphonuclear Leukocytes

*Julia Eisele[1,2†], Simone Schreiner[1†], Joscha Borho[1†], Stephan Fischer[1], Sebastian Heber[1], Sascha Endres[1], Maximilian Fellermann[1], Lisa Wohlgemuth[3], Markus Huber-Lang[3], Giorgio Fois[2], Michael Fauler[2], Manfred Frick[2] and Holger Barth[1]**

[1]Institute of Pharmacology and Toxicology, Ulm University Medical Center, Ulm, Germany, [2]Institute of General Physiology, Ulm University, Ulm, Germany, [3]Institute of Clinical and Experimental Trauma Immunology, Ulm University Medical Center, Ulm, Germany

The binary C2 toxin of *Clostridium* (*C.*) *botulinum* consists of two non-linked proteins, the enzyme subunit C2I and the separate binding/transport subunit C2II. To exhibit toxic effects on mammalian cells, proteolytically activated C2II (C2IIa) forms barrel-shaped heptamers that bind to carbohydrate receptors which are present on all mammalian cell types. C2I binds to C2IIa and the toxin complexes are internalized via receptor-mediated endocytosis. In acidified endosomal vesicles, C2IIa heptamers change their conformation and insert as pores into endosomal membranes. These pores serve as translocation-channels for the subsequent transport of C2I from the endosomal lumen into the cytosol. There, C2I mono-ADP-ribosylates G-actin, which results in depolymerization of F-actin and cell rounding. Noteworthy, so far morphological changes in cells were only observed after incubation with the complete C2 toxin, i.e., C2IIa plus C2I, but not with the single subunits. Unexpectedly, we observed that the non-catalytic transport subunit C2IIa (but not C2II) alone induced morphological changes and actin alterations in primary human polymorphonuclear leukocytes (PMNs, *alias* neutrophils) from healthy donors *ex vivo*, but not macrophages, epithelial and endothelial cells, as detected by phase contrast microscopy and fluorescent microscopy of the actin cytoskeleton. This suggests a PMN selective mode of action for C2IIa. The cytotoxicity of C2IIa on PMNs was prevented by C2IIa pore blockers and treatment with C2IIa (but not C2II) rapidly induced Ca^{2+} influx in PMNs, suggesting that pore-formation by C2IIa in cell membranes of PMNs is crucial for this effect. In addition, incubation of primary human PMNs with C2IIa decreased their chemotaxis *ex vivo* through porous culture inserts and in co-culture with human endothelial cells which is closer to the physiological extravasation process. In conclusion, the results suggest that C2IIa is a PMN-selective inhibitor of chemotaxis. This provides new knowledge for a pathophysiological role of C2 toxin as a modulator of innate immune cells and makes C2IIa an attractive candidate for the development of novel pharmacological strategies to selectively down-modulate the excessive and detrimental PMN recruitment into organs after traumatic injuries.

Keywords: binary C2 toxin, *Clostridium botulinum*, transport subunit C2IIa, trans-membrane channel, polymorphonuclear leukocytes, chemotaxis, migration

OPEN ACCESS

Edited by:
Jean-Marc Sabatier, Aix-Marseille Université, France

Reviewed by:
Kausik Chattopadhyay, Indian Institute of Science Education and Research Mohali, India
Michel R. Popoff, Institut Pasteur, France
Xuehua Xu, National Institute of Allergy and Infectious Diseases (NIH), United States

****Correspondence:***
Holger Barth
holger.barth@uni-ulm.de

[†]These authors have contributed equally to this work

Specialty section:
This article was submitted to Pharmacology of Ion Channels and Channelopathies, a section of the journal Frontiers in Pharmacology

Received: *07 November 2021*
Accepted: *24 January 2022*
Published: *11 February 2022*

Citation:
Eisele J, Schreiner S, Borho J, Fischer S, Heber S, Endres S, Fellermann M, Wohlgemuth L, Huber-Lang M, Fois G, Fauler M, Frick M and Barth H (2022) The Pore-Forming Subunit C2IIa of the Binary Clostridium botulinum C2 Toxin Reduces the Chemotactic Translocation of Human Polymorphonuclear Leukocytes. Front. Pharmacol. 13:810611. doi: 10.3389/fphar.2022.810611

INTRODUCTION

The C2 toxin of *Clostridium* (*C.*) *botulinum* is the prototype of the family of binary actin ADP-ribosylating toxins (Ohishi, 1983b; Aktories et al., 1986; Stiles et al., 2014). C2 toxin consists of two separate, non-linked proteins, which are secreted by the bacteria and assemble in solution or on the surface of eukaryotic target cells to form biologically active toxin complexes (Ohishi, 1983a; Ohishi et al., 1984; Ohishi and Miyake, 1985; Kurazono et al., 1987; Ohishi and Yanagimoto, 1992; Barth et al., 2000). One toxin subunit is the enzymatically active protein C2I (~50 kDa) (Aktories et al., 1986; Fuji et al., 1996; Barth et al., 1998a; Barth et al., 1998b), the other one is the binding/transport subunit C2II (~80 or ~100 kDa, depending on the *C. botulinum* strain) (Ohishi, 1987; Barth et al., 2000; Sterthoff et al., 2010). It was observed earlier by various groups that only the combination of C2I and C2II, but not the single subunits alone had cytotoxic effects when applied to cultured cells (Ohishi, 1983a; Ohishi et al., 1984; Barth et al., 1998a; Barth et al., 1998b; Barth et al., 2000) and the combination of C2I and C2IIa induced delayed caspase-dependent cell death in dividing cultured cells after 24–48 h (Heine et al., 2008).

We and others investigated the role of C2II in detail and found that the protein consists of four functionally different domains (Schleberger et al., 2006): The N-terminal domain 1 contains a cleavage site for proteases (Ohishi, 1987; Barth et al., 2000), domain 2 serves as binding site for C2I (Kaiser et al., 2006; Schleberger et al., 2006; Lang et al., 2008), domain 3 is crucial for membrane insertion (Blöcker et al., 2003; Knapp et al., 2016) and the C-terminally located domain 4 binds to the receptor on the surface of target cells (Blöcker et al., 2000). Limited proteolysis by host proteases removes a ~20 kDa peptide from the N-terminal domain of C2II, which generates the biologically active species C2IIa (Ohishi, 1987; Barth et al., 2000). C2IIa, but not C2II, forms barrel-shaped heptamers (Barth et al., 2000), which bind to complex and hybrid carbohydrate receptors on cells, which are present on all mammalian cell types (Eckhardt et al., 2000). Therefore, all cell types bind C2IIa and are sensitive towards C2 toxin. Moreover, C2IIa but not C2II forms pores in lipid bilayer membranes *in vitro* (Schmid et al., 1994). C2I binds to C2IIa but not to C2II (Barth et al., 2000; Kaiser et al., 2006), and subsequently the C2I/C2IIa complexes are internalized into cells via receptor-mediated endocytosis (Barth et al., 2000; Nagahama et al., 2009; Pust et al., 2010; Takehara et al., 2017). Noteworthy, C2IIa alone is also internalized by endocytosis (Nagahama et al., 2017). Following endocytosis of the C2IIa/C2I complexes, C2IIa mediates the release of C2I from early acidic endosomes into the cytosol (Barth et al., 2000; Barth et al., 2002). According to the current model, driven by the acidic conditions in the endosomal lumen, C2IIa heptamers change their conformation, insert into the endosomal membranes and form trans-membrane pores, which serve as translocation-channels for the transport of C2I across the endosomal membrane (Barth et al., 2000; Bachmeyer et al., 2001; Blöcker et al., 2003a; Blöcker et al., 2003b). In the cytosol, C2I mono-ADP-ribosylates G-actin at position arginine-177 (Aktories et al., 1986; Vandekerckhove et al., 1988), which turns G-actin into a capping protein that prevents further addition of G-actin to the growing end of actin filaments (Aktories et al., 1989; Uematsu et al., 2007). This results in depolymerization of F-actin and cell-rounding, which leads to a breakdown of biological barriers *in vivo* (Ohishi, 1983a; Ohishi, 1983b; Kurazono et al., 1987).

Recently, the initial steps of the internalization of C2 toxin were investigated in more detail by Nagahama and co-workers. According to their model built on observations in MDCK cells, binding of C2IIa to cells triggers a series of events resulting in the generation of microdomains in the plasma membrane, which facilitate the uptake of C2 toxin. Taken together, after binding to cells, a portion of cell-bound C2IIa forms pores in the plasma membrane, which causes Ca^{2+} influx into the cells (Nagahama et al., 2021). This Ca^{2+} influx triggers lysosomal exocytosis of enzymes including the cysteine protease cathepsin B (Nagahama et al., 2021). Cathepsin B activates acid sphingomyelinase, which hydrolyzes sphingomyelin and converts it to ceramide, thereby generating ceramide-rich microdomains in the plasma membranes that bud into cells, generate endosomal vesicles and thereby facilitate C2 toxin endocytosis (Nagahama et al., 2017). Moreover, this group reported that cells were protected from C2 toxin in the presence of inhibitors against acid sphingomyelinase and in the absence of calcium (Nagahama et al., 2017). Treatment of cells with heat-inactivated C2IIa or the neutralization of C2IIa with a specific antibody did not result in the production of ceramide (Nagahama et al., 2017). Thus, the authors concluded that C2IIa is essential to induce Ca^{2+} influx, lysosomal exocytosis, and finally endocytosis of C2 toxin, which extends the functions of C2IIa.

However, in previous studies, no morphological changes or cytotoxic effects were observed when cells were incubated with C2IIa in the absence of C2I (Ohishi, 1983a; Ohishi et al., 1984; Barth et al., 1998a; Barth et al., 1998b; Barth et al., 2000; Heine et al., 2008), suggesting that the pore formation in the plasma membrane does not result in cytotoxicity and might be limited to trigger toxin uptake. In the present study, we investigated the effect of C2IIa on cells in more detail using primary human PMNs. It was reported earlier that complete C2 toxin (C2IIa + C2I) inhibits migration of activated human neutrophils *ex vivo* (Norgauer et al., 1988) and that treatment of human PMNs with C2IIa + C2I, but not with C2IIa or C2I alone rapidly inhibited signal transduction via the N-formyl peptide receptor (Norgauer et al., 1989; Grimminger et al., 1991). Our results revealed that treatment of these cells with C2IIa alone, but not with the biologically inactive precursor C2II, caused obvious morphological changes and alterations in the actin cytoskeleton, which were prevented by C2IIa pore blockers. Moreover, incubation of primary human PMNs with C2IIa induced Ca^{2+} influx into the cytosol and decreased their chemotaxis through porous cell-culture inserts in the absence and presence of barrier-forming, co-cultured human endothelial cells *ex vivo*. In line with earlier studies,

there were no detectable effects of C2IIa on the morphology or viability of human endothelial and epithelial cells or macrophages.

MATERIALS AND METHODS

Purification of C2I and C2II and Activation of C2IIa

E. coli BL21 were transformed with pTRC99A:His_C2II, in which the amino acids ENLYFQ have been inserted C-terminally after Lys-181 to increase the efficiency of activation to C2IIa at 4°C. Five millilitre of LB-medium (1% tryptone, 0.5% yeast extract, 1% NaCl and 100 µg/ml ampicillin) were inoculated with a single colony and incubated at 37°C and 180 rpm for 5 h. A 150 ml LB-medium over-night culture was inoculated with the 5 ml preculture and incubated under the same conditions. 4 × 1l of main culture were each inoculated with 30 ml of the overnight culture and grown to an OD_{600} of 0.6 under the same conditions. Expression of His_C2II was induced by addition of 0.5 mM Isopropyl β-d-1-thiogalactopyranoside and performed at 16°C and 180 rpm overnight. The bacteria were harvested by centrifugation at 5,500 rcf and 4°C for 10 min and resuspended in 40 ml of NPI-20 (50 mM NaH_2PO_4, 300 mM NaCl, 20 mM imidazole, pH 8.0). 1% phenylmethylsulfonyl fluoride (100 mM in Ethanol) was added for protease inhibition. Bacteria were lysed by sonication (10 × 20 s pulses with 30 s breaks). The lysate was centrifuged at 13,000 rcf and 4°C for 20 min. The supernatant containing the protein of interest was filtered through 0.2 µm syringe filters and incubated overnight at 4°C with 1 ml bed-volume of PureCube 100 INDIGO Ni-agarose (Cube Biotech, Monheim am Rhein, Germany). Midi Plus columns (Cube Biotech, Monheim am Rhein, Germany) were used for protein extraction from Ni-agarose according to the instructions of the manufacturer at 4°C. NPI-20 was used as washing- and equilibration-buffer, NPI-250 (50 mM NaH_2PO_4, 300 mM NaCl, 250 mM imidazole, pH 8.0) was used as elution buffer. Fractions were analyzed by SDS-PAGE with subsequent Coomassie-staining. The fractions with high His_C2II concentration and low levels of impurities were combined. The protein was rebuffered in PBS (137 mM NaCl, 2.7 mM KCl, 8 mM Na_2HPO_4, 1.8 mM KH_2PO_4, pH 7.4) to a dilution factor <1:1,000 and concentrated by centrifugation (Vivaspin 20, 30.000 MWCO; Sartorius, Göttingen, Germany). The protein was frozen in liquid N_2 and stored at −80°C until activation. For proteolytic activation, the protein was thawed on ice. Trypsin was added to a stochastic ratio of 2:3 (n(trypsin):n(His_C2II)) and incubated for 15 min at 4°C for activation of His_C2II to C2IIa. Trypsin activity was inhibited by addition of an equal amount of trypsin inhibitor (m(trypsin) = m(trypsin inhibitor)) and incubation on ice for 1 h. Aggregated C2IIa was removed by centrifugation at 21,000 rcf for 10 min at 4°C. C2IIa purity and concentration was analyzed by SDS-PAGE with subsequent Coomassie staining and densitometric analysis. C2I was purified as described earlier (Barth et al., 1998b). The purity and identity of C2I, C2II and C2IIa were confirmed by SDS-PAGE and Western blotting with specific antibodies against C2I and C2II as described before (Barth et al., 1998b; Barth et al., 2000).

Cell Culture

Human umbilical vein endothelial cells (HUVEC) were obtained from ATCC® (Manassas, Virginia, United States) and maintained in Endothelial Cell Growth Medium MV2 containing 10% Growth Medium MV2 Supplement Mix (both PromoCell, Heidelberg, Germany) and 1% penicillin/streptomycin (Thermo Fisher Scientific, Ulm, Germany) at 37°C and 5% CO_2. For chemotaxis assays, HUVECs were seeded on 0.3 cm^2 translucent cell-culture inserts with a pore size of 3 µm (Sarstedt, Nümbrecht, Germany) coated with huAEC Coating Solution (InSCREENeX, Braunschweig, Germany) at a density of 5 × 10^4 cells/insert. Chemotaxis assays were performed between 48 and 72 h after seeding, when transendothelial electrical resistances of at least 15 Ω cm^2 (cellZscope, nanoAnalytics, zMünster, Germany) were reached. HUVEC were used in experiments until passage 9.

HeLa cells were obtained from DSMZ (Braunschweig, Germany) and maintained in Minimal Essential Medium (MEM) supplemented with 10% fetal calf serum (FCS), 1% Penicillin-Streptomycin, 1 mM Sodium Pyruvate, 0.1 mM MEM NEAA (all Thermo Fisher Scientific, Ulm, Germany) and 2 mM L-glutamine (Biochrom GmbH, Berlin, Germany) at 37°C and 5% CO_2. For cell seeding, see section *Cytotoxicity and Cell Viability Assays*.

Murine macrophage-like J774A.1 cells were obtained from DSMZ (Braunschweig, Germany) and maintained in Dulbecco's Modified Eagle's Medium (DMEM) containing 10% FCS, 1% penicillin/streptomycin, 0.1 mM MEM NEAA (all from Thermo Fisher Scientific, Ulm, Germany) and 2 mM L-glutamine (Biochrom GmbH, Berlin, Germany) at 37°C and 5% CO_2. For cell seeding, see section *Cytotoxicity and Cell Viability Assays*.

Isolation of Human Polymorphonuclear Cells (PMN)

PMNs were isolated from blood of healthy volunteers (ethics votum 24/16 of the Local Independent Ethics Committee of the University of Ulm). PMNs were purified using OptiPrep™ (Alere Technologies AS, Oslo, Norway) density gradient-medium following modified methods of the application sheet C12 (OptiPrep™ Application Sheet C12; 8th edition, January 2020) under endotoxin-free conditions. Isolation was performed at room temperature. One millilitre of 6% high-molecular weight dextran solution (Sigma-Aldrich, Hamburg, Germany) was added to 9 ml of freshly drawn blood, collected using S-Monovette® 7.5 ml K3 EDTA and Safety-Multifly®-Needle (both Sarstedt, Nümbrecht, Germany) and mixed by several very gentle inversions. After 40 min, the supernatant (leukocyte-rich plasma) was aspirated and layered over a density gradient. For this purpose, two centrifugation media with densities of 1.077 g/ml and 1.090 g/ml were prepared by mixing OptiPrep™-medium with appropriate amounts of BSS-A

(balanced salt solution A: 136.21 mM NaCl, 5.55 mM (D+)-glucose, 2.7 mM phosphate buffer, 10.65 mM HEPES, 5.4 mM KCl, pH 7.4 at room temperature, 285–295 mosmol/kg). After centrifugation (800 rcf, 25 min), polymorphonuclear leukocytes (PMN) were harvested from the lower interface of the gradient layer and gently diluted with an equal volume of BSS, followed by centrifugation for 10 min at 300 rcf. The pellet was resuspended in 5 ml RPMI Medium 1640 HEPES (IrvineScientific, Santa Ana, United States) with 10% FBS (Gibco by Thermo Fisher Scientific, Waltham, Massachusetts, United States). Cells were stained with calcein AM (Thermo Fisher Scientific, Ulm, Germany) at a final concentration of 200 nM for 20 min in the dark. Counting was performed using Countess™ II FL (Thermo Fisher Scientific, Ulm, Germany). PMN cell suspensions were adjusted to a density of 4×10^4 cells/µl with BSS-B (Balanced Salt Solution B: 132.79 mM NaCl, 5.55 mM (D+)-Glucose, 2.6 mM Phosphate buffer, 10.3 mM HEPES, 5.2 mM KCl, 1.9 mM $CaCl_2$, 1.3 mM $MgSO_4$., pH 7.0 at 37°C, 290 mosmol/kg). PMN isolations had a purity above 88% (mean 94.0% ± SD 4.4%) as confirmed by cytospin preparations (THARMAC® Laboratory Solutions, Wiesbaden, Germany) and Pappenheim-staining using the Hemacolor® staining kit (Merck, Darmstadt, Germany) according to the manufacturer's instructions.

Cytotoxicity and Cell Viability Assay

For morphology- and viability-based assays, cells were seeded (100 µl/well; HeLa: 4.25×10^4 cells/ml, HUVEC: 7.5×10^4 cells/ml, J774A.1: 7.7×10^4 cells/ml, PMNs: 5×10^5 cells/ml) in 96 well plates. HeLa and J774A.1 cells were grown for 1 day, HUVECs for 3 days, and PMNs (in RPMI Medium 1640 HEPES with 10% FBS) were seeded directly prior to the experiment. For intoxication, the medium was exchanged with fresh medium (100 µl) containing the respective toxin components at indicated concentrations and the cells were incubated at 37°C and 5% CO_2 for indicated time periods. To analyze morphological changes in cells, images were acquired on a LEICA DMi1 microscope (Leica Microsystems CMS GmbH, Wetzlar, Germany) connected to a LEICA MC170 HD camera (Leica Microsystems Ltd, Heerbrugg, Switzerland). Morphologically changed cells (defined as those cells that look substantially different from the majority of cells in the untreated control) were counted using neuralab software (Neuralab.de) and their percentage on the total number of cells per picture (one picture per well, three wells per condition) was calculated. Cell viability was determined by using the Cell Titer 96® AQueous One Solution Cell Proliferation Assay (MTS) from Promega (Walldorf, Germany), according to the manufacturer's instructions. Mock- and DMSO [20% (v/v)]-treated cells served as negative and positive control for cell viability, respectively. Following an incubation period of 24 h at 37°C, MTS [3-(4,5-dimethylthiazol-2-yl)-5-(3-carboxymethoxyphenyl)-2-(4-sulfophenyl)-2H-tetrazolium] was added to the medium of each well and the absorption was measured after 1 h at 490 nm using a microtiter plate reader.

Flow Cytometry Analysis of PMNs

Primary human PMNs were resuspended in phosphate-buffered saline containing calcium and magnesium (PBS, Gibco Thermo Fisher, Darmstadt, Germany) that was titrated to a physiological pH of 7.3. The cell concentration was adjusted to 2×10^6 cells/ml. PMNs were either incubated with phosphate buffer (PBS, for control), with N-formyl-Met-Leu-Phe (fMLF, 1 µM), C2I (1 µg/ml), C2IIa (2 µg/ml), or the combination of fMLF (1 µM) with either C2I (1 µg/ml) or C2IIa (1 µg/ml). PMNs were incubated at 37°C and measured after 5, 30, and 60 min using a Canto II flow cytometer (BD Biosciences, Heidelberg, Germany) as previously described (Hug et al., 2021). Doublets were excluded based on the linearity of the forward scatter area (FSC-A) and height. PMNs consisting mainly of neutrophils (at least 5×10^3 cells/measurement) were identified based on their FSC and side scatter properties.

Analysis of Cytosolic Ca^{2+} by Flow Cytometry

Cells were suspended at a density of 1×10^7 cells/ml in FACS buffer (143 mM NaCl, 6 mM KCl, 1 mM $MgSO_4$, 20 mM HEPES/NaOH, pH 7.4, 1 mM $CaCl_2$, and 5.6 mM glucose) and incubated for 45 min at 37°C and 10% CO_2 with 5 µM Indo-1-AM (I1223, Thermo Fisher Scientific, Waltham, Massachusetts, United States). The Ca^{2+} measurements were performed on a BD FACS Celesta™. In brief, 1×10^6 cells/sample in 0.5 ml of FACS buffer were pre-warmed for 10 min at 37°C. Next, the baseline intracellular cytosolic Ca^{2+} concentration ($[Ca^{2+}]_i$) was measured for 2 min before addition of C2IIa (5 µg/ml), C2II (5 µg/ml) or C2I (1 µg/ml). After an additional 4 min, 2 µM ionomycin (I0634, Sigma-Aldrich, Hamburg, Germany), a Ca^{2+}-selective ionophore (Beeler et al., 1979), was added to the samples to obtain maximum $[Ca^{2+}]_i$. Cells were kept at 37°C prior and during their injection from the sample tube into the flow cytometer instrument. The fluorescence ratio of Indo-1 violet (emission wavelength about 400 nm, Ca^{2+}-bound) to Indo-1 blue (emission wavelength about 475 nm; Ca^{2+}-free) following excitation at about 355 nm was measured by using FACSDiva™ software (BD Biosciences). For data evaluation, the experimental results contained in FCS files generated by the FACSDiva™ software (BD Biosciences) were imported into FlowJo™ v10.8 Software (BD Life Sciences) and analyzed using FlowJo™ kinetics platform. The individual points of the curves shown in **Figure 3A** correspond to the times in full seconds *versus* the medians of all fluorescence ratios representing $[Ca^{2+}]_i$, following normalization according to the maximal values reached after addition of 2 µM ionomycin.

Chemotaxis-Transmigration Assays With Human PMNs

0.3 cm^2 translucent cell-culture inserts with a pore size of 3 µm were coated with human fibronectin (1% solution in PBS, Advanced BioMatrix, Carlsbad, United States). 2×10^5 calcein AM stained PMNs were seeded in BSS-B into cell culture inserts (pore size 3 µm, Sarstedt, Nümbrecht, Germany) placed in 24 well plates (Greiner Bio-One, Kremsmünster, Austria) containing BSS-B. Cells were incubated for 2 h at 37°C in the presence or absence of C2IIa (2 µg/ml), C2I (1 µg/ml), the binary toxin (2 µg/ml C2IIa + 1 µg/

ml C2I) or cytochalasin B (5 µg/ml) (Sigma-Aldrich, Hamburg, Germany), serving as a positive migration-inhibitory control.

For transmigration assays through endothelial cell layers, control or toxin-treated PMNs were seeded on HUVEC monolayers with transendothelial resistances of at least 15 Ω cm^2 (see section *Cell Culture*) subsequently to pre-incubation of HUVECs with TNFα (10 ng/ml, Biomol, Hamburg, Germany). All measurements were performed in BSS-B.

Calcein fluorescence was repetitively measured from the top using a Tecan Infinite® M200 plate reader (Tecan Group, Männedorf, Switzerland) at 37°C (excitation 470–475 nm, emission measured at 513 nm after a lag time of 2 µs). fMLF (10 nM, Sigma-Aldrich, Hamburg, Germany) was applied to the lower chamber to trigger chemotaxis. Final volumes were 100 µl or 500 µl in the upper or lower compartments, respectively.

The chemoattractant fMLF triggered chemotaxis from the upper to the lower compartment of cell culture inserts. Therefore, the upper calcein-fluorescence signal declined with the transmigration of calcein-stained PMN through the membrane. Fluorescence data were normalized to the initial fluorescence intensity. Statistical analysis was performed for steady-state values after 90–95 min.

Measurement of the Effect of Binary C2 Toxin and Its Single Components on PMN Membrane Integrity

Isolated calcein-stained PMNs were seeded on a µ-slide 8 well slide (Ibidi) at a concentration of 1×10^5 cells/well. Cells were incubated for 1 h in bath solution (140 mM NaCl, 5 mM KCl, 1 mM $MgCl_2$, 2 mM $CaCl_2$, 5 mM glucose, 10 mM Hepes, pH 7.4) at 37°C 5% CO_2 to allow them to settle at the bottom of the well. Live cell fluorescence imaging was performed on an iMic digital microscope (Till Photonics, Germany) using a 488 nm excitation filter. Images were acquired with a 20x uPlanSapo objective (Olympus, Japan) at a rate of 0.3 Hz using iMic Online Analysis software (Till Photonics) for 30 min after stimulation with C2IIa (2 µg/ml), C2I (1 µg/ml), the binary C2 toxin (2 µg/ml C2IIa + 1 µg/ml C2I), ionomycin (2 µM, Sigma Germany) or saponin [0.2% (w/v)]. Images were captured for 30 min after stimulation at a rate of 0.3 Hz. Acquired images were analysed with FIJI software (Schindelin et al., 2012). Briefly, image stacks were aligned to compensate movement, subsequently images were background subtracted and a region of interest (ROI) was drawn around each cell and fluorescence was measured for each ROI in all images of the stack. Cells moving out of their ROI were excluded from the analysis. Further analysis was performed in Excel (Microsoft Office 365). Data was normalized to the average fluorescence intensity before treatment. Values before treatment (F0) and after 30 min (F30) were compared.

Assessment of Barrier-Integrity of Endothelial Cell Monolayers

In some transmigration experiments through HUVEC cell monolayers, fluorescence-labelled dextrans were added to the upper compartment. A damage of the endothelial cell layer, e.g., eventually caused by PMN transmigration, leads to an increased diffusion of dextrans to the lower compartment. Alexa Fluor™ 647-labelled 10 kDa and Texas Red™-labelled 70 kDa dextrans (both Thermo Fisher Scientific, Ulm, Germany) were added at final concentrations of 5 and 25 µg/ml, respectively. Fluorescence signals were measured with the top sensor of the Tecan Infinite M200 in addition to the calcein signal from PMN transmigration (see section *Chemotaxis-Transmigration Assay*). Raw fluorescence data was normalized to respective initial values. A stronger decline of normalized fluorescence intensity was interpreted as increased diffusion.

Statistics

Data was analyzed with Microsoft Excel (Microsoft Office 365) and GraphPad Prism 7 and 9 (GraphPad Software, San Diego, California, United States). Statistical significance was tested by applying the Kruskal–Wallis test with Dunn's correction for multiple comparison if not otherwise indicated in figure legends. *p*-values below 0.05 were considered statistically significant.

RESULTS

Treatment With C2IIa Results in a Changed Morphology of Primary Human PMNs

The identity of the recombinant proteins C2I, C2II and C2IIa that were prepared for the experiments was confirmed by SDS-PAGE and Western blotting (**Supplementary Figure S1**). To analyze whether treatment with C2IIa has an effect on PMNs, cells were prepared from blood of healthy donors and incubated for 3 h in the presence or absence of C2IIa. In parallel, cells were incubated with C2IIa + C2I to confirm that these cells are sensitive for C2 toxin and able to bind and internalize C2IIa. As further control, cells were incubated with C2I alone. The morphology of the cells was documented by phase contrast microscopy and the percentage of morphologically altered cells quantified from the pictures. As shown in **Figure 1A**, cells treated with complete C2 toxin showed an altered morphology, which was in line with earlier observations (Barth et al., 1998a; Barth et al., 1998b; Barth et al., 2000; Heine et al., 2008). As expected, cells treated with C2I alone did not change their morphology compared to untreated control cells. However, the cells treated with C2IIa alone showed an altered morphology, which was also observed by fluorescence microscopy of the actin cytoskeleton (**Figure 1B**) and this effect was time- and concentration-dependent (**Figure 1C**, **Supplementary Figure S2**). Untreated cells did not change their morphology over time and remained on a basal level (see **Figures 1A**, **2B**, **Supplementary Figure S2**). Additionally, the effect of C2IIa on human PMNs was analyzed by flow cytometry (**Figure 1D**). C2IIa but not C2I rapidly changed the size/morphology of PMNs. Moreover, C2IIa had no significant additional effect on the cellular size of PMNs that were at the same time stimulated with fMLF and C2IIa.

Cells were protected from C2IIa-induced morphological changes when they were incubated with C2IIa in the presence

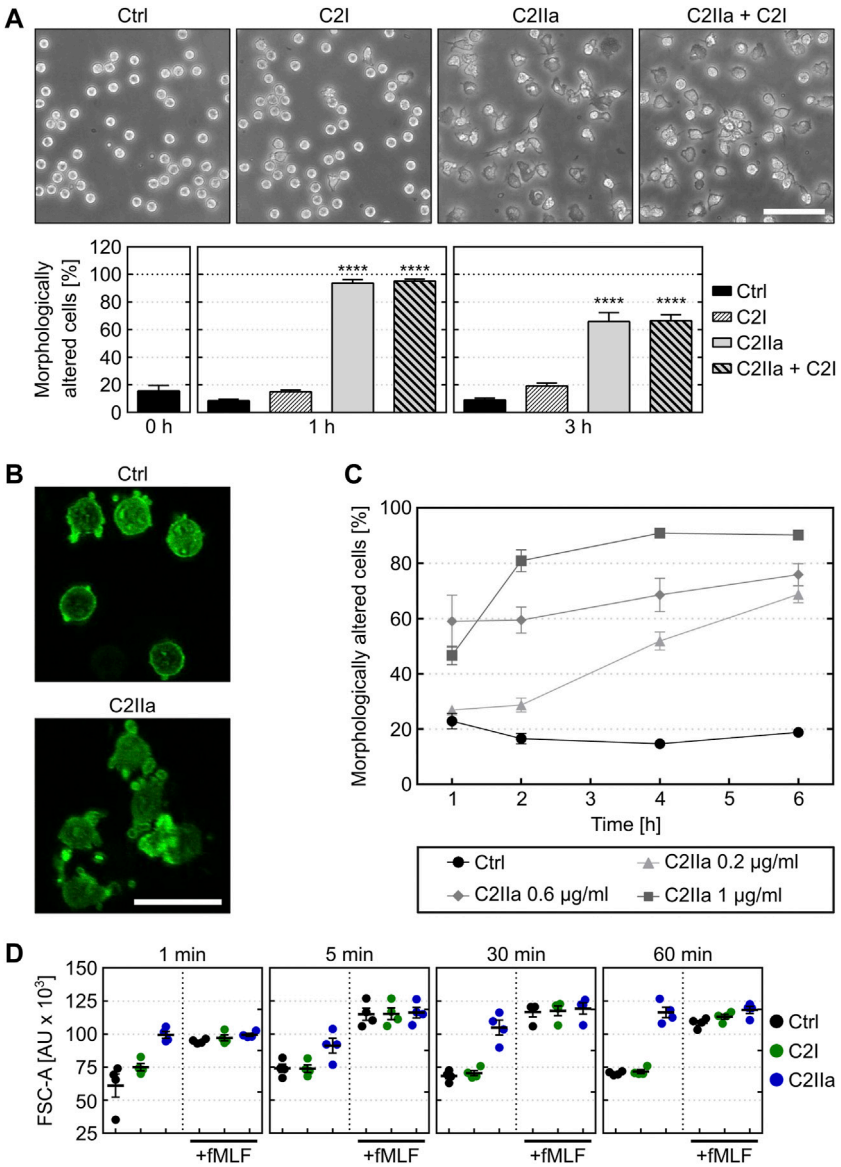

FIGURE 1 | Effect of C2IIa on the morphology of primary human neutrophils (PMNs) ex vivo. **(A)** Upper panel: Representative pictures show the morphology of PMNs incubated for 3 h at 37°C with C2IIa (2 µg/ml), C2I (1 µg/ml), both components (2 µg/ml C2IIa + 1 µg/ml C2I) or without any protein as control (Ctrl). Scale bar: 100 µm. Lower panel: Quantitative evaluation of morphologically altered PMNs after 1 and 3 h treatment at 37°C with C2IIa (2 µg/ml), C2I (1 µg/ml), both components (2 µg/ml C2IIa + 1 µg/ml C2I) or without any protein as control (Ctrl). Data show the results of 5 independent experiments, each with 3 technical replicates. Values represent the mean ± SEM (n = 15). Significance was tested against the untreated control (Ctrl) at each individual respective time point using Kruskal–Wallis test with Dunn's correction for multiple comparison (****$p < 0.0001$). Untreated cells (Ctrl) did not change their morphology over the time course of the experiment. At time point 0, all cells showed the same morphology as the untreated control cells when the respective proteins were applied to the individual groups of the cells. **(B)** Representative pictures of actin-stained (phalloidin-FITC) PMNs after 3 h incubation at 37°C with 1 µg/ml C2IIa or without any protein (Ctrl). Scale bar: 25 µm. **(C)** Quantitative analysis of morphological changes over time of PMNs treated with different concentrations of C2IIa or no C2IIa (Ctrl). Data show the results of 3 independent experiments, each with 3 technical replicates. Values represent the mean ± SEM (n = 9). **(D)** Flow cytometryc analysis of PMNs after treatment with C2IIa, C2I or PBS for control (Ctrl). Change of FSC was measured as surrogate for PMN cell size after incubation with C2I (1 µg/ml) or C2IIa (2 µg/ml). In parallel, PMNs were incubated with C2I (1 µg/ml) or C2IIa (2 µg/ml) in the presence of fMLF (1 µM), a chemoattractant peptide. PMNs from the same tube were analyzed after 1, 5, 30, and 60 min. Data is given as mean of four independent experiments ± SEM (n = 4).

of established C2IIa pore blockers HA1568 (Bronnhuber et al., 2014) or quinacrine (Kronhardt et al., 2016) (**Figure 2A**), confirming that the observed effect was mediated by transmembrane pores formed by C2IIa. Pretreatment of cells with bafilomycin A1, which inhibits the acidification of endosomal vesicles and protects cells from intoxication with complete C2 toxin (Barth et al., 2000), had no effect on the C2IIa-induced changes in morphology (**Figure 2B**). Since acidification is crucial for pore formation by C2IIa in endosomes, this result implicates that the observed

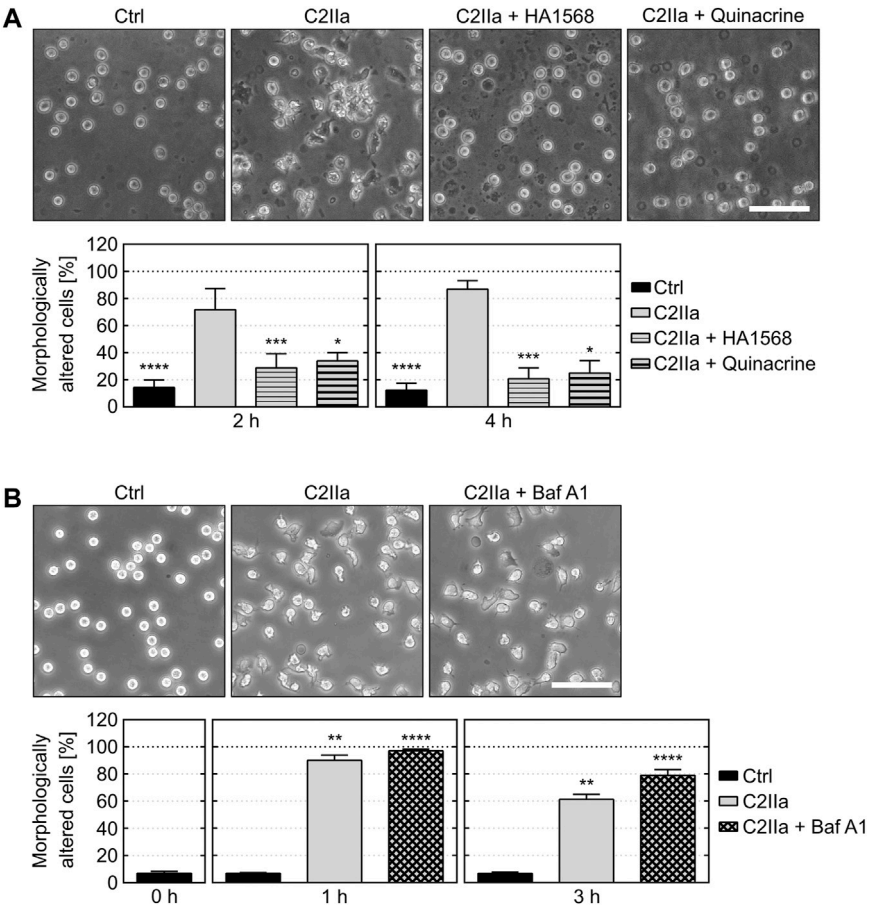

FIGURE 2 | Effect of pore blockers and bafilomycin A1 on C2IIa-induced changes in PMN morphology. **(A)** The pore blockers HA1568 and quinacrine protect PMNs from C2IIa-induced morphological changes. Upper panel: Representative pictures show the morphology of PMNs after 4 h treatment (37°C) with C2IIa (1 μg/ml) in the presence or absence of the established pore blockers HA1568 (100 μM) and quinacrine (5 μM). Additional PMNs were left untreated as control (Ctrl). Scale bar: 100 μm. Lower panel: The percentage of morphologically changed PMNs was quantified after 2 and 4 h and is depicted as mean ± SEM (n = 9–15, i.e., 3–5 independent experiments with 3 technical replicates for each condition, respectively). Significance was tested against the sample treated with C2IIa only using Kruskal–Wallis test with Dunn's correction for multiple comparison (*$p < 0.05$, ***$p < 0.001$, ****$p < 0.0001$). **(B)** Inhibition of endosomal acidification by bafilomycin A1 (Baf A1) has no impact on the C2IIa-induced morphological changes of PMNs. Upper panel: Representative pictures show the morphology of PMNs after 1 h treatment (37°C) with C2IIa (2 μg/ml) with or without Baf A1 (100 nM). Further PMNs were left untreated as control (Ctrl). Scale bar: 100 μm. Lower panel: The percentage of morphologically altered PMNs was quantified after the indicated time points and is depicted as mean ± SEM of three independent experiments, each with 3 technical replicates (n = 9). Significance was tested against the untreated control (Ctrl) using Kruskal–Wallis test combined with Dunn's multiple comparison test (**$p < 0.01$, ****$p < 0.0001$).

morphological changes after treatment with C2IIa are not induced by endosomal pore formation. To investigate the potential role of C2IIa pore formation in the plasma membrane of PMNs in more detail, the intracellular Ca^{2+} signal upon treating primary human PMN with C2IIa, its inactive precursor C2II and C2I were measured by flow cytometry. As shown in **Figure 3A** and **Supplementary Figure S3**, there was rapid increase of intracellular free Ca^{2+} concentration in PMNs after addition of C2IIa, while no comparable effect was measured after addition of C2II or C2I. This is in accordance with pore formation by C2IIa in the plasma membrane of PMNs, which seems to be crucial for the observed effects on PMNs, since morphological changes on PMNs can only be observed after treatment with C2IIa, but not with C2II (**Figure 3B**).

Prompted by the unexpected observation that C2IIa alone affects PMNs, we investigated the effect of C2IIa in direct comparison to C2IIa + C2I on other cell types including human epithelial cells (HeLa), human endothelial cells (HUVEC) and a murine macrophage line (J774A.1). Therefore, not only morphological changes, but also the viability of all cell types including PMNs were analyzed. As a control in the viability assays, DMSO was added to induce cell death. As shown in **Figures 4**, **5**, all cell types responded to complete C2 toxin (i.e., C2IIa + C2I), but not to C2I or C2IIa alone, even not when C2IIa was applied in the culture medium for 24 h in a higher concentration (5 μg/ml) compared to that used for PMN-intoxication (2 μg/ml). Moreover, C2IIa + C2I, but not C2I or C2IIa alone, reduced the amount of viable cells after 24 h of incubation (**Figure 5**, lower panel). This was expected from

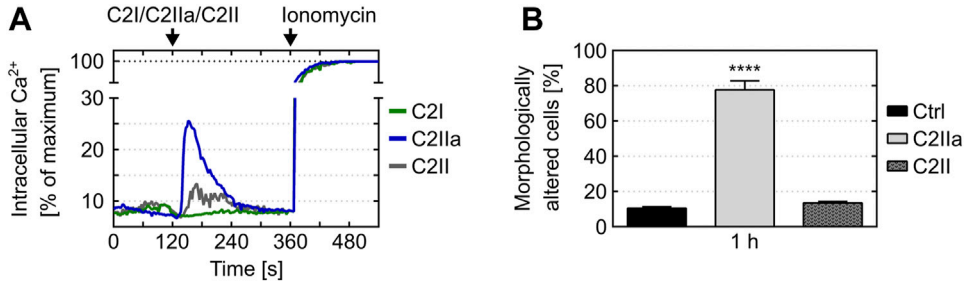

FIGURE 3 | Effect of C2IIa, C2II and C2I on $Ca^{(2+)}$ mobilization and morphological changes in primary human PMNs. **(A)** Treatment with C2IIa induces rapid Ca^{2+} influx into PMNs. Primary human PMNs were loaded with indo-1-AM. After pre-warming to 37°C, the cells were loaded into the flow cytometer and Ca^{2+} baseline was determined for 2 min. Afterwards, the cells were treated for 4 min with C2IIa (5 µg/ml), C2II (5 µg/ml) or C2I (1 µg/ml) and subsequently for 3 min with ionomycin. The individual points of the curves correspond to time in full seconds *versus* the medians of all fluorescence ratios representing $[Ca^{2+}]_i$, following their normalization according to the maximum values reached after addition of 2 µm ionomycin. Data is representative for three independent experiments. **(B)** Treatment with C2IIa but not with C2II induces changes in PMN morphology. Primary human PMNs were treated at 37°C with either C2IIa (5 µg/ml) or C2II (5 µg/ml) or without any protein as control (Ctrl). Pictures from the cells were taken after 1 h and quantitative analysis of morphological changes of PMNs was performed. Data show the results of 3 independent experiments, each with 3 technical replicates per condition. Values represent the mean ± SEM (n = 9). Significance was tested against the untreated control (Ctrl) using Kruskal–Wallis test with Dunn's correction for multiple comparison (****$p < 0.0001$).

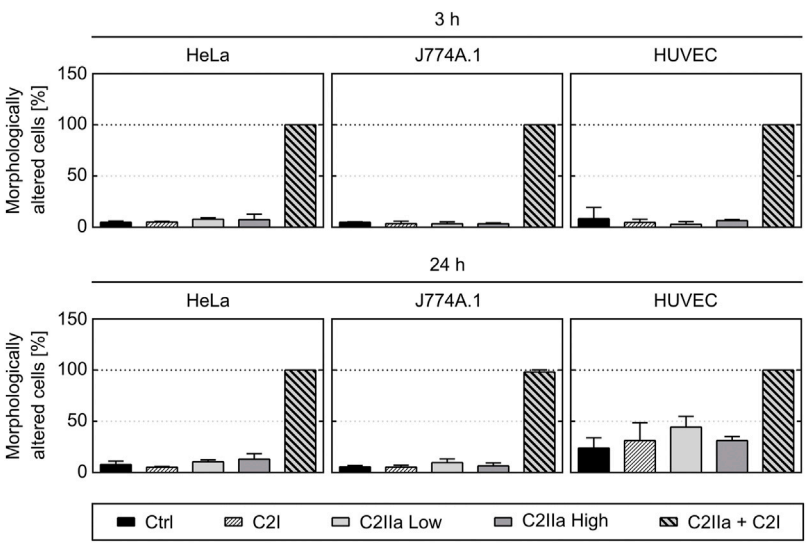

FIGURE 4 | Effect of complete C2 toxin and its single components C2IIa and C2I on the morphology of HeLa, HUVEC and J774A.1 cells. The percentage of morphologically changed cells was quantified after 3 and 24 h treatment (37°C) of different cell types with C2I (1 µg/ml), C2IIa Low (2 µg/ml), C2IIa High (5 µg/ml), the binary toxin (2 µg/ml C2IIa + 1 µg/ml C2I) or without any protein as control (Ctrl). Data is representative for at least three independent experiments per time point. Values represent the mean ± SD of 3 technical replicates.

earlier reports that C2 toxin induces apoptotic cell death after 24–48 h (Heine et al., 2008). After 3 h, all cell types including human primary PMNs were viable after treatment with C2IIa + C2I and C2IIa alone (**Figure 5**, upper and middle panel). Moreover, an incubation for 6 h with either C2IIa or complete C2 toxin (C2IIa + C2I) did not reduce the viability of primary human PMNs *ex vivo* (**Supplementary Figure S4**). Since primary PMNs do not survive for 24 h *ex vivo*, the effect of C2IIa on their viability could not be analyzed for prolonged incubation periods.

Taken together, the comparison between the different cell types confirmed earlier results that all cell types respond to the combination C2IIa + C2I, while treatment with the single components of C2 toxin had no effect on the tested cell types, except for PMNs, which selectively responded to C2IIa alone.

C2IIa Reduces the Chemotactic Translocation of Primary Human PMNs

To investigate whether C2IIa also affects PMN functions, the chemotactic activity of primary human PMNs was analyzed in a dual chamber system. To this end, PMNs were stained with the fluorescence dye calcein and added to the upper side of cell-culture inserts with 3 µm pores. Pores allow cells to migrate from the top to the bottom compartment of the chamber along a chemotactic gradient (Davidson and Patel, 2014). The PMNs in

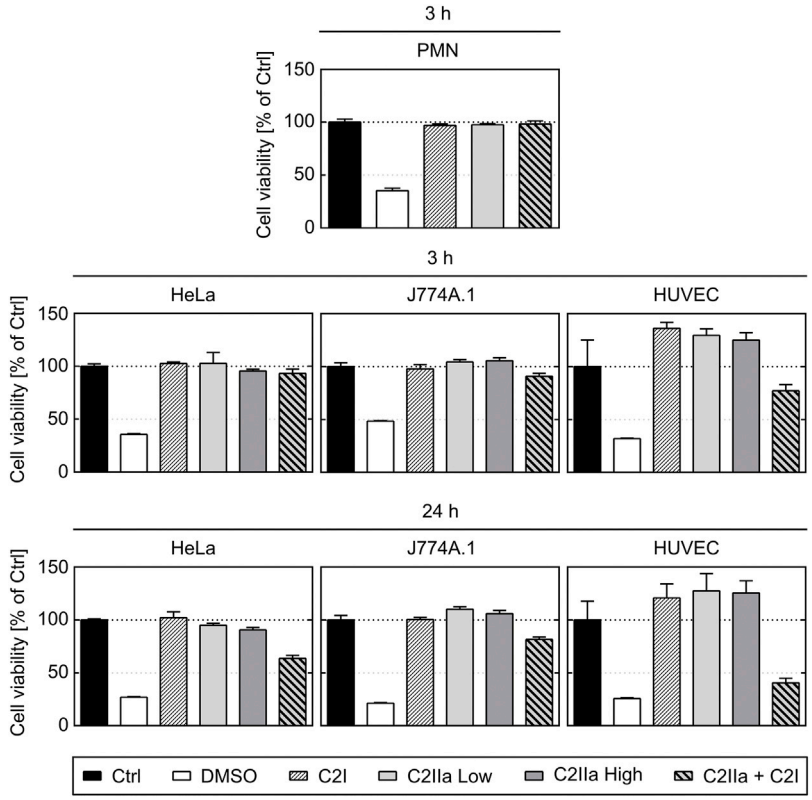

FIGURE 5 | Effect of complete C2 toxin and its single components C2IIa and C2I on the viability of primary human PMNs and on HeLa, HUVEC and J774A.1 cells. Relative viability (% of control) of different cell types after 3 and 24 h incubation (37°C) with DMSO (20%), C2I (1 µg/ml), C2IIa Low (2 µg/ml), C2IIa High (5 µg/ml), the binary toxin (2 µg/ml C2IIa + 1 µg/ml C2I) or without any component as control (Ctrl) was measured by MTS assay. Data is representative for at least three independent experiments per time point. Values represent the mean ± SD of 3 technical replicates.

the upper chamber were incubated for 2 h in the presence or absence of either C2IIa, C2I, C2 toxin (C2IIa + C2I) or cytochalasin B as an established migration-inhibiting compound. Subsequently, the chemoattractant fMLF was added to the lower compartment to trigger PMN chemotaxis. The amount of translocated PMNs was measured via the decline in the upper calcein fluorescence immediately after stimulation with fMLF over a period of 90 min. As expected, cytochalasin B and the binary C2 toxin (C2IIa + C2I) provoked a complete inhibition of fMLF-dependent translocation of PMNs, while C2I alone had no effect (**Figure 6A**). However, treatment with C2IIa alone resulted in a significant reduction of the amount of translocated PMNs, implicating that C2IIa inhibits the chemotactic migration of human PMNs *ex vivo*. This finding is further affirmed by the fact, that the fastest rate of PMN transmigration was drastically haltened by C2IIa but not C2I treatment (**Figure 6B**), suggesting that this mode of intoxication has the potential to effectively reduce leukocyte mass movement (Getter et al., 2019).

Since the described measurement is dependent on persistence of calcein in the cytosol of PMNs and C2IIa seem to be related to pore formation in the plasma membrane, a control experiment was performed to analyze whether treatment of PMNs with C2IIa leads to an efflux of calcein, a much larger molecule than Ca^{2+}, from the cells. Potentially, this could then result in a decreased fluorescent signal of C2IIa-treated PMNs and false-positive results. Therefore, calcein-stained PMNs were treated with either saponin, which is known to disrupt cell membranes, with the pore formation inducer ionomycin, with C2IIa, C2I, the complete binary C2 toxin (C2IIa + C2I), or with bath solution as control. As expected, saponin-treatment resulted in a complete loss of the fluorescence signal, which was calculated as the ratio of fluorescence between timepoint 30 min (F30) and timepoint zero (F0) (**Figure 6C**). In contrast, F30/F0 signals of PMNs exposed to any of the other compounds did not change (**Figure 6C**). This result excludes the possibility that the observed reduction of calcein is not a sole indicator of cellular translocation but also due to calcein loss through C2IIa pores in the plasma membrane.

C2IIa Reduces the Transendothelial Chemotactic Translocation of Primary Human PMNs But Does Not Affect the Endothelial Barrier Integrity

Prompted by this finding, we analyzed the chemotactic translocation of PMNs in co-culture with human endothelial cells, which is a better *in vitro* model of the physiological extravasation process (Filippi, 2016). To this end, a tight

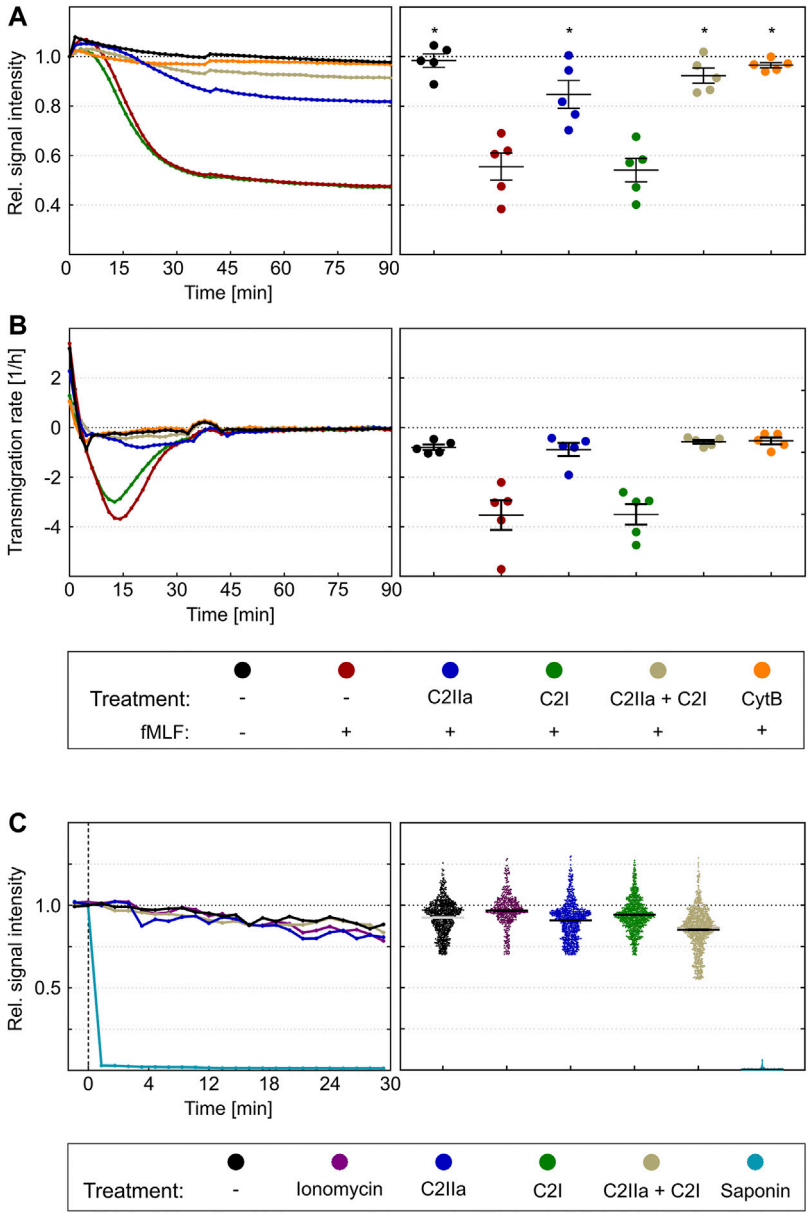

FIGURE 6 | Effect of complete C2 toxin and its single components C2IIa and C2I on the chemotactic translocation of primary human PMNs *ex vivo*. **(A)** Calcein stained PMNs were applied to the upper site of cell-culture inserts with 3 µm pores in the presence or absence of C2IIa (2 µg/ml), C2I (1 µg/ml), the binary toxin (2 µg/ml C2IIa + 1 µg/ml C2I) or cytochalasin B (5 µg/ml) as a positive control. After an intoxication time of 2 h, fMLF (10 nM) was added to the lower compartment to trigger chemotaxis. Calcein fluorescence was measured from the top immediately after stimulation over a period of 90 min. The decline in signal intensity is considered to be a measure of the fraction of cells migrated from the upper to the lower compartment. Its computation is described in the methods section. The left panel shows one representative recording. The right panel summarizes results of five independent experiments after 90 min. Values are given as mean ± SEM (n = 5). Significance was evaluated with the Kruskal–Wallis test and Dunn's correction for multiple comparison (*$p < 0.05$). Significant differences are all with respect to fMLF control samples. Symbols and colours are identical for **(A)** and **(B)**. **(B)** First time derivative of signals from experiments in **(A)** representing the transmigration rate [1/h]. The statistical analysis was performed with values of the maxima of the transmigration rates per individual experiment (n = 5), confirms an inhibition by the binary C2 toxin and the C2IIa component. **(C)** The left panel shows representative Fx (Fluorescence value at an timepoint x)/F0 curves of single cells over time. Immediately after addition of saponin the calcein signal is completely lost. On the opposite, treatment with ionomycin (2 µM), C2IIa (2 µg/ml), C2I (1 µg/ml) or both components (2 µg/ml C2IIa + 1 µg/ml C2I) show fluorescent signals similar to the untreated control. Right panel: Scatter plot shows F30/F0 for controls and treatment with ionomycin, C2IIa, C2I, both components of C2 toxin (C2IIa + C2I) or saponin. Values are given as mean ± SEM (Data are obtained from 3 independent experiments).

monolayer of human endothelial cells (HUVEC) was grown in the dual chamber device and activated by treatment with TNFα (Makó et al., 2010; Schildberger et al., 2010; Mehta and Malik, 2006). Calcein-stained PMNs were pre-incubated for 2 h in the presence or absence of either complete C2 toxin (C2IIa + C2I) or the single components C2IIa or C2I, respectively, and

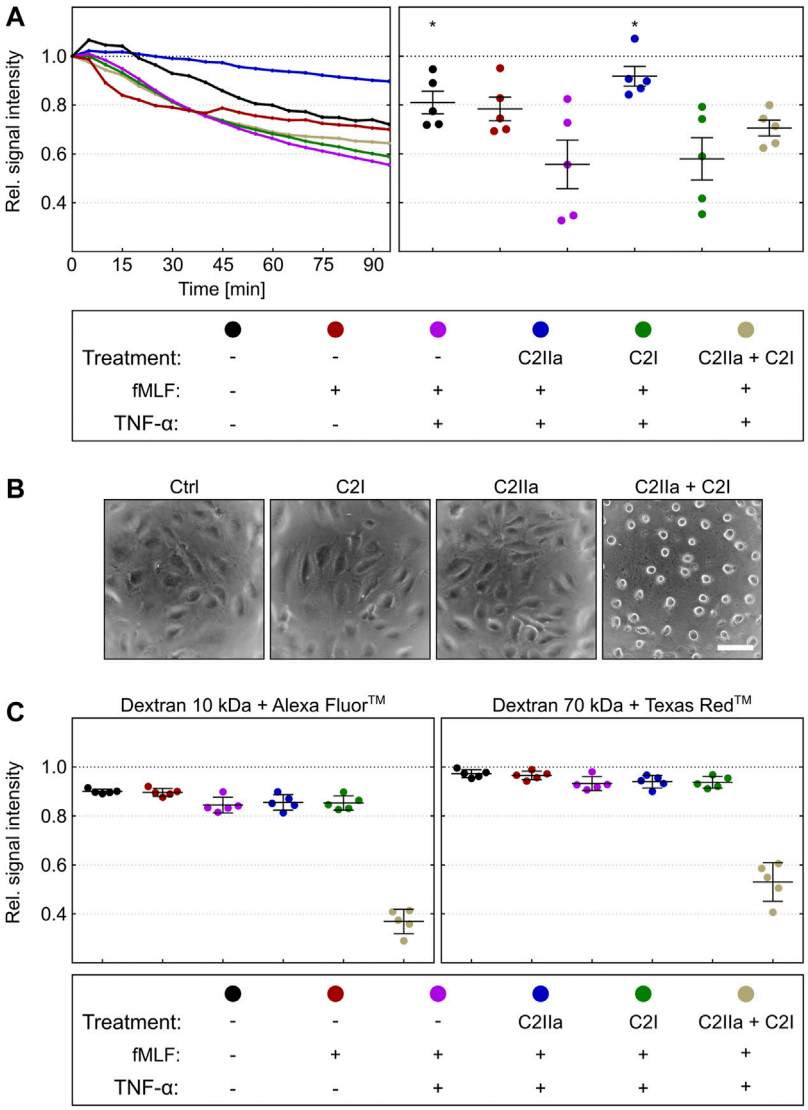

FIGURE 7 | Effect of complete C2 toxin and its single components C2IIa and C2I on the transendothelial chemotactic translocation of primary human PMNs *ex vivo* and on barrier integrity. **(A)** An endothelial monolayer (HUVEC) was cultured on filter inserts with 3 µm pore size and activated by TNFα (10 ng/ml). Calcein-stained PMNs were pre-incubated in the presence or absence of C2IIa (2 µg/ml), C2I (1 µg/ml) or both components (2 µg/ml C2IIa + 1 µg/ml C2I) for 2 h and subsequently seeded on the apical site of endothelial cells. PMN chemotaxis towards the lower chamber was stimulated by addition of fMLF (10 nM). Calcein fluorescence was measured from the top immediately after stimulation over a period of 95 min. The decline in signal intensity is considered to be a measure of the fraction of cells migrated through the endothelial monolayer within 95 min. Its computation is described in the methods section. The left panel shows one representative recording. The right panel summarizes results of five independent experiments after 95 min. Values are given as mean ± SEM (n = 5). Significance was tested with Wilcoxon matched-pairs signed rank test (one-tailed) by GraphPad software (*$p < 0.05$). Statistical tests refer to samples treated with fMLF + TNFα. **(B)** Representative pictures of HUVEC cells in a monolayer which were treated for 3 h at 37°C with solvent (Ctrl), C2IIa (2 µg/ml), C2I (1 µg/ml) or both components (2 µg/ml C2IIa + 1 µg/ml C2I). **(C)** The treatment of the co-culture (HUVEC) with C2IIa does not increase transendothelial fluxes of fluorescence dye-labelled dextrans with molecular weights of either 10 kDa or 70 kDa (left and right panels, respectively). In contrast to the single C2 toxin components, the whole toxin (2 µg/ml C2IIa + 1 µg/ml C2I) disrupted the endothelial barrier-integrity. Values are given as mean ± SEM of five independent experiments (n = 5).

subsequently seeded on the apical side of activated endothelial monolayers. As described before, PMNs were stimulated for transmigration by application of fMLF into the lower chamber. The amount of translocated PMNs was detected by fluorescence measurement over 95 min (**Figure 7A**, left panel) and the results of five independent experiments were evaluated (**Figure 7A**). These findings revealed that C2IIa alone significantly reduced the transmigration. As expected, C2I had no detectable effect. However, HUVEC cells rounded up after treatment with complete C2 toxin, indicating that they are sensitive for C2 toxin and able to bind C2IIa under these experimental conditions. Importantly, C2IIa did not affect the integrity of the endothelial barrier formed by HUVEC cells (**Figures 7B,C**). Treatment of the HUVEC/PMN co-culture

with C2IIa did not increase the transendothelial fluxes of fluorescence dye-labelled dextrans with molecular weights of either 10 or 70 kDa (**Figure 7C**, left and right panels, respectively). In contrast, complete C2 toxin (C2IIa + C2I) disrupted the endothelial barrier-integrity. In conclusion, the results suggest that C2IIa inhibits chemotactic diapedesis of human PMNs but does not exhibit cytotoxic effects on the endothelial cells.

DISCUSSION

Prompted by recent reports that the activated transport subunit of the binary C2 toxin, C2IIa, triggers the exocytosis of enzymes from lysosomes via Ca^{2+} influx through C2IIa pores formed in the plasma membrane of cells (Nagahama et al., 2017; Nagahama et al., 2021), we investigated the effect of C2IIa on various cell types. Taken all together, we found that C2IIa had no effects on cell morphology or viability of epithelial and endothelial cells as well as macrophages, but changed the morphology of primary human PMNs in a time- and concentration-dependent manner. However, concentrations of C2IIa in culture media used in the present experiments were higher than those required in combination with C2I for an effective intoxication of cells. The observed effect of C2IIa on the morphology of PMNs was prevented in the presence of compounds, which were previously described as blockers of C2IIa pores *in vitro* and in living cells (Bronnhuber et al., 2014; Knapp et al., 2016; Kronhardt et al., 2016; Kreidler et al., 2017), implicating that the effect of C2IIa on PMN morphology was mediated by C2IIa-dependent pore formation. Moreover, C2II, the precursor protein of C2IIa that does not form trans-membrane pores (Schmid et al., 1994) had no detectable effect on PMN morphology, supporting the hypothesis that C2IIa pores induce the changes in PMN morphology. However, bafilomycin A1, which prevents acidification of endosomal vesicles and protects cells from C2 toxin, had no effect on the C2IIa-induced changes of PMN morphology. This strongly suggests that C2IIa pores, which mediate the observed effect on PMNs, are formed in the cytoplasmic membranes of PMNs rather than in their endosomal membranes. This is supported by the finding that treatment of PMNs with C2IIa but not with C2II immediately increased the cytoplasmic amount of Ca^{2+}, most likely via influx at the plasma membrane caused by C2IIa pores.

In vitro, C2IIa forms pores in artificial black lipid bilayer membranes also at neutral pH conditions (Schmid et al., 1994), but pore formation is increased under acidic conditions (Bachmeyer et al., 2001). This is plausible since C2IIa trans-membrane pores are formed in the membranes of acidified endosomes for the delivery of C2I from the endosomal lumen into the host cell cytosol (Barth et al., 2000; Haug et al., 2003a; Haug et al., 2003b; Kaiser et al., 2009; Nagahama et al., 2009; Ernst et al., 2017). By measuring the release of radioactively labelled rubidium from cultured living cells, we discovered earlier that C2IIa, but not the inactive precursor C2II, forms pores in plasma membranes, but this pore formation essentially required acidic conditions while no detectable pore formation was measured in cells under neutral pH conditions (Barth et al., 2000; Bachmeyer et al., 2001; Blöcker et al., 2003a), suggesting that the number of C2IIa pores that are formed in the plasma membranes of cells to initiate the C2 toxin uptake via Ca^{2+} influx is likely limited. This could also explain why treatment with C2IIa in the absence of C2I did not induce cytotoxic effects or obvious morphological changes in the variety of cell types tested so far, except of PMNs, where Ca^{2+} influx at the plasma membrane and altered calcium homeostasis integrates chemotactic and adhesive signals (Schaff et al., 2008). In conclusion, the results of this present study strongly suggest that in the case of C2IIa, the pore formation by this protein in the plasma membrane is the cause for reduction in chemotaxis of human PMNs *ex vivo*.

The transport subunits of the related clostridial binary actin ADP-ribosylating iota toxin of *C. perfringens* and CDT of *Clostridioides difficile* (Popoff et al., 1988; Perelle et al., 1997a), Ib and CDTb, respectively, exhibit cytotoxic effects in the absence of their enzyme subunits by pore formation in the plasma membranes of mammalian cells even under neutral conditions (Nagahama et al., 2011; Landenberger et al., 2021; Ernst et al., 2021)). Incubation of cells with Ib (Nagahama et al., 2014) or CDTb (Ernst et al., 2021; Landenberger et al., 2021) results in morphological changes and loss of viability. However, cells are protected by pore blockers (Ernst et al., 2021; Landenberger et al., 2021), confirming that the cytotoxic effects of Ib or CDTb in the absence of their enzyme subunits is mediated by pore formation. C2IIa shows structure and function homology to Ib and CDTb (Perelle et al., 1997b; Stiles et al., 2014; Blonder et al., 2005) but the toxins show some differences in their cellular uptake mechanisms regarding the endocytotic pathways and the mechanisms underlying translocation of enzyme subunits from endosomes into the cytosol (Blöcker et al., 2001; Hale et al., 2004; Gibert et al., 2007; Gibert et al., 2011). Moreover, while C2IIa binds via carbohydrate structures to all cell types (Eckhardt et al., 2000), Ib and CDTb both exploit the surface protein LSR as a receptor (Papatheodorou et al., 2011). Therefore, only LSR-expressing cells respond to the toxins iota or CDT and to their transport subunits Ib or CDTb, respectively (Papatheodorou et al., 2011). In conclusion, the ability of C2IIa to exhibit cytotoxicity only to a specific cell type although it can bind to all cell types is unique among these three toxins.

Our results revealed that treatment with C2IIa reduced the chemotactic translocation of primary human PMNs *ex vivo* through a porous membrane and across the barrier of human endothelial cells. We could exclude that a loss of the calcein dye from the cells contributes to the detected decrease of fluorescence in these experiments with calcein-stained PMNs. Noteworthy, C2IIa did not affect endothelial cells or the barrier integrity of the endothelial monolayer, confirming the PMN-selectivity of C2IIa. Therefore, the findings suggest that C2IIa alone selectively targets PMNs and down-modulates their chemotactic translocation. This mode of action towards these important cells of the innate immune system might represent a pathophysiological contribution to the already established mode of action of the complete binary C2 toxin. Moreover, these novel findings might pave the way towards pharmacological strategies for targeted down-modulation of the excessive and detrimental chemotactic PMN translocation, which was observed in the context of (post-)

traumatic hyper-inflammatory conditions, for example, after blunt chest trauma and the associated lung contusion (Perl et al., 2012). Here, the local application of C2IIa could be beneficial to reduce the amount of PMNs extravasating into lung parenchyma without affecting other pulmonary cell types such as alveolar epithelial cells or macrophages.

DATA AVAILABILITY STATEMENT

The raw data supporting the conclusions of this article will be made available by the authors, without undue reservation.

ETHICS STATEMENT

The studies involving human participants were reviewed and approved by Ethics votum 24/16 of the Local Independent Ethics Committee of the University of Ulm. The patients/participants provided their written informed consent to participate in this study.

AUTHOR CONTRIBUTIONS

HB, MFe, MFr, SF, MH-L designed research; JE, SS, JB, SH, SE, LW, GF, MFa performed research; HB, MFr, MFe, SE, LW, MH-L, MFa, GF, SF, JB, JE, SS analyzed data; HB, MFr, SF, MH-L, JB wrote the paper.

FUNDING

The work in the Barth and Frick groups was funded by the Deutsche Forschungsgemeinschaft (DFG, German Research Foundation)-Project-ID 251293561—SFB 1149 (project A05). JB, JE, MFe, SH, SE, SS are members of the International Graduate School for Molecular Medicine, Ulm (IGradU); JE and SS are members of the research training program Experimental Medicine in IGradU.

ACKNOWLEDGMENTS

The authors thank Peter Gierschik for fruitful discussion and Anna Anastasia for technical assistance.

SUPPLEMENTARY MATERIAL

The Supplementary Material for this article can be found online at: https://www.frontiersin.org/articles/10.3389/fphar.2022.810611/full#supplementary-material

Supplementary Figure S1 | Analysis of recombinant C2I, C2II and C2IIa. The recombinant proteins were purified and C2IIa was activated as described in *Materials and Methods*. Proteins were subjected to 12.5% SDS-PAGE and analyzed by Coomassie blue staining (750 ng of each protein, left panel) or by Western blotting with specific antisera against C2I or C2II (350 ng of each protein, right and middle panel, respectively).

Supplementary Figure S2 | Effect of C2IIa on the morphology of primary human PMNs. Primary human PMNs were incubated without (Ctrl.) or with increasing concentrations of C2IIa at 37°C and analyzed by phase contrast microscopy. Pictures of the cells were taken 2 min before (indicated as untreated, UT) and immediately after protein addition into the medium (indicated as time point 0) and after 0.5, 1 and 6 h. The percentage of morphologically changed cells was quantified from the pictures. Data is representative for three independent experiments. Values represent the mean ± SD of three technical replicates.

Supplementary Figure S3 | The ability of C2IIa to mediate intracellular Ca^{2+} mobilization depends on the level of C2IIa stimulation. Primary human PMNs were loaded with Indo-1-AM. After pre-warming to 37°C, the cells were applied to the flow cytometer and the Ca^{2+} baseline was determined for 2 min. Subsequently, the cells were treated for 4 min with 0.2, 0.6, 1, 2, 5 and 10 µg/ml of C2IIa or with the PBS as control. Subsequently, ionomycin was added to the samples for 3 min. The individual points shown in the curves correspond to the times in full seconds versus the medians of all fluorescence ratios representing $[Ca^{2+}]_i$, following their normalization according to the maximal values reached after addition of 2 µM ionomycin. Data is representative for three independent experiments.

Supplementary Figure S4 | Effect of C2IIa and C2IIa + C2I on the viability of primary human PMNs *ex vivo*. Primary human PMNs were incubated without any protein (Ctrl.) or with either C2IIa (2 µg/ml) or complete C2 toxin (2 µg/ml C2IIa + 1 µg/ml C2I) at 37°C. After 6 h, the amount of viable cells was determined with the MTS cell viability assay and the percentage of viable cells calculated. Data is representative for three independent experiments. Values represent the mean ± SD of three technical replicates.

REFERENCES

Aktories, K., Bärmann, M., Ohishi, I., Tsuyama, S., Jakobs, K. H., and Habermann, E. (1986). Botulinum C2 Toxin ADP-Ribosylates Actin. *Nature* 322, 390–392. doi:10.1038/322390a0

Aktories, K., Reuner, K. H., Presek, P., and Bärmann, M. (1989). Botulinum C2 Toxin Treatment Increases the G-Actin Pool in Intact Chicken Cells: a Model for the Cytopathic Action of Actin-ADP-Ribosylating Toxins. *Toxicon* 27, 989–993. doi:10.1016/0041-0101(89)90149-9

Bachmeyer, C., Benz, R., Barth, H., Aktories, K., Gilbert, M., and Popoff, M. R. (2001). Interaction of Clostridium Botulinum C2 Toxin with Lipid Bilayer Membranes and Vero Cells: Inhibition of Channel Function by Chloroquine and Related Compounds *In Vitro* and Intoxification *In Vivo*. *FASEB J.* 15, 1658–1660. doi:10.1096/fj.00-0671fje

Barth, H., Blocker, D., Behlke, J., Bergsma-Schutter, W., Brisson, A., Benz, R., et al. (2000). Cellular Uptake of Clostridium Botulinum C2 Toxin Requires Oligomerization and Acidification. *J. Biol. Chem.* 275, 18704–18711. doi:10.1074/jbc.M000596200

Barth, H., Hofmann, F., Olenik, C., Just, I., and Aktories, K. (1998a). The N-Terminal Part of the Enzyme Component (C2I) of the Binary Clostridium Botulinum C2 Toxin Interacts with the Binding Component C2II and Functions as a Carrier System for a Rho ADP-Ribosylating C3-like Fusion Toxin. *Infect. Immun.* 66, 1364–1369. doi:10.1128/IAI.66.4.1364-1369.1998

Barth, H., Preiss, J. C., Hofmann, F., and Aktories, K. (1998b). Characterization of the Catalytic Site of the ADP-Ribosyltransferase *Clostridium Botulinum* C2 Toxin by Site-Directed Mutagenesis. *J. Biol. Chem.* 273, 29506–29511. doi:10.1074/jbc.273.45.29506

Barth, H., Roebling, R., Fritz, M., and Aktories, K. (2002). The Binary *Clostridium Botulinum* C2 Toxin as a Protein Delivery System: Identification of the Minimal Protein Region Necessary for Interaction of Toxin Components. *J. Biol. Chem.* 277, 5074–5081. doi:10.1074/jbc.M109167200

Beeler, T. J., Jona, I., and Martonosi, A. (1979). The Effect of Ionomycin on Calcium Fluxes in Sarcoplasmic Reticulum Vesicles and Liposomes. *J. Biol. Chem.* 254, 6229–6231. doi:10.1016/s0021-9258(18)50350-1

Blöcker, D., Bachmeyer, C., Benz, R., Aktories, K., and Barth, H. (2003a). Channel Formation by the Binding Component of *Clostridium Botulinum* C2 Toxin: Glutamate 307 of C2II Affects Channel Properties *In Vitro* and pH-dependent C2I Translocation *In Vivo*. *Biochemistry* 42, 5368–5377. doi:10.1021/bi034199e

Blöcker, D., Barth, H., Maier, E., Benz, R., Barbieri, J. T., and Aktories, K. (2000). The C Terminus of Component C2II of Clostridium Botulinum C2 Toxin Is Essential for Receptor Binding. *Infect. Immun.* 68, 4566–4573. doi:10.1128/iai.68.8.4566-4573.2000

Blöcker, D., Behlke, J., Aktories, K., and Barth, H. (2001). Cellular Uptake of the *Clostridium perfringens* Binary iota-toxin. *Infect. Immun.* 69, 2980–2987. doi:10.1128/IAI.69.5.2980-2987.2001

Blöcker, D., Pohlmann, K., Haug, G., Bachmeyer, C., Benz, R., Aktories, K., et al. (2003b). Clostridium Botulinum C2 Toxin: Low pH-Induced Pore Formation Is Required for Translocation of the Enzyme Component C2I into the Cytosol of Host Cells. *J. Biol. Chem.* 278, 37360–37367. doi:10.1074/jbc.M305849200

Blonder, J., Hale, M. L., Chan, K. C., Yu, L. R., Lucas, D. A., Conrads, T. P., et al. (2005). Quantitative Profiling of the Detergent-Resistant Membrane Proteome of iota-b Toxin Induced Vero Cells. *J. Proteome Res.* 4, 523–531. doi:10.1021/pr049790s

Bronnhuber, A., Maier, E., Riedl, Z., Hajós, G., Benz, R., and Barth, H. (2014). Inhibitions of the Translocation Pore of Clostridium Botulinum C2 Toxin by Tailored Azolopyridinium Salts Protects Human Cells from Intoxication. *Toxicology* 316, 25–33. doi:10.1016/j.tox.2013.12.006

Davidson, D., and Patel, H. (2014). Cytokine-induced Neutrophil Chemotaxis Assay. *Methods Mol. Biol.* 1172, 107–113. doi:10.1007/978-1-4939-0928-5_9

Eckhardt, M., Barth, H., Blöcker, D., and Aktories, K. (2000). Binding of *Clostridium Botulinum* C2 Toxin to Asparagine-Linked Complex and Hybrid Carbohydrates. *J. Biol. Chem.* 275, 2328–2334. doi:10.1074/jbc.275.4.2328

Ernst, K., Landenberger, M., Nieland, J., Nørgaard, K., Frick, M., Fois, G., et al. (2021). Characterization and Pharmacological Inhibition of the Pore-Forming Clostridioides Difficile CDTb Toxin. *Toxins (Basel)* 13, 390. doi:10.3390/toxins13060390

Ernst, K., Schmid, J., Beck, M., Hägele, M., Hohwieler, M., Hauff, P., et al. (2017). Hsp70 Facilitates Trans-membrane Transport of Bacterial ADP-Ribosylating Toxins into the Cytosol of Mammalian Cells. *Sci. Rep.* 7, 2724. doi:10.1038/s41598-017-02882-y

Filippi, M. D. (2016). Mechanism of Diapedesis: Importance of the Transcellular Route. *Adv. Immunol.* 129, 25–53. doi:10.1016/bs.ai.2015.09.001

Fujii, N., Kubota, T., Shirakawa, S., Kimura, K., Ohishi, I., Moriishi, K., et al. (1996). Characterization of Component-I Gene of Botulinum C2 Toxin and PCR Detection of its Gene in Clostridial Species. *Biochem. Biophys. Res. Commun.* 220, 353–359. doi:10.1006/bbrc.1996.0409

Getter, T., Margalit, R., Kahremany, S., Levy, L., Blum, E., Khazanov, N., et al. (2019). Novel Inhibitors of Leukocyte Transendothelial Migration. *Bioorg. Chem.* 92, 103250. doi:10.1016/j.bioorg.2019.103250

Gibert, M., Marvaud, J. C., Pereira, Y., Hale, M. L., Stiles, B. G., Boquet, P., et al. (2007). Differential Requirement for the Translocation of Clostridial Binary Toxins: iota Toxin Requires a Membrane Potential Gradient. *FEBS Lett.* 581, 1287–1296. doi:10.1016/j.febslet.2007.02.041

Gibert, M., Monier, M. N., Ruez, R., Hale, M. L., Stiles, B. G., Benmerah, A., et al. (2011). Endocytosis and Toxicity of Clostridial Binary Toxins Depend on a Clathrin-independent Pathway Regulated by Rho-GDI. *Cell. Microbiol.* 13, 154–170. doi:10.1111/j.1462-5822.2010.01527.x

Grimminger, F., Sibelius, U., Aktories, K., Just, I., and Seeger, W. (1991). Suppression of Cytoskeletal Rearrangement in Activated Human Neutrophils by Botulinum C2 Toxin. Impact on Cellular Signal Transduction. *J. Biol. Chem.* 266, 19276–19282. doi:10.1016/s0021-9258(18)54994-2

Hale, M. L., Marvaud, J. C., Popoff, M. R., and Stiles, B. G. (2004). Detergent-resistant Membrane Microdomains Facilitate Ib Oligomer Formation and Biological Activity of *Clostridium perfringens* iota-toxin. *Infect. Immun.* 72, 2186–2193. doi:10.1128/iai.72.4.2186-2193.2004

Haug, G., Leemhuis, J., Tiemann, D., Meyer, D. K., Aktories, K., and Barth, H. (2003a). The Host Cell Chaperone Hsp90 Is Essential for Translocation of the Binary *Clostridium Botulinum* C2 Toxin into the Cytosol. *J. Biol. Chem.* 278, 32266–32274. doi:10.1074/jbc.M303980200

Haug, G., Wilde, C., Leemhuis, J., Meyer, D. K., Aktories, K., and Barth, H. (2003b). Cellular Uptake of *Clostridium Botulinum* C2 Toxin: Membrane Translocation of a Fusion Toxin Requires Unfolding of its Dihydrofolate Reductase Domain. *Biochemistry* 42, 15284–15291. doi:10.1021/bi0354278

Heine, K., Pust, S., Enzenmüller, S., and Barth, H. (2008). ADP-ribosylation of Actin by the *Clostridium Botulinum* C2 Toxin in Mammalian Cells Results in Delayed Caspase-dependent Apoptotic Cell Death. *Infect. Immun.* 76, 4600–4608. doi:10.1128/IAI.00651-08

Hug, S., Bernhard, S., Stratmann, A. E. P., Erber, M., Wohlgemuth, L., Knapp, C. L., et al. (2021). Activation of Neutrophil Granulocytes by Platelet-Activating Factor Is Impaired during Experimental Sepsis. *Front. Immunol.* 12, 580. doi:10.3389/fimmu.2021.642867

Kaiser, E., Haug, G., Hliscs, M., Aktories, K., and Barth, H. (2006). Formation of a Biologically Active Toxin Complex of the Binary *Clostridium Botulinum* C2 Toxin without Cell Membrane Interaction. *Biochemistry* 45, 13361–13368. doi:10.1021/bi061459u

Kaiser, E., Pust, S., Kroll, C., and Barth, H. (2009). Cyclophilin A Facilitates Translocation of the *Clostridium Botulinum* C2 Toxin across Membranes of Acidified Endosomes into the Cytosol of Mammalian Cells. *Cel. Microbiol.* 11, 780–795. doi:10.1111/j.1462-5822.2009.01291.x

Knapp, O., Benz, R., and Popoff, M. R. (2016). Pore-forming Activity of Clostridial Binary Toxins. *Biochim. Biophys. Acta* 1858 (3), 512–525. doi:10.1016/j.bbamem.2015.08.006

Kreidler, A. M., Benz, R., and Barth, H. (2017). Chloroquine Derivatives Block the Translocation Pores and Inhibit Cellular Entry of Clostridium Botulinum C2 Toxin and Bacillus Anthracis Lethal Toxin. *Arch. Toxicol.* 91 (3), 1431–1445. doi:10.1007/s00204-016-1716-9

Kronhardt, A., Beitzinger, C., Barth, H., and Benz, R. (2016). Chloroquine Analog Interaction with C2- and Iota-Toxin *In Vitro* and in Living Cells. *Toxins (Basel)* 8 (8), 237. doi:10.3390/toxins8080237

Kurazono, H., Hosokawa, M., Matsuda, H., and Sakaguchi, G. (1987). Fluid Accumulation in the Ligated Intestinal Loop and Histopathological Changes of the Intestinal Mucosa Caused by *Clostridium Botulinum* C2 Toxin in the Pheasant and Chicken. *Res. Vet. Sci.* 42, 349–353. doi:10.1016/s0034-5288(18)30717-3

Landenberger, M., Nieland, J., Roeder, M., Nørgaard, K., Papatheodorou, P., Ernst, K., et al. (2021). The Cytotoxic Effect of Clostridioides Difficile Pore-Forming Toxin CDTb. *Biochim. Biophys. Acta Biomembr* 1863, 183603. doi:10.1016/j.bbamem.2021.183603

Lang, A. E., Neumeyer, T., Sun, J., Collier, R. J., Benz, R., and Aktories, K. (2008). Amino Acid Residues Involved in Membrane Insertion and Pore Formation of *Clostridium Botulinum* C2 Toxin. *Biochemistry* 47, 8406–8413. doi:10.1021/bi800615g

Makó, V., Czúcz, J., Weiszhár, Z., Herczenik, E., Matkó, J., Prohászka, Z., et al. (2010). Proinflammatory Activation Pattern of Human Umbilical Vein Endothelial Cells Induced by IL-1β, TNF-α, and LPS. *Cytometry* 77A, 962–970. doi:10.1002/cyto.a.20952

Mehta, D., and Malik, A. B. (2006). Signaling Mechanisms Regulating Endothelial Permeability. *Physiol. Rev.* 86, 279–367. doi:10.1152/physrev.00012.2005

Nagahama, M., Hagiyama, T., Kojima, T., Aoyanagi, K., Takahashi, C., Oda, M., et al. (2009). Binding and Internalization of *Clostridium Botulinum* C2 Toxin. *Infect. Immun.* 77, 5139–5148. doi:10.1128/IAI.00638-09

Nagahama, M., Kobayashi, K., Ochi, S., and Takehara, M. (2021). Internalization of *Clostridium Botulinum* C2 Toxin Is Regulated by Cathepsin B Released from Lysosomes. *Toxins (Basel)* 13 (4), 272. doi:10.3390/toxins13040272

Nagahama, M., Takahashi, C., Aoyanagi, K., Tashiro, R., Kobayashi, K., Sakaguchi, Y., et al. (2014). Intracellular Trafficking of Clostridium Botulinum C2 Toxin. *Toxicon* 82, 76–82. doi:10.1016/j.toxicon.2014.02.009

Nagahama, M., Takehara, M., Takagishi, T., Seike, S., Miyamoto, K., and Kobayashi, K. (2017). Cellular Uptake of Clostridium Botulinum C2 Toxin Requires Acid Sphingomyelinase Activity. *Infect. Immun.* 85 (4), e00966–16. doi:10.1128/IAI.00966-16

Nagahama, M., Umezaki, M., Oda, M., Kobayashi, K., Tone, S., Suda, T., et al. (2011). *Clostridium perfringens* iota-toxin B Induces Rapid Cell Necrosis. *Infect. Immun.* 79, 4353–4360. doi:10.1128/IAI.05677-11

Norgauer, J., Just, I., Aktories, K., and Sklar, L. A. (1989). Influence of Botulinum C2 Toxin on F-Actin and N-Formyl Peptide Receptor Dynamics in Human Neutrophils. *J. Cel Biol.* 109, 1133–1140. doi:10.1083/jcb.109.3.1133

Norgauer, J., Kownatzki, E., Seifert, R., and Aktories, K. (1988). Botulinum C2 Toxin ADP-Ribosylates Actin and Enhances O2- Production and Secretion but

Inhibits Migration of Activated Human Neutrophils. *J. Clin. Invest.* 82, 1376–1382. doi:10.1172/JCI113741

Ohishi, I. (1987). Activation of Botulinum C2 Toxin by Trypsin. *Infect. Immun.* 55, 1461–1465. doi:10.1128/IAI.55.6.1461-1465.1987

Ohishi, I. (1983a). Lethal and Vascular Permeability Activities of Botulinum C2 Toxin Induced by Separate Injections of the Two Toxin Components. *Infect. Immun.* 40, 336–339. doi:10.1128/IAI.40.1.336-339.1983

Ohishi, I., and Miyake, M. (1985). Binding of the Two Components of C2 Toxin to Epithelial Cells and brush Borders of Mouse Intestine. *Infect. Immun.* 48, 769–775. doi:10.1128/IAI.48.3.769-775.1985

Ohishi, I. (1983b). Response of Mouse Intestinal Loop to Botulinum C2 Toxin: Enterotoxic Activity Induced by Cooperation of Nonlinked Protein Components. *Infect. Immun.* 40, 691–695. doi:10.1128/IAI.40.2.691-695.1983

Ohishi, I., and Yanagimoto, A. (1992). Visualizations of Binding and Internalization of Two Nonlinked Protein Components of Botulinum C2 Toxin in Tissue Culture Cells. *Infect. Immun.* 60, 4648–4655. doi:10.1128/IAI.60.11.4648-4655.1992

Ohishi, I., Miyake, M., Ogura, H., and Nakamura, S. (1984). Cytopathic Effect of Botulinum C2toxin on Tissue-Culture Cells. *FEMS Microbiol. Lett.* 23, 281–284. doi:10.1111/j.1574-6968.1984.tb01078.x

Papatheodorou, P., Carette, J. E., Bell, G. W., Schwan, C., Guttenberg, G., Brummelkamp, T. R., et al. (2011). Lipolysis-stimulated Lipoprotein Receptor (LSR) Is the Host Receptor for the Binary Toxin *Clostridium difficile* Transferase (CDT). *Proc. Natl. Acad. Sci. U S A.* 108, 16422–16427. doi:10.1073/pnas.1109772108

Perelle, S., Gibert, M., Bourlioux, P., Corthier, G., and Popoff, M. R. (1997a). Production of a Complete Binary Toxin (Actin-specific ADP-Ribosyltransferase) by *Clostridium difficile* CD196. *Infect. Immun.* 65, 1402–1407. doi:10.1128/IAI.65.4.1402-1407.1997

Perelle, S., Scalzo, S., Kochi, S., Mock, M., and Popoff, M. R. (1997b). Immunological and Functional Comparison between *Clostridium perfringens* iota Toxin, *C. Spiroforme* Toxin, and Anthrax Toxins. *FEMS Microbiol. Lett.* 146, 117–121. doi:10.1111/j.1574-6968.1997.tb10180.x

Perl, M., Hohmann, C., Denk, S., Kellermann, P., Lu, D., Braumüller, S., et al. (2012). Role of Activated Neutrophils in Chest Trauma-Induced Septic Acute Lung Injury. *Shock* 38, 98–106. doi:10.1097/SHK.0b013e318254be6a

Popoff, M. R., Rubin, E. J., Gill, D. M., and Boquet, P. (1988). Actin-specific ADP-Ribosyltransferase Produced by a *Clostridium difficile* Strain. *Infect. Immun.* 56, 2299–2306. doi:10.1128/IAI.56.9.2299-2306.1988

Pust, S., Barth, H., and Sandvig, K. (2010). *Clostridium Botulinum* C2 Toxin Is Internalized by Clathrin- and Rho-dependent Mechanisms. *Cel. Microbiol.* 12, 1809–1820. doi:10.1111/j.1462-5822.2010.01512.x

Schaff, U. Y., Yamayoshi, I., Tse, T., Griffin, D., Kibathi, L., and Simon, S. I. (2008). Calcium Flux in Neutrophils Synchronizes Beta2 Integrin Adhesive and Signaling Events that Guide Inflammatory Recruitment. *Ann. Biomed. Eng.* 36, 632–646. doi:10.1007/s10439-008-9453-8

Schildberger, A., Rossmanith, E., Weber, V., and Falkenhagen, D. (2010). Monitoring of Endothelial Cell Activation in Experimental Sepsis with a Two-step Cell Culture Model. *Innate Immun.* 16 (5), 278–287. doi:10.1177/1753425909341885

Schindelin, J., Arganda-Carreras, I., Frise, E., Kaynig, V., Longair, M., Pietzsch, T., et al. (2012). Fiji: an Open-Source Platform for Biological-Image Analysis. *Nat. Methods* 9, 676–682. doi:10.1038/nmeth.2019

Schleberger, C., Hochmann, H., Barth, H., Aktories, K., and Schulz, G. E. (2006). Structure and Action of the Binary C2 Toxin from *Clostridium Botulinum*. *J. Mol. Biol.* 364, 705–715. doi:10.1016/j.jmb.2006.09.002

Schmid, A., Benz, R., Just, I., and Aktories, K. (1994). Interaction of Clostridium Botulinum C2 Toxin with Lipid Bilayer Membranes. Formation of Cation-Selective Channels and Inhibition of Channel Function by Chloroquine. *J. Biol. Chem.* 269, 16706–16711. doi:10.1016/s0021-9258(19)89448-6

Sterthoff, C., Lang, A. E., Schwan, C., Tauch, A., and Aktories, K. (2010). Functional Characterization of an Extended Binding Component of the Actin-ADP-Ribosylating C2 Toxin Detected in Clostridium Botulinum Strain (C) 2300. *Infect. Immun.* 78, 1468–1474. doi:10.1128/IAI.01351-09

Stiles, B. G., Pradhan, K., Fleming, J. M., Samy, R. P., Barth, H., and Popoff, M. R. (2014). Clostridium and bacillus Binary Enterotoxins: Bad for the Bowels, and Eukaryotic Being. *Toxins (Basel)* 6 (9), 2626–2656. doi:10.3390/toxins6092626

Takehara, M., Takagishi, T., Seike, S., Oda, M., Sakaguchi, Y., Hisatsune, J., et al. (2017). Cellular Entry of *Clostridium perfringens* Iota-Toxin and Clostridium Botulinum C2 Toxin. *Toxins (Basel)* 9 (8), 247. doi:10.3390/toxins9080247

Uematsu, Y., Kogo, Y., and Ohishi, I. (2007). Disassembly of Actin Filaments by Botulinum C2 Toxin and Actin-Filament-Disrupting Agents Induces Assembly of Microtubules in Human Leukaemia Cell Lines. *Biol. Cel* 99, 141–150. doi:10.1042/BC20060089

Vandekerckhove, J., Schering, B., Bärmann, M., and Aktories, K. (1988). Botulinum C2 Toxin ADP-Ribosylates Cytoplasmic Beta/gamma-Actin in Arginine 177. *J. Biol. Chem.* 263, 696–700. doi:10.1016/s0021-9258(19)35408-0

Conflict of Interest: The authors declare that the research was conducted in the absence of any commercial or financial relationships that could be construed as a potential conflict of interest.

The reviewer MRP declared a past collaboration with one of the authors HB to the handling editor.

Publisher's Note: All claims expressed in this article are solely those of the authors and do not necessarily represent those of their affiliated organizations, or those of the publisher, the editors, and the reviewers. Any product that may be evaluated in this article, or claim that may be made by its manufacturer, is not guaranteed or endorsed by the publisher.

frontiers in Pharmacology

ORIGINAL RESEARCH
published: 18 February 2022
doi: 10.3389/fphar.2022.800970

Three-Dimensional Structure Characterization and Inhibition Study of Exfoliative Toxin D From *Staphylococcus aureus*

Anwar Ullah[1]*, *Ajmal Khan*[2], *Ahmed Al-Harrasi*[2]*, *Kifayat Ullah*[1] and *Asghar Shabbir*[1]

[1]Department of Biosciences COMSATS University Islamabad, Islamabad, Pakistan, [2]Natural and Medical Sciences Research Center, University of Nizwa, Nizwa, Oman

The *Staphylococcus aureus* exfoliative toxins (ETs) are the main toxins that produce staphylococcal scalded skin syndrome (SSSS), an abscess skin disorder. The victims of the disease are usually newborns and kids, as well as grown-up people. Five ETs namely, exfoliative toxins A, B, C, D, and E have been identified in *S. aureus*. The three-dimensional (3D) structure of exfoliative toxins A, B, C and E is known, while that of exfoliative toxin D (ETD) is still unknown. In this work, we have predicted the 3D structure of ETD using protein modeling techniques (software used for 3D structure modeling comprising the MODELLER 9v19 program, SWISS-Model, and I-TESSER). The validation of the build model was done using PROCHECK (Ramachandran plot), ERRAT2, and Verify 3D programs. The results from 3D modeling show that the build model was of good quality as indicated by a GMQE score of 0.88 and by 91.1% amino acid residues in the most favored region of the Ramachandran plot, the ERRAT2 quality factor of 90.1%, and a verify3D score of >0.2 for 99.59% of amino acid residues. The 3D structure analysis indicates that the overall structure of ETD is similar to the chymotrypsin-like serine protease fold. The structure is composed of 13 β-strands and seven α-helices that fold into two well-defined six-strand β-barrels whose axes are roughly perpendicular to each other. The active site residues include histidine-97, aspartic acid-147, and serine-221. This represents the first structure report of ETD. Structural comparison with the other ETs shows some differences, particularly in the loop region, which also change the overall surface charge of these toxins. This may convey variable substrate specificity to these toxins. The inhibition of these toxins by natural (2S albumin and flocculating proteins from *Moringa oleifera* seeds) and synthetic inhibitors (suramin) was also carried out in this study. The results from docking indicate that the inhibitors bind near the C-terminal domain which may restrict the movement of this domain and may halt the access of the substrate to the active site of this enzyme. Molecular dynamic simulation was performed to see the effect of inhibitor binding to the enzyme. This work will further elucidate the structure–function relationship of this enzyme. The inhibition of this enzyme will lead to a new treatment for SSSS.

Keywords: *Staphylococcus aureus*, exfoliative toxins, exfoliative toxin D, comparative protein modeling, three-dimensional structure characterization, inhibition

OPEN ACCESS

Edited by:
Jean-Marc Sabatier,
Aix-Marseille Université, France

Reviewed by:
Dominik Gront,
University of Warsaw, Poland
Nousheen Bibi,
Shaheed Benazir Bhutto Women University, Pakistan

***Correspondence:**
Anwar Ullah
anwarullah@comsats.edu.pk
Ahmed Al-Harrasi
aharrasi@unizwa.edu.om

Specialty section:
This article was submitted to Pharmacology of Ion Channels and Channelopathies, a section of the journal Frontiers in Pharmacology

Received: *24 October 2021*
Accepted: *12 January 2022*
Published: *18 February 2022*

Citation:
Ullah A, Khan A, Al-Harrasi A, Ullah K and Shabbir A (2022) Three-Dimensional Structure Characterization and Inhibition Study of Exfoliative Toxin D From Staphylococcus aureus. *Front. Pharmacol. 13:800970. doi: 10.3389/fphar.2022.800970*

INTRODUCTION

Exfoliative toxins (ETs) of *Staphylococcus aureus* are the main causative agents of staphylococcal scalded skin syndrome (SSSS) (Hubiche et al., 2012; Kimberlin et al., 2015; Nguyen et al., 2021). The syndrome is characterized by a red rash and dissolution of the skin lying below the granular cell layer (Ladhani, 2003; Hanakawa and Stanley, 2004; Sahin-Tóth et al., 2021). The sites of infection include oral or nasal cavities, and the throat and umbilicus (Ladhani, 2003; Adhisivam and Mahadevan, 2006; Abril et al., 2020). The clinical symptoms start suddenly with fever, skin soreness, and itches, within a few hours to a few days of the infection (Amagai et al., 2000; Del Giudice, 2020). There are two common forms (localized and generalized) of SSSS that have been reported in the literature. The localized form (also called bullous impetigo) is recognized by the formation of minor patches on the skin, while the generalized form is characterized by the involvement of a large surface from the skin (Lyell, 1979; Cribier et al., 1984; Ladhani et al., 1999; Mannschreck et al., 2020; Del Giudice, 2020). Children under the age of 5 years are more susceptible to SSSS as compared to adults, due to the lack of removal for the exotoxins from the circulating system and the immature immune system (Oono et al., 1997; Shirin et al., 1998; Kapoor et al., 2008; Kadam et al., 2009; Doudoulakakis et al., 2021). Both of these are more developed in adults. The adults also have antibodies that specifically neutralize the toxins; however, in children, no such antibodies exist (Decleire et al., 2004). The SSSS-infected adults may show some symptoms like kidney dysfunction, immunodeficiency, and other long-term illness (Ladhani and Newson 2000; Decleire et al., 2004; Nguyen et al., 2021; Schwarz et al., 2021). The lethality rate from SSSS is under 5% (Melish, 1982; Cribier et al., 1984).

The ETs are highly specific toward their substrates, and these only cleave desmoglein 1 (Amagai et al., 2000; Amagai et al., 2002; Yamaguchi et al., 2002) and the cleavage occurs in a calcium-dependent confirmation of desmoglein 1 (Hanakawa et al., 2003). The removal of calcium from desmoglein 1, or pretreatment at 56°C or higher, or at low or high pH changes the conformation of desmoglein 1 and the ETs become unable to cleave it (Hanakawa et al., 2003). There is one unique site (following the glutamic acid at amino acid position 381) that is specifically cleaved by ETs in Dsg1 in mice and humans, and the ETs are unable to cleave identical substrates like Dsg3 and E-cadherin (Amagai et al., 2000; Hanakawa et al., 2002).

The ETs are serine proteinases with exotoxins enzymatic activity (Ladhani, 2003). Five types of ETs have been described in the literature, namely, exfoliative toxin A (ETA) (Cavarelli et al., 1997; Azarian et al., 2021), exfoliative toxin B (ETB) (Gemmell, 1997), exfoliative toxin C (ETC) (Sato et al., 1994), exfoliative toxin D (ETD) (Yamaguchi et al., 2002), and exfoliative toxin E (ETE) (Imanishi et al., 2019). The primary amino acid sequences of these contain 242–247 amino acid residues in their mature form (Cavarelli et al., 1997; Papageorgiou et al., 2000; Ladhani, 2003; Mariutti et al., 2015). The sequence identity among ETA, ETB, ETD, and ETE ranges from 43 to 63% (Ladhani, 2003); however, with ETC, these do not display any significant sequence identity (Ladhani, 2003). ETC, also known as adenylosuccinate lyase, is not toxic to humans, and its three-dimensional (3D) structure is also different from ETA, ETB, and ETE (Fyfe et al., 2010).

The crystal structures of ETA, ETB, ETC, and ETE have been described (Cavarelli et al., 1997; Papageorgiou et al., 2000; Fyfe et al., 2010; Mariutti et al., 2015). The crystal structure of ETD-like protein (Mariutti et al., 2015) described previously has now been renamed as ETE (Imanishi et al., 2019). The ETD-like protein has 59% sequence identity to ETD, and that is why it is called ETD-like (Imanishi et al., 2019). The 3D structure of ETs is similar to the classical serine proteinase, chymotrypsin-like fold (Cavarelli et al., 1997; Papageorgiou et al., 2000; Mariutti et al., 2015). Their 3D structure is composed of 13 β-strands and seven α-helices that fold into two well-organized six-stranded β-barrels whose axes are roughly perpendicular to each other (Cavarelli et al., 1997; Papageorgiou et al., 2000; Mariutti et al., 2015). The active site is positioned at the intersection of the two β-barrels, comprising of amino acid residues His-Asp-Ser, which are fully conserved in all the ETs and with other serine proteinases (Cavarelli et al., 1997; Papageorgiou et al., 2000; Mariutti et al., 2015).

Although the crystal structures of the ETs A, B, C, and E are known, the crystal structure of ETD is still unknown. This lack in the structure of ETD makes it difficult to establish a structure–function relationship and the mechanism of action and inhibition of this enzyme. The literature review indicates that most of the research work done on the ETD belongs to gene-level identification and characterization and the mode of spreading (Yamasaki et al., 2006; Mališová et al., 2020; Doudoulakakis et al., 2021). To better understand their 3D structure and mechanism of action, the present work depicts the model-based structure elucidation and characterization of ETD from *S. aureus*. A structure-based mechanism of action and inhibition study was carried out for ETD. Although this study is *in silico*, it will provide a better way to perform it in the lab for further verification.

MATERIALS AND METHODS

Sequence Extraction and Multiple Sequence Alignment

The primary amino acid sequence of ETD was retrieved from the National Centre for Biotechnology Information (NCBI) protein database (http://www.ncbi.nlm.nih.gov/protein), with the Gene Bank ID: AHC54578.1 (1–281 amino acid residues) (Paul et al., 2014) and the corresponding UniProt ID: Q8GAX8.

Prediction of Signal Peptide

The signal peptide in the primary structure of ETD was predicted using the program SignalP 3.0 server (Bendtsen et al., 2004), by providing the full-length amino acid sequence of ETD. The parameters used were organism group—Gram-positive bacteria and method—both neural network and Hidden Markov models, and the sequence was truncated to a maximum of 50 amino acid residues.

TABLE 1 | Percent sequence identities among ETD and other ETs.

Proteins	ETD_*Sa*	ETA_*Sa*	ETB_*Sa*	ETE_*Sa*	ExhC_*Ss*	TLP_*Sd*	TLP_*Sf*	TLP_*Sp*	ETB_*Sh*	ExhC_*Sc*
ETD_*Sa*	—	50%	62.62%	57.09%	45.16%	69.40%	67.50%	65.36%	66.60%	43.48%
ETA_*Sa*	50%	—	44.00%	43.35%	44.85%	42.98%	47.41%	43.32%	47.14%	38.61%
ETB_*Sa*	62.62%	44.00%	—	55.36%	37.19%	60.63%	64.64%	55.91%	59.48%	39.44%
ETE_*Sa*	57.09%	43.35%	55.36%	—	40.16%	56.38%	63.27%	58.91%	59.63%	43.03%
ExhC_*Ss*	45.16%	44.85%	37.19%	40.16%	—	40.41	46.88%	39.63%	44.24%	38.57%
TLP_*Sd*	69.40%	42.98%	60.63%	56.38%	40.41%	—	64.29%	64.29%	66.92%	39.29%
TLP_*Sf*	67.50%	47.41%	64.64%	63.27%	46.88%	64.29%	—	60.07%	67.16%	41.04%
TLP_*Sp*	65.36%	43.32%	55.91%	58.91%	39.63%	64.29%	60.07%	—	70.36%	39.13%
ETB_*Sh*	66.60%	47.14%	59.48%	59.63%	44.24%	66.92%	67.16%	70.36%	—	41.42%
ExhC_*Sc*	43.48%	38.61%	39.44%	43.03%	38.57%	39.29%	41.04%	39.13%	41.42%	—

ETD_Sa, exfoliative toxin D, Staphylococcus aureus*, Gene Bank ID: AHC54578.1; ETA_Sa, epidermolytic toxin A from* S. aureus*, PDB ID: 1AJGJ; ETB_Sa, crystal structure of exfoliative toxin B, PDB ID: 1DT2; ETE_Sa, exfoliative toxin E from* S. aureus*, Gene Bank ID: WP_054190843.1, PDB ID: 5C2Z; ExhC_Ss, exfoliative toxin ExhC from* S. sciuri*, Gene Bank ID: AEF13380.1; TLP_Sd, trypsin-like peptidase domain–containing protein from* S. delphini*, Gene Bank ID: WP_096546202.1; TLP_Sf, trypsin-like peptidase domain–containing protein from* S. felis*, Gene Bank ID: WP_103209705.1; TLP_Sp, trypsin-like peptidase domain–containing protein from* S. pseudintermedius*, Gene Bank ID: WP_100002848.1; ETB_Sh, exfoliative toxin B from* S. hyicus*, Gene Bank ID: BAA99411.1; ExhB_Sc: exfoliative toxin ExhB from* S. chromogenes*, Gene Bank ID: AAV98626.1.*

Biochemical Properties of the Exfoliative Toxin D

The molecular weight and isoelectric point (p*I*) of ETD was computed using the program ProtParam tools from the ExPASy Proteomics server (http://web.expasy.org/compute_pi/) (Gasteiger et al., 2005).

Generation of Sequence Logo From Multiple Sequence Alignment

For the creation of the sequence logo from the aligned sequences, WebLogo 3.2 (Crooks et al., 2004; Schneider and Stephens, 1990) was used by providing the default parameters.

Prediction of Glycosylation Sites

The potential glycosylation sites were predicted using the online webserver NetNGlyc 1.0 (Gupta et al., 2004), with parameters set to default.

Homology Model Building

For the generation of 3D homology model, we used numerous web-based protein modeling programs, including I-TESSER, MODELLER 9v19 program, and SWISS MODEL (Roy et al., 2010; Webb and Sali, 2016; Waterhouse et al., 2018). The atomic coordinates of ETE, with 63.71% identity (PDB ID: 5C2Z; Mariutti et al., 2015) was employed as a template.

Model Quality Validation and Assessment

The build ETD 3D model was validated and assessed by employing programs like PROCHECK (Laskowski et al., 2001; Laskowski et al., 1993), ERRAT version 2.0 (Colovos and Yeates, 1993), and Verify 3D (Bowie et al., 1991; Lüthy et al., 1992).

Molecular Docking

The protein and ligands were prepared for molecular docking by removing water molecules from the protein and adding hydrogen atoms. The ionization states of the atoms were kept in the ligand as mentioned in the database. The ligand geometry was optimized using the AM1 method (Dewar et al., 1985). The AM1-BCC method was used for calculating the partial charges of the ligands (Jakalian et al., 2002). The general AMBER force field (GAFF) method (Wang et al., 2004) was used for assigning the atoms type, bond angle, dihedral, and van der Waals parameters for the ligands. For molecular docking of the protein and ligands, the programs used were Molecular AutoDock 4.0, HADDOCK2.4, patchdock, and pardock (Schneidman-Duhovny et al., 2005; Gupta et al., 2007; Morris et al., 2009; van Zundert et al., 2016). The refinement of the protein–ligand complex was done using the FireDock (Mashiach et al., 2008).

Molecular Dynamics Simulation

The build 3D structure of ETD was assessed through various molecular dynamics (MD) simulation programs, like AMBER16 (Maier et al., 2015), GROMACS (Berendsen et al., 1995), MDweb, and MDMoby (Hospital et al., 2012). The FF14SB force field was used to measure all-atom protein interaction (Darden et al., 1993). The web server H++ (Anandakrishnan et al., 2012) was used to calculate the protonation states of the amino acid side chain, at neutral pH (7.0). The chloride ions (Cl^-) were used to neutralize the system. Then it was placed in a rectangular box of TIP3P water and expanded to at least 15 Å from any protein atom. The protein structure was optimized by minimizing the system for 500 conjugate gradient steps by applying a constant force constraint of 15 kcal/mol. The system was steadily heated from 0 to 300 K for 250 ps with a constant atom number, volume, and temperature all at once; simultaneously, the protein was restrained with a constant force of 10 kcal/mol Å2. The equilibration step was done using the constant atom number, pressure, and temperature ensemble for 500 ps, and the simulation was done for 100 ns with a 4 fs time step. The temperature and pressure were kept constant at 300 K and 1 atm, respectively, by Langevin coupling. The particle–mesh Ewald method (Darden et al., 1993) was used to compute the long-range electrostatic interactions. A cut-off distance of 10 Å to Van der Waals interactions was used during this process.

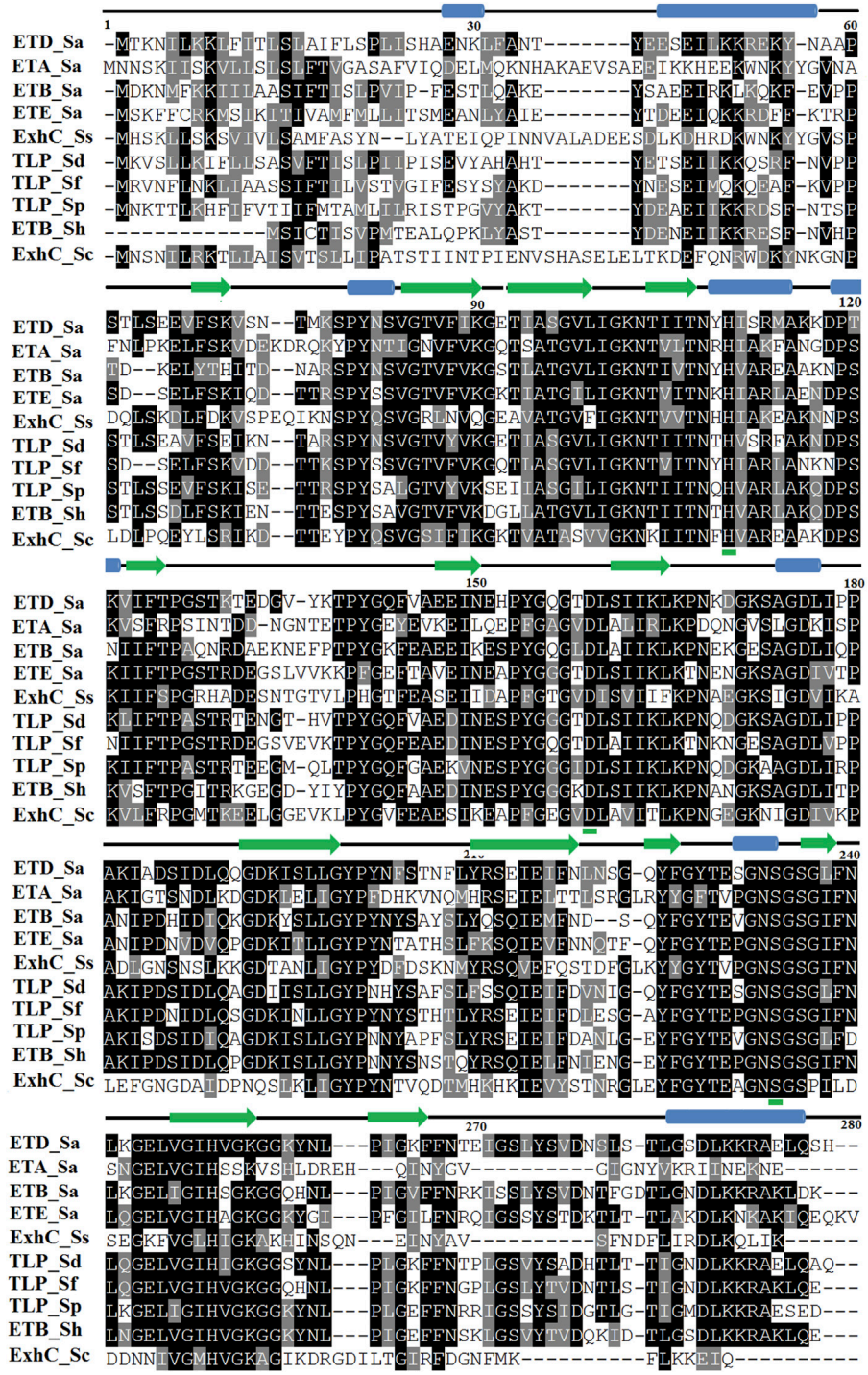

FIGURE 1 | Sequence alignment of ETs. ETD_*Sa*: exfoliative toxin D, *Staphylococcus aureus*, Gene Bank ID: AHC54578.1; ETA_*Sa*: epidermolytic toxin A from *S. aureus*, PDB ID: 1AJGJ; ETB_*Sa*: crystal structure of exfoliative toxin B, PDB ID: 1DT2; ETE_*Sa*: exfoliative toxin E from *S. aureus*, Gene Bank ID: WP_054190843.1, PDB ID: 5C2Z; ExhC_Ss: exfoliative toxin ExhC from *S. sciuri*, Gene Bank ID AEF13380.1; TLP_*Sd*: trypsin-like peptidase domain–containing protein from *S. delphini*, Gene Bank ID: WP_096546202.1; TLP_*Sf*: trypsin-like peptidase domain–containing protein from *S. felis*, Gene Bank ID: WP_103209705.1; TLP_Sp: trypsin-like peptidase domain–containing protein *S. pseudintermedius*, Gene Bank ID: WP_100002848.1; ETB_*Sh*: exfoliative toxin B from *S. hyicus*, Gene Bank ID: BAA99411.1, ExhB_*Sc*: exfoliative toxin ExhB *S. chromogenes*, Gene Bank ID: AAV98626.1. Amino acid residues involved in catalysis underlined with green. Secondary structural elements (alpha helices and beta strands) are shown above the sequence. Sequence numbering corresponds to the ETD_Sa precursor protein.

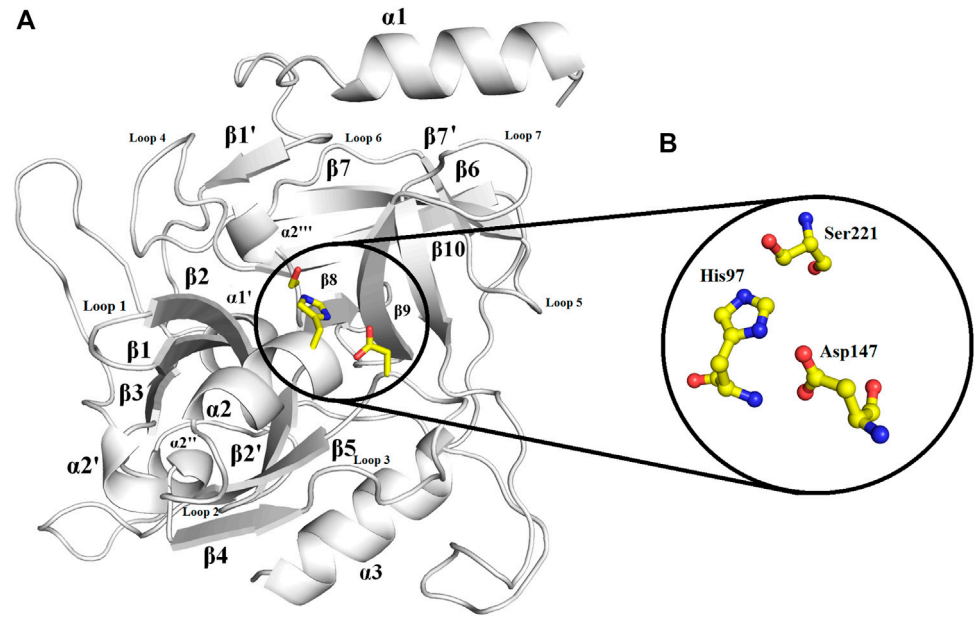

FIGURE 2 | Overall structure of ETD_Sa: **(A)** Cartoon representation. The active site residues are depicted as yellow sticks. The loops surrounding the active site cavity are also indicated **(B).** Residues involved in catalysis (catalytic triad) are highlighted. Numbering is according to mature ETD_Sa.

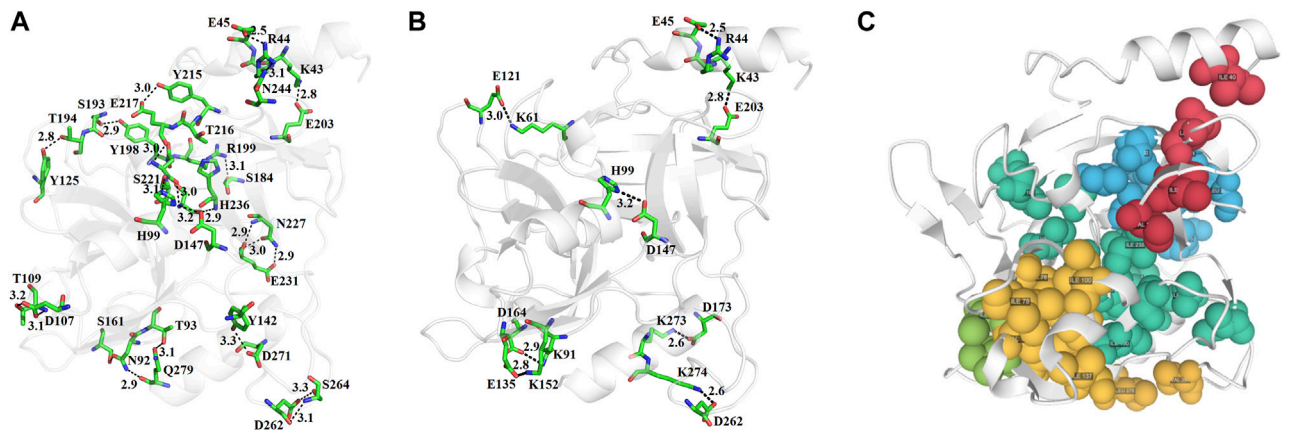

FIGURE 3 | (A) Hydrogen bonds, **(B)** disulfide bridges, and **(C)** hydrophobic interactions in ETD_*Sa* 3D structure.

The results from MD simulation were visualized using Visual Molecular Dynamics (Humphrey et al., 1996) and PyMOL (De Lano, 2002) molecular graphic visualization software.

Structure Alignment

The ETD structure was aligned to the other identical proteins using the PyMOL molecular graphics visualization program (De Lano, 2002).

Surface Charge Analysis

The PDB2PQR online server program was used to calculate the charge and radius (Dolinsky et al., 2004). The visualization of the surface and charge were carried out using the APBS tool from the PyMOL molecular graphics visualization program (De Lano, 2002).

RESULTS AND DISCUSSION

Multiple Sequence Alignment Analysis

The primary structure of ETD consists of 281 and 255 amino acid residues in the inactive (proenzyme) and active forms, respectively. The analysis of SignalP 3.0 shows that the first 26 amino acid residues of the proenzyme belong to the signal peptide (**Supplementary Figure S1**). The multiple sequence alignment analysis indicate a high sequence identity between ETD and the

TABLE 2 | Hydrogen bonds, salt bridges, and hydrophobic interactions in the 3D structure of ETD_*Sa*.

H-bonds

Network ID	Donor–acceptor	Distance	Angle DHA (degrees)
1	LYS43-NZ–GLU203-OE1	2.85	133.63
2	ARG44-NH2–GLU45-OE2	2.52	148.13
3	HIS99-ND1–ASP147-OD2	3.17	156.55
4	HIS99-NE2–SER221-OG	3.11	141.01
5	ARG199-NH2–SER184-OG	3.08	149.51
6	ASN220-ND2–SER223-OG	3.15	161.2
7	ASN227-ND2–GLU231-OE1	2.89	172.47
8	ASN244-ND2–ARG44-NH1	3.08	160.42
9	GLN279-NE2–THR93-OG1	2.92	137.44
10	THR109-OG1–ASP107-OD1	3.19	161.11
11	THR109-OG1–ASP107-OD2	3.32	142.7
12	TYR125-OH–THR194-OG1	2.8	167.92
13	TYR142-OH–ASP271-OD2	3.27	172.3
15	SER161-OG–ASN92-OD1	3.01	158.93
16	TYR198-OH–SER193-OG	2.9	176.31
17	TYR215-OH–GLU217-OE2	2.95	172.48
18	THR216-OG1–HIS236-NE2	3.2	152.06
19	SER264-OG–ASP262-OD2	3.14	161.6

Salt bridges

Residue 1	Residue 2	Distance (Å)
NZ LYS A 43	OE1 GLU A 203	2.8
NH2 ARG A 44	OE1 GLU A 45	2.5
NZ LYS A 61	OE1 GLU A 121	3.0
NZ LYS A 91	OD2 ASP A 164	2.9
NE2 HIS A 99	OD2 ASP A 147	3.2
OE1 GLU A 135	NZ LYS A 152	2.8
OD2 ASP A 174	NZ LYS A 273	2.6

Hydrophobic interactions

Cluster Id	Area (A)	No. contacts	Contacts/residue	Area (A)/residue
0	63.6	2	1.0	31.8
1	1922.9	49	3.3	39.2
2	926.2	21	2.6	44.1
3	62.9	2	1.0	31.5
4	75.1	2	1.0	37.6
5	1482.3	27	3.0	54.9
6	37.0	2	1.0	18.5
7	157.6	2	1.0	78.8

other ETs of *S. aureus* [ETA (50%), ETB (62.62%), and ETE (57.09%)] and ETs of *Staphylococcus sciuri* (ExhC, 45.16%), *Staphylococcus delphini* trypsin-like peptidase domain–containing protein (69.40%), *Staphylococcus felis* trypsin-like peptidase domain–containing protein (67.50%), *Staphylococcus pseudintermedius* trypsin-like peptidase domain–containing protein (65.36%), *Staphylococcus hyicus* ETB (66.60%), and *Staphylococcus chromogenes* ET ExhB (43.48%) (**Table 1**). The average sequence identity between ETD and other aligned ETs are 58.57%. The ETD shows very low sequence identity to *Staphylococcus epidermidis* glutamyl endopeptidases (30.59%). The amino acid residues of the catalytic triad (His110, Asp159, and Ser234) are completely conserved among all the aligned ETs (**Figure 1**). Besides the amino acid residues of the catalytic triad, the other fully conserved amino acid residues between ETD and others ETs include Pro80, Tyr81, Gly85, Gly100, Lys101, Asn102, Thr107, Asn108, Ala115, Pro119, Phe124, Pro126, Pro140, Gly 142, Pro153, Gly155, Gly157, Ileu163, Gly171, Gly175, Asp176, Ala181, Gly192, Asp193, Leu197, Gly199, Tyr200, Pro201, Glu215, Tyr225, Gly227, Thr229, Gly232, Asn233, Ser234, Gly235, Ser236, Gly247, and His249. The analysis of the sequence logo file produced using the WebLogo 3.2 indicates that the amino acids residues surrounding the active site are highly conserved among all the aligned ETs (**Supplementary Figure S2**).

Domain Analysis

The domain analysis carried out using conserved domain search (CD Search; Marchler-Bauer et al., 2017) and CDART (Conserved Domain Architecture Retrieval Tools; Geer et al., 2002) on the NCBI website indicate that the ETD is a single

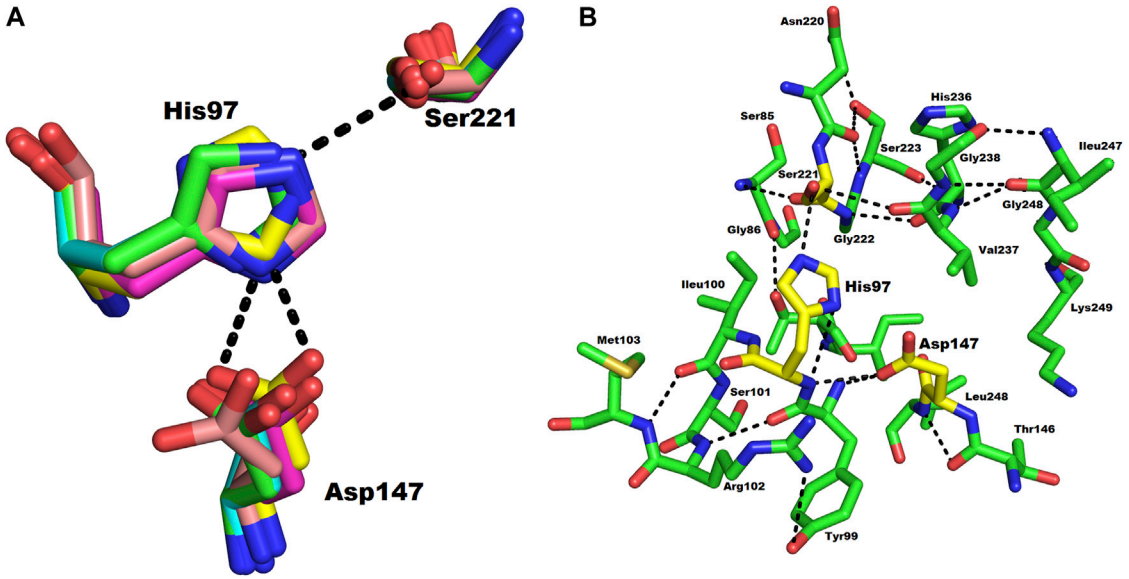

FIGURE 4 | (A) Structural alignment of the three catalytic residues (catalytic triad) of ETs. Green, magenta, yellow, and cyan represents the triad of ETD_*Sa* (model), ETA, ETB, and ETE, respectively. **(B)** Hydrogen bond network in the catalytic triad of ETD_*Sa*. The amino acid residues are shown as green sticks.

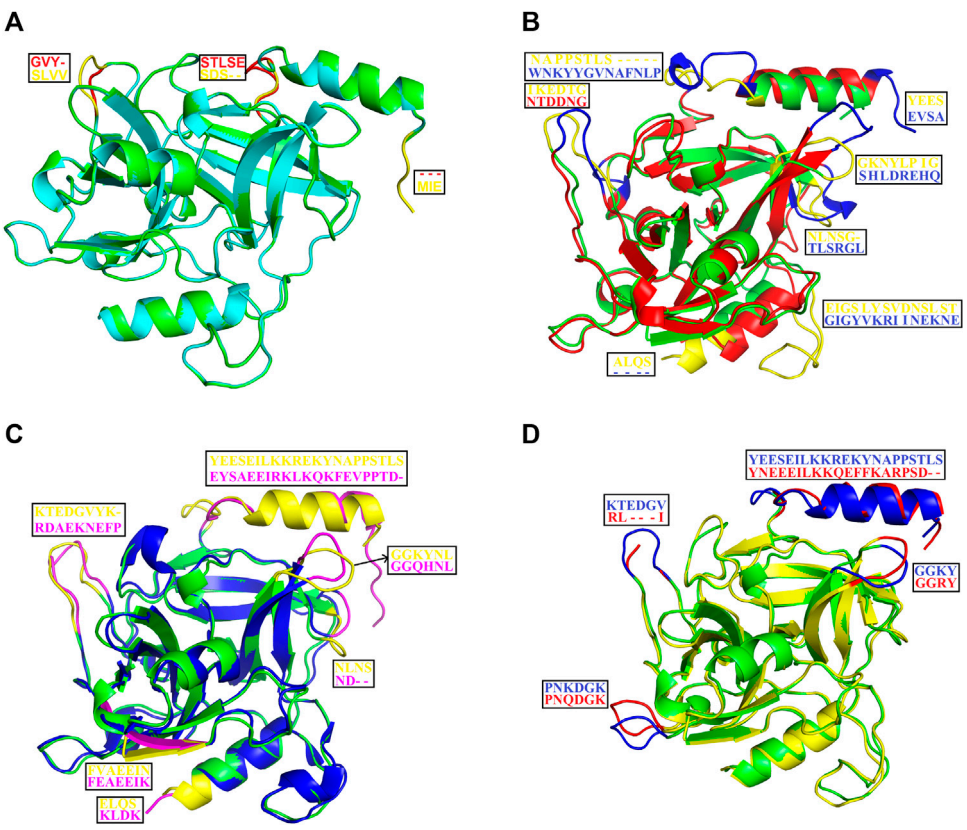

FIGURE 5 | Structural alignment among ETS. **(A)** ETD_Sa (green) aligns with ETE_ Sa (cyan). **(B)** ETD_Sa (green) aligns with ETA_ Sa (red). **(C)** ETD_Sa (green) aligns with ETB_ Sa (blue). **(D)** ETD_Sa (green) align ET_ Sp (yellow) (*S. pseudintermedius* exfoliative toxin EXI). The regions (loops) displaying differences and their corresponding amino acid residues (shown in the box) are colored in yellow, pink, blue, and red.

TABLE 3 | Root mean square deviation for structural alignment between ETD_*Sa* and other ETS.

Proteins	RMSD (Å)
ETD aligned ETE	0.060
ETD aligned ETA	0.618
ETD aligned ETB	0.632
ETD aligned EXI	0.516

domain protein belonging to trypsin-like serine proteinases (Tryp_SPc super family; 61–236 amino acid residues matching) most of which are synthesized as inactive precursors or zymogens. These are converted to the active form after limited proteolysis.

The MotifFinder analysis indicates that ETD is a trypsin-2 peptidase and belongs to the trypsin-like peptidase domain (84–235 amino acid residues matching) (**Supplementary Figure S3**).

Glycosylation

Although Rogolsky et al. (1974) have shown that ETs of *S. aureus* contain 9% carbohydrates; the NetGlycan 4.0 server (Steentoft et al., 2013) indicates that ETD is not glycosylated. The crystal structures of other ETs (A, B, and E) also do not have any glycosylation (Cavarelli et al., 1997; Papageorgiou et al., 2000; Mariutti et al., 2015).

Biochemical Properties

The molecular weights of precursor and mature ETDs were 30.80 and 27.90 kDa, with corresponding p*I*s 8.90 and 7.99, respectively. These values are in agreement with the previously calculated values for ETs (De Azavedo et al., 1988; Gasteiger et al., 2005).

The Scoop (Pucci et al., 2017) analysis for protein thermal stability shows the melting temperature (Tm) of ETD is 56.5°C (**Supplementary Figure S4**), which is in agreement with the previous experimentally measured value for ETA, ETB, and ETE (Piemont et al., 1986; Mariutti et al., 2015).

Homology Modeling, Model Evaluation, and Molecular Docking

For 3D structural characterization, the homology model of ETD was generated by applying various software including the SWISS MODEL (Waterhouse et al., 2018), MODELLER 9v19 program (Webb and Sali, 2016), and I-TESSER (Roy et al., 2010). The atomic coordinates of ETE, with 63.71% identity (PDB ID: 5C2Z; Mariutti et al., 2015) was employed as a template (**Supplementary Figure S5**). After a comparison of the build models from all the three programs, the model built by the SWISS MODEL was selected based on GMQE which depicts the quality estimation of it (**Supplementary Tables S1, S2**). The GMQE score is given as a number between 0 and 1. Higher numbers show higher accuracy. So, the model has the GMQE value of 0.88, reflecting good accuracy of the model. The build model of ETD was validated using PROCHECK (Ramachandran plot) (Laskowski et al., 1993), ERRAT2 (Colovos and Yeates, 1993), and Verify3D (Bowie et al., 1991; Lüthy et al., 1992). The Ramachandran plot analysis shows that 91.1% of the amino

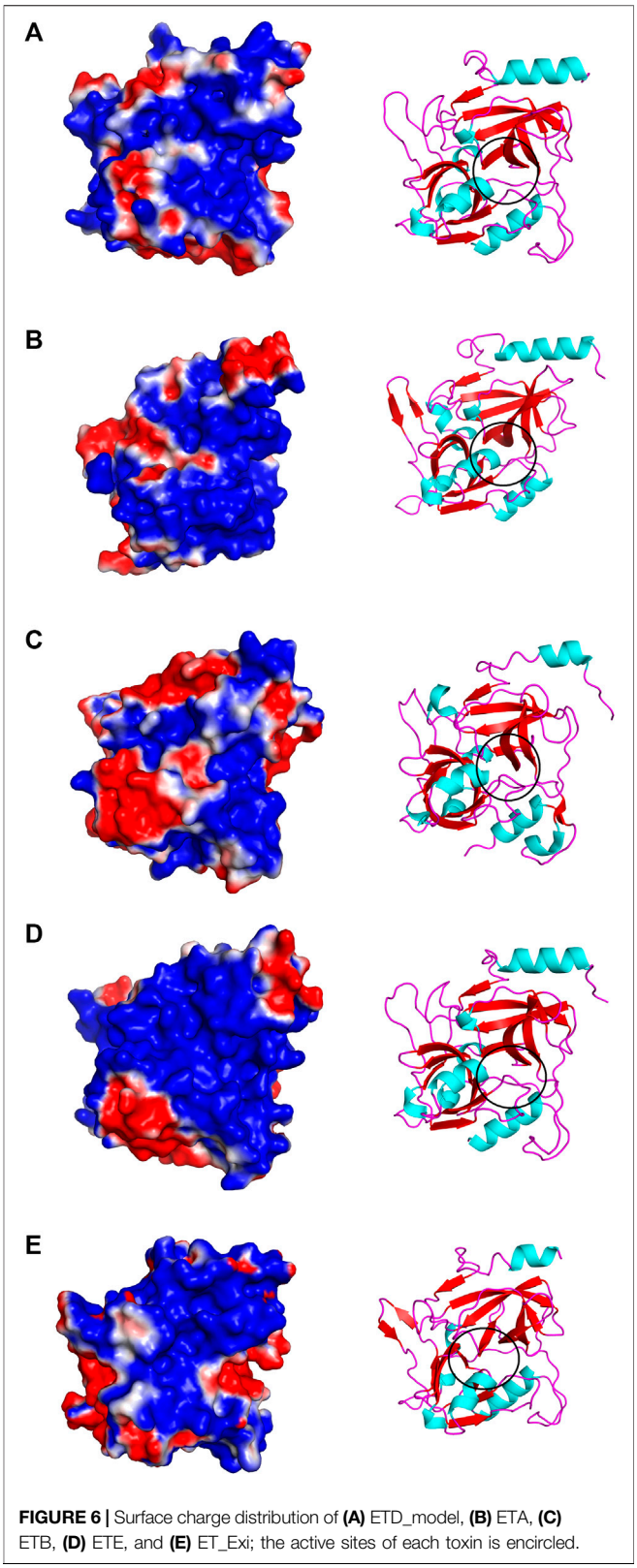

FIGURE 6 | Surface charge distribution of **(A)** ETD_model, **(B)** ETA, **(C)** ETB, **(D)** ETE, and **(E)** ET_Exi; the active sites of each toxin is encircled.

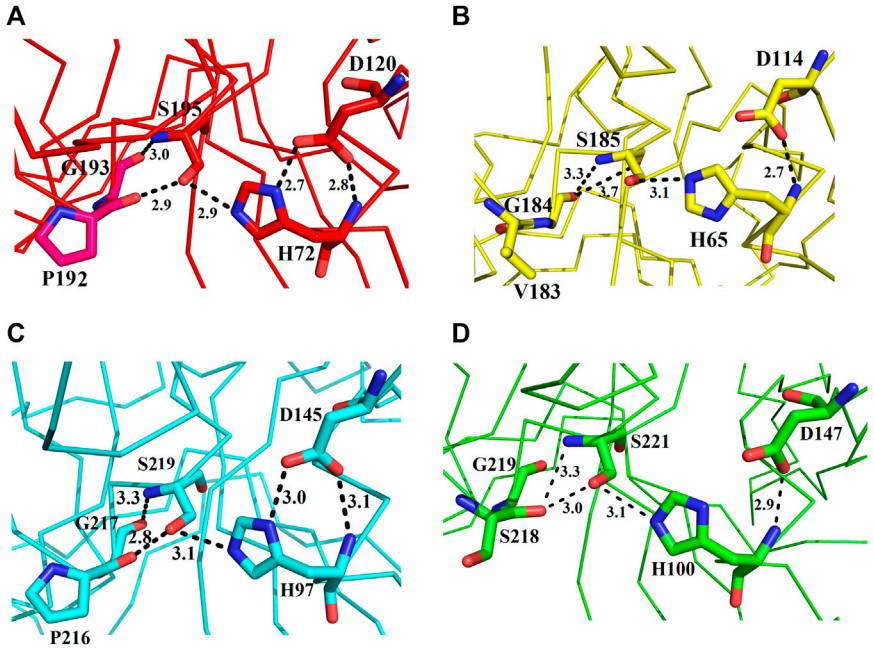

FIGURE 7 | Representation of amino acid residues that make the ETs inactive: **(A)** ETA, **(B)** ETB, **(C)** ETE, and **(D)** ETD_model.

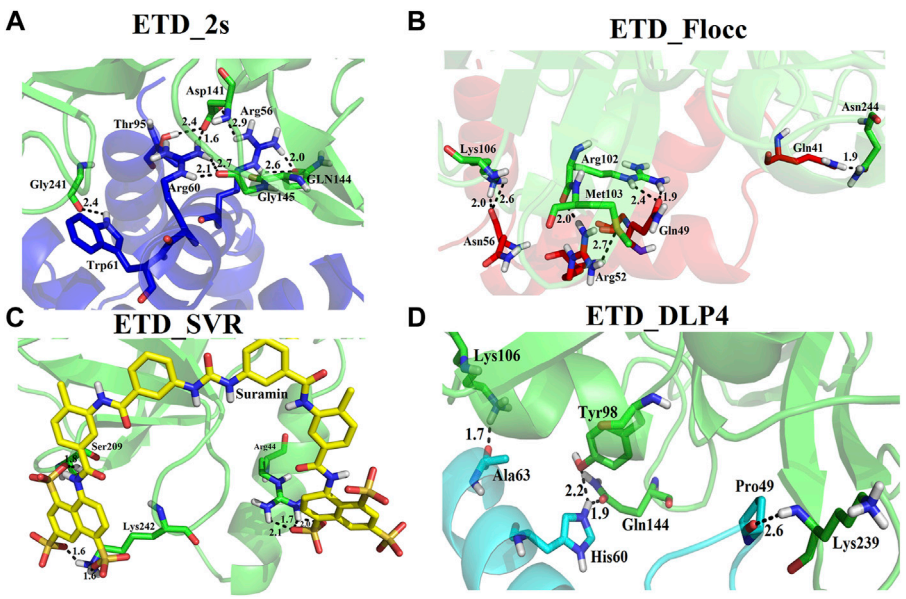

FIGURE 8 | Proposed mechanisms for ETs. **(A)** The catalytic triad (His72, Asp120, and Ser195) and the amino acid residues Pro192, Gly193 (red sticks), and hydrolytic water (green sphere); the enzyme is inactive in this state. **(B)** The enzyme (red) becomes active after binding to the substrate (green), by disrupting the bond with Pro192. **(C)** The enzyme attacks the substrate (peptide) (green sticks) carboxyl group. **(C)** Tetrahedral intermediate. **(D)** Donation of H+ by His72 to peptide for leaving group, and breakage of the tetrahedral intermediate and release of the first product. **(E)** Splitting of the hydrolytic water molecule into H+ and OH–. **(F)** The OH– attacks the bond between Ser195 and the peptide C-terminal end and liberates this part from the enzyme. **(G)** ET (red) and enzyme (green) complex.

acid residues were in the most favored region and 8.8% were in the additionally allowed region with no amino acid residue in generously allowed and disallowed regions (**Supplementary Figure S6**). The ERRAT2 inspection indicates the overall quality factor of 90.13%, which comes in the average range of protein 3D structure quality according to the program developer (**Supplementary Figure S7**). The results obtained from Verify3D display 99.59% of amino acid residues having a 3D–1D score >0.2

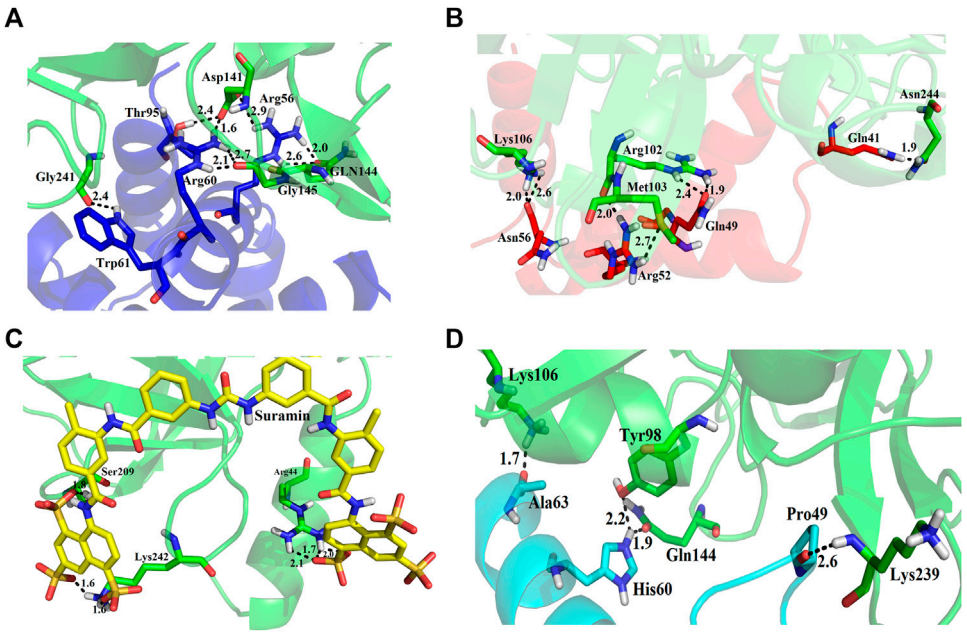

FIGURE 9 | Inhibition of ETD_*Sa* (green sticks) by **(A)** 2S albumin (blue sticks), **(B)** flocculating protein (red sticks), **(C)** suramin (yellow sticks), and **(D)** DLP-4 (cyan sticks).

(**Supplementary Figure S8**). No poor area (zero or negative) in the ETD build model was detected by the Verify3D program, indicating a suitable environment for each amino acid residue in the determined structure (**Supplementary Figure S8**). The entire structural criterion including chirality and unusual *cis/trans* configuration was perfect, and there were no steric clashes in the build model (**Supplementary Figure S9A**), as indicated by results coming from molecular dynamic simulation (MDWeb analysis). The radius of gyration was constant at 68.8–68.9 Å during the whole process, with only 0.1 Å variations (**Supplementary Figure S9B**). The B-factor and RMSD per residue values indicate some regions with flexibility, mostly confined to the loop region of ETD structure (**Supplementary Figures S9C,D**).

The molecular docking results produced by AutoDock 4.0, HADDOCK2.4, patchdock, and pardock (Schneidman-Duhovny et al., 2005; Gupta et al., 2007; Morris et al., 2009; van Zundert et al., 2016) were nearly the same; however, we select the results from HADDOCK2.4 based on the RMSD value and various forms of energy released during the docking process (**Supplementary Figures S13A,D, S14A**). Also, the results from HADDOCK2.4 were very similar to MD simulation results from GROMACS, both of which give the same number of H-bonds between the ETD_*Sa* and the ligands (**Supplementary Figures S13C,F**; **Figure 11**).

Overall Structure

The overall structure of ETD is similar to the chymotrypsin-like serine protease fold. The structure is composed of 13 β-strands and seven α-helices (**Figure 2**; **Supplementary Figure S10**) that fold into two well-defined six-stranded β-barrels whose axes are roughly perpendicular to each other. The β-strands are antiparallel to each other. To make its structure simpler for general discussion, it can be split into two domains, namely, N-terminal and C-terminal domains.

The N-terminal domain is composed of amino acid residues from Tyr35 to Leu148 and Leu228 to Lys242, from the C-terminal part of the protein. This domain comprises four α-helices (α1, α1′, α2, and α2′) and seven β-strands (β1′, β1, β2′, β2, β3, β4, and β9) (**Supplementary Figure S10**). This domain starts with a long α-helix which lies adjacent to the C-terminal β-barrel (**Figure 2A**). This alpha helix is charged having both acidic and basic amino acid residues (Asp, Glu, Lys, and Arg). The C-terminal domain is made up of amino acid residues from Ser149 to Asn227 and Tyr243 to Ser280. This domain contains three α-helices (α2″, α2‴, and α3) and five β-strands (β5, β6, β7, β7′, and β8) (**Supplementary Figure S10**). The active site which is composed of the three catalytic residues (catalytic triads) His, Asp, and Ser is located at the junction of the two domains (**Figures 2A,B**). The active site is surrounded by various loops from all four sides (**Figure 2A**). In several chymotrypsin-like serine proteinases, the loops 1, 2, 3, and 4 are known to participate in the determination of subsite preference, while loops 5, 6, and 7 are important to influence the specificity of the S1 site (Perona, and Craik, 1995). Although, like other serine proteinases, there are no disulfide bridges in the structure of ETD, the 3D structure of this enzyme (and other ETs) is highly stable due to various hydrogen bonds, salt bridges, and hydrophobic interactions (**Figures 3A–C**; **Table 2**).

The PredictProtein server (Rost et al., 2004; Bigelow et al., 2004) indicates that the secondary structure of ETD is composed of 7.83% α-helices, 24.56% β-strands, and 67.62% loops

TABLE 4 | List of protein (ETD)–ligand (suramin) interactions.

Hydrogen bonds

	<----- A T O M 1 ----->					<----- A T O M 2 ----->					
	Atom no.	Atom name	Res name	Res no.	Chain		Atom no.	Atom name	Res name	Res no.	Chain	Distance
1.	106	NH1	ARG	44	A	-->	2350	O30	SVR	205	B	2.85
2.	1672	OG	SER	209	A	-->	2423	O79	SVR	205	B	2.69
3.	1672	OG	SER	209	A	<--	2423	O79	SVR	205	B	2.69
4.	1962	NZ	LYS	242	A	-->	2411	O80	SVR	205	B	2.49
5.	1962	NZ	LYS	242	A	-->	2416	O85	SVR	205	B	2.53

Non-bonded contacts

	<----- A T O M 1 ----->					<----- A T O M 2 ----->					
	Atom no.	Atom name	Res name	Res no.	Chain		Atom no.	Atom name	Res name	Res no.	Chain	Distance
1.	105	CZ	ARG	44	A	---	2350	O30	SVR	205	B	3.07
2.	105	CZ	ARG	44	A	---	2351	O28	SVR	205	B	3.79
3.	106	NH1	ARG	44	A	---	2350	O30	SVR	205	B	2.85
4.	109	NH2	ARG	44	A	---	2348	S21	SVR	205	B	3.07
5.	109	NH2	ARG	44	A	---	2350	O30	SVR	205	B	2.54
6.	109	NH2	ARG	44	A	---	2351	O28	SVR	205	B	2.57
7.	619	CG	HIS	99	A	---	2385	C50	SVR	205	B	3.78
8.	620	ND1	HIS	99	A	---	2385	C50	SVR	205	B	3.30
9.	1065	O	GLY	145	A	---	2395	C59	SVR	205	B	3.77
10.	1065	O	GLY	145	A	---	2396	C60	SVR	205	B	3.60
11.	1075	N	ASP	147	A	---	2395	C59	SVR	205	B	3.26
12.	1078	CB	ASP	147	A	---	2395	C59	SVR	205	B	3.53
13.	1081	OD2	ASP	147	A	---	2385	C50	SVR	205	B	3.17
14.	1081	OD2	ASP	147	A	---	2386	C52	SVR	205	B	3.00
15.	1671	CB	SER	209	A	---	2423	O79	SVR	205	B	3.59
16.	1672	OG	SER	209	A	---	2420	C69	SVR	205	B	3.71
17.	1672	OG	SER	209	A	---	2421	S73	SVR	205	B	3.62
18.	1672	OG	SER	209	A	---	2423	O79	SVR	205	B	2.69
19.	1923	CG1	VAL	237	A	---	2386	C52	SVR	205	B	3.78
20.	1944	O	LYS	239	A	---	2380	N44	SVR	205	B	3.85
21.	1957	CA	LYS	242	A	---	2409	O81	SVR	205	B	3.73
22.	1958	CB	LYS	242	A	---	2409	O81	SVR	205	B	3.54
23.	1959	CG	LYS	242	A	---	2408	S75	SVR	205	B	3.71
24.	1959	CG	LYS	242	A	---	2409	O81	SVR	205	B	2.83
25.	1959	CG	LYS	242	A	---	2411	O80	SVR	205	B	3.74
26.	1960	CD	LYS	242	A	---	2408	S75	SVR	205	B	3.79
27.	1960	CD	LYS	242	A	---	2409	O81	SVR	205	B	3.21
28.	1960	CD	LYS	242	A	---	2411	O80	SVR	205	B	3.24
29.	1961	CE	LYS	242	A	---	2408	S75	SVR	205	B	3.74
30.	1961	CE	LYS	242	A	---	2409	O81	SVR	205	B	3.75
31.	1961	CE	LYS	242	A	---	2411	O80	SVR	205	B	2.80
32.	1961	CE	LYS	242	A	---	2413	C72	SVR	205	B	3.28
33.	1961	CE	LYS	242	A	---	2414	C76	SVR	205	B	3.79
34.	1961	CE	LYS	242	A	---	2415	S83	SVR	205	B	3.88
35.	1961	CE	LYS	242	A	---	2416	O85	SVR	205	B	2.88
36.	1962	NZ	LYS	242	A	---	2408	S75	SVR	205	B	3.85
37.	1962	NZ	LYS	242	A	---	2411	O80	SVR	205	B	2.49
38.	1962	NZ	LYS	242	A	---	2413	C72	SVR	205	B	3.39
39.	1962	NZ	LYS	242	A	---	2414	C76	SVR	205	B	3.85
40.	1962	NZ	LYS	242	A	---	2415	S83	SVR	205	B	3.46
41.	1962	NZ	LYS	242	A	---	2416	O85	SVR	205	B	2.53
42.	1962	NZ	LYS	242	A	---	2417	O86	SVR	205	B	3.61
43.	1986	CG	ASN	244	A	---	2352	C12	SVR	205	B	3.87
44.	1988	ND2	ASN	244	A	---	2352	C12	SVR	205	B	3.79
45.	1988	ND2	ASN	244	A	---	2353	C7	SVR	205	B	3.45
46.	1988	ND2	ASN	244	A	---	2358	O4	SVR	205	B	3.64
47.	2015	CD1	ILE	247	A	---	2389	O54	SVR	205	B	3.83

Number of hydrogen bonds: 5

Number of non-bonded contacts: 47

(**Supplementary Figure S11A**). The results obtained from this program also showed that ETD has 43.06% amino acid where the residues are surface exposed, 51.63% are buried, and 5.34% are intermediate (**Supplementary Figure S11B**). These results are in agreement with the results obtained for other ETs (Mariutti et al., 2015).

Active Site

The active site of ETD is made up of three amino acid residues (His, Asp, and Ser) which are called the catalytic triad. These three amino acid residues are fully conserved among all the aligned ETs (**Figure 1**). These amino acid residues are also aligned well structurally to each other (**Figure 4A**). The amino acid residues of the active site are stabilized by hydrogen bonds among themselves and with other amino acids residues nearby (**Figure 4B**). The His97 is H-bonded to Ser221, while Asp147 is bonded to the main chain of His97 and also to Tyr99, and Ser221 to the main chain of Val237 (**Figure 4B**).

Metal Ion/Ligand Binding Sites

The analysis of the results forms Ion Com–Ion Ligand binding site prediction (Hu et al., 2016), identifies the amino acid residues (Glu5, Tyr64, His65, Glu101, His106, Asp147, Glu167, Phe171, Asn172, Phe179, Tyr181, Glu183, Ser184, G185, Asn186, Ser187, His202, Arg241, Ala242, Glu243, Leu244, Gln245, and Ser246 as potential binding sites for Zn^{+2}, and Ileu49, Ala50, His65, Ileu66, Tyr181, Thr182, Glu183, Ser184, Gly185, Asn186, Ser187, His202, Val203, Gly204, Lys205, and Pro212 as potential binding sites for K^{+}). Zn^{+2} and K^{+} have been also encountered in the 3D structure of an alkaline form of v8 proteinase from *S. aureus* (PDB ID: 1WCZ, unpublished work, PDB ID: 1QY6, Prasad et al., 2004). In this v8 proteinase, Zn^{+2} is tetrahedrally coordinated by Asp7, His9, and Lys147 (**Supplementary Figure S12A**), while K^{+} is coordinated by His107 only (**Supplementary Figure S12B**).

Structural Comparisons Among Exfoliative Toxins

The structural alignment analysis between ETD and other ETs indicates that all of these align well to each other with some differences in the loop regions (**Figures 5A–D**). The highest differences were found with ETA and ETB with an RMSD value of 0.618 and 0.632, respectively (**Table 3**). These differences were mostly due to amino acid residues confined to the loop regions (**Figures 5A–D**). The surface charge distribution of these enzymes also varies considerably because of these variations in the amino acid residues in the loop regions (**Figures 6A–E**). The surface charge of ETD is partially positive and partially neutral around the active site (**Figure 6A**) while that of ETA is partially positive and partially negative (**Figure 6B**). Similarly, the **Figure 6C** surface charge of ETB is highly negative (**Figure 6C**) and that of ETE is highly positive around the active site (**Figure 6D**).

These enzymes are usually inactive in their free state due to the hydrogen bonds between Pro192 and G193 (donor–acceptor distances of 2.9–3.0 Å, ETA), V183 and G184 (donor–acceptor distances of 3.3–3.7 Å, ETB), P216 and G217 (donor–acceptor distances of 2.8–3.3 Å, ETE), and S218 and G219 (donor–acceptor distances of 3.0–3.3 Å, ETD (**Figures 7A–D**). A mean distance of 3.0 Å (donor–acceptor) is required for

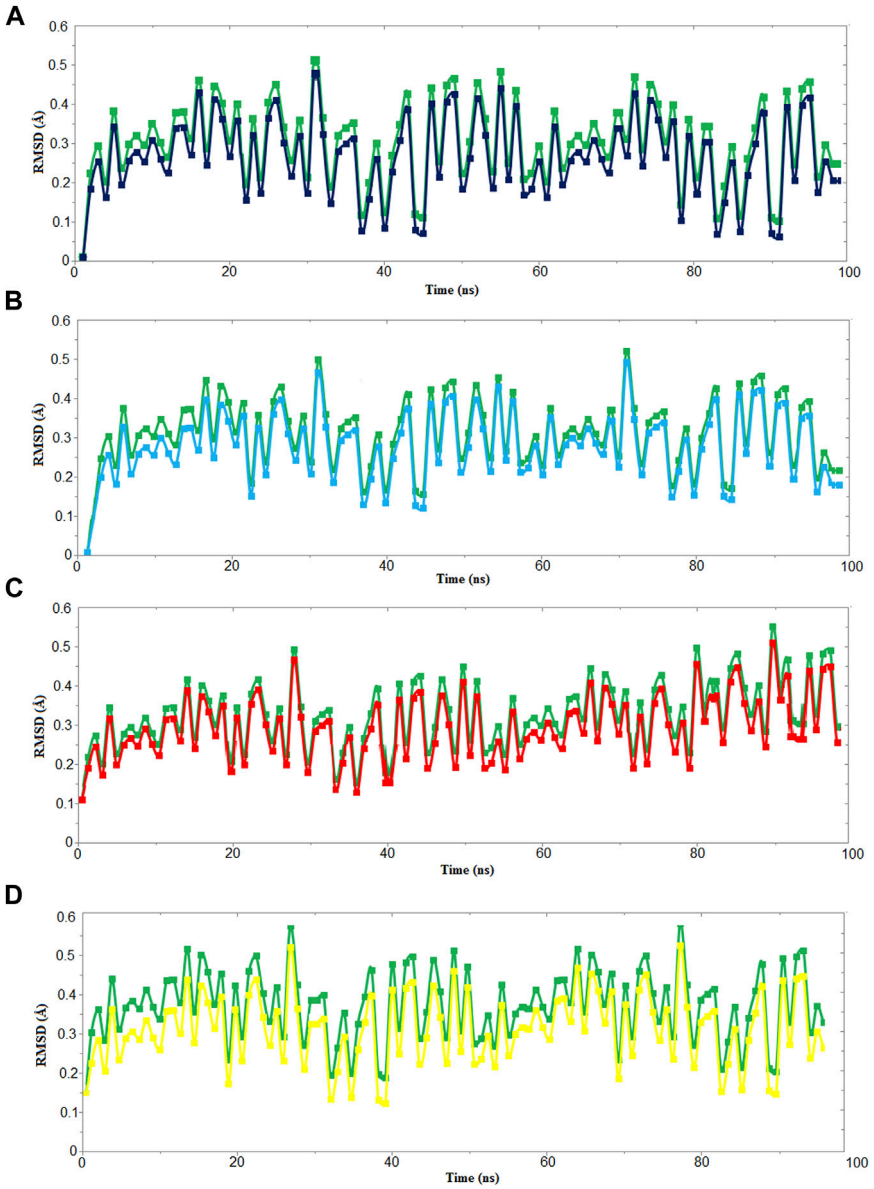

FIGURE 10 | RMSD vs time graph for 100 ns MD simulation of ETD_*Sa* (green) with **(A)** 2S albumin, **(B)** flocculating protein (black), **(C)** suramin (red), and **(D)** DLP4 (yellow).

hydrogen bond formation in protein secondary structure (Rajagopal et al., 2005; Dev et al., 2015). Depending on the distance between donor and acceptor, the hydrogen bond can be classified into three main classes (Jeffrey, 1997). These are strong hydrogen bonds (often covalent) (donor–acceptor distances of 2.2–2.5 Å), medium hydrogen bonds (largely electrostatic) (2.5–3.2 Å), and weak hydrogen bond (electrostatic) (3.2–4.0 Å). Keeping this in view, the hydrogen bond between active site serine residue and other amino acid residues (Pro, Gly, Val, and Ser) are classified as medium (ETA and ETE) and weak (ETB and ETD). Thus ETA and ETE are inactive in their native states and ETB and ETD are active. According to Steitz and Shulman (1982), most of the serine proteinases are inactive in their native state and become active only when substrate binds to these enzymes.

Mechanism of Action

The ETs use the same catalytic mechanisms as used by the other serine proteinases-like chymotrypsin to hydrolyze their substrate (Hartley and Kilby, 1954; Polgár, 1971; Katona et al., 2002). However, there is no oxyanion hole formation in ETs (Papageorgiou et al., 2000). The three catalytic amino acid residues (H57, D102, and S195—catalytic triad) are fully conserved in all ETs (**Figure 1**) and also in other serine proteinases (Birktoft et al., 1976; Steitz and Shulman, 1982; Bagley and Altman, 1996). These ETs follow the general

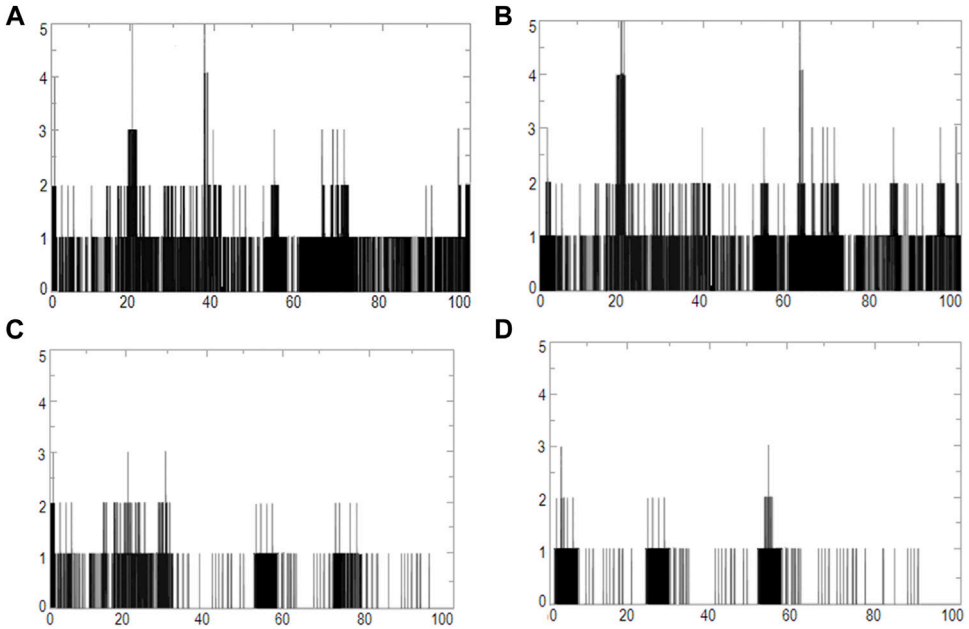

FIGURE 11 | Graphs of hydrogen bonds plotted vs time for 100 ns range simulations of ETD_Sa and **(A)** 2S albumin, **(B)** flocculating protein, **(C)** suramin, and **(D)** DLP4.

acid–base catalysis (Anderson et al., 1961; Polgár and Bender, 1969; Polgár, 1971). They are inactive in their free state due to the hydrogen bond formed between active site serine and some other specific residues (**Figures 7A-D**, **Figure 8**). A twist of 180° in these amino acid residues (**Figure 8B**) results when the N-terminal helix binds to a specific epidermal receptor, that make the toxins active (Vath et al., 1999 and 1997). His72 then takes a proton from Ser195 (**Figure 8B**) and makes the serine residue a strong electrophile (**Figure 10C**) that attacks on the sessile peptide bond between Glu381 and G382 (**Figure 8C**). This leads to the construction of a tetrahedral intermediate which is formed between Ser195 and desmoglein-1 (substrate of ETs) (**Figure 8D**). This intermediate is unstable, and electrons rearrangement leads to breakage: the C-terminus of the substrate is detached and released (**Figure 8E**). The N-terminus of the substrate is still attached to the enzyme (**Figure 8F**). An attack from OH– of water on the bond between the enzyme and N-terminus of the substrate causes breakage of the N-terminus of the substrate, and this part also departs from the enzyme and is restored to its original state.

Inhibition Study of Exfoliative Toxin D by Natural and Synthetic Inhibitors

We used four inhibitors: two natural [2S albumin (PDB ID: 5DOM, Ullah et al., 2015) and flocculating protein [PDB ID: 5WUZ, Kini et al., 2016 (Unpublished) *Moringa oleifera*] and two synthetics [suramin (PubChem CID: 5361) and defensin-like peptide 4 (DLP4) (UniProtKB ID: W5U4X3)]. The 2S albumin and flocculating protein are highly positively charged with several arginine residues located on their surfaces. Both of these inhibitors bind to the middle and C-terminal regions of the ETD (**Figures 9A,B**). The 2S albumin and flocculating protein make six hydrogen bonds (**Supplementary Figures S13A–C**). However, 2S albumin makes two salt bridges and 64 nonbonded contacts, while the flocculating protein makes one salt bridge and 84 nonbonded contacts (**Supplementary Figures S13A–C**). In the case of synthetic inhibitors, suramin binds to the N- and C-terminal of ETD and makes five hydrogen bonds and 47 nonbonded contacts (**Figure 9C**; **Table 4**), while DLP4 binds to the middle and C-terminal regions of ETD and make four hydrogen and 40 nonbonded contacts (**Figure 9D**; **Supplementary Figures S14A–C**). The 2S albumin and flocculating protein have already been used as inhibitors for Coronavirus $3CL^{Mpro}$ (Ullah and Ullah, 2021), while suramin has been shown to inhibit the function of human thrombin, snake venom thrombin like enzymes, and phospholipases A2 enzymes (Monteiro et al., 2004; Murakami et al., 2005; Fernandes et al., 2007; Lima et al., 2009; Ullah et al., 2018). The inhibition of ETD from *S. hyicus* has been done with DLP4 (Li et al., 2020; Ma et al., 2021). The results of MD simulation (GROMACS) indicate that the interactions between ETD_*Sa* and all the four ligands were stable throughout the simulation process (**Figure 10**), and 2S albumin and flocculating proteins made 4–6 bonds while suramin and DLP4 formed 2–4 hydrogen bonds (**Figure 11**).

Differences Between Exfoliative Toxins and Other Serine Proteinases

The ETs differ from other serine proteinases by possessing an N-terminal α-helix that is highly charged (Vath et al., 1997; Cavarelli et al., 1997), and they also have two amino acid residues [proline (192)–glycine (193), ETA and valine (183)–glycine (184), ETB] which make a hydrogen bond with the active site serine and make

them inactive (Ladhani, 2003). In the catalytic reactions of ETs, there is no formation of oxyanion hole formation (Papageorgiou et al., 2000). The serine proteinases from other organisms are highly stable by having many disulfide bridges (Ullah et al., 2018); however, the ETs lack any such disulfide bridges (Mariutti et al., 2015; Piemont et al., 1986; Papageorgiou et al., 2000). The serine proteinases are highly glycosylated, while ETs do not have any carbohydrates in their 3D structure (Piemont et al., 1986; Papageorgiou et al., 2000; Mariutti et al., 2015).

S. aureus not only causes diseases in human beings but also in other organisms like small piglets (Schwarz et al., 2021; Malik et al., 2021) and dogs (Sahin-Tóth et al., 2021). These bacteria show resistance to methicillin and are also called methicillin-resistant *S. aureus* (Hirose et al., 2019). Their resistance to methicillin is a serious issue because these bacteria are the main cause of skin infections in animals (Hirose et al., 2019; Del Giudice, 2020). To find a new treatment for skin diseases caused by *S. aureus*, many researchers around the world are trying to find out novel inhibitors for the toxins produced by these bacteria. Mohan and Venugopal (2020) have carried out molecular binding and simulation studies of flavonoids those inhibit the ETA of *S. aureus* and have come to know that these make three hydrogen bonds with the ETA. Li et al., 2020 have used DLP4 and its derivatives as antimicrobial agents against *S. aureus* (Li et al., 2020). Suramin is used as an antitrypanosomal drug, and it has been shown to inhibit human thrombin (Lima et al., 2009), snake venom phospholipases A2 (Salvador et al., 2018), snake venom serine proteinases (Ullah et al., 2018), nucleocapsid protein from novel bunyavirus (Jiao et al., 2013), RNA-dependent RNA polymerase of murine norovirus (Mastrangelo et al., 2012), and pyruvate kinase of *Leishmania mexicana* (Morgan et al., 2011). In the majority of the studies carried out using suramin as inhibitor, it has been found that it binds to the C-terminal part of the protein (Lima et al., 2009; Ullah et al., 2018). In the current study, suramin was found to bind to the C-terminal of ETD also (**Figure 11C**). The 2S albumin seed storage proteins (Ullah et al., 2015) and flocculating protein (Sousa et al., 2020) from *M. oleifera* are highly positively charged proteins. In our previous study, we had shown that these proteins bind to SARS-CoV-2 3CL M^{pro} in-between domain II and III and restrict their moment (Ullah and Ullah, 2021). This may result in the inactivation of this enzyme. In the present study, the 2S albumin seed storage proteins and flocculating protein bind in-between the N- and C-termini of ETD (**Figures 11A,B**) and may restrict the moments in these parts.

CONCLUSIONS AND FUTURE PERSPECTIVES

In conclusion, the model-based structure characterization of ETD_*Sa* and its sequence and structural comparison with other ETs were studied in this work. ETD_*Sa* displays a high sequence identity with the other ETs. The build ETD_*Sa* model also aligned well to the 3D structures of other ETs, with some differences that were confined to the loop regions. The differences in amino acid residues in the loop regions cause a different surface charge distribution to these enzymes which may also convey variable substrate specificity to these enzymes. The proposed mechanism of the ET was elucidated based on their 3D structure. The inhibition study of these enzymes by natural and synthetic inhibitors will further facilitate the treatment of SSSS. Finally, for further validation of the current study, the 3D structure of ETD_*Sa* may be determined by X-ray crystallography.

DATA AVAILABILITY STATEMENT

The datasets presented in this study can be found in online repositories. The names of the repository/repositories and accession number(s) can be found in the article/ **Supplementary Material**.

AUTHOR CONTRIBUTIONS

AU: Drafted, written, and reviewed the manuscript. AK, KU and AS: Proofread and correct the manuscript. AH: Funding Acquisition, Validation, analysis, and interpretation of data.

FUNDING

The project was supported by grant from The Oman Research Council (TRC) through the funded project (BFP/RGP/CBS/19/220). A part of the project was supported by higher education commission (HEC), Pakistan, (HEC-No: 7709/Federal/NRPU/R8D/HEC/ 2017).

ACKNOWLEDGMENTS

The authors would like to thank the University of Nizwa for the generous support of this project and Oman Research Council (TRC) through the funded project (BFP/RGP/CBS/19/220). We thank technical staff for assistance.

SUPPLEMENTARY MATERIAL

The Supplementary Material for this article can be found online at: https://www.frontiersin.org/articles/10.3389/fphar.2022.800970/full#supplementary-material

REFERENCES

Adhisivam, B., and Mahadevan, S. (2006). Abscess of the Nasal Septum with Staphylococcal Scalded Skin Syndrome. *Indian Pediatr.* 43 (4), 372–373.

Amagai, M., Matsuyoshi, N., Wang, Z. H., Andl, C., and Stanley, J. R. (2000). Toxin in Bullous Impetigo and Staphylococcal Scalded-Skin Syndrome Targets Desmoglein 1. *Nat. Med.* 6, 1275–1277. doi:10.1038/81385

Amagai, M., Nishifuji, K., Yamaguchi, T., Hanakawa, Y., Sugai, M., and Stanley, J. R. (2002). Staphylococcal Exfoliative Toxin B Specifically Cleaves

Desmoglein 1. *J. Invest. Dermatol.* 118 (5), 845–850. doi:10.1046/j.1523-1747.2002.01751.x

Anandakrishnan, R., Aguilar, B., and Onufriev, A. V. (2012). H++ 3.0: Automating pK Prediction and the Preparation of Biomolecular Structures for Atomistic Molecular Modeling and Simulations. *Nucleic Acids Res.* 40, W537–W541. doi:10.1093/nar/gks375

Anderson, B. M., Cordes, E. H., and Jencks, W. P. (1961). Reactivity and Catalysis in Reactions of the Serine Hydroxyl Group and of O-Acyl Serines. *J. Biol. Chem.* 236, 455–463. doi:10.1016/s0021-9258(18)64384-4

Azarian, T., Cella, E., Baines, S. L., Shumaker, M. J., Samel, C., Jubair, M., et al. (2021). Genomic Epidemiology and Global Population Structure of Exfoliative Toxin A-Producing Staphylococcus aureus Strains Associated with Staphylococcal Scalded Skin Syndrome. *Front. Microbiol.* 12, 663831. doi:10.3389/fmicb.2021.663831

Bagley, S. C., and Altman, R. B. (1996). Conserved Features in the Active Site of Nonhomologous Serine Proteases. *Fold Des* 1 (5), 371–379. doi:10.1016/S1359-0278(96)00052-1

Bendtsen, J. D., Nielsen, H., von Heijne, G., and Brunak, S. (2004). Improved Prediction of Signal Peptides: SignalP 3.0. *J. Mol. Biol.* 340 (4), 783–795. doi:10.1016/j.jmb.2004.05.028

Berendsen, H. J. C., van der Spoel, D., and van Drunen, R. (1995). GROMACS: A Message-Passing Parallel Molecular Dynamics Implementation. *Comp. Phys. Commun.* 91, 43–56. doi:10.1016/0010-4655(95)00042-e

Bigelow, H. R., Petrey, D. S., Liu, J., Przybylski, D., and Rost, B. (2004). Predicting Transmembrane Beta-Barrels in Proteomes. *Nucleic Acids Res.* 32 (8), 2566–2577. doi:10.1093/nar/gkh580

Birktoft, J. J., Kraut, J., and Freer, S. T. (1976). A Detailed Structural Comparison between the Charge Relay System in Chymotrypsinogen and in Alpha-Chymotrypsin. *Biochemistry* 15 (20), 4481–4485. doi:10.1021/bi00665a023

Bowie, J. U., Lüthy, R., and Eisenberg, D. (1991). A Method to Identify Protein Sequences that Fold into a Known Three-Dimensional Structure. *Science* 253, 164–170. doi:10.1126/science.1853201

Cavarelli, J., Prévost, G., Bourguet, W., Moulinier, L., Chevrier, B., Delagoutte, B., et al. (1997). The Structure of Staphylococcus aureus Epidermolytic Toxin A, an Atypic Serine Protease, at 1.7 A Resolution. *Structure* 5 (6), 813–824. doi:10.1016/s0969-2126(97)00235-9

Colovos, C., and Yeates, T. O. (1993). Verification of Protein Structures: Patterns of Nonbonded Atomic Interactions. *Protein Sci.* 2, 1511–1519. doi:10.1002/pro.5560020916

Cribier, B., Piemont, Y., and Grosshans, E. (1984). Staphylococcal Scalded Skin Syndrome in Adults. A Clinical Review Illustrated with a New Case. *J. Am. Acad. Dermatol.* 30, 319–324. doi:10.1016/s0190-9622(94)70032-x

Crooks, G. E., Hon, G., Chandonia, J. M., and Brenner, S. E. (2004). WebLogo: A Sequence Logo Generator. *Genome Res.* 14, 1188–1190. doi:10.1101/gr.849004

Darden, T., York, D., and Pedersen, L. (1993). Particle mesh Ewald: An N log (N) method for Ewald sums in large systems. *J. Chem. Phys.* 98, 10089–10092. doi:10.1063/1.464397

De Azavedo, J. C., Arbuthnott, J. P., and Arbuthnott, J. P. (1988). Assays for Epidermolytic Toxin of Staphylococcus aureus. *Methods Enzymol.* 165, 333–338. doi:10.1016/s0076-6879(88)65049-x

De Lano, W. L. (2002). *The PyMOL Molecular Graphics System*. San Carlos, CA, USA: DeLano Scientific.

Decleire, P. Y., Blondiaux, G., Delaere, B., and Glupczynski, Y. (2004). Staphyloccocal Scalded Skin Syndrome in an Adult. *Acta Clin. Belg.* 59 (6), 365–368. doi:10.1179/acb.2004.053

Del Giudice, P. (2020). Skin Infections Caused by Staphylococcus aureus. *Acta Derm Venereol.* 100 (9), adv00110. doi:10.2340/00015555-3466

Dev, S., Maheshwari, S., and Roy Choudhury, A. (2015). Insights into the C-H···F-C Hydrogen Bond by Cambridge Structural Database Analyses and Computational Studies. *RSC Adv.* 5, 26932–26940. doi:10.1039/c5ra03063c

Dewar, M. J. S., Zoebisch, E. G., Healy, E. F., and Stewart, J. J. P. (1985). Development and Use of Quantum Mechanical Molecular Models. 76. AM1: a New General Purpose Quantum Mechanical Molecular Model. *J. Am. Chem. Soc.* 107 (13), 3902–3909. doi:10.1021/ja00299a024

Dolinsky, T. J., Nielsen, J. E., McCammon, J. A., and Baker, N. A. (2004). PDB2PQR: an Automated Pipeline for the Setup of Poisson-Boltzmann Electrostatics Calculations. *Nucleic Acids Res.* 32, W665–W667. doi:10.1093/nar/gkh381

Doudoulakakis, A., Spiliopoulou, I., Giormezis, N., Syridou, G., Nika, A., Bozavoutoglou, E., et al. (2021). Methicillin-resistant Staphylococcus aureus Transmission and Hospital-Acquired Bacteremia in a Neonatal Intensive Care Unit in Greece. *J. Infect. Chemother.* 28(2), 176–180.doi:10.1016/j.jiac.2021.07.013

Fernandes, R. S., Assafim, M., Arruda, E. Z., Melo, P. A., Zingali, R. B., and Monteiro, R. Q. (2007). Suramin Counteracts the Haemostatic Disturbances Produced by *Bothrops jararaca* Snake Venom. *Toxicon* 49 (7), 931–938. doi:10.1016/j.toxicon.2007.01.002

Fyfe, P. K., Dawson, A., Hutchison, M. T., Cameron, S., and Hunter, W. N. (2010). Structure of Staphylococcus aureus Adenylosuccinate Lyase (PurB) and Assessment of its Potential as a Target for Structure-Based Inhibitor Discovery. *Acta Crystallogr. D Biol. Crystallogr.* 66 (Pt 8), 881–888. doi:10.1107/S0907444910020081

G Abril, A. A., G Villa, T. T., Barros-Velázquez, J., Cañas, B., Sánchez-Pérez, A., Calo-Mata, P., et al. (2020). *Staphylococcus aureus* Exotoxins and Their Detection in the Dairy Industry and Mastitis. *Toxins (Basel)* 12 (9), 537. doi:10.3390/toxins12090537

Gasteiger, E., Hoogland, C., Gattiker, A., Duvaud, S. e., Wilkins, M. R., Appel, R. D., et al. (2005). "Protein Identification and Analysis Tools on the ExPASy Server," in *The Proteomics Protocols Handbook*. Editor J. M. Walker (Totowa, USA: Humana Press), 571–607. doi:10.1385/1-59259-890-0:571

Geer, L. Y., Domrachev, M., Lipman, D. J., and Bryant, S. H. (2002). CDART: Protein Homology by Domain Architecture. *Genome Res.* 12 (10), 1619–1623. doi:10.1101/gr.278202

Gemmell, C. G. (1997). Staphylococcal Scalded Skin Syndrome. *J. Med. Microbiol.* 43, 318–327. doi:10.1099/00222615-43-5-318

Gupta, A., Gandhimathi, A., Sharma, P., and Jayaram, B. (2007). ParDOCK: An All Atom Energy Based Monte Carlo Docking Protocol for Protein-Ligand Complexes. *Protein Pept. Lett.* 14 (7), 632–646. doi:10.2174/092986607781483831

Gupta, R., Jung, E., and Brunak, S. (2004). Prediction of N-Glycosylation Sites in Human Proteins. Available online: http://www.cbs.dtu.dk/services/NetNGlyc/ (Accessed on October 12, 2021).

Hanakawa, Y., Schechter, N. M., Lin, C., Garza, L., Li, H., and Yamaguchi, T. (2002). Molecular mechanisms of blister formation in bullous impetigo and staphylococcal scalded skin syndrome. *Sci. Rep.* 110 (1), 53-60. doi:10.1172/JCI15766

Hanakawa, Y., Selwood, T., Woo, D., Lin, C., Schechter, N. M., and Stanley, J. R. (2003). Calcium-dependent Conformation of Desmoglein 1 Is Required for its Cleavage by Exfoliative Toxin. *J. Invest. Dermatol.* 121 (2), 383–389. doi:10.1046/j.1523-1747.2003.12362.x

Hanakawa, Y., and Stanley, J. R. (2004). Mechanisms of Blister Formation by Staphylococcal Toxins. *J. Biochem.* 136 (6), 747–750. doi:10.1093/jb/mvh182

Hartley, B. S., and Kilby, B. A. (1954). The Reaction of P-Nitrophenyl Esters with Chymotrypsin and Insulin. *Biochem. J.* 56, 288–297. doi:10.1042/bj0560288

Hirose, M., Aung, M. S., Fukuda, A., Murata, Y., Saitoh, M., KobayashiPrevalence, N., et al. (2019). Prevalence and Genetic Characteristics of Methicillin-ResistantStaphylococcus Aureusand Coagulase-Negative Staphylococci Isolated from Oral Cavity of Healthy Children in Japan. *Microb. Drug Resist.* 25 (3), 400–407. doi:10.1089/mdr.2018.0333

Hospital, A., Andrio, P., Fenollosa, C., Cicin-Sain, D., Orozco, M., and Gelpí, J. L. (2012). MDWeb and MDMoby: An Integrated Web-Based Platform for Molecular Dynamics Simulations. *Bioinformatics* 28, 1278–1279. doi:10.1093/bioinformatics/bts139

Hu, X., Dong, Q., Yang, J., and Zhang, Y. (2016). Recognizing Metal and Acid Radical Ion-Binding Sites by Integrating Ab Initio Modeling with Template-Based Transferals. *Bioinformatics* 32 (21), 3694–3269. doi:10.1093/bioinformatics/btw637

Hubiche, T., Bes, M., Roudiere, L., Langlaude, F., Etienne, J., and Del Giudice, P. (2012). Mild Staphylococcal Scalded Skin Syndrome: an Underdiagnosed Clinical Disorder. *Br. J. Dermatol.* 166 (1), 213–215. doi:10.1111/j.1365-2133.2011.10515.x

Humphrey, W., Dalke, A., and Schulten, K. (1996). VMD: Visual Molecular Dynamics. *J. Mol. Graph* 14 (1), 33–38.27-8 doi:10.1016/0263-7855(96)00018-5

Imanishi, I., Nicolas, A., Caetano, A. B., Castro, T. L. P., Tartaglia, N. R., and Mariutti, R. (1996). Exfoliative toxin E, a new Staphylococcus aureus virulence factor with host-specific activity. *Sci. Rep.* 9 (1), 16336. doi:10.1038/s41598-019-52777-3

Jakalian, A., Jack, D. B., and Bayly, C. I. (2002). Fast, Efficient Generation of High-Quality Atomic Charges. AM1-BCC Model: II. Parameterization and Validation. *J. Comput. Chem.* 23 (16), 1623–1641. doi:10.1002/jcc.10128

Jeffrey, G. A. (1997). *An Introduction to Hydrogen Bonding*. New York: Oxford University Press.

Jiao, L., Ouyang, S., Liang, M., Niu, F., Shaw, N., Wu, W., et al. (2013). Structure of Severe Fever with Thrombocytopenia Syndrome Virus Nucleocapsid Protein in Complex with Suramin Reveals Therapeutic Potential. *J. Virol.* 87 (12), 6829–6839. doi:10.1128/JVI.00672-13

Kadam, S., Tagare, A., Deodhar, J., Tawade, Y., and Pandit, A. (2009). Staphylococcal Scalded Skin Syndrome in a Neonate. *Indian J. Pediatr.* 76 (10), 1074. doi:10.1007/s12098-009-0212-0

Kapoor, V., Travadi, J., and Braye, S. (2008). Staphylococcal Scalded Skin Syndrome in an Extremely Premature Neonate: a Case Report with a Brief Review of Literature. *J. Paediatr. Child. Health* 44 (6), 374–376. doi:10.1111/j.1440-1754.2008.01316.x

Katona, G., Berglund, G. I., Hajdu, J., Gráf, L., and Szilágyi, L. (2002). Crystal Structure Reveals Basis for the Inhibitor Resistance of Human Brain Trypsin. *J. Mol. Biol.* 315 (5), 1209–1218. doi:10.1006/jmbi.2001.5305

Kimberlin, D. W., Brady, M. T., Jackson, M. A., and Long, S. S. (2015). *Staphylococcal Infections*. 30th. Elk Grove Village, IL: American Academy of Pediatrics Red Book, 715. 22.

Ladhani, S., Joannou, C. L., Lochrie, D. P., Evans, R. W., and Poston, S. M. (1999). Clinical, Microbial, and Biochemical Aspects of the Exfoliative Toxins Causing Staphylococcal Scalded-Skin Syndrome. *Clin. Microbiol. Rev.* 12, 224–242. doi:10.1128/CMR.12.2.224

Ladhani, S., and Newson, T. (2000). Familial Outbreak of Staphylococcal Scalded Skin Syndrome. *Pediatr. Infect. Dis. J.* 19, 578–579. doi:10.1097/00006454-200006000-00021

Ladhani, S. (2003). Understanding the Mechanism of Action of the Exfoliative Toxins of Staphylococcus aureus. *FEMS Immunol. Med. Microbiol.* 39 (2), 181–189. doi:10.1016/S0928-8244(03)00225-6

Laskowski, R. A., MacArthur, M. W., Moss, D. S., and Thornton, J. M. (1993). PROCHECK: A Program to Check the Stereochemical Quality of Protein Structures. *J. Appl. Cryst.* 26, 283–291. doi:10.1107/s0021889892009944

Laskowski, R. A., MacArthur, M. W., and Thornton, J. M. (2001). "PROCHECK: Validation of Protein Structure Coordinates," in *International Tables of Crystallography: Volume F: Crystallography of Biological Macromolecules*. Editors M. G. Rossmann and E. Arnold (Dordrecht, Netherlands: Kluwer Academic Publishers), 722–725.

Li, B., Yang, N., Wang, X., Hao, Y., Mao, R., Li, Z., et al. (2020). An Enhanced Variant Designed from DLP4 Cationic Peptide against *Staphylococcus aureus* CVCC 546. *Front. Microbiol.* 11, 1057. doi:10.3389/fmicb.2020.01057

Lima, L. M., Becker, C. F., Giesel, G. M., Marques, A. F., Cargnelutti, M. T., de Oliveira Neto, M., et al. (2009). Structural and Thermodynamic Analysis of Thrombin:suramin Interaction in Solution and crystal Phases. *Biochim. Biophys. Acta* 1794 (6), 873–881. doi:10.1016/j.bbapap.2009.03.011

Lüthy, R., Bowie, J. U., and Eisenberg, D. (1992). Assessment of Protein Models with Three-Dimensional Profiles. *Nature* 356, 83–85. doi:10.1038/356083a0

Lyell, A. (1979). Toxic Epidermal Necrolysis (The Scalded Skin Syndrome): a Reappraisal. *Br. J. Dermatol.* 100, 69–86. doi:10.1111/j.1365-2133.1979.tb03571.x

Ma, X., Yang, N., Mao, R., Hao, Y., Yan, X., Teng, D., et al. (2021). The Pharmacodynamics Study of Insect Defensin DLP4 against Toxigenic *Staphylococcus Hyicus* ACCC 61734 *In Vitro* and *Vivo*. *Front. Cel Infect. Microbiol.* 11, 638598. doi:10.3389/fcimb.2021.638598

Maier, J. A., Martinez, C., Kasavajhala, K., Wickstrom, L., Hauser, K. E., and Simmerling, C. (2015). ff14SB: Improving the Accuracy of Protein Side Chain and Backbone Parameters from ff99SB. *J. Chem. Theor. Comput.* 11 (8), 3696–3713. doi:10.1021/acs.jctc.5b00255

Malik, M., Chiers, K., Boyen, F., Croubels, S., and Maes, D. (2021). Porcine Ear Necrosis. *Vet. J.* 271, 105655. doi:10.1016/j.tvjl.2021.105655

Mališová, L., Jakubů, V., Musílek, M., Kekláková, J., and Žemličková, H. (2020). Phenotype and Genotype Characteristics of *Staphylococcus aureus* Resistant to Methicillin/Oxacillin Carrying Gene *mecC* in the Czech Republic from 2002 to 2017. *Microb. Drug Resist.* 26 (8), 918–923. doi:10.1089/mdr.2019.0319

Mannschreck, D., Feig, J., Selph, J., and Cohen, B. (2020). Disseminated Bullous Impetigo and Atopic Dermatitis: Case Series and Literature Review. *Pediatr. Dermatol.* 37 (1), 103–108. doi:10.1111/pde.14032

Marchler-Bauer, A., Bo, Y., Han, L., He, J., Lanczycki, C. J., Lu, S., et al. (2017). CDD/SPARCLE: Functional Classification of Proteins via Subfamily Domain Architectures. *Nucleic Acids Res.* 45 (D1), 200–203. doi:10.1093/nar/gkw1129

Mariutti, R. B., Souza, T. A. C. B., Ullah, A., Caruso, I. P., de Moraes, F. R., Zanphorlin, L. M., et al. (2015). Crystal Structure of *Staphylococcus aureus* Exfoliative Toxin D-like Protein: Structural Basis for the High Specificity of Exfoliative Toxins. *Biochem. Biophysical Res. Commun.* 467 (1), 171–177. doi:10.1016/j.bbrc.2015.08.083

Mashiach, E., Schneidman-Duhovny, D., Andrusier, N., Nussinov, R., and Wolfson, H. J. (2008). FireDock: a Web Server for Fast Interaction Refinement in Molecular Docking. *Nucleic Acids Res.* 36, W229–W232. Web Server. doi:10.1093/nar/gkn186

Mastrangelo, E., Pezzullo, M., Tarantino, D., Petazzi, R., Germani, F., Kramer, D., et al. (2012). Structure-based Inhibition of Norovirus RNA-dependent RNA Polymerases. *J. Mol. Biol.* 419 (3-4), 198–210. doi:10.1016/j.jmb.2012.03.008

Melish, M. E. (1982). Staphylococci, Streptococci and the Skin: Review of Impetigo and Staphylococcal Scalded Skin Syndrome. *Semin. Dermatol.* 1, 101–109.

Mohan, R., and Venugopal, S. (2020). Molecular Binding and Simulation Studies of Staphylococcus aureus Superantigens with Flavonoid Compounds. *Infect. Disord. Drug Targets* 20 (4), 531–542. doi:10.2174/1871526519666190207092307

Monteiro, R. Q., Campana, P. T., Melo, P. A., and Bianconi, M. L. (2004). Suramin Interaction with Human Alpha-Thrombin: Inhibitory Effects and Binding Studies. *Int. J. Biochem. Cel Biol.* 36, 2077–2085. doi:10.1016/j.biocel.2004.03.007

Morgan, H. P., McNae, I. W., Nowicki, M. W., Zhong, W., Michels, P. A. M., Auld, D. S., et al. (2011). The Trypanocidal Drug Suramin and Other Trypan Blue Mimetics Are Inhibitors of Pyruvate Kinases and Bind to the Adenosine Site. *J. Biol. Chem.* 286 (36), 31232–31240. doi:10.1074/jbc.M110.212613

Morris, G. M., Huey, R., Lindstrom, W., Sanner, M. F., Belew, R. K., Goodsell, D. S., et al. (2009). AutoDock4 and AutoDockTools4: Automated Docking with Selective Receptor Flexibility. *J. Comput. Chem.* 30 (16), 2785–2791. doi:10.1002/jcc.21256

Murakami, M. T., Arruda, E. Z., Melo, P. A., Martinez, A. B., Calil-Eliás, S., Tomaz, M. A., et al. (2005). Inhibition of Myotoxic Activity of *Bothrops asper* Myotoxin II by the Anti-trypanosomal Drug Suramin. *J. Mol. Biol.* 350 (3), 416–426. doi:10.1016/j.jmb.2005.04.072

Nguyen, Q. D., Vu, M. N., and Hebert, A. A. (2021). Recognizing and Managing Staphylococcal Scalded Skin Syndrome in the Emergency Department. *Pediatr. Emerg. Care*. doi:10.1097/PEC.0000000000002564

Oono, T., Kanzaki, H., Yoshioka, T., and Arata, J. (1997). Staphylococcal Scalded Skin Syndrome in an Adult. *Dermatology* 195 (3), 268–270. doi:10.1159/000245958

Papageorgiou, A. C., Plano, L. R., Collins, C. M., and Acharya, K. R. (2000). Structural Similarities and Differences in *Staphylococcus aureus* Exfoliative Toxins A and B as Revealed by Their crystal Structures. *Protein Sci.* 9 (3), 610–618. doi:10.1110/ps.9.3.610

Paul, S. K., Ghosh, S., Kawaguchiya, M., Urushibara, N., Hossain, M. A., Ahmed, S., et al. (2014). Detection and Genetic Characterization of PVL-Positive ST8-MRSA-IVa and Exfoliative Toxin D-Positive European CA-MRSA-Like ST1931 (CC80) MRSA-IVa Strains in Bangladesh. *Microb. Drug Resist.* 20 (4), 325–336. doi:10.1089/mdr.2013.0153

Perona, J. J., and Craik, C. S. (1995). Structural Basis of Substrate Specificity in the Serine Proteases. *Protein Sci.* 4, 337–360. doi:10.1002/pro.5560040301

Piemont, Y., Piemont, E., and Gerard, D. (1986). Fluorescence Studies Stability of Staphylococcal Exfoliative Toxins A and B. *FEMS Microbiol. Lett.* 36, 245e249.

Polgár, L. (1971). On the Mechanism of Proton Transfer in the Catalysis by Serine Proteases. *J. Theor. Biol.* 31, 165–169.

Polgár, L., and Bender, M. L. (1969). The Nature of General Base-General Acid Catalysis in Serine Proteases. *Proc. Natl. Acad. Sci. U. S. A.* 64, 1335–1342.

Prasad, L., Leduc, Y., Hayakawa, K., and Delbaere, L. T. J. (2004). The Structure of a Universally Employed Enzyme: V8 Protease fromStaphylococcus Aureus. *Acta Crystallogr. D Biol. Cryst.* 60 (2), 256–259. doi:10.1107/s090744490302599x

Pucci, F., Kwasigroch, J. M., and Rooman, M. (2017). SCooP: an Accurate and Fast Predictor of Protein Stability Curves as a Function of Temperature. *Bioinformatics* 33 (21), 3415–3422. doi:10.1093/bioinformatics/btx417

Rajagopal, S., and Vishveshwara, S. (2005). Short Hydrogen Bonds in Proteins. *FEBS J.* 272 (8), 1819–1832. doi:10.1111/j.1742-4658.2005.04604.x

Rogolsky, M., Wiley, B. B., Keyhani, M., and Glasgow, L. A. (1974). Interaction of Staphylococcal Exfoliative Toxin with Concanavalin A. *Infect. Immun.* 10 (6), 1260–1265. doi:10.1128/iai.10.6.1260-1265.1974

Rost, B., Yachdav, G., and Liu, J. (2004). The PredictProtein Server. *Nucleic Acids Res.* 32, W321–W326. Web Server issue. doi:10.1093/nar/gkh377

Roy, A., Kucukural, A., and Zhang, Y. (2010). I-TASSER: A Unified Platform for Automated Protein Structure and Function Prediction. *Nat. Protoc.* 5 (4), 725–738. doi:10.1038/nprot.2010.5

Sahin-Tóth, J., Kovács, E., Tóthpál, A., Juhász, J., Forró, B., Bányai, K., et al. (2021). Whole Genome Sequencing of Coagulase Positive Staphylococci from a Dog-And-Owner Screening Survey. *PLoS One* 16 (1), e0245351. doi:10.1371/journal.pone.0245351

Salvador, G. H. M., Dreyer, T. R., Gomes, A. A. S., Cavalcante, W. L. G., dos Santos, J. I., de Oliveira Neto, M., et al. (2018). Structural and Functional Characterization of Suramin-Bound MjTX-I from Bothrops Moojeni Suggests a Particular Myotoxic Mechanism. *Sci. Rep.* 8 (1), 10317. doi:10.1038/s41598-018-28584-7

Sato, H., Matsumori, Y., Tanabe, T., Saito, H., Shimizu, A., Kawano, J., et al. (1994). A New Type of Staphylococcal Exfoliative Toxin from a Staphylococcus aureus Strain Isolated from a Horse with Phlegmon. *Infect. Immun.* 62 (9), 3780–3785. doi:10.1128/iai.62.9.3780-3785.1994

Schneider, T. D., and Stephens, R. M. (1990). Sequence Logos: A New Way to Display Consensus Sequences. *Nucl. Acids Res.* 18 (20), 6097–6100. doi:10.1093/nar/18.20.6097

Schneidman-Duhovny, D., Inbar, Y., Nussinov, R., and Wolfson, H. J. (2005). PatchDock and SymmDock: Servers for Rigid and Symmetric Docking. *Nucleic Acids Res.* 33, W363–W367. Web Server. doi:10.1093/nar/gki481

Schwarz, L., Loncaric, I., Brunthaler, R., Knecht, C., Hennig-Pauka, I., and Ladinig, A. (2021). Exudative Epidermitis in Combination with Staphylococcal Pyoderma in Suckling Piglets. *Antibiotics* 10 (7), 840. doi:10.3390/antibiotics10070840

Shirin, S., Gottlieb, A. B., and Stahl, E. B. (1998). Staphylococcal Scalded Skin Syndrome in an Immunocompetent Adult: Possible Implication of Low-Dosage Prednisone. *Cutis* 62, 223–224.

Sousa, A. M. P., Salles, H. O., Oliveira, H. D., Souza, B. B. P., Cardozo Filho, J. L., Sifuentes, D. N., et al. (2020). Mo-HLPs: New Flocculating Agents Identified from Moringa Oleifera Seeds Belong to the Hevein-like Peptide Family. *J. Proteomics* 217, 103692. doi:10.1016/j.jprot.2020.103692

Steentoft, C., Vakhrushev, S. Y., Joshi, H. J., Kong, Y., Vester-Christensen, M. B., Schjoldager, K. T.-B. G., et al. (2013). Precision Mapping of the Human O-GalNAc Glycoproteome through SimpleCell Technology. *EMBO J.* 32 (10), 1478–1488. doi:10.1038/emboj.2013.79

Steitz, T. A., and Shulman, R. G. (1982). Crystallographic and NMR Studies of the Serine Proteases. *Annu. Rev. Biophys. Bioeng.* 11 (1), 419–444. doi:10.1146/annurev.bb.11.060182.002223

Ullah, A., Mariutti, R. B., Masood, R., Caruso, I. P., Costa, G. H., Millena de Freita, C., et al. (2015). Crystal structure of mature 2S albumin from Moringa oleifera seeds. *468(1-2)* 114, 365–371. doi:10.1016/j.bbrc.2015.10.087

Ullah, A., Masood, R., Ali, I., Ullah, K., Ali, H., Akbar, H., et al. (2018). Thrombin-like Enzymes from Snake Venom: Structural Characterization and Mechanism of Action. *Int. J. Biol. Macromolecules* 114, 788–811. doi:10.1016/j.ijbiomac.2018.03.164

Ullah, A., and Ullah, K. (2021). Inhibition of SARS-CoV-2 3CL Mpro by Natural and Synthetic Inhibitors: Potential Implication for Vaccine Production against COVID-19. *Front. Mol. Biosci.* 8, 640819. doi:10.3389/fmolb.2021.640819

van Zundert, G. C. P., Rodrigues, J. P. G. L. M., Trellet, M., Schmitz, C., Kastritis, P. L., Karaca, E., et al. (2016). The HADDOCK2.2 Web Server: User-Friendly Integrative Modeling of Biomolecular Complexes. *J. Mol. Biol.* 428 (4), 720–725. doi:10.1016/j.jmb.2015.09.014

Vath, G. M., Earhart, C. A., Monie, D. D., Iandolo, J. J., Schlievert, P. M., and Ohlendorf, D. H. (1999). The Crystal Structure of Exfoliative Toxin B: A Superantigen with Enzymatic Activity,. *Biochemistry* 38 (32), 10239–10246. doi:10.1021/bi990721e

Vath, G. M., Earhart, C. A., Rago, J. V., Kim, M. H., Bohach, G. A., Schlievert, P. M., et al. (1997). The Structure of the Superantigen Exfoliative Toxin A Suggests a Novel Regulation as a Serine Protease,. *Biochemistry* 36 (7), 1559–1566. doi:10.1021/bi962614f

Wang, J., Wolf, R. M., Caldwell, J. W., Kollman, P. A., and Case, D. A. (2004). Development and Testing of a General AMBER Force Field. *J. Comput. Chem.* 25 (9), 1157–1174. doi:10.1002/jcc.20035

Waterhouse, A., Bertoni, M., Bienert, S., Studer, G., Tauriello, G., Gumienny, R., et al. (2018). SWISS-MODEL: Homology Modelling of Protein Structures and Complexes. *Nucleic Acids Res.* 46 (W1), W296–W303. doi:10.1093/nar/gky427

Webb, B., and Sali, A. (2016). Comparative Protein Structure Modeling Using MODELLER. *Curr. Protoc. Bioinformatics* 54 (1), 3. doi:10.1002/cpbi.3

Yamaguchi, T., Nishifuji, K., Sasaki, M., Fudaba, Y., Aepfelbacher, M., Takata, T., et al. (2002). Identification of the Staphylococcus aureus Etd Pathogenicity Island Which Encodes a Novel Exfoliative Toxin, ETD, and EDIN-B. *Infect. Immun.* 70 (10), 5835–5845. doi:10.1128/iai.70.10.5835-5845.2002

Yamasaki, O., Tristan, A., Yamaguchi, T., Sugai, M., Lina, G., Bes, M., et al. (2006). Distribution of the Exfoliative Toxin D Gene in Clinical Staphylococcus aureus Isolates in France. *Clin. Microbiol. Infect.* 12 (6), 585–588. doi:10.1111/j.1469-0691.2006.01410.x

Conflict of Interest: The authors declare that the research was conducted in the absence of any commercial or financial relationships that could be construed as a potential conflict of interest.

Publisher's Note: All claims expressed in this article are solely those of the authors and do not necessarily represent those of their affiliated organizations, or those of the publisher, the editors, and the reviewers. Any product that may be evaluated in this article, or claim that may be made by its manufacturer, is not guaranteed or endorsed by the publisher.

frontiers in Pharmacology

ORIGINAL RESEARCH
published: 21 February 2022
doi: 10.3389/fphar.2022.828269

The Bioflavonoids Rutin and Rutin Succinate Neutralize the Toxins of *B. jararaca* Venom and Inhibit its Lethality

Ana Teresa Azevedo Sachetto[1,2], *Jackson Gabriel Miyamoto*[3], *Alexandre Keiji Tashima*[3], *Ana Olívia de Souza*[4] *and Marcelo Larami Santoro*[1,2]*

[1]*Laboratory of Pathophysiology, Institute Butantan, São Paulo, Brazil,* [2]*Department of Medical Sciences, School of Medicine, University of São Paulo, São Paulo, Brazil,* [3]*Department of Biochemistry, Escola Paulista de Medicina, Federal University of São Paulo, (EPM/UNIFESP), São Paulo, Brazil,* [4]*Laboratory of Development and Innovation, Institute Butantan, São Paulo, Brazil*

The venom of the Brazilian pit viper *Bothrops jararaca* (BjV) is a complex mixture of molecules, and snake venom metalloproteinases (SVMP) and serine proteinases (SVSP) are the most abundant protein families found therein. Toxins present in BjV trigger most of the deleterious disturbances in hemostasis observed in snakebites, i.e., thrombocytopenia, hypofibrinogenemia and bleedings. The treatment of patients bitten by snakes still poses challenges and the bioflavonoid rutin has already been shown to improve hemostasis in an experimental model of snakebite envenomation. However, rutin is poorly soluble in water; in this study, it was succinylated to generate its water-soluble form, rutin succinate (RS), which was analyzed comparatively regarding the chemical structure and characteristic features of rutin. Biological activities of rutin and RS were compared on hemostatic parameters, and against toxic activities of crude BjV *in vitro*. *In vivo*, C57BL/6 mice were injected i.p. with either BjV alone or pre-incubated with rutin, RS or 1,10-phenanthroline (o-phe, an SVMP inhibitor), and the survival rates and hemostatic parameters were analyzed 48 h after envenomation. RS showed the characteristic activities described for rutin – i.e., antioxidant and inhibitor of protein disulfide isomerase – but also prolonged the clotting time of fibrinogen and plasma *in vitro*. Differently from rutin, RS inhibited typical proteolytic activities of SVMP, as well as the coagulant activity of BjV. Importantly, both rutin and RS completely abrogated the lethal activity of BjV, in the same degree as o-phe. BjV induced hemorrhages, falls in RBC counts, thrombocytopenia and hypofibrinogenemia in mice. Rutin and RS also improved the recovery of platelet counts and fibrinogen levels, and the development of hemorrhages was totally blocked in mice injected with BjV incubated with RS. In conclusion, RS has anticoagulant properties and is a novel SVMP inhibitor. Rutin and RS showed different mechanisms of action on hemostasis. Only RS inhibited directly BjV biological activities, even though both flavonoids neutralized *B. jararaca* toxicity *in vivo*. Our results showed clearly that rutin and RS show a great potential to be used as therapeutic compounds for snakebite envenomation.

Keywords: coagulation, hemostasis, rutin, snake venom, antivenom

OPEN ACCESS

Edited by:
Herve Kovacic,
Aix Marseille Université, France

Reviewed by:
Zeliha Selamoglu,
Niğde Ömer Halisdemir University, Turkey
Ana Karina Oliveira,
University of Virginia, United States

***Correspondence:**
Marcelo Larami Santoro
marcelo.santoro@butantan.gov.br
marcelosantoro@yahoo.com

Specialty section:
This article was submitted to Translational Pharmacology, a section of the journal Frontiers in Pharmacology

Received: *03 December 2021*
Accepted: *27 January 2022*
Published: *21 February 2022*

Citation:
Sachetto ATA, Miyamoto JG, Tashima AK, de Souza AO and Santoro ML (2022) The Bioflavonoids Rutin and Rutin Succinate Neutralize the Toxins of B. jararaca Venom and Inhibit its Lethality. Front. Pharmacol. 13:828269. doi: 10.3389/fphar.2022.828269

INTRODUCTION

Snakebite envenomation is a priority among the tropical neglected diseases recognized by the World Health Organization (WHO) (World Health Organization, 2021). In Brazil, *Bothrops* snakes stand out for being responsible for 90% of the snakebite accidents. Acknowledging that, *Bothrops jararaca* (*B. jararaca*) is considered by WHO as a species with high medical relevance (World Health Organization, 2021; Sistema de Informação de, 2022).

Snake venom is used for predation and defense, which led to a natural evolution toward a high complexity and specificity (Gutiérrez et al., 2017). *Bothrops* venom is mainly composed by proteins, as snake venom metalloproteinases (SVMP), serine proteases (SVSP), phospholipases A_2 (PLA_2), C-type lectins, L-amino acid oxidases, hyaluronidases, among others (Koh et al., 2006; Deolindo et al., 2010; Sajevic et al., 2011; Takeda et al., 2012; Izidoro et al., 2014). These proteins are responsible for the toxic and lethal activities of the venom, which induce an inflammatory response, oxidative/nitrosative stress and hemostatic disturbances, as thrombocytopenia, consumptive coagulopathy and bleedings (Kamiguti et al., 1986; Maruyama et al., 1990; Santoro et al., 1994; Barraviera et al., 1995; Gonçalves and Mariano, 2000; Gutiérrez and Rucavado, 2000; Petricevich et al., 2000; Avila-Agüero et al., 2001; Sano-Martins et al., 2003; Schattner et al., 2005; Santoro et al., 2008a; Santoro et al., 2008b; Zychar et al., 2010; Moura-da-Silva and Baldo, 2012; Ferraz et al., 2015; Gutiérrez et al., 2017).

Although snakebite envenomation is a complex disease, its only official and prescribed treatment is the administration of animal-derived antivenoms, which directly inhibits venom toxins. *Bothrops* antivenom is used to treat patients bitten by *Bothrops* snakes, but it has limitations to block the snakebite-induced local effects and secondary complications as oxidative/nitrosative stress (Cardoso et al., 1993; Jorge et al., 1995; Battellino et al., 2003; Strapazzon et al., 2014). Therefore, studies have been conducted aiming to search for and develop new complementary medicinal products.

Several polyphenols from plant sources were shown to have beneficial activities for human and animal health (Selamoglu, 2017). Flavonoids are included on the class of polyphenols and were already tested to combat snake venom effects on victims (Castro et al., 1999; Nishijima et al., 2009; Pithayanukul et al., 2010). Among the several compounds with therapeutic potential, quercetin-3-rutinose (rutin) was elected for being a compound derived from plants, easily accessible, with low-cost and a broad range of activities, and can be produced in several pharmaceutical formulations (Behling et al., 2004; Pietta, 2000; Kandaswami and Middleton, 1994; Afanas'ev et al., 1989; Ganeshpurkar and Saluja, 2017). Rutin is a flavonoid which presents the core structure of a quercetin (3,5,7,3′-4′-pentahydroxyl flavone) and two glycosides at the 3′ position of the C ring. However, the use of rutin shows limitations regarding its aqueous solubility and bioavailability. As alternatives for these challenges, either using compounds analogous to rutin (as isoquercetin and troxerutin), or chemically modifying rutin to improve its solubility – e.g., by conjugation of rutin with metal ions or succinylation of hydroxyl groups in rutin glycosides (Krewson and Couch, 1952; Alluis et al., 2000; Pedriali et al., 2008a; Gullón et al., 2017) – have been tested.

Rutin exhibits different activities, as an antioxidant, anti-inflammatory, antithrombotic, pro-hemostatic and protein disulfide isomerase (PDI) inhibitor (Afanas'ev et al., 1989; Ganeshpurkar and Saluja, 2017; Choi et al., 2015; Jasuja et al., 2012; Stopa et al., 2017; Schulman et al., 2016; Sharma et al., 2013; Panche et al., 2016; Kauss et al., 2008; Kirchner et al., 2013). This turns rutin into a promising therapeutic agent against complex diseases as snakebite envenomation. In fact, rutin and analogous compounds have been studied for their properties against snake venoms for more than 7 decades (Seba, 1949). However, a recent study from our group (Sachetto et al., 2018) showed that rutin potential towards snake envenomation is much broader than previously observed. Therefore, we aimed to synthetize and characterize a water-soluble form of rutin, named rutin succinate (RS), and investigate the possible inhibitory effects of both rutin and RS on venom toxins activities *in vitro* and *in vivo*.

MATERIAL AND METHODS

Materials

Lyophilized venom from adult specimens of *B. jararaca* snakes was obtained from the Laboratory of Herpetology, Instituto Butantan (Sistema Nacional de Gestão do Patrimônio Genético e do Conhecimento Tradicional Associado, SisGen AF375C2). *Bothrops* antivenom was kindly donated by Instituto Butantan (lot: 1305077). Di-eosin-GSSG and purified PDI were kindly donated by Dr. Francisco Laurindo, INCOR, USP. Rutin (code R5143), succinic acid, succinic anhydride, 1,10-phenantroline (o-phe), AEBSF, bovine fibrinogen, porcine skin gelatin, casein, collagenase from *Clostridium histolyticum*, and bacitracin A were obtained from Sigma-Aldrich (United States). All other reagents were of analytical grade or better.

Animals

Male C57BL/6 mice, weighing 18–22 g, were obtained from the Animal Facility of Instituto Butantan, and were maintained with free access to food and water. Experimental procedures involving mice were in accordance with National Guidelines, the Conselho Nacional de Controle de Experimentação Animal (CONCEA) and were approved by the Institutional Animal Care and Use Committees (Instituto Butantan, 4491070319 and Faculdade de Medicina da Universidade de São Paulo, 1334/2019).

Rutin Succinate Synthesis

Rutin succinate (RS) was synthetized by succinylation of the hydroxyl groups present in the sugar moieties of rutin (Pedriali et al., 2008b) (**Figure 1**). A solution of rutin (2.5 g), succinic anhydride (3.75 g) and pyridine (100 ml) was heated at 70°C por 24 h in a dry-bath. The reaction product (RS) was rotaevaporated (rotaevaporator R-210, Buchi) to remove pyridine, solubilized in warm butanol, cooled and filtered with cooled diethyl ether. Organic solvents were removed by rotaevaporation and the final product (RS) was solubilized in methanol and totally

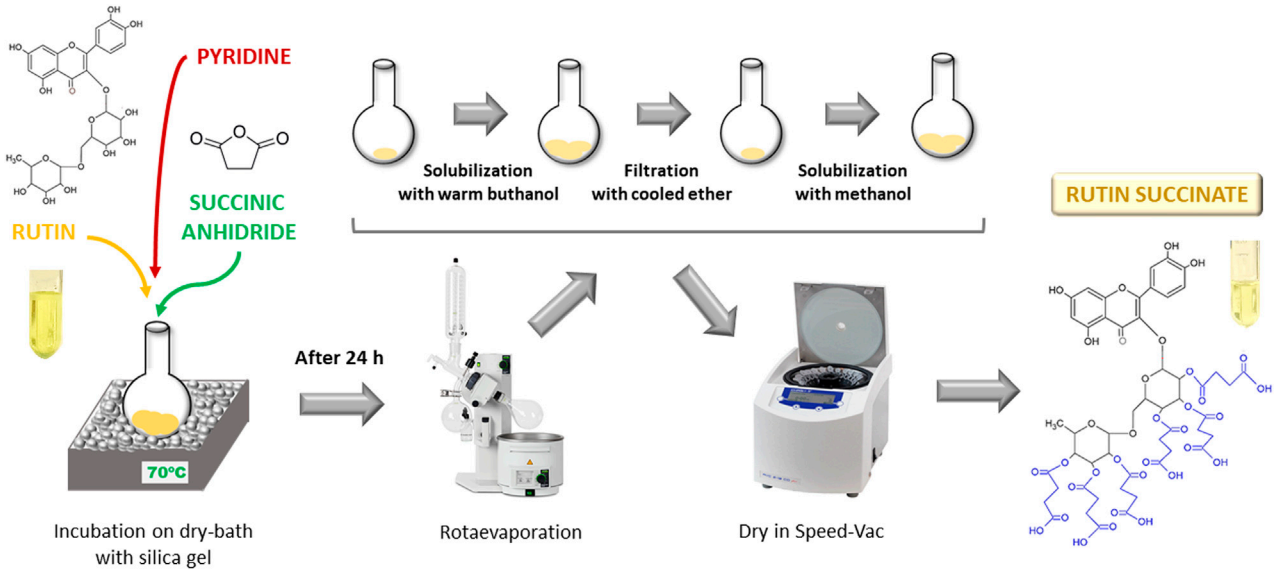

FIGURE 1 | Schematic representation of rutin succinate synthesis.

dried in a Speed-Vac equipment (RVC 2-18 CD Plus, Christ) and stored at room temperature.

Characterization of RS

UV-Visible Spectrophotometry

UV-visible spectrophotometry was utilized to verify if the core flavonoid chemical structure of RS was intact following rutin succinylation. Solutions of rutin and RS (205 µM in methanol) were analyzed in a quartz 96-well microplate (Molecular Devices, United States) at a spectrum of 240 nm–450 nm in a microplate reader (SpectraMax 190, Molecular Devices).

High Performance Liquid Chromatography

The chromatographic analysis of RS and rutin was performed by reversed-phase high performance liquid chromatography (HPLC) [Äkta Purifier 10 HPLC system, GE (Cytiva)]. For that, aliquots (20 µl) of rutin or RS (5 mg/ml in methanol) were loaded into a C18 column (ACE, 250 × 4.6 mm), and eluted at a flow rate of 1 ml/min, using a gradient from 45 to 70% B (mobile phases A: 99.9% H_2O/0.1% trifluoroacetic acid (TFA) and B: 90.0% methanol/9.9% H_2O/0.1% TFA) during 25 min. The absorbance UV/Vis detector was set to the wavelengths of 214, 254, and 280 nm. The analytical profiles of succinic anhydride (10 µl of a 5 mg/ml solution), succinic acid (10 µl of a 5 mg/ml solution), pyridine (3 µl) and diethyl ether (40 µl) were obtained and compared to that of the RS preparations.

Mass Spectrophotometry (LC-MS/MS)

Liquid chromatography-mass spectrometry (LC-MSE) analyses were performed on a Synapt G2 HDMS mass spectrometer (Waters) coupled to the chromatographic system nanoAcquity UPLC (Waters). Rutin and RS were dissolved in methanol and diluted in formic acid 0.1% to a final concentration of 10 ng/µl and 100 ng/µl, respectively. Samples of rutin and RS (10 and 500 ng respectively) were loaded into a trap column (Acquity UPLC M-Class Symmetry C18 Trap Column, 100 Å, 5 µm, 300 µm × 25 mm, Waters) at 8 µl/min in phase A (0.1% formic acid) for 5 min. Samples were subsequently eluted in an analytical column (Acquity UPLC M-Class HSS T3 Column, 1.8 µm, 300 µm × 150 mm, Waters) with a gradient of 20%–60% of phase B (0.1% formic acid in ACN) over 15 min at a flow rate of 3 µl/min. Analyses were performed in the data independent acquisition (DIA) method MSE (Silva et al., 2006; Abreu et al., 2017), in the m/z range of 50–2,000 and set up in resolution mode. Precursor ions were fragmented by collision-induced dissociation (CID), switching from low (4 eV) to high (ramped from 20 to 30 eV) collision energy, for accurate measurement of both precursor and fragment ions. Scan times were set to 1.0 s. The ESI source was operated in the positive mode with a capillary voltage of 3.0 kV, block temperature of 100°C, and cone voltage of 15 V. The column temperature was set at 55°C. For lock mass correction, a [Glu1]-Fibrinopeptide B solution (500 fmol/ml in 50% methanol, 0.1% formic acid; Peptide 2.0) was infused through the reference sprayer at 2 µl/min and sampled every 60 s for external calibration (Pedroso et al., 2017).

Total Antioxidant Capacity

The total antioxidant capacity (TAC) of rutin and RS was assayed based on the CUPRAC colorimetric method (Ribeiro et al., 2011; Sachetto et al., 2018). The final concentrations of rutin and RS in the assay were 0.015, 0.029, 0.059, and 0.118 mM. As a standard curve, 2-fold serially dilutions of reduced L-glutathione (GSH), ranging from 12.5 to 300 µM, were used. Results were expressed as mM of GSH.

Quenching of Calcium, Magnesium and Zinc Ions

The ability of rutin and RS to quench divalent metal ions was tested using commercial assays (Magnesium kit for $MgCl_2$ and $ZnCl_2$, and Ca arsenazo Liquiform kit for $CaCl_2$, Labtest, Brazil).

Rutin, RS and succinic acid (SA, free form of succinic anhydride) were two-fold serially diluted (using 1% DMSO in saline) and added to the standards (2 mg/ml $MgCl_2$, 25 mM $ZnCl_2$ or 10 mg/ml $CaCl_2$). The assays were carried out following manufacturer's instructions and the final concentration of rutin, RS or succinic acid were: 1.11, 2.23, 4.46, 8.92, and 17.84 μM (calcium assay); 0.26, 0.52, 1.04, 2.08, and 4.15 μM (magnesium assay); and 31.25, 62.5, 125, 250, and 500 μM (zinc assay).

Analysis of PDI Structure and Activity

PDI structure was analyzed testing the intrinsic fluorescence of tryptophan residues (Trp) (Ado et al., 2006). In 96-well black microplates (Costar, United States), a PDI solution (300 nM, 50 μl/well) and 50 μl of rutin or RS solutions (0.59 mM in Tris-HCl buffer (20 mM Tris, 140 mM NaCl, 1 mM $CaCl_2$, pH 8.0 and 1% DMSO). After 15 min of incubation at room temperature, the fluorescence spectrum was recorded (excitation. 280 nm, and emission: 360–510 nm). PDI reductase activity were determined using di-eosin-GSSG probe as previously described (Raturi and Mutus, 2007; Montano et al., 2014; Oliveira et al., 2019). Rutin or RS was diluted in 1% DMSO in phosphate buffer to final concentrations of 60 μM. Results were expressed as relative fluorescence units (RFU) and Vmax were also analyzed.

Activities of Rutin and RS on Hemostatic Parameters *In Vitro*

Prothrombin Time and Activated Partial Thromboplastin Time

Commercial kits for prothrombin time (DiaPlastin, DiaMed, Brazil) and aPTT (TTPA CLOT, Bios Diagnostica, Brazil) were used according to manufacturer's instructions. Mouse plasma was diluted in saline (1:10 for PT and 1:5 for aPTT) and pre-incubated with rutin or RS solutions for 10 min at 37°C before the assays. Rutin and RS were two-fold serially diluted in 154 mM NaCl solution containing 1% DMSO.

Thrombin Time

Thrombin time assay was performed by pre-incubating 100 μl of mouse plasma [diluted 1:4 in Tyrode buffer (137 mM NaCl, 2.7 mM KCl, 3 mM NaH_2PO_4, 10 mM HEPES, 5.6 mM dextrose, 1 mM $MgCl_2$, 2 mM $CaCl_2$, pH 7.4)] or bovine fibrinogen solution (4 mg/ml in Tyrode buffer) with 12.5 μl of Tyrode buffer or solutions of rutin, RS or SA for 15 min at 37°C. After incubation, 12.5 μl of thrombin-calcium solution (10 U/ml thrombin and 100 mM $CaCl_2$) were added, and the clotting time was determined until 300 s in a coagulometer (STart 4, Diagnostica Stago). The final concentrations of rutin, RS and SA were 0.18, 0.37, 0.74, 1.47, and 2.95 mM, respectively.

Absorbance and Fluorescence Profile of Fibrinogen and Albumin

Rutin, RS and SA were two-fold serially diluted as described previously for thrombin time. The formation of fibrinogen complexes was tested analyzing the turbidity of fibrinogen solutions (Zhang et al., 2013). In a quartz 96-well microplate, aliquots (50 μl/well) of a fibrinogen solution (6.4 mg/ml in PBS, pH 7.4), followed by addition of aliquots (50 μl/well) of PBS, rutin, RS or SA. Absorbances were read at 405 nm. Moreover, the structure of fibrinogen and bovine serum albumin (BSA) were analyzed by the addition of fibrinogen or BSA solutions diluted in Tyrode buffer (0.8 mg/ml, final concentration), and pre-incubation with rutin, RS or SA solutions for 15 min at 37°C. The fluorescence of Trp was measured as described above.

Activities of Rutin and RS on BjV Activities *In Vitro*

The following experiments were performed after pre-incubations of BjV with buffer containing DMSO (control of reaction), rutin, RS or SA for 30 min at 37°C. Different concentrations of rutin, RS and SA were used, depending on the concentration of BjV, with a range of 2.25, 4.5, 9, 18, and 36 times the amount of BjV. As positive controls of inhibition, BjV was pre-incubated with 8 mM AEBSF (inhibitor of SVSP), and/or 13 mM o-phe or Na_2EDTA (inhibitors of SVMP) for 1 h at 37°C (Yamashita et al., 2014). The results were calculated as percentage of activity based on BjV (considered 100% of activity) if not specified otherwise.

Analysis of BjV and Jararhagin Structure

The fluorescence of Trp in BjV proteins and jararhagin (an important SVMP isolated from BjV) (Moura-da-Silva and Baldo, 2012) was analyzed as described above. BjV or jararhagin was diluted in Tris-HCl buffer (20 mM Tris, 140 mM NaCl, 1 mM $CaCl_2$, pH 8.0), both in final concentration of at 0.2 mg/ml, and incubated with solutions of rutin, RS or SA two-fold serially diluted in Tris-HCl buffer (containing 1% DMSO), with final concentrations ranging from 0.07375 to 1.18 mM.

L-Amino Acid Oxidase, Hyaluronidase and SVSP Activities

The activities of LAAO, hyaluronidases and SVSP were analyzed using L-leucine, hyaluronic acid and BAPNA as substrates, respectively (Antunes et al., 2010; Sachetto et al., 2018). BjV was diluted on the specific assay buffers, so that the final concentrations of BjV in the assays were 17 μg/ml for LAAO, 66 μg/ml for hyaluronidases, and 44 μg/ml for SVSP. Rutin, RS and SA were diluted in the same buffer as BjV with the addition of DMSO and final concentrations ranging from 0.23 to 2.69 mM (LAAO), 0.18 mM–3.9 mM (hyaluronidases) and 0.13–2.01 (SVSP) were tested.

Activities of SVMP

SVMP were tested regarding their collagenolytic, gelatinolytic, caseinolytic, fibrinogenolytic and activator of prothrombin activities (Antunes et al., 2010; Sachetto et al., 2018). For the collagenolytic activity, azocoll collagen (Antunes et al., 2010; Sachetto et al., 2018) was incubated with 0.072 mg/ml BjV and rutin, RS or SA, at final concentrations ranging from 0.11 to 1.76 mM. The gelatinolytic, caseinolytic and fibrinogenolytic activity (Santoro and Sano-Martins, 1993; Antunes et al., 2010) was determined by the analysis of the degradation profile of intact proteins by SDS-PAGE, using mixtures of BjV

(17 μg/ml, final concentration), and rutin, RS or SA at final concentrations ranging from 0.07 to 1.13 mM. The degradation of fibrinogen and gelatin was also tested using jararhagin and collagenase from *C. histolyticum* (38 μg/ml, Sigma), respectively. The densitometric analysis was performed using the software ImageJ (Fiji), and differences between the intact proteins and the proteins incubated with BjV was considered as 100% of activity. The prothrombin activating activity was determined as described previously (Yamada and Morita, 1997; Antunes et al., 2010), using BjV at 0.8 μg/ml (final concentration), and rutin, RS or SA at final concentrations ranging from 3.03 to 48.49 mM.

Coagulant Activity

The coagulant activity of BjV was tested using mouse plasma or bovine fibrinogen using a modification of the minimum coagulant dose technique. BjV was used at 50 μg/ml, and rutin, RS or SA at 0.18 mM–2.95 mM (final concentrations).

In Vivo Experimental Groups and Procedures

BjV, RS or SA were dissolved in sterile saline and rutin was dissolved in equal parts of propylene glycol and sterile saline. Two doses of BjV were utilized: 3.2 mg/kg b.w. i.p., i.e., 2× lethal dose 50% of BjV (LD_{50}, moderate envenomation), and 4.8 mg/kg b.w. i.p. (3×LD_{50}, severe envenomation) (Antunes et al., 2010). Rutin and RS were utilized at doses 9 times higher than BjV (28.8 or 43.2 mg/kg b.w. i.p.), as previously described (Sachetto et al., 2018). To better understand RS activities, SA was used at 9.6 mg/kg b.w. i.p. (same molarity as rutin and RS). SVMP or SVSP were inhibited with the use of 13 mM o-phe or 8 mM AEBSF, respectively. Bacitracin A (80 mg/kg p.v. i.p.) was used to verify the contribution of thiol isomerases in the severe envenomation (Cho et al., 2008). BjV was pre-incubated with these solutions and injected into animals. Male C57BL/6 mice (18 g–22 g) were randomly allocated in different experimental groups: saline (negative control), BjV (positive control), BjV + rutin, BjV + RS, BjV + SA, BjV + AEBSF, BjV + o-phe and BjV + bacitracin A.

Survival Analysis

The survival of mice was analyzed after injection of 3× LD_{50} of BjV alone [severe envenomation, (Antunes et al., 2010)] or pre-incubated with rutin RS, SA, o-phe, or bacitracin A. The number of surviving animals was recorded at each hour from 1 to 9 h, and at 24 and 48 h after the injection of solutions.

Blood and Organ Collection

After 48 h, blood was collected from surviving mice and used for complete blood cell counts (CBC) and plasma collection, as described previously (Sachetto et al., 2018). For histological analysis, fragments of liver, kidney, lungs, heart, pancreas, spleen, intestine, diaphragm and intestinal wall from dead or euthanized mice were collected, submersed on Bouin's solution until processing of histological material.

Hemostatic Parameters

CBC was performed in an automated cell counter BC-2800 Vet (Mindray, China). Plasma fibrinogen was measured in citrated plasma using a colorimetric assay (Ratnoff and Menzie, 1951; Sachetto, 2018).

Statistical Analysis

Normal distribution and homoscedasticity of the results were analyzed using the software STATA™, version 10, and data were transformed whenever necessary. One-way or Kruskal-Wallis test was used, followed by *post-hoc* tests (Bonferroni or Dunn's tests). The software SPSS (version22), Sigma Plot (version 12.0) and R (version 4.00) were employed for these analyses. Data was considered statistically significant when $p < 0.05$, and results were expressed as mean ± standard error of mean (SEM).

RESULTS

RS Synthesis and Characterization

RS showed a yellow coloration and a powdered aspect, as rutin; however, RS is more hygroscopic than rutin, and then it was maintained in the desiccator at room temperature. RS solubility in water is 115 times higher than that of rutin (14.4 g/L vs. 0.125 g/L, respectively). In the following experiments, RS molecular weight was considered as if it was the same of rutin (610.52). Regarding the absorbance spectrum, both rutin and RS showed peaks at 260 and 360 nm (**Figures 2A,B**), as expected for the aromatic rings A and B of flavonoids (Bondarev and Knyukshto, 2013; Kumar and Pandey, 2013).

Rutin and RS showed different analytical profiles when analyzed by HPLC (**Figures 2C,D**). Rutin presented a major peak with retention time (RT) at 13 min and absorption in 214, 154, and 280 nm. It is important to observe that this peak attributed to rutin was not present in the RS chromatographic profile, which displayed several peaks also with absorption in 214, 154, and 280 nm. These peaks in RS chromatogram are likely due to the different extent of succinylation of the hydroxyl groups present in rutinoside moieties of rutin. The presence of chemical residuals in RS synthesis was also analyzed by HPLC. Retention time for the peaks of chemicals used in synthesis (succinic acid: 6 min, succinic anhydride: 12 min, pyridine: 5 min, diethyl ether: 23 and 33 min) were not observed in RS samples, and therefore, RS synthesis and purification were considered successful and without chemical contaminants. Further purification of rutin peaks was not carried out, and the RS samples used in the experiments is therefore a combination of different succinylation forms of rutin.

Rutin was analyzed by LC-MSE and eluted at 6.84 min, showing the expected precursor ion at m/z 611.18+ and main fragments at 303.06+ and 465.12+ (**Figures 3A,B**). Rutin has six possible succinylation sites on the free hydroxyl groups of its rutinoside (**Figures 3C,D**).

Ion chromatograms of RS showed that several succinylated forms co-exist, composing a complex mixture of 1–6 succinyl substitutions (**Figure 3E**). Six possible forms exist for 1 succinyl

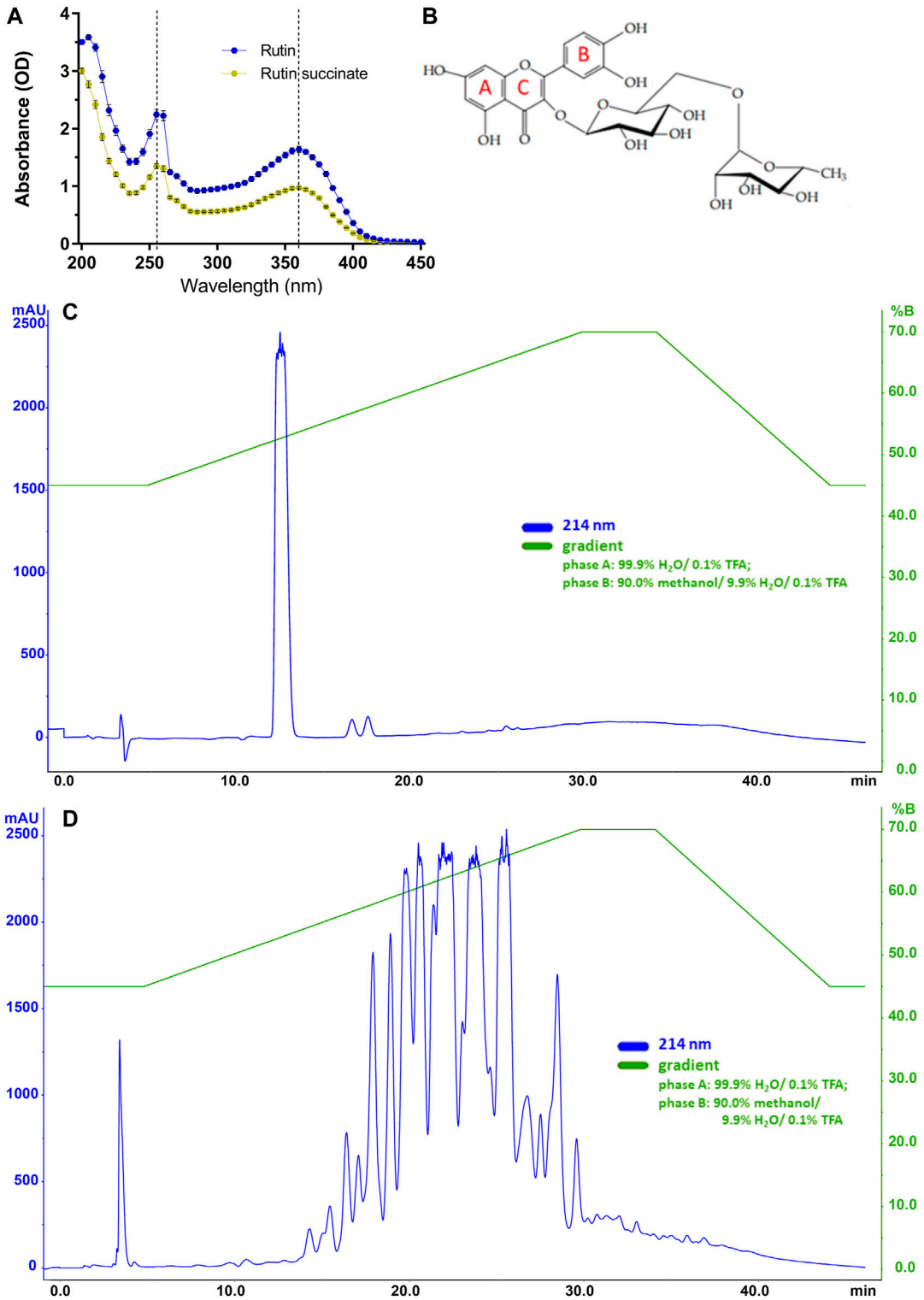

FIGURE 2 | (A) The absorbance spectra of rutin and RS. **(B)** Molecular structure of rutin with indications of aromatic rings A, B and C; Chromatographic profiles obtained for **(C)** rutin and **(D)** RS analyzed by HPLC using a C18 column (250 × 4.6 mm). Chromatographic conditions: ACE C18 column (250 × 4.6 mm); mobile phase A: 99.9% H_2O/0.1% TFA and B: 90.0% methanol/9.9% H_2O/0.1% TFA); flow rate of 1.0 ml/min; λ = 214 nm; and injection volume of 20 µl.

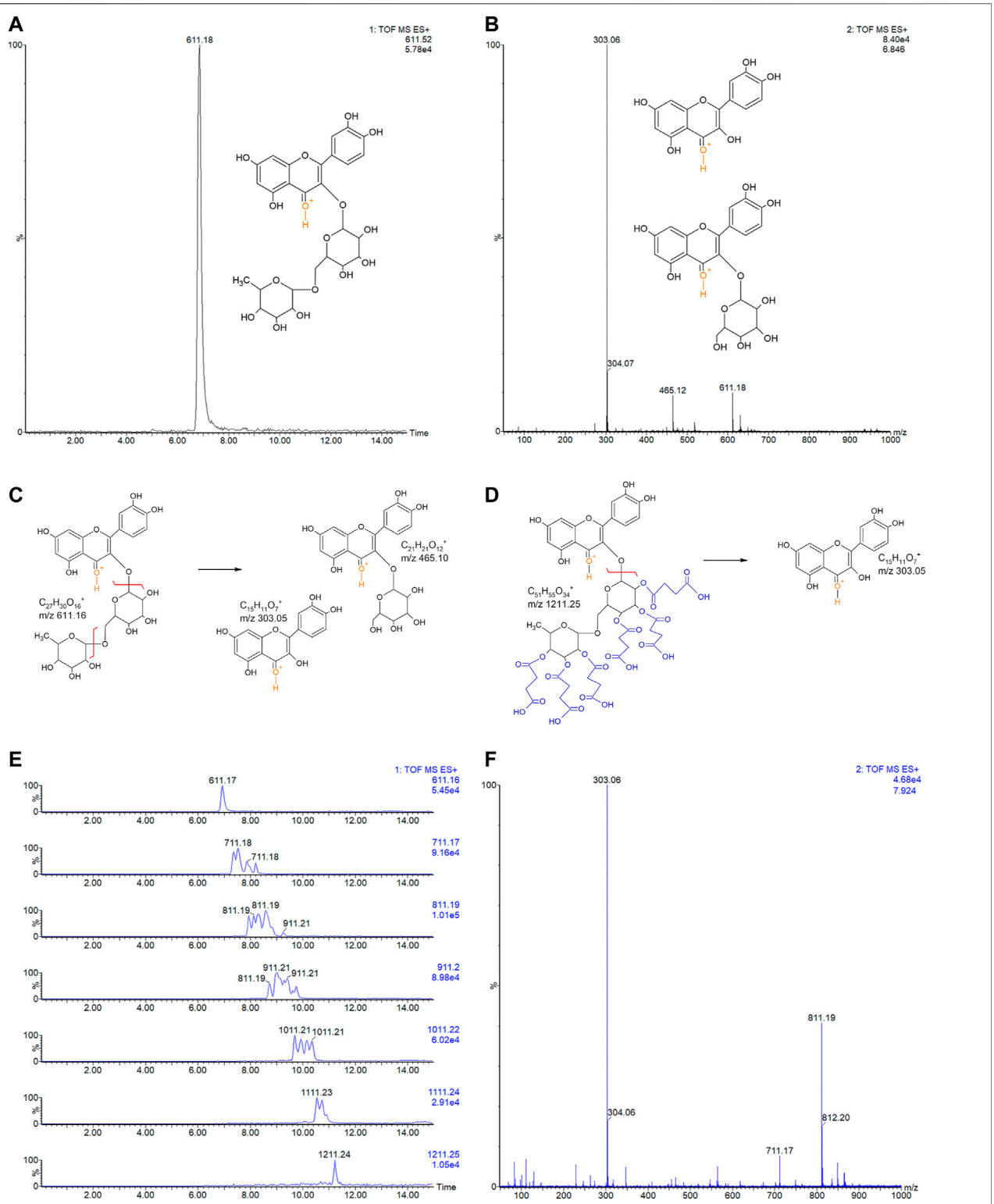

FIGURE 3 | (A) LC-MSE chromatogram of rutin (10 ng, RT 6.84). **(B)** CID-MS/MS spectrum of rutin: main fragment ions observed at m/z 303.06+ and 465.12+. Remaining precursor ion at 611.18+ due to the DIA analysis. Proposed fragmentation routes of **(C)** rutin and **(D)** RS by ESI-CID-MS/MS. **(E)** LC-MSE chromatograms of RS (500 ng) with multiple succinylations (1–6), and **(F)** representative CID-MS/MS spectrum of RS with 2 and 3 succinylations, at RT 7.924. Remaining precursor ions (at m/z 711.17+ and m/z 811.19+) due to the DIA analysis.

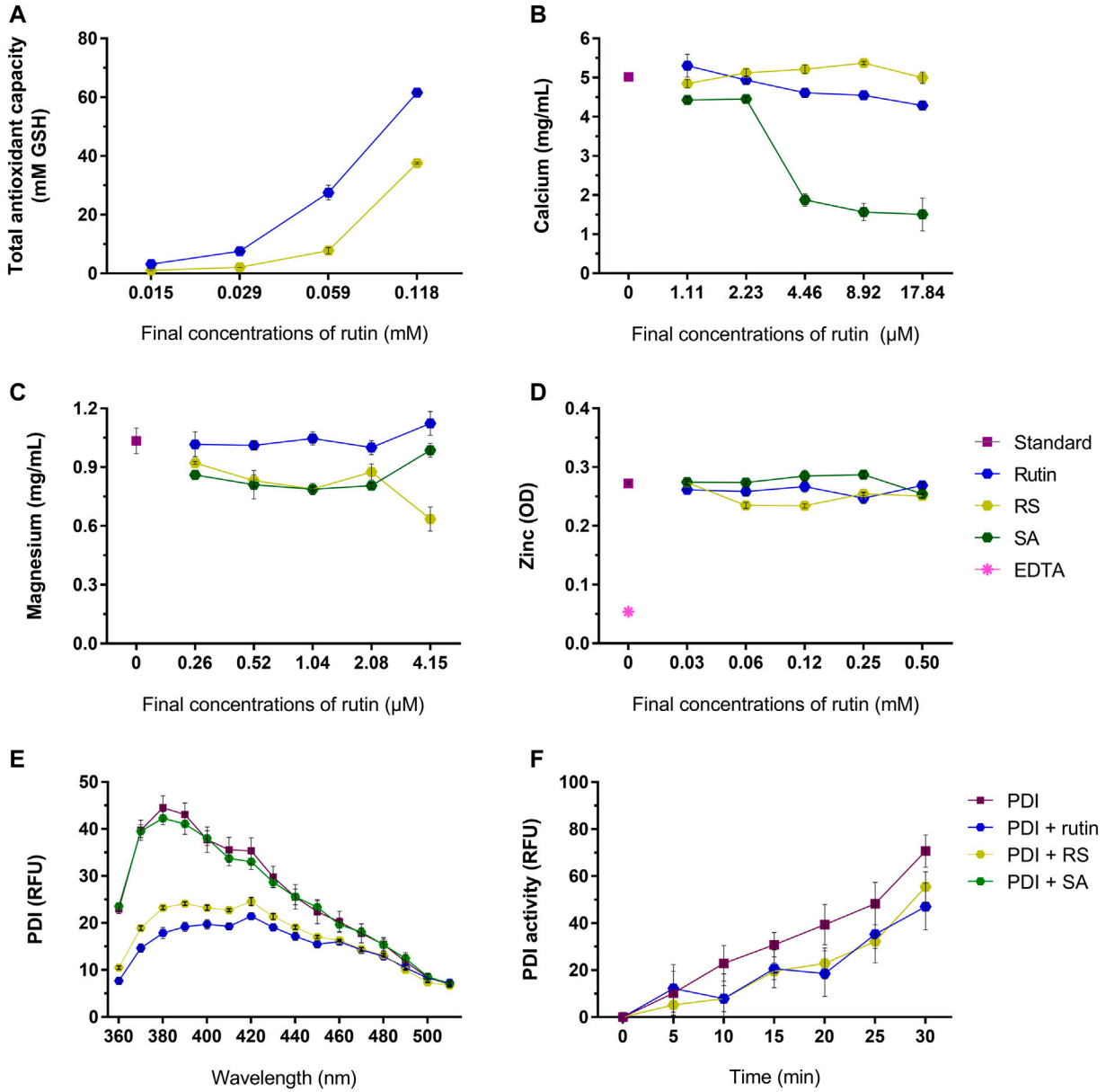

FIGURE 4 | (A) Total antioxidant capacity of rutin and RS at different concentrations, analyzed by the CUPRAC method. Data were expressed as GSH equivalents (mM). Quenching of **(B)** calcium, **(C)** magnesium and **(D)** zinc by the pre-incubation with rutin, RS, SA or Na_2EDTA at different concentrations. Data were expressed as concentration of free calcium or magnesium (mg/ml) or as optical density units (OD) for zinc. **(E)** Fluorescence spectra of PDI or PDI pre-incubated with rutin, RS or AS. Data were expressed as relative fluorescence units (RFU). **(F)** PDI reductase activity, evaluated by change in the fluorescence of di-eosine-GSSG probe (150 nM); PDI was tested alone or PDI pre-incubated with rutin, RS and SA (60 μM). Data were expressed as relative fluorescence units (RFU). Assays for **(A–D)** were carried out in duplicate and for **(E,F)** in triplicate.

substitution on rutin and 15, 20, 15, and 6 forms exist for 2, 3, 4, and 5 succinyl substitutions, respectively. Indeed, the 2–5 RS shows the isomeric forms in the chromatograms of their precursor ions (**Figure 3F**). Each succinyl substitution adds 100.016 Da to rutin, so that the precursor ions of RS for 1–6 substitutions are observed at m/z 711.2, 811.2, 911.2, 1011.2, 1111.2, and 1211.2, respectively. Only the original rutin and the 6-succinylated rutin show single forms and single-peak chromatograms (**Figure 3E**). Therefore, a total of 63 RS forms co-exist in the mixture, plus part of the remaining original non-substituted rutin. Low percentages of rutin and RS with 5 and 6 succinates are present in the sample (3.9, 4.8, and 0.6%, respectively). Medium rates are observed for 1 and 4 succinate RS (17.3 and 15.3%); however, the RS sample is mostly composed by RS with 2 and 3 succinates (30.7 and 27.6% of the sample).

Rutin has a broad range of activities, therefore it was relevant to investigate if RS also exhibit these activities, as antioxidant (Ganeshpurkar and Saluja, 2017), quencher of metal ions

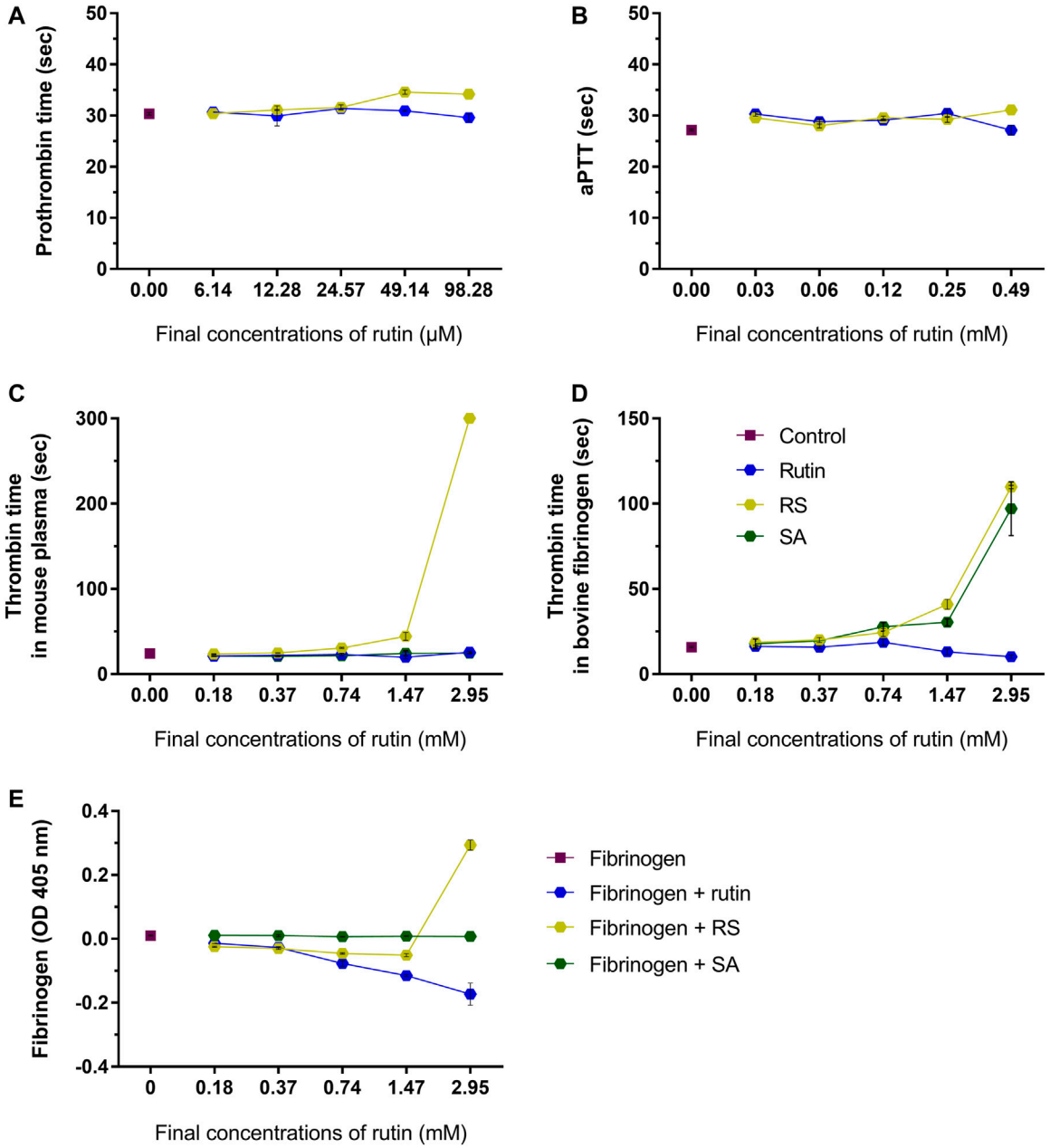

FIGURE 5 | Activity of rutin and RS at different concentrations on **(A)** prothrombin time in mouse plasma; **(B)** aPTT in mouse plasma. Activity of rutin, RS and SA at different concentrations on **(C)** thrombin time in mouse plasma; **(D)** thrombin time in bovine fibrinogen; **(E)** formation of complexes with fibrinogen. Data are representative of assays in triplicate.

(Behling et al., 2004; Pietta, 2000; Kandaswami and Middleton, 1994; Afanas'ev et al., 1989; Ganeshpurkar and Saluja, 2017) and PDI inhibitor (Jasuja et al., 2012). Rutin and RS showed a concentration-dependent antioxidant activity (**Figure 4A**), but RS expressed a lower antioxidant potential. Differently, rutin and RS did not show expressive quenching of calcium (**Figure 4B**), magnesium (**Figure 4C**) or zinc (**Figure 4D**) ions; however succinic acid (SA, the free-form of succinic anhydride) quenched calcium ions in a concentration-dependent manner.

Rutin is a known PDI inhibitor (Jasuja et al., 2012), as it modulates PDI structure and function. Rutin and RS, but not SA, altered PDI chemical structure, decreasing the fluorescence of Trp residues of PDI (**Figure 4E**). Congruently, pre-incubating rutin or RS with PDI decreased its reductase activity, evidenced by the decrease in the RFU of the probe (**Figure 4F**), as well as the decrease in the Vmax of the reaction (PDI alone: 0.043 ± 0.0003 units/second, PDI + rutin: 0.030 ± 0.004 and PDI + RS: 0.03 3 ± 0.001 units/second). Therefore, both rutin and RS

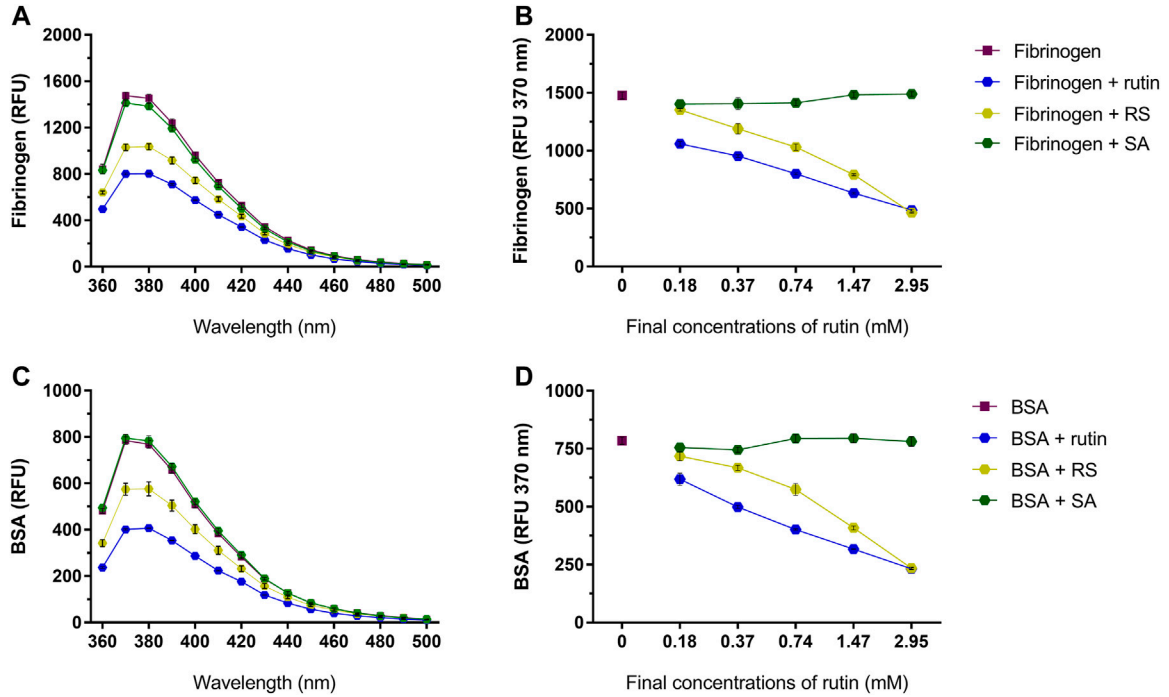

FIGURE 6 | Activity of rutin, RS and SA at different concentrations on the fluorescence spectra of **(A,B)** bovine fibrinogen and **(C,D)** BSA. Data are expressed as RFU, and assays were carried out in triplicate.

inhibited PDI reductase activity and acted as antioxidants, since RS presented the same core chemical structure of the flavonoid rutin (Pedriali et al., 2008b).

RS Alters Hemostatic Parameters *In Vitro*

Besides rutin activity as a PDI inhibitor, studies have already shown that rutin may modulate other hemostatic components *in vitro* (Kuntić et al., 2011; Choi et al., 2015). Therefore, we investigated the direct activity of rutin and RS in hemostatic parameters *in vitro*, as well as on abundant proteins present in blood, as fibrinogen and albumin. To better understand RS activities, SA was also analyzed comparatively, since RS was synthetized by succinylation of rutin.

RS prolongated moderately prothrombin time (**Figure 5A**) and aPTT (**Figure 5B**) (maximum of 3.6 and 3.9 s compared to control, respectively), which indicated that RS could affect some component(s) of the common pathway of the coagulation cascade. Later on, thrombin time was analyzed using mouse plasma (**Figure 5C**) or bovine fibrinogen (**Figure 5D**) as substrates. Compared to control, the thrombin time was prolonged when RS was added (maximum of >300 s for mouse plasma and 93.7 s for fibrinogen). SA prolonged the thrombin time when fibrinogen solution was used as the substrate (increase of 81 s), whereas rutin shortened the thrombin time in 6.5 s.

Since fibrinogen is a key component of hemostasis, the influence of rutin, RS and SA was investigated in this protein. The analysis of possible complexes with fibrinogen (**Figure 5E**) revealed that only the highest concentration of RS induced an increase in fibrinogen turbidity, which indicates a possible formation of complex by electrostatic interaction (Zhang et al., 2013). SA did not form complexes with fibrinogen, and the inhibition of thrombin time by SA may be more related with its activity as a calcium quenching molecule, as demonstrated above. Since only RS altered all hemostatic parameters, its activity on coagulation is different from that shown by rutin, and not due solely to the presence of succinates in its structure.

Pre-incubation of rutin and RS with fibrinogen (**Figures 6A,B**) or albumin (**Figures 6C,D**) decreased the fluorescence of their Trp residues, indicating a possible alteration of their 3D structure, which was not observed by pre-incubation with SA.

RS Inhibits BjV Activities *In Vitro*

As the focus of this work is the use of rutin and RS as therapeutic compounds for the treatment of snakebites, the possible modulation of BjV biological activities by rutin and RS was first assessed *in vitro*. Secondly, the direct activity of rutin, RS and SA was also tested in jararhagin – the most abundant SVMP in BjV (Sugiki et al., 1995). As observed for fibrinogen, albumin and PDI, rutin and RS decreased the fluorescence of Trp residues in BjV proteins (**Figure 7A**) and jararhagin (**Figure 7B**). However, SA only modulated the fluorescence of jararhagin. In order to verify whether protein conformational alterations were also modifying BjV activities, *in vitro* tests were undertaken.

Rutin and RS minimally inhibited LAAO activity (max. of 30.1 and 22.3% of inhibition, respectively) (**Figure 7C**). However, differently from rutin, RS inhibited BjV hyaluronidase activity (**Figure 7D**) in a concentration-dependent manner, showing a

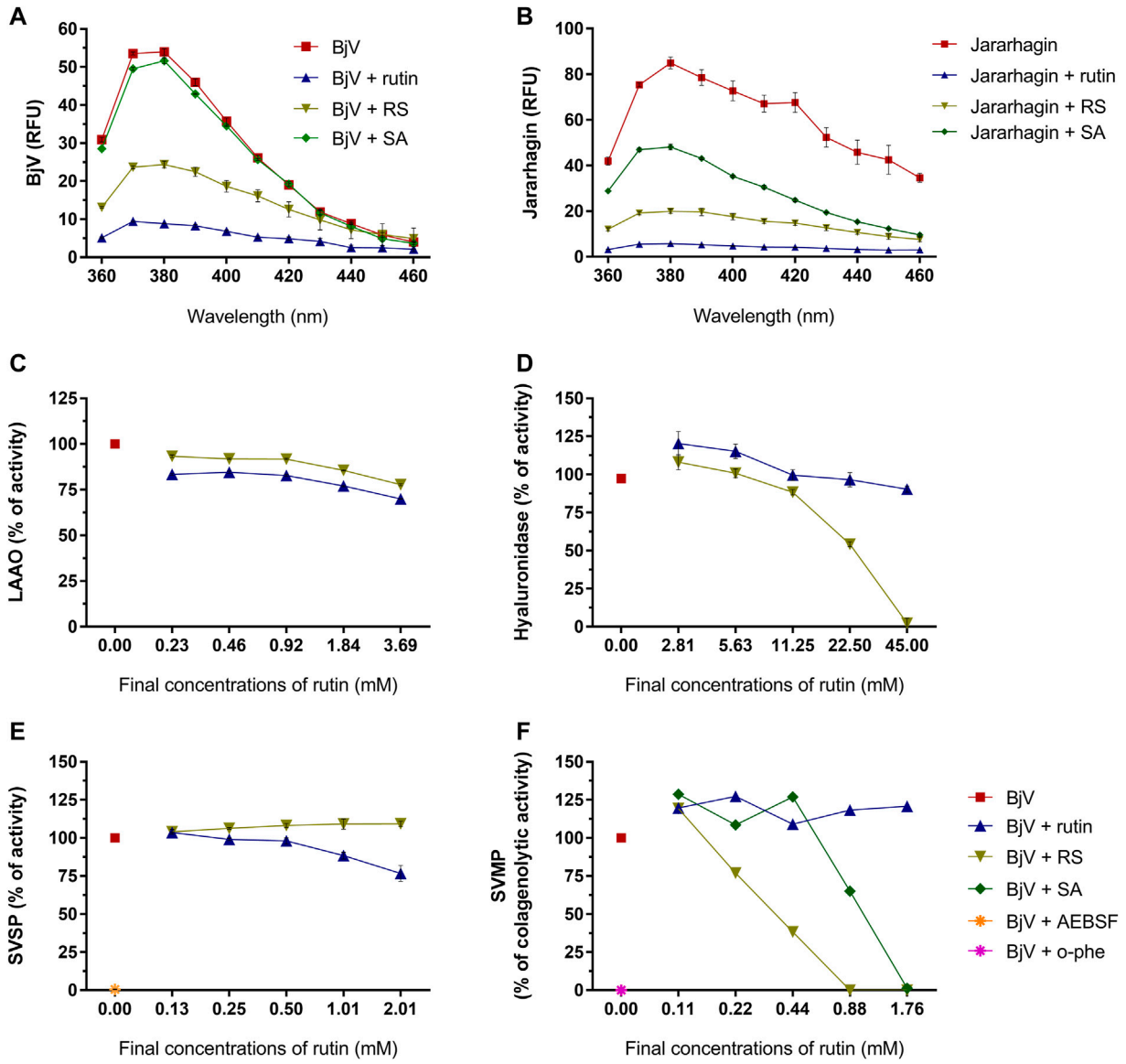

FIGURE 7 | Activity of rutin, RS and SA on the fluorescence spectra of **(A)** BjV and **(B)** jararhagin. Data were expressed as RFU. Activity of rutin, RS, SA, AEBSF (SVSP inhibitor) and o-phe (SVMP inhibitor) on enzymatic activities of BjV protein families *in vitro*: **(C)** LAAO, **(D)** hyaluronidase, **(E)** SVSP and **(F)** SVMP. SA and o-phe were tested only for SVMP activity, and AEBSF was tested only for SVSP activity. Data were expressed as percentage of the maximum enzymatic activity; assays were carried out in duplicates/triplicates.

maximum of 97.7% of inhibition. LAAO and hyaluronidase are minor parts of BjV, and therefore, other major protein families of BjV were chosen to be tested, as SVSP and SVMP.

SVSP activity (**Figure 7E**) was completely inhibited (99.4%) by AEBSF, an SVSP inhibitor, and modestly inhibited by the pre-incubation with rutin (max. of 23.3% of inhibition), but not by RS. On the other hand, rutin did not alter the collagenolytic activity of SVMP (**Figure 7F**), while BjV pre-incubated with o-phe, an SVMP inhibitor totally blocked this activity. Similarly, pre-incubation of BjV with RS or SA inhibited the collagenolytic activity in a concentration-dependent manner, achieving 100% of inhibition on the highest concentrations tested. To confirm RS and SA ability to inhibit SVMP, other SVMP activities were tested.

The proteolytic activity of BjV was analyzed on the substrates gelatin, casein and bovine fibrinogen (**Figures 8–10**, lanes 2). BjV alone cleaved protein bands of 75 kDa–250 kDa bands for gelatin, 25 kDa–30 kDa bands for casein (α-casein) and 60 kDa bands for fibrinogen (α-chain), and subsequent increases in lower molecular weight bands, related to products of protein degradation of substrates. BjV pre-incubated with AEBSF (**Figures 8A–10A,E**) or rutin (**Figures 8A–10A,B**, lanes 3–7) minimally attenuated proteolysis (maximum of 19.8% of inhibition) of those substrates. As expected, the inhibition of

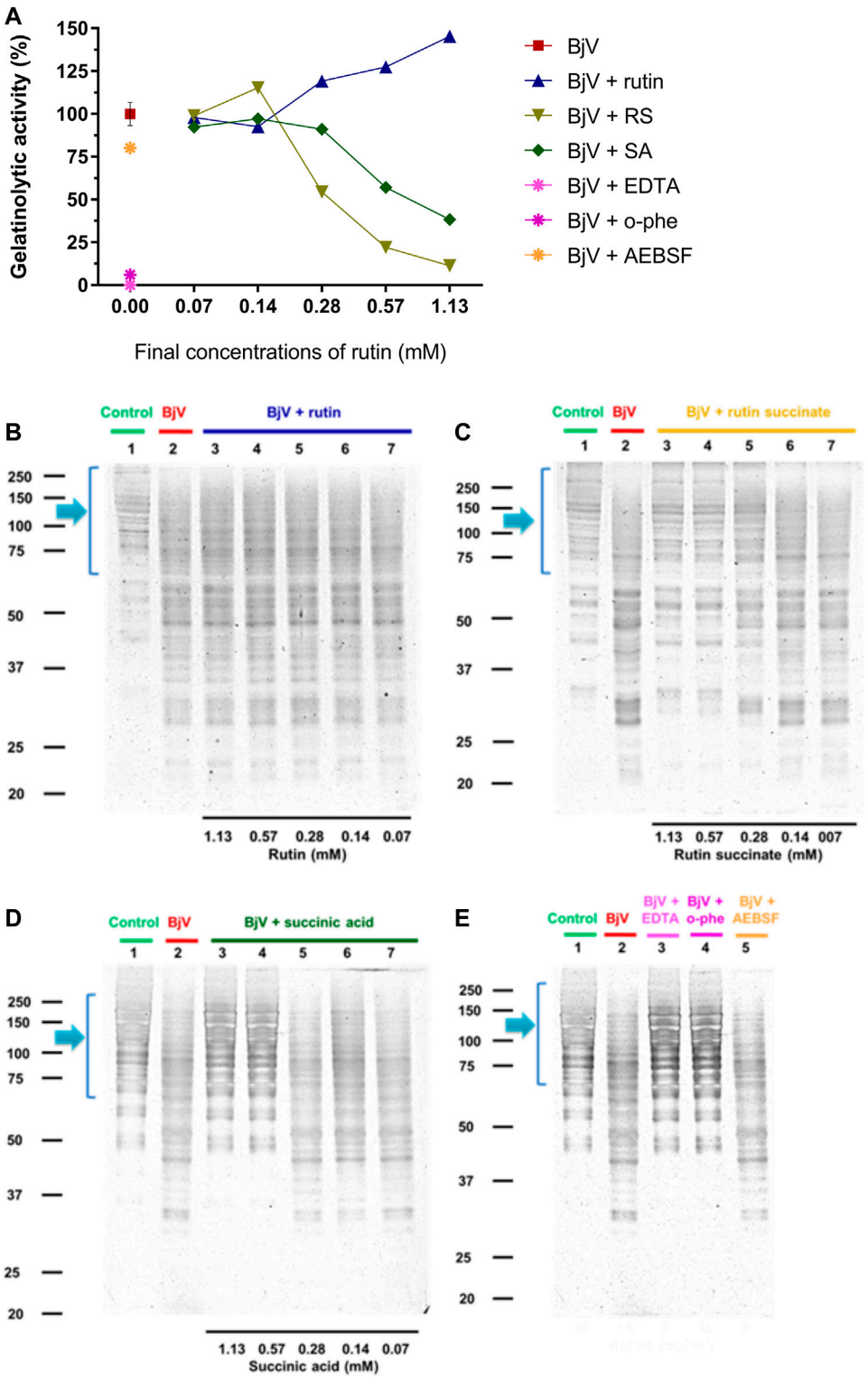

FIGURE 8 | (A–D) Activity of rutin, RS and SA at different concentration on BjV-induced gelatinolytic activity *in vitro*. **(A)** data were expressed as percentage of gelatinolytic activity induced by BjV alone; **(B–E)** gelatin degradation by BjV evaluated by means of SDS-PAGE gels (10%). Gelatin incubated without BjV (lanes 1) or with BjV solutions at 1.0 mg/ml (lanes 2); [**(B)**, BjV + rutin], lanes 3–7, rutin concentrations ranging from 1.13 to 0.07 mM; [**(C)**, BjV + RS], lanes 3–7, RS concentrations ranging from 1.13 to 0.07 mM; [**(D)**, BjV + SA], lanes 3–7, SA concentrations ranging from 1.13 to 0.07 mM; **(E)** BjV + Na_2EDTA (lane 3), BjV + o-phe (lane 4) and BjV + AEBSF (lane 5). Arrows refer to interest bands of 75 kDa–250 kDa, relative to non-degraded gelatin.

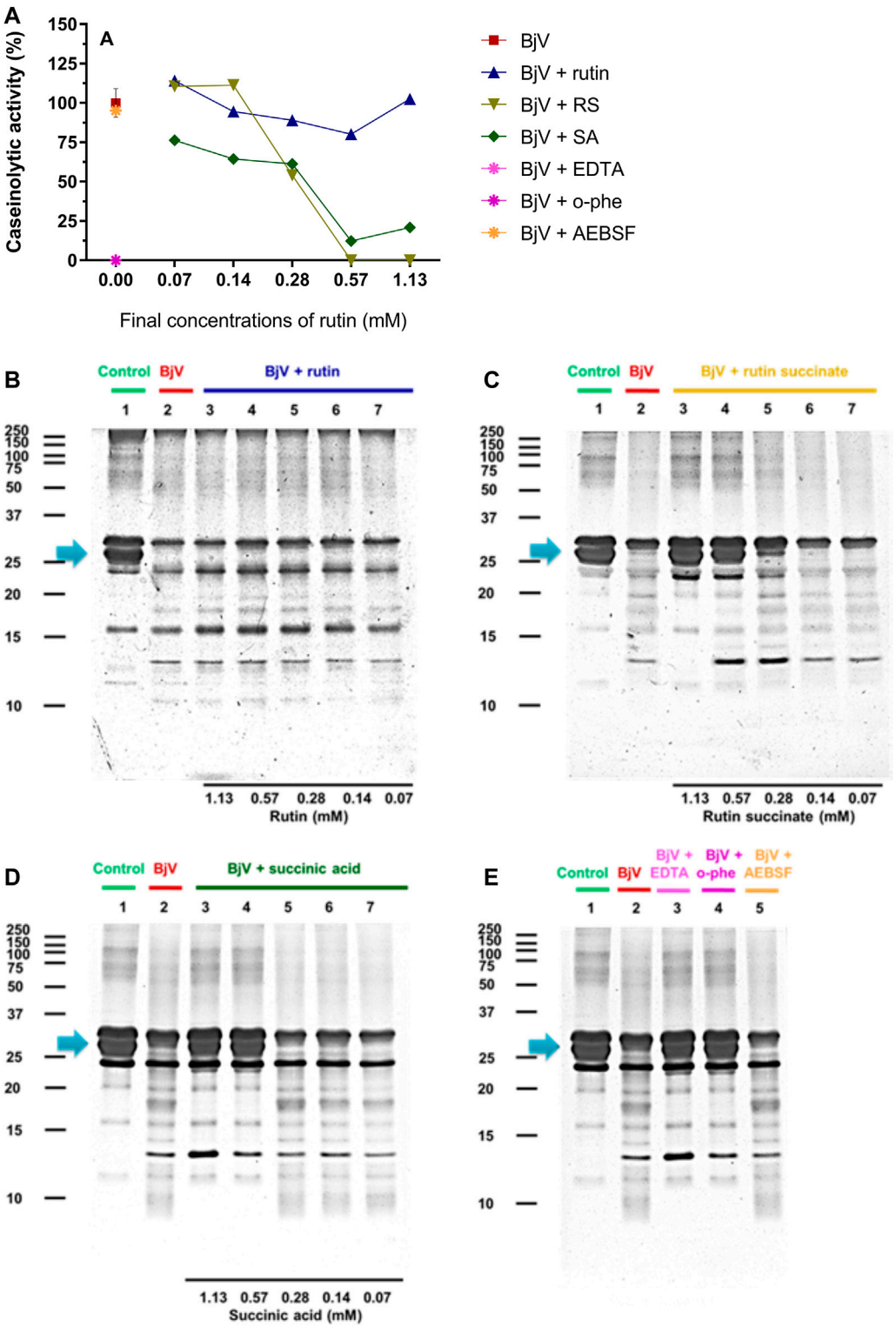

FIGURE 9 | (A–D) Activity of rutin, RS and SA at different concentration on BjV-induced caseinolytic activity *in vitro*. **(A)** data were expressed as percentage of caseinolytic activity induced by BjV alone; **(B–E)** casein degradation by BjV evaluated by means of SDS-PAGE gels (10%). Casein incubated without BjV (lanes 1) or with BjV solutions at 1.0 mg/ml (lanes 2); [**(B)**, BjV + rutin], lanes 3–7, rutin concentrations ranging from 1.13 to 0.07 mM; [**(C)**, BjV + RS], lanes 3–7, RS concentrations ranging from 1.13 to 0.07 mM; [**(D)**, BjV + SA], lanes 3–7, SA concentrations ranging from 1.13 to 0.07 mM; **(E)** BjV + Na_2EDTA (lane 3), BjV + o-phe (lane 4) and BjV + AEBSF (lane 5). Arrows refer to interest bands of 25 kDa–30 kDa (approximately), relative to non-degraded α-casein.

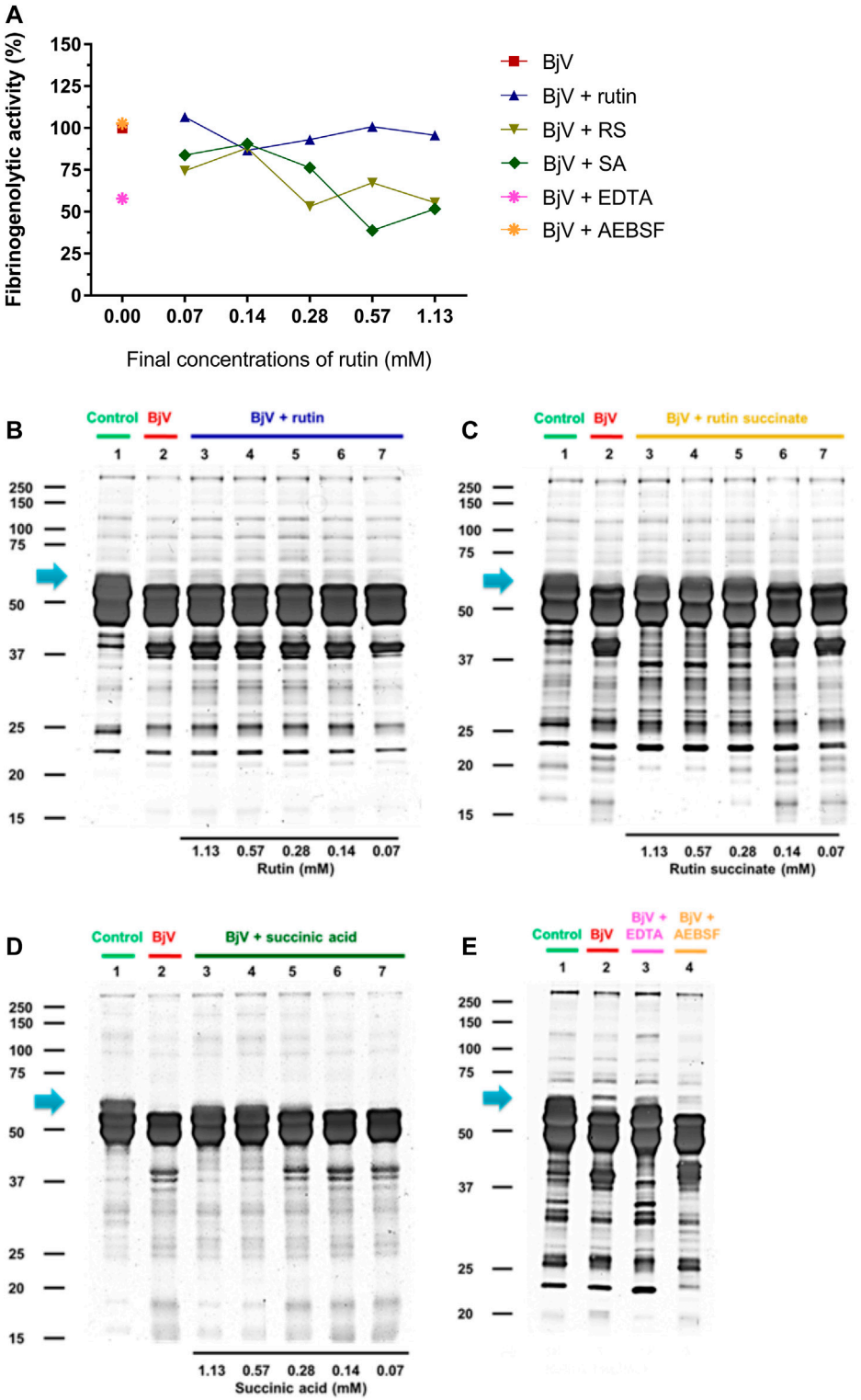

FIGURE 10 | (A–D) Activity of rutin, RS and SA at different concentration on BjV-induced fibrinogenolytic activity *in vitro*. **(A)** Data were expressed as percentage of fibrinogenolytic activity induced by BjV alone; **(B–E)** fibrinogen degradation by BjV was evaluated by means of SDS-PAGE gels (10%). Fibrinogen incubated without BjV (lanes 1) or with BjV solutions at 1.0 mg/ml (lanes 2); [**(B)**, BjV + rutin], lanes 3–7, rutin concentrations ranging from 1.13 to 0.07 mM; [**(C)**, BjV + RS], lanes 3–7, RS concentrations ranging from 1.13 to 0.07 mM; [**(D)**, BjV + SA], lanes 3–7, SA concentrations ranging from 1.13 to 0.07 mM; **(E)** BjV + Na_2EDTA (lane 3), BjV + o-phe (lane 4) and BjV + AEBSF (lane 5). Arrows refers to interest bands of 60 kDa (approximately), relative to non-degraded fibrinogen α-chain.

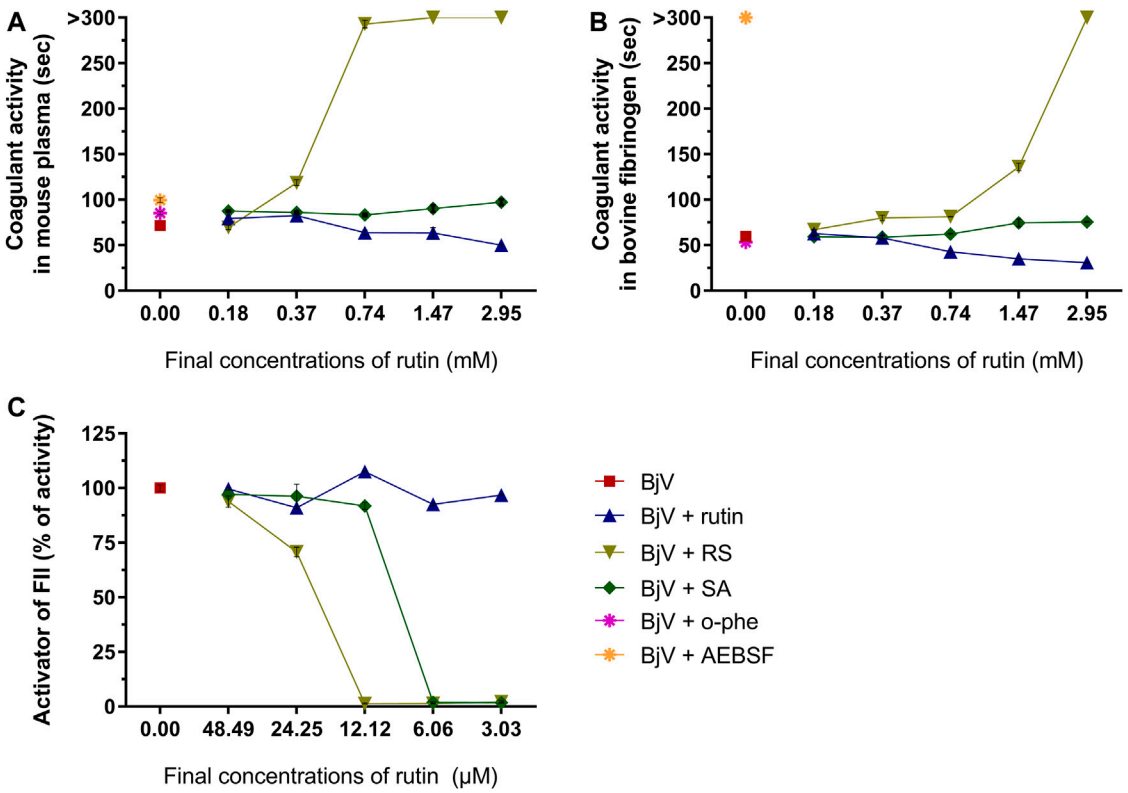

FIGURE 11 | Activity of rutin, RS or AS at different concentrations on BjV activities *in vitro*: **(A)** clotting of mouse plasma or **(B)** bovine fibrinogen. Data were expressed as clotting activity in seconds after the addition of BjV (0.25 mg/ml). **(C)** Prothrombin activation. Data were expressed as percentage of activity, and assays were carried out in triplicates.

SVMP by Na_2EDTA or o-phe decreased the BjV proteolytic activity (**Figures 8A–10A,E**): 100% for caseinolytic effect, 93.4% for gelatinolytic, and 42.2% for fibrinogenolytic activity. Likewise, RS inhibited SVMP activity more intensely than Na_2EDTA or o-phe (**Figures 8A–10A,C**, lanes 3–7), in a concentration-dependent manner, and inhibition rates as high as 100% was noticed for caseinolytic activity, around 90% for gelatinolytic and 47% for fibrinogenolytic activity. As observed for the collagenolytic activity, SA exhibited lower rates of proteolysis inhibition than RS (**Figures 8A–10A,D**, lanes 3–7), and maximum decreases of 61.2%–79.1% were observed for the three substrates. In addition, RS and SA decreased the degradation of fibrinogen by jararhagin and the degradation of gelatin by the collagenase from *C. histolyticum*, indicating a broader modulation of different agents and toxins.

Besides the proteolysis of proteins, SVMP also showed clotting activity due to the activation of coagulation factors, as factor X and prothrombin (Sano-Martins et al., 2003; Serrano et al., 2014). Rutin interfered minimally (9% inhibition) with the activation of prothrombin by BjV (**Figure 11C**). However, the pre-incubation of BjV with RS and SA at the 2 higher concentrations tested decreased 98%–99% the activation of prothrombin induced by BjV. Since the *in vitro* clotting activity is a well-established characteristic of BjV, this property was tested for rutin, RS or SA using bovine fibrinogen (**Figure 11B**) or mouse plasma (**Figure 11A**) as substrates. The clotting time of fibrinogen or mouse plasma was minimally decreased by rutin (5.1% maximum inhibition), SA (21% maximum inhibition) or o-phe (16.6% maximum inhibition); however, SVSP inhibition by AEBSF inhibited completely fibrinogen clotting by BjV. Differently, RS decreased BjV clotting activity in a concentration-dependent manner, ranging from 11.3 to 100% inhibition for fibrinogen clotting, and 30%–100% inhibition for plasma clotting.

Therefore, rutin minimally interfered with BjV activities *in vitro*. Nonetheless, pre-incubation of RS or SA with BjV inhibited important activities thereof, mainly those related to SVMP activity. In addition, RS also displayed broader effects related to a direct modulation of coagulation, evidencing its potential as an anticoagulant compound.

Since rutin showed potential beneficial effects on envenomation *in vivo* (Sachetto et al., 2018) and RS directly inhibited BjV *in vitro*, both rutin and RS were tested using an experimental model of envenomation. For *in vivo* experiments, rutin and RS were tested in concentrations 9 times higher than those used for BjV, and therefore, at this dosage, rutin pre-incubated with BjV did not alter its proteins, while pre-incubation with RS (or SA) inhibited partially the SVMP biological activities.

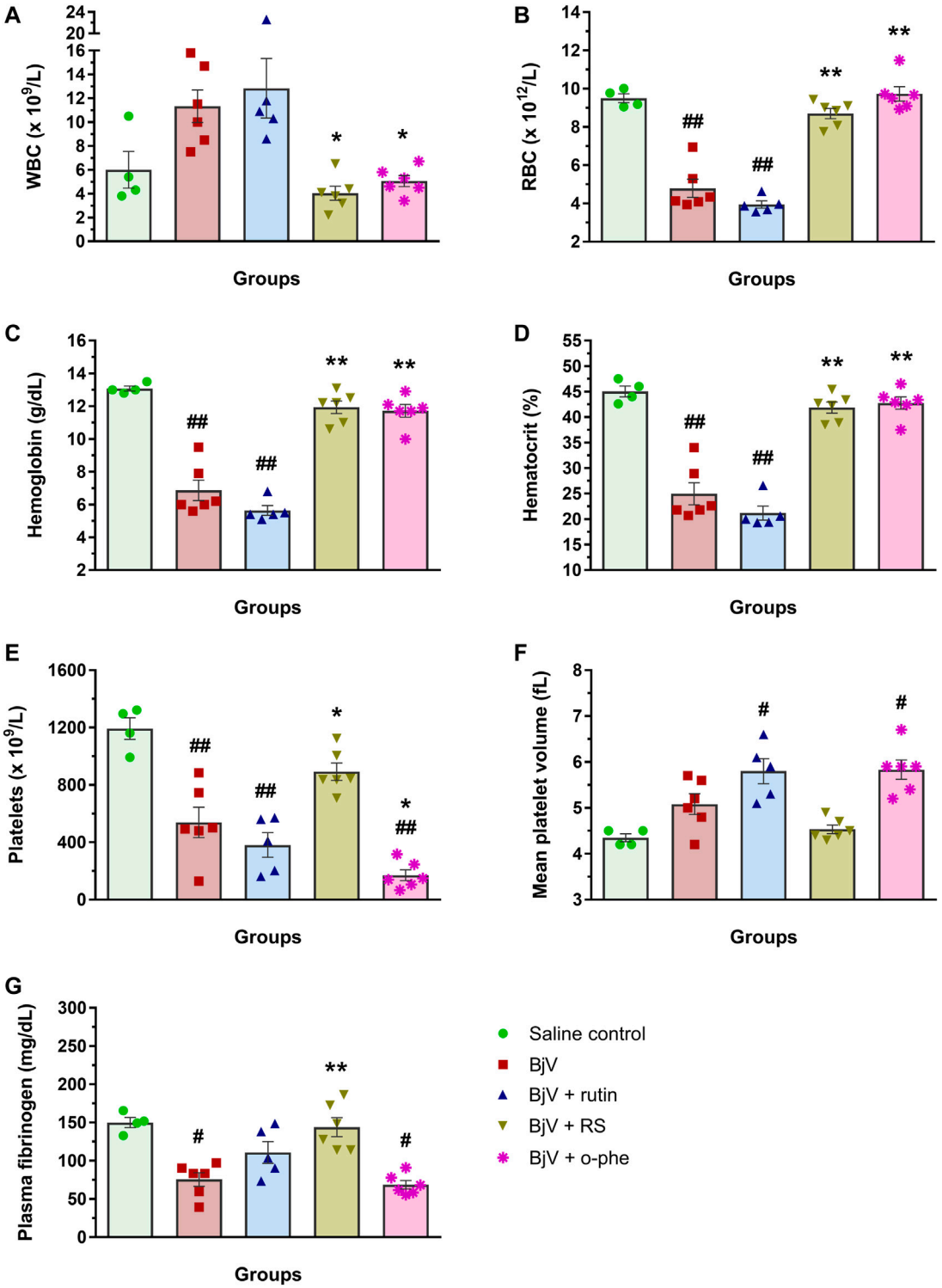

FIGURE 12 | (A) WBC counts, **(B)** RBC counts, **(C)** hemoglobin, **(D)** hematocrit, **(E)** platelet counts, **(F)** MPV and **(G)** plasma fibrinogen in mice 48 h after the injection of saline, BjV, BjV + rutin, BjV + RS or BjV + o-phe (BjV dose: 2×LD_{50}). One-way ANOVA was used, followed by Bonferroni *post-hoc* test; #$p < 0.05$ and ##$p < 0.001$ when compared to saline control group; *$p < 0.05$ and **$p < 0.001$ when compared to BjV group. Data are expressed as mean ± SEM. (n = 4–6/group).

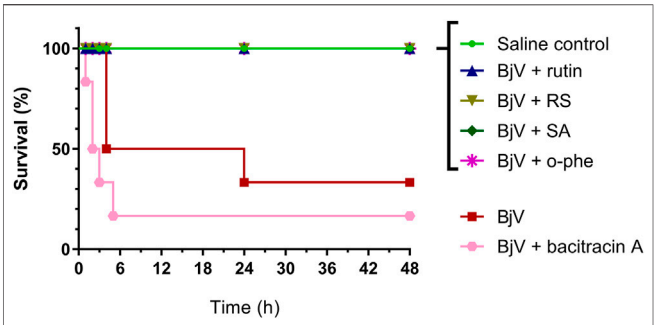

FIGURE 13 | Survival curves of mice during 48 h after the injection of saline, BjV, BjV + rutin, BjV + RS, BjV + SA, BjV + o-phe and BjV + bacitracin A (BjV dose: 3×LD_{50}). Log-rank test was used, and survival curves showed significant difference ($p = 0.005$). Data were expressed as percentage of survival (n = 3–6/group).

Rutin and RS Suppressed BjV Toxicity and Lethality

To analyze mouse survival as well as hemostatic disturbance, BjV was intraperitoneally injected in mice. Two different doses of BjV were used: 2×LD_{50} was used to simulate moderate envenomation and evaluate hemostatic parameters, whereas 3×LD_{50} was used to evaluate severe envenomation. Both rutin and RS were preincubated with BjV, and tested regarding its protective potential *in vivo*.

The moderate envenomation model did not induce mortality in mice in 48 h. The hematologic analysis revealed that preincubating BjV with RS or o-phe decreased circulating WBC (**Figure 12A**) compared to BjV group ($p < 0.050$). BjV alone induced a characteristic decrease of 44%–58% in RBC parameters (**Figures 12B–D**) ($p < 0.001$), but BjV + RS and BjV + o-phe hindered such fall, and results similar to the control ($p = 1.000$) and different from BjV ($p < 0.001$) were noticed. BjV also evokes other hemostatic disturbances *in vivo*, as thrombocytopenia and hypofibrinogenemia. The experimental groups BjV, BjV + rutin and BjV + o-phe had 53%–86% lower platelet counts and 16%–33% higher mean platelet volume (MPV, $p < 0.050$, **Figure 12F**) than the saline control ($p < 0.001$, **Figure 12E**). BjV and BjV + o-phe groups also showed a marked decrease in plasma fibrinogen levels ($p < 0.050$, **Figure 12G**), but rutin partially prevented the drop in fibrinogen levels, not differing from control ($p = 0.201$). As observed for the RBC, platelet counts and fibrinogen levels in the BjV + RS group were similar to the those of the control group ($p = 1.000$), and higher than those of mice injected with BjV alone ($p < 0.050$ for platelets and $p < 0.0001$ for fibrinogen). In addition to the hemostatic disturbances described above, BjV also evoked hemorrhages in the abdominal wall of all envenomed mice. However, the pre-incubation of BjV with RS or o-phe completely prevented it.

The severe envenomation model allowed the observation of mice survival for 48 h after 3×LD_{50} BjV injection (**Figure 13**). All animals from saline control, BjV + rutin, BjV + SA and BjV + o-phe groups survived. However, when injected with BjV alone, 50% of animals died after 4 h and the final survival rate at 48 h was 33.3%. Animals injected with BjV and bacitracin A (a thiol isomerase inhibitor) showed even lower survival rates (16.7%) after 48 h. Survival curves (**Figure 13**) showed significant differences among groups ($p < 0.001$). The results indicated that rutin, RS, AS and o-phe inhibited the toxic activity of BjV, preserving mice survival in a severe model of systemic envenomation. Furthermore, the thiol isomerase inhibition by bacitracin A reduced mice survival, which indicate a protective role of these enzymes in the organism during envenomation.

After 48 h of venom administration, hemostatic parameters of surviving mice were analyzed. WBC counts (**Figure 14A**) showed no alterations among groups ($p > 0.129$); nevertheless, RBC parameters (**Figures 14B–D**) showed results similar to those observed in the moderate envenomation model. BjV decreased RBC counts, hemoglobin and hematocrit ($p < 0.001$ compared to control), but the group BjV + RS and BjV + SA were similar to the control saline ($p = 1.000$) and different from the BjV group ($p < 0.050$). However, contrary to the moderate envenomation, BjV + o-phe group still showed a decrease of 43%–45% in RBC parameters compared to the control ($p < 0.001$). The analysis of blood smears revealed that envenomed mice presented morphological alterations as the presence of anisocytosis, polychromasia, schizocytes, dacryocytes and acanthocytes. This indicated that SVMP inhibition and rutin did not prevent RBC drop in the severe envenomation. However, RS and SA could prevent it, indicating the effectiveness of succinate groups on this parameter, regardless of SVMP inhibition. A marked thrombocytopenia was observed in all envenomed mice (**Figure 14E**) compared to controls ($p < 0.001$), as well as an increase in MPV (**Figure 14F**) in BjV + rutin, BjV + SA and BjV + o-phe groups ($p < 0.050$), but BjV + RS group showed the less intense decrease in platelet counts (42%). Plasma fibrinogen levels (**Figure 14G**) also decreased around 38%–60% in all envenomed animals ($p < 0.050$), and results showed that fibrinogen levels of BjV + rutin mice were similar in both moderate and severe envenomation.

Like the moderate envenomation model, severe envenomation induced hemorrhages in the abdominal and diaphragm of the animals, except in mice from the saline control, BjV + RS, BjV + SA and BjV + o-phe. Interestingly, BjV + rutin mice did not developed diaphragm hemorrhages neither. In one mouse that received BjV alone and died before 48 h, organs were collected for histological analyses. Skeletal muscles in the abdominal wall, at the face that had peritoneum intermediating their direct contact with BjV, showed paler eosinophilic coloration in their cytoplasm, implying that they had been damaged. Areas of hemorrhage were also observed at this face, but inflammatory infiltrate was not extensive. Muscle fibers present in the diaphragm showed the same lesions. In mice that received BjV preincubated with rutin and that survived for 48 h, a decreased extension of muscle fibers, in the abdominal wall and diaphragm showed decreased coloration of cytoplasm, and hemorrhage was less intense. In the mouse that received BjV preincubated with RS, no changes were observed. Thereby, the results of *in vivo* envenomation showed that BjV induced systemic hematological and hemostatic alterations and evoked animal

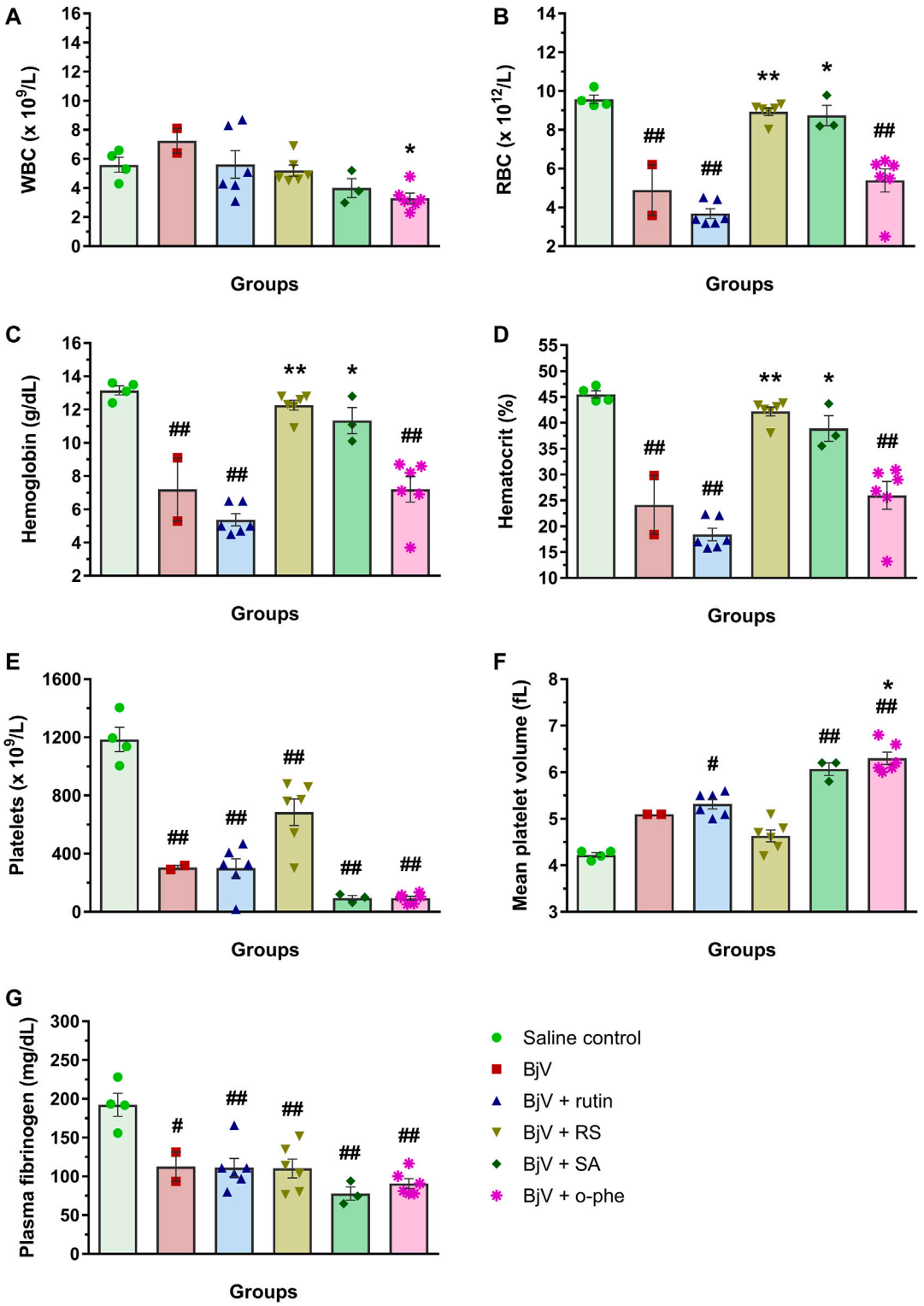

FIGURE 14 | (A) WBC counts, **(B)** RBC counts, **(C)** hemoglobin, **(D)** hematocrit, **(E)** platelet counts, **(F)** MPV and **(G)** plasma fibrinogen of mice 48 h after the injection of saline, BjV, BjV + rutin, BjV + RS, BjV + SA and BjV + o-phe (BjV dose: $3LD_{50}$). One-way ANOVA was used, followed by Bonferroni *post-hoc* test; #$p < 0.05$ and ##$p < 0.001$ when compared to saline control group; *$p < 0.05$ and **$p < 0.001$ when compared to BjV group. Data are expressed as mean ± SEM. (n = 3–6/group).

lethality. SVMP inhibition (by o-phe and SA) prevented the hemorrhagic and lethal activity of BjV, but did not show effects on other parameters. Whereas rutin induced a partial improvement of fibrinogen levels, RS improved hematological and hemostatic parameters and completely inhibited BjV-induced hemorrhagic activity. This indicates that RS effectiveness is not limited to its succinate moieties nor SVMP inhibitory activity. Moreover, rutin and RS ensured mice survival, showing their potential to neutralize the venom toxic activities, preventing the lethality evoked by BjV.

DISCUSSION

BjV is composed by a complex mixture of biomolecules, mostly proteins, as SVMP, SVSP, LAAO, hyaluronidases, among others (Koh et al., 2006; Deolindo et al., 2010; Sajevic et al., 2011; Takeda et al., 2012; Izidoro et al., 2014). These proteins present *in vitro* and *in vivo* activities, both in experimental models as well as in bitten patients, inducing hemostatic disturbances, bleeding and inflammatory reactions (Sano-Martins et al., 2003; Baldo et al., 2010; Gutiérrez, 2016; Kini and Koh, 2016; Gutiérrez et al., 2017). The severity of *Bothrops* envenomation is stratified as mild, moderate or severe, for proper patient treatment and antivenom administration (França et al., 2003). *B. jararaca* snakebite envenomation induces systemic alterations, as thrombocytopenia, a decrease in RBC counts and hypofibrinogenemia, both in animal models (Yamashita et al., 2014; Sachetto et al., 2018) and bitten patients (Maruyama et al., 1990; Santoro et al., 2008c). Thus, the analysis of hemostatic disturbances, such as blood incoagulability, hypofibrinogenemia, and other hematological alterations are relevant parameters to evaluate both the severity of envenomation and the effectiveness of antivenom administration (Santoro et al., 2008c). Therefore, the possible inhibitory potential of rutin and RS were tested regarding the characteristic enzymatic activities of BjV *in vitro*, as well as their potential to inhibit the toxicity and lethality of BjV in experimental envenomation models.

In order to achieve that, RS was synthetized. It showed higher water-solubility than rutin, in agreement with previous findings that reported an increase in 80 times in its solubility (Pedriali et al., 2008b). There was no alteration at the RS core chemical structure, as shown by the absorbance of their aromatic rings A and B (Bondarev and Knyukshto, 2013; Kumar and Pandey, 2013), and the CID-MS/MS fragments (Ou-yang et al., 2013; Chen et al., 2015), maintaining thereby the features of a flavonoid, like rutin. Furthermore, the differences between rutin and RS by HPLC and LC-MSE analyses were related to the substitutions of hydroxyl groups in the sugar moieties of rutin for succinate groups, as shown previously (Pedriali, 2006), which indicated the effectiveness of the rutin succinylation process. Rutin succinylation did not alter the characteristic activities of rutin, however the observed difference between rutin and RS antioxidant capacity may be due to the normal range of antioxidant activity of the flavonoids, which differs even within quercetin molecules. Besides, the results are in accordance with previous reports in which it was shown that RS has a lower antioxidant activity due to its lack of stabilization of carboxyl groups by hydroxyl groups in RS (Pedriali, 2006; Pedriali et al., 2008b). Differently from rutin and RS, succinic acid presented a calcium quenching activity, which may be related to its ability of interacting and forming complexes with metal ions (Domingo et al., 1988; Pathan et al., 2014).

Another key feature of rutin is its ability to inhibit PDI. It is known that PDI is susceptible to alterations of structure and function depending on the redox state and its interaction with substrates (Bekendam et al., 2016). PDI possesses 5 Trp residues, and it was already observed that GSSG – a known substrate that interacts with PDI (Raturi and Mutus, 2007) – induces a decrease in fluorescence of Trp residues in PDI (Ado et al., 2006), as observed herein. Congruently, rutin binds to the hydrophobic pocked of PDI b' domain, which induces a conformational alteration to a more compact structure, preventing other substrates to bind and inhibiting PDI reductase activity (Lin et al., 2015). It was already shown that only quercetins with glycosides at 3′ position in C ring are able to bind and inhibit PDI (Furie and Flaumenhaft, 2014), and in the present work it was observed that rutin and RS impacted in PDI structure, but not AS, which does not present the chemical structure and properties of rutin. Extracellular PDI is important for thrombus formation *in vivo* and rutin inhibits PDI both *in vitro* and *in vivo*. Rutin and analogous components inhibit thrombus formation in mice, as evaluated by the decrease in platelet accumulation and fibrin deposition (Jasuja et al., 2012). However, inhibition of the thiol isomerase family by bacitracin A was inefficient to protect mice from envenomation, therefore other activities of rutin – as anti-inflammatory, antioxidant, and modulator of vascular tonus and permeability – are likely involved therein (Afanas'ev et al., 1989; Ganeshpurkar and Saluja, 2017; Choi et al., 2015; Jasuja et al., 2012; Stopa et al., 2017; Schulman et al., 2016; Sharma et al., 2013; Panche et al., 2016; Kauss et al., 2008; Kirchner et al., 2013).

In addition, rutin was already shown to have the potential of interfering with other proteins in the blood, as showed by the results for BSA and fibrinogen. The activity of rutin on BSA was demonstrated earlier, and the decrease in albumin fluorescence was related with rutin binding by means of hydrogen bridges and weak van der Waals forces (Sengupta et al., 2018). The decrease in Trp residue fluorescence is also associated with conformational alterations of fibrinogen, since the Trp residues are mostly located in the hydrophobic portion of fibrinogen (Zhang et al., 2013). Our results confirm the interaction of rutin and RS with BSA and fibrinogen, which is important to understand their role *in vivo*, since BSA is relevant for the transport and bioavailability of exogenous components in the organism, whereas fibrinogen is a key component of hemostasis.

Regarding hemostasis components, SVSP and SVMP – the major protein families found in BjV – are both responsible for the clotting activity of BjV (Santoro and Sano-Martins, 1993; Yamashita et al., 2014; Sachetto et al., 2018), as also demonstrated herein. SVMP act as procoagulant proteins due to its ability to directly activate factor X and prothrombin (Antunes et al., 2010; Sachetto and Mackman, 2019), and were already related to the hemostatic disturbances evoked by BjV (Yamashita et al., 2014); (Senise et al., 2015). SVSP may act as

thrombin-like enzymes, which are capable of inducing *in vitro* and *in vivo* coagulation (Santoro and Sano-Martins, 1993; Sano-Martins et al., 2003; Antunes et al., 2010; Yamashita et al., 2014), and have been pointed out as important toxins for venom-induced coagulopathy (Nahas et al., 1979; Stocker et al., 1982). Quercetins reversely inhibit serine proteases, as human thrombin and, possibly, thrombin-like enzymes (Mozzicafreddo et al., 2006; Cuccioloni et al., 2009; Xue et al., 2017). This effect is concentration-dependent, as observed for the inhibition of SVSP activity by rutin. Moreover, the different structures of flavonoids interfere on their potential to bind to serine proteases (Mozzicafreddo et al., 2006), and therefore it is possible that the succinate groups of RS favor the inhibition of BjV thrombin-like enzymes, preventing their clotting ability.

Rutin was previously studied when pre-incubated with BjV, and it did not show significant inhibitory activity on BjV activities *in vitro* (Sachetto et al., 2018), as also observed herein. However, the reduction in fluorescence of Trp residues has been considered an indicative of conformational alterations of proteins present in snake venoms (Hashkel et al., 2018), and quercetin has been already demonstrated to bind to *Bothrops* venom components and induce that change (Kumar et al., 2017). In fact, the modest inhibition of BjV toxins by rutin may be due to its indirect activities, as an antioxidant that neutralizes H_2O_2 generation by LAAO *in vitro*, or due to other effects that occurred only when high concentrations of rutin, as for SVSP inhibition, were used. However, RS displayed a higher ability to inhibit BjV toxins *in vitro*, as hyaluronidases and SVMP. Snake venom hyaluronidases are often related to the degradation of extracellular matrix components, mainly hyaluronic acid, contributing to local damage and venom propagation *in vivo*. Flavonoids are hyaluronidase inhibitors (Bala et al., 2018) and the marked effectiveness of RS compared to rutin may be due to chemical differences between them, and/or superior water solubility of RS.

The SVMP protein family is the most abundant in BjV and show several activities *in vitro* and *in vivo* (Markland and Swenson, 2013). As demonstrated previously (Sachetto et al., 2018), rutin did not modulate SVMP function, however the inhibition of SVMP proteolytic activity by RS and SA seemed to be directly related to the succinyl groups in these molecules. Degradation of protein components is an important activity of SVMP, mainly related to the hydrolysis of basal membrane components of capillary vessels, which is a fundamental step for the development of hemorrhages induced by venom *in vivo* (Gutiérrez et al., 2016a; Gutiérrez et al., 2016b). Studies have demonstrated the relevance of SVMP on systemic envenomation caused by *B. asper*, and that SVMP inhibitors decreased the clotting activity of venom *in vitro,* and defibrinogenation and hemorrhagic activities *in vivo* (Rucavado et al., 2004). As showed herein, RS effectively inhibited both hemorrhagic and defibrinogenating activities of BjV on the moderate model of envenomation. However, these inhibitors only partially prevented the increase in vascular permeability and mortality of envenomed animals (Rucavado et al., 2004; Chacón et al., 2015). The lethality of Viperidae snake venoms is attributed to intravascular consumption of coagulation factors induced by procoagulating venoms, and to blood leakage that leads to cardiovascular collapse by hemorrhagic venoms (Gutierrez et al., 2017). Studies suggest that *Bothrops* venoms lethality is multifactorial (Maria et al., 1998), which may comprise SVMP activities and the increase in inflammation and vascular permeability (Chacón et al., 2015). Our results demonstrate that BjV SVMP inhibition (by RS, SA or o-phe) is effective on preventing the hemorrhages and lethality induced by BjV. However, RS effects were certainly broader, and not only due to SVMP inhibition, as demonstrated by the beneficial effect of RS on blood cell counts during envenomation.

The decrease in RBC parameters by *Bothrops* envenomation has been already related to the occurrence of local and systemic bleedings and microangiopathic hemolytic anemia in animals (Senise et al., 2015; Sachetto et al., 2018)and patients (Santoro et al., 2008c; Málaque et al., 2019). Accordingly, our results showed that mice with lower RBC counts also manifested morphologic alterations of RBC – indicating that venom-induced intravascular hemolysis occurred (Senise et al., 2015) – and abdominal hemorrhage, suggesting a connection between bleedings and the decrease in RBC counts. The precise mechanisms of thrombocytopenia in *B. jararaca* envenomation are not completely elucidated yet, although it is known that it is not related to SVMP, SVSP or local hemorrhagic injury (Yamashita et al., 2014). Furthermore, more severely envenomed patients manifested a more prominent platelet decrease (Santoro et al., 2008c), as reported herein for mice. As mentioned above, blood incoagulability is attributed to SVMP and SVSP activities (Yamashita et al., 2014; Senise et al., 2015; Sachetto et al., 2018), and its association with thrombocytopenia increases the tendency to development of systemic bleedings (Kamiguti et al., 1991).

The use of plant compounds or extracts – including flavonoids – may inhibit totally or partially the lethality and hemorrhages induced by BjV (da Silva et al., 2015; de Souza et al., 2020; Domingos et al., 2015; Ferreira et al., 2019), however the compounds and mechanisms by which this inhibition occurs have not been described yet. Inasmuch as rutin and RS completely inhibited the lethality evoked by BjV and modulated BjV-induced hemostatic disturbances, it is likely that this effect is also due to a direct action in the organism, hindering the damaging consequences of envenomation.

It is important to notice that rutin is already commercialized as a food supplement in several countries and it is considered safe by the Food and Drug Administration (FDA) in recommended doses of 2 g per day for human beings. Chemical formulations containing rutin or analogous compounds (Varemoid®, Relvene®, Venoruton® e Paroven®) are commercialized since the 1960's for the topical treatment of venous disturbances. Furthermore, quercetin and isoquercetin are being tested in clinical trials using oral administration (Heinz et al., 2010; Stopa et al., 2013; Flaumenhaft et al., 2015; Kooshyar et al., 2017; Di Lorenzo, 2018; Zwicker, 2018). Mice treated with rutin and other quercetins showed similar results on the inhibition of thrombus formation, either by oral or intravenous treatments (Jasuja et al., 2012). Reasoning that rutin and/or RS could be used as a first-choice medicinal product for snakebite treatment, so that their administration

occurred prior to antivenom therapy at hospitals, it will be essential to evaluate different administration routes -- as topical, intravenous, and oral ones -- to verify their influences on outcomes.

In conclusion, rutin and RS exhibit different and direct activities towards BjV proteins. Pre-incubation of BjV with RS inhibited its coagulant and proteolytic activities, whereas pre-incubation with rutin did not show important changes *in vitro*. Otherwise, RS acted as an anticoagulant compound *in vitro*, possibly by its interaction with fibrinogen. *In vivo*, RS inhibited hemostatic disturbances partially, while local hemorrhage was completely blocked. Therefore, RS directly inhibits BjV SVMP *in vitro* and *in vivo*. Furthermore, rutin and RS showed important effectiveness on protecting mice from BjV toxicity, ensuring mice survival and improving hemostatic balance. Further studies are necessary to investigate the therapeutic potential rutin and RS in other envenomation models, and at different time intervals, as well as its use as a complementary agent to antivenom therapy.

DATA AVAILABILITY STATEMENT

The raw data supporting the conclusion of this article will be made available by the authors, without undue reservation.

ETHICS STATEMENT

The animal study was reviewed and approved by Institutional Animal Care and Use Committees (Instituto Butantan, 4491070319 and Faculdade de Medicina da Universidade de São Paulo, 1334/2019).

AUTHOR CONTRIBUTIONS

Conceptualization: AS, MS. Methodology: AS, JM, and AOS. Investigation and data analysis; AS, MS, AOS, JM, and AK. Funding acquisition MS, AK: Project administration: MS. Supervision: MS, AT. Original draft writing: AS. Review and editing of the manuscript: AS, MS, AOS, JM, and AT.

FUNDING

This study was supported by the São Paulo Research Foundation (FAPESP, www.fapesp.br), grants # 2008/06524-3 (AOS), 2013/25177-0 (MS), 2018/26015-8 (AS), and 2019/07618-6 (MS); Conselho Nacional de Desenvolvimento Científico e Tecnológico (CNPq, www.cnpq.br), grant # 312469/2018-7 and 309980/2021-6 (MS); and Fundação Butantan (www.fundacaobutantan.org.br, FAPESP 2017/20106-9 (AT)).

ACKNOWLEDGMENTS

We are indebted to Dr. Francisco Laurindo (Instituto do Coração, Faculdade de Medicina, USP) for the donation of di-eosin-GSSG and purified PDI. We are also grateful to Magna A. Maltauro Soares for technical assistance with routine histological technique, and Rafael Conrado for technical expertise in HPLC analyses.

REFERENCES

Abreu, T. F., Sumitomo, B. N., Nishiyama, M. Y., Oliveira, U. C., Souza, G. H., Kitano, E. S., et al. (2017). Peptidomics of Acanthoscurria Gomesiana Spider Venom Reveals New Toxins with Potential Antimicrobial Activity. *J. Proteomics* 151, 232–242. doi:10.1016/j.jprot.2016.07.012

Ado, K., Takeda, N., Kikuchi, M., and Taniguchi, Y. (2006). The Pressure Effect on the Structure and Functions of Protein Disulfide Isomerase. *Biochim. Biophys. Acta* 1764, 586–592. doi:10.1016/j.bbapap.2006.01.015

Afanas'ev, I. B., Dorozhko, A. I., Brodskii, A. V., Kostyuk, V. A., and Potapovitch, A. I. (1989). Chelating and Free Radical Scavenging Mechanisms of Inhibitory Action of Rutin and Quercetin in Lipid Peroxidation. *Biochem. Pharmacol.* 38, 1763–1769. doi:10.1016/0006-2952(89)90410-3

Alluis, B., Pérol, N., El hajji, H., and Dangles, O. (2000). Water-soluble Flavonol (=3-Hydroxy-2-Phenyl-4h-1-Benzopyran-4-One) Derivatives: Chemical Synthesis, Colouring, and Antioxidant Properties. *Hca* 83, 428–443. doi:10.1002/(sici)1522-2675(20000216)83:2<428:aid-hlca428>3.0.co;2-j

Antunes, T. C., Yamashita, K. M., Barbaro, K. C., Saiki, M., and Santoro, M. L. (2010). Comparative Analysis of Newborn and Adult *Bothrops jararaca* Snake Venoms. *Toxicon* 56, 1443–1458. doi:10.1016/j.toxicon.2010.08.011

Avila-Agüero, M. L., París, M. M., Hu, S., Peterson, P. K., Gutiérrez, J. M., Lomonte, B., et al. (2001). Systemic Cytokine Response in Children Bitten by Snakes in Costa Rica. *Pediatr. Emerg. Care* 17, 425–429. doi:10.1097/00006565-200112000-00006

Bala, E., Hazarika, R., Singh, P., Yasir, M., and Shrivastava, R. (2018). A Biological Overview of Hyaluronidase: a Venom Enzyme and its Inhibition with Plants Materials. *Mater. Today Proc.* 5, 6406–6412. doi:10.1016/j.matpr.2017.12.252

Baldo, C., Jamora, C., Yamanouye, N., Zorn, T. M., and Moura-da-Silva, A. M. (2010). Mechanisms of Vascular Damage by Hemorrhagic Snake Venom Metalloproteinases: Tissue Distribution and *In Situ* Hydrolysis. *Plos Negl. Trop. Dis.* 4, e727. doi:10.1371/journal.pntd.0000727

Barraviera, B., Lomonte, B., Tarkowski, A., Hanson, L. Å., and Meira, D. A. (1995). Acute-phase Reactions, Including Cytokines, in Patients Bitten by Bothrops and Crotalus Snakes in Brazil. *J. Venom. Anim. Toxins* 1, 11–22. doi:10.1590/s0104-79301995000100003

Battellino, C., Piazza, R., da Silva, A. M., Cury, Y., and Farsky, S. H. (2003). Assessment of Efficacy of Bothropic Antivenom Therapy on Microcirculatory Effects Induced by *Bothrops jararaca* Snake Venom. *Toxicon* 41, 583–593. doi:10.1016/s0041-0101(02)00389-6

Behling, E. B., Sendão, M. C., Francescato, H. D. C., Antunes, L. M. G., and Bianchi, Md. L. P. (2004). Flavonóide quercetina: aspectos gerais e ações biológicas. *Alim Nutr.* 15, 285–292.

Bekendam, R. H., Bendapudi, P. K., Lin, L., Nag, P. P., Pu, J., Kennedy, D. R., et al. (2016). A Substrate-Driven Allosteric Switch that Enhances PDI Catalytic Activity. *Nat. Commun.* 7, 12579. doi:10.1038/ncomms12579

Bondarev, S. L., and Knyukshto, V. N. (2013). Fluorescence and Phosphorescence of Rutin. *J. Lumin.* 142, 236–240. doi:10.1016/j.jlumin.2013.03.047

Cardoso, J. L., Fan, H. W., França, F. O., Jorge, M. T., Leite, R. P., Nishioka, S. A., et al. (1993). Randomized Comparative Trial of Three Antivenoms in the Treatment of Envenoming by Lance-Headed Vipers (*Bothrops jararaca*) in São Paulo, Brazil. *Q. J. Med.* 86, 315–325.

Castro, O., Gutiérrez, J. M., Barrios, M., Castro, I., Romero, M., and Umaña, E. (1999). Neutralización del efecto hemorrágico inducido por veneno de *Bothrops asper* (Serpentes: Viperidae) por extractos de plantas tropicales. *Revista de Biología Trop.* 47, 605–616. doi:10.15517/rbt.v47i3.19215

Chacón, F., Oviedo, A., Escalante, T., Solano, G., Rucavado, A., and Gutiérrez, J. M. (2015). The Lethality Test Used for Estimating the Potency of Antivenoms against *Bothrops asper* Snake Venom: Pathophysiological Mechanisms, Prophylactic Analgesia, and a Surrogate *In Vitro* Assay. *Toxicon* 93, 41–50. doi:10.1016/j.toxicon.2014.11.223

Chen, M., Zhang, X., Wang, H., Lin, B., Wang, S., and Hu, G. (2015). Determination of Rutin in Rat Plasma by Ultra Performance Liquid Chromatography Tandem Mass Spectrometry and Application to Pharmacokinetic Study. *J. Chromatogr. Sci.* 53, 519–525. doi:10.1093/chromsci/bmu078

Cho, J., Furie, B. C., Coughlin, S. R., and Furie, B. (2008). A Critical Role for Extracellular Protein Disulfide Isomerase during Thrombus Formation in Mice. *J. Clin. Invest.* 118, 1123–1131. doi:10.1172/JCI34134

Choi, J. H., Kim, D. W., Park, S. E., Lee, H. J., Kim, K. M., Kim, K. J., et al. (2015). Anti-thrombotic Effect of Rutin Isolated from *Dendropanax Morbifera* Leveille. *J. Biosci. Bioeng.* 120, 181–186. doi:10.1016/j.jbiosc.2014.12.012

Cuccioloni, M., Mozzicafreddo, M., Bonfili, L., Cecarini, V., Eleuteri, A. M., and Angeletti, M. (2009). Natural Occurring Polyphenols as Template for Drug Design. Focus on Serine Proteases. *Chem. Biol. Drug Des.* 74, 1–15. doi:10.1111/j.1747-0285.2009.00836.x

da Silva, G. A., Domingos, T. F., Fonseca, R. R., Sanchez, E. F., Teixeira, V. L., and Fuly, A. L. (2015). The Red Seaweed *Plocamium Brasiliense* Shows Anti-snake Venom Toxic Effects. *J. Venom Anim. Toxins Incl Trop. Dis.* 21, 2. doi:10.1186/s40409-015-0002-2

de Souza, J. F., de Oliveira, E. C., da Silva, A. C. R., da Silva, V. P., Coelho Kaplan, M. A., Figueiredo, M. R., et al. (2020). Potential Use of Extract of the Plant Schwartiza Brasiliensis (Choisy) Bedell Ex gir.-Cañas against the Toxic Effects of the Venom of *Bothrops jararaca* or B. Jararacussu. *Biomed. Pharmacother.* 125, 109951. doi:10.1016/j.biopha.2020.109951

Deolindo, P., Teixeira-Ferreira, A. S., DaMatta, R. A., and Alves, E. W. (2010). L-amino Acid Oxidase Activity Present in Fractions of *Bothrops jararaca* Venom Is Responsible for the Induction of Programmed Cell Death in *Trypanosoma Cruzi*. *Toxicon* 56, 944–955. doi:10.1016/j.toxicon.2010.06.019

Di Lorenzo, G. (2018). Isoquercetin as an Adjunct Therapy in Patients with Kidney Cancer Receiving First-Line Sunitinib: a Phase I/II Trial (QUASAR). ClinicalTrials.gov Identifier: NCT02446795. Available at: https://clinicaltrials.gov/ct2/show/NCT02446795 (cited Jul 03, 2018).

Domingo, J. L., Gómez, M., Llobet, J. M., and Corbella, J. (1988). Comparative Effects of Several Chelating Agents on the Toxicity, Distribution and Excretion of Aluminium. *Hum. Toxicol.* 7, 259–262. doi:10.1177/096032718800700305

Domingos, T. F., Vallim, M. A., Cavalcanti, D. N., Sanchez, E. F., Teixeira, V. L., and Fuly, A. L. (2015). Effect of Diterpenes Isolated of the marine Alga Canistrocarpus Cervicornis against Some Toxic Effects of the Venom of the bothrops Jararaca Snake. *Molecules* 20, 3515–3526. doi:10.3390/molecules20033515

Ferraz, C. R., Calixto-Campos, C., Manchope, M. F., Casagrande, R., Clissa, P. B., Baldo, C., et al. (2015). Jararhagin-induced Mechanical Hyperalgesia Depends on TNF-α, IL-1β and NFκB in Mice. *Toxicon* 103, 119–128. doi:10.1016/j.toxicon.2015.06.024

Ferreira, L. G., da Silva, A. C. R., Noseda, M. D., Fuly, A. L., de Carvalho, M. M., Fujii, M. T., et al. (2019). Chemical Structure and Snake Antivenom Properties of Sulfated Agarans Obtained from *Laurencia Dendroidea* (Ceramiales, Rhodophyta). *Carbohydr. Polym.* 218, 136–144. doi:10.1016/j.carbpol.2019.04.066

Flaumenhaft, R., Furie, B., and Zwicker, J. I. (2015). Therapeutic Implications of Protein Disulfide Isomerase Inhibition in Thrombotic Disease. *Arterioscler Thromb. Vasc. Biol.* 35, 16–23. doi:10.1161/ATVBAHA.114.303410

França, F. O. S., and Málaque, C. M. S. (2003). "Acidente Botrópico," in *Animais Peçonhentos no Brasil - Biologia, Clínica e Terapêutica dos Acidentes*. Editors J. L. C. Cardoso, F. O. S. França, F. H. Wen, C. M. S. Málaque, and V. J. Haddad. 1 ed. (São Paulo: Savier), 72–86.

Furie, B., and Flaumenhaft, R. (2014). Thiol Isomerases in Thrombus Formation. *Circ. Res.* 114, 1162–1173. doi:10.1161/CIRCRESAHA.114.301808

Ganeshpurkar, A., and Saluja, A. K. (2017). The Pharmacological Potential of Rutin. *Saudi Pharm. J.* 25, 149–164. doi:10.1016/j.jsps.2016.04.025

Gonçalves, L. R., and Mariano, M. (2000). Local Haemorrhage Induced by *Bothrops jararaca* Venom: Relationship to Neurogenic Inflammation. *Mediators Inflamm.* 9, 101–107. doi:10.1080/096293500411569

Gullón, B., Lú-Chau, T. A., Moreira, M. T., Lema, J. M., and Eibes, G. (2017). Rutin: A Review on Extraction, Identification and Purification Methods, Biological Activities and Approaches to Enhance its Bioavailability. *Trends Food Sci. Tech.* 67, 220–235. doi:10.1016/j.tifs.2017.07.008

Gutiérrez, J. M., Calvete, J. J., Habib, A. G., Harrison, R. A., Williams, D. J., and Warrell, D. A. (2017). Snakebite Envenoming. *Nat. Rev. Dis. Primers* 3, 17063. doi:10.1038/nrdp.2017.63

Gutiérrez, J. M., Escalante, T., Rucavado, A., Herrera, C., and Fox, J. W. (2016). A Comprehensive View of the Structural and Functional Alterations of Extracellular Matrix by Snake Venom Metalloproteinases (SVMPs): Novel Perspectives on the Pathophysiology of Envenoming. *Toxins (Basel).* 8. doi:10.3390/toxins8100304

Gutiérrez, J. M., Escalante, T., Rucavado, A., and Herrera, C. (2016). Hemorrhage Caused by Snake Venom Metalloproteinases: a Journey of Discovery and Understanding. *Toxins (Basel)* 8, 93. doi:10.3390/toxins8040093

Gutiérrez, J. M., and Rucavado, A. (2000). Snake Venom Metalloproteinases: Their Role in the Pathogenesis of Local Tissue Damage. *Biochimie* 82, 841–850. doi:10.1016/s0300-9084(00)01163-9

Gutierrez, J. M., Solano, G., Pla, D., Herrera, M., Segura, A., Vargas, M., et al. (2017). Preclinical Evaluation of the Efficacy of Antivenoms for Snakebite Envenoming: State-Of-The-Art and Challenges Ahead. *Toxins (Basel)* 9, 163. doi:10.3390/toxins9050163

Gutiérrez, J. M. (2016). Understanding and Confronting Snakebite Envenoming: the Harvest of Cooperation. *Toxicon* 109, 51–62. doi:10.1016/j.toxicon.2015.11.013

Hashkel, A. M., Sadawe, E. A., Mohamed, A., Magel, N. M., Mrema, I. A., Bensaber, S. M., et al. (2018). Differentiation between Snake and Bee Venoms Using Fluorescence Spectroscopy and Computational Approach. *COJ Rev. Res.* 1, 2. doi:10.31031/cojrr.2018.01.000510

Heinz, S. A., Henson, D. A., Austin, M. D., Jin, F., and Nieman, D. C. (2010). Quercetin Supplementation and Upper Respiratory Tract Infection: a Randomized Community Clinical Trial. *Pharmacol. Res.* 62, 237–242. doi:10.1016/j.phrs.2010.05.001

Izidoro, L. F., Sobrinho, J. C., Mendes, M. M., Costa, T. R., Grabner, A. N., Rodrigues, V. M., et al. (2014). Snake Venom L-Amino Acid Oxidases: Trends in Pharmacology and Biochemistry. *Biomed. Res. Int.* 2014, 196754. doi:10.1155/2014/196754

J. Stopa, B. Furie, R. Flaumenhaft, and J. Zwicker (Editors) (2013). *Human Clinical Trials Evaluating Protein Disulfide Isomerase as an Antithrombotic Target: Pharmacodynamic and Pharmacokinetic Studies of Oral Quercetin and Isoquercetin* (XXIV Congress of the International Society of Thrombosis and Haemostasis).

Jasuja, R., Passam, F. H., Kennedy, D. R., Kim, S. H., van Hessem, L., Lin, L., et al. (2012). Protein Disulfide Isomerase Inhibitors Constitute a New Class of Antithrombotic Agents. *J. Clin. Invest.* 122, 2104–2113. doi:10.1172/JCI61228

Jorge, M. T., Cardoso, J. L. C., Castro, S. C. B., Ribeiro, L., França, F. O. S., de Almeida, M. E. S., et al. (1995). A Randomized 'blinded' Comparison of Two Doses of Antivenom in the Treatment of Bothrops Envenoming in São Paulo, Brazil. *Trans. R. Soc. Trop. Med. Hyg.* 89, 111–114. doi:10.1016/0035-9203(95)90678-9

Kamiguti, A. S., Cardoso, J. L., Theakston, R. D., Sano-Martins, I. S., Hutton, R. A., Rugman, F. P., et al. (1991). Coagulopathy and Haemorrhage in Human Victims of *Bothrops jararaca* Envenoming in Brazil. *Toxicon* 29, 961–972. doi:10.1016/0041-0101(91)90079-7

Kamiguti, A. S., Matsunaga, S., Spir, M., Sano-Martins, I. S., and Nahas, L. (1986). Alterations of the Blood Coagulation System after Accidental Human Inoculation by *Bothrops jararaca* Venom. *Braz. J. Med. Biol. Res.* 19, 199–204.

Kandaswami, C., and Middleton, E. (1994). Free Radical Scavenging and Antioxidant Activity of Plant Flavonoids. *Adv. Exp. Med. Biol.* 366, 351–376. doi:10.1007/978-1-4615-1833-4_25

Kauss, T., Moynet, D., Rambert, J., Al-Kharrat, A., Brajot, S., Thiolat, D., et al. (2008). Rutoside Decreases Human Macrophage-Derived Inflammatory Mediators and Improves Clinical Signs in Adjuvant-Induced Arthritis. *Arthritis Res. Ther.* 10, R19. doi:10.1186/ar2372

Kini, R. M., and Koh, C. Y. (2016). Metalloproteases Affecting Blood Coagulation, Fibrinolysis and Platelet Aggregation from Snake Venoms: Definition and Nomenclature of Interaction Sites. *Toxins (Basel)* 8. doi:10.3390/toxins8100284

Kirchner, T., Hermann, E., Möller, S., Klinger, M., Solbach, W., Laskay, T., et al. (2013). Flavonoids and 5-aminosalicylic Acid Inhibit the Formation of

Neutrophil Extracellular Traps. *Mediators Inflamm.* 2013, 710239. doi:10.1155/2013/710239

Koh, D. C., Armugam, A., and Jeyaseelan, K. (2006). Snake Venom Components and Their Applications in Biomedicine. *Cell Mol Life Sci* 63, 3030–3041. doi:10.1007/s00018-006-6315-0

Kooshyar, M. M., Mozafari, P. M., Amirchaghmaghi, M., Pakfetrat, A., Karoos, P., Mohasel, M. R., et al. (2017). A Randomized Placebo- Controlled Double Blind Clinical Trial of Quercetin in the Prevention and Treatment of Chemotherapy-Induced Oral Mucositis. *J. Clin. Diagn. Res.* 11, ZC46–ZC50. doi:10.7860/JCDR/2017/23975.9571

Krewson, C. F., and Couch, J. F. (1952). Preparation of Water-Soluble Metal Complexes of Rutin and Related Flavonols. *J. Am. Pharm. Assoc. Am. Pharm. Assoc.* 41, 83–86. doi:10.1002/jps.3030410211

Kumar, R., Caruso, I. P., Ullah, A., Lopes Cornelio, M., Andres Fossey, M., Pereira de Souza, F., et al. (2017). Exploring the Binding Mechanism of Flavonoid Quercetin to Phospholipase A2: Fluorescence Spectroscopy and Computational Approach. *Eur. J. Exp. Biol.* 07. doi:10.21767/2248-9215.100033

Kumar, S., and Pandey, A. K. (2013). Chemistry and Biological Activities of Flavonoids: an Overview. *Scientific World J.* 2013, 162750. doi:10.1155/2013/162750

Kuntić, V., Filipović, I., and Vujić, Z. (2011). Effects of Rutin and Hesperidin and Their Al(III) and Cu(II) Complexes on *In Vitro* Plasma Coagulation Assays. *Molecules* 16, 1378–1388. doi:10.3390/molecules16021378

Lin, L., Gopal, S., Sharda, A., Passam, F., Bowley, S. R., Stopa, J., et al. (2015). Quercetin-3-rutinoside Inhibits Protein Disulfide Isomerase by Binding to its B'x Domain. *J. Biol. Chem.* 290, 23543–23552. doi:10.1074/jbc.M115.666180

Málaque, C. M. S., Duayer, I. F., and Santoro, M. L. (2019). Acute Kidney Injury Induced by Thrombotic Microangiopathy in Two Cases of *Bothrops* Envenomation. *Clin. Toxicol. (Phila)* 57, 213–216. doi:10.1080/15563650.2018.1510129

Maria, W. S., Cambuy, M. O., Costa, J. O., Velarde, D. T., and Chávez-Olórtegui, C. (1998). Neutralizing Potency of Horse Antibothropic Antivenom. Correlation between *In Vivo* and *In Vitro* Methods. *Toxicon* 36, 1433–1439. doi:10.1016/s0041-0101(98)00077-4

Markland, F. S., Jr., and Swenson, S. (2013). Snake Venom Metalloproteinases. *Toxicon* 62, 3–18. doi:10.1016/j.toxicon.2012.09.004

Maruyama, M., Kamiguti, A. S., Cardoso, J. L., Sano-Martins, I. S., Chudzinski, A. M., Santoro, M. L., et al. (1990). Studies on Blood Coagulation and Fibrinolysis in Patients Bitten by *Bothrops jararaca* (Jararaca). *Thromb. Haemost.* 63, 449–453. doi:10.1055/s-0038-1645064

Montano, S. J., Lu, J., Gustafsson, T. N., and Holmgren, A. (2014). Activity Assays of Mammalian Thioredoxin and Thioredoxin Reductase: Fluorescent Disulfide Substrates, Mechanisms, and Use with Tissue Samples. *Anal. Biochem.* 449, 139–146. doi:10.1016/j.ab.2013.12.025

Moura-da-Silva, A. M., and Baldo, C. (2012). Jararhagin, a Hemorrhagic Snake Venom Metalloproteinase from *Bothrops jararaca*. *Toxicon* 60, 280–289. doi:10.1016/j.toxicon.2012.03.026

Mozzicafreddo, M., Cuccioloni, M., Eleuteri, A. M., Fioretti, E., and Angeletti, M. (2006). Flavonoids Inhibit the Amidolytic Activity of Human Thrombin. *Biochimie* 88, 1297–1306. doi:10.1016/j.biochi.2006.04.007

Nahas, L., Kamiguti, A. S., and Barros, M. A. (1979). Thrombin-like and Factor X-Activator Components of *Bothrops* Snake Venoms. *Thromb. Haemost.* 41, 314–328. doi:10.1055/s-0038-1646781

Nishijima, C. M., Rodrigues, C. M., Silva, M. A., Lopes-Ferreira, M., Vilegas, W., and Hiruma-Lima, C. A. (2009). Anti-hemorrhagic Activity of Four Brazilian Vegetable Species against *Bothrops jararaca* Venom. *Molecules* 14, 1072–1080. doi:10.3390/molecules14031072

Oliveira, P. V. S., Garcia-Rosa, S., Sachetto, A. T. A., Moretti, A. I. S., Debbas, V., De Bessa, T. C., et al. (2019). Protein Disulfide Isomerase Plasma Levels in Healthy Humans Reveal Proteomic Signatures Involved in Contrasting Endothelial Phenotypes. *Redox Biol.* 22, 101142. doi:10.1016/j.redox.2019.101142

Ou-yang, Z., Cao, X., Wei, Y., Zhang, W.-W. -Q., Zhao, M., and Duan, J.-a. (2013). Pharmacokinetic Study of Rutin and Quercetin in Rats after Oral Administration of Total Flavones of mulberry Leaf Extract. *Revista Brasileira de Farmacognosia* 23, 776–782. doi:10.1590/s0102-695x2013000500009

Panche, A. N., Diwan, A. D., and Chandra, S. R. (2016). Flavonoids: an Overview. *J. Nutr. Sci.* 5, e47–15. doi:10.1017/jns.2016.41

Pathan, J., Janrao, D. M., Agarwal, B. R., and Farooqui, M. (2014). Studies on Metal Ligand Stability Constant of Allopurinol and Succinic Acid with Some Metal Ions in Aqueos media. *Int. J. Chem. Stud.* 1, 36–41.

Pedriali, C. A. (2006). *Síntese química de derivados hidrossolúveis da rutina: determinação de suas propriedades físico-químicas e avaliação de suas atividades antioxidantes*. São Paulo: Universidade de São Paulo.

Pedriali, C. A., Fernandes, A. U., Bernusso, L. d. C., and Polakiewicz, B. (2008). The Synthesis of a Water-Soluble Derivative of Rutin as an Antiradical Agent. *Quím. Nova* 31, 2147–2151. doi:10.1590/s0100-40422008000800039

Pedriali, C. A., Fernandes, A. U., Bernusso, L. d. C., and Polakiewicz, B. (2008). The Synthesis of a Water-Soluble Derivative of Rutin as an Antiradical Agent. *Quím. Nova* 31, 2147–2151. doi:10.1590/s0100-40422008000800039

Pedroso, A. P., Souza, A. P., Dornellas, A. P., Oyama, L. M., Nascimento, C. M., Santos, G. M., et al. (2017). Intrauterine Growth Restriction Programs the Hypothalamus of Adult Male Rats: Integrated Analysis of Proteomic and Metabolomic Data. *J. Proteome Res.* 16, 1515–1525. doi:10.1021/acs.jproteome.6b00923

Petricevich, V. L., Teixeira, C. F., Tambourgi, D. V., and Gutiérrez, J. M. (2000). Increments in Serum Cytokine and Nitric Oxide Levels in Mice Injected with *Bothrops asper* and *Bothrops jararaca* Snake Venoms. *Toxicon* 38, 1253–1266. doi:10.1016/s0041-0101(99)00227-5

Pietta, P. G. (2000). Flavonoids as Antioxidants. *J. Nat. Prod.* 63, 1035–1042. doi:10.1021/np9904509

Pithayanukul, P., Leanpolchareanchai, J., and Bavovada, R. (2010). Inhibitory Effect of tea Polyphenols on Local Tissue Damage Induced by Snake Venoms. *Phytother Res.* 24 Suppl 1 (Suppl. 1), S56–S62. doi:10.1002/ptr.2903

Ratnoff, O. D., and Menzie, C. (1951). A New Method for the Determination of Fibrinogen in Small Samples of Plasma. *J. Lab. Clin. Med.* 37, 316–320.

Raturi, A., and Mutus, B. (2007). Characterization of Redox State and Reductase Activity of Protein Disulfide Isomerase under Different Redox Environments Using a Sensitive Fluorescent Assay. *Free Radic. Biol. Med.* 43, 62–70. doi:10.1016/j.freeradbiomed.2007.03.025

Ribeiro, J. P., Magalhães, L. M., Reis, S., Lima, J. L., and Segundo, M. A. (2011). High-throughput Total Cupric Ion Reducing Antioxidant Capacity of Biological Samples Determined Using Flow Injection Analysis and Microplate-Based Methods. *Anal. Sci.* 27, 483–488. doi:10.2116/analsci.27.483

Rucavado, A., Escalante, T., and Gutiérrez, J. M. (2004). Effect of the Metalloproteinase Inhibitor Batimastat in the Systemic Toxicity Induced by *Bothrops asper* Snake Venom: Understanding the Role of Metalloproteinases in Envenomation. *Toxicon* 43, 417–424. doi:10.1016/j.toxicon.2004.01.016

Sachetto, A. T. A. (2018). *Alterações hemostáticas e de estado redox no envenenamento por* Bothrops jararaca*: modulação pelo antioxidante natural rutina (quercetina-3-rutinosídeo)*. São Paulo: Faculdade de Medicina da Universidade de São Paulo.

Sachetto, A. T. A., and Mackman, N. (2019). Modulation of the Mammalian Coagulation System by Venoms and Other Proteins from Snakes, Arthropods, Nematodes and Insects. *Thromb. Res.* 178, 145–154. doi:10.1016/j.thromres.2019.04.019

Sachetto, A. T. A., Rosa, J. G., and Santoro, M. L. (2018). Rutin (Quercetin-3-rutinoside) Modulates the Hemostatic Disturbances and Redox Imbalance Induced by *Bothrops jararaca* Snake Venom in Mice. *Plos Negl. Trop. Dis.* 12, e0006774. doi:10.1371/journal.pntd.0006774

Sajevic, T., Leonardi, A., and Križaj, I. (2011). Haemostatically Active Proteins in Snake Venoms. *Toxicon* 57, 627–645. doi:10.1016/j.toxicon.2011.01.006

Sano-Martins, I. S., and Santoro, M. L. (2003). "Distúrbios Hemostáticos em Envenenamentos por Animais Peçonhentos no Brasil," in Animais Peçonhentos no Brasil - *Biologia, Clínica e Terapêutica dos Acidentes*. Editors J. L. C. Cardoso, F. O. S. França, F. H. Wen, C. M. S. Málaque, and V. J. Haddad. 1 ed. (São Paulo: São PauloSavier), 289–309.

Santoro, M. L., Sano-Martins, I. S., and Chamone, D. A. (1994). *In Vivo* platelet Activation Induced by *Bothrops jararaca* Venom in Rabbits. *Platelets* 5, 162–170. doi:10.3109/09537109409005530

Santoro, M. L., and Sano-Martins, I. S. (1993). Different Clotting Mechanisms of *Bothrops jararaca* Snake Venom on Human and Rabbit Plasmas. *Toxicon* 31, 733–742. doi:10.1016/0041-0101(93)90379-w

Santoro, M. L., Sano-Martins, I. S., Fan, H. W., Cardoso, J. L., Theakston, R. D., Warrell, D. A., et al. (2008). Haematological Evaluation of Patients Bitten by the Jararaca, *Bothrops jararaca*, in Brazil. *Toxicon* 51, 1440–1448. doi:10.1016/j.toxicon.2008.03.018

Santoro, M. L., Sano-Martins, I. S., Fan, H. W., Cardoso, J. L., Theakston, R. D., Warrell, D. A., et al. (2008). Haematological Evaluation of Patients Bitten by the Jararaca, *Bothrops jararaca*, in Brazil. *Toxicon* 51, 1440–1448. doi:10.1016/j.toxicon.2008.03.018

Santoro, M. L., Sano-Martins, I. S., Fan, H. W., Cardoso, J. L., Theakston, R. D., and Warrell, D. A. (2008). Haematological Evaluation of Patients Bitten by the Jararaca, *Bothrops jararaca*, in Brazil. *Toxicon* 51, 1440–1448. doi:10.1016/j.toxicon.2008.03.018

Schattner, M., Fritzen, M., Ventura, Jde. S., de Albuquerque Modesto, J. C., Pozner, R. G., Moura-da-Silva, A. M., et al. (2005). The Snake Venom Metalloproteases Berythractivase and Jararhagin Activate Endothelial Cells. *Biol. Chem.* 386, 369–374. doi:10.1515/BC.2005.044

Schulman, S., Bendapudi, P., Sharda, A., Chen, V., Bellido-Martin, L., Jasuja, R., et al. (2016). Extracellular Thiol Isomerases and Their Role in Thrombus Formation. *Antioxid. Redox Signal.* 24, 1–15. doi:10.1089/ars.2015.6530

Seba, R. A. (1949). Efeitos vasculares Do veneno de "*Bothrops atrox*" sua inibição pela rutina e um antihistaminico. *Revista Fluminense de Medicina* 14, 179–188.

Selamoglu, Z. (2017). Polyphenolic Compounds in Human Health with Pharmacological Properties. *J. Traditional Med. Clin. Naturopathy* 6. doi:10.4172/2573-4555.1000e138

Sengupta, P., Sardar, P. S., Roy, P., Dasgupta, S., and Bose, A. (2018). Investigation on the Interaction of Rutin with Serum Albumins: Insights from Spectroscopic and Molecular Docking Techniques. *J. Photochem. Photobiol. B* 183, 101–110. doi:10.1016/j.jphotobiol.2018.04.019

Senise, L. V., Yamashita, K. M., and Santoro, M. L. (2015). *Bothrops jararaca* Envenomation: Pathogenesis of Hemostatic Disturbances and Intravascular Hemolysis. *Exp. Biol. Med. (Maywood)* 240, 1528–1536. doi:10.1177/1535370215590818

Serrano, S. M. T., Oliveira, A. K., Menezes, M. C., and Zelanis, A. (2014). The Proteinase-Rich Proteome ofBothrops Jararacavenom. *Toxin Rev.* 33, 169–184. doi:10.3109/15569543.2014.922581

Sharma, S., Ali, A., Ali, J., Sahni, J. K., and Baboota, S. (2013). Rutin : Therapeutic Potential and Recent Advances in Drug Delivery. *Expert Opin. Investig. Drugs* 22, 1063–1079. doi:10.1517/13543784.2013.805744

Silva, J. C., Gorenstein, M. V., Li, G. Z., Vissers, J. P., and Geromanos, S. J. (2006). Absolute Quantification of Proteins by LCMSE: A Virtue of Parallel Ms Acquisition. *Mol. Cel Proteomics* 5, 144–156. doi:10.1074/mcp.M500230-MCP200

Sistema de Informação de Agravos de Notificação (SINAN) (2022). Available at: www.saude.gov.br/sinanweb January 25, 2022).

Stocker, K., Fischer, H., and Meier, J. (1982). Thrombin-like Snake Venom Proteinases. *Toxicon* 20, 265–273. doi:10.1016/0041-0101(82)90225-2

Stopa, J. D., Neuberg, D., Puligandla, M., Furie, B., Flaumenhaft, R., and Zwicker, J. I. (2017). Protein Disulfide Isomerase Inhibition Blocks Thrombin Generation in Humans by Interfering with Platelet Factor V Activation. *JCI Insight* 2, e89373. doi:10.1172/jci.insight.89373

Strapazzon, J. O., Parisotto, E. B., Moratelli, A. M., Garlet, T. R., Bastos, J., Zimermann, I. R., et al. (2014). Systemic Oxidative Stress in Victims of *Bothrops* Snakebites. *J. Appl. Biomed.* 13, 161–167.

Sugiki, M., Maruyama, M., Yoshida, E., Mihara, H., Kamiguti, A. S., and Theakston, D. G. (1995). Enhancement of Plasma Fibrinolysis *In Vitro* by Jararhagin, the Main Haemorrhagic Metalloproteinase in *Bothrops jararaca* Venom. *Toxicon* 33, 1605–1617. doi:10.1016/0041-0101(95)00102-6

Takeda, S., Takeya, H., and Iwanaga, S. (2012). Snake Venom Metalloproteinases: Structure, Function and Relevance to the Mammalian ADAM/ADAMTS Family Proteins. *Biochim. Biophys. Acta* 1824, 164–176. doi:10.1016/j.bbapap.2011.04.009

World Health Organization (2021). Snakebite Envenoming. Available at: https://www.who.int/news-room/fact-sheets/detail/snakebite-envenoming (cited January 25, 2022).

Xue, G., Gong, L., Yuan, C., Xu, M., Wang, X., Jiang, L., et al. (2017). A Structural Mechanism of Flavonoids in Inhibiting Serine Proteases. *Food Funct.* 8, 2437–2443. doi:10.1039/c6fo01825d

Yamada, D., and Morita, T. (1997). Purification and Characterization of a Ca2+-dependent Prothrombin Activator, Multactivase, from the Venom of Echis Multisquamatus. *J. Biochem.* 122, 991–997. doi:10.1093/oxfordjournals.jbchem.a021862

Yamashita, K. M., Alves, A. F., Barbaro, K. C., and Santoro, M. L. (2014). *Bothrops jararaca* Venom Metalloproteinases Are Essential for Coagulopathy and Increase Plasma Tissue Factor Levels during Envenomation. *Plos Negl. Trop. Dis.* 8, e2814. doi:10.1371/journal.pntd.0002814

Zhang, W., Zhong, D., Liu, Q., Zhang, Y., Li, N., Wang, Q., et al. (2013). Effect of Chitosan and Carboxymethyl Chitosan on Fibrinogen Structure and Blood Coagulation. *J. Biomater. Sci. Polym. Ed.* 24, 1549–1563. doi:10.1080/09205063.2013.777229

Zwicker, J. (2018). Cancer Associated Thrombosis and Isoquercetin. ClinicalTrials.gov Identifier: NCT02195232. Available at: https://clinicaltrials.gov/ct2/show/NCT02195232 (cited Jul 03, 2018).

Zychar, B. C., Dale, C. S., Demarchi, D. S., and Gonçalves, L. R. (2010). Contribution of Metalloproteases, Serine Proteases and Phospholipases A2 to the Inflammatory Reaction Induced by *Bothrops jararaca* Crude Venom in Mice. *Toxicon* 55, 227–234. doi:10.1016/j.toxicon.2009.07.025

Conflict of Interest: The authors declare that the research was conducted in the absence of any commercial or financial relationships that could be construed as a potential conflict of interest.

Publisher's Note: All claims expressed in this article are solely those of the authors and do not necessarily represent those of their affiliated organizations, or those of the publisher, the editors and the reviewers. Any product that may be evaluated in this article, or claim that may be made by its manufacturer, is not guaranteed or endorsed by the publisher.

frontiers in Pharmacology

ORIGINAL RESEARCH
published: 28 February 2022
doi: 10.3389/fphar.2022.821181

The Pharmacological and Structural Basis of the AahII–$Na_V1.5$ Interaction and Modulation by the Anti-AahII Nb10 Nanobody

Riadh Hmaidi[1,2], *Ayoub Ksouri*[1], *Rahma Benabderrazek*[1], *Viviane Antonietti*[3], *Pascal Sonnet*[3], *Mathieu Gautier*[2†*], *Balkiss Bouhaouala-Zahar*[1,4*†] and *Halima Ouadid-Ahidouch*[2*†]

[1]Laboratory of Biomolecules, Venoms, and Theranostic Applications, Institut Pasteur Tunis, University of Tunis El Manar, Tunis, Tunisia, [2]Laboratory of Cellular and Molecular Physiology UR 4667, UFR of Sciences, University of Picardie Jules Verne, Amiens, France, [3]Infectious Agents, Resistance and Chemotherapy UR 4294, UFR of Pharmacy, University of Picardie Jules Verne, Amiens, France, [4]Medical School of Tunis, University of Tunis El Manar, Tunis, Tunisia

Scorpion α-toxins are neurotoxins that target the fast inactivation mechanism of voltage-gated sodium (Na_V) channels leading to several neuro- and cardiotoxic effects in mammals. The toxin AahII is the most active α-toxin from the North African scorpion *Androctonus australis Hector* that slows the fast inactivation of Na_V channels. To fight scorpion envenomation, an anti-AahII nanobody named NbAahII10 (Nb10) was developed. The efficiency of this nanobody has been evaluated *in vivo* on mice, but its mechanism of action at the cellular level remains unknown. Here we have shown that AahII toxin slows the fast inactivation of the adult cardiac $Na_V1.5$ channels, expressed in HEK293 cells, in a dose-dependent manner, while current amplitude was not affected. The inactivation of $Na_V1.5$ is slower by a factor of 4, 7, and 35 in the presence of [AahII] at 75, 150, and 300 nM, respectively. The washout partially reversed the toxin effect on inactivation from 8.3 ± 0.9 ms to 5.2 ± 1.2 ms at 75 nM. We have also demonstrated that the highly neutralizing Nb10 can fully reverse the effect of AahII toxin on the channel inactivation kinetics even at the 1:1 M ratio. However, the 1:0.5 M ratio is not able to neutralize completely the AahII effect. Therefore, the application of Nb10 promotes a partial abolishment of AahII action. Bioinformatic analysis and prediction of $Na_V1.5$-driven docking with AahII show that Ala39 and Arg62 of AahII play a crucial role to establish a stable interaction through H-bound interactions with Gln1615 and Lys1616 (S3–S4 extracellular loop) and Asp1553 (S1–S2 loop) from the voltage-sensing domain IV (VSD4) of $Na_V1.5$, respectively. From this, we notice that AahII shares the same contact surface with Nb10. This strongly suggests that Nb10 dynamically replaces AahII toxin from its binding site on the $Na_V1.5$ channel. At the physiopathological level, Nb10 completely neutralized the enhancement of breast cancer cell invasion induced by AahII. In summary, for the first time, we made an electrophysiological and structural characterization of the neutralization potent of Nb10 against the α-scorpion toxin AahII in a cellular model overexpressing $Na_V1.5$ channels.

Keywords: scorpion toxin, AahII, $Na_v1.5$, nanobody, patch-clamp, docking, inactivation

OPEN ACCESS

Edited by:
Jean-Marc Sabatier, Aix-Marseille Université, France

Reviewed by:
Thomas Durek, The University of Queensland, Australia
Enrico Leipold, University of Lübeck, Germany
Allan Douglas Cembella, Alfred Wegener Institute Helmholtz Centre for Polar and Marine Research (AWI), Germany

***Correspondence:**
Mathieu Gautier
mathieu.gautier@u-picardie.fr
Balkiss Bouhaouala-Zahar
balkiss.bouhaouala@fmt.utm.tn
Halima Ouadid-Ahidouch
halima.ahidouch-ouadid@u-picardie.fr

[†]These authors have contributed equally to this work

Specialty section:
This article was submitted to Pharmacology of Ion Channels and Channelopathies, a section of the journal Frontiers in Pharmacology

Received: *23 November 2021*
Accepted: *17 January 2022*
Published: *28 February 2022*

Citation:
Hmaidi R, Ksouri A, Benabderrazek R, Antonietti V, Sonnet P, Gautier M, Bouhaouala-Zahar B and Ouadid-Ahidouch H (2022) The Pharmacological and Structural Basis of the AahII–$Na_V1.5$ Interaction and Modulation by the Anti-AahII Nb10 Nanobody. Front. Pharmacol. 13:821181. doi: 10.3389/fphar.2022.821181

INTRODUCTION

Voltage-gated sodium (Na_V) channels are large transmembrane proteins responsible for the initiation and propagation of action potentials in excitable cells (Ahern et al., 2016). After voltage-dependent opening, Na_V channels undergo a rapid spontaneous inactivation process that terminates Na^+ permeation (Armstrong et al., 1973; Ahern et al., 2016). Fast inactivation is the main hallmark of eukaryotic Na_V channel function that allows cells to repolarize and Na_V channels to become ready for reactivation (Ulbricht 2005; Ahern et al., 2016). Eukaryotic Na_V channels count 9 isoforms ($Na_V1.1$–$Na_V1.9$), encoded by 9 distinct genes (SCN1–5A and SCN8–11A) with almost 50% of homology in the amino acid sequences (Goldin et al., 2000; Catterall et al., 2005). These channels consist of the heteromeric assembly of an α-subunit which forms the channel pore and provides its function with two auxiliary β-subunits. The α-subunit of Na_V channels contains four homologous, nonidentical domains, each consisting of six transmembrane segments (S1–S6) (Ren et al., 2001; Catterall 2014). Each domain is organized into two parts, the voltage-sensing domain (VSD) from S1 to S4 and the pore module (PM) between S5 and S6 (Catterall et al., 2017). The S4 segments known as voltage sensors modules are positively charged due to four to eight arginine/lysine residues flanked by two hydrophobic residues (Ahern et al., 2016; Catterall et al., 2017). This positively charged motif serves as a gating charge and moves outward upon depolarization to initiate the channel activation.

Rapid inactivation of Na_V channels results from the occlusion of the pore by a cytosolic inactivation motif that consists of a cluster of hydrophobic residues, isoleucine, phenylalanine, and methionine (IFM) in the intracellular loop connecting domain III (DIII) and DIV (Armstrong et al., 1973; Goldin 2003). In fact, during the activation process, the movement of the voltage sensors, particularly the DIV voltage sensor (VSD4), exposes a hydrophobic site between the S3 and S4 segments. The binding of the IFM motif to this site leads to a physical blockage of ion movement in the cell (Goldin 2003; Catterall 2014). Because VSD1–3 respond more rapidly to membrane depolarization than VSD4 (Chanda and Bezanilla, 2002), inactivation generally occurs after channel activation. Therefore, the inactivation process is intimately linked to channel activation following the movement of VSD4. Indeed, mutation of the IFM motif can completely abolish fast inactivation in Na_V channels (Ahern et al., 2016; Catterall et al., 2017).

Several venomous animals including scorpions have developed an arsenal of toxins that target and disrupt Na_V inactivation to immobilize prey or predators (Bosmans and Tytgat, 2007; Hanck and Sheets, 2007). AahII from *Androctonus australis Hector* is the most toxic polypeptide responsible for the noxious effects of the venom with an LD50 < 3 ng at an intracerebroventricular administration in a 20 g mouse (Devaux et al., 2004). At the pharmacological level, AahII is an α-scorpion toxin that targets site 3 on Na_V channels and slows the inactivation to sustain sodium influx (Martin et al., 1987; Catterall et al., 2007; Clairfeuille et al., 2019). At the structural level, AahII is a 64-amino-acid peptide stabilized by four disulfide bonds to form a compact β1–α1–β2–β3 scaffold that can highly interact with multiple mammalian Na_V channel subtypes (Housset et al., 1994).

To affect the fast inactivation mechanism, AahII interacts with VSD4 by trapping it in a deactivated state. AahII does not disturb channel activation because DI–III voltage sensors can ensure the opening of the channel even if VSD4 remains deactivated. In the absence of AahII, the S4 helix of VSD4 moves outward to unlatch the intracellular fast inactivation gating machinery, as described before (Clairfeuille et al., 2019).

Another well-known α-scorpion toxin with a similar effect is LqhIII from *Leiurus quinquestriatus hebraeus* (Jiang et al., 2021). It was recently reported that LqhIII anchors on top of VSD4 and traps the gating charges of the S4 segment in a unique intermediate-activated state stabilized by four ion pairs. This conformation weakens the binding of the fast inactivation gate and favors the opening of the activation gate (Jiang et al., 2021).

In order to counteract human envenoming caused by scorpion stings, several toxin-specific antivenoms were developed using different approaches. The standard immunotherapy method consists of using purified polyclonal antibody F (ab′)2 fragments prepared from equine hyperimmune sera (Chippaux and Goyffon, 1998; Bouaziz et al., 2008). However, the use of these antibody fragments of ≈100 kDa is only moderately effective due to their polyclonal nature and may cause dangerous adverse effects such as anaphylactic shocks (Pepin-Covatta et al., 1996).

Another method based on the use of murine monoclonal antibodies was later developed to neutralize the effect of the AahII toxin. This study led to the development of the murine 4C1 antibody (Bahraoui et al., 1988), subsequently used to develop an AahII-specific scFv (single-chain variable fragment) (Mousli et al., 1999). Similarly, other studies have allowed the development of an scFv against the AahI that belongs to a distinct antigenic and structural group of *Androctonus australis Hector* scorpion toxins (Devaux et al., 2001). Some years later, a bispecific scFv construct against both AahI and AahII toxins was obtained by engineering techniques able to protect mice against the whole *Androctonus australis Hector* venom (Juste et al., 2007).

However, all these constructs mentioned above have the major problem of synchronization of kinetic diffusion which is due to the huge difference between the molecular weight of antibodies (MW of approx. 150 kDa), F (ab′)2 (MW of approx. 100 kDa), and their target toxins (MW of approx. 7 kDa). Likewise, the ScFv fragment was not lastingly effective due to a VH–VL unstable complex interaction. Moreover, the neutralizing capacity remains moderate, and their use as a human therapeutic might still generate an undesirable human anti-mouse antibody response (HAMA).

More recently, we have developed an antivenom using another type of toxin binders based on the variable domains of the dromedary heavy-chain antibodies (HCAbs, heavy-chain antibody) naturally lacking light chains and CH1 domains of heavy chains, named VHHs. The specified VHH variable domain encodes an antibody fragment, also named Nb (nanobody), that represents the smallest, intact, natural antigen-binding fragment (Hmila et al., 2008), which has been used to develop an anti-*Androctonus australis Hector* venom that recognizes specifically the AahI′ toxin from Aah scorpion venom. This anti-AahI′ can neutralize 3 LD_{50} when tested *in vivo* using s.c. injection in Swiss mice.

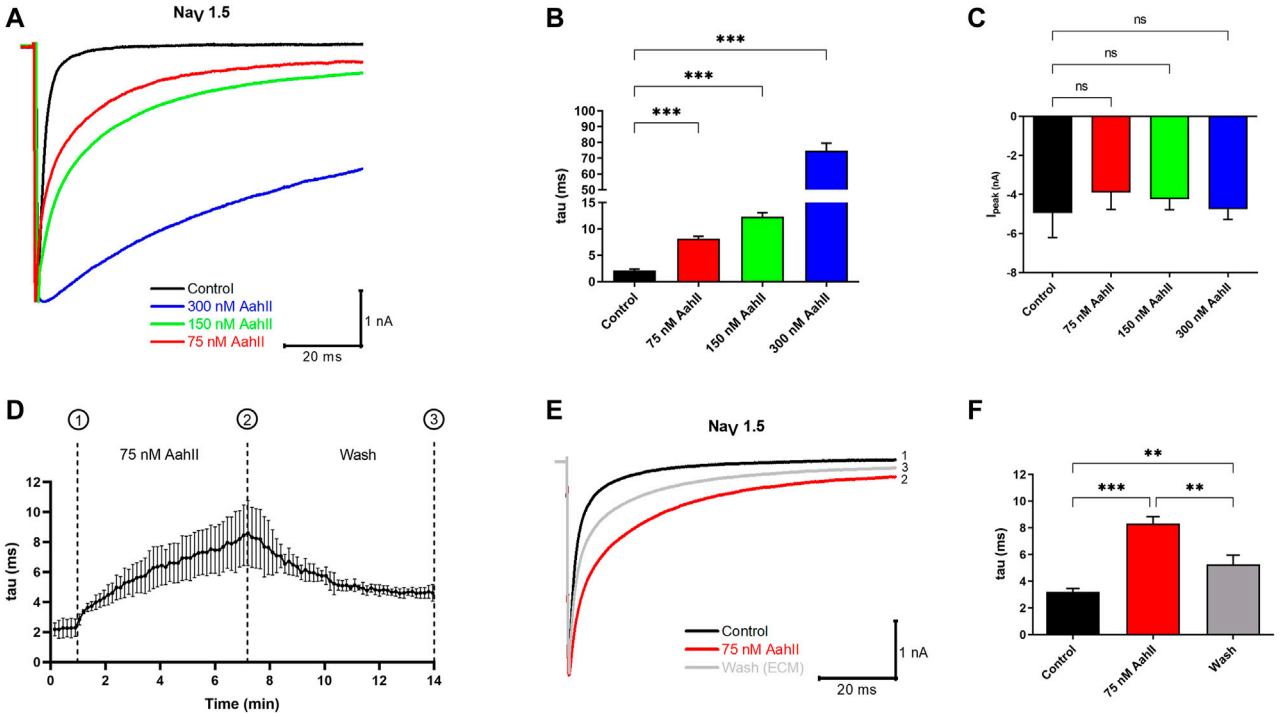

FIGURE 1 | The pharmacological effect of AahII toxin on the Na$_V$1.5 channel overexpressed in HEK293 cells. **(A)** Original whole-cell Na^+ current traces recorded in control condition (control = extracellular medium = ECM) and in the presence of different concentrations of AahII toxin. **(B)** Mean of Na$_V$1.5 inactivation time constant (tau) in the control condition and following application of AahII toxin at different concentrations (75, 150, and 300 nM). Values are the mean of 5 independent experiments, n = 5. All data are presented as mean ± standard error (***$p < 0.001$). **(C)** Mean of current amplitude, Ipeak (nA) measured at −40 mV in the same conditions as in panel **(B)**. Values are representative of independent experiments, $n = 5$. All data are presented as mean ± SE (***$p < 0.001$). **(D)** Mean of the kinetics of inactivation time constant of the Na$_V$1.5 channel (tau) following perfusion of AahII toxin at 75 nM from 1 to 7 min followed by washing with ECM up to 14 min. Traces are representative of independent experiments, $n = 3$. All data are presented as mean ± SE. **(E)** Representative of original whole-cell current traces showing the reversible effect of AahII observed in panel **(D)**. Trace 1: current trace recorded in control medium, Trace 2: current obtained at 7 min represents the maximum effect of AahII toxin at 75 nM, and Trace 3: current trace after washing the AahII toxin during 14 min. Traces are representative of independent experiments, $n = 3$. **(F)** Mean of inactivation time constant of the Na$_V$1.5 channel (tau) following a similar protocol as in panel **(D)**.

Later, by the same approach, an Nb that neutralizes the most toxic compound of Aah venom, AahII toxin, was developed. The so-called Nb10 is an anti-AahII that targets a unique epitope on AahII and neutralizes 7 LD_{50} when tested *in vivo* using Swiss mice (Abderrazek et al., 2009). *In silico* studies demonstrated whether Nb10 binds the active site of AahII toxin (Ksouri et al., 2018).

These two Nbs are characterized by their small size (MW of approx. 15 kDa), good stability, high level of expression in prokaryotic systems, high solubility, and suitable specificity. At the preclinical level, the performance of a bispecific NbF12-10 toxin-specific Nb format (including the anti-AahII Nb10) was demonstrated in an envenoming simulated animal model (Hmila et al., 2010; Hmila et al., 2012).

While Nb10 constitutes the best candidate that neutralizes AahII toxic effects, the precise functional and structural mechanism by which Nb10 neutralizes AahII and interacts with the AahII–Na$_V$ channel complex remains unknown. Here, we studied at the electrophysiological and structural levels the interactions of a purified AahII toxin and Nb10 nanobody with the Na$_V$1.5 channel stably expressed in a HEK cell model. Our data reveal the mode of action and structural basis of AahII and the α-scorpion toxins in general, on the Na$_V$1.5 channel, and proposes Nb10 as a promising antivenom candidate against *Androctonus australis Hector* scorpion stings.

RESULTS

Effect of AahII on Na$_V$1.5 Channel Activity

First, we investigated, by patch-clamp technique, the effect of AahII toxin purified from the venom of *Androctonus australis Hector* scorpion on a cardiac sodium channel Na$_V$1.5 subunit using the human embryonic kidney cell line HEK293 stably transfected with α subunit of Na$_V$1.5 of human origin. The activity of Na$_V$1.5 was recorded by a whole-cell patch clamp. In control conditions, Na currents activate rapidly and inactivate within 2–3 ms. Perfusion of increasing concentrations of AahII progressively slows the inactivation kinetics of the Na$_V$1.5 channel. This inactivation was slower by a factor of 4, 7, and 35 in the presence of [AahII] at 75, 150, and 300 nM, respectively, when compared to the control conditions (**Figures 1A,B**; $n = 5$, ***$p < 0.001$), while current amplitude was not affected (**Figure 1C**; $n = 5$, ***$p < 0.001$). In a second series, we investigated whether the effect of AahII was reversible. After

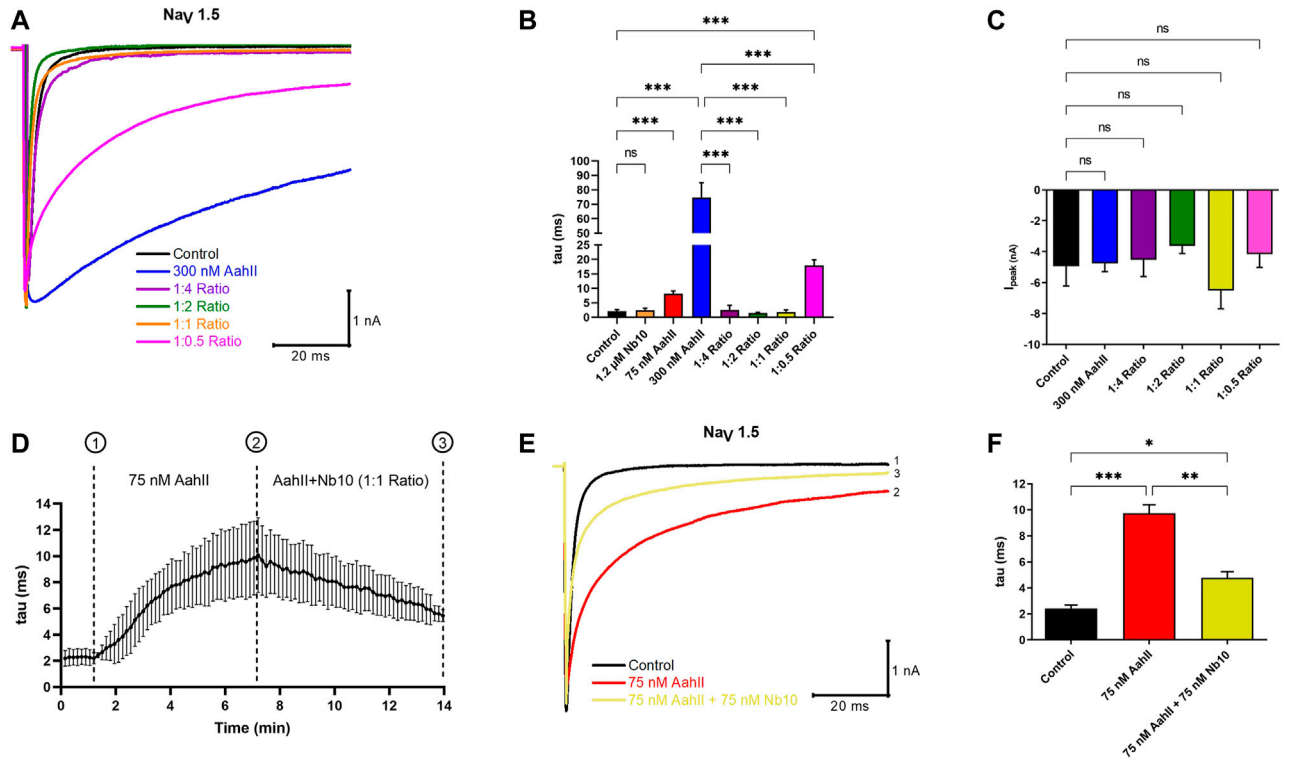

FIGURE 2 | Nb10 interacts with AahII on the Na$_V$1.5 channel. **(A)** Original whole-cell Na^+ current traces recorded at −40 mV in control conditions (Control), in the presence of 300 nM AahII alone, 1.2 µM Nb10 alone, or at different ratios of [AahII]: [Nb10]. 1:4 ratio ([AahII] = 300 nM: [Nb10] = 1.2 µM); 1:2 ratio ([AahII] = 300 nM: [Nb10] = 600 nM), 1:1 ratio ([AahII] = 300 nM: [Nb10] = 300 nM), and 1:0.5 ratio ([AahII] = 300 nM: [Nb10] = 150 nM). **(B)** Mean of Na$_V$1.5 channel inactivation time constant (tau) in control conditions (control), AahII, and Nb10 alone and combined at different ratios. Values are representative of independent experiments, $n = 5$. All data are presented as mean ± SE (***$p < 0.001$). **(C)** Mean of Na^+ current amplitude recorded at -40 mV in the same conditions as in panel **(A)**. Values are representative of independent experiments, $n = 5$. All data are presented as mean ± SE (***$p < 0.001$). **(D)** Mean of kinetics of the inactivation time constant of the Na$_V$1.5 channel (tau) following perfusion of AahII toxin at 75 nM from 1 to 7 min followed by the perfusion of a mixture of AahII and Nb10 at a 1:1 ratio up to 14 min. Traces are representative of independent experiments, $n = 3$. All data are presented as mean ± SE. **(E)** Representative of whole-cell Na^+ current traces recorded at -40 mV in the same conditions as in panel **(D)**, Na^+ current recorded in control conditions (Trace 1), after 7 min of AahII perfusion (Trace 2), and perfusion of AahII and Nb10 at a 1:1 ratio up to 14 min (Trace 3). Traces are representative of independent experiments, $n = 3$. **(F)** Mean of inactivation time constant of the Na$_V$1.5 channel (tau) following a similar protocol as in panel (D). Values are representative of independent experiments, $n = 3$. All data are presented as mean ± SE (***$p < 0.001$).

current stabilization by perfusing the control solution for 1 min, (AahII) at 75 nM was perfused throughout 7 min until the current was stabilized. Then, the cell was washed by control solution perfusion (**Figure 1D**; $n = 3$, ***$p < 0.001$). As expected, AahII slowed the constant time inactivation (tau) from 3.2 ± 0.4 ms in control conditions to 8.3 ± 0.9 ms in AahII treatment conditions at 75 nM (**Figures 1E,F**; $n = 3$, ***$p < 0.001$). The washout partially reversed the toxin effect on inactivation to 5.2 ± 1.2 ms (**Figures 1E,F**; $n = 3$, ***$p < 0.001$), suggesting its extracellular specific binding.

The Nb10 Reverses the AahII Effect on Na$_V$ Inactivation

We investigated whether Nb10 is able to reverse the Na$_V$ slow inactivation kinetic induced by 300 nM of AahII by whole-cell patch clamp experiments using four different AahII:Nb10 M ratios. Interestingly, the 1:4 ([AahII] = 300 nM: [Nb10] = 1.2 µM), 1:2 ([AahII] = 300 nM: [Nb10] = 600 nM), and 1:1 ([AahII] = 300 nM: [Nb10] = 300 nM) ratios are able to neutralize the effect of AahII toxin on slowing the fast inactivation of the Na$_V$1.5 channel and allow to obtain values comparable to the control values (tau = 2 ± 0.6 ms), (**Figures 2A,B**; $n = 5$, ***$p < 0.001$). In contrast, at a lower ratio (1:0.5) ([AahII] = 300 nM: [Nb10] = 150 nM), the toxin–antibody complex reduced the toxin effect on inactivation slowdown (**Figures 2A,B**; $n = 5$, ***$p < 0.001$). It is also worth noting that neither Nb10 alone nor the AahII–Nb10 complexes affect the current amplitude (**Figure 2C**; $n = 5$, ***$p < 0.001$).

In order to investigate whether the perfusion of Nb10 is able to affect the binding of AahII on Na$_V$1.5, we established a protocol to follow the inactivation time constant (tau) through different conditions (**Figure 2D**; $n = 3$, ***$p < 0.001$). After current stabilization by perfusion of the control solution (tau = 2.4 ± 0.4 ms), [AahII] = 75 nM was perfused throughout 7 min until the current stabilization (tau = 9.7 ± 1.2 ms); from 7 min up to 14 min, cells were perfused by a 1:1 AahII–Nb10 ratio at 75 nM (75 nM AahII +75 nM Nb10). The application of Nb10 promotes

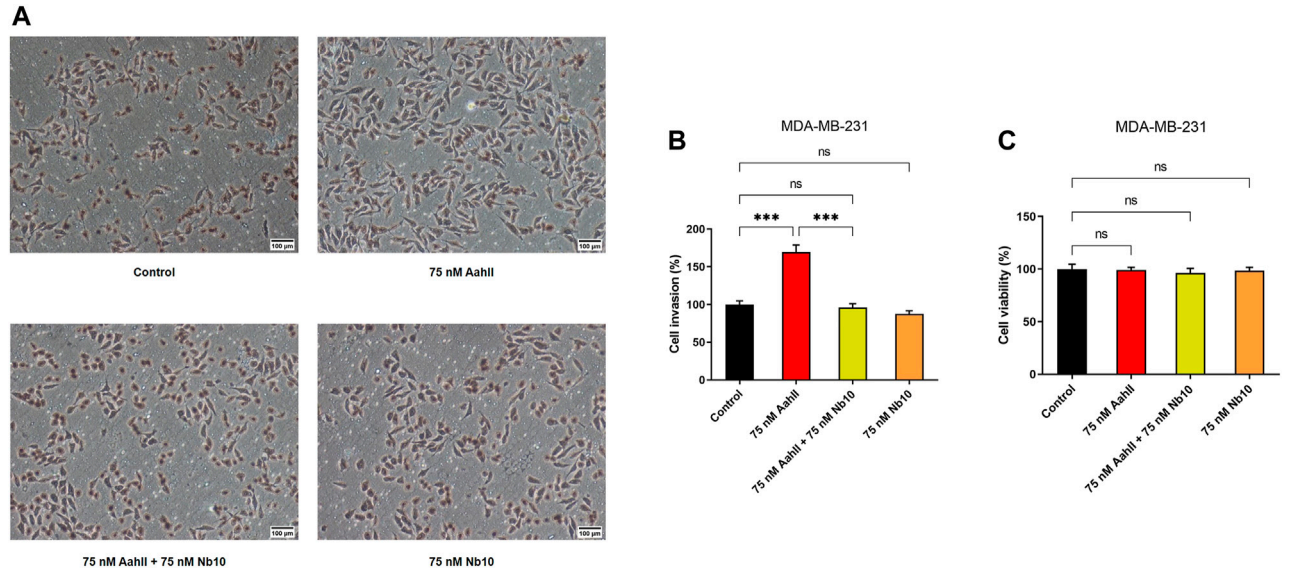

FIGURE 3 | Nb10 can reverse the effect of AahII on MDA-MB-231 cell invasion. **(A)** Microscopic pictures of fields at different conditions. **(B)** Cell invasion was measured after 24 h of incubation in the control condition (control) and in the presence of AahII and Nb10 alone or combined at a 1:1 ratio. Results shown are representative of independent experiments, $n = 3$. All data are presented as mean ± SE (***$p < 0.001$). **(C)** Cell viability was performed in the same condition as **(B)**. Results shown are representative of independent experiments, $n = 3$. All data are presented as mean ± SE (*ns*, $p > 0.05$).

a partial abolishment of AahII action (tau = 4.7 ± 0.8 ms, **Figures 2D–F**; $n = 3$, ***$p < 0.001$).

Similar results are found when we perfused first 75 nM AahII during 7 min (tau = 9.6 ± 0.9 ms), followed by the perfusion of 75 nM Nb10 alone until 14 min (tau = 4.6 ± 0.4) (**Supplemental Figures S2D–F**, $n = 3$, $p < 0.001$).

These results strongly suggest that Nb10 can displace the AahII toxin from its binding site on the $Na_V1.5$ channel.

Nb10 Reverses the Effect of AahII on MDA-MB-231 Cell Invasion of Breast Cancer Cells

We investigated the effect of AahII and Nb10 alone and together on MDA-MB-231 cell invasion in the Boyden chamber. Nb10, alone, at 75 nM was without effect on MDA-MB-231 cell invasion (**Figures 3A,B**). At 75 nM, AahII alone increases cell invasion by 67.16 ± 9% (**Figures 3A,B**; $n = 3$, ***$p < 0.001$). In contrast, AahII failed to affect invasion in the presence of Nb10 at a 1:1 ratio (**Figures 3A,B**; $n = 3$, ***$p < 0.001$). Moreover, both AahII and Nb10 alone and the AahII:Nb10 ratio have no effect on proliferation (**Figure 3C**; $n = 3$, ***$p < 0.001$).

Structural *in-Silico* Simulation of $Na_V1.5$-AahII Toxin Interaction Complex

Molecular simulations were designed based on a benchmarking approach to predict the $Na_V1.5$–AahII complex of interaction. Several molecular docking methods and classes were tested. Both rigid and flexible dockings were performed in blind and driven manners. In total, around 4,500 complexes were generated (data not shown). The best complex orientation was found with the flexible high ambiguity driven protein–protein docking (HADDOCK). The orientation has been established according to extracellular topological domains of the $Na_V1.5$ α-subunit. A total of 150 generated complexes were obtained and grouped into five main clusters. Cluster 1 is the largest with 121 among the 150 complexes containing the best-score docking-oriented complex with a HADDOCK score of -100.9. Data of generated complexes are shown in **Table 1**.

The best complex conformation shows the AahII scorpion toxin oriented to the S3–S4 extracellular loop (1,608–1,620). In general, this part of the $Na_V1.5$ α-subunit is dedicated to α-toxins' interactions. The selected stable orientation is based on the strong molecular interaction manner. First, the 3D complex showed that the Ala39 residue of AahII plays a crucial role to establish a stable bond through H-bound interactions with $Na_V1.5$ α-subunit Gln1615 and Lys1616 residue positions. A second significant interaction involves an H-bound interaction between the AahII Arg62 residue with the Asp1553 of the $Na_V1.5$ α-subunit extracellular topological domain (S1–S2 loops) (**Figure 4**).

DISCUSSION

The pharmacology of scorpion α-toxins is a great gateway to studying the structure and function of ion channels in order to increase our knowledge of their properties. In this report, we studied and characterized the α-scorpion toxin AahII mode of interaction with the $Na_V1.5$ channel and the modulation of the complex interaction by Nb10, a highly neutralizing anti-AahII

TABLE 1 | Molecular docking (Na$_V$1.5–AahII) HADDOCK grouped 150 structures into 5 clusters, representing 94.0% of the water-refined HADDOCK models. The statistics of the top 5 clusters are presented in this table. The top cluster is the most reliable according to the HADDOCK score. The Z-score indicates the number of standard deviations from the mean of this cluster in terms of score (the most negative HADDOCK score is the best).

Top 10	Cluster 1	Cluster 3	Cluster 2	Cluster 6	Cluster 4	Cluster 5
Nr 1 best complexes						
HADDOCK score	−100.9 ± 6.8	−79.0 ± 6.9	−72.7 ± 7.3	−70.7 ± 10.7	−64.0 ± 14.9	−58.5 ± 6.9
Cluster size	121	9	6	4	4	6
RMSD from the overall lowest-energy structure	1.4 ± 0.1	2.5 ± 0.1	2.9 ± 0.2	2.7 ± 0.1	2.2 ± 0.3	1; 8 ± 0.0
Van der Waals energy	−50.8 ± 5.8	−53.1 ± 3.6	−53.4 ± 8.2	−68.7 ± 1.0	−49.2 ± 5.5	−58.6 ± 4.9
Electrostatic energy	−84.6 ± 41.0	−10.6 ± 11.3	−9.1 ± 43.7	−9.0 ± 55.2	−8.1 ± 59.0	−6.4 ± 30.7
Desolvation energy	−34.8 ± 8.0	−28.7 ± 5.7	−25.2 ± 7.6	−10.8 ± 2.9	−24.1 ± 9.4	−17.7 ± 12.2
Restraint violation energy	16.3 ± 14.14	49.3 ± 47.15	59.3 ± 50.53	64.5 ± 33.83	69.9 ± 153.62	70.3 ± 98.97
Buried surface area	1538.6 ± 119.9	1737.9 ± 50.4	1760.9 ± 129.3	2147.0 ± 124.8	1753.7 ± 82.6	2072.7 ± 61.6
Z-score	−2.2	−0.6	−0.5	−0.3	0.1	0.3

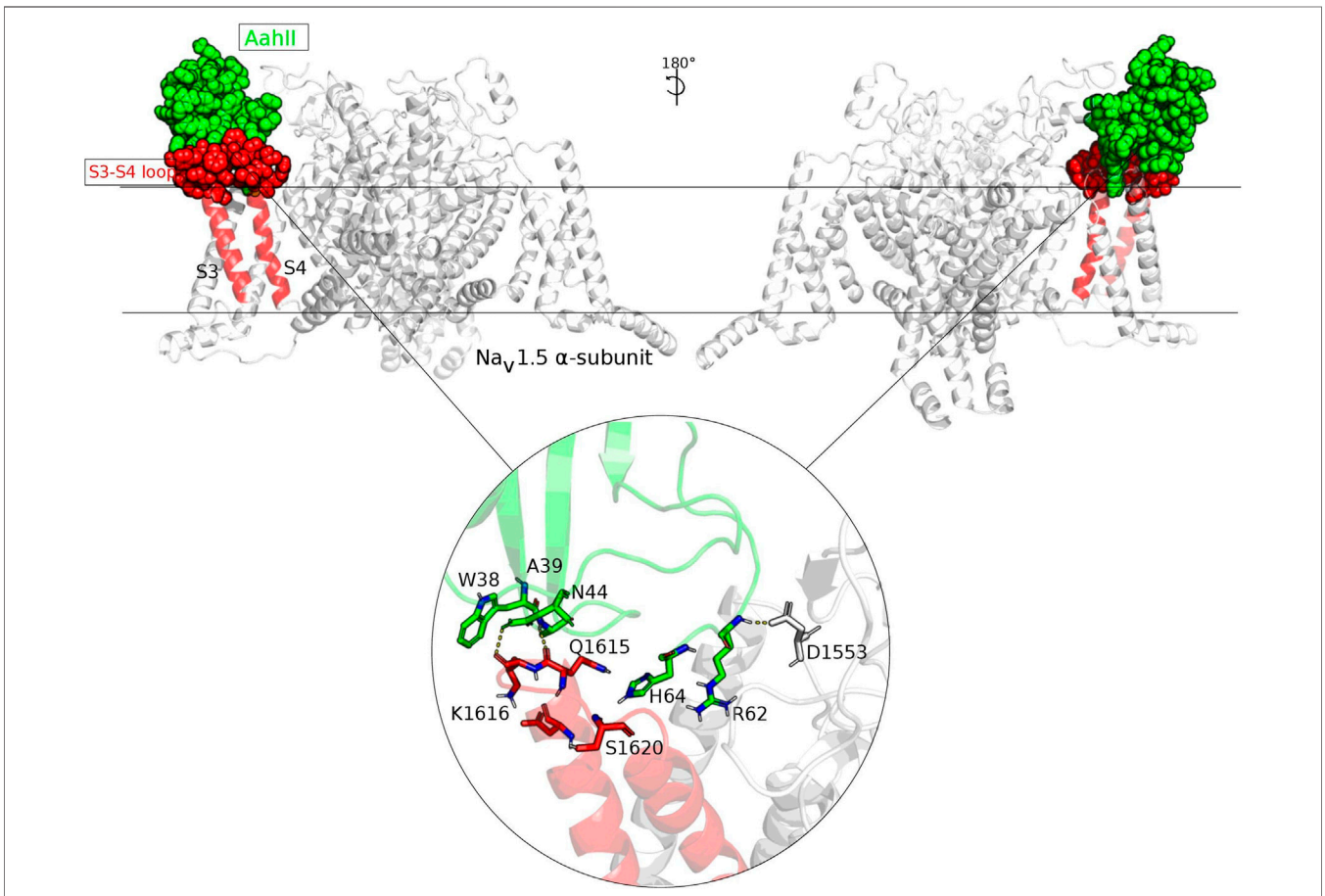

FIGURE 4 | Two faces of the Na$_V$1.5–AahII molecular interaction presentation. The two faces of the Na$_V$1.5–AahII molecular interaction are presented with an orientation of 180°. The subunit involved in the interaction was colored in red and AahII scorpion toxin in green. The extracellular S3–S4 loop part of the subunit interacting with AahII is presented in spheres. This molecular orientation is selected among hundreds of poses according to a very accurate molecular docking approach. The zoomed part illustrated in a circle shows the most crucial residues involved in the complex interaction and maintaining a stable molecular orientation. These residues make H-bounds, as well as hydrophobic and hydrophilic interactions.

nanobody (Abderrazek et al., 2009). For this accomplishment, we used a functional Na$_V$1.5 channel alpha subunit vector of an adult isoform transfected in HEK293.

Significantly, the AahII toxin slows the fast inactivation of the Na$_V$1.5 channel by a factor of 4 at 75 nM while current amplitude was not affected, demonstrating its nanomolar ranging effect.

Our results agree with a recently reported study showing that AahII toxin slows the $Na_V1.7$ fast inactivation mechanism when used at 300 nM (EC_{50} = 51.7 ± 1.5 nM) (Clairfeuille et al., 2019). Their investigations of the cryo-EM-based structural AahII-$Na_V1.7$ channel interaction showed that α-scorpion toxin AahII binds to two different sites on a nonfunctional chimera in both DI and DIV. However, they did not demonstrate whether AahII bound to either of these sites was functionally active in the chimera (Clairfeuille et al., 2019). In this paper and using a wash perfusion protocol to follow the kinetics of Na_V inactivation, we demonstrated that AahII slows the time inactivation of $Na_V1.5$ at a low concentration (75 nM) and that the binding of AahII is extracellular.

In the past, pharmacological studies retained a single neurotoxin receptor (site 3) per Na_V channel located in VSD4 at which related gating modifier toxins, such as scorpion α-toxins and sea anemone toxins, bind (Rogers et al., 1996; Gordon et al., 2007). To address this question, we performed a $Na_V1.5$ site 3 driven docking with AahII and generated 4,500 complexes from which the best orientation showed the involvement of the AahII C-terminal (Arg62 and His64) in the interaction with the DIV-S4 (1,575–1,615 residues) of $Na_V1.5$. Our data are in accordance with a recent similar study that focuses on LqhIII α-toxin from the deathstalker scorpion *Leiurus quinquestriatus hebraeus* and the $Na_V1.5$ channel, showing that LqhIII binds at the extracellular end of the aqueous cleft formed by S1–S2 and S3–S4 helical hairpins in VSD4 through its β2β3 loop and its C-terminal domain (Jiang et al., 2021). Other structure–activity relationship studies show that AahII interacts with Na_V channels through the β2–β3 loop from Gln37 to Pro60 (Clairfeuille et al., 2019) and its C-terminal segment especially involving Arg62 and His64 which are critical for potent modulation of Na_V channels by targeting neurotoxin receptor site 3 (Wang et al., 2003; Benkhadir et al., 2004; Clairfeuille et al., 2019). Indeed, the residues Phe15 and Trp38 and Asn44 from AahII establishing the β2–β3 loop have been described to recognize the VSD4 of the Na_V channels and play an important role in bioactivity of the α-toxin (Kharrat et al., 1989; Gur et al., 2011; Clairfeuille et al., 2019).

It is well admitted that scorpion α-toxins bind to the neurotoxin receptor in a voltage-dependent manner, with a high-affinity binding in the resting state (Clairfeuille et al., 2019; Jiang et al., 2021). Likely, depolarization of the channel reduces toxin affinity and causes its dissociation (Clairfeuille et al., 2019; Jiang et al., 2021). The binding of α-toxins prevents the outward movement of the gating charges of the DIV-S4 segment. In standard conditions, this normal outward movement of the DIV-S4 segment is followed by the unbending of the elbow formed by the DIV S4–S5 loop and the opening of the receptor site for binding of the IFM motif to guarantee the fast inactivation. The binding of AahII α-toxin would counteract this succession of conformational events that lead to fast inactivation.

We have previously demonstrated that Nbs are better tools to interact with toxins and neutralize their effects because of their small size, good stability, high level of expression in a prokaryotic systems, high solubility, and suitable specificity.

Following the development of a highly AahII-specific Nbs, we obtained Nb10 which was the "best-in-class" nanobody able to neutralize the most toxic scorpion α-toxin. This encouraged us to study and characterize the capacity of Nb10 to modulate the interaction of AahII with $Na_V1.5$ using a whole-cell patch clamp. Nb10 was produced in a prokaryotic system and purified from *E. coli* bacterial periplasm that meets the required quality control standards (Abderrazek et al., 2009), which allowed us to have enough purified Nb10 quantity that specifically recognizes and binds AahII. Nb10 is a 14 kDa protein able to neutralize 7 LD_{50} AahII toxicity when injected in mice (association rate constant: $K_{on} = 1.14 \times 10^6\ M^{-1}.S^{-1}$; dissociation rate constants: $K_{off} = 5.69 \times 10^{-4}\ s^{-1}$; equilibrium dissociation constant: K_D = 0.49 nM) (Abderrazek et al., 2009).

By an electrophysiological approach, we demonstrated that Nb10 can fully abolish the AahII effect on fast inactivation of the $Na_V1.5$ channel, with a 1:1 ratio, while current amplitude was not affected. Indeed, perfusion kinetics monitoring of (AahII + Nb10) shows that Nb10 can abolish the AahII-binding action, strongly suggesting that Nb10 shifted or at least altered the AahII-binding site of interaction with VSD4, which releases the DIV-S4 segment to adopt its normal movement and initiates the rapid inactivation of the $Na_V1.5$ channel.

Recent *in silico* 3D modeling of the interaction of AahII with Nb10 revealed the potential contribution of the Trp38 residue from AahII with Met103, Arg108, Tyr105, and Ala111 of Nb10 (Ksouri et al., 2018). Indeed, the segment from Ala39 to Ala45 in AahII has been identified as the main region responsible for antigenic reactivity (Devaux et al., 1993).

The *in-silico* prediction of the AahII–Nav1.5 alpha-subunit interaction showed that AahII binds at the extracellular end of the aqueous cleft formed by the S1–S2 and S3–S4 helical hairpins *via* its loop (from Trp38 to Asn44) and its C-terminal (Arg62 and His64). Our findings are comparable to the Cryo-EM experimentally solved results which revealed the structure of LqhIII bound to $Na_V1.5$ at the 3.3 Å resolution, showing that the LqhIII scorpion toxin anchors on top of VSD4, wedged between the S1–S2 and S3–S4 linkers, and through the β2–β3 loop and the C-terminal of the LqhIII α-Scorpion toxins (Jiang et al., 2021). This confirms that α-Scorpion toxins bind to neurotoxin receptor site 3 in a voltage-dependent manner, with high-affinity binding to the resting state (Catterall 1977; Catterall 1979).

Despite the topological difference of the implicated amino acids in the interaction with the two distinct scorpion toxins (AahII and LqhIII), the positions of the bound toxin with the S1–S2 and S3–S4 helical hairpins are remarkably similar. Therefore, we can trust the structural outputs based on a very accurate computational approach. Herein, 3D modeling of the best AahII-$Na_V1.5$ α-subunit complex showed that AahII Ala39 and Arg62 residues play a crucial role in establishing a stable interaction, through H-bounds, with $Na_V1.5$ Gln1615 and Lys1616 residues.

These results indicated that Nb10 recognizes a similar or identical surface that directly interacts with the DIV-S4 segment of the $Na_V1.5$ channel, involving two major residues at positions 39 and 62 in AahII. Indeed, the C-terminal AahII

His64 and Arg62 are similarly involved in the Nb10–AahII and $Na_V1.5$–AahII interaction complexes and participate in the AahII active site (Ksouri et al., 2018).

Furthermore, to address the need for a highly physiological characterization of the interaction between AahII and Nb10 on cells, we performed invasion assays using MDA-MB-231 cells that express a neonatal isoform of $Na_V1.5$. This $Na_V1.5$ channel is involved in both migration and invasion processes of the MDA-MB-231 triple-negative breast cancer cell line and promotes metastasis (Roger et al., 2003; Kamarulzaman et al., 2017; Zhang et al., 2018; Luo et al., 2020). Interestingly, as expected AahII increases the invasion of MDA-MB-231 cells by 67.16 ± 9%; the equimolar range of Nb10 can completely suppress this effect (1:1 M ratio). Therefore, both AahII and Nb10 may be useful for biomedical models assessing the involvement of Na_V channel subtypes in the invasion process capability of several tumor cell lines as well as drug delivery into tissues.

Altogether, our results suggest that Nb10 perfectly fits both AahII toxin-binding surfaces on the Na_V channel (β2–β3 loop and C-terminal domain) and dynamically blocks AahII–$Na_V1.5$ interactions. The two amino acid positions in AahII are crucial for both interactions with $Na_V1.5$ and Nb10.

MATERIALS AND METHODS

Scorpion Venom Fractionation and AahII Toxin Purification

Androctonus australis Hector crude venom was extracted and purified by gel filtration chromatography according to the well-established protocol (Miranda et al., 1970) with slight optimization (Hmila et al., 2008) **(Supplemental Figure S1A)**. The toxic fraction containing toxins with molecular weight ranging from 3,000 to 7,500 Da named AahG50 was collected and then fractionated by FPLC (GE ÄKTA) on a cation exchange RESOURCE S chromatography column pre-equilibrated with of 0.05 M ammonium acetate buffer solution. Peptides were eluted over 80 min of linear gradient from 0.05 to 0.5 M ammonium acetate, pH 6.6, at a flow rate of 0.8 ml/min. Peptides are detected at an absorbance of 280 nm **(Supplemental Figure S1B)**. The toxic fraction 9 from FPLC was applied to a reverse-phase high-performance liquid chromatography (RT-HPLC) Dionex on a C8 column (Spherisorb 5 μm, L × I.D. 25 cm × 4.6 mm). The main peptides were eluted from the column at the rate of 0.8 ml/min using a three-step gradient. The initial mobile phase is 100% A [0.1% trifluoroacetic acid (TFA, Sigma-Aldrich, St. Louis, MO, USA) in water] and 0% B [0.1% TFA in acetonitrile (Sigma-Aldrich)]. The percentage of mobile phase B increases all over the three steps, from 0% to 20% over 4 min, beginning at 0 min; from 20% to 40% over 40 min, beginning at 4 min; and from 40% to 100% over 5 min, beginning at 44 min. Elution was performed at a flow rate of 0.8 ml/min. Absorbance was monitored at 280 nm **(Supplemental Figure S1C)**. The concentration of purified proteins was quantified by the QuantiPro BCA Assay Kit.

Nb10 Expression and Purification

The recombinant vector displaying the VHH gene transcript encoding Nb10, subcloned into the pHEN6 expression vector using the restriction enzymes NcoI or PstI and BstEII, was used to transform non-suppressive and competitive *WK6 E. coli* electrocompetent cells that met the required quality control standards. The expression of Nb10 was performed as previously described (Abderrazek et al., 2009). The obtained periplasmic extract containing His-tagged proteins was incubated with nickel-Sepharose beads (Sigma-Aldrich) for 1 h at 4°C under gentle agitation. The mixture was then poured into a PD-10 column (Cytiva, Marlborough, MA, USA) and allowed to drain by gravity. The HIS-Select adsorbent was washed with 20 column volumes of PBS 1× and allowed to drain by gravity. The washing step ends when the OD280 nm of the last droplet of the eluate approaches 0. Elution of the Ni-ion-bound protein fraction was done by adding 5 ml of concentrated PBS/imidazole at 500 mM. The purity of the eluted protein was checked by SDS-polyacrylamide gel electrophoresis and visualized using Coomassie brilliant blue. The protein of interest has a molecular weight of about 14 kDa **(Supplemental Figure 1D)**. The final yield was determined from the UV absorption at 280 nm and the theoretical extinction coefficient of Nb10.

Cell Cultures

HEK293 and MDA-MB-231 cells were cultured in Eagle's Minimal Essential Medium (EMEM; Life Technologies, Saint Aubin, France) supplemented with 20 mM HEPES, 2 mM Glutamine (Life Technologies, Saint Aubin, France), and 5% fetal bovine serum (FBS, Life Technologies, Saint Aubin, France). The medium is changed every 48 h. Cells are kept in the incubator at 5% CO_2 and 37°C and weekly trypsinized using trypsin-EDTA. The absence of *mycoplasma* is checked twice a month.

Patch Clamp Experiments

HEK293 cells stably expressing $Na_V1.5$ were generously gifted by Prof. Hugues Abriel (Institute of Biochemistry and Molecular Medicine, University of Bern, Switzerland). Cells were cultured in 35-mm Petri dishes at a density of 1×10^4 cells at least 2 days before patch-clamp experiments. Before recording, cells were washed with the saline solution used as an extracellular medium for control conditions. Whole-cell patch-clamp recordings were obtained using a patch-clamp amplifier (Axon Axopatch 200B, Molecular Devices, Sunnyvale, CA, USA). The recording pipette intracellular solution contained the following (in mM): 8 Na-gluconate, 145 Cs-methane sulfonate, 10 EGTA, and 10 HEPES (pH 7.2 adjusted with NaOH, osmolarity 326 mOsm). The extracellular recording solution contained the following (in mM): 150 Na-gluconate, 5 K-gluconate, 2 Mg-gluconate, 2 Ca-gluconate, 10 HEPES, and 5 glucose (pH 7.4 adjusted with NaOH, osmolarity 337 mOsm). All electrophysiological experiments were performed at room temperature. The whole-cell recording of the patch-clamp technique was used with no coated pipettes (Hirschmann®, Laborgerate, Eberstadt, Germany) with resistance between 3 and 5 MΩ. Seal resistance was typically more than 1 GΩ

before the break of the membrane to access the whole-cell configuration. Perfusion of different concentrations of AahII and Nb10 was performed using a perfusion system with a flow rate of 5 ml/min. Currents were recorded at the frequency of 0.2 Hz. Signals were filtered at 1 kHz and digitized at 5 kHz. Cells were voltage-clamped at −140 mV, and Na^+ currents were recorded following membrane depolarization from −140 to −40 mV for 200 ms every 5 s. Cell capacitances were not compensated. Data were analyzed using Clampfit 10.7 (Molecular Devices, Inc., San Jose, CA, USA), then plotted in OriginPro 2018 (Software, Inc., USA).

The inactivation time constant (tau) value is calculated directly using a single exponential function fitting on Clampfit 10.7 (Molecular Devices, Inc., San Jose, CA, United States)

Cell Invasion Assays

Cell invasion experiments were performed by Boyden chamber with Matrigel assay. The upper compartment that contains 0% FBS-treated medium was seeded with 4×10^4 cells. The lower compartment contains a 5% FBS-treated medium to promote chemotaxis. After 24 h of incubation at 37°C, inserts were washed with PBS (Sigma-Aldrich, Darmstadt Germany), fixed 10 min by methanol (Sigma-Aldrich, Darmstadt Germany), and colored 5 min with hematoxylin (Sigma-Aldrich, Darmstadt Germany). Two supplementary washes with water are performed to eliminate the rest of hematoxylin. The remaining cells on the upper side were removed from the membrane by rubbing. Invasive cells in the lower compartment are then counted on 20 fields at ×20 magnification with an inverted microscope (Zeiss, Cambridge, England). For each experiment, the number of invasive cells per area for each condition was normalized by the mean of invasive cells in the control condition. Experiments are done in duplicate for each condition.

Cell Viability Assays

Cell viability was performed by MTT assay as previously described (Lefebvre et al., 2020). Cells were seeded in 6-well plates in double of density as invasion assays at the rate of 8×10^4 cells per well. After 24 h of incubation, the medium is replaced by 800 µl of MTT (tetrazolium salts of 3-(4,5-dimethyl-2-thiazolyl)-2,5-diphenyl-2H-tetrazolium bromide, Sigma-Aldrich, Darmstadt Germany) solubilized in culture medium without FBS at 0.5 mg/ml in each well. Plates were then incubated for 50 min at 37°C in obscurity. To dissolve purple formazan crystals formed by living cells, the culture medium was replaced with DMSO (dimethyl sulfoxide, Sigma-Aldrich, Darmstadt Germany). Absorbance of each well was quantified at 550 nm using an Infinite® 200 Pro Reader (Tecan Trading AG, Männedorf, Switzerland).

Statistical Data Analysis

Data are presented as mean ± SEM, and *n* refers to the number of individual cells. All the experiments were performed in at least 3 different cell passages. Data analysis and figure conception were made using GraphPad Prism 9.0 (GraphPad Software, Inc., La Jolla, CA, USA), Origin 2018 (Microcal Software, Inc., Los Angeles, CA, USA), and Clampfit 10.7 (Molecular Devices, Inc., USA). The mean values of more than two groups were tested using a two-way analysis of variance (ANOVA) followed by Holm–Sidak *post hoc* tests. Differences between the values were considered significant when $p < 0.05$. The *p*-values < 0.05, <0.01, and <0.001 are represented as *, **, and ***, respectively.

Structural *in Silico* Simulation of $Na_V1.5$-AahII Interaction

The 3D structure of $Na_V1.5$ at 3.2–3.5 Å resolution was extracted from the protein data bank (PDB ID: 6UZ3). The corresponding $Na_V1.5$ channel structure enables at a functional level to generate cardiac action potentials and initiates the heartbeat. The $Na_V1.5$ subunit α is described from 1 to 1,838 in the linear amino acid sequence. This structure was extracted, cleaned, then relaxed using several parsing PDB files, bioinformatics tools, and python scripts. The 3D crystal structure of toxin II from the scorpion *Androctonus australis Hector* refined at 1.3 Å resolution was extracted from the protein data bank (PDB ID: 1PTX). The flexible computational docking simulation was performed between AahII as a blinded driven molecule and $Na_V1.5$ structures *via* its α-toxin-specific binding region of the DIV voltage sensor. The HADDOCK (high ambiguity driven protein–protein docking) was used as the driven flexible docking tool for modeling biomolecular complexes.

Restraint data to drive the docking as active residues were implicated without excluding surrounding surface residues or passive residues around the active residues, to avoid bias molecular interaction output information.

Linux command lines were used to generate molecular complexes. Clustering of molecular complexes based on a specific HADDOCK score allows the best understanding of interaction molecular behaviors; therefore, the best-oriented complex can be well selected based on several molecular docking features as the main component of the HADDOCK score, such as interface-RMSD calculated on the backbone (I-RMSD), ligand-RMSD calculated on the backbone atoms (l-RMSD), and fraction of common contacts (FFC).

The selected molecular complex was analyzed, and residues with crucial interactions were highlighted through an amino acid sequence contact map with a threshold of 5 Å.

Generated complex structures and interactions were then visualized *via* the molecular visualization software PyMOL (Schrödinger et al., 2020).

DATA AVAILABILITY STATEMENT

The original contributions presented in the study are included in the article/**Supplementary Material**; further inquiries can be directed to the corresponding authors.

AUTHOR CONTRIBUTIONS

RH did the experiments (Scorpion venom fractionation and AahII toxin purification, NbAahII10 expression and purification, cell culture, treatments, cell viability, and invasion assays, patch-clamp experiments) and wrote the original draft,

AK did the structural *in silico* simulations, RB contributed to the NbAahII10 production and purification, VA and PS contributed to the crude venom analyses and AahII toxin purification MG, BB-Z, and HO-A designed the study and supervised the work. BB-Z revised the manuscript. All authors have read and agreed to the published version of the manuscript.

FUNDING

This work was supported in part by the University of Picardie Jules Verne and the University of Tunis El Manar and in part by the VenoMATIcs IPIN project, Tunisia.

ACKNOWLEDGMENTS

The authors thank Professor Hechmi Louzir, General Director of Pasteur Institute, for constant encouragement. The authors would like to thank Thouraya Chagour and Marie-Sophie Telliez for their technical assistance.

SUPPLEMENTARY MATERIAL

The Supplementary Material for this article can be found online at: https://www.frontiersin.org/articles/10.3389/fphar.2022.821181/full#supplementary-material

REFERENCES

Abderrazek, R. B., Hmila, I., Vincke, C., Benlasfar, Z., Pellis, M., Dabbek, H., et al. (2009). Identification of Potent Nanobodies to Neutralize the Most Poisonous Polypeptide from Scorpion Venom. *Biochem. J.* 424 (424), 263–272. doi:10.1042/BJ20090697

Ahern, C. A., Payandeh, J., Bosmans, F., and Chanda, B. (2016). The Hitchhiker's Guide to the Voltage-Gated Sodium Channel Galaxy. *J. Gen. Physiol.* 147, 1–24. doi:10.1085/jgp.201511492

Armstrong, C. M., Bezanilla, F., and Rojas, E. (1973). Destruction of Sodium Conductance Inactivation in Squid Axons Perfused with Pronase. *J. Gen. Physiol.* 62, 375–391. doi:10.1085/jgp.62.4.375

Bahraoui, E., Pichon, J., Muller, J. M., Darbon, H., Elayeb, M., Granier, C., et al. (1988). Monoclonal Antibodies to Scorpion Toxins. Characterization and Molecular Mechanisms of Neutralization. *J. Immunol.* 1141, 214–220.

Benkhadir, K., Kharrat, R., Cestèle, S., Mosbah, A., Rochat, H., El Ayeb, M., et al. (2004). Molecular Cloning and Functional Expression of the Alpha-Scorpion Toxin BotIII: Pivotal Role of the C-Terminal Region for its Interaction with Voltage-dependent Sodium Channels. *Peptides* 25, 151–161. doi:10.1016/j.peptides.2004.01.009

Bosmans, F., and Tytgat, J. (2007). Voltage-gated Sodium Channel Modulation by Scorpion Alpha-Toxins. *Toxicon* 49, 142–158. doi:10.1016/j.toxicon.2006.09.023

Bouaziz, M., Bahloul, M., Kallel, H., Samet, M., Ksibi, H., Dammak, H., et al. (2008). Epidemiological, Clinical Characteristics and Outcome of Severe Scorpion Envenomation in South Tunisia: Multivariate Analysis of 951 Cases. *Toxicon* 52, 918–926. doi:10.1016/j.toxicon.2008.09.004

Catterall, W. A. (1979). Binding of Scorpion Toxin to Receptor Sites Associated with Sodium Channels in Frog Muscle. Correlation of Voltage-dependent Binding with Activation. *J. Gen. Physiol.* 74, 375–391. doi:10.1085/jgp.74.3.375

Catterall, W. A., Cestèle, S., Yarov-Yarovoy, V., Yu, F. H., Konoki, K., and Scheuer, T. (2007). Voltage-gated Ion Channels and Gating Modifier Toxins. *Toxicon* 49, 124–141. doi:10.1016/j.toxicon.2006.09.022

Catterall, W. A., Goldin, A. L., and Waxman, S. G. (2005). International Union of Pharmacology. XLVII. Nomenclature and Structure-Function Relationships of Voltage-Gated Sodium Channels. *Pharmacol. Rev.* 57, 397–409. doi:10.1124/pr.57.4.4

Catterall, W. A. (1977). Membrane Potential-dependent Binding of Scorpion Toxin to the Action Potential Na+ Ionophore. Studies with a Toxin Derivative Prepared by Lactoperoxidase-Catalyzed Iodination. *J. Biol. Chem.* 252, 8660–8668. doi:10.1016/s0021-9258(19)75272-7

Catterall, W. A. (2014). Structure and Function of Voltage-Gated Sodium Channels at Atomic Resolution. *Exp. Physiol.* 99, 35–51. doi:10.1113/expphysiol.2013.071969

Catterall, W. A., Wisedchaisri, G., and Zheng, N. (2017). The Chemical Basis for Electrical Signaling. *Nat. Chem. Biol.* 13 (13), 455–463. doi:10.1038/nchembio.2353

Chanda, B., and Bezanilla, F. (2002). Tracking Voltage-dependent Conformational Changes in Skeletal Muscle Sodium Channel during Activation. *J. Gen. Physiol.* 120, 629–645. doi:10.1085/jgp.20028679

Chippaux, J. P., and Goyffon, M. (1998). Venoms, Antivenoms and Immunotherapy. *Toxicon* 36, 823–846. doi:10.1016/s0041-0101(97)00160-8

Clairfeuille, T., Cloake, A., Infield, D. T., Llongueras, J. P., Arthur, C. P., Li, Z. R., et al. (2019). Structural Basis of α-scorpion Toxin Action on Nav Channels. *Science* 363, 363. doi:10.1126/science.aav8573

Devaux, C., Jouirou, B., Naceur Krifi, M., Clot-Faybesse, O., El Ayeb, M., and Rochat, H. (2004). Quantitative Variability in the Biodistribution and in Toxinokinetic Studies of the Three Main Alpha Toxins from the Androctonus Australis hector Scorpion Venom. *Toxicon* 43, 661–669. doi:10.1016/j.toxicon.2004.02.021

Devaux, C., Juin, M., Mansuelle, P., and Granier, C. (1993). Fine Molecular Analysis of the Antigenicity of the Androctonus Australis hector Scorpion Neurotoxin II: a New Antigenic Epitope Disclosed by the Pepscan Method. *Mol. Immunol.* 30, 1061–1068. doi:10.1016/0161-5890(93)90152-2

Devaux, C., Moreau, E., Goyffon, M., Rochat, H., and Billiald, P. (2001). Construction and Functional Evaluation of a Single-Chain Antibody Fragment that Neutralizes Toxin AahI from the Venom of the Scorpion Androctonus Australis hector. *Eur. J. Biochem.* 268, 694–702. doi:10.1046/j.1432-1327.2001.01923.x

Goldin, A. L., Barchi, R. L., Caldwell, J. H., Hofmann, F., Howe, J. R., Hunter, J. C., et al. (2000). Nomenclature of Voltage-Gated Sodium Channels. *Neuron* 28, 365–368. doi:10.1016/s0896-6273(00)00116-1

Goldin, A. L. (2003). Mechanisms of Sodium Channel Inactivation. *Curr. Opin. Neurobiol.* 13, 284–290. doi:10.1016/s0959-4388(03)00065-5

Gordon, D., Karbat, I., Ilan, N., Cohen, L., Kahn, R., Gilles, N., et al. (2007). The Differential Preference of Scorpion Alpha-Toxins for Insect or Mammalian Sodium Channels: Implications for Improved Insect Control. *Toxicon* 49 (49), 452–472. doi:10.1016/j.toxicon.2006.11.016

Gur, M., Kahn, R., Karbat, I., Regev, N., Wang, J., Catterall, W. A., et al. (2011). Elucidation of the Molecular Basis of Selective Recognition Uncovers the Interaction Site for the Core Domain of Scorpion Alpha-Toxins on Sodium Channels. *J. Biol. Chem.* 286, 28635209–28635217. doi:10.1074/jbc.M111.259507

Hanck, D. A., and Sheets, M. F. (2007). Site-3 Toxins and Cardiac Sodium Channels. *Toxicon* 49, 181–193. doi:10.1016/j.toxicon.2006.09.017

Hmila, I., Abdallah R, B. A., Saerens, D., Benlasfar, Z., Conrath, K., Ayeb, M. E., et al. (2008). VHH, Bivalent Domains and Chimeric Heavy Chain-Only Antibodies with High Neutralizing Efficacy for Scorpion Toxin AahI'. *Mol. Immunol.* 45, 3847–3856. doi:10.1016/j.molimm.2008.04.011

Hmila, I., Cosyns, B., Tounsi, H., Roosens, B., Caveliers, V., Abderrazek, R. B., et al. (2012). Pre-clinical Studies of Toxin-specific Nanobodies: Evidence of *In Vivo* Efficacy to Prevent Fatal Disturbances Provoked by Scorpion Envenoming. *Toxicol. Appl. Pharmacol.* 264, 222–231. doi:10.1016/j.taap.2012.07.033

Hmila, I., Saerens, D., Ben Abderrazek, R., Vincke, C., Abidi, N., Benlasfar, Z., et al. (2010). A Bispecific Nanobody to Provide Full protection against Lethal Scorpion Envenoming. *FASEB J.* 24, 3479–3489. doi:10.1096/fj.09-148213

Housset, D., Habersetzer-Rochat, C., Astier, J. P., and Fontecilla-Camps, J. C. (1994). Crystal Structure of Toxin II from the Scorpion Androctonus Australis Hector Refined at 1.3 A Resolution. *J. Mol. Biol.* 238, 23888–24103. doi:10.1006/jmbi.1994.1270

Jiang, D., Tonggu, L., Gamal El-Din, T. M., Banh, R., Pomes, R., Zheng, N., et al. (2021). Structural Basis for Voltage-Sensor Trapping of the Cardiac Sodium Channel by a Deathstalker Scorpion Toxin. *Nat. Commun.* 4, 12128. doi:10.1038/s41467-020-20078-3

Juste, M., Martin-Eauclaire, M. F., Devaux, C., Billiald, P., and Aubrey, N. (2007). Using a Recombinant Bispecific Antibody to Block Na+ -channel Toxins Protects against Experimental Scorpion Envenoming. *Cell Mol Life Sci* 64, 206–218. doi:10.1007/s00018-006-6401-3

Kamarulzaman, N. S., Dewadas, H. D., Leow, C. Y., Yaacob, N. S., and Mokhtar, N. F. (2017). The Role of REST and HDAC2 in Epigenetic Dysregulation of Nav1.5 and nNav1.5 Expression in Breast Cancer. *Cancer Cel Int* 17, 74. doi:10.1186/s12935-017-0442-6

Kharrat, R., Darbon, H., Rochat, H., and Granier, C. (1989). Structure/activity Relationships of Scorpion Alpha-Toxins. Multiple Residues Contribute to the Interaction with Receptors. *Eur. J. Biochem.* 181, 181381–181390. doi:10.1111/j.1432-1033.1989.tb14735.x

Ksouri, A., Ghedira, K., Ben Abderrazek, R., Shankar, B. A. G., Benkahla, A., Bishop, O. T., et al. (2018). Homology Modeling and Docking of AahII-Nanobody Complexes Reveal the Epitope Binding Site on AahII Scorpion Toxin. *Biochem. Biophys. Res. Commun.* 496 (496), 1025–1032. doi:10.1016/j.bbrc.2018.01.036

Luo, Q., Wu, T., Wu, W., Chen, G., Luo, X., Jiang, L., et al. (2020). The Functional Role of Voltage-Gated Sodium Channel Nav1.5 in Metastatic Breast Cancer. *Front. Pharmacol.* 11, 1111. doi:10.3389/fphar.2020.01111

Martin, M. F., Rochat, H., Marchot, P., and Bougis, P. E. (1987). Use of High Performance Liquid Chromatography to Demonstrate Quantitative Variation in Components of Venom from the Scorpion Androctonus Australis Hector. *Toxicon* 25, 569–573. doi:10.1016/0041-0101(87)90293-5

Miranda, F., Kupeyan, C., Rochat, H., Rochat, C., and Lissitzky, S. (1970). Purification of Animal Neurotoxins. Isolation and Characterization of Eleven Neurotoxins from the Venoms of the Scorpions Androctonus Australis hector, Buthus Occitanus Tunetanus and Leiurus Quinquestriatus Quinquestriatus. *Eur. J. Biochem.* 16, 514–523. doi:10.1111/j.1432-1033.1970.tb01111.x

Mousli, M., Devaux, C., Rochat, H., Goyffon, M., and Billiald, P. (1999). A Recombinant Single-Chain Antibody Fragment that Neutralizes Toxin II from the Venom of the Scorpion Androctonus Australis hector. *FEBS Lett.* 442, 442183–442188. doi:10.1016/s0014-5793(98)01647-0

Pépin-Covatta, S., Lutsch, C., Grandgeorge, M., Lang, J., and Scherrmann, J. M. (1996). Immunoreactivity and Pharmacokinetics of Horse Anti-scorpion Venom F(ab')2-scorpion Venom Interactions. *Toxicol. Appl. Pharmacol.* 141, 272–277. doi:10.1006/taap.1996.0284

Ren, D., Navarro, B., Xu, H., Yue, L., Shi, Q., and Clapham, D. E. (2001). A Prokaryotic Voltage-Gated Sodium Channel. *Science* 294, 2372–2375. doi:10.1126/science.1065635

Roger, S., Besson, P., and Le Guennec, J. Y. (2003). Involvement of a Novel Fast Inward Sodium Current in the Invasion Capacity of a Breast Cancer Cell Line. *Biochim. Biophys. Acta* 1616, 1616107–1616111. doi:10.1016/j.bbamem.2003.07.001

Rogers, J. C., Qu, Y., Tanada, T. N., Scheuer, T., and Catterall, W. A. (1996). Molecular Determinants of High Affinity Binding of Alpha-Scorpion Toxin and Sea Anemone Toxin in the S3-S4 Extracellular Loop in Domain IV of the Na+ Channel Alpha Subunit. *J. Biol. Chem.* 271, 27115950–27115962. doi:10.1074/jbc.271.27.15950

Schrödinger, L., and DeLano, W. J. T. P. M. G. S. (2020). Pymol.2. Version

Ulbricht, W. (2005). Sodium Channel Inactivation: Molecular Determinants and Modulation. *Physiol. Rev.* 85, 1271–1301. doi:10.1152/physrev.00024.2004

Wang, C. G., Gilles, N., Hamon, A., Le Gall, F., Stankiewicz, M., Pelhate, M., et al. (2003). Exploration of the Functional Site of a Scorpion Alpha-like Toxin by Site-Directed Mutagenesis. *Biochemistry* 42 (42), 4699–4708. doi:10.1021/bi0270438

Zhang, B., Deng, Z., Zeng, B., Yang, S., Chen, X., Xu, X., et al. (2018). *In-vitro* Effects of the FS50 Protein from Salivary Glands of Xenopsylla Cheopis on Voltage-Gated Sodium Channel Activity and Motility of MDA-MB-231 Human Breast Cancer Cells. *Anticancer Drugs* 29, 880–889. doi:10.1097/CAD.0000000000000662

Conflict of Interest: The authors declare that the research was conducted in the absence of any commercial or financial relationships that could be construed as a potential conflict of interest.

Publisher's Note: All claims expressed in this article are solely those of the authors and do not necessarily represent those of their affiliated organizations, or those of the publisher, the editors, and the reviewers. Any product that may be evaluated in this article, or claim that may be made by its manufacturer, is not guaranteed or endorsed by the publisher.

frontiers in Pharmacology

ORIGINAL RESEARCH
published: 07 March 2022
doi: 10.3389/fphar.2022.815069

Isolation and Pharmacological Characterization of α-Elapitoxin-Oh3a, a Long-Chain Post-Synaptic Neurotoxin From King Cobra (*Ophiophagus hannah*) Venom

Tam M. Huynh[1], *Anjana Silva*[1,2], *Geoffrey K. Isbister*[1,3] *and Wayne C. Hodgson*[1]*

[1]Monash Venom Group, Department of Pharmacology, Biomedical Discovery Institute, Monash University, Clayton, VIC, Australia, [2]Department of Parasitology, Faculty of Medicine and Allied Sciences, Rajarata University of Sri Lanka, Anuradhapura, Sri Lanka, [3]Clinical Toxicology Research Group, University of Newcastle, Newcastle, NSW, Australia

The King Cobra (*Ophiophagus hannah*) is the world's largest venomous snake and has a widespread geographical distribution throughout Southeast Asia. Despite proteomic studies indicating the presence of postsynaptic neurotoxins in *O. hannah* venom, there are few pharmacological investigations of these toxins. We isolated and characterized α-elapitoxin-Oh3a (α-EPTX-Oh3a; 7,938 Da), a long-chain postsynaptic neurotoxin, which constitutes 5% of *O. hannah* venom. α-EPTX-Oh3a (100–300 nM) caused concentration-dependent inhibition of indirect twitches and inhibited contractile responses of tissues to exogenous acetylcholine and carbachol, in the chick biventer cervicis nerve-muscle preparation. The prior incubation of tissues with Thai Red Cross Society King Cobra antivenom (1 ml/0.8 mg) prevented the *in vitro* neurotoxic effects of α-EPTX-Oh3a (100 nM). The addition of Thai Red Cross Society King Cobra antivenom (1 ml/0.8 mg), at the t_{90} time point partially reversed the *in vitro* neurotoxicity of α-EPTX-Oh3a (100 nM). Repeatedly washing the tissue did not allow significant recovery from the *in vitro* neurotoxic effects of α-EPTX-Oh3a (100 nM). α-EPTX-Oh3a demonstrated pseudo-irreversible antagonism of concentration-response curves to carbachol, with a pA_2 of 8.99. *De novo* sequencing of α-EPTX-Oh3a showed a long-chain postsynaptic neurotoxin with 72 amino acids, sharing 100% sequence identity with Long neurotoxin OH-55. In conclusion, the antivenom is useful for reversing the clinically important long-chain α-neurotoxin-mediated neuromuscular paralysis.

Keywords: ***Ophiophagus hannah*, snake, antivenom, neuromuscular paralysis, neurotoxin**

OPEN ACCESS

Edited by:
Yuri N. Utkin,
Institute of Bioorganic Chemistry (RAS), Russia

Reviewed by:
Christian Legros,
Université d'Angers, France
Fernanda C. Cardoso,
The University of Queensland, Australia

***Correspondence:**
Wayne C. Hodgson
wayne.hodgson@monash.edu

Specialty section:
This article was submitted to Pharmacology of Ion Channels and Channelopathies, a section of the journal Frontiers in Pharmacology

Received: *15 November 2021*
Accepted: *31 January 2022*
Published: *07 March 2022*

Citation:
Huynh TM, Silva A, Isbister GK and Hodgson WC (2022) Isolation and Pharmacological Characterization of α-Elapitoxin-Oh3a, a Long-Chain Post-Synaptic Neurotoxin From King Cobra (Ophiophagus hannah) Venom. Front. Pharmacol. 13:815069. doi: 10.3389/fphar.2022.815069

INTRODUCTION

The King Cobra (*Ophiophagus hannah*) is widely distributed in Southeast Asia, some parts of the Indian subcontinent and Southern China (O'Shea, 2008). Despite typically avoiding human habitat, *O. hannah* is considered to be a medically important species since, as the world's largest venomous snake, it is able to inject a large amount of venom in a single bite (Gowtham et al., 2012). Envenoming by *O. hannah* causes life-threatening neuromuscular paralysis and is usually treated by

administration of monovalent Thai Red Cross Society King Cobra antivenom (Tin et al., 1991; Tun et al., 1995).

Few pharmacological studies have investigated the mechanism of action of *O. hannah* venom, and isolated neurotoxins, at the skeletal neuromuscular junction. Snake venom neurotoxins are generally classified by their target site at the neuromuscular junction (i.e., post-synaptic or pre-synaptic). Proteomic studies of the venom of *O. hannah* have indicated a large relative abundance of "postsynaptic" neurotoxins (Petras et al., 2015; Tan et al., 2015), which inhibit neurotransmission by acting as antagonists at the skeletal nicotinic acetylcholine receptor (nAChR) (Barber et al., 2013). Postsynaptic neurotoxins are further classified as short-chain or long-chain neurotoxins, and their structural and functional differences have been previously described in detail (Barber et al., 2013; Utkin, 2019). Recent research has shown that long-chain α-neurotoxins are more clinically important in human envenoming, compared to short-chain α-neurotoxins, due to their higher potency and poor reversibility on the human nAChR (Silva et al., 2018).

Although several α-neurotoxins have been previously isolated from *O. hannah* venom to study their protein structure (Lin et al., 1995a; Lin et al., 1995b; Chang et al., 1995; Lin et al., 1997; Chang et al., 2000; Roy et al., 2010), there is a need for pharmacological studies to characterize the main neurotoxins that potentially contribute to human neuromuscular paralysis. This study aimed to isolate the main neurotoxins from *O. hannah* venom and identify the mode of action, as well as determine the *in vitro* efficacy of Thai Red Cross Society King Cobra antivenom in neutralizing them.

MATERIALS AND METHODS

Venoms and Antivenoms

Freeze-dried *O. hannah* venom from Indonesia was a gift from Venom Supplies Tanunda (South Australia). Thai Red Cross Society King Cobra antivenom was purchased from Thai Red Cross Society (Bangkok, Thailand; Batch No: LH00118, expiry date: 13/02/2023). According to the manufacturer's instructions, 1 ml of the antivenom neutralizes 0.8 mg of *O. hannah* venom. The amount of antivenom required for neutralizing the *in vitro* neurotoxicity of the isolated toxin was calculated based on the relative abundance of the toxin in the whole venom.

Chemicals and Reagents

The following chemicals and drugs were used: acetylcholine chloride (Sigma-Aldrich, St. Louis, MO, United States), acetic acid sodium salt (sodium acetate, Merck, Darmstadt, Germany), acetonitrile (ACN, Merck, Darmstadt, Germany), ammonium bicarbonate (Sigma-Aldrich, St. Louis, MO, United States), carbamylcholine chloride (carbachol; Sigma-Aldrich, St. Louis, MO, United States), dithiothretiol (Merck, Darmstadt, Germany), formic acid (Sigma-Aldrich, St. Louis, MO, United States), iodoacetamide (GE Healthcare, Uppsala, Sweden), LCMS grade acetonitrile (Fisher Scientific, Loughborough, United Kingdom), potassium chloride (KCl, Ajax Finechem Pty. Ltd., Taren Point, Australia), proteomics grade bovine trypsin (Sigma-Aldrich, St. Louis, MO, United States), trifluoroacetic acid (TFA, Auspep, Melbourne, Australia), d-tubocurarine (Sigma-Aldrich, St. Louis, MO, United States) and trifluroethanol (Sigma-Aldrich, St. Louis, MO, United States). Unless otherwise indicated, all chemicals were dissolved or diluted in milli-Q water.

Isolation and Purification of Toxin

Chromatography was performed using a high-performance liquid chromatography (HPLC) system (Shimadzu, Kyoto, Japan).

Reverse-Phase HPLC

Freeze-dried *O. hannah* venom (2 mg) was reconstituted in 500 µl milli-Q water (Millipore Corporation, Billerica, MA, United States) and centrifuged at 12,000 rpm for 10 min before being loaded into a Phenomenex Jupiter semi-preparative C18 column (5 µm, 250 mm × 10 mm; Phenomenex, Torrance, CA, United States) equilibrated with solvent A (0.1% TFA) at a flow rate of 2 ml/min. The fractions were then eluted using a gradient of solvent B (90% ACN in 0.09% TFA); 0–25% over 10 min, 25%–80% between 10 and 60 min and 80–0% between 60 and 65 min. The eluent was monitored at 214 nm. Fractions were collected manually according to the peaks in the chromatogram and freeze-dried immediately, then later screened using the chick biventer cervicis nerve-muscle preparation to identify those with neurotoxicity.

Ion-Exchange Chromatography

Freeze-dried, single run sample of the peak eluting at 19 min from reverse-phase HPLC was reconstituted in 500 µl of buffer A (5 mM sodium acetate; pH 5.1) and loaded into a Mono S strong cation exchange column (8 µm, 8 mm × 75 mm; Showa Denko; Japan). The column was equilibrated with buffer A at a flow rate of 0.5 ml/min. The fractions were eluted using the following gradient of buffer B (5 mM sodium acetate and 0.5 M sodium chloride; pH 5.1): 0% over 10 min, 0–60% between 10 and 70 min and 60–0% between 70 and 75 min. The eluent was monitored at 280 nm. Toxin 1C was collected manually at 52 min and then subsequently freeze-dried to be ready for further analysis.

Mass Spectrometry and Amino Acid Sequencing

Intact Protein Analysis With Matrix Associated Laser Desorption Time of Flight (MALDI-TOF) Mass Spectrometry

Venom fractions were analysed by LC-MS using a quadrupole TOF mass spectrometer (MicroTOFq, Bruker Daltonics, Bremen, Germany) coupled online with a 1,200 series capillary HPLC (Agilent Technologies, Santa Clara, CA, United States). Samples were injected onto a MabPac SEC-1 5um 300A 50 × 4 mm (Thermo Scientific) column with 50% acetonitrile 0.05% TFA, 0.05% FA at a flow rate of 50 µl/min. The protein was eluted over a 20 min run-time monitored by UV detection at 254 nm. The eluant was nebulised and ionised using the Bruker electrospray

source with a capillary voltage of 4500 V dry gas at 180°C, a flow rate of 4 l/min and nebuliser gas pressure at 300 mbar. After 20 min, the flow path was switched to infuse Low concentration Tune mix (Agilent Technologies, Santa Clara, CA, United States) to calibrate the spectrum post-acquisition. The spectra were extracted and deconvoluted using Data explorer software version 3.4 build 192 (Bruker Daltonics, Bremen, Germany).

Electrospray-Ionisation Coupled With Mass-Spectrometry/Mass Spectrometry (ESI-LCMS/MS)

The sample (2.5–5 μg) was buffer exchanged into 50 mM ammonium bicarbonate and reduced in 2.5 mM DTT at 60°C for 5 min followed by alkylation with 10 mM chloroacetamide for 30 min at room temperature. The enzyme was then added at the rate of 0.5 μg per 10 μg of protein and incubated at 37°C overnight. For chymotrypsin digests 50 mM Tris buffer was used in place of ammonium bicarbonate.

All enzyme digests were analysed by LC-MS/MS using the QExactive mass spectrometer (Thermo Scientific, Bremen, Germany) coupled online with a RSLC nano HPLC (Ultimate 3,000, Thermo Scientific, Bremen, Germany). Sample (200 ng) was injected and concentrated on a 100 μm, 2 cm nanoviper pepmap100 trap column with 97.5% buffer A (0.1% TFA) at a flow rate of 15 μl/min. The peptides then eluted and separated with a Thermo RSLC pepmap100, 75 μm × 50 cm, 100 Å pore size, reversed phase nano column with a 30 min gradient of 92.5% buffer A (0.1% formic acid) to 42.5% B (80% ACN 0.1% formic acid), at a flow rate of 250 nl/min. The eluant was nebulised and ionised using the Thermo nano electrospray source with a distal coated fused silica emitter (New Objective, Woburn, MA, United States) with a capillary voltage of 1900 V. Peptides were selected for MSMS analysis in Full MS/dd-MS2 (TopN) mode with the following parameter settings: TopN 10, resolution 70,000, MSMS AGC target 5e5, 118 ms Max IT, NCE 27, 1.8 m/z isolation window, dynamic exclusion was set to 10 s.

De Novo Protein Sequencing

Data from the LCMS/MS acquisitions was analysed using Peaks AB Ver. 2.0 (Bioinformatics Solutions Inc., Ont, Canada), to derive a *de novo* protein sequence. The following search parameters were used: missed cleavages, 2; peptide mass tolerance, ± 10 ppm; peptide fragment tolerance, ± 0.05 Da; fixed modifications, carbamidomethyl (Cys); Variable modification, oxidation (Met).

Sequences were validated using Byonic (ProteinMetrics) V 3.1–19 and a precursor and fragment mass tolerance of 20 ppm. Modifications specified were Carbamidomethyl @C fixed and Oxidation @M Variable common 1. The protein output was set to 1% FDR.

Chick Biventer Cervicis Nerve-Muscle Preparation

Male chickens (aged 4–10 days) were killed by exsanguination following CO_2 inhalation. Biventer cervicis nerve-muscle preparations were dissected and then mounted on wire tissue holders under 1 g resting tension in 5 ml organ baths. Tissues were maintained at 34°C, bubbled with 95% O_2 and 5% CO_2, in physiological salt solution of the following composition (mM): 118.4 NaCl, 4.7 KCl, 1.2 $MgSO_4$, 1.2 KH_2PO_4, 2.5 $CaCl_2$, 25 $NaHCO_3$ and 11.1 glucose. Indirect twitches were evoked by stimulating the motor nerve (0.1 Hz; 0.2 ms) at supramaximal voltage (10–20 V), using a Grass S88 stimulator (Grass Instruments, Quincy, MA). Selective stimulation of the nerve was confirmed by the abolishment of twitches by the addition of d-tubocurarine (10 μM). Tissues were then repeatedly washed with physiological salt solution to restore twitch response to nerve stimulation. Contractile responses of the tissues to exogenous acetylcholine (ACh; 1 mM for 30 s), carbachol (CCh; 20 μM for 60 s) and KCl (40 mM for 30 s) were obtained in the absence of nerve stimulation. Nerve stimulation was then recommenced for at least 30 min before the addition of the toxin or antivenom.

To examine the ability of antivenom to neutralise α-elapitoxin-Oh3a (i.e., prevention study), tissues were equilibrated with antivenom for 10 min before the toxin was added. To determine the ability of antivenom to reverse α-elapitoxin-Oh3a induced neurotoxicity (i.e., reversal study), antivenom was added at t_{90} (i.e., time at which the initial twitch height was inhibited by 90%). To examine the reversible nature of the binding of α-elapitoxin-Oh3a to skeletal nAChR, organ baths were repeatedly washed for a period of 10 s every 5 min until any recovery of twitch responses had plateaued.

At the conclusion of each experiment, ACh, CCh and KCl were re-added as above. Twitch responses and responses to exogenous agonists were measured *via* a Grass FT03 force displacement transducer and recorded on a PowerLab system (ADInstruments Pty Ltd., Australia).

Cumulative Concentration-Response Curves to Carbachol

In order to determine the potency (i.e., pA_2 value) of α-elapitoxin-Oh3a, cumulative concentration–response curves to CCh (0.6–80 μM) were obtained by adding increasing concentrations of the agonist to unstimulated chick preparations without washing the preparation between each addition. After the maximum response was achieved, the tissue was repeatedly washed and allowed to recover for 30 min. Then α-elapitoxin-Oh3a (1–30 nM) or vehicle (milli-Q water) was allowed to equilibrate with the tissue for 60 min before the cumulative concentration–response curve to CCh was repeated in the presence of toxin or vehicle.

Data Analysis

The quantity of α-elapitoxin-Oh3a in the whole venom was determined by measuring the area under the curve of the reverse-phase HPLC and ion-exchange chromatograms with the single peak representing α-elapitoxin-Oh3a being expressed as a percentage of the total area under the curve of whole venom.

Nerve-mediated twitch responses and responses to ACh (30 s), CCh (60 s) and KCl (30 s) were measured via a Grass FT03 force

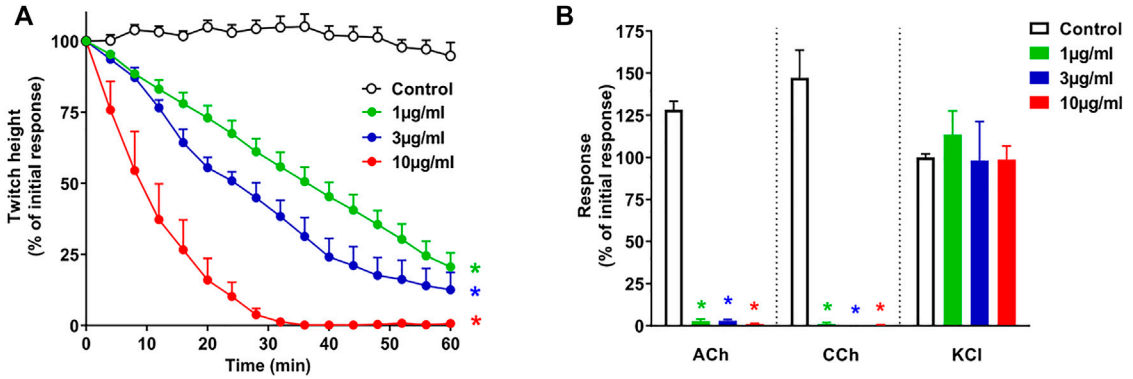

FIGURE 1 | Concentration-dependent *in vitro* neurotoxicity of *O. hannah* venom (1–10 µg/ml) on **(A)** indirect twitches and **(B)** responses to exogenous agonists ACh (1 mM), CCh (20 µM) and KCl (40 mM) in the chick biventer cervicis nerve-muscle preparation. *$p < 0.05$, significantly different from **(A)** control at 60 min (one-way ANOVA; $n = 4$) or **(B)** pre-toxin response to same agonist (paired *t*-test, $n = 4$).

displacement transducer and recorded on PowerLab system (ADInstruments Pty Ltd., Australia). Post-venom/toxin responses were expressed as a percentage of their initial responses. An unpaired *t*-test or one-way analysis of variance (ANOVA) was used to compare the effect on twitch height of different pre-treatments. Comparison of responses to exogenous agonists before and after pre-treatment was made using a Student's paired *t*-test. In order to determine the antagonist potency (i.e., pA_2) of α-elapitoxin-Oh3a, the shifts in the cumulative concentration-response curves to CCh, in the absence or presence of α-elapitoxin-Oh3a, were analysed using the modified Lew Angus method. All ANOVAs were followed by a Bonferroni's multiple comparison post-hoc test. Data presented are in the form of mean ± standard error of the mean (SEM) of n experiments. All data and statistical analyses were performed using PRISM 9.2.0 (GraphPad Software, San Diego, CA, United States, 2016). For all statistical tests, $p < 0.05$ was considered statistically significant.

RESULTS

In Vitro Neurotoxicity of the Whole Venom

O. hannah venom (1–10 µg/ml) caused concentration-dependent inhibition of indirect twitches in the chick biventer cervicis nerve-muscle preparation ($n = 4$; $p < 0.05$, one-way ANOVA; **Figure 1A**). All concentrations of the venom also abolished contractile responses of tissues to exogenous ACh and CCh ($n = 4$; $p < 0.05$, paired *t*-test; **Figure 1B**), but not KCl. The reduction of responses to ACh and CCh, without affecting the responses to KCl, indicates a postsynaptic mode of action.

Fractionation of Venom *via* Reverse-phase HPLC and Ion-Exchange Chromatography

α-Elapitoxin-Oh3a was isolated from *O. hannah* venom using reverse-phase HPLC followed by ion-exchange chromatography. Fractionation of whole venom by reverse-phase HPLC on a Jupiter C18 semi-preparative column yielded several major and minor peaks (**Figure 2A**). Initial screening of all fractions from reverse-phase HPLC, in the chick biventer nerve-muscle preparation, showed that peak 1, peak 2, peak 3 and peak 4, which eluted at 19, 20, 22 and 23 min, respectively, displayed postsynaptic neurotoxicity. Peak 1 was further purified using ion-exchange chromatography on a Mono S strong cation exchange column, producing several additional fractions (**Figure 2B**). Initial screening of these fractions, in the chick biventer nerve-muscle preparation, showed that peak 1C, which eluted at 52 min, displayed postsynaptic neurotoxicity. Fraction 1C, subsequently named α-elapitoxin-Oh3a, was subjected to further purification using ion-exchange chromatography, resulting in a clean peak (**Figure 2C**). α-Elapitoxin-Oh3a is estimated to constitute approximately 5% of the whole venom protein content. The neurotoxins within peak 2, peak 3 and peak 4 could not be further purified using the current chromatographic methods.

Intact Protein Analysis With MALDI-TOF Mass Spectrometry

Intact protein analysis of α-elapitoxin-Oh3a using MALDI-TOF showed a single mass with a molecular weight of 7,938.4 Da (**Figure 3**).

De Novo Protein Sequencing and Protein Identification

Enzyme digest using ESI-LCMS/MS generated the following full amino acid sequence of α-elapitoxin-Oh3a (72 amino acids) which was validated using Byonic (ProteinMetrics) V 3.1–19.

TKCYVTPDVKSETCPAGQDICY TETWCDAWCTSRGKRVNLGCAATCPIVKPGV EIKCCSTDNCNPFPTRKRP

α-Elapitoxin-Oh3a showed 100% sequence identity with Long neurotoxin OH-55 (UniProtKB–Q53B58) and was assigned the name "α-elapitoxin-Oh3a" based on the rational nomenclature

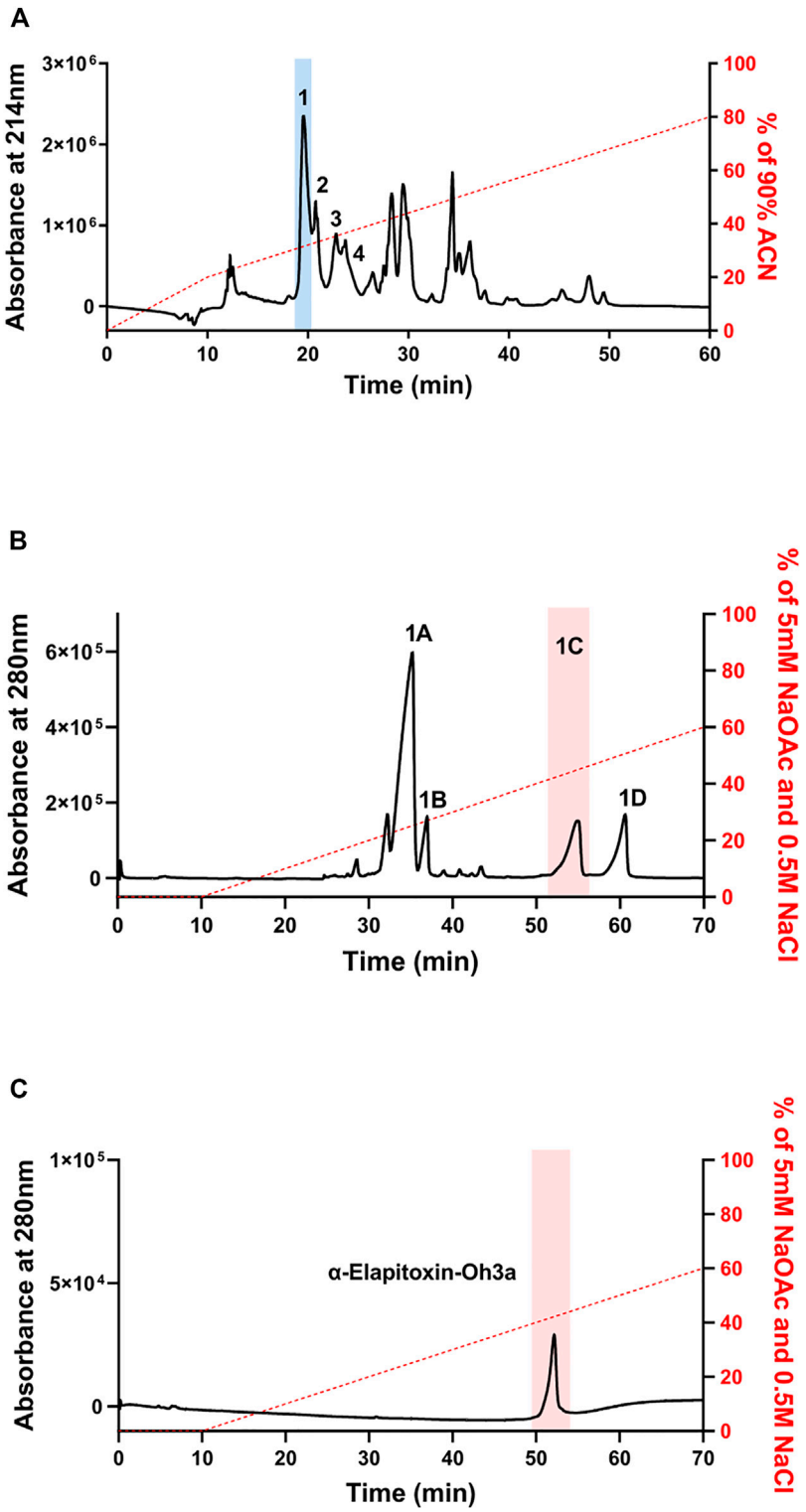

FIGURE 2 | Chromatograms of *O. hannah* venom showing the fractionation steps to purify α-Elapitoxin-Oh3a. **(A)** *O. hannah* venom by reverse-phase HPLC on a Jupiter C18 semi-preparative column; **(B)** fractionation of peak 1 by ion-exchange chromatography on a Mono S strong cation exchange column; **(C)** further purification of peak 1C by ion-exchange chromatography on a Mono S strong cation exchange column.

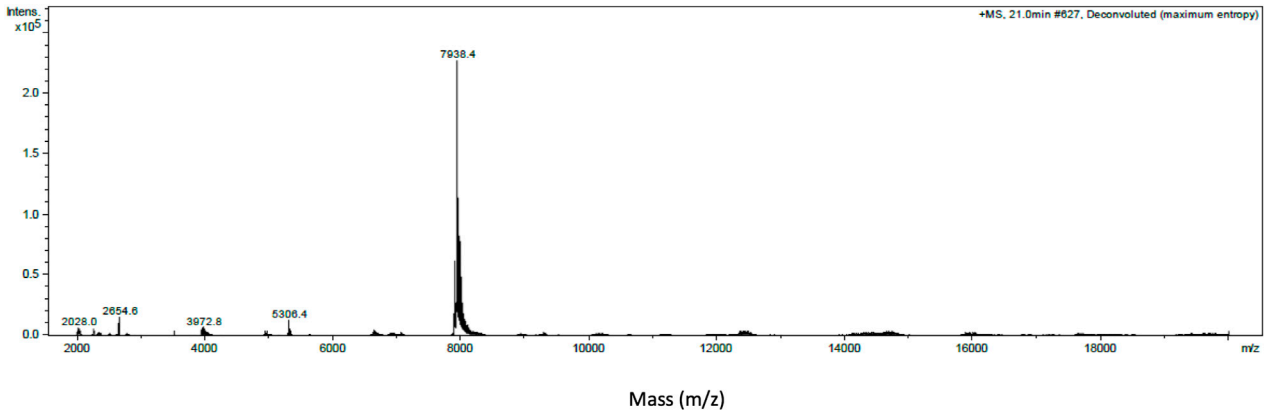

FIGURE 3 | Intact protein MALDI-TOF chromatogram of α-Elapitoxin-Oh3a indicating an intact mass of 7,938.4 Da.

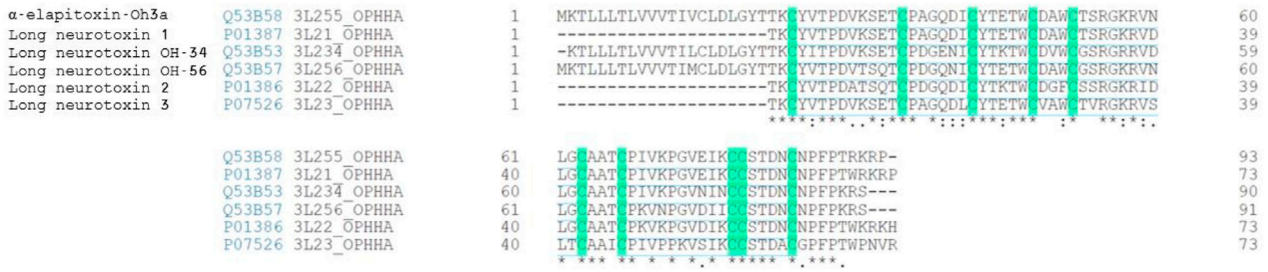

FIGURE 4 | Sequence alignment (from BLAST search) of α-Elapitoxin-Oh3a with long-chain alpha neurotoxins from *O. hannah* venom. Highlighted amino acids are the 10 cysteine residues present in identical positions of all long-chain alpha neurotoxins that make the five disulfide bonds. Amino acids with (*) are fully conserved in all toxins, conserved amino acids with (.) are weakly similar properties group and amino acids with (:) are strongly similar properties group.

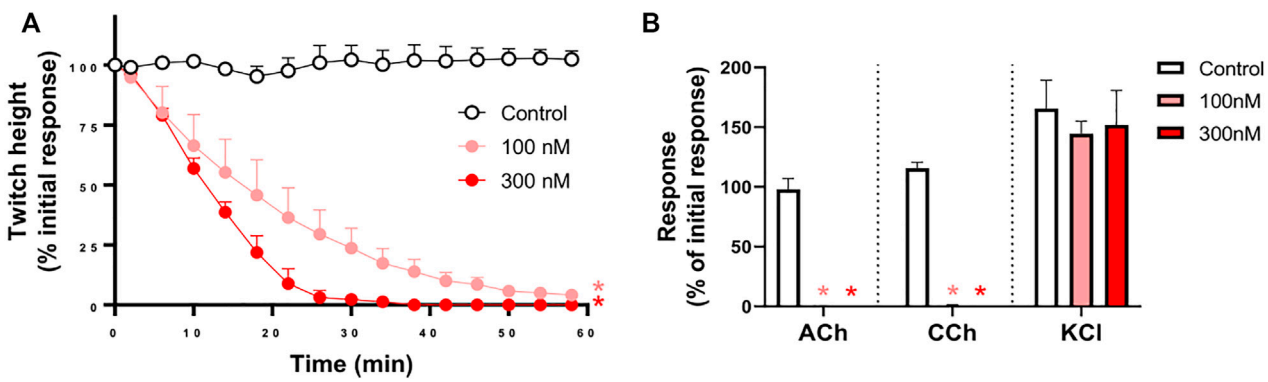

FIGURE 5 | The concentration-dependent *in vitro* neurotoxic effects of α-elapitoxin-Oh3a (100–300 nm) on **(A)** indirect twitches and **(B)** responses to exogenous agonists ACh (1 mM), CCh (20 μM) and KCl (40 mM) in the chick biventer cervicis nerve-muscle preparation. *$p < 0.05$, significantly different from **(A)** control at 60 min (one-way ANOVA; $n = 4$) or **(B)** pre-toxin response to same agonist (paired *t*-test, $n = 4$).

for naming peptide toxins from spiders and other venomous animals suggested by King et al. (2008). α-Elapitoxin-Oh3a showed more than 80% sequence homology with the long-chain α-neurotoxins, long neurotoxin 1, long neurotoxin 2, long neurotoxin 3, long neurotoxin OH-34, long neurotoxin OH-56 isolated from the venom of *O. hannah* (**Figure 4**).

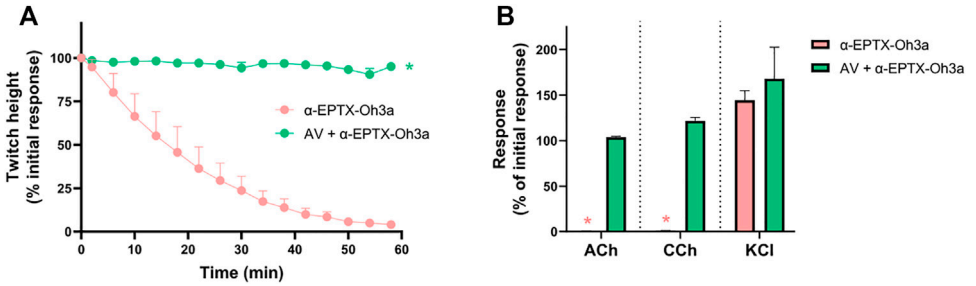

FIGURE 6 | The effect of α-elapitoxin-Oh3a (100 nM) in the absence and presence of Thai Red Cross Society King Cobra antivenom (AV; at the recommended concentration; 1 ml/0.8 mg) on **(A)** indirect twitches and **(B)** responses to exogenous agonists ACh (1 mM), CCh (20 μM) and KCl (40 mM) in the chick biventer cervicis nerve-muscle preparation. *$p < 0.05$, significantly different from **(A)** α-elapitoxin-Oh3a alone at 60 min (unpaired *t*-test; $n = 4$) or **(B)** pre-toxin response to same agonist (paired *t*-test, $n = 4$).

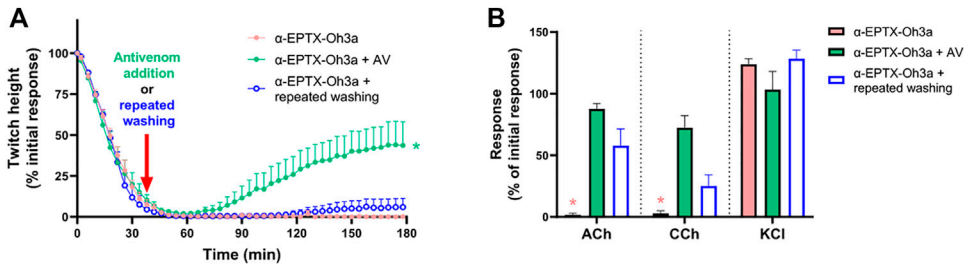

FIGURE 7 | The effect of α-elapitoxin-Oh3a (100 nM) in the absence and presence of Thai Red Cross Society King Cobra antivenom (AV; at the recommended concentration; 1 ml/0.8 mg) or repeated washing of the tissue at the t_{90} time point on **(A)** indirect twitches and **(B)** responses to exogenous agonists ACh (1 mM), CCh (20 μM) and KCl (40 mM) in the chick biventer cervicis nerve-muscle preparation. *$p < 0.05$, significantly different from **(A)** α-elapitoxin-Oh3a alone at 180 min (one-way ANOVA; $n = 4$) or **(B)** pre-toxin response to same agonist (paired *t*-test, $n = 4$).

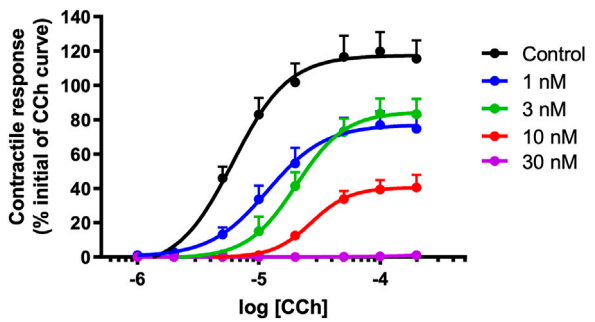

FIGURE 8 | Concentration-dependent effects of α-elapitoxin-Oh3a (1–30 nM; $n = 5$) on cumulative concentration-response curves to carbachol (CCh) in the unstimulated chick biventer cervicis nerve-muscle preparation.

In Vitro Neurotoxicity of α-Elapitoxin-Oh3a

Concentration-Dependent Inhibition of Twitches and Exogenous Agonists Responses

α-Elapitoxin-Oh3a (100–300 nM) caused concentration-dependent inhibition of indirect twitches in the chick biventer cervicis nerve-muscle preparation ($n = 4$; $p < 0.05$, one-way ANOVA; **Figure 5A**). Both concentrations of the toxin inhibited responses of tissues to exogenous ACh and CCh ($n = 4$; $p < 0.05$, paired *t*-test; **Figure 5B**), but not KCl. The reduction of responses to ACh and CCh, without affecting the responses to KCl, indicates a postsynaptic mode of action.

In Vitro Neurotoxicity Antivenom Prevention Study

The prior incubation of tissues with Thai Red Cross Society King Cobra antivenom (1 ml/0.8 mg) prevented the inhibition of indirect twitches by α-elapitoxin-Oh3a (100 nM; $n = 4$; $p < 0.05$, unpaired *t*-test; **Figure 6A**) and prevented the reduction of contractile responses to ACh and CCh ($n = 4$; $p < 0.05$, paired *t*-test; **Figure 6B**).

In Vitro Neurotoxicity Antivenom Reversal and Washing Study

The addition of Thai Red Cross Society King Cobra antivenom (1 ml/0.8 mg), at the t_{90} time point following the effect of α-elapitoxin-Oh3a (100 nM), partially restored the twitch responses to 42.0 ± 14.3% ($n = 4$; $p < 0.05$, one-way ANOVA; **Figure 7A**) of the pre-toxin twitch height by the 180 min time point. The toxin-induced reduction of responses to ACh and CCh was also significantly prevented by the delayed addition of antivenom ($n = 4$; $p < 0.05$, paired *t*-test; **Figure 7B**).

Repeatedly washing the tissue for 10 s every 5 min, commencing at the t_{90} time point following addition of α-elapitoxin-Oh3a (100 nM), only caused a slight recovery of the twitch responses to 6.4 ± 5.6% ($n = 4$; **Figure 7A**). Repeated

washing also partially reversed the inhibition of responses to ACh and CCh ($n = 4$; $p < 0.05$, paired *t*-test; **Figure 7B**).

Carbachol Cumulative Concentration-Response Curves

α-Elapitoxin-Oh3a (1–30 nM) caused a concentration-dependent non-parallel shift of the cumulative concentration-response curve to CCh, with a concentration-dependent reduction of the maximum response in unstimulated chick biventer cervicis nerve-muscle preparations (**Figure 8**). This indicates that α-elapitoxin-Oh3a is pseudo-irreversible antagonist at the skeletal nAChR. Using the modified Lew and Angus method, the pA_2 value of α-elapitoxin-Oh3a was calculated to be 8.99 (95% c.l.: 8.00–9.90).

DISCUSSION

In this study, we examined the *in vitro* neurotoxicity of *O. hannah* venom, and isolated and characterized a long-chain postsynaptic α-neurotoxin, α-elapitoxin-Oh3a. The *in vitro* neurotoxicity of α-elapitoxin-Oh3a was neutralized, and partially reversed, by Thai Red Cross Society King Cobra antivenom. Administration of antivenom provided more recovery than repeated washing of the tissue. α-Elapitoxin-Oh3a also demonstrated irreversible or "pseudo-irreversible" antagonism at avian skeletal nAChR.

O. hannah venom demonstrated postsynaptic neurotoxicity in the indirectly stimulated chick biventer nerve-muscle preparation as indicated by the concentration-dependent inhibition of indirect twitches and reduction in contractile responses to external nicotinic agonists. This observation is consistent with proteomic reports suggesting a large abundance of postsynaptic neurotoxins in the venom (Petras et al., 2015; Tan et al., 2015).

α-Elapitoxin-Oh3a was isolated using reverse-phase HPLC and ion-exchange chromatography, and shown to constitute approximately 5% of *O. hannah* venom. With a molecular mass of 7,938.4 Da, and consisting of 72 amino acids, α-elapitoxin-Oh3a exhibits traits consistent with those of long-chain postsynaptic neurotoxins (Barber et al., 2013). Further, α-elapitoxin-Oh3a was calculated to have a pA_2 value of 8.99, indicating a high potency in terms of its antagonist activity at the nAChR. For comparison, the pA_2 of α-bungarotoxin, a potent long-chain α-neurotoxin, determined using the same methodology as the current study, was calculated to be 8.71 (Wickramaratna et al., 2004). Our experiments also suggest that the antagonism of α-elapitoxin-Oh3a is irreversible or pseudo-irreversible. All the above are suggestive of α-elapitoxin-Oh3a being a typical long-chain α-neurotoxin (Barber et al., 2013).

Additionally, we identified three fractions from reverse-phase HPLC which displayed postsynaptic neurotoxicity, but the α-neurotoxins within these fractions could not be further purified using ion-exchange chromatography. The presence of multiple α-neurotoxins in *O. hannah* venom from Indonesia, has also been previously indicated by proteomic analysis (Petras et al., 2015), with approximately 37% of the venom protein identified as postsynaptic neurotoxins. α-Elapitoxin-Oh3a showed 100% sequence identity with Long neurotoxin OH-55, which was also reported by the aforementioned study to constitute approximately 12% of the venom, slightly more than the relative abundance suggested in the current study.

Long neurotoxin OH-55 has also been isolated from *O. hannah* venom by He et al. (2004). In this previous study, a 24 h LD_{50} assay of the isolated α-neurotoxins from *O. hannah* venom in mice showed Long neurotoxin OH-55 to have a LD_{50} of 120 ng/g (i.p.), likely due to a high potency on the mouse (rodent) nAChR. Unlike short-chain α-neurotoxins, long-chain α-neurotoxins do not show a difference in the potency and reversibility between human and rodent nAChR. Therefore, they are likely to be more clinically important and capable of causing neuromuscular paralysis in humans (Silva et al., 2018). Hence, it could be assumed that α-elapitoxin-Oh3a, which constitutes 5–12% of the whole venom, would be of high clinical importance in causing neuromuscular paralysis in envenomed humans.

Thai Red Cross Society King Cobra antivenom was able to fully prevent the neurotoxic effects of α-elapitoxin-Oh3a, indicating the presence of antibody fragments against the toxin. Further, the antivenom was able to partially restore (~40%) the indirect twitches of the chick biventer preparation after they were fully inhibited by the toxin. The continuous physical removal of α-elapitoxin-Oh3a, by repeated washing of the preparation, did not result in any significant reversal of the neurotoxic effect of the toxin on indirect twitches although there was partial restoration of the responses to exogenous agonists. Since the constant removal of toxin from the surrounding physiological environment is unable to effectively reverse the neuromuscular block, this suggests that the role of antivenom may not be limited to antibodies binding to epitopes at the pharmacological site of unbound toxins, preventing their antagonism at nAChRs, but antibodies may also bind to epitopes more distant from the pharmacological site of nAChR-bound toxins, triggering conformational changes in the toxin that would reduce its affinity for nAChRs (Silva and Isbister, 2020). This was previously demonstrated by commercially used antivenoms and high-affinity monoclonal antibodies which could accelerate the detachment of *Naja nigricollis* toxin α from nAChRs (Boulain and Ménez, 1982; Boulain et al., 1985; Gatineau et al., 1988). In contrast to α-elapitoxin-Oh3a, toxin α is a short-chain postsynaptic neurotoxin, which generally have a lower potency and higher reversibility at nAChRs, and likely to be of lesser clinical importance (Silva et al., 2018). The important observation made in this study is that antivenom can reverse the clinically important long-chain α-neurotoxin-mediated neuromuscular paralysis.

In conclusion, we have shown that α-Elapitoxin-Oh3a (7,938 Da), a long-chain a-neurotoxin from *O. hannah* venom, is a highly potent pseudo-irreversible antagonist at nAChR in avian skeletal muscle. The neurotoxic effects of α-Elapitoxin-Oh3a are prevented, and partially reversed, by Thai Red Cross Society King Cobra antivenom. α-Elapitoxin-Oh3a is likely to be a key contributor the neuromuscular paralysis that can result by envenoming by the King Cobra.

DATA AVAILABILITY STATEMENT

The protein sequence data reported in this paper is available in the UniProt Knowledgebase under the accession number Q53B58.

ETHICS STATEMENT

The animal study was reviewed and approved by Monash University Ethics Committee on 18 December 2019; ethics number 22575.

AUTHOR CONTRIBUTIONS

TH: experiments, data acquisition, data analysis, writing. AS: experiment design, data analysis, writing. GI: experiment design, data analysis, writing, funding acquisition. WH: experiment design, data analysis, writing, funding acquisition.

FUNDING

This study was supported by an Australian National Health and Medical Research Council (NHMRC) Senior Research Fellowship (ID: 1154503) awarded to GI, and a NHMRC Centres for Research for Excellence Grant (ID: 1110343) awarded to GI and WH.

ACKNOWLEDGMENTS

We would also like to acknowledge the Monash Proteomics & Metabolomics Facility and Dr David Steer for determining the intact mass and amino acid sequence of the toxin.

REFERENCES

Barber, C. M., Isbister, G. K., and Hodgson, W. C. (2013). Alpha Neurotoxins. *Toxicon* 66, 47–58. doi:10.1016/j.toxicon.2013.01.019

Boulain, J. C., and Ménez, A. (1982). Neurotoxin-Specific Immunoglobulins Accelerate Dissociation of the Neurotoxin-Acetylcholine Receptor Complex. *Science* 217, 732–733. doi:10.1126/science.7100919

Boulain, J. C., Fromageot, P., and Ménez, A. (1985). Further Evidence Showing that Neurotoxin-Acetylcholine Receptor Dissociation Is Accelerated by Monoclonal Neurotoxin-specific Immunoglobulin. *Mol. Immunol.* 22, 553–556. doi:10.1016/0161-5890(85)90178-6

Chang, C.-C., Lin, P.-M., Chang, L.-S., and Kuo, K.-W. (1995). Chemical Modification of Tryptophan Residues in α-neurotoxins from *Ophiophagus hannah* (king Cobra) Venom. *J. Protein Chem.* 14, 89–94. doi:10.1007/bf01888366

Chang, L., Chang, C., and Lin, S. (2000). Differential Contribution of the Conserved Tyrosine Residues to Activity and Structural Stability of *Ophiophagus hannah* α-Neurotoxins. *J. Pept. Res.* 55, 240–245. doi:10.1034/j.1399-3011.2000.00176.x

Gatineau, E., Lee, C. Y., Fromageot, P., and Menez, A. (1988). Reversal of Snake Neurotoxin Binding to Mammalian Acetylcholine Receptor by Specific Antiserum. *Eur. J. Biochem.* 171, 535–539. doi:10.1111/j.1432-1033.1988.tb13822.x

Gowtham, Y. J., Kumar, M. S., Girish, K. S., and Kemparaju, K. (2012). Hemostatic Interference of Indian King Cobra (*Ophiophagus hannah*) Venom. Comparison with Three Other Snake Venoms of the Subcontinent. *Biochemistry (Mosc)* 77, 639–647. doi:10.1134/s0006297912060119

He, Y. Y., Lee, W. H., and Zhang, Y. (2004). Cloning and Purification of α-Neurotoxins from king Cobra (*Ophiophagus hannah*). *Toxicon* 44, 295–303. doi:10.1016/j.toxicon.2004.06.003

King, G. F., Gentz, M. C., Escoubas, P., and Nicholson, G. M. (2008). A Rational Nomenclature for Naming Peptide Toxins from Spiders and Other Venomous Animals. *Toxicon* 52, 264–276. doi:10.1016/j.toxicon.2008.05.020

Lin, S. R., Chi, S. H., Chang, L. S., Kuo, K. W., and Chang, C. C. (1995a). Chemical Modification of Cationic Groups of a Novel α-Neurotoxin (Oh-4) from King Cobra (*Ophiophagus hannah*) Venom. *J. Biochem.* 118, 297–301. doi:10.1093/oxfordjournals.jbchem.a124906

Lin, S. R., Chi, S. H., Chang, L. S., Kuo, K. W., and Chang, C. C. (1995b). Chemical Modification of Cationic Residues in Toxin a from King Cobra (*Ophiophagus hannah*) Venom. *J. Protein Chem.* 15, 95–101. doi:10.1007/bf0188681510.1007/BF01886815

Lin, S. R., Leu, L. F., Chang, L. S., and Chang, C. C. (1997). Amino Acid Sequence and Chemical Modification of a Novel α-Neurotoxin (Oh-5) from King Cobra (*Ophiophagus hannah*) Venom. *J. Biochem.* 121, 690–695. doi:10.1093/oxfordjournals.jbchem.a021641

O'Shea, M. (2008). *Venomous Snakes of the World*, London, UK. New Holland Publishers.

Petras, D., Heiss, P., Süssmuth, R. D., and Calvete, J. J. (2015). Venom Proteomics of Indonesian King Cobra, *Ophiophagus hannah*: Integrating Top-Down and Bottom-Up Approaches. *J. Proteome Res.* 14, 2539–2556. doi:10.1021/acs.jproteome.5b00305

Roy, A., Zhou, X., Chong, M. Z., D'Hoedt, D., Foo, C. S., Rajagopalan, N., et al. (2010). Structural and Functional Characterization of a Novel Homodimeric Three-Finger Neurotoxin from the Venom of *Ophiophagus hannah* (King Cobra). *J. Biol. Chem.* 285, 8302–8315. doi:10.1074/jbc.M109.074161

Silva, A., and Isbister, G. K. (2020). Current Research into Snake Antivenoms, Their Mechanisms of Action and Applications. *Biochem. Soc. Trans.* 48, 537–546. doi:10.1042/BST20190739

Silva, A., Cristofori-Armstrong, B., Rash, L. D., Hodgson, W. C., and Isbister, G. K. (2018). Defining the Role of post-synaptic α-neurotoxins in Paralysis Due to Snake Envenoming in Humans. *Cell. Mol. Life Sci.* 75, 4465–4478. doi:10.1007/s00018-018-2893-x

Tan, C. H., Tan, K. Y., Fung, S. Y., and Tan, N. H. (2015). Venom-Gland Transcriptome and Venom Proteome of the Malaysian King Cobra (*Ophiophagus hannah*). *BMC Genomics* 16, 687. doi:10.1186/s12864-015-1828-2

Tin, M., Rai, M., Maung, C., Tun, P., and Warrell, D. A. (1991). Bites by the King Cobra (*Ophiophagus hannah*) in Myanmar: Successful Treatment of Severe Neurotoxic Envenoming. *Q. J. Med.* 80, 751–762.

Tun, P., Aye-Aye-Myint, M., Warrell, D. A., and Tin, M. (1995). King Cobra (*Ophiophagus hannah*) Bites in Myanmar: Venom Antigen Levels and Development of Venom Antibodies. *Toxicon* 33, 379–382. doi:10.1016/0041-0101(94)00157-4

Utkin, Y. N. (2019). Last Decade Update for Three-Finger Toxins: Newly Emerging Structures and Biological Activities. *World J. Biol. Chem.* 10, 17–27. doi:10.4331/wjbc.v10.i1.17

Wickramaratna, J. C., Fry, B. G., Loiacono, R. E., Aguilar, M. I., Alewood, P. F., and Hodgson, W. C. (2004). Isolation and Characterization at Cholinergic Nicotinic Receptors of a Neurotoxin from the Venom of the *Acanthophis* Sp. Seram Death Adder. *Biochem. Pharmacol.* 68, 383–394. doi:10.1016/j.bcp.2004.03.033

Conflict of Interest: The authors declare that the research was conducted in the absence of any commercial or financial relationships that could be construed as a potential conflict of interest.

Publisher's Note: All claims expressed in this article are solely those of the authors and do not necessarily represent those of their affiliated organizations, or those of the publisher, the editors and the reviewers. Any product that may be evaluated in this article, or claim that may be made by its manufacturer, is not guaranteed or endorsed by the publisher.

frontiers in Pharmacology

ORIGINAL RESEARCH
published: 21 March 2022
doi: 10.3389/fphar.2022.816795

Australian Sea Snake Envenoming Causes Myotoxicity and Non-Specific Systemic Symptoms - Australian Snakebite Project (ASP-24)

Christopher I. Johnston[1]*, *Theo Tasoulis*[1] and *Geoffrey K. Isbister*[1,2]

[1]Clinical Toxicology Research Group, University of Newcastle, Newcastle, NSW, Australia, [2]National Poison Centre Network, Westmead Children's Hospital, Sydney, NSW, Australia

Background: Sea snakes are venomous snakes found in the warm parts of the Indo-Pacific, including around Australia. Most sea snake envenoming causes myotoxicity, but previous Australian case reports describe neurotoxicity. We aimed to describe the epidemiology and clinical presentation of Australian sea snake envenoming and the effectiveness of antivenom.

Methods: Patients were recruited to the Australian Snakebite Project (ASP), an Australia-wide prospective observational study recruiting all patients with suspected or confirmed snakebite >2 years. Information about demographics, bite circumstances, species involved, clinical and laboratory features of envenoming, and treatment is collected and entered into a purpose-built database.

Results: Between January 2002 and August 2020, 13 patients with suspected sea snake bite were recruited to ASP, 11 were male; median age was 30 years. Bites occurred in Queensland and Western Australia. All patients were in or around, coastal waters at the time of bite. The species involved was identified in two cases (both *Hydrophis zweifeli*). Local effects occurred in 9 patients: pain (5), swelling (5), bleeding (2), bruising (1). Envenoming occurred in eight patients and was characterised by non-specific systemic features (6) and myotoxicity (2). Myotoxicity was severe (peak CK 28200 and 48100 U/L) and rapid in onset (time to peak CK 13.5 and 15.1 h) in these two patients. Non-specific systemic features included nausea (6), headache (6), abdominal pain (3), and diaphoresis (2). Leukocytosis, neutrophilia, and lymphopenia occurred in both patients with myotoxicity and was evident on the first blood test. No patients developed neurotoxicity or coagulopathy. Early Seqirus antivenom therapy was associated with a lower peak creatine kinase.

Conclusion: While relatively rare, sea snake envenoming is associated with significant morbidity and risk of mortality. Early antivenom appears to have a role in preventing severe myotoxicity and should be a goal of therapy.

Keywords: Australian, sea snake, envenoming, envenomation, antivenom, myotoxicity

Edited by:
Jean-Marc Sabatier, Aix-Marseille Université, France

Reviewed by:
Carlo Pietro Campobasso, University of Campania Luigi Vanvitelli, Italy
Sam Kularatne, University of Peradeniya, Sri Lanka

***Correspondence:**
Christopher I. Johnston
Christopher.I.Johnston@uon.edu.au

Specialty section:
This article was submitted to Translational Pharmacology, a section of the journal Frontiers in Pharmacology

Received: *17 November 2021*
Accepted: *15 February 2022*
Published: *21 March 2022*

Citation:
Johnston CI, Tasoulis T and Isbister GK (2022) Australian Sea Snake Envenoming Causes Myotoxicity and Non-Specific Systemic Symptoms - Australian Snakebite Project (ASP-24). Front. Pharmacol. 13:816795. doi: 10.3389/fphar.2022.816795

INTRODUCTION

Sea snakes (*Hydrophiini* or true sea snakes) are a diverse clade of venomous Elapidae, that are part of the Hydrophiinae sub-family, which also include all Australia-Papuan/Melanesian terrestrial elapids and sea kraits (*Laticauda*) (Strickland et al., 2016; Zaher et al., 2019). True sea snakes live exclusively in water and are commonly found in the warm tropical and subtropical parts of the Indian and Pacific Oceans, where they live in shallow coastal waters, estuaries, the open ocean, and occasionally inland lakes and rivers (Phillips, 2002; Sanders et al., 2008; Lane and Shine, 2011). Until recently some sea snake species in Australian waters were thought to be the same as those found in Asia. Recent morphological and molecular evidence has demonstrated distinct lineages in Australia. An important example is the previously recognised beaked sea snake *Enhydrina schistosa* in Australia has now been made a separate species, *Hydrophis zweifeli* (Ukuwela et al., 2013; Rasmussen et al., 2014). Sea snakes are easily identifiable by their vertically flattened, paddle-shaped tail, and most species are not considered to be aggressive unless they are being handled, threatened, or it is mating season (Mcgoldrick and Marx, 1991). World-wide sea snake bites are rare, with many sea snake bites occurring from fishing activities (Marsden and Reid, 1961; Reid, 1975b; Limpis, 1978).

Sea snake venoms have been studied extensively, with numerous toxins identified and studied in animal models. Myotoxins (Fohlman and Eaker, 1977; Ali et al., 2000) and neurotoxins (pre- and post-synaptic) (Geh and Chan, 1973; Tu, 1974; Chetty et al., 2004) are the most important venom components Other toxins that have been identified include cytotoxins (Tamiya and Yagi, 2011) and haemolysins (Tu et al., 1970; Tu, 1974), although the clinical relevance of these toxins is unclear.

Most published cases of sea snake envenoming come from Malaysia (Marsden and Reid, 1961; Reid, 1975b), Sri Lanka (Kularatne et al., 2014), and Thailand (Sitprija et al., 1971), with male fisherman the highest risk group (Reid, 1975b). The reported rate of envenoming after witnessed bites was 32% (Reid, 1975b). The commonest clinical effects are systemic myotoxicity, with muscle pain and tenderness, muscle stiffness and spasm, weakness, elevated serum creatine kinase (CK), myoglobinuria, and myonecrosis on muscle biopsy (Reid, 1961a; Marsden and Reid, 1961; Kularatne et al., 2014). A small proportion of patients with myotoxicity developed an acute kidney injury with associated uraemia, severe hyperkalaemia and anuria, with some treated with renal replacement therapy (Marsden and Reid, 1961; Sitprija et al., 1971). Several deaths are reported from respiratory failure, hyperkalaemia and acute kidney injury (Marsden and Reid, 1961). In some cases, features of neurotoxicity are reported, with ptosis, ophthalmoplegia, flaccid paralysis, and loss of tendon reflexes. These neurological features were believed by the investigators to be a result of severe myotoxicity, rather than a direct neurotoxic effect (Marsden and Reid, 1961; Reid, 1975a; Kularatne et al., 2014). Other features of sea snake envenoming that were reported include leucocytosis and vomiting (Reid, 1961a; Reid, 1975a). Minimal local bite site effects were noted (Reid, 1961b).

Few sea snake envenoming cases have been reported in Australia, and the envenoming syndrome remains poorly characterised (Mercer et al., 1981; Fulde and Smith, 1984; Dobb, 1986; Patterson and Swallow, 1991). Neurotoxicity is the commonest finding reported in case reports, with slurred speech, paraesthesia, ptosis, diplopia, ophthalmoplegia, muscle weakness and flaccid paralysis, and other neurological signs (hyperreflexia, drowsiness, loss of consciousness and confusion) (Mercer et al., 1981; Fulde and Smith, 1984; Dobb, 1986; Patterson L, 1991). Myotoxicity has also been reported, as well as opisthotonos, respiratory distress, headache, vomiting, mild coagulopathy, and leucocytosis (Mercer et al., 1981; Fulde and Smith, 1984; Dobb, 1986; Patterson and Swallow, 1991; Seqirus Pty Ltd, 2019). A case of fatal sea snake envenoming in Australian waters has been reported, with rapid onset of neurotoxic features and death from respiratory failure (Tiemensma and Byard, 2021).

There is a commercial sea snake antivenom (Seqirus®) available for the treatment of sea snake envenoming, which is raised against Malaysian *Hydrophis schistosa* (beaked sea snake) venom in horses (Ukuwela et al., 2013; Seqirus Pty Ltd, 2019). The product is manufactured in Australia as vials to be diluted and given as an intravenous infusion (Seqirus Pty Ltd., 14th November 2019). The product requires refrigeration and has a shelf life of 3 years (Therapeutic Goods AdministrationA. G., 2020). It's cost and cold chain storage requirements limit availability in many countries that have cases of sea snake envenoming, with some availability and usage described in Malaysia and Singapore (Tan, 2010; Tan et al., 2015). Despite being raised against only one sea snake venom to a species not found in Australian waters, the product is recommended for envenoming from all sea snake types in Australia (Seqirus Pty Ltd, 2019). Efficacy in animal models of neurotoxicity and lethality has been demonstrated with the venoms from many sea snake species (Tu, 1987; Chetty et al., 2004). The antivenom appeared to be effective in a small series of patients from Malaysia (Reid, 1962; Reid, 1975a).

The objective of this study is to examine the epidemiology and clinical presentation of Australian sea snake envenoming and investigate the effectiveness of sea snake antivenom in its treatment.

METHODS

We undertook a review of all sea snakebites recruited to the Australian snakebite project. The Australian snakebite project is a prospective multi-centre observational study of patients with suspected snakebite from all Australian states and territories. All patients with suspected or confirmed snakebite over the age of two are eligible for recruitment. Human research ethics approval was obtained from major State and Territory human research ethics committees (HRECs) responsible covering all recruiting hospitals including the Northern Territory Department of Health and Menzies School of Health Research (reference, 04/08), the

Hunter New England Area Health Service and the University of Newcastle (reference, 07/11/21/3.06), the Royal Perth Hospital Ethics Committee and South Metro Area Health Service (reference, RA-08/003), the Western Australian Country Health Service (reference, 2008:03), the Tasmania Network (reference, H00109965), and the Gold Coast Health Service District (reference, 200835), as well as for a further ten HRECs of participating facilities. Written informed consent was obtained from the patient or their next of kin, parent or guardian (for minors or those unable to provide consent themselves).

Patients are referred to the ASP investigators for recruitment after identification of snakebites by onsite clinicians, local investigators, staff of the Australian Poisons Information Centre Network or laboratory staff. Patient information sheets, consent forms, data collection forms and laboratory procedures are faxed to the treating site. After the patient has provided informed consent, information is collected on demographics, bite circumstance, clinical data, treatment given and response, in purpose designed datasheets that are completed by the treating team. Missing data is collected from patient medical records if required. Patient treatment is determined by the local treating team, in many cases in consultation with a Clinical Toxicologist from the Australian Poisons Information Centre Network. Collected data are entered into a purpose designed database by trained research assistants and then reviewed by the chief investigator.

Clinical syndromes are defined based on signs and symptoms of envenoming and serial laboratory findings, according to pre-determined criteria (Johnston et al., 2017). Myotoxicity was defined as patients with a CK greater than 1000 U/L and severe myotoxicity as a CK greater than 10,000 U/L (Johnston and Isbister, 2020). Systemic hypersensitivity reactions to antivenom are defined by the National Guidelines of Allergy and Infectious Disease—Food Allergy and Anaphylaxis Network criteria (Sampson et al., 2006), with severity defined by the grading system proposed by Brown (2004).

The ASP database was searched from January 2002 to August 2020 for all potential cases of sea snakebite, including both envenomed and non-envenomed patients. Included patients were those with likely sea snakebite, defined as either: 1) a patient bitten by a sea snake in which there was expert identification of the snake involved or 2) there was witnessed bite by a snake with a paddle-shaped tail in, or nearby, coastal waters. Information extracted from the database included patient demographic data, bite circumstance and location, clinical findings, laboratory investigations, snakebite treatment and time to hospital discharge post-bite.

Descriptive statistical analysis is carried out on continuous outcomes, with normality of the data assessed by the Kolmogorov-Smirnov test and the Shapiro-Wilk normality test. All descriptive data is presented as medians with interquartile ranges (IQR) and ranges. All analyses and graphics were done in GraphPad Prism version 9.0.2 for Windows, GraphPad Software, San Diego California, United States.

RESULTS

Between January 2002 and August 2020 there were 2,292 patients recruited to the Australian Snakebite Project. Thirteen sea snake bites were identified, making up only 0.6% of all snakebites. Eleven of 13 were male and the median patient age was 30 years (4–68 years). One patient was a snake handler (**Table 1**).

All bites occurred in the wild on the coast of, or waters off, Queensland and Western Australia, of which the most southern location was Hervey Bay, Queensland (**Figure 1**). All patients were in or near the water at the time of the bite: four on boats, four swimming in the ocean, three standing on land (two on the beach, one on a river bank) and two standing in shallow water. The only inland bite occurred on the bank of the Fitzroy river at Rockhampton (approximately 56 km inland) (**Figure 1**). Activity at the time of bite included fishing (11), swimming (2), standing on the snake (1), handling a snake found on land (1) and collecting marine animals for research (1). There were nine patients bitten on the upper limb, three on the lower limb and one patient who was bitten on the face (**Table 1**). There was identification of the snake species involved in two cases, both *Hydrophis zweifeli* (Beaked sea snake—formerly known as Australian *Enhydrina schistosa*; **Figure 2**).

Local effects in 9 patients included pain (5) that was only mild, minimal swelling (5) local bleeding (2) and bruising (1) (**Figure 3**). Systemic envenoming occurred in eight of the 13 patients and was characterised by non-specific systemic symptoms (6) and myotoxicity (2). In addition to those with myotoxicity four further envenomed patients had small elevations in creatine kinase (CK) of 275 U/L, 804 U/L, 919 U/L, and 939 U/L (**Table 1**; **Figure 4**). Non-specific systemic symptoms included nausea (6), headache (6), abdominal pain (3), and diaphoresis (2). Median time to onset of first non-specific systemic symptoms was 22.5 min (IQR: 5–119 min, range 5–385 min). Five envenomed patients had musculoskeletal symptoms, including local myalgia (4), local muscle tenderness (2), generalised myalgia (2), and trismus (1). Median time to onset of first musculoskeletal symptoms was 30 min (IQR: 12.5–195 min; range 10–210 min). Two patients had myotoxicity with a peak CK of 48,100 U/L and 28,200 U/L, and therefore severe myotoxicity. Neither developed an acute kidney injury. The time to peak CK was 15.1 and 13.5 h, respectively in these two patients (**Figure 4**). They had elevated serum transaminases, peak aspartate transaminase (AST) of 2350 U/L and 748 U/L, and peak alanine transaminase (ALT) of 514 and 241 U/L, respectively. Both patients with myotoxicity also had an elevated white cell count (WCC of 14.2×10^9/L and 15.7×10^9/L), evident on the first blood test (7 and 8.6 h). Both had neutrophilia and lymphopenia. Serum AST and ALT results were available in five of the other patients, respectively, and were within normal limits in all of these patients. Nine of the eleven other patients had WCC results and only one patient (who was non-envenomed) had an elevated WCC of 11.6×10^9/L. No patients had objective evidence of neurotoxicity, venom-induced consumption coagulopathy, anticoagulant coagulopathy, thrombocytopenia, haemolysis, hyperkalaemia, or acute kidney injury.

Pressure bandage with immobilisation was performed in ten of the patients. Antivenom was given to seven of the eight

TABLE 1 | Summary of patient characteristics and clinical features of 13 patients with sea snake bite.

Age/ Sex	Location	Activity	Bite site	Sea snake type	PBI used	Envenomed	Features of envenoming	Muscle pain/ tenderness	Peak CK (U/L)	AV given	Time to first AV post-bite (h)	Antivenom reaction	Time to discharge post bite (h)
4/M	Beach (in water)	Swimming	Hand	Unknown	No	Yes	Myotoxicity, NSSS	General	48,100	Yes	9	No	26.0
12/M	Beach (in water)	Fishing	Ankle	Unknown	Yes	Yes	Myotoxicity	Local	28,200	Yes	11.5	No	166.0
30/M	Ocean	Fishing on trawling vessel	Finger	Unknown	Yes	Yes	NSSS	Local	939	Yes	5.5	No	35.5
15/F	Beach (in water)	Swimming	Leg	Unknown	Yes	No	Mild envenoming*	No	919	Yes	14.75	Moderate	45.0
23/M	Ocean	Fishing on trawling vessel	Finger	Unknown	Yes	Yes	NSSS	No	804	Yes	4.25	Mild	36.0
52/M	Ocean	Spear fishing	Face	Unknown	No	Yes	NSSS	General	275	Yes	4	No	22.5
51/M	Ocean	Collecting research specimens	Finger	*Hydrophis zweifeli*	Yes	Yes	NSSS	No	146	No	N/A	No	18.8
17/F	Beach (in water)	Walking in shallow water	Foot	Unknown	Yes	Yes	NSSS	Local	86	Yes	4.75	No	16.9
30/M	Ocean	Fishing on trawling vessel	Finger	Unknown	No	No	Non-envenomed	No	Not available	No	N/A	No	14.3
16/M	River bank	Fishing	Finger	*Hydrophis zweifeli*	Yes	No	Non-envenomed	No	223	No	N/A	No	19.5
62/M	Beach (on sand)	Fishing	Finger	Unknown	Yes	No	Non-envenomed	No	210	No	N/A	No	9.0
68/M	Ocean	Fishing on trawling vessel	Finger	Unknown	Yes	No	Non-envenomed	No	203	Yes	6.5	No	22.0
47/M	Beach (on sand)	Recovering unwell snake	Finger	Unknown	Yes	No	Non-envenomed	No	58	No	N/A	No	11.5

*NSSS, Non-specific systemic symptoms. *—Mild envenoming with rapid rise in CK (but peak less than 1000 U/L thus not meeting definition of myotoxicity).*

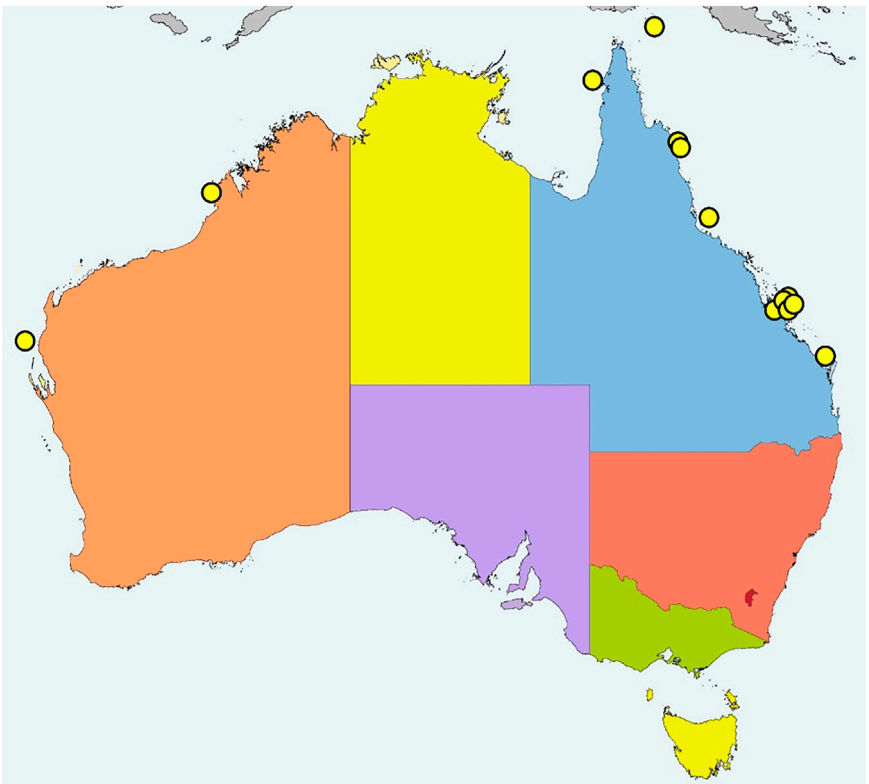

FIGURE 1 | Distribution of 13 sea snake bites in Australia from January 2002 to August 2020.

envenomed patients, and one non-envenomed patient. All patients initially received one vial of antivenom, and only one patient received a second vial. The median time to the first dose of antivenom post-bite was 6 h (IQR: 4.4–18.9; range 4–14.8 h). Administration of antivenom within 6 h in patients with envenoming appeared to be associated with lower peak CK in envenomed patients, with a peak CK measurements of 919, 28,200, and 48,100 U/L for the ≥ 6-h group, versus 86, 275, 804, and 939 U/L for the < 6-h group. Two patients had immediate hypersensitivity reactions to antivenom. The first had a mild hypersensitivity reaction limited to urticaria managed with an antihistamine and adrenaline infusion. The second developed a moderate hypersensitivity reaction with cough and angioedema, managed with an antihistamine and corticosteroid.

All patients survived to discharge and the median time to discharge post-bite for the 13 patients was 22 h (IQR: 15.6–35.8; range 9–166 h) (**Table 1**). Time to discharge for the two patients with myotoxicity were 26 and 166 h post-bite, respectively (**Table 1**).

DISCUSSION

Australian sea snake bites are extremely rare, with less than one case per year on average, and only half of these envenomed. We found that sea snake envenoming in Australia is characterised by non-specific systemic symptoms and myotoxicity, the latter is both rapid in onset and severe. Neurotoxicity was not observed in this case series, consistent with the international literature (Marsden and Reid, 1961; Sitprija et al., 1971; Kularatne et al., 2014). Laboratory abnormalities included increased CK consistent with muscle injury, elevated AST and to a lesser extent ALT, and neutrophilia and lymphopenia. The elevated AST and ALT are more likely to be due to muscle injury, rather than liver injury, because the more specific liver enzyme ALT was less elevated. Venom induced consumption coagulopathy and anticoagulant coagulopathy did not occur, in contrast to most important Australian terrestrial snakes (Johnston et al., 2017). Administration of antivenom within 6 h appeared to be associated with a reduction in the severity of myotoxicity.

The relative rarity is surprising, given the wide distribution of several sea snake species in Australian waters and the marked potential for occupational exposure, particularly with the prawn trawling activity off the north coast of Australia, with tens of thousands of sea snakes caught in fishing nets per year (Wassenberg et al., 1994). More importantly, the rarity of sea snakebites makes it more difficult to have antivenom available for patients, which was reflected in the longer times to antivenom administration compared to terrestrial snake envenoming (Johnston et al., 2017).

This case series lacked fatal cases of sea snake envenoming, previously seen particularly in published research from Malaysia (Marsden and Reid, 1961), and described previously in Australia (Tiemensma and Byard, 2021). There are a number of potential reasons for this, including variations involving the snake (snake

FIGURE 2 | Photograph of a *Hydrophis zweifeli* (Beaked sea snake—formerly known as Australian *Enhydrina schistosa*) (credit: Jamie Seymour).

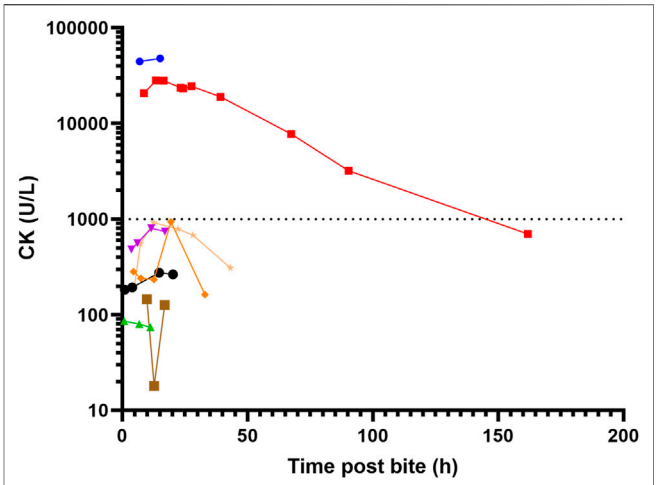

FIGURE 4 | Serial creatine kinase (CK) measurement for eight patients with sea snake envenoming, two with myotoxicity (peak CK > 1000 U/L).

type, regional variation in snake venom toxicity, age of the snake), bite circumstances (part of body affected, amount of venom injected), patient (age, weight and comorbidities), and treatment (first aid administered and time to access of hospital care, investigations, antivenom, and supportive care). There were no cases of sea snake envenoming identified post-mortem in a previous series including coronial cases of snake envenoming (Johnston et al., 2017). This may be due to the relative rarity of sea snake envenoming in Australia and the quality of care, as well as the difficulty conclusively diagnosing sea snake envenoming post-mortem (Feola et al., 2020).

While only present in two patients, the myotoxicity that occurred was striking in both the speed of onset and severity. Both patients had markedly elevated CK on first blood test results at 7 and 8 h respectively, which was different to myotoxicity reported from Australian terrestrial snakes, in which the median time to first abnormal CK was 11.1 h and the median time to peak CK was 34.3 h (Johnston and Isbister, 2020). For the one patient with serial CK results available, the CK peaked early at 13.5 h. Unfortunately, the other patient was discharged after the second CK result of 48,100 U/L, because he was clinically well (**Figure 4**). The speed of onset is in keeping with several fatal cases caused by severe myotoxicity described by Marsden and Reid in Malaysia, in which death occurred less than 24 h post-bite (Marsden and Reid, 1961). Some previously described musculoskeletal features of envenoming, such as severe muscle spasms, were not observed in these patients. Isolated elevation in serum transaminases is a previously described phenomenon in Australian snakebite associated myotoxicity (Johnston and Isbister, 2020), and likely relates to release of release of transaminases from damaged skeletal muscle, rather than primary hepatotoxic effect.

Neurotoxicity, a feature previously described in Australian cases of sea snake envenoming, including one fatal case, did not occur in this series (Tiemensma and Byard, 2021). Even though several neurotoxins have been identified in sea snake venoms, they are of

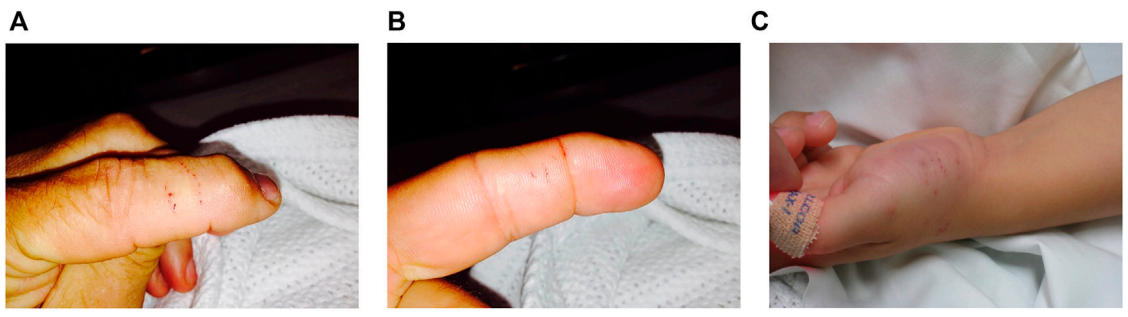

FIGURE 3 | (A–C): Fang marks of patients bitten by sea snakes.

unclear clinical relevance in human envenoming, or there is known inter-species variation in response to neurotoxins, as is the case with the lack of binding site for short chain neurotoxins from *H. schistosa* venom in humans (Harris, 1989). In a Malaysian case series of sea snake envenoming fatalities, early mortality from issues such as paresis and respiratory failure is described, features often attributed to neurotoxicity (Marsden and Reid, 1961). Subsequent autopsy on some cases in the Malaysian series demonstrated marked necrosis of intercostal and diaphragmatic muscle, with myotoxicity, rather than neurotoxicity, attributed as the cause of death (Marsden and Reid, 1961). In a small number of sea snake envenoming cases from Sri Lanka (Kularatne et al., 2014) and Thailand (Sitprija et al., 1971) neuromuscular transmission and nerve conduction studies have been carried out, demonstrating myopathy as the cause of neurological symptoms in the patients. The authors of the Thai case series also proposed that myotoxic sensitisation of skeletal muscle could potentiate the paralytic effects of hyperkalaemia and uraemia, with rapid improvement in symptoms noted when patients were treated with haemodialysis with associated correction of serum potassium and urea excess (Sitprija et al., 1971). However, neurotoxicity may occur in only some species of sea snakes, which may not have caused bites in this series.

To date, there is minimal clinical evidence published to support the recommended treatment for Australian sea snake envenoming, Seqirus sea snake antivenom®. Potential limitations of the treatment include that it is monovalent and raised against venom from *Enhydrina schistosa* (beaked sea snakes) of Malaysian origin, especially given recent recognition of Australian *E. schistosa* actually being a distinct species, *Hydrophis zweifeli* (Reid, 1961b; Ukuwela et al., 2013). Despite this, the antivenom is recommended for all envenomed cases from a diverse local sea snake fauna (Seqirus Pty Ltd, 2019). Whilst *in vitro* and animal modelling of antivenom efficacy has been demonstrated, it is unclear if the models chosen or inter-species variability in response translates into effectiveness in human cases for all sea snake types. In the absence of being able to confirm specific sea snake type and quantify effectiveness in a larger group of patients, this study demonstrates the potential value of early antivenom in preventing severe myotoxicity. The use of tiger snake antivenom for the management of sea snake envenoming, a practice that was previously recommended if sea snake antivenom was not available (Acott, 1986) prior to antivenom manufacturing changes (Chetty et al., 2004), was not observed and is not recommended.

There are several limitations to this study, the most important of which is the lack of venom-specific enzyme immunoassay, which can allow identification of snake species involved, quantify venom present, allow correlation of venom concentration with clinical presentation, and measure the efficacy of sea snake antivenom at binding circulating venom. Given the diverse sea snake fauna in Australia, it is difficult to obtain venom samples from this broad range of difficult to catch snakes and prepare polyclonal antibodies for all potential snakes. This, coupled with snake specimens or photo availability, led to identification of the involved sea snake being possible in only two cases. The generalisability of observational data (some of which is secondary data, such as physical examination and clinical features that are not directly collected by the research team) in the small number of cases described in this series to sea snake bite from any species in Australia is also not known.

Despite the rarity of sea snake bite in Australia, half of the patients were envenomed and envenoming appears to be associated with significant morbidity and potentially mortality when it occurs. Whilst difficult to definitively diagnose without the presence of coagulopathy, patients with potential sea snakebite based on appearance of the snake and locality, should have close serial physical examination and laboratory testing. Strong consideration of early antivenom therapy (<6 h) should be given for patients with non-specific systemic features, muscle pain and tenderness, or neutrophilia, with a goal of preventing fulminant myotoxicity from developing.

DATA AVAILABILITY STATEMENT

The raw data supporting the conclusion of this article will be made available by the authors, without undue reservation.

ETHICS STATEMENT

The studies involving human participants were reviewed and approved by the major State and Territory human research ethics committees (HRECs) responsible covering all recruiting hospitals including the Northern Territory Department of Health and Menzies School of Health Research (reference, 04/08), the Hunter New England Area Health Service and the University of Newcastle (reference, 07/11/21/3.06), the Royal Perth Hospital Ethics Committee and South Metro Area Health Service (reference, RA-08/003), the Western Australian Country Health Service (reference, 2008:03), the Tasmania Network (reference, H00109965), and the Gold Coast Health Service District (reference, 200835), as well as for a further ten HRECs of participating facilities. Written informed consent to participate in this study was provided by the participant, or their legal guardian/next of kin.

AUTHOR CONTRIBUTIONS

Conceived and designed the study: CJ and GI. Analysed the data: CJ, TT, and GI. Wrote the paper: CJ, TT, and GI. Recruitment of patients at hospital sites: CJ and GI.

FUNDING

The study is supported by an NHMRC Centre for Research Excellence Grant ID 1110343. GI is funded by an NHMRC Senior Research Fellowship ID 1154503.

ACKNOWLEDGMENTS

We acknowledge the support of the large number of clinicians and laboratory staff that have made the Australian Snakebite

Project possible. In particular, we thank all the research administrative staff of the Clinical Toxicology Research Group for collecting and recording data, maintaining the database, and organising transport of blood samples, including Jen Robinson, Kylie Tape, Marea Herden, Renai Kearney, and Shane Jenkins.

REFERENCES

Acott, C. J. (1986). Sea-snake Envenomation. *Med. J. Aust.* 144, 448. doi:10.5694/j.1326-5377.1986.tb128437.x

Ali, S. A., Alam, J. M., Abbasi, A., Zaidi, Z. H., Stoeva, S., and Voelter, W. (2000). Sea Snake Hydrophis Cyanocinctus Venom. II. Histopathological Changes, Induced by a Myotoxic Phospholipase A2 (PLA2-H1). *Toxicon* 38, 687–705. doi:10.1016/s0041-0101(99)00184-1

Brown, S. G. (2004). Clinical Features and Severity Grading of Anaphylaxis. *J. Allergy Clin. Immunol.* 114, 371–376. doi:10.1016/j.jaci.2004.04.029

Chetty, N., Du, A., Hodgson, W. C., Winkel, K., and Fry, B. G. (2004). The *In Vitro* Neuromuscular Activity of Indo-Pacific Sea-Snake Venoms: Efficacy of Two Commercially Available Antivenoms. *Toxicon* 44, 193–200. doi:10.1016/j.toxicon.2004.05.022

Dobb, G. J. (1986). Sea-snake Envenomation. *Med. J. Aust.* 144, 112. doi:10.5694/j.1326-5377.1986.tb113687.x

Feola, A., Marella, G. L., Carfora, A., Della Pietra, B., Zangani, P., and Campobasso, C. P. (2020). Snakebite Envenoming a Challenging Diagnosis for the Forensic Pathologist: a Systematic Review. *Toxins (Basel)* 12, 699. doi:10.3390/toxins12110699

Fohlman, J., and Eaker, D. (1977). Isolation and Characterization of a Lethal Myotoxic Phospholipase A from the Venom of the Common Sea Snake *Enhydrina schistosa* Causing Myoglobinuria in Mice. *Toxicon* 15, 385–393. doi:10.1016/0041-0101(77)90116-7

Fulde, G. W., and Smith, F. (1984). Sea Snake Envenomation at Bondi. *Med. J. Aust.* 141, 44–45. doi:10.5694/j.1326-5377.1984.tb132670.x

Geh, S. L., and Chan, K. E. (1973). The Pre-junctional Site of Action of *Enhydrina schistosa* Venom at the Neuromuscular junction. *Eur. J. Pharmacol.* 21, 115–120. doi:10.1016/0014-2999(73)90215-x

Harris, J. B. (1989). Snake Venoms in Science and Clinical Medicine. 3. Neuropharmacological Aspects of the Activity of Snake Venoms. *Trans. R. Soc. Trop. Med. Hyg.* 83, 745–747. doi:10.1016/0035-9203(89)90313-1

Johnston, C. I., and Isbister, G. K. (2020). Australian Snakebite Myotoxicity (ASP-23). *Clin. Toxicol. (Phila)*, 1–8. doi:10.1080/15563650.2020.1836377

Johnston, C. I., Ryan, N. M., Page, C. B., Buckley, N. A., Brown, S. G., O'leary, M. A., et al. (2017). The Australian Snakebite Project, 2005-2015 (ASP-20). *Med. J. Aust.* 207, 119–125. doi:10.5694/mja17.00094

Kularatne, S. A., Hettiarachchi, R., Dalpathadu, J., Mendis, A. S., Appuhamy, P. D., Zoysa, H. D., et al. (2014). *Enhydrina schistosa* (Elapidae: Hydrophiinae) the Most Dangerous Sea Snake in Sri Lanka: Three Case Studies of Severe Envenoming. *Toxicon* 77, 78–86. doi:10.1016/j.toxicon.2013.10.031

Lane, A., and Shine, R. (2011). Phylogenetic Relationships within Laticaudine Sea Snakes (Elapidae). *Mol. Phylogenet. Evol.* 59, 567–577. doi:10.1016/j.ympev.2011.03.005

Limpis, C. J. (1978). *Toxicology of the Venom of Subtropical Queensland Hydrophiidae*. Toxins: Elsevier, 341–363.

Marsden, A. T., and Reid, H. A. (1961). Pathology of Sea-Snake Poisoning. *Br. Med. J.* 1, 1290–1293. doi:10.1136/bmj.1.5235.1290

Mcgoldrick, J., and Marx, J. A. (1991). Marine Envenomations; Part 1: Vertebrates. *J. Emerg. Med.* 9, 497–502. doi:10.1016/0736-4679(91)90223-3

Mercer, H. P., Mcgill, J. J., and Ibrahim, R. A. (1981). Envenomation by Sea Snake in Queensland. *Med. J. Aust.* 1, 130–132. doi:10.5694/j.1326-5377.1981.tb135383.x

Patterson, L. S. S., and Swallow, S. (1991). Sea Snake Envenomation. *Med. J. Aust.* 155, 850. doi:10.5694/j.1326-5377.1991.tb94065.x

Phillips, C. M. (2002). Sea Snake Envenomation. *Dermatol. Ther.* 15, 58–61. doi:10.1046/j.1529-8019.2002.01504.x

Rasmussen, A. R., Sanders, K. L., Guinea, M. L., and Amey, A. P. (2014). Sea Snakes in Australian Waters (Serpentes: Subfamilies Hydrophiinae and Laticaudinae)-Aa Review with an Updated Identification Key. *Zootaxa* 3869, 351–371. doi:10.11646/zootaxa.3869.4.1

Reid, H. A. (1975a). Antivenom in Sea-Snake Bit Poisoning. *Lancet* 1, 622–623. doi:10.1016/s0140-6736(75)91897-8

Reid, H. A. (1961b). Diagnosis, Prognosis, and Treatment of Sea-Snake Bite. *Lancet* 2, 399–402. doi:10.1016/s0140-6736(61)92483-7

Reid, H. A. (1975b). Epidemiology of Sea-Snake Bites. *J. Trop. Med. Hyg.* 78, 106–113.

Reid, H. A. (1961a). Myoglobinuria and Sea-Snake-Bite Poisoning. *Br. Med. J.* 1, 1284–1289. doi:10.1136/bmj.1.5235.1284

Reid, H. A. (1962). Sea-snake Antivenene: Successful Trial. *Br. Med. J.* 2, 576–579. doi:10.1136/bmj.2.5304.576

Sampson, H. A., Muñoz-Furlong, A., Campbell, R. L., Adkinson, N. F., Jr, Bock, S. A., Branum, A., et al. (2006). Second Symposium on the Definition and Management of Anaphylaxis: Summary Report-Ssecond National Institute of Allergy and Infectious Disease/Food Allergy and Anaphylaxis Network Symposium. *Ann. Emerg. Med.* 47, 373–380. doi:10.1016/j.annemergmed.2006.01.018

Sanders, K. L., Lee, M. S., Leys, R., Foster, R., and Keogh, J. S. (2008). Molecular Phylogeny and Divergence Dates for Australasian Elapids and Sea Snakes (Hydrophiinae): Evidence from Seven Genes for Rapid Evolutionary Radiations. *J. Evol. Biol.* 21, 682–695. doi:10.1111/j.1420-9101.2008.01525.x

Seqirus Pty Ltd. (2019). "Australian Product Information - Sea Snake Antivenom Injection").

Sitprija, V., Sribhibhadh, R., and Benyajati, C. (1971). Haemodialysis in Poisoning by Sea-Snake Venom. *Br. Med. J.* 3, 218–219. doi:10.1136/bmj.3.5768.218

Strickland, J. L., Carter, S., Kraus, F., and Parkinson, C. L. (2016). Snake Evolution in Melanesia: Origin of the Hydrophiinae (Serpentes, Elapidae), and the Evolutionary History of the Enigmatic New Guinean elapidToxicocalamus. *Zool J. Linn. Soc.* 178, 663–678. doi:10.1111/zoj.12423

Tamiya, N., and Yagi, T. (2011). Studies on Sea Snake Venom. *Proc. Jpn. Acad. Ser. B Phys. Biol. Sci.* 87, 41–52. doi:10.2183/pjab.87.41

Tan, C. H., Tan, N. H., Tan, K. Y., and Kwong, K. O. (2015). Antivenom Cross-Neutralization of the Venoms of Hydrophis Schistosus and Hydrophis Curtus, Two Common Sea Snakes in Malaysian Waters. *Toxins (Basel)* 7, 572–581. doi:10.3390/toxins7020572

Tan, H. H. (2010). Epidemiology of Snakebites from a General Hospital in Singapore: A 5-year Retrospective Review (2004-2008). *Ann. Acad. Med. Singap* 39, 640–647.

Therapeutic Goods Administration, A.G (2020). Summary for Artg Entry: 74901 Sea Snake Antivenom (Equine) 1000u Injection via [Online]. Available at: https://tga-search.clients.funnelback.com/s/search.html?query=&collection=tga-artg (Accessed 01 23, 2022).

Tiemensma, M., and Byard, R. W. (2021). Fatal Sea Snake Envenomation. The American Journal of Forensic Medicine and Pathology.

Tu, A. T. (1987). Biotoxicology of Sea Snake Venoms. *Ann. Emerg. Med.* 16, 1023–1028. doi:10.1016/s0196-0644(87)80752-7

Tu, A. T., Passey, R. B., and Toom, P. M. (1970). Isolation and Characterization of Phospholipase A from Sea Snake, Laticauda Semifasciata Venom. *Arch. Biochem. Biophys.* 140, 96–106. doi:10.1016/0003-9861(70)90013-5

Tu, A. T. (1974). Sea Snake Venoms and Neurotoxins. *J. Agric. Food Chem.* 22, 36–43. doi:10.1021/jf60191a034

Ukuwela, K. D., De Silva, A., Mumpuni, B. G., Fry, B. G., Lee, M. S., and Sanders, K. L. (2013). Molecular Evidence that the Deadliest Sea Snake *Enhydrina schistosa* (Elapidae: Hydrophiinae) Consists of Two Convergent Species. *Mol. Phylogenet. Evol.* 66, 262–269. doi:10.1016/j.ympev.2012.09.031

Wassenberg, T., Salini, J., Heatwole, H., and Kerr, J. (1994). Incidental Capture of Sea-Snakes (Hydrophiidae) by Prawn Trawlers in the Gulf of Carpentaria, Australia. *Mar. Freshw. Res.* 45, 429–443. doi:10.1071/mf9940429

Zaher, H., Murphy, R. W., Arredondo, J. C., Graboski, R., Machado-Filho, P. R., Mahlow, K., et al. (2019). Large-scale Molecular Phylogeny, Morphology, Divergence-Time Estimation, and the Fossil Record of Advanced Caenophidian Snakes (Squamata: Serpentes). *PloS one* 14, e0216148. doi:10.1371/journal.pone.0216148

Conflict of Interest: CIJ is an employee of Boehringer Ingelheim. This research is unrelated to his employment and is not in a therapeutic area related to any company research or development.

The remaining authors declare that the research was conducted in the absence of any commercial or financial relationships that could be construed as a potential conflict of interest.

Publisher's Note: All claims expressed in this article are solely those of the authors and do not necessarily represent those of their affiliated organizations, or those of the publisher, the editors and the reviewers. Any product that may be evaluated in this article, or claim that may be made by its manufacturer, is not guaranteed or endorsed by the publisher.

frontiers | Frontiers in Pharmacology

ORIGINAL RESEARCH
published: 19 May 2022
doi: 10.3389/fphar.2022.846992

Structural and Functional Characterization of a Novel Scorpion Toxin that Inhibits $Na_V1.8$ via Interactions With the DI Voltage Sensor and DII Pore Module

*Kiran George[1†], Diego Lopez-Mateos[2,3†], Tarek Mohamed Abd El-Aziz[4,5,6†], Yucheng Xiao[7†], Jake Kline[1], Hong Bao[1], Syed Raza[1], James D. Stockand[4], Theodore R. Cummins[7], Luca Fornelli[1], Matthew P. Rowe[1], Vladimir Yarov-Yarovoy[2,3,8] and Ashlee H. Rowe[1,9]**

[1]Department of Biology, University of Oklahoma, Norman, OK, United States, [2]Department of Physiology and Membrane Biology, University of California, Davis, Davis, CA, United States, [3]Biophysics Graduate Group, University of California, Davis, Davis, CA, United States, [4]Department of Cellular and Integrative Physiology, University of Texas Health Science Center San Antonio, San Antonio, TX, United States, [5]Zoology Department, Faculty of Science, Minia University, El-Minia, Egypt, [6]Amsaal Venom Farm L.L.C., Abu Dhabi, United Arab Emirates, [7]Department of Biology, School of Science, Indiana University-Purdue University Indianapolis, Indianapolis, IN, United States, [8]Department of Anesthesiology and Pain Medicine, University of California, Davis, Davis, CA, United States, [9]Graduate Program in Cellular and Behavioral Neurobiology, University of Oklahoma, Norman, OK, United States

OPEN ACCESS

Edited by:
Jean-Marc Sabatier, Aix-Marseille Université, France

Reviewed by:
Christin Schroeder, The University of Queensland, Australia
Wandi Zhu, Harvard Medical School, United States

***Correspondence:**
Ashlee H. Rowe
ahrowe@ou.edu

[†]These authors have contributed equally to this work

Specialty section:
This article was submitted to Pharmacology of Ion Channels and Channelopathies, a section of the journal Frontiers in Pharmacology

Received: *31 December 2021*
Accepted: *05 April 2022*
Published: *19 May 2022*

Citation:
George K, Lopez-Mateos D, Abd El-Aziz TM, Xiao Y, Kline J, Bao H, Raza S, Stockand JD, Cummins TR, Fornelli L, Rowe MP, Yarov-Yarovoy V and Rowe AH (2022) Structural and Functional Characterization of a Novel Scorpion Toxin that Inhibits $Na_V1.8$ via Interactions With the DI Voltage Sensor and DII Pore Module. Front. Pharmacol. 13:846992. doi: 10.3389/fphar.2022.846992

Voltage-gated sodium channel $Na_V1.8$ regulates transmission of pain signals to the brain. While $Na_V1.8$ has the potential to serve as a drug target, the molecular mechanisms that shape $Na_V1.8$ gating are not completely understood, particularly mechanisms that couple activation to inactivation. Interactions between toxin producing animals and their predators provide a novel approach for investigating Na_V structure-function relationships. Arizona bark scorpions produce Na^+ channel toxins that initiate pain signaling. However, in predatory grasshopper mice, toxins inhibit $Na_V1.8$ currents and block pain signals. A screen of synthetic peptide toxins predicted from bark scorpion venom showed that peptide NaTx36 inhibited Na^+ current recorded from a recombinant grasshopper mouse $Na_V1.8$ channel ($OtNa_V1.8$). Toxin NaTx36 hyperpolarized $OtNa_V1.8$ activation, steady-state fast inactivation, and slow inactivation. Mutagenesis revealed that the first gating charge in the domain I (DI) S4 voltage sensor and an acidic amino acid (E) in the DII SS2 – S6 pore loop are critical for the inhibitory effects of NaTx36. Computational modeling showed that a DI S1 – S2 asparagine (N) stabilizes the NaTx36 – $OtNa_V1.8$ complex while residues in the DI S3 – S4 linker and S4 voltage sensor form electrostatic interactions that allow a toxin glutamine (Q) to contact the first S4 gating charge. Surprisingly, the models predicted that NaTx36 contacts amino acids in the DII S5 – SS1 pore loop instead of the SS2 – S6 loop; the DII SS2 – S6 loop motif (QVSE) alters the conformation of the DII S5 – SS1 pore loop, enhancing allosteric interactions between toxin and the DII S5 – SS1 pore loop. Few toxins have been identified that modify $Na_V1.8$ gating. Moreover, few toxins have been described that modify sodium channel gating via the DI S4 voltage sensor. Thus, NaTx36 and $OtNa_V1.8$ provide tools for investigating the structure-activity relationship

between channel activation and inactivation gating, and the connection to alternative pain phenotypes.

Keywords: Nav1.8, voltage-gated sodium channel, AZ bark scorpion, grasshopper mice, NaTx36, slow inactivation, venom, neurotoxin

INTRODUCTION

Voltage gated sodium ion channels (Na_V) are transmembrane protein pores that generate the action potentials underlying neuronal signaling and muscle contraction (Catterall, 1980; Catterall, 1992; Catterall, 2000; Catterall et al., 2005; Ahern et al., 2016). Mammals express nine genes that encode Na_V isoforms expressed in different tissues and at different developmental time points (Ahern et al., 2016). Na_V generate action potentials by regulating the flux of Na^+ ions across excitable cell membranes (Catterall, 1992; Catterall, 2000). These channels are activated by voltage (initiating Na^+ influx), and inactivated by terminating Na^+ flux (Catterall, 2014). Na_V have four domains, each consisting of six helices (S1 – S6) (**Figure 1A**). In each domain, the transmembrane re-entrant loop between S5 and S6 form the ion-permeating pore and Na^+ selectivity filter, while the extracellular loops that link S5 to the pore (S5 – SS1) and the pore to S6 (SS2 – S6) form the mouth of the pore. Positively charged amino acids in the S4 segment of each domain function as voltage sensor gating charges (GC). The intracellular loop that links DIII and DIV contains an isoleucine-phenylalanine-methionine (IFM) motif that forms the fast inactivation mechanism. The extracellular loops linking S3 to S4 in DII and DIV serve as binding sites for scorpion β and α toxins, respectively. At resting membrane potential, the channel is closed (**Figure 1B**). Depolarization of the cell membrane alters the electrostatic forces that move S4 helices outward, opening the channel (Catterall, 2000; Catterall, 2014). While the movement of the S4 helices in DI – DIII are associated with channel activation (opening), the movement of the S4 helix in DIV initiates the fast inactivation mechanism (Armstrong, 2006). During fast inactivation, the DIII – DIV loop acts as an inactivation particle to occlude the pore. Slow inactivation is a second form of inactivation that involves a rearrangment of the

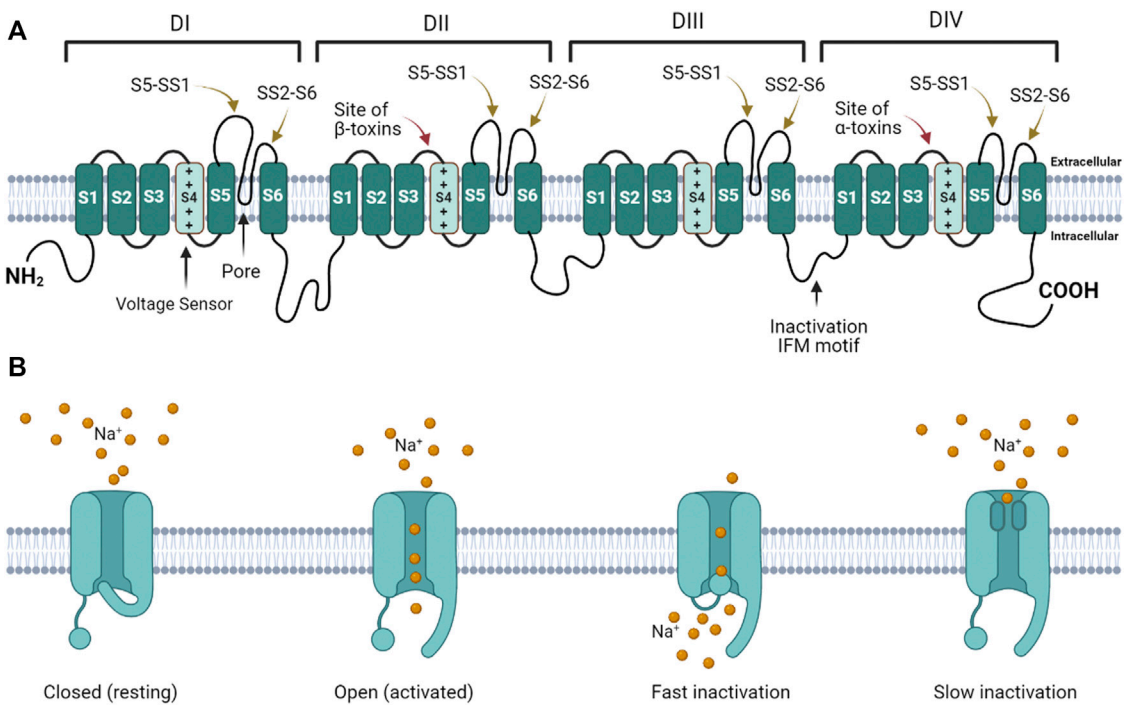

FIGURE 1 | Voltage gated sodium channel structure and function. **(A)** The channel consists of four homologous domains (DI – DIV). Each domain consists of six transmembrane helices (S1 – S6). The fourth helix (S4) in each domain contains basic amino acids that act as voltage-sensor gating charges. The re-entrant loops between S5 and S6 in each domain form the pore (black arrow points to pore in DI). The extracellular loops connecting S5 to the pore (S5 – SS1) and the pore to S6 (SS2 – S6) form the mouth of the pore. The intracellular loop connecting DIII to DIV forms the fast inactivation hinged lid. The isoleucine-phenylalanine-methionine (IFM) motif is critical for fast inactivation gating. The DII and DIV S3 – S4 linkers form the primary scorpion β and α toxin binding sites, respectively. **(B)** When the channel is in the resting state, the activation gate is closed. When the channel is activated, the gate opens. During activation the inactivation gate (hinged lid) is disengaged. During fast inactivation, the hinged lid occludes the intracellular side of the pore. When the channel transitions into the slow inactivated state, the pore loops change conformation to obstruct the pore.

segments that line the pore (Vilin and Ruben, 2001; Silva, 2014; Chatterjee et al., 2018).

Three Na_V (Nav1.7, 1.8, 1.9) are expressed in peripheral nociceptive neurons where they contribute to membrane excitability (Vilin and Ruben, 2001; Blair and Bean, 2002; Blair and Bean, 2003; Sokolov et al., 2008). $Na_V1.8$ generates the majority of Na^+ current underlying the upstroke of action potentials in small-diameter nociceptive neurons, and thus, is a key ion channel governing the excitability of sensory neurons and transmission of pain signals (Cummins and Waxman, 1997; Renganathan et al., 2001; Blair and Bean, 2002; Blair and Bean, 2003; Cummins et al., 2007; Dib-Hajj et al., 2010). Numerous studies have implicated $Na_V1.8$ currents in mechanical, cold, neuropathic, and inflammatory pain – highlighting the potential for $Na_V1.8$ to serve as a target for drug therapy (Cummins et al., 2007; Basbaum et al., 2009; Cavanaugh et al., 2009; Le Pichon and Chesler, 2014; Barbosa et al., 2016; Peirs and Seal, 2016). While progress has been made elucidating the role of $Na_V1.8$ in regulating the excitability of nociceptive neurons and transmission of pain signals, the molecular mechanisms that govern $Na_V1.8$ gating are not completely understood. Animal-derived venoms and peptide toxins are useful tools for investigating Na_V structure-function relationships. For example, scorpion toxins were used to examine the structure and function of voltage sensors ($Na_V1.2$) and the fast inactivation mechanism ($Na_V1.7$) (Cestèle et al., 1998; Bosmans and Tytgat, 2007; Bosmans and Swartz, 2010; Zhang et al., 2011; Clairfeuille et al., 2019). However, until recently, few animal toxins had been identified that modify $Na_V1.8$ gating (Ye et al., 2015), prompting efforts to construct chimeras of $Na_V1.8$ that could bind peptide toxins by exchanging extracellular loops on $Na_V1.8$ with corresponding toxin binding sites from $Na_V1.2$ (Gilchrist and Bosmans, 2018). More recently, additional peptide toxins have been discovered that modify $Na_V1.8$ gating, providing insight into structure-activity relationships between voltage sensors and gating mechanisms (Zhang et al., 2019; Deuis et al., 2021; Finol-Urdaneta et al., 2022).

Toxin-producing animals and their predators provide an alternative approach for using toxin – Na_V interactions to examine the relationship between voltage sensors and gating processes. Arizona (AZ) bark scorpions (Centruroides sculpturatus) produce venom that is painful as well as potentially lethal (Curry et al., 1983; Boyer et al., 2009). The venom is a cocktail of peptide toxins that bind Na^+ and K^+ channels in nerve and muscle tissue (Couraud et al., 1984; Simard et al., 1992; Possani et al., 1999; Possani et al., 2000; Corona et al., 2001; Rodríguez de la Vega and Possani, 2004; Rodríguez de la Vega and Possani, 2005). The peptides do not cause pain by damaging tissue; they activate $Na_V1.7$, hyperexciting nociceptive neurons (Vandendriessche et al., 2010; Rowe et al., 2011; Rowe et al., 2013). Anecdotal reports describe the venom as producing the sensation of burning pain, coupled with hypersensitivity to touch and pressure. Thus, bark scorpion venom provides a source of novel biochemicals for probing ion channels that regulate nociceptive neuron excitability and pain-related behavior. Southern grasshopper mice (Onychomys torridus) prey on bark scorpions. Compared to house mice, grasshopper mice show little response when either stung by scorpions or injected with venom (Rowe and Rowe, 2006; Rowe and Rowe, 2008; Rowe et al., 2013). Electrophysiological analyses showed that bark scorpion venom inhibited $Na_V1.8$ currents and blocked the propagation of action potentials in dissociated, small-diameter dorsal root ganglia (DRG) neurons from grasshopper mice (Rowe et al., 2013). In contrast, bark scorpion venom had no effect on house mice $Na_V1.8$ currents. Instead of blocking action potentials in house mice DRG neurons, the venom increased the propagation of action potentials. Moreover, pre-injecting grasshopper mice with venom decreased their pain-related behavior in response to formalin. Pre-injecting house mice with venom only increased their pain related behavior in response to formalin. Collectively, the findings demonstrate that grasshopper mice have evolved resistance to painful venom. Our hypothesis is that grasshopper mice have amino acid variants in $Na_V1.8$ that enable the channel to bind peptide toxins which inhibit channel activity and block pain signals. Thus, bark scorpions and grasshopper mice provide a novel system for investigating $Na_V1.8$ amino acid variants that alter the structure-activity relationship between the channel and venom peptides, and for determining the biophysical mechanisms that decrease nociceptive-neuron excitability and pain-related behavior in a rodent model.

We previously isolated a venom subfraction (F11-E) from the AZ bark scorpion and showed that it inhibited tetrodotoxin resistant (TTX-R) Na^+ current recorded from the grasshopper mouse recombinant $OtNa_V1.8$ channel (Mohamed Abd El-Aziz et al., 2021). Using liquid chromatography mass spectrometry (LC MS), we showed that subfraction F11-E contained four peptides each having the mass and primary structure characteristic of scorpion sodium channel toxins (NaTx) (Mohamed Abd El-Aziz et al., 2021). The AZ bark scorpion venom gland transcriptome (NCBI GenBank accession number PRJNA340270) was used to confirm the primary structure of the novel peptides (NaTx4, NaTx13, NaTx22, NaTx36) (Mohamed Abd El-Aziz et al., 2021). Our goal is to identify peptides that inhibit $OtNa_V1.8$ and to functionally characterize the inhibitory activity. To this end, the peptides were chemically synthesized by SB-PEPTIDE (SmartBioscience SAS, France) and then tested on $OtNa_V1.8$. Here, we report that NaTx36 inhibits $OtNa_V1.8$ TTX-R Na^+ current in a concentration and voltage dependent manner, recapitulating the inhibitory effects of AZ bark scorpion venom on $OtNa_V1.8$. Electrophysiological analyses show that NaTx36 modulates $OtNa_V1.8$ activation and inactivation gating, while site-directed mutagenesis and computational modeling suggest that amino acids in the DI voltage sensor and the DII pore module are critical for channel inhibition. These results are significant because few toxins have been identified that target $Na_V1.8$ (Ye et al., 2015; Zhang et al., 2019; Deuis et al., 2021). Moreover, few toxins have been described that modify Na_V gating mechanisms via interaction with the DI voltage sensor (Xiao et al., 2014; Clairfeuille et al., 2019). The interactions between NaTx36 and $OtNa_V1.8$ provide a toolkit for investigating the structure-activity relationship between channel activation and inactivation gating mechanisms.

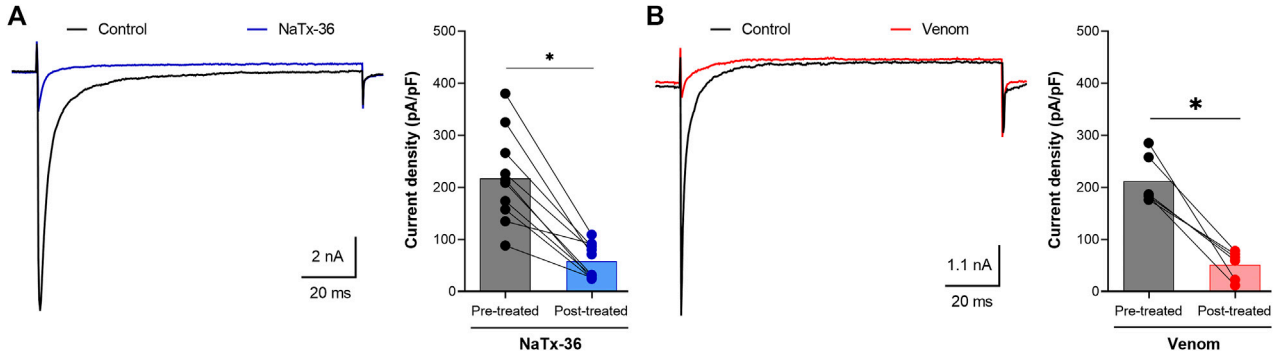

FIGURE 2 | Effects of NaTx36 on grasshopper mouse recombinant OtNa$_V$1.8 Na^+ current density. Na^+ currents were elicited by a 100-ms depolarization to +20 mV from a holding potential of −80 mV. Tetrodotoxin (TTX, 500 nM) was added to the bath solution to block endogenous TTX sensitive Na^+ currents. Representative Na^+ current traces and current density (pA/pF) recorded from whole-cell voltage-clamped ND7/23 cells transfected with OtNa$_V$1.8. Na^+ currents were recorded before and after application of NaTx36 and AZ bark scorpion venom. **(A)** NaTx36 (blue symbols, 10 μg/ml, $n = 9$ cells), and **(B)** venom (red symbols, 1.0 μg/ml, $n = 6$ cells) inhibited tetrodotoxin resistant (TTX-R) Na^+ currents. Filled circles represent current density values for individually recorded cells. Histograms represent mean current density reported as picoamps divided by picofarads (pA/pF, * $p < 0.05$).

RESULTS

NaTx36 Inhibits Recombinant Grasshopper Mouse OtNa$_V$1.8 Na^+ Current

We used whole-cell patch clamp electrophysiology to measure the effects of synthetic peptide toxins on TTX-R Na^+ current recorded from OtNa$_V$1.8 expressed in ND7/23 cells. Custom peptide toxins were synthesized by SB-PEPTIDE (SmartBioscience SAS, France) using the amino acid sequence of the primary structures previously determined for NaTx36, NaTx22, NaTx13, NaTx4 (Mohamed Abd El-Aziz et al., 2021). SB-PEPTIDE purified the final peptides using High Performance Liquid Chromatography (HPLC), confirmed the mass using Liquid Chromatography Mass Spectrometry (LC MS), and quantified the peptides using OD280. The purity, intact mass and amino acid sequence of each peptide was validated in this study using LC MS, and bottom-up MS/MS, respectively (**Supplementary Figures S1 –S8**).

A sample of each peptide toxin was separately diluted in bath solution to the desired final concentration. Na^+ currents were elicited by a 100-millisecond depolarization to +20 mV from a holding potential of −80 mV before and after application of toxins. Toxin NaTx36 significantly decreased OtNa$_V$1.8 Na^+ current density from 217.5 ± 27.83 pA/pF to 57.82 ± 10.47 pA/pF (10 μg/ml, $n = 9$ cells, $p < 0.05$) (**Figure 2A**). The inhibitory effect of NaTx36 was characteristic of the effect of AZ bark scorpion venom on OtNa$_V$1.8, with the exception that a lower concentration of venom is required to inhibit OtNa$_V$1.8. Venom decreased current density from 212.1 ± 19.18 pA/pF to 51.56 ± 11.25 pA/pF (1.0 μg/ml, $n = 6$ cells, $p < 0.05$) (**Figure 2B**).

Synthetic peptide toxins NaTx4, NaTx22, and NaTx13 were also tested on OtNa$_V$1.8 using the protocol described above (**Supplementary Figure S9A**). NaTx4 (pre-treated: 255.7 ± 31.05 pA/pF, post-treated: 251.3 ± 29.45 pA/pF, $n = 7$ cells), NaTx22 (pre-treated: 220.5 ± 32.46 pA/pF, post-treated: 196.4 ± 29.45 pA/pF, $n = 8$ cells), and NaTx13 (pre-treated: 240.3 ± 31.01 pA/pF, post-treated: 223.3 ± 25.77 pA/pF, $n = 9$ cells) had no effect on OtNa$_V$1.8 current density (all toxins tested at 10 μg/ml) (**Supplementary Figures S9B–D**). These results demonstrate that peptides NaTx4, NaTx22 and NaTx13 are not biologically active against OtNav1.8. Given that the peptides were chemically synthesized (SB-PEPTIDE, SmartBioscience SAS, France), it is possible that the peptides were not bio-active because they did not fold properly.

Our previous work demonstrated that AZ bark scorpion venom had no effect on house mouse Na$_V$1.8 (Rowe et al., 2013). An alignment of grasshopper mouse Na$_V$1.8 with house mouse sequence revealed variation in the position of an acidic residue (E) within the DII SS2 – S6 loop. In grasshopper mice, the position of E (859QVSE862) is shifted by three amino acids compared to house mice (859EVSQ862). Site-directed mutagenesis showed that the position of the E is critical for the inhibitory effects of AZ bark scorpion venom (Rowe et al., 2013). Thus, we hypothesized that grasshopper mice had evolved amino acid substitutions that enabled their Na$_V$1.8 to bind venom peptides and block channel activity. Because human Na$_V$1.8 is like the house mouse channel, expressing the E at position 859 (Rowe et al., 2013) (see also **Figure 12B** in this study), we predicted that NaTx36 would have no effect on human Na$_V$1.8 (hNa$_V$1.8). To determine whether NaTx36 inhibits human Na$_V$1.8, we tested the peptide on a recombinant hNa$_V$1.8 channel expressed in ND7/23 cells. Na^+ currents were elicited by a 50-ms depolarizing pulse to +10 mV before and after application of NaTx36 (**Supplementary Figure S10A**). To determine the effect of NaTx36 on the hNa$_V$1.8 current-voltage relationship, Na^+ currents were induced by 50-ms depolarizing steps to various potentials ranging from −80 to +40 mV in 5-mV increments (**Supplementary Figure S10B**). Neither 100 nM nor 1.0 μM NaTx36 inhibited hNav1.8.

NaTx36 Inhibits OtNa$_V$1.8 Activity in a Concentration-Dependent Manner

We previously showed that AZ bark scorpion venom inhibits OtNa$_V$1.8 TTX-R Na^+ current in a concentration-dependent

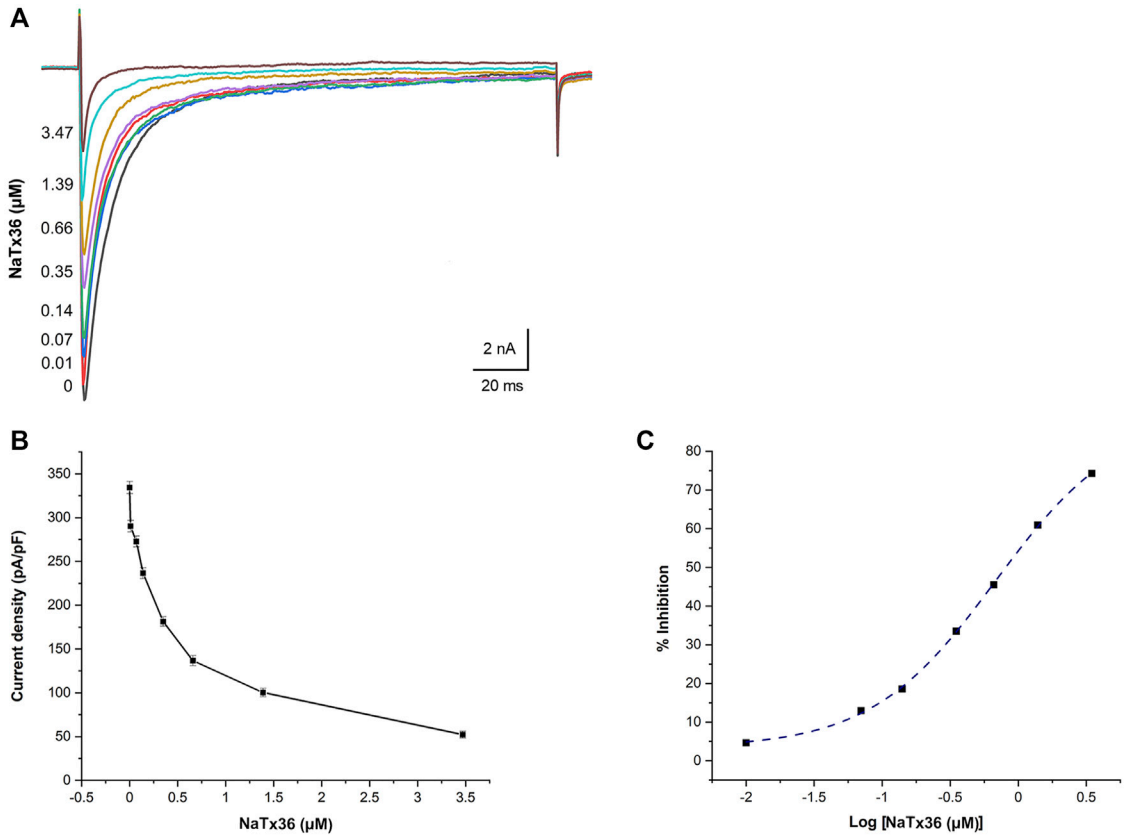

FIGURE 3 | NaTx36 inhibits OtNa$_V$1.8 in a concentration dependent manner. **(A)** TTX-R Na^+ current traces and **(B)** current density (pA/pF) recorded from ND7/23 cells expressing OtNav1.8 before and after application of NaTx36. Na^+ currents were elicited by a 100-ms depolarization to +20 mV from a holding potential of −80 mV before and after application of NaTx36. Tetrodotoxin (TTX, 500 nM) was added to the bath solution to block endogenous TTX sensitive Na^+ currents. Currents decrease in response to samples of NaTx36 ranging from 0.01 to 3.47 μM (n = 5 – 6 cells per concentration). **(C)** Na^+ current values in response to NaTx36 were fit to a Dose-response equation with variable Hill slope to estimate the half-maximum inhibitory concentration (IC_{50} = 0.68 ± 0.05 μM).

manner (Rowe et al., 2013). To evaluate the dose response effect of NaTx36, we applied a range of toxin concentrations to OtNa$_V$1.8 expressed in ND7/23 cells. Na^+ currents were elicited by a 100-millisecond depolarization to +20 mV from a holding potential of −80 mV before and after application of NaTx36. Similar to the inhibitory effect of venom, increasing concentrations of NaTx36 decreased OtNa$_V$1.8 current density (0 μM = 334.33 ± 7.02 pA/pF, 0.1 μM = 290.16 ± 5.53 pA/pF, 0.07 μM = 272.66 ± 4.16 pA/pF, 0.14 μM = 236.66 ± 7.26 pA/pF, 0.35 μM = 181.33 ± 5.38 pA/pF, o.66 μM = 136.66 ± 6.77 pA/pF, 1.39 μM = 100.33 ± 4.83 pA/pF, 3.47 μM = 52.33 ± 4.63 pA/pF, n = 5 – 6 cells per concentration) (**Figures 3A,B**). The half-maximum inhibitory concentration (IC_{50}) of NaTx36 = 0.68 ± 0.05 μM (**Figure 3C**).

Hyperpolarizing Holding Potentials Reduce NaTx36 Inhibitory Effects on OtNa$_V$1.8

We previously showed that the inhibitory effect of venom is voltage-dependent (Mohamed Abd El-Aziz et al., 2021). To determine if the inhibitory effect of NaTx36 on OtNa$_V$1.8 is also voltage dependent, we tested NaTx36 on OtNa$_V$1.8 at two different holding potentials. Currents were induced by 50-ms depolarizing steps to various potentials ranging from −80 to +40 mV in 5-mV increments. All currents induced before and after application of NaTx36 were normalized to the maximum amplitude of control peak current. At +20 mV, NaTx36 (100 nM) reduced Na^+ current amplitude by 66.0 ± 0.9% (control n = 5 cells, NaTx36 n = 4 cells) (**Figure 4A**). However, when cells were hyperpolarized to a holding potential of −120 mV, the inhibitory effects of NaTx36 (100 nM) were reduced. At +20 mV, the toxin inhibition was reduced from 66.0 ± 0.9% to 20.8 ± 0.8% (−80 mV, n = 4 cells; −120 mV, n = 3 cells) (**Figure 4B**). In addition, the results show that NaTx36 enhances OtNa$_V$1.8 activation at more hyperpolarized membrane potentials (**Figures 4A,B**). This suggests that NaTx36 acts as a typical scorpion beta toxin by opening channels at more hyperpolarized membrane potentials (Qu et al., 1998; Cestèle and Catterall, 2000; Mantegazza and Cestèle, 2005).

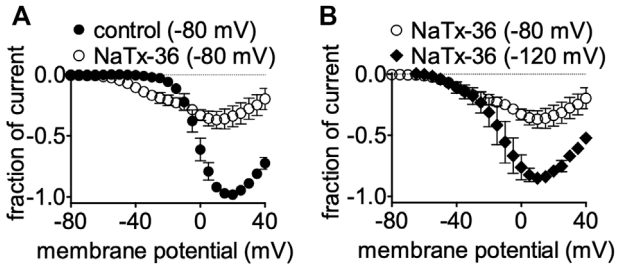

FIGURE 4 | Effects of NaTx36 on OtNa$_V$1.8 current-voltage relationship (I-V curves). Cells were pretreated with 500 nM TTX to block TTX-sensitive sodium channels, and currents were elicited by 50-ms depolarizing steps to various voltages ranging from −80 to +40 mV in 5-mV increments. All Na^+ currents were normalized to the maximum amplitude of control peak current. **(A)** Representative I-V curves before and after 100 nM NaTx36. When the holding potential was −80 mV, NaTx36 could inhibit TTX-R Na^+ current recorded from ND7/23 cells transfected with recombinant OtNav1.8 (control, $n = 5$; NaTx36, $n = 4$). NaTx36 also enhanced activation by hyperpolarizing the membrane potential at which channels begin opening. **(B)** When the holding potential was changed to −120 mV, inhibition of OtNa$_V$1.8 by 100 nM NaTx36 was substantially reduced (−80 mV, $n = 4$; −120 mV, $n = 3$).

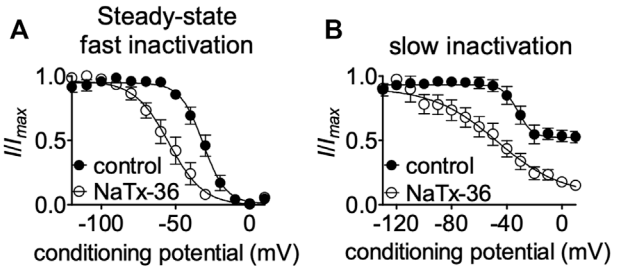

FIGURE 5 | Effects of NaTx36 on OtNav1.8 steady-state fast and slow inactivation. **(A,B)** Representative steady-state fast inactivation and slow inactivation curves before and after 100 nM NaTx36 application to ND7/23 cells transfected with recombinant OtNav1.8. Cells were pretreated with 500 nM TTX to block TTX-sensitive sodium channels. All Na^+ currents were normalized to the maximum amplitude of control peak current. **(A)** Using a double-pulse protocol, Na^+ currents were induced by a 20-ms depolarizing potential of +30 mV following a 500-ms prepulse at voltages ranging from −120 to +10 mV. Currents were plotted as a fraction of the maximum peak current. NaTx36 shifted the voltage dependence of steady-state fast inactivation to hyperpolarized membrane potentials (control, $n = 5$ cells; NaTx36, $n = 3$ cells). **(B)** Using a standard stimulus protocol, slow inactivation was induced with 5 s pre-pulses ranging from −130 to +10 mV, followed by 10 ms pulses to −80 mV to allow recovery from fast inactivation. A 20 ms test pulse to +30 mV was then used to determine the fraction of current available. Currents were plotted as a fraction of the maximum peak current. NaTx36 shifted the voltage dependence of slow inactivation to hyperpolarized membrane potentials (control, $n = 5$ cells; NaTx36, $n = 4$ cells).

NaTx36 Shifts the Voltage Dependence of OtNa$_V$1.8 Steady-State Fast and Slow Inactivation

To gain insight into mechanisms underlying NaTx36 inhibition of OtNa$_V$1.8, we determined the effects of the toxin on steady-state fast and slow inactivation. ND7/23 cells were transfected with OtNa$_V$1.8 and then pretreated with 500 nM TTX to block TTX-sensitive sodium channels. The voltage dependence of steady-state fast inactivation was measured with a double-pulse protocol where Na^+ currents were induced by a 20-ms depolarizing potential of +30 mV following a 500-ms prepulse at voltages ranging from −120 to +10 mV. Currents were plotted as a fraction of the maximum peak current. NaTx36 (100 nM) shifted the voltage dependence of steady-state fast inactivation to hyperpolarized membrane potentials (control, $n = 5$ cells; NaTx36, $n = 3$ cells) (**Figure 5A**).

Next, we asked whether NaTx36 alters the steady-state slow inactivation curve. Using a standard stimulus protocol, slow inactivation was induced with 5 s pre-pulses ranging from −130 to +10 mV, followed by 10 ms pulses to −80 mV to allow recovery from fast inactivation. A 20 ms test pulse to +30 mV was then used to determine the fraction of current available. Currents were plotted as a fraction of the maximum peak current. NaTx36 (100 nM) shifted the voltage dependence of slow inactivation to hyperpolarized membrane potentials (control, $n = 5$ cells; NaTx36, $n = 4$ cells) (**Figure 5B**).

Site-Directed Mutagenesis: Residues in the DI S4 Voltage Sensor and DII SS2 – S6 Pore Loops Are Critical for the Inhibitory Effects of Venom and NaTx36

We previously showed that AZ bark scorpion venom inhibited grasshopper mouse Na$_V$1.8 TTX-R Na^+ current while having no effect on house mouse Na$_V$1.8 (Rowe et al., 2013). This suggested that grasshopper mice had evolved amino acid substitutions in their Na$_V$1.8 that enabled venom peptides to bind the channel and block Na^+ current. We sequenced the gene (Scn10a) encoding grasshopper mice Na$_V$1.8 and found a four amino acid motif (859QVSE862) in the DII SS2 – S6 pore loop that differed from house mice (859EVSQ862) by altering the position of an acidic residue (Rowe et al., 2013). We used site-directed mutagenesis to mutate the OtNa$_V$1.8 DII SS2 – S6 loop to exchange the glutamine for the glutamic acid at position 859 (Q859E) and the glutamic acid for the glutamine at position 862 (E862Q), and demonstrated that the 859QVSE862 motif is critical for the inhibitory effects of bark scorpion venom (Rowe et al., 2013). Insertion of the glutamic acid at position 862 into the house mouse recombinant Na$_V$1.8 (mNa$_V$1.8) inhibited approximately 30% of the TTX-R Na^+ current, demonstrating that the E862 is necessary but not sufficient for the inhibitory effects of venom (Rowe et al., 2013). This suggests that other amino acids in the grasshopper mouse OtNa$_V$1.8 channel contribute to the docking and/or inhibitory activity of venom peptides. Given that the inhibitory effects of the venom are voltage dependent, we reasoned that a voltage sensor might be involved in the mechanism. To test this, we mutated the first and second GC in the OtNa$_V$1.8 DI S4 (R215G/R218G) and DII S4 (R756G/R759G) voltage sensors and measured the effect of venom on gating pore currents. Gating pore currents can serve as tools to examine the specificity with which toxins modulate Na$_V$ (**Figures 6A–C**) (Xiao et al., 2014). Cells held at −80 mV were stimulated by 50-ms hyperpolarizing steps to various potentials that ranged from −200 to +40 mV in 10-mV

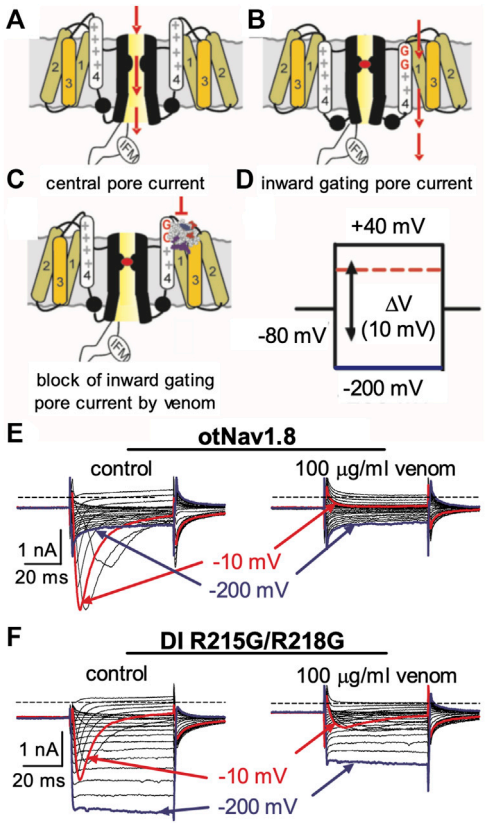

FIGURE 6 | Effects of AZ bark scorpion venom on DI inward gating pore currents. Gating pore currents were generated by glycine mutation of the first and second gating charges (two outermost arginine residues) on $OtNa_V1.8$ DI S4 (R215G/R218G). **(A–C)** Schematic diagram depicting channel central pore current **(A)**, generation of inward gating-pore current **(B)**, and block of inward gating pore current by venom **(C)**. **(D)** A typical protocol was used to elicit inward gating pore current. Cells held at –80 mV were stimulated by 50-ms hyperpolarizing steps to various potentials that ranged from –200 to +40 mV in 10-mV increments. **(E)** 100 µg/ml venom completely inhibited central pore current of wild type $OtNa_V1.8$ channels but failed to affect background leak currents. **(F)** 100 µg/ml venom only partially inhibited central pore currents recorded from $OtNa_V1.8$ mutant channels, suggesting that the double mutation (R215G/R218G) on DI S4 could reduce venom binding affinity towards $OtNa_V1.8$ channels. Venom also depressed inward gating pore currents through the DI voltage sensor domain (VSD). Blue and red traces represent typical leak current (gating pore current) and central pore current at –200 and –10 mV, respectively.

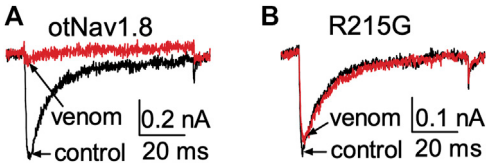

FIGURE 7 | Effects of AZ bark scorpion venom on Na^+ currents recorded from a DI S4 voltage sensor mutant. **(A)** Venom inhibits wildtype OtNav1.8 Na+ currents. **(B)** The first GC arginine (R215) in the DI S4 voltage sensor was exchanged for a glycine (R215G). TTX (500 nM) was added to the bath solution to block TTX-sensitive currents. Na^+ currents were elicited by a 50 ms depolarization to +20 mV from a holding potential of –80 mV before and after application of venom (10 µg/ml). Venom inhibited wildtype OtNav1.8, but not the DI S4 voltage sensor mutant (R215G) channels expressed in ND7/23 cells (n = 3).

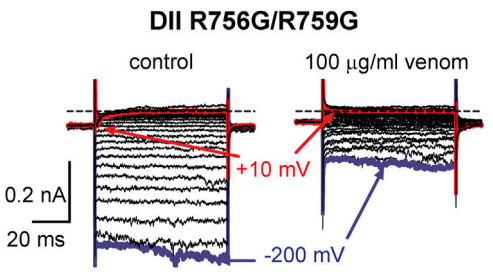

FIGURE 8 | Effects of AZ bark scorpion venom on DII inward gating pore currents. Gating pore currents were generated by glycine mutation of the first and second gating charges (two outermost arginine residues) on $OtNa_V1.8$ DII S4 (R756G/R759G). A typical protocol was used to elicit inward gating pore current (see schematic, **Figure 6D**). Cells held at –80 mV were stimulated by 50-ms hyperpolarizing steps to various potentials that ranged from –200 to +40 mV in 10-mV increments. As observed for wildtype $OtNa_V1.8$ channels, venom completely inhibited $OtNa_V1.8$ DII S4 R756G/R759G mutant channels, suggesting that the mutations did not affect venom binding affinity. Blue and red traces represent typical leak current (gating pore current) and central pore current at –200 and –10 mV, respectively.

increments (**Figure 6D**). Venom (100 µg/ml) completely inhibited central pore currents recorded from wild type $OtNa_V1.8$ channels but failed to affect background leak currents (**Figure 6E**). Venom (100 µg/ml) only partially inhibited central pore currents recorded from $OtNa_V1.8$ mutant channels, suggesting that the DI S4 double mutation (R215G/R218G) could reduce venom binding affinity towards $OtNa_V1.8$ channels (**Figure 6F**). Venom also significantly depressed inward gating pore currents through the DI voltage sensing domain, suggesting that venom might be a DI S4 gating modifier. To further examine the effects of venom on the DI S4 voltage sensor, we made a single DI mutant by mutating only the first GC R215G. Na^+ currents were elicited by a 50-millisecond depolarization to +20 mV from a holding potential of –80 mV before and after application of venom (10 µg/ml). After mutating the first GC, venom could no longer inhibit the $OtNa_V1.8$ channel (R215G, n = 3 cells) (**Figure 7**). These results suggest that the DI voltage sensor is critical for the inhibitory effects of venom. However, they also raise an interesting question regarding differences in the inhibitory effects of venom on single (first GC) and double (first and second GC) voltage sensor mutants. It is possible that the DI S4 second GC allosterically alters the conformation of the first gating charge, which in turn enhances interaction with venom toxins.

To determine if the DII S4 voltage sensor plays a role in venom inhibition, we mutated the first and second GC R756G/R759G. Venom (100 µg/ml) completely inhibited $OtNa_V1.8$ DII R756G/R759G mutant channels, suggesting that the mutation of the two outer most GC in the DII S4 voltage sensor did not affect venom binding affinity (**Figure 8**). However, while we show that venom altered gating pore currents generated by the DII voltage sensor

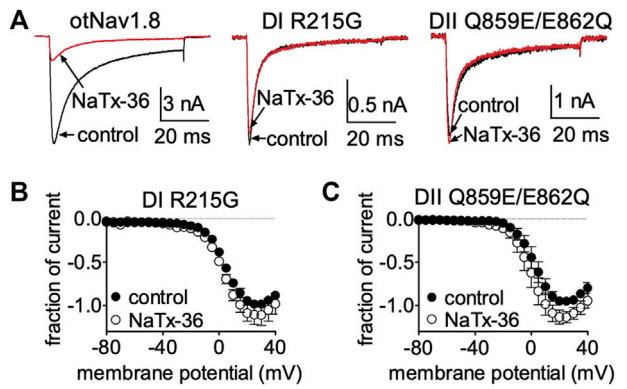

FIGURE 9 | Effects of NaTx36 on DI S4 voltage sensor and DII SS2 – S6 pore loop mutants. **(A)** Representative Na^+ current traces were elicited by a 50-ms depolarization to +20 mV from a holding potential of −80 mV before and after application of NaTx36 to ND7/23 cells transfected with either DI or DII mutant OtNav1.8. **(B,C)** To determine the fraction of current after toxin treatment, Na^+ currents were elicited by 50-ms depolarizing steps to various voltages ranging from −80 to +40 mV in 5-mV increments. All Na^+ currents were normalized to the maximum amplitude of control peak current. **(B)** NaTx36 (100 nM) did not inhibit the $OtNa_V1.8$ DI voltage sensor S4 R215G mutant (control, n = 3; NaTx36, n = 3; p = 0.23). **(C)** In addition, NaTx36 (100 nM) had no effect on the DII SS2 – S6 pore loop Q859E/E862Q mutant (control, n = 5; NaTx36, n = 5; p = 0.08). All cells were pretreated with 500 nM TTX to block TTX-sensitive sodium channels.

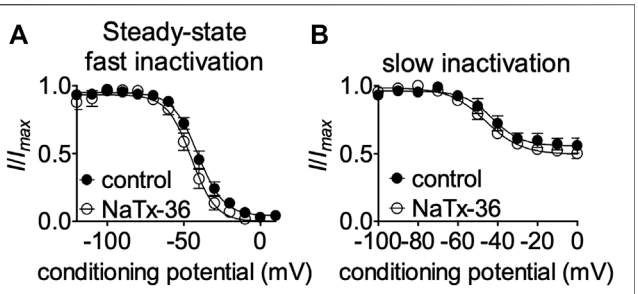

FIGURE 10 | Effects of DI S4 mutation R215G on steady-state fast inactivation and slow inactivation. **(A,B)** Representative steady-state fast inactivation and slow inactivation curves before and after 100 nM NaTx36 application to ND7/23 cells transfected with $OtNa_V1.8$ DI S4 first GC R215G mutant channels. Cells were pretreated with 500 nM TTX to block TTX-sensitive sodium channels. All Na^+ currents were normalized to the maximum amplitude of control peak current. **(A)** Steady-state fast inactivation was measured by a standard double-pulse protocol in which sodium currents were elicited by a 20-ms depolarizing potential of +30 mV following a 500-ms prepulse at voltages ranging from −120 to +10 mV. 100 nM NaTx36 did not affect steady-state fast inactivation of the R215G mutant channels (control, n = 8; NaTx36, n = 5). **(B)** Steady-state slow inactivation was measured with 5 s pre-pulses ranging from −130 to +10 mV, followed by 10 ms pulses to −80 mV to allow recovery from fast inactivation followed by a 20-ms depolarizing potential of +30 mV. 100 nM NaTx36 did not affect steady-state fast inactivation of the R215G mutant channels (control, n = 5 cells; NaTx36, n = 4 cells).

mutant R756G/R759G, we did not show if the double mutation altered the binding of venom peptides to $OtNa_V1.8$. Thus, we cannot completely rule out that the DII voltage sensor may contribute to interaction between venom peptides and $OtNa_V1.8$.

Collectively, these results suggest that venom peptides may be inhibiting $OtNa_V1.8$ via interactions with the first GC (R215) in the DI S4 voltage sensor, and with the acidic residue (E862) in the DII SS2 – S6 pore loop. To determine if these amino acids are also critical for the inhibitory effects of NaTx36, we applied the toxin to the $OtNa_V1.8$ DI S4 voltage sensor and DII SS2 – S6 pore loop mutants. Cells were pretreated with 500 nM TTX to block TTX-sensitive sodium channels. Representative Na^+ current traces were elicited by a 50-ms depolarization to +20 mV from a holding potential of −80 mV before and after application of NaTx36 to ND7/23 cells transfected with either wildtype, DI S4 (R215), or DII SS2 – S6 (Q859E/E862Q) mutant OtNav1.8 (**Figure 9A**). To determine the fraction of current after toxin treatment, Na^+ currents were elicited by 50-ms depolarizing steps to various voltages ranging from −80 to +40 mV in 5-mV increments. All Na^+ currents were normalized to the maximum amplitude of control peak current. NaTx36 (100 nM) failed to inhibit TTX-R Na^+ currents recorded from the DI voltage sensor mutant (R215G) channels. The fraction of current was 110.9% ±11.1% of control current (control, n = 3; NaTx36, n = 3; p = 0.23) (**Figure 9B**). In addition, NaTx36 (100 nM) failed to inhibit TTX-R Na^+ currents recorded from the DII SS2 – S6 pore loop (Q859E/E862Q) mutant channels. The fraction of current after toxin treatment was 136.0% ± 19.7% of control current (control, n = 5; NaTx36, n = 5; p = 0.08) (**Figure 9C**). These results suggest that the DI S4 first GC R215 and the acidic residue (E862) in the DII SS2 – S6 pore loop are critical for NaTx36 inhibition of $OtNa_V1.8$.

NaTx36 shifts the voltage-dependence of steady-state fast inactivation and slow inactivation of wildtype $OtNa_V1.8$ channels to hyperpolarized membrane potentials (**Figure 5**). Given that mutation of the DI S4 R215G abolishes the inhibitory effects of NaTx36 on wildtype $OtNa_V1.8$, we asked whether NaTx36 could still shift the voltage dependence of steady-state fast inactivation and slow inactivation of DI S4 R215G mutant channels. To test this, ND7/23 cells were transfected with DI S4 R215G mutant clones. Steady-state fast inactivation was measured by a standard double-pulse protocol in which sodium currents were induced by a 20-ms depolarizing potential of +30 mV following a 500-ms prepulse at voltages ranging from −120 to +10 mV. NaTx36 (100 nM) failed to shift the voltage dependence of steady-state fast inactivation for the R215G mutant channels (control, n = 8; NaTx36, n = 5) (**Figure 10A**). Steady-state slow inactivation was measured with 5 s pre-pulses ranging from −130 to +10 mV, followed by 10 ms pulses to −80 mV to allow recovery from fast inactivation followed by a 20-ms depolarizing potential of +30 mV NaTx36 (100 nM) also failed to shift the voltage dependence of steady-state slow inactivation for the R215G mutant channels (control, n = 5; NaTx36, n = 4) (**Figure 10B**). These data suggest that the DI S4 R215 is critical for the effects of NaTx36 on $OtNa_V1.8$ steady-state fast inactivation and slow inactivation. The data also suggest a link between toxin-induced Na^+ current inhibition and channel inactivation mechanisms.

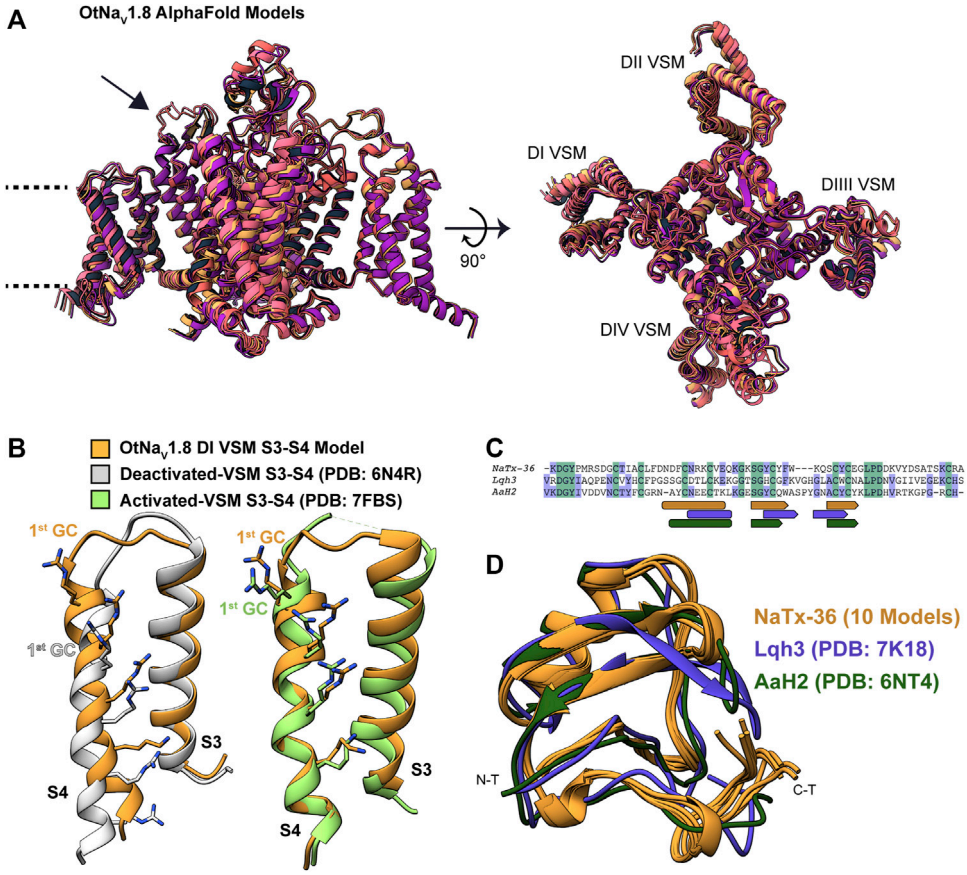

FIGURE 11 | Computational modeling of OtNa$_V$1.8 and NaTx36 structures. **(A)** Representative ribbon structures for the five top models of OtNa$_V$1.8 generated by AlphaFold; dashed lines represent approximate membrane boundaries, and the black arrow points to the DII S5 – SS1 loop. **(B)** Position of gating charges (GC) within the DI voltage sensor S4 segment of the OtNa$_V$1.8 model. DI S3 – S4 segments from the OtNa$_V$1.8 model are compared with experimental structures of activated and deactivated voltage sensor segments to illustrate that the OtNa$_V$1.8 DI S3 – S4 was modelled in the activated (outward) state. In the activated state, the first GC R215 is exposed to the extracellular solvent. **(C)** Sequence alignment of NaTx36 with two other scorpion toxins, Lqh3 and AaH2, whose biological actions on voltage-gated sodium channels are well-described; rounded rectangles indicate sequence segments corresponding to alpha-helices, and pentagons indicate beta strands. **(D)** NaTx36 models generated by AlphaFold and RosettaFold are superimposed onto the experimental structures of scorpion toxins Lqh3 and AaH2.

Computational Models: Residues in the DI S1 – S2 and S3 – S4 Linkers, and in the DII S5 – SS1 Pore Loops Are Critical for NaTx36 – OtNa$_V$1.8 Interactions

Electrophysiological analyses of OtNa$_V$1.8 DI and DII mutant channels suggest that residues in the DI S4 voltage sensor (R215) and DII pore loop SS2 – S6 (E862) are critical for the inhibitory effects of both AZ bark scorpion venom and NaTx36. To further investigate the molecular determinants underlying NaTx36 inhibition of OtNa$_V$1.8 Na^+ current, we computationally modelled the toxin protein bound to grasshopper mouse OtNa$_V$1.8.

Modeling OtNa$_V$1.8 channel: We used AlphaFold to model the OtNa$_V$1.8 channel based on Na$_V$1.8 sequence from grasshopper mice (Onychomys torridus, GenBank: KF717604.1) (**Figure 11A**). The five predicted structures showed remarkable agreement [root mean square deviation (RMSD) between backbone atoms = 0.6–0.8 Å] apart from conformational differences corresponding to the DII pore module (**Figure 11A, arrow**). The electrophysiological data from the OtNa$_V$1.8 DI S4 mutant (R215G) showed that the first GC R215 is critical for NaTx36 inhibition of OtNa$_V$1.8 (**Figure 9B**). This suggests that GC R215 in OtNa$_V$1.8 is in the activated (outward) position where it could be exposed to the toxin. We compared the relative position of GC R215 in the OtNa$_V$1.8 DI S4 segment with Protein Data Bank (PDB) experimental structures of deactivated (PDB: 6N4R) and activated (PDB: 7FBS) voltage sensors and confirmed that the position of the first GC R215 in the OtNa$_V$1.8 DI S4 voltage sensor was modelled in the outward conformation (**Figure 11B**).

Modeling NaTx36 toxin: We used RosettaFold (five models) and AlphaFold (five models) to generate models of NaTx36. The ten models demonstrated outstanding agreement [root mean square deviation (RMSD) between backbone atoms = 0.2–0.7 Å] with only minor differences in the carboxyl terminal (C-T) region (**Figures 11C,D**) that are most likely due to conformational flexibility of this region. We compared

the predicted fold of NaTx36 with the experimental structures of scorpion toxins Lqh3 (Leiurus quinquestriatus) and AaH2 (Androctonus australis) since their mechanisms of action on Na_V channels are structurally well-described (Clairfeuille et al., 2019; Jiang et al., 2021). Sequence identity between NaTx36 and Lqh3 is 29.85%, and between NaTx36 and AaH2 is 34.33% (**Figure 11C**). The overall structural folds of NaTx36, Lqh3, and AaH2 are remarkably similar; only differing slightly in the position and length of the secondary structure elements (**Figure 11D**). These differences highlight the ability of scorpions to produce functionally diverse peptide toxins from a structural core that is stabilized by multiple disulfide bonds. This unique structure-function relationship allows a large degree of sequence sampling without disrupting the original folding pattern. Notably, Lqh3, AaH2, and other scorpion peptide toxins have been reported to interact with the DIV S4 voltage sensor in sodium channels (Possani et al., 1999; Possani et al., 2000) while our experimental results suggest that NaTx36 inhibits $OtNa_V1.8$ Na^+ current through manipulation of the DI S4 voltage sensor.

Determination of amino acids in $OtNa_V1.8$ critical for binding toxin NaTx36. NaTx36 modifies $OtNa_V1.8$ gating (**Figures 4**, **5**), which suggests that NaTx36 inhibits $OtNa_V1.8$ by manipulating a channel voltage sensor. Electrophysiological characterization of the $OtNa_V1.8$ DI S4 voltage sensor mutant showed that the first GC R215 is critical for the inhibitory effects of both venom and toxin NaTx36 (**Figures 6**–**9**). To test the hypothesis that residues in the DI voltage sensor interact with NaTx36, we conducted local ensemble docking using RosettaDock4.0 (Marze et al., 2018) by placing NaTx36 in different initial positions proximal to the $OtNa_V1.8$ DI voltage sensing region. This docking protocol is a multi-scale Monte-Carlo based algorithm in which toxin protein properties (translation, rotation, backbone torsional angles, side chain rotamers) are randomly perturbed while multiple conformational ensembles from both the channel and the toxin are queried. Progression through sample space via Monte-Carlo search is scored using a predefined energy function. Perturbations are either accepted or rejected using the Metropolis criterium.

After generating approximately 20,000 models, we observed that the models converged toward an interface energy minimum (**Supplementary Figure S11**) suggesting they had reached a near-native binding conformation between NaTx36 and $OtNa_V1.8$. By analyzing the binding interface of top scoring models, we identified three regions of the channel interacting with the toxin (**Figure 12**). Regions one and two correspond to the DI voltage sensing module (S1 – S4) (**Figure 12A**). Within the voltage sensing module, the $OtNa_V1.8$ DI S1 – S2 linker has a unique QN (glutamine, asparagine) motif that is replaced by an RT (arginine, threonine) motif at corresponding positions in house mouse and human $Na_V1.8$ (**Figure 12A**). In grasshopper mice, the QN motif represents two polar uncharged residues with large side chains that replace the positively charged R and polar uncharged T (small side chain) in house mice and human Nav1.8. These changes in grasshopper mice would alter the surface charge and conformation of the DI S1 – S2 linker. The second binding interface was identified in the DI S3 – S4 linker near the extracellular end of the S4 segment (**Figure 12A**). This region is highly conserved among grasshopper mice, house mice and humans. The third binding interface was identified within the DII pore module (S5 – SS1, SS2 – S6) (**Figure 12B**). Proximal to the extracellular end of the DI voltage sensing module (**Figure 11A, black arrow**), contacts are identified in the DII S5 – SS1 loop (**Figure 12B**). This region shows a large degree of sequence variability among grasshopper mouse, house mouse and human $Na_V1.8$, and it corresponds to the region of the model that differed among AlphaFold predictions (**Figure 11A, black arrow**). These data suggest that this loop might exhibit increased conformational flexibility compared to other structural regions in the channel. Notably, the DII SS2 – S6 QVSE motif that was experimentally determined to be necessary but not sufficient for the inhibitory effects of either venom (Rowe et al., 2013) or NaTx36 (**Figure 9C**) on $OtNa_V1.8$, is located distally from the DII S5 – SS1 interacting region. The NaTx36 – $OtNa_V1.8$ model did not predict any contacts between the toxin and amino acids in the DII SS2 – S6 (**Figure 12B, orange bar**). These data suggest that while NaTx36 does not directly contact residues in the DII SS2 – S6, these residues may cause allosteric interactions with the DII S5 – SS1 loop that contribute to $OtNa_V1.8$ inhibition.

Further examination of the models of the NaTx36 – $OtNa_V1.8$ complex provided important insights into the nature of the interactions between NaTx36 and $OtNa_V1.8$ (**Figure 13**), as well as possible explanations for the importance of the DII SS2 – S6 QVSE motif observed in electrophysiological analyses of $OtNa_V1.8$ mutant channels. The models revealed that NaTx36 establishes contacts with channel residues from the three regions described above by adopting a position at the extracellular end of the DI voltage sensing module where the toxin projects its secondary structure elements toward the pore (**Figure 13A**). This NaTx36 docking pose contrasts with Lqh3 and AaH2 scorpion toxins which bind to Na_V DIV S3 – S4 linkers by positioning the beta sheet and alpha-helix away from the pore (Clairfeuille et al., 2019; Jiang et al., 2021).

Interactions with the channel DI S1 – S2 linker (**Figure 13D**) are established by toxin residues located at the bottom of the toxin alpha-helix. Detailed analysis showed favorable interactions between toxin residues L16, F17 and D18 and channel residue N150 which is uniquely present in $OtNa_V1.8$. Notably, Protein Interface Z Score Assessment (PIZSA) software analysis (Roy et al., 2019) of the binding interface revealed that these contacts between the toxin and channel residue N150 account for most of the stabilizing interactions (**Supplementary Table S1**). Channel residue D151 also interacts with the toxin, although these interactions may contribute less to the binding. Residues L16, F17 and D18 are also utilized by the toxin to engage the DII pore module by strongly interacting with C815.

The $OtNa_V1.8$ DI S3 – S4 linker also underlies relevant interactions with charged residues in the toxin (**Figure 13C**). For example, toxin residue R62, located in the C-terminal tail of NaTx36, interacts with channel residue D207. Toxin residues K40 and Q41 establish a complex set of electrostatic interactions with channel residues R209 in the DI S3 – S4 linker and R215 (first GC) in the DI S4 enabling Q41

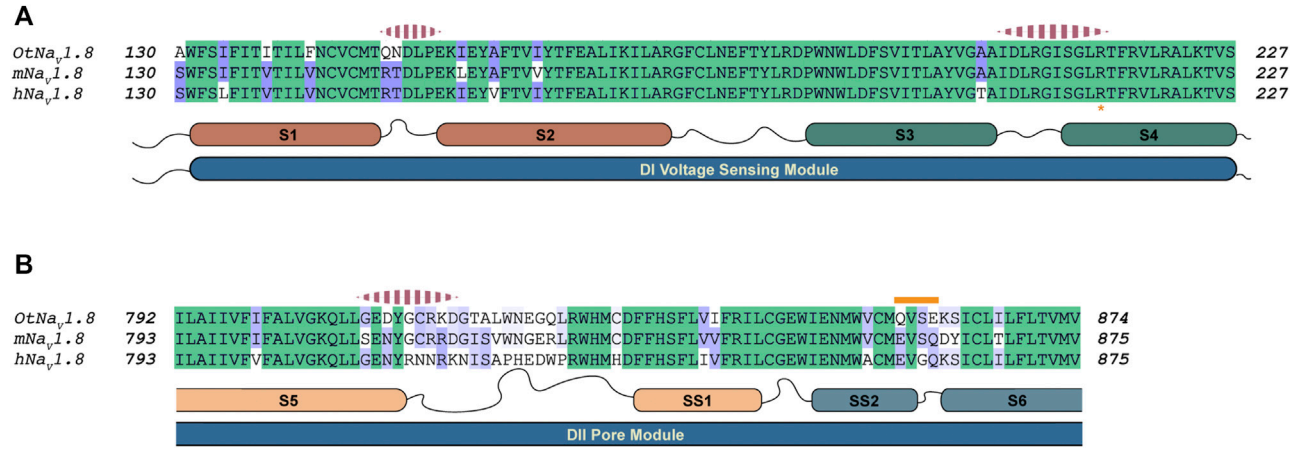

FIGURE 12 | Alignment of $Na_V1.8$ from grasshopper mice, house mice, and humans comparing predicted interaction regions between $Na_V1.8$ and NaTx36. Sequence from grasshopper mouse ($OtNa_V1.8$) DI voltage sensing module (S1 – S2 and S3 – S4) and DII pore module (S5 – SS1, SS2 – S6) was aligned with house mouse (mNav1.8) and human (hNav1.8) sequences to identify motifs uniquely present in $OtNa_V1.8$. The alignment color coding is based on sequence identity (high, green; medium, purple; low, white). Regions of the channel that were identified by docking simulations to interact with the toxin are highlighted with pink dashed segments above the corresponding channel sequence. **(A)** Sequence alignment DI voltage sensing module; Orange asterisk at the bottom of the alignment highlights the first gating charge within the S4 segment. **(B)** Sequence alignment corresponding to the second Pore module. The orange bar above the sequence highlights the QVSE motif necessary for NaTx36 inhibitory effect on $OtNa_V1.8$.

to wedge into the voltage sensor to interact with R215. This result might explain why the $OtNa_V1.8$ R215G mutant lost sensitivity to NaTx36 inhibition.

In the channel pore module, the DII S5 – SS1 loop interacts with NaTx36 through a set of aromatic (F17, Y35, Y37, F38, W39) and polar uncharged (N19) residues (**Figure 13B**). Channel residues C815, R816 and K817 interact strongly with toxin residue N19, accounting for the second most important hotspot identified by PIZSA (**Supplementary Table S1**). In addition, toxin aromatic residues interact with channel residues Q807, E811 and R816, although it is possible that these residues are also important for membrane embedding.

To explain the observation that the QVSE motif in the DII SS2 – S6 loop is required for the inhibitory effect of the toxin, we located these residues in our model (**Figure 13B**, blue segment). We observed that, although these residues are located far from the interface with NaTx36, they closely interact with the DII S5 – SS1 region, which our model predicts is crucial for toxin binding. This observation together with the variability observed in the predicted structure for DII S5 – SS1 loop by AlphaFold, suggests that this loop might have relatively high conformational flexibility. If so, interactions with the QVSE motif in DII SS2 – S6 might modulate the relative occupancy of different conformational states and, thus, affect NaTx36 toxin binding. To test this hypothesis, we used AlphaFold to model $OtNa_V1.8$ with the QVSE motif changed to EVSQ (Q859E/E862Q) (**Figure 14**). We found that AlphaFold predicts two different conformations of the DII S5 – SS1 loop for the WT $Na_V1.8$. However, all mutant Q859E/E862Q – OtNaV1.8 models presented the same conformation in this loop. Interestingly, the loop conformation present in our model of NaTx36 bound to WT $OtNa_V1.8$ is the one missing in the mutant models. These results suggest a role for the QVSE motif in regulating DII S5 – SS1 loop conformational flexibility. Future experimental testing to confirm functional differences should be conducted to evaluate this hypothesis.

DISCUSSION

AZ bark scorpion venom inhibits grasshopper mouse $Na_V1.8$ Na^+ current and blocks transmission of pain signals to the brain (Rowe et al., 2013). We fractioned bark scorpion venom and showed that subfraction F11-E inhibits a recombinant grasshopper mouse $Na_V1.8$ channel ($OtNa_V1.8$) (Mohamed Abd El-Aziz et al., 2021). We chemically synthesized the four peptide toxins (NaTx4, NaTx13, NaTx22, NaTx36) identified from F11-E and tested them on $OtNa_V1.8$. Toxin NaTx36 inhibits $OtNa_V1.8$ Na^+ current in a concentration and voltage dependent manner (**Figures 2–4**). To gain insight into the molecular basis underlying NaTx36 inhibition of $Na_V1.8$, we determined the biological action of NaTx36 on $OtNa_V1.8$ and identified amino acids that are critical for the toxin-channel interaction complex.

NaTx36 Enhances Grasshopper Mouse $Na_V1.8$ Channel Activation Through a Three-Point Binding Motif

Whole-cell patch clamp electrophysiology demonstrated that NaTx36 lowers the threshold for channel opening by shifting the voltage dependence of activation to hyperpolarized membrane potentials. Current-voltage curves show that in the presence of NaTx36, $OtNa_V1.8$ channels begin to open around −60 mV (**Figure 4**). This suggests that the biological action of NaTx36 is like scorpion β-toxins, which enhance activation through a voltage sensor trapping mechanism. The mechanism proposes that scorpion β-toxins bind Na_V at rest and then trap

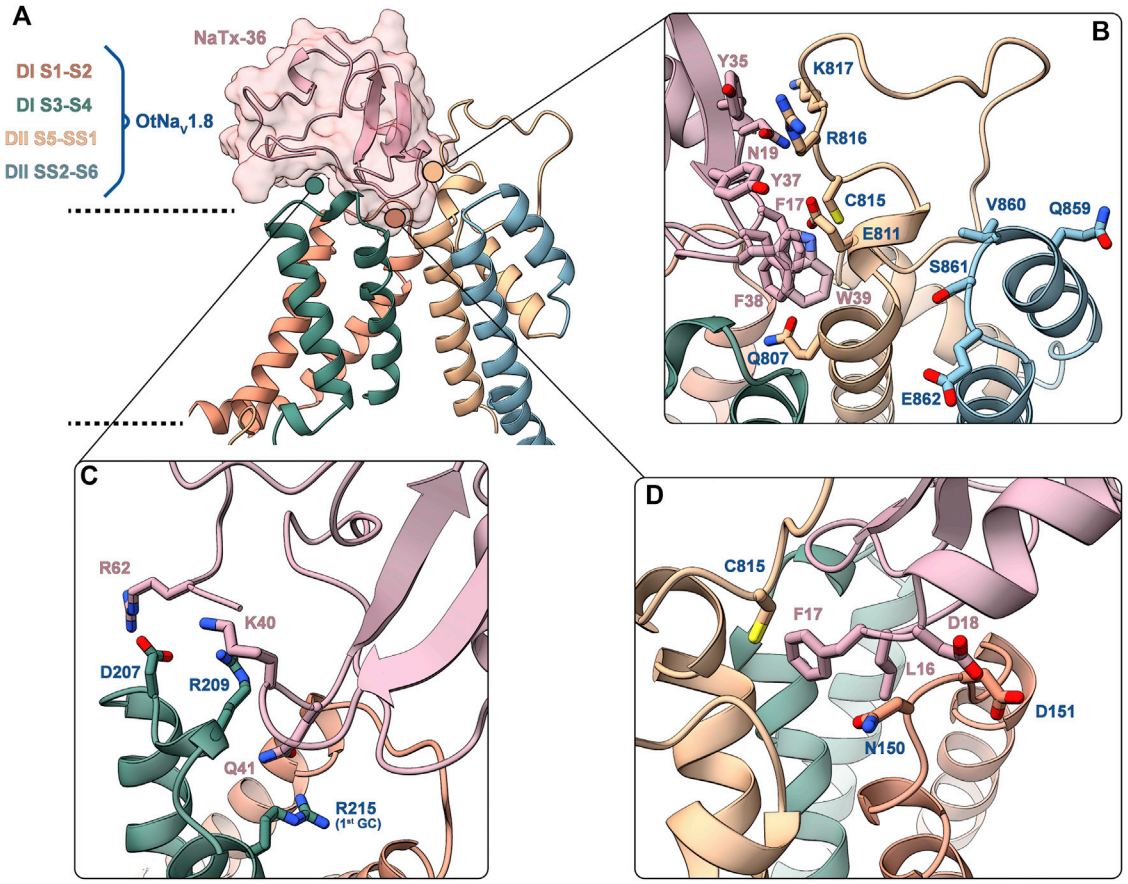

FIGURE 13 | Predicted binding interface between NaTx36 and OtNa$_V$1.8. **(A)** Binding interface overview. Dashed lines represent approximate membrane boundaries. Cartoon representation is used for both the channel and the toxin, the molecular surface of NaTx36 is shown with transparency. **(B)** DII S5 – SS1 – NaTx36 interface. QVSE motif within SS2 – S6 is colored blue. **(C)** DI S3 – S4 – NaTx36 interface. **(D)** DI S1 – S2 – NaTx36 interface. Side chains for residues of interest are shown in stick representation.

the DII S4 voltage sensor in the activated (outward) position, increasing the probability that channels will open at or near resting membrane potentials (Qu et al., 1998; Cestèle and Catterall, 2000; Catterall et al., 2007). Scorpion β-toxins have a three-point binding site on Na$_V$ where the wedge-shaped toxins fit into a solvent accessible cleft formed by the DII voltage sensing module S1 – S2 and S3 – S4 linkers, and the neighboring DIII SS2 – S6 pore loop (Zhang et al., 2011; Zhang et al., 2012). The primary binding site includes residues in the DII S3 – S4 linker that are critical for β-toxins to trap the S4 voltage sensor (Zhang et al., 2011). Secondary binding sites include residues in the DII S1 – S2 linker and the DIII SS2 – S6 pore loop (Zhang et al., 2012). Na$_V$ three-dimensional channel structure is organized such that the voltage sensing module (S1 – S4) of each domain is adjacent to the pore module (S5 – S6) of its neighboring domain (domain swapping). Thus, the three points of the DII/DIII β-toxin binding motif are physically close. In contrast to the typical β-toxin DII/DIII binding motif, site-directed mutagenesis and computational models in this study demonstrate that NaTx36 uses residues in the DI voltage sensor and DII pore module to inhibit OtNa$_V$1.8. A comparison of gating pore currents from DI S4 (R215G/R218G) and DII S4 (R756G/R759G) double mutant channels suggest that the DI S4 voltage sensor is critical for venom inhibition of OtNa$_V$1.8 (**Figures 6**, **8**). A DI S4 (R215G) single mutant channel confirmed that the first GC (R215) in the DI S4 voltage sensor is critical for the inhibitory effects of venom (**Figure 7**) and NaTx36 (**Figure 9**). Moreover, the DII mutant channel showed that the pore loop SS2 – S6 Q859E/E862Q motif is important for the inhibitory effects of NaTx36. While the data suggest that NaTx36 employs a DI/DII binding motif as opposed to the characteristic β-toxin DII/DIII motif, the DI/DII reflects a similar domain swapping arrangement that enables the toxin to modulate channel gating via the voltage sensing module.

Computational modeling of the NaTx36 – OtNa$_V$1.8 complex supported the experimental electrophysiological data showing that the DI voltage sensor and the DII pore module are critical for NaTx36 activity. However, the models revealed additional details on residues that mediate toxin-channel interactions. First, NaTx36 and OtNa$_V$1.8 establish a highly stable complex through interactions between toxin residues L16, F17, and D18 with channel residue N150 in the DI S1 – S2 linker (**Figure 13D**). NaTx36 also forms electrostatic interactions between toxin

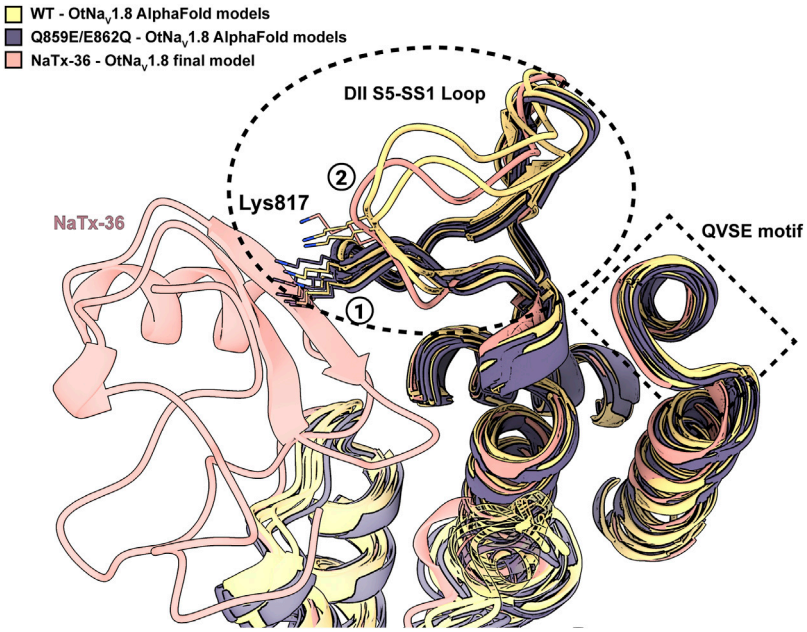

FIGURE 14 | DII S5 – SS1 loop conformations in WT-OtNa$_V$1.8 and mutant SS2 – S6 Q859E/E862Q – OtNa$_V$1.8. AlphaFold models predict two different conformations for the DII S5 – SS1 loop in the WT channel (see circled 1 and 2); three models in the first conformation and two in the second (yellow models). The second loop conformation is the one predicted by RosettaDock to bind NaTx36 (pink model). However, the second loop conformation is not present in the predicted models for the mutant channel. In the mutant channel SS2 – S6 Q859E/E862Q – OtNa$_V$1.8, the DII S5 – SS1 loop was modelled by AlphaFold only in the first conformation observed for the WT (black models). Interestingly, superimposed models predict a steric clash between channel residue Lys817 and NaTx36 if the DII S5 – SS1 loop occupies the first conformation.

residues R62 and K40 and channel residues D207 and R209 in the DI S3 – S4 linker, and toxin residue Q41 with the DI S4 GC R215 (**Figure 13C**). This motif enables toxin residue Q41 to wedge into the DI voltage sensor to interact with the first GC R215. Further, the models predicted that instead of directly contacting residues in the DII SS2 – S6 pore loop, toxin residues L16, F17, and D18 interact with residue C815 in the channel DII S5 – SS1 pore loop, establishing a link between the toxin and domains DI and DII. Models of the mutant QVSE/EVSQ channel predict that the QVSE motif in the DII SS2 – S6 loop allosterically alters the conformation of the S5 – SS1 loop to enhance toxin-channel interactions. The toxin and channel DI/DII complex may be further stabilized by interactions between a set of aromatic (F17, Y35, Y37, F38, W39) and polar uncharged (N19) residues in NaTx36 and residues C815, R816 and K817 in the channel DII S5 – SS1 pore loop.

Collectively, the site-directed mutagenesis and modeling analyses suggest that NaTx36 enhances activation of OtNa$_V$1.8 via a three-point binding motif that includes direct and allosteric interactions with residues in the DI voltage sensing module (S1 – S2 and S3 – S4 linkers, S4 segment) and the DII pore module (S5 – SS1 and SS2 – S6 loops). This motif suggests a potential mechanism for NaTx36 to dock with OtNa$_V$1.8 and then trap the DI S4 voltage sensor in the outward position, enhancing channel activation. While the majority of scorpion β- and α-toxin studies suggest that voltage sensors in DII and DIV, respectively, are the primary targets, other systems provide examples of how toxin binding/activity relationships involve additional channel domains. For example, Xiao et al. showed that the spider toxin ProTx-II interacts with a sodium channel DI voltage sensor to modify the voltage dependence of gating pore currents (Xiao et al., 2014). However, the DII S4 voltage sensor was the most critical sensor for interactions with ProTx-II. Using cryo-EM, Clairfeuille et al. discovered that the scorpion α-toxin AaH2, which blocks fast inactivation, binds a site in the DI voltage sensing module in addition to its high affinity binding site in the DIV voltage sensor (Clairfeuille et al., 2019). Given that NaTx36 hyperpolarizes the voltage dependence of OtNa$_V$1.8 steady-state fast inactivation, and DIII and DIV play a role in fast inactivation, future work on the NaTx36 – OtNa$_V$1.8 complex should investigate the effects of NaTx36 on the DIII and DIV voltage sensors.

NaTx36 Modifies Grasshopper Mouse Na$_V$1.8 Fast Inactivation Gating

Na$_V$ S4 voltage sensors respond to depolarizing membrane potentials by moving outward. Movement of the DI – DIII voltage sensors combined with partial movement of the DIV voltage sensor initiates opening of the channel activation gate; movement of the DIV voltage sensor triggers fast inactivation gating (Armstrong, 2006; Gilchrist and Bosmans, 2018). As described above, NaTx36 enhances OtNa$_V$1.8 opening by lowering the threshold for channel activation. In addition, NaTx36 modifies steady-state fast inactivation gating in OtNa$_V$1.8 by substantially shifting the voltage dependence to

hyperpolarized potentials (**Figure 5A**). Notably, few scorpion toxins have been characterized in terms of their effects on the voltage dependence of fast inactivation gating. Typically, scorpion toxins are characterized regarding effects on the voltage dependence of activation (β-toxins trap the DII voltage sensor in the outward position, shifting activation to hyperpolarized potentials that open channels) or effects on fast inactivation kinetics (α-toxins trap the DIV voltage sensor in the inward position, delaying fast inactivation gating) (Qu et al., 1998; Cestèle and Catterall, 2000; Catterall et al., 2007; Campos et al., 2008; Clairfeuille et al., 2019). However, the relationship between activation and inactivation gating, and how toxins alter the voltage dependent properties of that relationship, can provide insight into channel availability. For example, the scorpion β-toxin BMK I shifts the voltage dependence of both activation and fast inactivation gating to hyperpolarized potentials in rat $Na_V1.8$, causing an increase in small diameter DRG TTX-R Na^+ current and pain-related behavior (Ye et al., 2015). Similarly, the recently described tarantula toxin β-theraphotoxin-Eo1a activates $Na_V1.8$ and causes pain in house mice by hyperpolarizing activation and steady-state fast inactivation (Deuis et al., 2021). The DIV voltage-sensor-binding toxins Hm1a and LqqIV shift the voltage dependence of $Na_V1.1$ fast inactivation gating to depolarized potentials, increasing channel availability and window currents (Osteen et al., 2017). These window currents were attributed to toxin effects on fast inactivation gating as opposed to delayed inactivation kinetics. In contrast, the cobra toxin Na1a inhibits rat $Na_V1.8$ activity by depolarizing activation and hyperpolarizing fast inactivation (Zhang et al., 2019). Collectively, these studies highlight the importance of examining the effects of toxins on the voltage dependence of activation and inactivation gating to determine how toxins alter channel excitability. Further examination of the effects of NaTx36 on $OtNa_V1.8$ activation and fast inactivation gating will be critical for estimating channel availability, and for determining whether decreased availability underlies NaTx36 inhibition of $OtNa_V1.8$.

NaTx36 Modifies Grasshopper Mouse $Na_V1.8$ Slow Inactivation Gating

In addition to modifying activation and fast inactivation gating, NaTx36 modifies slow inactivation gating in $OtNa_V1.8$ by substantially shifting the voltage dependence to hyperpolarized membrane potentials (**Figure 5B**). Slow inactivation differs from fast inactivation in voltage- and time-dependent properties. While fast inactivation inhibits Na_V excitability within milliseconds of action potential firing, slow inactivation develops in response to prolonged membrane depolarization (tens of seconds) or a series of action potentials, inhibiting Na_V excitability over longer timescales (seconds to minutes) (Vilin and Ruben, 2001; Ulbricht, 2005; Gawali et al., 2016; Ghovanloo et al., 2016). Transition into the slow inactivated state is characterized by a decrease in Na^+ current amplitude due to a reduction in the population of channels available to fire action potentials. The number of channels rendered unavailable during slow inactivation is proportional to the duration and frequency of the membrane depolarizations that initiate slow inactivation. For example, Blair and Bean (Blair and Bean, 2003) demonstrated that nociceptive sensory neurons transitioned into the slow inactivated state following prolonged electrical and chemical stimulation. Sustained excitation of DRG membranes by either electrical stimulation or capsaicin caused a decrease in $Na_V1.8$ TTX-R Na^+ currents and action potential firing. More recently, Zhang and Bean showed that cannabidiol (CBD) inhibited house mouse $Na_V1.8$ in a state-dependent manner that decreased channel availability (Zhang and Bean, 2021). During depolarizing potentials, CBD induced fast binding to inactivated channels, while repolarizing potentials induced slow unbinding from channels. Zhang and Bean concluded that CBD reduces repetitive action potential firing and DRG neuronal excitability by enhancing the slow inactivated state of $Na_V1.8$. Thus, the hyperpolarizing effects of NaTx36 on $OtNa_V1.8$ slow inactivation may contribute to inhibition of Na^+ current by reducing the population of available channels. Given that NaTx36 also hyperpolarizes $OtNa_V1.8$ activation and fast inactivation, it is plausible that the relationship between activation and fast inactivation gating prolong the excitability of $OtNa_V1.8$ or induce repetitive action potentials, triggering channel transition to a slow inactivated state. Moreover, to reverse slow inactivation, membranes must be hyperpolarized. Holding $OtNa_V1.8$ at hyperpolarized potentials reduced the inhibitory effects of NaTx36 (**Figure 4**). Further examination of activation-inactivation (fast and slow) gating relationships, and how toxins alter those relationships, will be critical for characterizing the mechanisms underlying NaTx36 inhibition of $OtNa_V1.8$.

Summary and Conclusion

In primary sensory nociceptive neurons, $Na_V1.8$ is crucial for transmitting pain signals to the brain. Given that $Na_V1.8$ is linked to neuropathic and inflammatory pain, it has the potential to serve as a drug target. However, the mechanisms that regulate $Na_V1.8$ gating are not completely understood. While animal-derived toxins have provided tools for examining structure-activity relationships in several Na_V, fewer toxins have been identified that modify $Na_V1.8$ gating (Ye et al., 2015; Zhang et al., 2019; Deuis et al., 2021). AZ bark scorpions produce venoms rich in peptide toxins that modify the gating mechanisms of Na^+ ion channels in nerve and muscle tissue (Jaimovich et al., 1982; Couraud et al., 1984; Possani et al., 1999; Corona et al., 2001; Rodríguez de la Vega and Possani, 2005; Carcamo-Noriega et al., 2018). Toxins induce extreme pain in sensitive animals (Rowe et al., 2011; Rowe et al., 2013; Niermann et al., 2020). Southern grasshopper mice prey on bark scorpions, having evolved reduced sensitivity to pain-inducing toxins via amino acid substitutions in Nav1.8 (Rowe and Rowe, 2006; Rowe and Rowe, 2008; Rowe et al., 2013). In this study, we tested four synthetic versions of peptide toxins (NaTx4, NaTx13, NaTx22, NaTx36) identified from a subfraction of AZ bark scorpion venom that inhibited a recombinant grasshopper mouse $Na_V1.8$ channel ($OtNa_V1.8$). Of the four peptides, NaTx36 inhibited $OtNa_V1.8$ in a concentration and voltage dependent manner recapitulating the effects of venom. Interestingly, NaTx36 hyperpolarized the voltage dependence of $OtNa_V1.8$

activation, fast inactivation, and slow inactivation gating. Site-directed mutagenesis and computational modeling demonstrated that NaTx36 interacts with $OtNa_V1.8$ via amino acids in the DI voltage sensor and DII pore module, as opposed to most scorpion β-toxins that interact with Na_V via residues in the DII voltage sensor and DIII pore module. Thus, interactions between NaTx36 and $OtNa_V1.8$ provide a novel system for investigating links between activation – inactivation gating relationships, Na_V channel availability, and mechanisms that inhibit $Na_V1.8$ activity and pain-related behavior. Moreover, NaTx36 may serve as a template for structure-guided development of Na_V targeting peptides to treat pain without addiction (Nguyen and Yarov-Yarovoy, 2022).

METHODS AND MATERIALS

Venom Extraction

AZ bark scorpions were collected from the Santa Rita Experimental Range (University of Arizona, Santa Rita Mountains, AZ, United States). Crude venom was extracted from the venom glands using electrical stimulation according to previously published protocols (Clairfeuille et al., 2019). The crude venom samples were hydrated in sterile water, centrifuged, and filtered (0.45 µm sterile filter) to remove insoluble components. Aliquots of the supernatant (hereafter referred to as venom) were lyophilized and stored at −80°C.

Toxin Peptide Synthesis

Peptide toxins NaTx4, NaTx13, NaTx22, and NaTx36 were chemically synthesized by SB-PEPTIDE (SmartBioscience SAS, France) using the amino acid sequence of peptide primary structures previously determined (Mohamed Abd El-Aziz et al., 2021). Peptides were assembled stepwise using Fmoc-based Solid Phase Peptide Synthesis (SPPS) on a PTI Symphony synthesizer on resin. The Fmoc protecting group was removed using 20% piperidine in DMF and free amine was coupled using tenfold excess of Fmoc amino acids and HCTU/DIEA activation in NMP/DMF (3 × 15 min). Linear peptides were de-protected and cleaved from the resin with a cleavage cocktail, then precipitated out in cold diethyl ether. The resulting white solids were washed twice with diethyl ether and re-suspended. Oxidative folding of the crude linear peptides was conducted at room temperature (RT) in oxidative conditions. Final peptides were purified using Reverse-Phase High Performance Liquid Chromatography (RP HPLC). Samples were injected into a C18 column (150 × 4.6 mm, 130 Å, 2.5 µm) using the following gradient:

Time (min)	%B
0	5
2	5
22	60
22.1	95
27	95

Buffer A = 0.1% TFA in H20 and Buffer B = 0.1% TFA in acetonitrile. Peptides were controlled by ESI-HRMS and HPLC on Agilent systems, then freeze-dried. SB-PEPTIDE confirmed the mass using Liquid Chromatography Mass Spectrometry (LC MS) (copies of the SB-PEPTIDE Certificate of Analysis, HPLC, and MS data available upon request). Peptides were quantified using OD280 and checked using Nanodrop at 205 nM wavelength. The purity, intact mass and amino acid sequence of each peptide was then validated by co-authors in this study using HPLC, LC MS, and bottom-up MS/MS, respectively (see **Sections 4.3** and **4.4** below for method details, see also **Supplementary Figures S1–S8**).

LC-MS Validation of Synthetic Toxin Peptides

BioPharma Finder 4.1 (Thermo Scientific) was used for deconvoluting the intact mass spectrum of synthetic peptide toxins (NaTx36, NaTx4, NaTx13, NaTx22), using the Xtract algorithm to calculate the monoisotopic mass. A fit factor of 0.65 was applied together with a signal-to-noise ratio cutoff of 3. Bottom-up proteomics data were searched using the SEQUEST algorithm included in Proteome Discoverer 4.0 (Thermo Scientific) against a custom database containing the non-processed sequence (i.e., signal peptide included) of (NaTx36, NaTx4, NaTx13, NaTx22). The following search parameters were used in SEQUEST: precursor mass tolerance 10 ppm; fragment mass tolerance 0.1 Da; carbamidomethylation as dynamic modification of Cysteines.

Mass Spectrometry-Base Validation of Synthetic Toxin Peptides

The intact forms of the synthetic peptide toxins NaTx36, NaTx4, NaTx13, and NaTx22 were analyzed after proteolysis to confirm the primary structure and the absence of modifications using liquid chromatography on-line coupled to mass spectrometry (LC-MS). All mass spectrometry measurements were performed on an Orbitrap Eclipse mass spectrometer (Thermo Scientific, San Jose, CA, United States), while liquid chromatography analysis of the whole toxin or its proteolytic peptides was carried out using an Ultimate 3000 UHPLC chromatographic system (Thermo Scientific). For all LC-MS runs, the mobile phases were composed as follows: mobile phase A, 5% acetonitrile (v/v) and 0.2% formic acid (v/v) in water; mobile phase B, 5% water (v/v) and 0.2% formic acid (v/v) in acetonitrile. All solvents were LC-MS grade. For intact mass determination, the synthetic sample was desalted using C4 ZipTips (MilliporeSigma, St. Louis, Missouri) and about 200 ng were loaded onto a nanobore column (100 µm × 200 mm) in-house packed with PLRP-S (Agilent, Santa Clara, California). Separation was conducted using a 45 min gradient, and electrosprayed toxin cations were detected over a 400–2,000 m/z window using 120,000 resolving power (at m/z 200), with the Orbitrap Eclipse set in "protein mode". For bottom-up proteomics, 5 µg of sample were dissolved in 8 M guanidinium chloride and denatured by heating at 100°C for 30 min. Disulfide bond reduction was then performed using

200 mM tris(2-carboxyethyl)phosphine for 30 min at 100°C, and was followed by Cys alkylation incubating the sample with 25 mM iodoacetamide for 20 min at 37°C in the dark. Guanidinium chloride was then diluted to 0.5 M using 100 mM Tris-HCl at pH 8.5 and the sample was digested using 0.4 µg of trypsin for 18 h at 37°C under shaking. Proteolytic peptides were desalted using a C18 spin column (Thermo Scientific) according to the manufacturer's instructions. LC-MS experiments were based on a commercial trap and analytical nanobore C18 column (Acclaim PepMap, 75 µm × 150 mm, Thermo Scientific) and separation was conducted over a 45 min gradient. The Orbitrap Eclipse was operated in "peptide mode" using a Top-S data-dependent acquisition method (3 s cycle); broadband spectra were collected over a 375–2,000 m/z window using 120,000 resolving power (at m/z 200), while peptides were fragmented via higher-energy collisional dissociation (NCE = 35%) and tandem mass spectra were recorded in the Orbitrap at 15,000 resolving power (at m/z 200). Dynamic exclusion was set to 30 s.

Culture and Transfection of ND7/23 Cells

Venom and NaTx36 samples were screened for inhibitory activity against a recombinant Nav1.8 clone from grasshopper mice. The gene encoding O. torridus Nav1.8 was inserted into a plasmid with a fluorescent marker (pcDNA3.1-EGFP) for expression in a hybrid cell line (ND7/23). The recombinant Nav1.8 clone is referred to as OtNav1.8. ND7/23 cells were purchased from Novagene [European Collection of Cell Cultures (ECCC), Salisbury, United Kingdom] and cultured under standard conditions according to guidelines provided by the ECCC (37°C in a humidified incubator supplying 5% CO_2, in Dulbecco's modified Eagle medium supplemented with 10% fetal bovine serum and 1% penicillin-streptomycin). For patch clamp recording (see below), ND7/23 cells were plated on cover glass chips treated with 0.01% Poly-L-lysine (Sigma, St. Louis, MO, United States). Plated cells were transfected with plasmids encoding α-, β1-, and β2-OtNav1.8 subunits genetically linked to NH2-terminal eGFP using Lipofectamine 3000 reagent (L3000015, Invitrogen, Carlsbad, CA, United States), as described in the manufacturer's protocol. In brief, 60% confluent cells in a 35-mm dish were treated with 14 µg of total plasmid cDNA for 24–48 h. Cells exhibiting green fluorescence were used for patch clamp recording.

Electrophysiology Recording

Whole-cell patch clamp electrophysiology was used to record the effects of venom and peptide toxins on $OtNa_V1.8$ Na^+ current expressed in ND7/23 cells. Lyophilized venom and toxin peptide samples were hydrated in sterile, double distilled water to make stock solutions. Concentrations of stock solutions were confirmed using the average of three nanodrop readings. Samples of venom and peptide toxins were then diluted in external bath solution (containing in mM: 140 NaCl, 3 KCl, 1 $MgCl_2$, 1 $CaCl_2$, and 10 HEPES; pH was adjusted to 7.3 with NaOH) to the desired final concentration. Tetrodotoxin (TTX; 500 nM) was added to the bath solution when recording recombinant $OtNa_V1.8$ currents from ND7/23 cells to remove TTX-sensitive Na^+ currents. The whole-cell membrane currents were recorded at room temperature (21–24°C) using a low noise patch clamp amplifier (Axopatch 200B) interfaced via a Digidata 1550B system to a PC running the pClamp 11 software (Axon Instruments, Molecular Devices, San Jose, CA, United States). All currents were filtered at 1 kHz. Patch pipettes were pulled from borosilicate glass capillaries (World Precision Instruments, Inc., FL, United States) using either a P-97 or P-1000 Flaming/Brown micropipette puller (Sutter Instrument, Novato, CA, United States) and fire-polished on a micro-forge (MF-830; Narishige Scientific Instrument, Japan). The initial resistance was 0.8–1.5 MΩ when filled with the pipette internal solution (containing in mM: 140 CsF, 10 NaCl, 1.1 EGTA, and 10 HEPES; pH adjusted to 7.3 with CsOH). Current traces were evoked by a 100-millisecond depolarizing potential of +20 mV from the holding potential at −80 mV. Current–voltage curves were generated by voltage-clamp protocols consisting of a holding potential of −80 mV followed by a series of 50-ms depolarizations from −80 to +60 mV in 5-mV increments. In the hyperpolarization experiments, the current–voltage curve was generated by voltage-clamp protocols consisting of a holding potential of −120 mV for 30 s followed by a series of 50-ms depolarizations from −80 to +60 mV in 5-mV increments. All venom and venom protein effects were compared to baseline values obtained in vehicle (bath solution) in the same cell. After control responses were obtained, samples of either venom or peptide toxin NaTx36 (concentrations ranging from 0.1 to 25 µg/ml) were added to the chamber (either 87 or 250 µl total volume) and protocols were repeated. The pClamp 11.1 software (Axon Instruments, Molecular Devices) was used for signal acquisition and analysis. The data were filtered at 1 kHz and digitized at 1 kHz using a data acquisition interface 1550B (Axon Instruments, Molecular Devices, San Jose, CA, United States). The whole cell capacitance transient and series resistances were compensated (70%–85%).

Statistics

Data were analyzed and plotted using ClampFit 11.1 (Molecular Devices), GraphPad Prism 9 (GraphPad Software, Inc., San Diego, CA, United States) and OriginPro 2021b (OriginLab Corp. Northampton, United States). Summarized whole-cell current data are reported as the mean ± SEM of the $OtNa_V1.8$ current density. Summarized data were compared using Student's unpaired t-test, with $p < 0.05$ considered significant. The half inhibitory concentration (IC_{50}) of NaTx36 on $OtNa_V1.8$ channels was estimated by fitting the data to a Dose-response equation with variable Hill slope [y = A1 + (A2 - A1)/(1 + 10^((Log X0 – X) * p))] where A1 = bottom asymptote, A2 = top asymptote, Log X0 = center, and p = Hill slope.

Site-Directed Mutagenesis

Site-directed mutagenesis was conducted to introduce mutations into the DI voltage sensor and the DII pore module of the OtNav1.8 recombinant channel. Mutations were introduced using either Agilent QuikChange II (Agilent Technologies, Inc., Santa Clara, CA, United States) or New England Biolabs Q5 (Ipswich, MA, United States) site-directed mutagenesis kits, according to the manufacturer's protocol. PCR products were used to transform DH5α competent cells (New England Biolabs). Mutations were confirmed using sanger sequencing.

Primers

R215G forward: 5′-CGAGGAATCTCAGGCCTAGGGACA TTCCG-3′
R215G reverse: 5′-CGGAATGTCCCTAGGCCTGAGATT CCTCG-3′
R215G/R218G forward: 5′-CCTAGGGACATTCGGAGT TCTCAGGGCC-3′
R215G/R218G reverse: 5′-GGCCCTGAGAACTCCGAATGT CCCTAGG-3′
E862Q forward: 5′-GGTCTGCATGCAAGTCAGTCAGAA ATCCATCTGC-3′
E862Q reverse: 5′-GCAGATGGATTTCTGACTGACTTG CATGCAGACC-3′
Q859E/E862Q forward: 5′-GGTCTGCATGGAAGTCAG TCAGAAATCCATCTGC-3′
Q859E/E862Q reverse: 5′-GCAGATGGATTTCTGACTGAC TTCCATGCAGACC-3′
R756G/R759G forward: 5′-TCTGTGCTTGGGACCTTCGGT TTGCTGCG-3′
R756G/R759G reverse: 5′-CGCAGCAAACCGAAGGTCCCA AGCACAGA-3′

$OtNa_V1.8$ Modeling

The complete sequence for $Na_V1.8$ from grasshopper mice (O. torridus, GenBank: KF717604.1) was trimmed to remove N and C terminal intracellular regions as well as two, large intracellular interdomain loops that are usually not resolved in available experimental structures of mammalian sodium channels. Trimmed sequence was used as input for AlphaFold (Jumper et al., 2021) in Google Colab (Mirdita et al., 2021) with 24 max recycles. Five models of OtNaV1.8 were generated and optimized using Rosetta FastRelax protocol (Conway et al., 2014) and ref2015 energy function (Alford et al., 2017).

NaTx36 Modeling

NaTx36 amino acid sequence (Mohamed Abd El-Aziz et al., 2021) was used as input for AlphaFold and RosettaFold (Baek et al., 2021) to generate 10 models, 5 with each method. Resulting models were fast relaxed as performed for $OtNa_V1.8$ models.

Computational Docking of NaTx36 to $OtNa_V1.8$ DI Voltage Sensing Module

Relaxed models of both toxin and channel were used to generate conformational ensembles as previously described (Marze et al., 2018). NaTx36 was located in three different initial positions and orientations around the $OtNa_V1.8$ DI voltage sensing module (S1 – S4) to generate the inputs for RosettaDock4.0 (Marze et al., 2018). Approximately 20,000 docked models were generated and analyzed. Automatic analysis and counting of interacting residues from top scoring models were accomplished by making use of the Protein Interface Z Score Assessment (PIZSA) software (Roy et al., 2019). Selection of the final model was based on the lowest interface score (I_sc).

Molecular Graphics Visualization

All models were processed and analyzed using UCSF ChimeraX (Goddard et al., 2018).

DATA AVAILABILITY STATEMENT

The gene encoding Onychomys torridus scn10a and the dataset for the AZ Bark scorpion venom gland transcriptome can be found in the following repositories: https://www.ncbi.nlm.nih.gov/genbank/, KF717604; https://www.ncbi.nlm.nih.gov/genbank/, PRJNA340270. The electrophysiology, mass spectrometry, and computational modeling datasets for this study are available upon request.

AUTHOR CONTRIBUTIONS

Conceptualization, YX, VY-Y, MR and AR; methodology and data collection, KG, DL-M, TE-A, YX, VY-Y, LF, JK, HB, SR, MR and AR; software, DL-M, VY-Y and AR; validation, DL-M, VY-Y, LF, JK and AR; formal analysis, KG, DL-M, TE-A, YX, VY-Y, LF, JK, MR and AR; resources, VY-Y, TC, JS, LF, MR and AR; data curation, DL-M, VY-Y, LF, JK, and AR; writing—original draft preparation, AR; writing—review and editing, KG, DL-M, VY-Y, TE-A, YX, SR, JS, TC, LF, MR and AR; visualization, KG, DL-M, VY-Y, TE-A, YX, LF, JK, SR and AR; supervision, AR; project administration, MR and AR; funding acquisition, AR All authors have read and agreed to the published version of the manuscript.

FUNDING

This research was funded by IDeA NIH NIGMS P20GM103640-08, NSF IOS Neural Systems Cluster 1448393, and University of Oklahoma start-up funds to AR; NIH R21NS109896 to YX; NIH R01NS053422 to TC; University of CA at Davis start-up funds to VY-Y; postdoctoral support through IDeA NIH NIGMS P20GM103640-08 to KG, HB, and JK.

ACKNOWLEDGMENTS

Thanks to Alyse Heaston for assistance collecting scorpions and extracting venom; to Bret Blum, Mark Heitlinger and the Santa Rita Experimental Station, University of Arizona for permission to collect specimens of *C. sculpturatus*; and to Ann West, Christina Bourne, Robert Cichewicz, and members of the University of Oklahoma Center for Structural Biology for suggestions related to project methodology.

SUPPLEMENTARY MATERIAL

The Supplementary Material for this article can be found online at: https://www.frontiersin.org/articles/10.3389/fphar.2022.846992/full#supplementary-material

REFERENCES

Ahern, C. A., Payandeh, J., Bosmans, F., and Chanda, B. (2016). The Hitchhiker's Guide to the Voltage-Gated Sodium Channel Galaxy. *J. Gen. Physiol.* 147, 1–24. doi:10.1085/jgp.201511492

Alford, R. F., Leaver-Fay, A., Jeliazkov, J. R., O'Meara, M. J., DiMaio, F. P., Park, H., et al. (2017). The Rosetta All-Atom Energy Function for Macromolecular Modeling and Design. *J. Chem. Theor. Comput* 13, 3031–3048. doi:10.1021/acs.jctc.7b00125

Armstrong, C. M. (2006). Na Channel Inactivation from Open and Closed States. *Proc. Natl. Acad. Sci. U S A.* 103, 17991–17996. doi:10.1073/pnas.0607603103

Baek, M., DiMaio, F., Anishchenko, I., Dauparas, J., Ovchinnikov, S., Lee, G. R., et al. (2021). Accurate Prediction of Protein Structures and Interactions Using a Three-Track Neural Network. *Science* 373 (6557), 871–876. doi:10.1126/science.abj8754

Barbosa, C., and Cummins, T. R. (2016). "Unusual Voltage-Gated Sodium Currents as Targets for Pain," in *Current Topics in Membranes*. Editors J. F. Robert and N. S. Yu (Cambridge, Massachusetts, United States: Academic Press), Vol. 78, 599–638. doi:10.1016/bs.ctm.2015.12.005

Basbaum, A. I., Bautista, D. M., Scherrer, G., and Julius, D. (2009). Cellular and Molecular Mechanisms of Pain. *Cell* 139, 267–284. doi:10.1016/j.cell.2009.09.028

Blair, N. T., and Bean, B. P. (2003). Role of Tetrodotoxin-Resistant Na+ Current Slow Inactivation in Adaptation of Action Potential Firing in Small-Diameter Dorsal Root Ganglion Neurons. *J. Neurosci.* 23, 10338–10350. doi:10.1523/jneurosci.23-32-10338.2003

Blair, N. T., and Bean, B. P. (2002). Roles of Tetrodotoxin (TTX)-Sensitive Na+ Current, TTX-Resistant Na+ Current, and Ca2+ Current in the Action Potentials of Nociceptive Sensory Neurons. *J. Neurosci.* 22, 10277–10290. doi:10.1523/jneurosci.22-23-10277.2002

Bosmans, F., and Swartz, K. J. (2010). Targeting Voltage Sensors in Sodium Channels with Spider Toxins. *Trends Pharmacol. Sci.* 31, 175–182. doi:10.1016/j.tips.2009.12.007

Bosmans, F., and Tytgat, J. (2007). Voltage-gated Sodium Channel Modulation by Scorpion Alpha-Toxins. *Toxicon* 49, 142–158. doi:10.1016/j.toxicon.2006.09.023

Boyer, L. V., Theodorou, A. A., Berg, R. A., Mallie, J., Chávez-Méndez, A., García-Ubbelohde, W., et al. (2009). Antivenom for Critically Ill Children with Neurotoxicity from Scorpion Stings. *N. Engl. J. Med.* 360, 2090–2098. doi:10.1056/NEJMoa0808455

Campos, F. V., Chanda, B., Beirão, P. S., and Bezanilla, F. (2008). Alpha-scorpion Toxin Impairs a Conformational Change that Leads to Fast Inactivation of Muscle Sodium Channels. *J. Gen. Physiol.* 132, 251–263. doi:10.1085/jgp.200809995

Carcamo-Noriega, E. N., Olamendi-Portugal, T., Restano-Cassulini, R., Rowe, A., Uribe-Romero, S. J., Becerril, B., et al. (2018). Intraspecific Variation of Centruroides Sculpturatus Scorpion Venom from Two Regions of Arizona. *Arch. Biochem. Biophys.* 638, 52–57. doi:10.1016/j.abb.2017.12.012

Catterall, W. A. (1992). Cellular and Molecular Biology of Voltage-Gated Sodium Channels. *Physiol. Rev.* 72, S15–S48. doi:10.1152/physrev.1992.72.suppl_4.S15

Catterall, W. A., Cestèle, S., Yarov-Yarovoy, V., Yu, F. H., Konoki, K., and Scheuer, T. (2007). Voltage-gated Ion Channels and Gating Modifier Toxins. *Toxicon* 49, 124–141. doi:10.1016/j.toxicon.2006.09.022

Catterall, W. A. (2000). From Ionic Currents to Molecular Mechanisms: the Structure and Function of Voltage-Gated Sodium Channels. *Neuron* 26, 13–25. doi:10.1016/s0896-6273(00)81133-2

Catterall, W. A., Goldin, A. L., and Waxman, S. G. (2005). International Union of Pharmacology. XLVII. Nomenclature and Structure-Function Relationships of Voltage-Gated Sodium Channels. *Pharmacol. Rev.* 57, 397–409. doi:10.1124/pr.57.4.4

Catterall, W. A. (1980). Neurotoxins that Act on Voltage-Sensitive Sodium Channels in Excitable Membranes. *Annu. Rev. Pharmacol. Toxicol.* 20, 15–43. doi:10.1146/annurev.pa.20.040180.000311

Catterall, W. A. (2014). Structure and Function of Voltage-Gated Sodium Channels at Atomic Resolution. *Exp. Physiol.* 99, 35–51. doi:10.1113/expphysiol.2013.071969

Cavanaugh, D. J., Lee, H., Lo, L., Shields, S. D., Zylka, M. J., Basbaum, A. I., et al. (2009). Distinct Subsets of Unmyelinated Primary Sensory Fibers Mediate Behavioral Responses to Noxious thermal and Mechanical Stimuli. *Proc. Natl. Acad. Sci. U S A.* 106, 9075–9080. doi:10.1073/pnas.0901507106

Cestèle, S., and Catterall, W. A. (2000). Molecular Mechanisms of Neurotoxin Action on Voltage-Gated Sodium Channels. *Biochimie* 82, 883–892. doi:10.1016/s0300-9084(00)01174-3

Cestèle, S., Qu, Y., Rogers, J. C., Rochat, H., Scheuer, T., and Catterall, W. A. (1998). Voltage Sensor-Trapping: Enhanced Activation of Sodium Channels by Beta-Scorpion Toxin Bound to the S3-S4 Loop in Domain II. *Neuron* 21, 919–931. doi:10.1016/s0896-6273(00)80606-6

Chatterjee, S., Vyas, R., Chalamalasetti, S. V., Sahu, I. D., Clatot, J., Wan, X., et al. (2018). The Voltage-Gated Sodium Channel Pore Exhibits Conformational Flexibility during Slow Inactivation. *J. Gen. Physiol.* 150, 1333–1347. doi:10.1085/jgp.201812118

Clairfeuille, T., Cloake, A., Infield, D. T., Llongueras, J. P., Arthur, C. P., Li, Z. R., et al. (2019). Structural Basis of α-scorpion Toxin Action on Nav Channels. *Science* 363, eaav8573. doi:10.1126/science.aav8573

Conway, P., Tyka, M. D., DiMaio, F., Konerding, D. E., and Baker, D. (2014). Relaxation of Backbone Bond Geometry Improves Protein Energy Landscape Modeling. *Protein Sci.* 23, 47–55. doi:10.1002/pro.2389

Corona, M., Valdez-Cruz, N. A., Merino, E., Zurita, M., and Possani, L. D. (2001). Genes and Peptides from the Scorpion Centruroides Sculpturatus Ewing, that Recognize Na(+)-Channels. *Toxicon* 39, 1893–1898. doi:10.1016/s0041-0101(01)00174-x

Couraud, F., and Jover, E. (1984). "Mechanism of Action of Scorpion Toxins," in *Handbook of Natural Toxins*. Editor A. T. Tu (New York City, NY, USANew York, N.Y.: Marcel Dekker), 2, 659–678.

Cummins, T. R., Sheets, P. L., and Waxman, S. G. (2007). The Roles of Sodium Channels in Nociception: Implications for Mechanisms of Pain. *Pain* 131, 243–257. doi:10.1016/j.pain.2007.07.026

Cummins, T. R., and Waxman, S. G. (1997). Downregulation of Tetrodotoxin-Resistant Sodium Currents and Upregulation of a Rapidly Repriming Tetrodotoxin-Sensitive Sodium Current in Small Spinal Sensory Neurons after Nerve Injury. *J. Neurosci.* 17, 3503–3514. doi:10.1523/jneurosci.17-10-03503.1997

Curry, S. C., Vance, M. V., Ryan, P. J., Kunkel, D. B., and Northey, W. T. (1983). Envenomation by the Scorpion Centruroides Sculpturatus. *J. Toxicol. Clin. Toxicol.* 21, 417–449. doi:10.3109/15563658308990433

Deuis, J. R., Ragnarsson, L., Robinson, S. D., Dekan, Z., Chan, L., Jin, A. H., et al. (2021). The Tarantula Venom Peptide Eo1a Binds to the Domain II S3-S4 Extracellular Loop of Voltage-Gated Sodium Channel NaV1.8 to Enhance Activation. *Front. Pharmacol.* 12, 789570. doi:10.3389/fphar.2021.789570

Dib-Hajj, S. D., Cummins, T. R., Black, J. A., and Waxman, S. G. (2010). Sodium Channels in normal and Pathological Pain. *Annu. Rev. Neurosci.* 33, 325–347. doi:10.1146/annurev-neuro-060909-153234

Finol-Urdaneta, R. K., Ziegman, R., Dekan, Z., McArthur, J. R., Heitmann, S., Luna-Ramirez, K., et al. (2022). Multitarget Nociceptor Sensitization by a Promiscuous Peptide from the Venom of the King Baboon Spider. *Proc. Natl. Acad. Sci. U S A.* 119, e2110932119. doi:10.1073/pnas.2110932119

Gawali, V. S., and Todt, H. (2016). "Mechanism of Inactivation in Voltage-Gated Na+ Channels," in *Current Topics in Membranes*. Editors J. F. Robert and N. Sergei Yu (Cambridge, Massachusetts, United States: Academic Press), Vol. 78, 409–450. doi:10.1016/bs.ctm.2016.07.004

Ghovanloo, M.-R., Aimar, K., Ghadiry-Tavi, R., Yu, A., and Ruben, P. C. (2016). "Physiology and Pathophysiology of Sodium Channel Inactivation," in *Current Topics in Membranes*. Editors J. F. Robert and N. Sergei Yu (Cambridge, Massachusetts, United States: Academic Press), Vol. 78, 479–509. doi:10.1016/bs.ctm.2016.04.001

Gilchrist, J., and Bosmans, F. (2018). Using Voltage-Sensor Toxins and Their Molecular Targets to Investigate NaV 1.8 Gating. *J. Physiol.* 596, 1863–1872. doi:10.1113/JP275102

Goddard, T. D., Huang, C. C., Meng, E. C., Pettersen, E. F., Couch, G. S., Morris, J. H., et al. (2018). UCSF ChimeraX: Meeting Modern Challenges in Visualization and Analysis. *Protein Sci.* 27, 14–25. doi:10.1002/pro.3235

Jaimovich, E., Ildefonse, M., Barhanin, J., Rougier, O., and Lazdunski, M. (1982). Centruroides Toxin, a Selective Blocker of Surface Na+ Channels in Skeletal Muscle: Voltage-Clamp Analysis and Biochemical Characterization of the Receptor. *Proc. Natl. Acad. Sci. U. S. A.* 79, 3896–3900. doi:10.1073/pnas.79.12.3896

Jiang, D., Tonggu, L., Gamal El-Din, T. M., Banh, R., Pomes, R., Zheng, N., et al. (2021). Structural Basis for Voltage-Sensor Trapping of the Cardiac Sodium Channel by a Deathstalker Scorpion Toxin. *Nat. Commun.* 12, 128. doi:10.1038/s41467-020-20078-3

Jumper, J., Evans, R., Pritzel, A., Green, T., Figurnov, M., Ronneberger, O., et al. (2021). Highly Accurate Protein Structure Prediction with AlphaFold. *Nature* 596, 583–589. doi:10.1038/s41586-021-03819-2

Le Pichon, C. E., and Chesler, A. T. (2014). The Functional and Anatomical Dissection of Somatosensory Subpopulations Using Mouse Genetics. *Front. Neuroanat.* 8, 21–18. doi:10.3389/fnana.2014.00021

Mantegazza, M., and Cestèle, S. (2005). Beta-scorpion Toxin Effects Suggest Electrostatic Interactions in Domain II of Voltage-dependent Sodium Channels. *J. Physiol.* 568, 13–30. doi:10.1113/jphysiol.2005.093484

Marze, N. A., Roy Burman, S. S., Sheffler, W., and Gray, J. J. (2018). Efficient Flexible Backbone Protein-Protein Docking for Challenging Targets. *Bioinformatics* 34, 3461–3469. doi:10.1093/bioinformatics/bty355

Mirdita, M., Ovchinnikov, S., and Steinegger, M. (2021). ColabFold - Making Protein Folding Accessible to All. *bioRxiv*. doi:10.1101/2021.08.15.456425

Mohamed Abd El-Aziz, T., Xiao, Y., Kline, J., Gridley, H., Heaston, A., Linse, K. D., et al. (2021). Identification and Characterization of Novel Proteins from Arizona Bark Scorpion Venom that Inhibit Nav1.8, a Voltage-Gated Sodium Channel Regulator of Pain Signaling. *Toxins* 13, 501. doi:10.3390/toxins13070501

Nguyen, P. T., and Yarov-Yarovoy, V. (2022). Towards Structure-Guided Development of Pain Therapeutics Targeting Voltage-Gated Sodium Channels. *Front. Pharmacol.* 13, 842032. doi:10.3389/fphar.2022.842032

Niermann, C. N., Tate, T. G., Suto, A. L., Barajas, R., White, H. A., Guswiler, O. D., et al. (2020). Defensive Venoms: Is Pain Sufficient for Predator Deterrence? *Toxins (Basel)* 12, 260. doi:10.3390/toxins12040260

Osteen, J. D., Sampson, K., Iyer, V., Julius, D., and Bosmans, F. (2017). Pharmacology of the Nav1.1 Domain IV Voltage Sensor Reveals Coupling between Inactivation Gating Processes. *Proc. Natl. Acad. Sci. U S A.* 114, 6836–6841. doi:10.1073/pnas.1621263114

Peirs, C., and Seal, R. P. (2016). Neural Circuits for Pain: Recent Advances and Current Views. *Science* 354, 578–584. doi:10.1126/science.aaf8933

Possani, L. D., Becerril, B., Delepierre, M., and Tytgat, J. (1999). Scorpion Toxins Specific for Na+-Channels. *Eur. J. Biochem.* 264, 287–300. doi:10.1046/j.1432-1327.1999.00625.x

Possani, L. D., Merino, E., Corona, M., Bolivar, F., and Becerril, B. (2000). Peptides and Genes Coding for Scorpion Toxins that Affect Ion-Channels. *Biochimie* 82, 861–868. doi:10.1016/s0300-9084(00)01167-6

Qu, S. Y., Rogers, J. C., Rochat, H., Scheuer, T., and Catterall, W. A. (1998). Voltage Sensor-Trapping. *Neuron* 21, 919–931. doi:10.1016/s0896-6273(00)80606-6

Renganathan, M., Cummins, T. R., and Waxman, S. G. (2001). Contribution of Na(v)1.8 Sodium Channels to Action Potential Electrogenesis in DRG Neurons. *J. Neurophysiol.* 86, 629–640. doi:10.1152/jn.2001.86.2.629

Rodríguez de la Vega, R. C., and Possani, L. D. (2004). Current Views on Scorpion Toxins Specific for K+-channels. *Toxicon* 43, 865–875. doi:10.1016/j.toxicon.2004.03.022

Rodríguez de la Vega, R. C., and Possani, L. D. (2005). Overview of Scorpion Toxins Specific for Na+ Channels and Related Peptides: Biodiversity, Structure-Function Relationships and Evolution. *Toxicon* 46, 831–844. doi:10.1016/j.toxicon.2005.09.006

Rowe, A. H., and Rowe, M. P. (2008). Physiological Resistance of Grasshopper Mice (Onychomys spp.) to Arizona Bark Scorpion (Centruroides Exilicauda) Venom. *Toxicon* 52, 597–605. doi:10.1016/j.toxicon.2008.07.004

Rowe, A. H., Xiao, Y., Rowe, M. P., Cummins, T. R., and Zakon, H. H. (2013). Voltage-gated Sodium Channel in Grasshopper Mice Defends against Bark Scorpion Toxin. *Science* 342, 441–446. doi:10.1126/science.1236451

Rowe, A. H., Xiao, Y., Scales, J., Linse, K. D., Rowe, M. P., Cummins, T. R., et al. (2011). Isolation and Characterization of CvIV4: a Pain Inducing α-scorpion Toxin. *PLoS One* 6, e23520. doi:10.1371/journal.pone.0023520

Rowe, A. H., and Rowe, M. P. (2006). Risk Assessment by Grasshopper Mice (Onychomys spp.) Feeding on Neurotoxic Prey (Centruroides spp.). *Anim. Behav.* 71, 725–734. doi:10.1016/j.anbehav.2005.08.003

Roy, A. A., Dhawanjewar, A. S., Sharma, P., Singh, G., and Madhusudhan, M. S. (2019). Protein Interaction Z Score Assessment (PIZSA): an Empirical Scoring Scheme for Evaluation of Protein-Protein Interactions. *Nucleic Acids Res.* 47, W331–W337. doi:10.1093/nar/gkz368

Silva, J. (2014). Slow Inactivation of Na(+) Channels. *Handb Exp. Pharmacol.* 221, 33–49. doi:10.1007/978-3-642-41588-3_3

Simard, J. M., Meves, H., and Watt, D. D. (1992). "Toxicolgy, Chemistry and Safety," in *Natural Toxins*. Editors R. F. Keeler, N. B. Mandava, and A. T. Tu (Fort Collins, CO: Alaken, Inc.), 1, 236–263.

Sokolov, S., Scheuer, T., and Catterall, W. A. (2008). Depolarization-activated Gating Pore Current Conducted by Mutant Sodium Channels in Potassium-Sensitive Normokalemic Periodic Paralysis. *Proc. Natl. Acad. Sci. U S A.* 105, 19980–19985. doi:10.1073/pnas.0810562105

Ulbricht, W. (2005). Sodium Channel Inactivation: Molecular Determinants and Modulation. *Physiol. Rev.* 85, 1271–1301. doi:10.1152/physrev.00024.2004

Vandendriessche, T., Olamendi-Portugal, T., Zamudio, F. Z., Possani, L. D., and Tytgat, J. (2010). Isolation and Characterization of Two Novel Scorpion Toxins: The Alpha-toxin-like CeII8, Specific for Na(v)1.7 Channels and the Classical Anti-mammalian CeII9, Specific for Na(v)1.4 Channels. *Toxicon* 56, 613–623. doi:10.1016/j.toxicon.2010.06.008

Vilin, Y. Y., and Ruben, P. C. (2001). Slow Inactivation in Voltage-Gated Sodium Channels: Molecular Substrates and Contributions to Channelopathies. *Cell Biochem Biophys* 35, 171–190. doi:10.1385/CBB:35:2:171

Xiao, Y., Blumenthal, K., and Cummins, T. R. (2014). Gating-Pore Currents Demonstrate Selective and Specific Modulation of Individual Sodium Channel Voltage-Sensors by Biological Toxins. *Mol. Pharmacol.* 86, 159–167. doi:10.1124/mol.114.092338

Ye, P., Jiao, Y., Li, Z., Hua, L., Fu, J., Jiang, F., et al. (2015). Scorpion Toxin BmK I Directly Activates Nav1.8 in Primary Sensory Neurons to Induce Neuronal Hyperexcitability in Rats. *Protein Cell* 6, 443–452. doi:10.1007/s13238-015-0154-4

Zhang, F., Zhang, C., Xu, X., Zhang, Y., Gong, X., Yang, Z., et al. (2019). Naja Atra Venom Peptide Reduces Pain by Selectively Blocking the Voltage-Gated Sodium Channel Nav1.8. *J. Biol. Chem.* 294, 7324–7334. doi:10.1074/jbc.RA118.007370

Zhang, H. B., and Bean, B. P. (2021). Cannabidiol Inhibition of Murine Primary Nociceptors: Tight Binding to Slow Inactivated States of Nav1.8 Channels. *J. Neurosci.* 41, 6371–6387. doi:10.1523/JNEUROSCI.3216-20.2021

Zhang, J. Z., Yarov-Yarovoy, V., Scheuer, T., Karbat, I., Cohen, L., Gordon, D., et al. (2012). Mapping the Interaction Site for a β-Scorpion Toxin in the Pore Module of Domain III of Voltage-Gated Na+ Channels. *J. Biol. Chem.* 287, 30719–30728. doi:10.1074/jbc.m112.370742

Zhang, J. Z., Yarov-Yarovoy, V., Scheuer, T., Karbat, I., Cohen, L., Gordon, D., et al. (2011). Structure-Function Map of the Receptor Site for β-Scorpion Toxins in Domain II of Voltage-Gated Sodium Channels. *J. Biol. Chem.* 286, 33641–33651. doi:10.1074/jbc.m111.282509

Conflict of Interest: TE-A was employed by Amsaal Venom Farm after data was collected for this project.

The remaining authors declare that the research was conducted in the absence of any commercial or financial relationships that could be construed as a potential conflict of interest.

Publisher's Note: All claims expressed in this article are solely those of the authors and do not necessarily represent those of their affiliated organizations, or those of the publisher, the editors and the reviewers. Any product that may be evaluated in this article, or claim that may be made by its manufacturer, is not guaranteed or endorsed by the publisher.

Advantages of publishing in Frontiers

OPEN ACCESS
Articles are free to read for greatest visibility and readership

FAST PUBLICATION
Around 90 days from submission to decision

HIGH QUALITY PEER-REVIEW
Rigorous, collaborative, and constructive peer-review

TRANSPARENT PEER-REVIEW
Editors and reviewers acknowledged by name on published articles

Frontiers
Avenue du Tribunal-Fédéral 34
1005 Lausanne | Switzerland

Visit us: www.frontiersin.org
Contact us: frontiersin.org/about/contact

REPRODUCIBILITY OF RESEARCH
Support open data and methods to enhance research reproducibility

DIGITAL PUBLISHING
Articles designed for optimal readership across devices

FOLLOW US
@frontiersin

IMPACT METRICS
Advanced article metrics track visibility across digital media

EXTENSIVE PROMOTION
Marketing and promotion of impactful research

LOOP RESEARCH NETWORK
Our network increases your article's readership